

IntechOpen

# Steam Generator Systems

## Operational Reliability and Efficiency

*Edited by Valentin Uchanin*





---

# **STEAM GENERATOR SYSTEMS: OPERATIONAL RELIABILITY AND EFFICIENCY**

---

Edited by **Valentin Uchanin**

## **Steam Generator Systems: Operational Reliability and Efficiency**

<http://dx.doi.org/10.5772/622>

Edited by Valentin Uchanin

### **Contributors**

Dong-Jin Kim, Seong Sik Hwang, Man Kyo Jung, HongPyo Kim, Joung Soo Kim, Michio Murase, Takashi Nagae, Noritoshi Minami, Akio Tomiyama, Lucia Bonavigo, Mario De Salve, Luben Sabotinov, Patrick Chevrier, Sung-Woo Kim, Hong Pyo Kim, Didier Costes, Alois Hoeld, Dumitra R Lucan, Toshinobu Sasa, Hiroyuki Oigawa, Zilvinas Bazaras, Boris Timofeev, Adolfo Cobo, Jesús Ma Mirapeix, David Solana, Alfonso Álvarez-De-Miranda, José Miguel López-Higuera, Pilar-Beatriz García-Allende, Olga M<sup>a</sup> Conde, Leon Cizelj, Guy Roussel, Duck-Gun Park, Kwon-Sang Ryu, Derac Son, Jonas Bredberg, Valentin Nikolaj Uchanin, Zaki Su'ud

### **© The Editor(s) and the Author(s) 2011**

The moral rights of the and the author(s) have been asserted.

All rights to the book as a whole are reserved by INTECH. The book as a whole (compilation) cannot be reproduced, distributed or used for commercial or non-commercial purposes without INTECH's written permission.

Enquiries concerning the use of the book should be directed to INTECH rights and permissions department ([permissions@intechopen.com](mailto:permissions@intechopen.com)).

Violations are liable to prosecution under the governing Copyright Law.



Individual chapters of this publication are distributed under the terms of the Creative Commons Attribution 3.0 Unported License which permits commercial use, distribution and reproduction of the individual chapters, provided the original author(s) and source publication are appropriately acknowledged. If so indicated, certain images may not be included under the Creative Commons license. In such cases users will need to obtain permission from the license holder to reproduce the material. More details and guidelines concerning content reuse and adaptation can be found at <http://www.intechopen.com/copyright-policy.html>.

### **Notice**

Statements and opinions expressed in the chapters are those of the individual contributors and not necessarily those of the editors or publisher. No responsibility is accepted for the accuracy of information contained in the published chapters. The publisher assumes no responsibility for any damage or injury to persons or property arising out of the use of any materials, instructions, methods or ideas contained in the book.

First published in Croatia, 2011 by INTECH d.o.o.

eBook (PDF) Published by IN TECH d.o.o.

Place and year of publication of eBook (PDF): Rijeka, 2019.

IntechOpen is the global imprint of IN TECH d.o.o.

Printed in Croatia

Legal deposit, Croatia: National and University Library in Zagreb

Additional hard and PDF copies can be obtained from [orders@intechopen.com](mailto:orders@intechopen.com)

Steam Generator Systems: Operational Reliability and Efficiency

Edited by Valentin Uchanin

p. cm.

ISBN 978-953-307-303-3

eBook (PDF) ISBN 978-953-51-5987-2



# We are IntechOpen, the world's leading publisher of Open Access books Built by scientists, for scientists

4,000+

Open access books available

116,000+

International authors and editors

120M+

Downloads

151

Countries delivered to

Our authors are among the  
Top 1%

most cited scientists

12.2%

Contributors from top 500 universities



WEB OF SCIENCE™

Selection of our books indexed in the Book Citation Index  
in Web of Science™ Core Collection (BKCI)

Interested in publishing with us?  
Contact [book.department@intechopen.com](mailto:book.department@intechopen.com)

Numbers displayed above are based on latest data collected.  
For more information visit [www.intechopen.com](http://www.intechopen.com)





# Meet the editor



After graduating as an electro-physical engineer at the Lviv Technical University in 1971, Valentin Uchanin joined the Karpenko Physico-Mechanical Institute of Academy of Sciences, Lviv. Post-graduate research education in correspondent form received at the Institute of Aviation Materials (Moscow) from 1978-1982. Doctor Degree obtained from Central Technological Institute of Mechanical Engineering Technology (Moscow) in 1983 with dissertation titled "The research and development of eddy current method and means for detection and parameter estimation of flaws in aircraft materials". His interests include research and development in eddy current, electrical, magnetic nondestructive evaluation and diagnostics, such as modeling, signal analysis, probe and device design, flaw sizing, material degradation. Dr. V. Uchanin is member of the board of Ukrainian Society for Non-destructive Testing and Technical Diagnostics and the Head of Western Branch, member of editorial board of Journal "Technical Diagnostics and Nondestructive Testing (Kiev) and Editor-in-chief of collection of scientific articles "Physical Methods and Means to Media, Material and Product Testing". He is the Chairmen of Organizing Committee of the Annual International NDT Conference "LEOTEST" (1996-2011).



---

# Contents

---

## **Preface XIII**

### **Part 1 Material Degradation and Fracture Mechanisms 1**

- Chapter 1 **Degradations of Incoloy 800  
Steam Generator Tubing 3**  
Dumitra Lucan
- Chapter 2 **Analysis of Oxide on Steam Generator Tubing  
Material in High Temperature Alkaline Leaded Solution 21**  
Dong-Jin Kim, Seong Sik Hwang,  
Joung Soo Kim, Yun Soo Lim,  
Sung Woo Kim and Hong Pyo Kim
- Chapter 3 **Burst and Leak Behaviour  
of SCC Degraded SG Tubes of PWRs 41**  
Seong Sik Hwang, Man Kyo Jung,  
Hong Pyo Kim and Joung Soo Kim
- Chapter 4 **In-situ Monitoring of SCC  
of Alloy 600 SG Tubing in PWR using EN Analysis 61**  
Sung-Woo Kim, Hong-Pyo Kim,  
Seong-Sik Hwang and Dong-Jin Kim
- Chapter 5 **Effect of Long-Term Thermal Influence  
on Mechanical Properties of Welded Joints  
for Carbon Steels used in Power Engineering 75**  
Zilvinas Bazaras and Boris Timofeev
- Chapter 6 **Primary to Secondary Leakage  
at PSB-VVER Test Facility,  
Simulated by CATHARE 2 Code 99**  
Luben Sabotinov and Patrick Chevrier
- Chapter 7 **Reliability of Degraded Steam Generator Tubes 117**  
Leon Cizelj and Guy Roussel

**Part 2 Nondestructive Evaluation and Diagnostics 143**

- Chapter 8 **The Development of Eddy Current Technique for WWER Steam Generators Inspection 145**  
Valentin Uchanin and Vladimir Najda
- Chapter 9 **Detection of Magnetic Phase in the Steam Generator Tubes of NPP 165**  
Duck-Gun Park, Kwon-Sang Ryu and Derac Son
- Chapter 10 **Optical Methods for On-line Quality Assurance of Welding Processes in Nuclear Steam Generators 185**  
Adolfo Cobo, Jesús M<sup>a</sup> Mirapeix, David Solana, Alfonso Álvarez-de-Miranda, Pilar-Beatriz García-Allende, Olga M<sup>a</sup> Conde and José Miguel López-Higuera

**Part 3 Heat Transfer and Coolant Flow Processes 203**

- Chapter 11 **Countercurrent Flow in a PWR Hot Leg under Reflux Condensation 205**  
Noritoshi Minami, Michio Murase and Akio Tomiyama
- Chapter 12 **Evaluation of Non-condensable Gas Recirculation Flow in Steam Generator U-tubes during Reflux Condensation 227**  
Michio Murase, Takashi Nagae and Noritoshi Minami
- Chapter 13 **Coolant Channel Module CCM. An Universally Applicable Thermal-Hydraulic Drift-Flux Based Separate-Region Mixture-Fluid Model 247**  
Alois Hoeld
- Chapter 14 **The Thermal-hydraulic U-tube Steam Generator Model and Code UTSG-3 (Based on the Universally Applicable Coolant Channel Module CCM) 289**  
Alois Hoeld
- Chapter 15 **Computation of Flows in Steam Generators 327**  
Jonas Bredberg
- Chapter 16 **Semi Analytical Analysis of Steady State Condition of Steam Generator 353**  
Zaki Su'ud

**Part 4 Safety and Maintenance Management 369**

- Chapter 17 **Issues for Nuclear Power Plants Steam Generators 371**  
Lucia Bonavigo and Mario De Salve

- Chapter 18 **Shielding Analysis of the Secondary Coolant  
Circuit of Accelerator Driven Systems 393**  
Toshinobu Sasa and Hiroyuki Oigawa
- Chapter 19 **Starting Fast Reactors Again 413**  
Didier Costes





---

## Preface

---

Operational productivity, reliability and safety of power generating plants are strongly connected with effectiveness and behaviour of applied steam generator system. It is especially crucial for nuclear power plants with two circuit heat exchange arrangement when only few millimeters of tube wall material separate the primary and secondary circuits. Whereas the first circuit is connected with reactor core and has high level of radioactive contamination, the tube integrity preservation is very important for ecological safety. In addition, it is necessary to note that the steam generator components are exposed to permanent and simultaneous influences of high temperature, pressure, stresses and corrosion-erosion wear.

Therefore, the material degradation of steam generator components in a common sense (united different corrosion phenomena, fatigue cracking, structure changes and another fracture processes) is one of the most relevant and inseparable factor for appearance of the leakage between the primary and the secondary circuits.

Because of long-term operation and fracture inevitability the role of nondestructive evaluation based on different physical phenomena for on-time defect detection to prevent possible accidents is also very significant. At present, the eddy current method became the most applicable for steam generator tube operational inspection along the full tube length with application of different types of internal probes due to many advantages in comparison with other methods.

By optimizing of the heat transfer, cooling and flaw processes on the base of theoretical simulation and computer codes the higher level of the nuclear power plant efficiency and availability can be achieved.

This book consists of 19 chapters allocated between four parts:

- Material degradation and fracture mechanisms,
- Nondestructive evaluation and diagnostics,
- Heat transfer and coolant flow processes,
- Safety and maintenance management.

The authors from different countries all over the world (Germany, France, Italy Japan, Slovenia, Indonesia, Belgium, Romania, Lithuania, Russia, Spain, Sweden, Korea and Ukraine) prepared chapters for this book. Such a broad geography indicates the high significance of considered subjects.

The book is intended for practical engineers, researchers, students and other people dealing with the reviewed problems. We hope that the presented book will be beneficial to all readers and initiate further inquiry and development with aspiration for better future.

In the name of all authors, I want to express our gratitude to publishing process manager Ms. Ana Nikolic for patience and understanding

**Dr. Valentin Uchanin**

Karpenko Physico-Mechanical Institute of National Academy of Sciences  
Department of Structural Fracture Mechanics and Material Properties Optimization  
Lviv,  
Ukraine

# **Part 1**

## **Material Degradation and Fracture Mechanisms**



# Degradations of Incoloy 800 Steam Generator Tubing

Dumitra Lucan

*Department of Corrosion and Circuits Chemistry,  
Institute for Nuclear Research, POB 78, Pitesti  
Romania*

## 1. Introduction

In our days, the nuclear energy becomes more and more important. The efficient operation of a Nuclear Power Plant (NPP) supposes the assurance of the performances established by design for all entire life of the NPP key components. Steam Generator (SG) is one of the key components for a NPP because this equipment assures the separation boundary between the primary and secondary circuit and its unavailability suppose the NPP shutdown. The synergetic action of the high pressures and temperatures, constraints (stresses, vibrations) and the chemical parameters of the cooling agents make the steam generator susceptible for more types of degradations. Because of the unavailability of the measures for monitoring and mitigation of these degradations the performances of the steam generators decrease and determine direct and indirect losses. The replacement of the steam generator is very expensive and very difficult. For these reasons it becomes necessary the assurance of the steam generator performances for the entire life established by design, 30 years with the possibility of extension to 40 or 60 years.

The optimization of the steam generator operation, by implementation of the management complex system for the monitoring of the operation processes, periodical inspections, and preventive maintenance determine economies by order of hundreds of millions dollars, for entire life of a nuclear power plant.

In this scope it is very important to intensify of the applicative research in the purpose of establishing the newest solutions, methods, mechanisms in order to characterize the specific processes for the operation of the steam generator. The principal objective of the research consists in the establishing of the fundamental knowledge, theories, methods and models necessary for qualitative and quantitative characterization of steam generator degradation processes. The complementary research activity should be oriented towards the management of ageing and, implicitly, towards the preservation of the steam generator structural integrity.

The principal objective of the work presented in this chapter consists in the characterization of specific processes and mechanisms referring to steam generator tubing degradation.

The specific objectives are the following: the establishment of the main corrosive degradation mechanisms which contribute at steam generator tubing material (Incolloy-800) failures; knowledge of the phenomena which appear in steam generator because of the material/environment interaction; elucidation of corrosion product release, transport and

deposition mechanisms in the secondary circuit of the steam generator, which depend by physical-mechanical properties of materials and physical-chemical properties of thermal agent (temperature, pressure, pH, electrochemical potential).

All steam generator tube failures result in the transfer of the radioactive materials from the primary coolant circuit to the steam generator secondary circuit, and necessitate downtime to locate and plug failed tubes. For the particular case of the CANDU plants, any steam generator tube failure results in an additional economic penalty through the loss of heavy water. Nearly all the failures were attributed to secondary side water chemistry conditions and excursions, many of which resulted from condenser cooling water ingress.

The investigation of the structural materials corrosion in correlation with the water chemistry, as well as the impurities and corrosion products concentration and deposition and their removing from the CANDU steam generators is a very active field and both the experimental works and the understanding of the mechanisms involved are submitted to some rapid changes and permanently open to the research. To provide information about the corrosion behaviour of the structural materials from CANDU steam generators under normal and abnormal conditions of operation and to identify the failure types produced by corrosion were performed a lot of corrosion experiments. These experiments consisted in chemical accelerated tests, static autoclaving and electrochemical investigations.

The goal of this work consists in the assessment of corrosion behaviour of the tubes material, Incoloy-800, at normal secondary circuit parameters ((temperature - 260°C, pressure - 5.1MPa). The testing environment was the demineralised water without impurities, at different pH values regulated with morpholine and cyclohexylamine (all volatile treatment - AVT).

The results are presented like micrographics and graphics representing weight loss of metal due to corrosion, corrosion rate, total corrosion products formed, the adherent corrosion products, released corrosion products, release rate of corrosion products and release rate of the metal.

This work contributes to the establishing of causes that produced components degradation, the knowledge of mechanisms degradation, evaluation of corrosion evolution in time by extrapolation of obtained results and estimation of remaining safe operation life for the nuclear power plant key-components.

The knowledge of corrosion behavior of structural materials of equipments from nuclear power plants gives the possibility to effectuate of some correct diagnosis and following of necessary measures to prevent and diminish the ageing process of which the evolution supposes some considerable economic costs.

## **2. Types of corrosion specific to the steam generator**

The maintenance operations in a Nuclear Power Plant are particularly complex and difficult due to its specific nature. It is, therefore, necessary that by an appropriate design and a proper choice of construction materials assisted by a correct operation, long operation periods be ensured, (IAEA, 1997).

The important steps of a maintenance program for NPP related facilities are the disassembling and the inspection of components in order to:

1. detect of the problems that occurred after the last inspection, including:
  - a. the determination of their causes;
  - b. the notification of the supplier if a material defect is involved;

2. correct the actions proposal considering the estimated period that the component is still able to operate, implying either the elimination of the main defect causes or the re-design of the part.
3. implement corrective measures by:
  - a. the cleaning operations;
  - b. the repairs;
  - c. the replacement of the defective component, if possible by an upgraded one, if this exists.

Maintenance should be done periodically, according to a pre-established plan. In this way, besides repairing the known defects, others can be identified, as well as their causes and the corrective actions required. Maintenance is especially difficult at nuclear facilities due to the presence of radiation fields and to the complexity of the facilities.

The SG tubing degradation caused by corrosion and other age-related mechanisms continues to be a significant safety and cost concern for many SGs. The understanding SG degradation mechanisms is the key to effective management of SG ageing and consists in the knowledge of SG materials and these one properties, stressors and operating conditions, like degradation sites and wear mechanisms.

The Steam Generators, equipments that ensure the connection between the primary and the secondary circuits, create several safety problems during operation, mainly due to corrosion and mechanical damages. Maintenance is also difficult in the SG because of the limited access to various components and because of the presence of the high radiation field existing on the side of the primary circuit.

For manufacturing the SG, several types of steels are used, whose coexistence in the environmental conditions of the steam generator arises special problems with respect to corrosion.

Corrosion and the mechanical damage in the SG are the result of complex interaction between various factors:

- strict control of water chemistry;
- adequate thermo-hydraulic design;
- selection of generator construction materials;
- utilisation of compatible materials for the entire secondary circuit;
- conditions of achieving equipments and facilities;
- the operation technique.

This is why a careful analysis of corrosion problems is required, necessary both from an economic point of view and for the safe operation.

#### ***Materials and environment conditions specific to the steam generator***

The most important element in selecting the SG construction materials is their resistance to corrosion in special operation conditions.

The main operation parameters of the SG are:

D <sub>2</sub> O	H <sub>2</sub> O
t <sub>in</sub> = 309°C	t <sub>in</sub> = 187.2°C
t <sub>ou</sub> = 290°C	t <sub>ou</sub> = 260°C
P <sub>in</sub> = 9.887 MPa	P <sub>in</sub> = 6.700 MPa
P <sub>ou</sub> = 9.625 MPa	P <sub>ou</sub> = 4.695 MPa

Incoloy-800 is utilised for tubes having in view the following reasons:

- presents good resistance to stress corrosion cracking, as compared to Inconel-600;
- releases a much smaller amount of radioactive products in the primary circuit;
- has a high resistance to cracking corrosion in alkaline environment (20% higher than Inconel-600).

The SG includes the following types of steels: Incoloy-800 (tubes), Inconel-600 (tubesheet cladding), stainless steel SA 240-410S (intermediate supports), carbon steel SA 516-gr. 70 (shells), carbon steel SA 508 cl.2 (tubesheet).

The chemical control of water is done by maintaining of the parameters between certain limits that influence the corrosion behaviour of SG materials: the amount and composition of corrosion products, impurities (especially dissolved salts) and oxidation agents.

Although the corrosion products are not directly responsible for corrosion, they are the main cause of the accumulation and concentration of aggressive species that can lead to a variety of corrosion forms. The corrosion products will be carried from the SG in the entire system, determining the occurrence of corrosion-related inconveniences, even and in areas where apparently this would not be possible. The main source of penetration of oxygen and impurities is coolant leakage from the condenser. The impurities concentration is responsible for the initiation, propagation and acceleration of corrosion processes of the SG tubing. This is why it is compulsory a careful control of water chemistry, of reactants addition and of the cleaning degree after maintenance or repairs.

Degradations due to corrosion can be divided into two large groups: degradations that end up in cracking and those which do not imply cracking. Corrosive degradations produced in the absence of a significant stress (applied, residual or due to corrosion products deposition) will not end up in cracking, except for certain cases such as intergranular corrosion.

Corrosion that does not imply cracking can appear under the following three specific forms:

1. generalised corrosion;
2. localised corrosion (pitting of Incoloy-800 tubes);
3. crevice corrosion.

The corrosion cracking degradations are favoured by the following conditions:

- a. stress corrosion cracking (SCC) under constant stress in the thermally affected area close to welds.
- b. SCC under monotonous increasing stress, during denting occurrence in the SG.
- c. fatigue (wear) corrosion of Incoloy-800 tubes under cyclic stress.

### **Generalised corrosion**

Many research workers have demonstrated that stainless steels and nickel-rich alloys present in the SG undertake a generalized corrosion; their corrosion rates vary in time approximately parabolically.

The corrosion products release rates decrease in time, following various kinetics.

Generalized corrosion prevails in the case of carbon steels.

Since most of the studies were performed in static autoclaves, particular care is required if one desires the extrapolation of results for typical conditions in nuclear facilities, where the influence of the thermal transfer and of coolant circulation is added, due to thermo-hydraulic parameters.

The corrosion mechanism of these materials consists in the formation of two overlapped layers of compounds, the outer one being crystalline. Based on this model, Lesurf assumed that the total rate of the film formation is controlled by the migration rate of iron species



soluble in water through the pores of the oxide layer: part of the oxidized iron is included in the magnetite formed in the area of contact with the metallic under-layer (forming thus the inner film), while the remaining is carried into the solution, at the outer edge of the oxide layer where it can precipitate, forming the crystalline outer film, or its release can occur in the solution mass, precipitating at random.

The corrosion products entailed in the working fluid will deposit in the restricted circulation regions, thus contributing to the initiation of corrosion in those areas.

### **Localized corrosion**

Localized corrosion supposes the fast local dissolving on a significant depth and it can induce destruction of the base material.

Localized corrosion is an extremely dangerous phenomenon, since it usually takes place in less aggressive environments - where generalized corrosion is negligible - and it is quite difficult to be detected, due to its location and very small dimensions.

### **Denting corrosion**

If the cooling water was phosphate-treated and then treated with volatile amines (AVT) one noticed the occurrence of a corrosive attack called denting. This means the deformation of Incoloy-800 tubing due to the increase in volume of corrosion products formed between the intermediary carbon steel support plate and the Incoloy-800 tube.

Around each Incoloy-800 tube that penetrates the intermediary support plate there is a gap of a few tenths of a millimetre. Within this space an accelerated corrosion of carbon steel was noticed, resulting in magnetite. Magnetite accumulates in time and exerts a compression force on the tube; this one can distort, leading to a local stiction in the tube, called dent.

This denting corrosion can also lead to the blocking of the sondes used in eddy-current examinations of the tubular bundle.

Consequently, denting is a form of corrosion in the crevice between the tube and the support plate, where an initial concentration of acid species (chlorides, sulphates) takes place.

The oxygen, copper and nickel ions act as accelerators of denting. The occurrence of this event can be avoided by choosing appropriate construction solutions for the intermediate supports, utilization of stainless steel for these supports, treatment, from the very beginning, with volatile amines and removal of copper from the composition of the secondary circuit equipments.

### **Corrosion under the impurities layer (wastage)**

Another type of corrosion likely to occur when treating water with phosphates is the "wastage" corrosion. This one takes place under the deposits on the tube surface, in the areas where wet and dry periods alternate.

It is known that during SG operation a sludge accumulates on the tubesheet, reaching a height of 30 cm or more. As the sludge content increases, the coolant cannot reach the surface in order to replace the evaporated liquid. The temperature in this region becomes equal to that of the coolant. The area where the strongest corrosion is encountered is the interface, where wetting and drying alternate, which determines the thinning of the Incoloy-800 tubes.

Using adequate constructive solutions can diminish the phenomenon.

### **Pitting corrosion**

Pitting corrosion can appear both on the Incoloy-800 tubing and on the tubesheet. Thus, pits with a depth of 0.02-0.05 mm have been observed on the Incoloy-800 tubes in the crevices where denting occurred, determined by a high concentration of chlorides. Pitting was also observed on the tubesheet, especially under the sludge.

### **Stress corrosion cracking (SCC)**

This type of corrosion was more frequently identified on the U-shaped upper region of Incoloy-800 tubes, but cracks have been noticed in other areas, too.

The crack that appeared in the U-bend region has been generally initiated from the inside of the tube. The examination of such tubes shows that these cracks initiated on the side of the primary agent are of intergranular nature, oriented along the longitudinal axis of the tubes. The factors involved in the cracking of the U-bend region are:

- microstructural factors, features referring to material strength and hardness;
- residual or latent stresses that emerge during fabrication, bending and installation;
- shape of the tube, bending radius resulting from processing;
- the extent and frequency of cycling, shape of strains induced during SG operation;
- environment chemistry or environment factors.

The inspection of cracks on the unbended side of damaged tubes revealed that SCC appeared in points where denting progressed to such extent so that the tubes became ovalized or wave-shaped, instead of circular. Cracks occurrence was noticed in places where the highest strain was applied; they were initiated either on the inner or on the outer surface. A third type of SCC initiated by granular attack from the interior is in the transfer region from the expanded area to the non-expanded one - at the joint with the tubesheet - where high strains affect the tube walls.

### **Mechanical degradations of the SG tubing**

Mechanical degradations that may alter SG tubing can be divided into: vibrations wear (fretting) and fatigue wear.

These degradations belong to the category of localized attack.

The strength that determines them is produced by tubes vibration, induced by flow circulation.

This time, corrosion appears as an additional factor that accelerates mechanical degradation of the tubes; it acts synergistically. The effect of the synergetic action of the two factors varies from the erosion of passive films on the materials surface to the accelerating effects of certain aggressive environments on the quality of the metal.

Due to vibrations in the region of contact tube - tubesheet, the tube can notably reduce its thickness, sometimes displaying cracks. Vibrations are also responsible for the excessive degradation of anti-vibration bars used in some SG: their replacement is prescribed. In the case of cracks initiated on defects (for example in regions where local thinning of tubing walls took place) a transgranular attack was identified on the tubes outer surface. The mechanism of these cracks includes the fatigue fretting corrosion in the presence of corrosive species in the environment, (Lucan, D. 2006; Lucan, D. et al., 2007; Lucan, D. et al., 2008).

Fig. 1. is a schematic layout of corrosive attacks specific to Steam Generators.

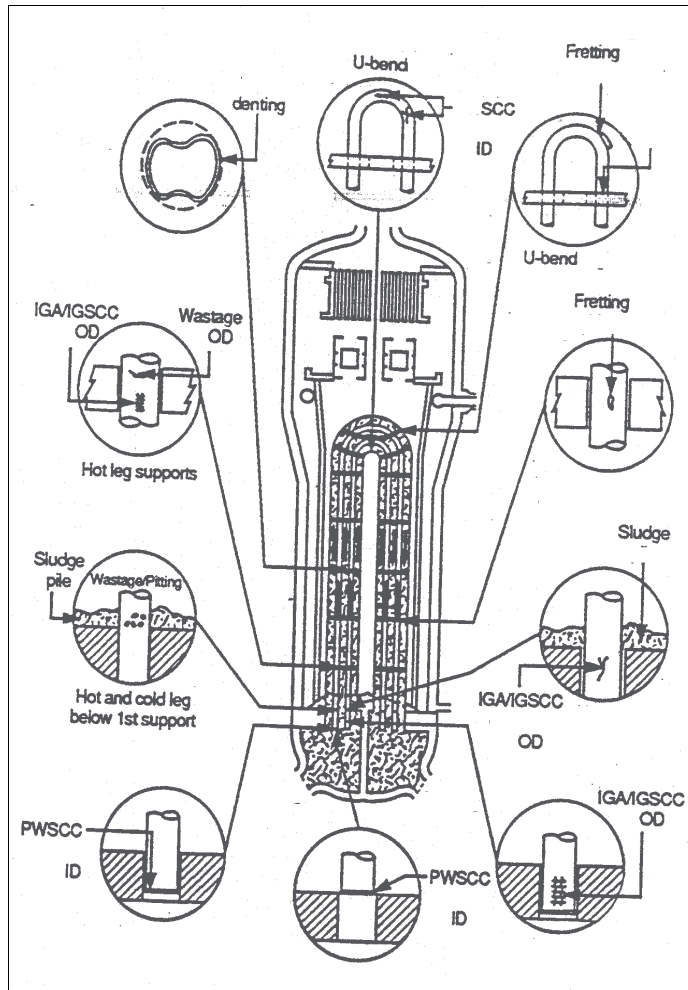


Fig. 1. Types of corrosion specific to the steam generator, (IAEA, 1997)

### 3. Experimental

The generalized corrosion is an undesirable process because it is accompanied by deposition of the corrosion products which affect the steam generator performances. It is very important to understand the corrosion mechanism with the purpose of evaluating the quantities of corrosion products which exist in the steam generator after a determined period of operation, (IAEA, 1997).

The nickel-based alloys (Incoloy-800) are currently used as corrosion resistant materials in the nuclear industry because their corrosion rates are quite low. This behavior is attributable to the protective character of the oxide film formed on their surface when the contact with the pressurized high-temperature water environment is realized. Nevertheless, oxidation processes or deposition of corrosion products can promote the development of particular corrosion problems. These phenomena result from changes in the structure of the oxide films throughout the cooling circuit, (Iglesias & Calderon, 2003).

Corrosion experiments included in the present work have been carried out on the Incoloy-800 samples by autoclaving in static autoclaves at parameters specific for the secondary circuit of the CANDU steam generator: temperature 260°C, pressure 5.1MPa. The specimens used were from Incoloy-800, steam generator tube, (15.9mm outside diameter and 1.13mm wall thickness) which was sectioned on the diameter into 15 mm long pieces polished with grit papers and cleaned ultrasonically. The testing environments utilized were demineralised water with pH = 7.5, 8.5 and 9.5 (AVT). The testing periods were 240h, 2050h and 3550h. Demineralised water had a dissolved oxygen content was below 2ppm (oxygen was released by thermal degassing at 100°C). The water pH and conductivity were measured with Multi - Channel Analyser CONSORT C835. Experimental work included: gravimetric analyses, optical microscopically analyses and electrochemical measurements (potentiodynamic polarization). The weight modifications due to oxidation or corrosion products removal by different methods were measured using a Shimadzu AUW 220 analytically balance providing a precision of  $\pm 0.01$  mg. The surfaces morphologies and the cross sections of the corrosion samples were analyzed with the optical microscope OLYMPUS GX 71. The corrosion kinetic was additionally evaluated by potentiodynamic measurements using a PAR 2273 device.

#### 4. Results and discussions

The goal of the work consists in the assessment of the kinetics corrosion for the Incoloy-800 - material of the tubes - tested in demineralised water with different pH values and the experimental results processing with the purpose of including results in a future database of a steam generator. To investigate the water chemistry effects on characteristics of corrosive films formed on Incoloy-800 material, a number of corrosion experiments by electrochemical methods and static autoclaving were performed. The electrochemical determinations were performed by potentiostatic method in aqueous solutions with different pH, at room temperature, (Lucan, D., 2010).

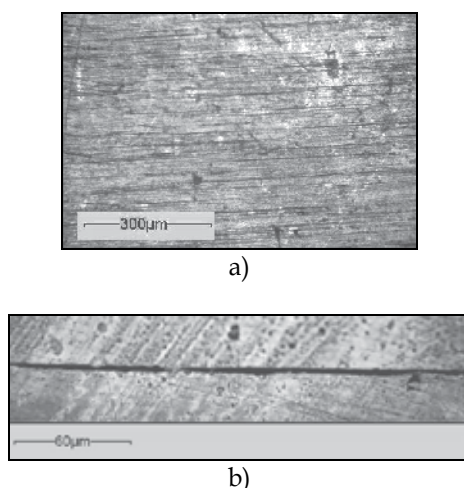
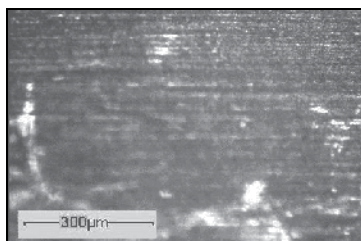
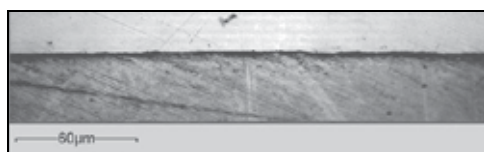


Fig. 2. Surface morphology (x200) (a) and aspect of the superficial layer (x1000) (b) for Incoloy-800 exposed for 1680h in demineralised water, pH=7.5, T=260°C and p=5.1MPa

The chemical composition of Incoloy-800 in percent weight is: C=0.02%, Mn=0.64%, Si=0.49%, S=0.01%, Ni=33.40%, Cr=21.90%, Cu=0.01%, Al=0.24%, Ti=0.41% and Fe=42.88%. Some examples of experimental results for the testing of the Incoloy-800 samples for different times in demineralised water environments with pH=7.5, pH=8.5 and pH=9.5 (AVT) at secondary circuit steam generator specifically parameters (260°C and 5.1MPa) are presented in the Fig.2 ÷ Fig.4.

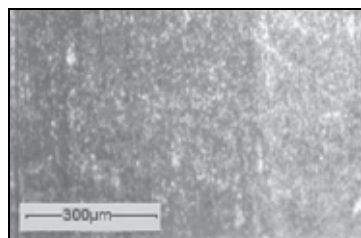


a)



b)

Fig. 3. Surface morphology (x200) (a) and aspect of the superficial layer (x1000) (b) for Incoloy-800 exposed for 3600h in demineralised water, pH=8.5, T=260°C, p=5.1MPa



a)



b)

Fig. 4. Surface morphology (x200) (a) and aspect of the superficial layer (x1000) (b) for Incoloy-800 exposed for 3192h in demineralised water, pH=9.5, T=260°C, p=5.1MPa

The exposure times for the metallographic analysis of samples tested at a pH=7.5 were: 264h, 456h, 696h, 960h and 1680h. For the Incoloy-800 samples, tested for 264h in demineralised water at a pH=7.5 a uniform, continuous, adherent oxide layer is noticed, with thickness smaller than or equal to 0.6μm. When the testing time was 456h in the same

conditions the presence of the oxide is noticed on samples surface, brown-red in colour. The samples surface is entirely covered by oxide and there are no uncovered spots while the visual aspect is almost identical for the entire surface. Thickness of the oxide layer is about  $0.8\text{ }\mu\text{m}$ . The oxide layer on the samples tested for 696h is uniform, continuous, adherent, while its thickness ranges between  $0.6\text{ }\mu\text{m}$ – $1.2\text{ }\mu\text{m}$ . The results of the 960 hours exposure was the occurrence of an oxide layer with a thickness of  $0.9\text{ }\mu\text{m}$ – $1.5\text{ }\mu\text{m}$ .

The thickness of the oxide layer existing on the samples tested for 1680h is about  $3\text{ }\mu\text{m}$ .

The aspect of the surface and film formed on the samples tested 1680h in demineralised water at a pH=7.5 are presented in Fig.2. The exposure times for the metallographic analysis of the samples tested at a pH=8.5 were: 240h, 720h, 1200h, 1416h, 1656h, 1824h, 2064h, and 3600h. On the Incoloy-800 samples, tested for 240h in demineralised water with a pH=8.5 adjusted with morpholine and cyclohexylamine, at  $260^{\circ}\text{C}$  and a pressure of 5.1MPa a uniform, continuous and adherent oxide layer is noticed, whose thickness is smaller than or equal to  $1.9\text{ }\mu\text{m}$ . The surface morphology for some samples exposed for 240h in demineralised water at a pH=8.5 (AVT) at parameters specific to the steam generator secondary circuit shows the presence of the oxide, its colour being brown-red. The samples surface is completely covered by oxide and there are no uncovered spots, while the visual aspect is almost identical for the entire surface. It is to be noticed that the oxide layer for the samples tested 720h in demineralised water with a pH=8.5 is in this case, uniform, continuous, adherent and its thickness ranges between  $0.7\text{ }\mu\text{m}$  and  $0.8\text{ }\mu\text{m}$ . The oxide is uniform, with brown-red shadows and formed in continuous film on the samples surface. For the Incoloy-800 samples tested for 1200h in demineralised water with a pH=8.5 the result of the exposure was the formation of an oxide layer with a uniform thickness of  $1.2\text{ }\mu\text{m}$ . In this case the oxide uniformity is noticed. The aspect of the oxide layer existing on the samples tested 1416h is shown that the film thickness on these samples is about  $0.8\text{ }\mu\text{m}$ . The surface morphology for the samples exposed for 1416h has a uniform aspect.

The aspect of the oxide layer existing on the surface of samples tested for 1656h in demineralised water with pH=8.5 is uniform, continuous and adherent. The uniformity and continuity of the oxide film is observed and the surface morphology for the samples exposed for 1656h in demineralised water with pH=8.5. The oxide film is uniform, continuous, adherent and has a thickness smaller than  $2.6\text{ }\mu\text{m}$  for a sample exposed for 1824h in demineralised water with a pH=8.5 in conditions specific to the operation of the secondary circuit.

The aspect of the oxide layer on the surface of samples tested for 2064h in demineralised water with a pH=8.5 is uniform, continuous and adherent. The uniformity and continuity of the oxide layer can be noticed by the surface morphology of samples exposed for 3600h in demineralised water with a pH=8.5, Fig.3. The oxide layer is uniform, continuous and adherent and has a thickness smaller than  $3.5\text{ }\mu\text{m}$ . The aspect of the oxide layer and the surface morphology, respectively, for a sample exposed for 3192h in demineralised water at a pH=9.5 under operating conditions specific to the secondary circuit are presented in Fig.4.

#### 4.1 Comparison of outputs of tests performed at pH=7.5, pH=8.5 and pH=9.5

After autoclaving operation the samples were descaled in two stage alkaline permanganate – citrox, (Taylor, 1977). Fig.5 ÷ Fig.11 comparatively present the corrosion kinetics for: metal loss by corrosion; corrosion rate; totally formed corrosion products; adherent corrosion products, released corrosion products; corrosion products release, and the release rate of

metal at a pH=7.5, pH=8.5 and pH=9.5, respectively. The Table 1 presents the equations for the corrosion kinetics. For the weight loss due to corrosion and corrosion rate it is noticed that, in the case of a pH=9.5 these have the smallest values (Fig.5 and Fig.6), (Lucan et al., 1998; Lucan et al., 2001; Lucan et al., 2003; Lucan et al., 2005; Cojan et al., 2008). The results are confirmed by the experiments presented in articles from specialty journals, (Taylor, 1977; Stellwag, 1998; Iglesias & Calderon, 2003).

No.	Parameter	pH=7.5	pH=8.5	pH=9.5
1	Loss of metal by corrosion	$y=0.1249\ln(x)+0.0337$	$y=0.2201x^{0.2705}$	$y=0.10501x^{0.277}$
2	Corrosion rate	$y=0.2275x^{-0.831}$	$y=0.3439x^{-0.8377}$	$y=0.2579x^{-0.8434}$
3	Total corrosion products	$y=0.1626\ln(x)+0.1055$	$y=0.2417\ln(x)-0.0648$	$y=0.0973\ln x+0.2721$
4	Adherent corrosion products	$y=0.2924x^{0.142}$	$y=0.2962x^{0.2602}$	$y=0.0757\ln x+0.2827$
5	Released corrosion products	$y=0.0511\ln(x)-0.0328$	$y=0.0296\ln(x)-0.0461$	$y=0.0216\ln x-0.0106$
6	Release rate of corrosion products	$y=0.0206x^{-0.4336}$	$y=0.0217x^{-0.6715}$	$y=0.0168x^{-0.6354}$
7	Release rate of metal	$y=0.0031x^{-0.6542}$	$y=0.0174x^{-0.7571}$	$y=0.0031x^{-0.6715}$

Table 1. The equations for the kinetic corrosion specific parameters

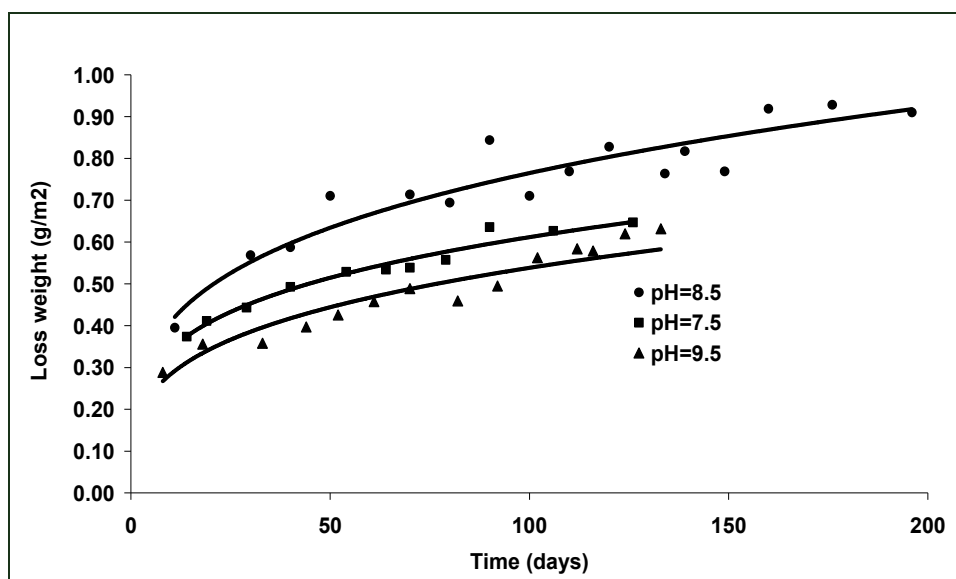


Fig. 5. Loss of metal by corrosion vs. time

Also, in the case of totally formed corrosion products the smallest values have been obtained in exposure in solution at a pH=9.5 (Fig.7). In the case of adherent corrosion products, the smallest values have been reached for the solution with a pH = 7.5 (Fig.8), but the values for

the tests at pH = 9.5 solution are similar, without significant differences between the two cases.

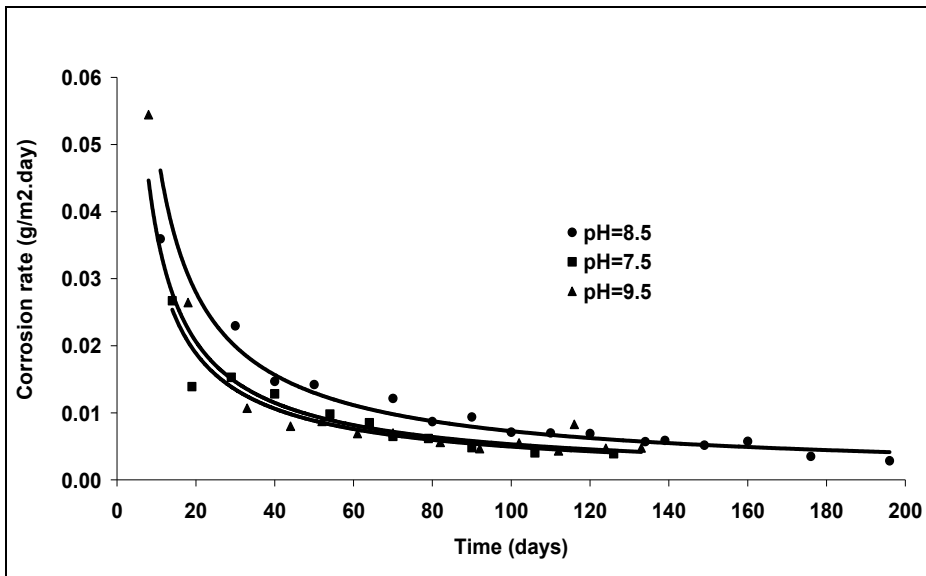


Fig. 6. Corrosion rate vs. time

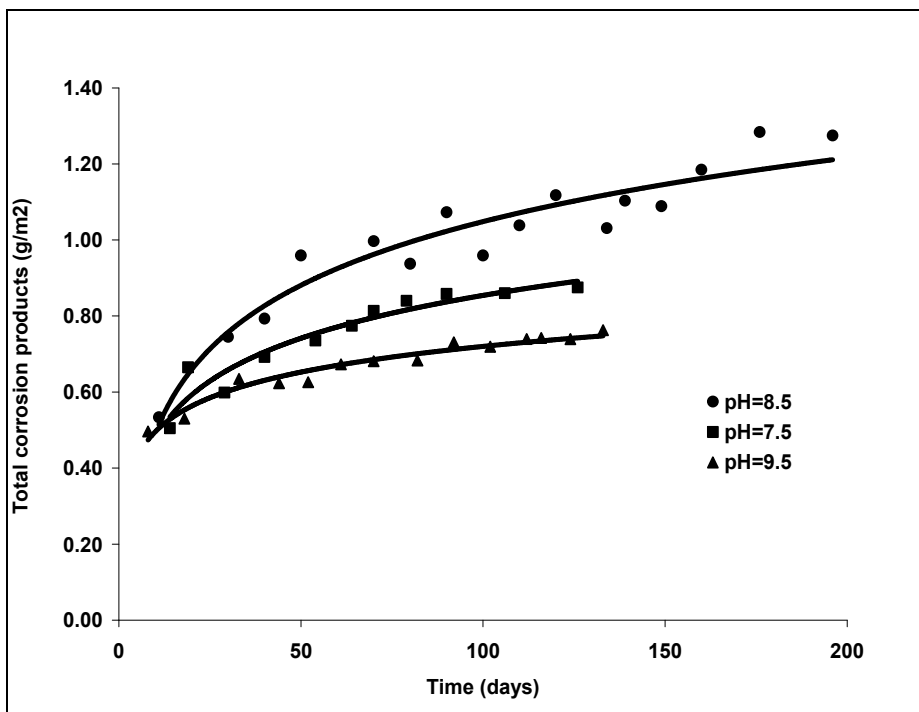


Fig. 7. Total corrosion products vs. time



In the case of released corrosion products, the release rate for products and metal the highest values are obtained for the samples tested in the solution with a pH=7.5 (Fig.9÷Fig.11). This can be explained by the fact that magnetite solubility has higher values for solutions with a smaller pH.

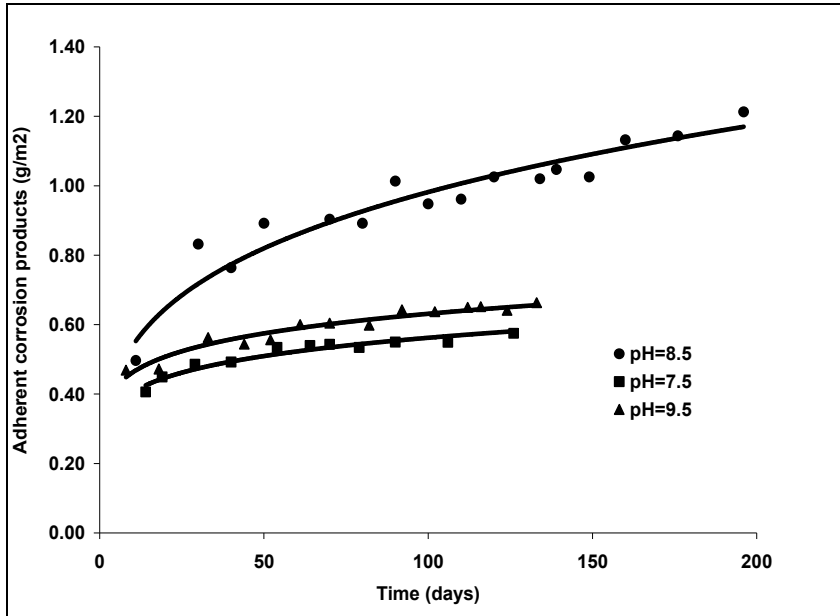


Fig. 8. Adherent corrosion products vs. time

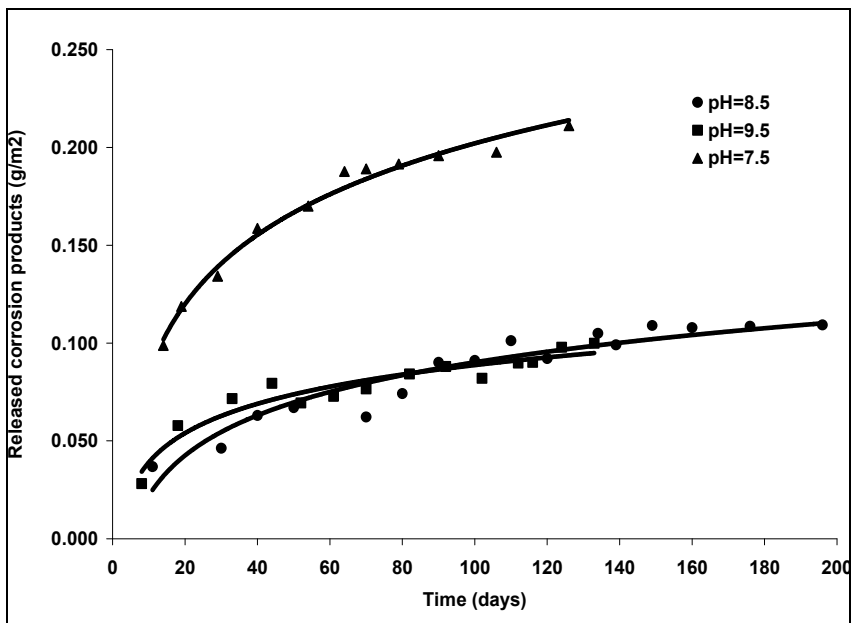


Fig. 9. Released corrosion products vs. time

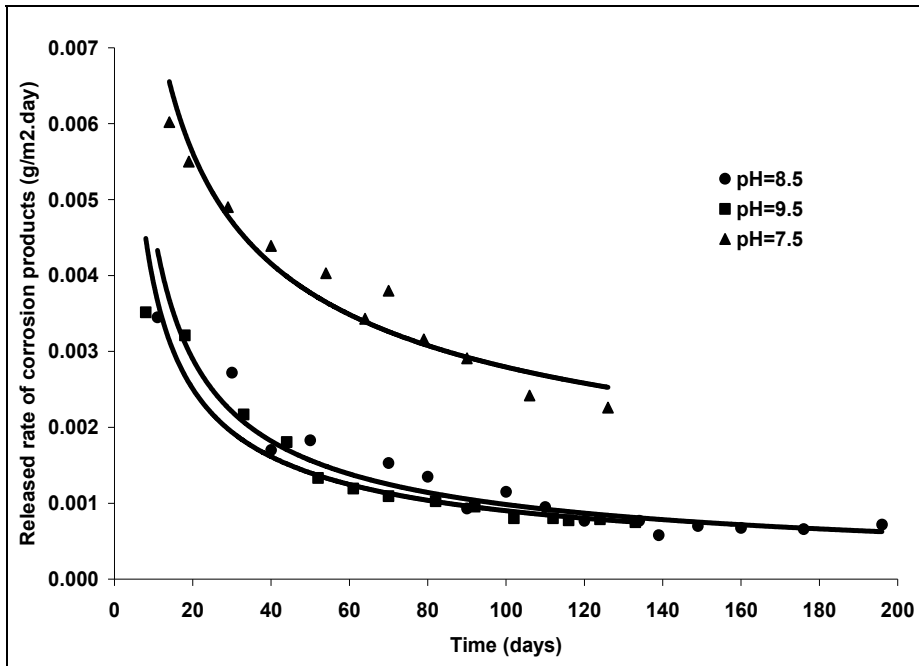


Fig. 10. Released rate of corrosion products vs. time

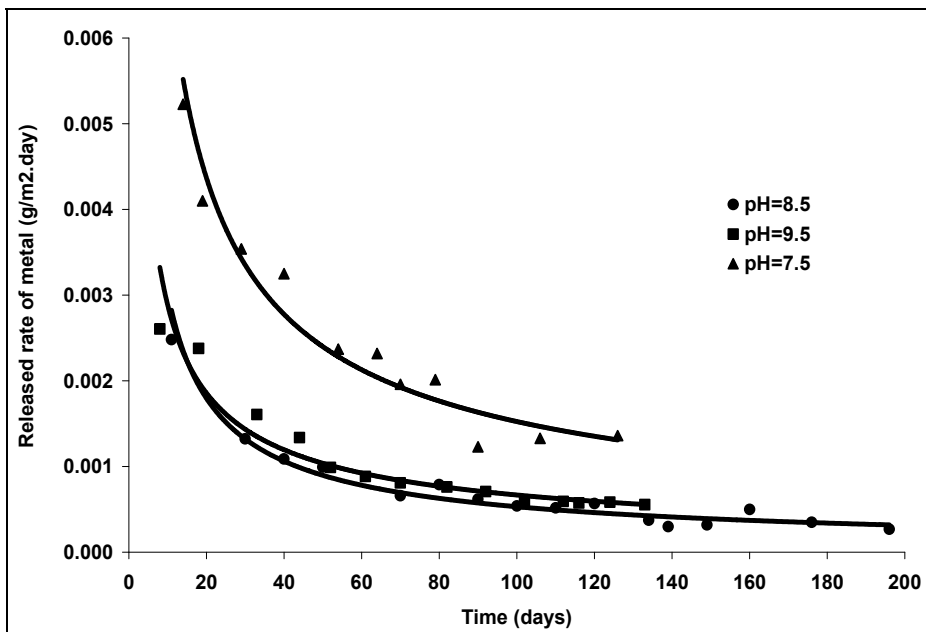


Fig. 11. Released rate of metal vs. time

An example in this sense is the fact that, at 200°C the magnetite solubility is 2µg/kg for a solution with pH=9.5 while for a pH=8.5 the magnetite solubility increases, reaching

60 $\mu$ g/kg. It can be stated that corrosion kinetics for: metal loss by corrosion; corrosion rate; totally formed corrosion products; adherent corrosion products; released corrosion products and the metal release rate at a pH=7.5, pH=8.5 and pH=9.5, respectively, evolve following power-type or logarithmic laws: the smallest corrosion rates are obtained in the case of exposure in a pH=9.5 solution.

Fig.12 and Fig.13 show the results of electrochemical measurements performed by the potentiodynamic method. The electrochemical potential values measured in demineralised water at a pH=9.5 for samples tested by autoclaving at a pH=7.5: PD 35 – tested 10 days, PD 39 – tested 19 days and PD 33- initial status; and pH=8.5 for samples tested by autoclaving at a pH=8.5: PD 36 – tested 10 days, PD 37 – tested 47 days, PD 38 – tested 96 days and PD 34- initial status, show that the oxide films formed on the samples surface at higher exposure times provides them a relatively high corrosion resistance.

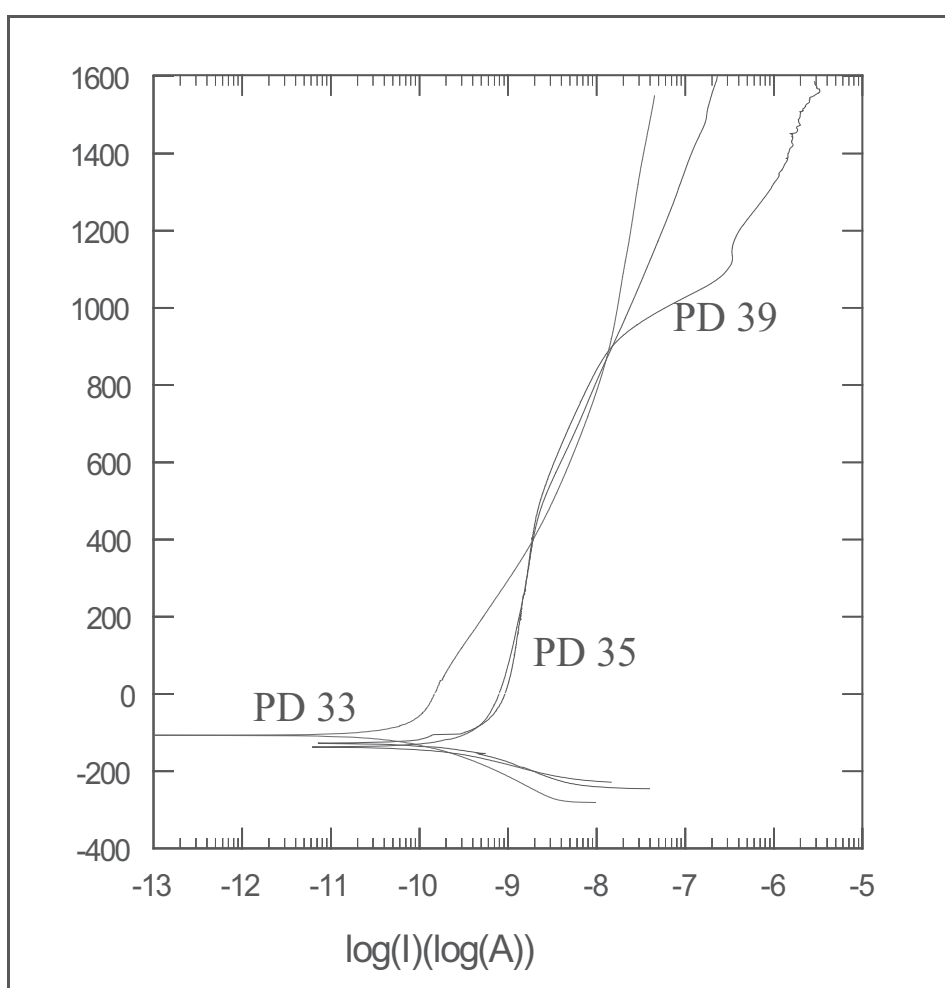


Fig. 12. Potentiodynamic curves Incoloy-800 tested pH=7.5: PD 33- as received; PD 35 – tested 10 days; PD 39 – tested 19 days

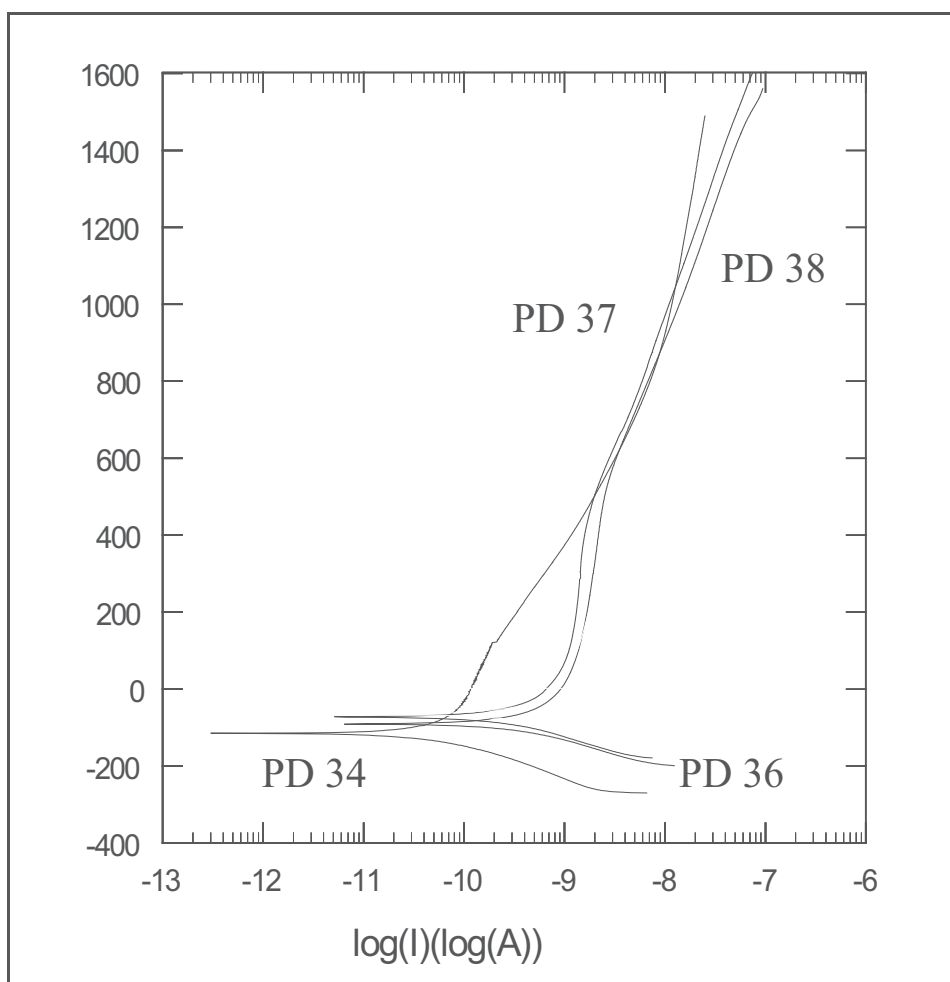


Fig. 13. Potentiodynamic curves Incoloy-800 tested pH=8.5: PD 34- as received; PD 36 – tested 10 days; PD 37 –tested 47days; PD 38 – tested 76 days

## 5. Conclusions

This work presents in the first place the types of degradations specific to the steam generators and in the second place the correlation between the nature of materials used for the construction of the steam generator tubing, the chemical characteristics of the circulating environment and the way in which certain of their pH values can lead to the development of different types of oxide layers.

Corrosion testing has been performed for Incoloy-800 alloy samples for 3600h at a pH=7.5, 3600h at a pH=8.5 and 4800h at a pH=9.5.

By using gravimetric analysis and descaling of filmed samples assayed at certain intervals of time, the corrosion kinetics of the Incoloy-800 alloy has been established.

The films formed on samples after autoclaving and the morphology of samples surfaces have been assessed by metallographic microscopy.

In the case of samples tested in solution of pH=7.5 for 264h the thickness of the films is 0.6 $\mu$ m, this one increasing with the increase of the testing time, reaching 3 $\mu$ m after 1680h of testing.

For the samples tested in solution of a pH=8.5 for 240h thickness of the films is 1.9 $\mu$ m, this one increasing with the increase of the testing time, reaching 3.5 $\mu$ m after 3600h of testing.

The corrosion kinetics has been established for the corrosion-induced loss of metal, corrosion rate, total formed corrosion products, adherent corrosion products, released corrosion products, released rate of corrosion products and released rate of metal.

The work also presents the kinetic curves and the equations which describe these curves for the tests performed at the three values of the pH.

A comparison is presented between the corrosion kinetics for the normal value of the operation pH=9.5, and also for the values 7.5 and 8.5. For the corrosion-induced loss of weight and for the corrosion rate it is noticed that in the case of pH=9.5 solution these have the smallest values.

In the case of released corrosion products, their release rate and metal release rate, the highest values are obtained for the samples tested in a pH=7.5 solution. This can be explained by the fact that magnetite solubility has higher values for solutions with a smaller pH.

The work does a correlation of the normal/abnormal chemical system of the steam generator secondary circuit with the corrosion of the tubing material exposed in respective environment.

The future research will have like objective experimental studies on the behaviour of the principal steam generator structural materials in the presence of the impurities and the synergetically effect of the simultaneously presence of impurities especially in the regions with restrictive flow and/or in the presence of crevices.

## 6. References

- Barber, D. & Lister, D. H. (1983). Chemistry of the water circuits of CANDU reactors, *Proceedings of a Symposium Water Chemistry and Corrosion Problems in Nuclear Power Plants*, Vienna, pp. 149-161.
- Cattant, F. (1997), Lessons learned from the examination of tubes pulled from Electricite de France steam generators, in *Nuclear Engineering and Design*, 168, pp. 241-253.
- Cojan, M., Muscaloiu, C., Pirvan, I., Roth, M. & Lucan, D. (2008). R&D Support to CANDU 6 NPP lifetime management, in CD-ROM *Proc. of the WEC Regional Energy Forum – FOREN 2008*, Neptun, Romania, Paper 021, pp. 1-8.
- IAEA. (1997). Assessment and management of ageing of major nuclear power plant components important to safety: *Steam generators*, in IAEA-TEC-DOC-981.
- Iglesias, A.M. & Calderon, R. (2003), Thermal resistance contributions of oxides growth on Incoloy 800 steam generator tubes, in *Nuclear Engineering and Design*, 219, pp. 1-10.
- Lucan, D., Fulger, M., Pirvan, I., Radulescu, M. & Jinescu, Ghe. (1998). Corrosion of tube-tubesheet joint in the CANDU steam generator at operation resuming after the chemical cleaning deposits occurred due to the contamination of condense by the cooling water, in *Proceedings of International Nuclear Congress ENC'98*, Nice, France, pp. 348-352.

- Lucan, D., Fulger, M. & Jinescu, Ghe. (2001). The ageing of CANDU steam generator due to localized corrosion, in *Proceedings of the 5-th International Seminar on Primary and Secondary Side Water Chemistry of Nuclear Power Plants*, Eger, Hungary, pp. 1-5.
- Lucan, D., Fulger, M., Velciu, L. & Savu, Gh. (2003). Corrosion kinetics of Incoloy-800 in high temperature and pressure water with pH 9.5, Institute for Nuclear Research Pitesti, Internal Report.
- Lucan, D., Fulger, M., Savu, Gh., Velciu L. & Lucan, G. (2005). Experimental research concerning CANDU steam generator components, in CD-ROM *Proceedings of International Congress on Advanced Nuclear Power Plants*, Seoul, KOREA, Paper 5431, pp. 1-8.
- Lucan, D. (2006). Behavior of Steam Generator tubing in the presence of silicon compounds, in *Power Plant Chemistry – Journal of All Power Plant Chemistry Areas*, ISSN 1438-5325, Power Plant Chemistry GmbH, P.O.Box 1269, 68806, Neulussheim, Germany vol.8, no.6 pp.361-369.
- Lucan, D., Fulger, M. & Jinescu, Ghe. (2007). Corrosion of SA 508 in high temperature and pressure water containing silicon compounds, in *Rev. Chim.*, ISSN 0034-7752, CHIMINFORM DATA S.A., vol.58, no.12, pp.1182-1189.
- Lucan, D. Fulger, M. & Jinescu, Ghe. (2008). Corrosion process of Incoloy-800 in high pressure and temperature aqueous environment, in *Rev. Chim.*, ISSN 0034-7752, CHIMINFORM DATA S.A., vol.59, no.9, pp.1026-1029.
- Lucan, D. (2010). Behaviour of the steam generator tubing in water with different pH values, (in press) *Nuclear Engineering and Design* (a part of the chapter reprinted from this article with permission from Elsevier).
- Stellwag, B. (1998). The mechanism of oxide film formation on austenitic stainless steels in high temperature water, in *Corros. Sci.*, 40 (2/3), pp. 337-70.
- Taylor, G.F. (1977), Corrosion monitoring in CANDU nuclear generating stations, in AECL-5648, *Corrosion* 77, Paper 119, pp. 1-21.

# Analysis of Oxide on Steam Generator Tubing Material in High Temperature Alkaline Leaded Solution

Dong-Jin Kim, Seong Sik Hwang, Joung Soo Kim, Yun Soo Lim,  
Sung Woo Kim and Hong Pyo Kim  
*Korea Atomic Energy Research Institute*  
1045 Daedeok-Daero, Yuseong-Gu, Daejeon 305-353  
Republic of Korea

## 1. Introduction

Nuclear power plants (NPP) using Alloy 600 as a heat exchanger tube of the steam generator (SG) have experienced various corrosion problems such as pitting, intergranular attack (IGA) and stress corrosion cracking (SCC). In spite of much effort to reduce the material degradations, SCC is still one of important problems to overcome.

Secondary water pH which affects SCC behavior substantially spans widely from acid to alkaline in crevice depending on water chemistry control, water chemistry in crevice, plant specific condition, etc. Especially, specific chemical species are accumulated in the crevice as the sludge leading to a specific condition of crevice chemistry. Among these chemical species, lead is known to be one of the most deleterious species in the reactor coolants that cause SCC of the alloy (Sarver, 1987; Castano-Marin et al., 1993; Wright and Mirzai, 1999; Staehle, 2003). Even Alloy 690, as an alternative of Alloy 600 because of outstanding superiority to SCC, is also susceptible to lead in alkaline solution (Vaillant et al., 1996; Kim et al., 2005; Kim and Kim, 2009).

Lead has been effectively detected in all tubesheet samples, crevice deposits and surface scales removed from SGs. Typical concentrations are 100 to 500 ppm but in some plants, concentrations as high as 2,000 to 10,000 ppm have been detected (Fruzzetti, 2005). The best method to prevent lead induced SCC (PbSCC) is to eliminate the harmful lead from the NPP chemistry, which is not possible and most NPPs are already contaminated by lead. Moreover only a very low level of sub ppm affects PbSCC.

During a long exposure time of more than 30 years under a high temperature and high pressure water chemical environment, an Alloy 600 surface experiences an oxide formation, breakdown and modification depending on the nature of the grown oxide, combined with a residual stress induced by a tube expansion which is introduced to fix a tube to a tube sheet. Therefore it is strongly anticipated that a SCC is inevitably related to an oxide properties, formed on an Alloy 600 surface, because a crack initiates and propagates through a breakdown and alteration of a surface oxide, fundamentally speaking. An oxide properties should be investigated for the elucidation of a lead induced mechanism and its countermeasure.

It is expected that an addition of lead into a solution modifies the oxide property affecting SCC behavior. A discovery of the way to avoid this modification can give us a key to control PbSCC such as an inhibitor.

The thickness, composition, passivity and structure of an oxide formed and grown on Alloy 600 are influenced by the temperature, pH, time, chemical species and so on, in a very complex manner (McIntyre et al., 1979; Kim et al., 2008). The very complicated and nano-sized thin oxides formed in aqueous/non aqueous conditions have been successfully analysed by using a transmission electron microscopy (TEM), an x-ray photoelectron spectroscopy (XPS), an Auger electron spectroscopy (AES) and an electrochemical impedance spectroscopy (EIS) (Machet et al., 2004; Yi et al., 2005; Rincón et al., 2007; Hwang et al., 2007).

In the present work, the oxides formed on Alloy 600 in aqueous solutions with and without lead were examined by using a transmission electron microscopy (TEM), an energy dispersive x-ray spectroscopy (EDXS), an x-ray photoelectron spectroscopy (XPS) and an electrochemical impedance spectroscopy (EIS). The oxide property was compared with the SCC behaviors tested in caustic solutions in the presence of lead and NiB as an inhibitor as well as in the absence of both impurities by using a slow strain rate tension (SSRT) test.

## 2. Experimental details

The test specimens were fabricated from a 19.05 mm (0.75 inches) outside diameter Alloy 600 steam generator tubing material which was thermally treated (TT) at 704°C for 15 hours following solution annealing at 975°C for 20 minutes or high temperature mill annealed (HTMA) at 1024°C for 3 minutes. The chemical compositions are given in Table 1. High-purity water (18M $\Omega$  cm at RT) was used as the reference solution. Aqueous solutions used were shown in Table 2. Reagent grade PbO was added to the reference solution at an amount of 5,000 or 10,000 ppm as a source of lead. The performance of a NiB inhibitor was evaluated by adding 4 g/l of NiB into the leaded solution. Deaeration was carried out by purging with a high purity nitrogen gas to remove the dissolved oxygen for 20 hours before the tests commenced.

Material	C	Si	Mn	P	Cr	Ni	Fe	Co	Ti	Cu	Al	B	S	N	Ce
Alloy 600TT	0.03	0.07	0.003	0.024	16.12	74.42	9.06	0.007	0.005	0.003		0.006	0.001	0.0103	0.003
Alloy 600 HTMA	0.025	0.05	0.22	0.07	15.67	75.21	8.24	0.005	0.39	0.011	0.15	0.0014	0.001	0.0103	

Table 1. Chemical compositions of the Alloy 600 TT and Alloy 600 HTMA

The electrochemical tests were performed for rectangular plate specimens (10 mm x 10 mm) fabricated from the thermally treated tubing. The surface of the specimens was polished up to 1  $\mu$ m using a diamond suspension. An Alloy 600 wire was spot welded to the specimen, and the wire was shielded with a heat-shrinkable polytetrafluoroethylene (PTFE) tubing. The test specimens were immersed in a 1-gallon nickel autoclave at 315°C for 14 days. The electrochemical impedance measurements were carried out in the frequency range of 10<sup>6</sup> to 10<sup>-3</sup> Hz at the OCP with a 10 mV perturbation. A Solartron 1255 frequency response analyser was used with a Solartron 1287 electrochemical interface. Experimental matrix was shown in



Table 2. Separate autoclaves were used for the leaded and the unleaded test solutions to avoid a cross contamination.

Environment	pH(315°C) by MULTEQ	Remark	Experiment
-H <sub>2</sub> O	5.8	Neutral	SSRT test
-10,000ppm PbO	7.9	pH increase	
-10,000ppm PbO + 4g/L NiB	7.9	Deaeration	
-0.01M Na <sub>2</sub> SO <sub>4</sub> + 0.01M NaHSO <sub>4</sub>	5.6	Acid	SSRT test
-10,000ppm PbO	8.7	pH increase	
-10,000ppm PbO + 4g/L NiB	8.7	Deaeration	
-0.01M Na <sub>2</sub> SO <sub>4</sub>	5.8	Neutral	SSRT test
-10,000ppm PbO	8.6	pH increase	
-10,000ppm PbO + 4g/L NiB	8.6		
-Ammonia	6.3	Mild caustic	Immersion test
-5,000ppm PbO	7.9	pH increase	
-5,000ppm PbO + 4g/L NiB	7.9	Deaeration	
-0.1M NaOH (Deaeration)	9.9	Caustic the Same pH	SSRT, immersion test
-5,000/10,000ppm PbO (Deaeration)	9.9		
-5,000/10,000ppm PbO (Non-deaeration)	9.9		
-10wt% NaOH	10.4	Strong caustic	SSRT test
-10,000ppm PbO	10.4	Deaeration	
-40wt% NaOH	10.9	Strong caustic	SSRT test
-10,000ppm PbO	10.9	Deaeration	

Table 2. Various aqueous solutions and their pHs for SSRT and immersion (electrochemical impedance) tests at 315°C (MULTEQ, 2008)

After the immersion test, the plate specimens were examined. The surface oxide layer and its composition was examined by using a field emission TEM, equipped with an EDXS (JEM-2100F, JEOL). The information on the chemical binding was obtained by using an XPS (AXIS-NOVA, KRATOS Analytical). The spectra for Ni 2p, Cr 2p, O 1s and Pb 4f were recorded with an AlK $\alpha$  radiation ( $h\nu = 1486.6$  eV), at a pass energy of 20 eV. The take-off angle, the base pressure and the sputter rate for a depth profiling were 45°, 5.0x10<sup>-9</sup> torr and 0.04nm/s in SiO<sub>2</sub>, respectively. To analyse the XPS results, an online database was used (<http://www.laserface.com>).

The SSRT tests were performed for uniaxial tension specimens fabricated from a HTMA tubing in unleaded, and leaded solutions, and a leaded one with a NiB addition. The tests were carried out in 0.5-gallon nickel autoclaves at 315°C and an equilibrium pressure. The test specimens were at an open circuit potential (OCP) without an impressed electrochemical current. The strain rate was 2 x 10<sup>-7</sup> s<sup>-1</sup>. After the SSRT test, surface was observed to determine SCC ratio by using a SEM (JSM6360).

### 3. Results and discussion

#### 3.1 Analysis of oxide in solution without lead

Figs. 1 (a) and (b) are the TEM images and the results of the TEM-EDXS analyses for a cross-section of the surface oxide layer that was formed in the ammonia solution without/with

NiB at 315°C, respectively. Similar appearance was observed for the two oxide layers formed in the two kinds of solutions with about a 400 – 500 nm thickness. An inner oxide layer can be more clearly differentiated in the surface oxide formed in the ammonia solution with NiB. It is worthwhile noting that an outer layer seems to be more porous compared to an inner layer.

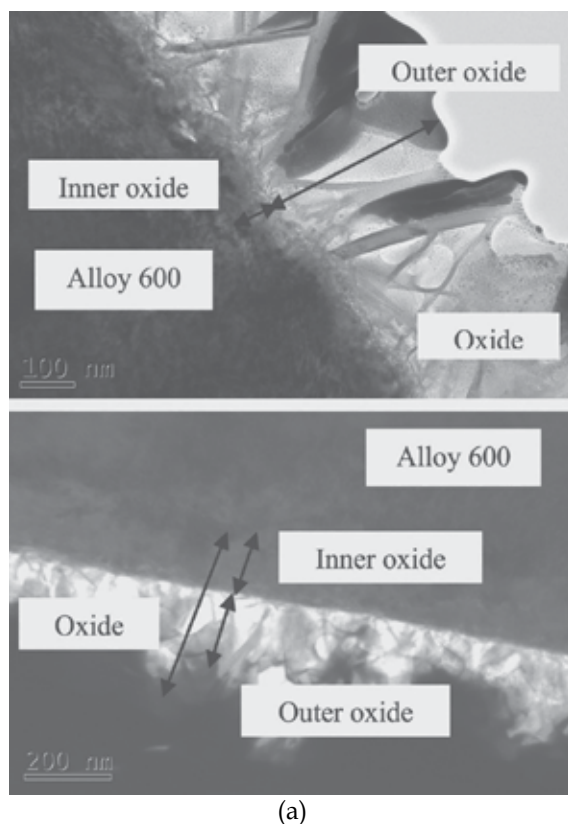


Fig. 1. (a) TEM images for surface oxides formed on Alloy 600 specimens

From Fig. 1(b) of the TEM-EDXS results, the surface oxide layers are composed of a duplex oxide layer, i.e., nickel rich outer layer and chromium rich inner layer, irrespective of the used aqueous solution. A chromium rich inner layer of the surface oxide formed in the ammonia solution with NiB is thicker than that of the surface oxide layer in the ammonia solution without NiB. Based on the similar chemical composition and surface appearance of both surface oxide layers, except for the oxide thickness, the TEM diffraction pattern for the surface oxide formed in the ammonia solution with NiB was analysed because it is easier to observe a thicker oxide.

Figs. 2 (a) and (b) are the diffraction patterns, mainly obtained from an outer surface oxide and an inner surface oxide, respectively. From the diffraction patterns, there are two ring patterns and two spot patterns. The same patterns corresponding to outer ring and spot pattern I are observed in Figs. 2 (a) and (b) because the beam size is too wide to differentiate a duplex layer, i.e. an outer surface oxide and an inner oxide, completely, even though the diffraction pattern was investigated at different sites. By analysing the diffraction pattern for

the surface oxide formed in the ammonia solution with NiB at 315°C, an outer ring and an inner ring originated from an inner oxide and an outer oxide, respectively. It was revealed that a porous outer oxide is mainly composed of NiO and a relatively dense inner layer consists of  $\text{Cr}_2\text{O}_3$  (JCPDS card no. 47-1049; JCPDS card no. 74-0326). It seems that spot patterns I and II are related to another nickel oxide such as  $\text{Ni}(\text{OH})_2$  rather than NiO and Alloy 600, respectively.

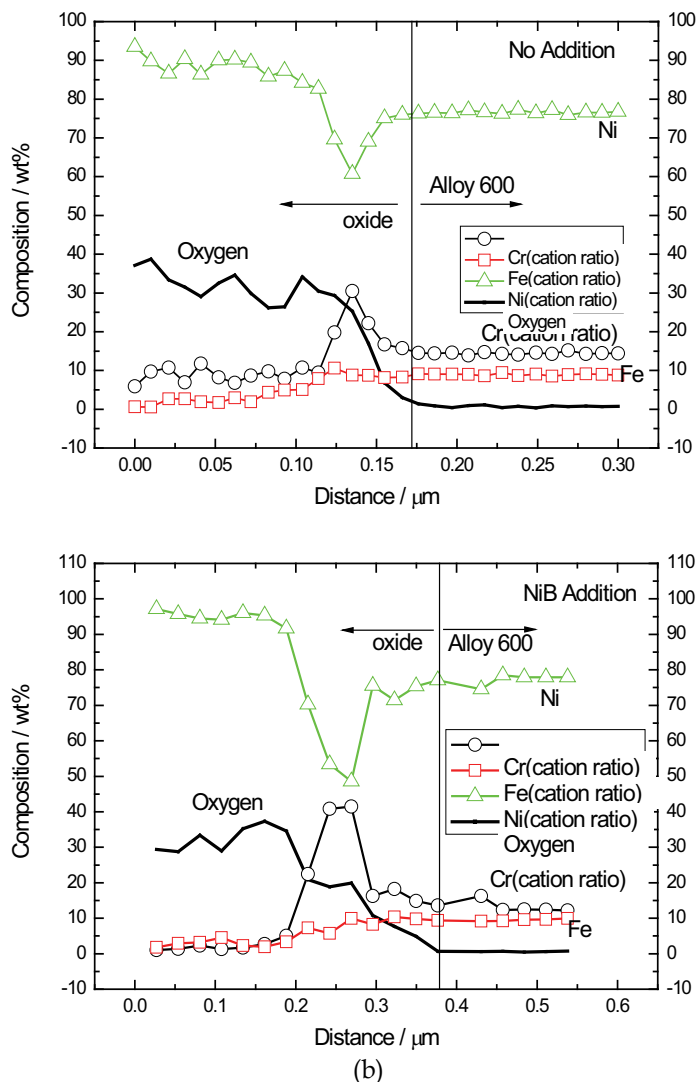


Fig. 1. (b) TEM-EDXS analyses for in-depth chemical compositions for surface oxide layer formed on Alloy 600 specimens in ammonia solutions without/with NiB at 315°C (Kim, D.-J. et al., 2010)

Figs. 3 (a) and (b) are the XPS results for the surface oxide formed in the ammonia solution with NiB. Ni metal with a binding energy in the range of 852.8~853 eV was detected near

the top surface oxide and its intensity increased rapidly to a saturation value with the etching time while the intensities for NiO and Ni(OH)<sub>2</sub> with binding energies near 855 eV and 856.6 eV, respectively, were very small even at a 10s etching time and their values were decreased to a background level only at a 1430s etching time. From the results of the diffraction pattern and XPS, it was found that an outer oxide is composed of NiO and Ni(OH)<sub>2</sub>.

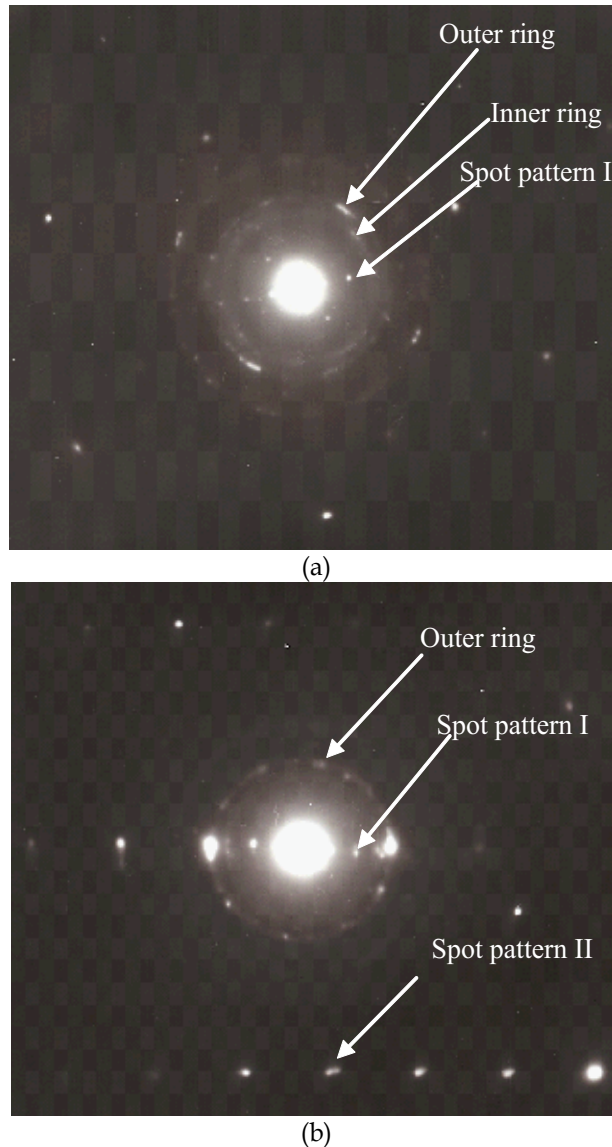


Fig. 2. Diffraction patterns for (a) outer surface oxide and (b) inner surface oxide formed on Alloy 600 in an ammonia solution with NiB at 315°C (Kim, D.-J. et al., 2010)

Apart from Ni, Cr metal with a binding energy of 574.2 eV did not appear at an early stage and the intensity of the metallic chromium increased with the sputtering time while the

intensity for the Cr oxide with a binding energy in the range of 576.6 to 577.3 eV revealed a large value at an early stage and decreased slowly with the etching time indicating that the Cr oxide is relatively dense.

Combining the results of the TEM and XPS, it can be concluded that the nickel oxides of NiO and Ni(OH)<sub>2</sub> are very porous and hence a porous outer oxide is sputtered easily leading to an early appearance of unreacted nickel while Cr oxide composed of an inner layer is much denser than an outer layer. It has been reported that metallic ions in a solution are re-deposited to form a porous outer oxide layer (Robertson, 1989). Growth processes of an inner layer and an outer layer occur at the metal/oxide and oxide/electrolyte interfaces, respectively. The growth rates are controlled by a transport of the layer forming species through a layer, i.e. by an inward diffusion of electrolyte species including oxygen and an outward diffusion of metal cations.

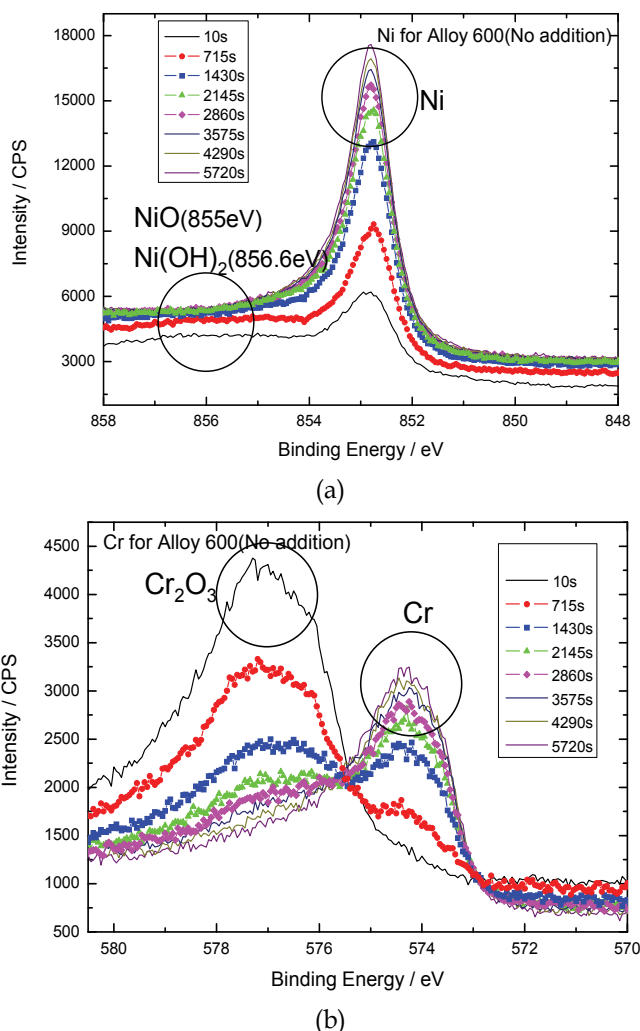


Fig. 3. X-ray photoelectron spectra of (a) Ni(2p<sub>3/2</sub>) and (b) Cr(2p<sub>3/2</sub>) for surface oxide layer formed in an ammonia solution without additive at 315°C (Kim, D.-J. et al., 2010)

### 3.2 Analysis of oxide in solution with lead

Fig. 4 is TEM micrographs for the surface oxide layer formed on the TT Alloy 600 specimens in aqueous solutions at 315°C of (a) unleaded 0.1M NaOH (reference) and (b) with PbO. In the unleaded solution, porous outer oxide and inner oxide are observed while only an oxide layer is observed in the leded solution.

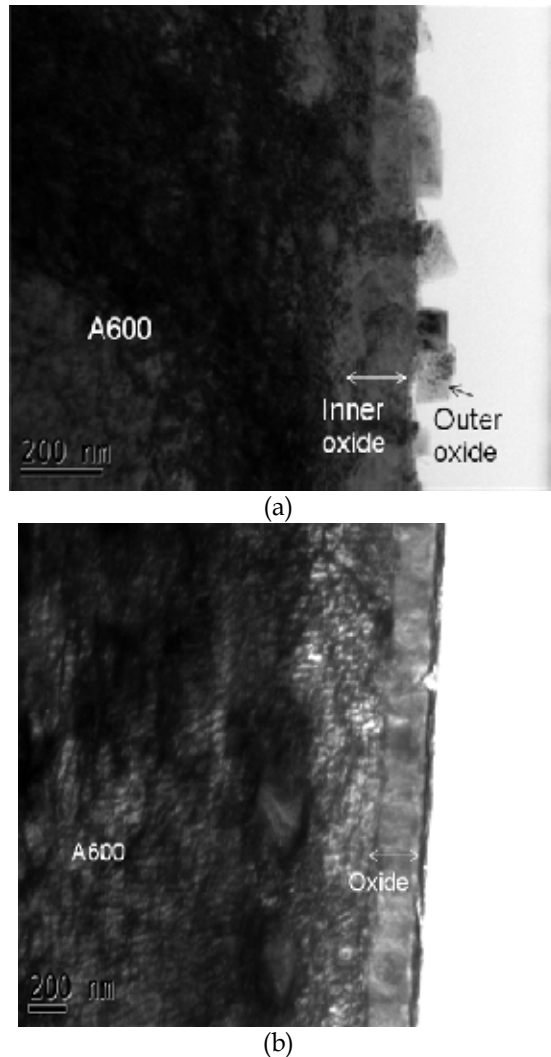
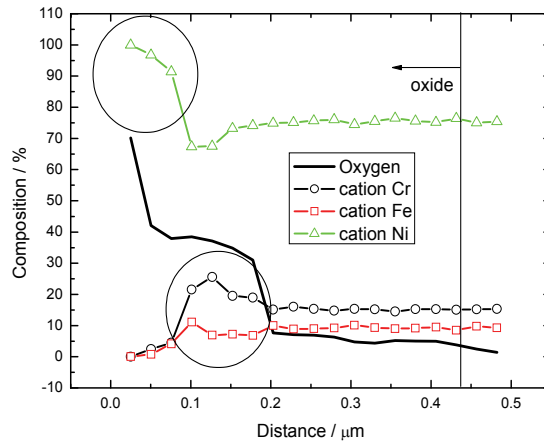


Fig. 4. TEM micrographs for the surface oxide layer formed on the TT Alloy 600 specimens in aqueous solutions at 315°C; (a) unleaded 0.1M NaOH (reference) and (b) with PbO

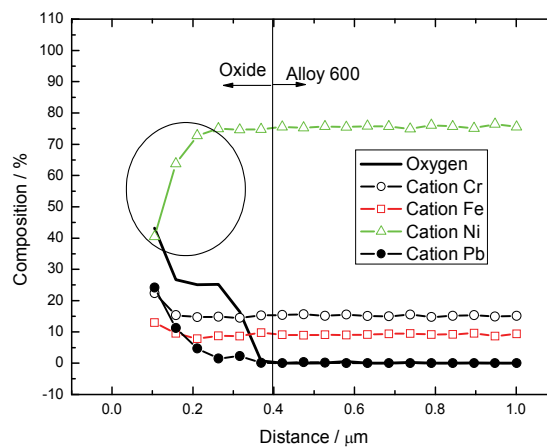
Fig. 5 shows the TEM-EDXS analyses for the specimens tested in the unleaded reference 0.1M NaOH solution (Fig. 5a) and in the leaded solution (Fig. 5b). From the results of Figs. 4 and 5, a duplex oxide layer was formed at the surface, i.e., porous nickel-rich outer layer and dense chromium-rich inner layer similar to the experimental results obtained in unleaded ammonia solution. In the leaded solution, a large amount of lead was observed at about 25

% on the surface. Cations such as Cr and especially Ni were depleted in the oxide layer. The duplex oxide layer observed in the unleaded solution was not examined in the leaded solution.



(a)

Line 5

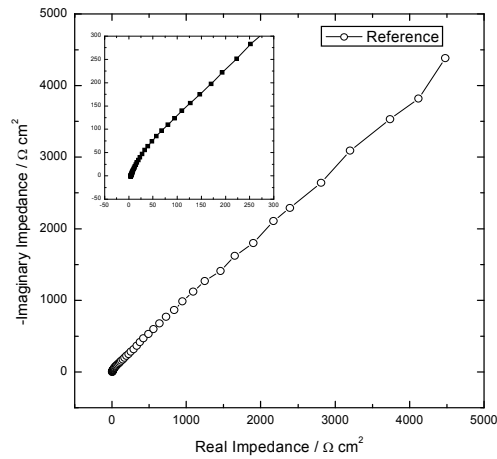


(b)

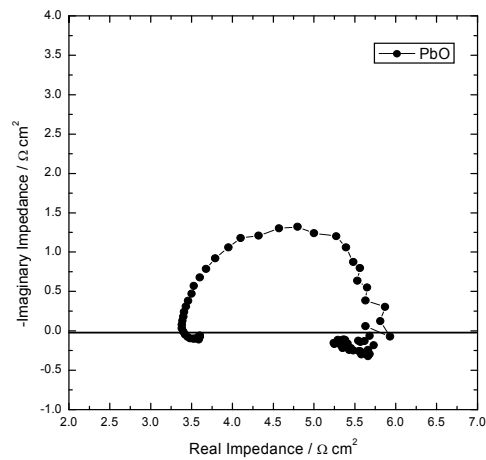
Fig. 5. TEM-EDXS analyses for the in-depth chemical compositions for the surface oxide layer formed on the TT Alloy 600 specimens in aqueous solutions at 315°C; (a) unleaded 0.1M NaOH (reference) and (b) with PbO

It is interesting to see the electrochemical impedance spectroscopy (EIS) results obtained for the specimens immersed in the aqueous solutions without/with PbO. Fig. 6 presents the Nyquist plots obtained for the TT Alloy 600 specimens in the 0.1 M NaOH solutions at 315°C of (a) the unleaded reference and (b) the leaded solution. From the impedance spectra

obtained for the unleaded solution, it can be assumed that the equivalent circuit is composed of a series of a solution resistance and a parallel of a capacitance and a resistance originating from a passive oxide and a constant phase element which may be related to a diffusion process of an electrolyte or a metallic cation, connected to an oxide resistance.



(a)



(b)

Fig. 6. Nyquist plots obtained from the electrochemical impedance measurements for the TT Alloy 600 immersed in the 0.1 M NaOH solutions at 315°C: (a) unleaded reference and (b) leaded with PbO

However, by adding lead oxide to the solution, the total impedance was considerably decreased indicating that an oxide passivity was greatly decreased. An inductive loop which might be caused by a lead incorporation into the oxide was observed. This inductive loop may be attributed to conduction path by the incorporated lead.



Fig. 7 shows the XPS results for the specimen tested in the lead ammonia solution. Lead is incorporated into the oxide layer at a metallic state (136.7 eV) and as a lead oxide (138.9 eV) (<http://www.lasurface.com>).

Based on thermodynamics, an equilibrium electrochemical potential of  $\text{Pb}^{2+}/\text{Pb}$  is higher than an equilibrium potential of  $\text{Ni}^{2+}/\text{Ni}$  leading to increase of OCP of Alloy 600 in the lead solution (Pourbaix, 1966). Hence, Pb can be deposited electrochemically in the lead solution at OCP, which is consistent to Pb metal detected by XPS. However it is not unequivocal yet which one between metallic Pb and PbO affects PbSCC more.

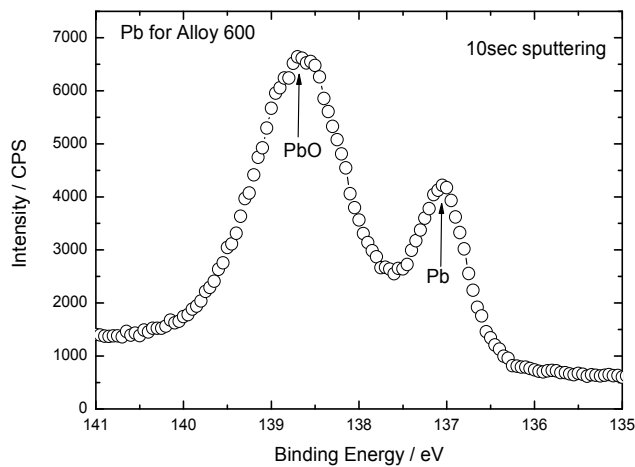


Fig. 7. X-ray photoelectron spectrum of the surface oxide layer formed for TT Alloy 600 in the lead ammonia solution

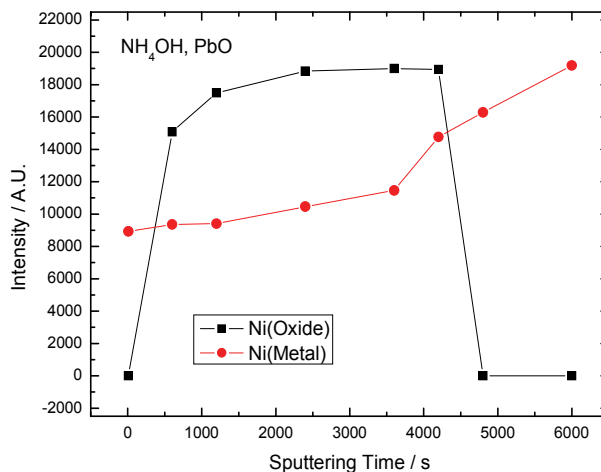
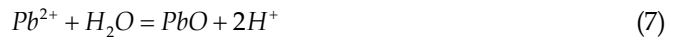
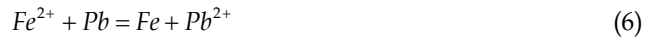
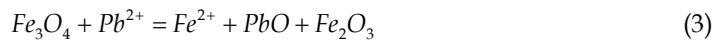
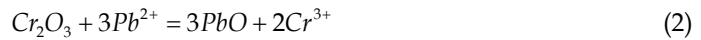


Fig. 8. Plot of XPS intensity of nickel as a metallic state and metal as an oxide state against sputtering time obtained for a TT Alloy 600 specimen immersed in lead ammonia solution

Fig. 8 is a plot of the XPS intensity of Ni as a metallic state and Ni as an oxide state against sputtering time obtained for a specimen immersed in leaded ammonia solution. Fig. 8 was obtained by integration the XPS signal acquired around binding energy level of the Ni species as a metallic state and an oxide state as a function of the sputtering time. Depletion of nickel as an oxide state and a metallic state was observed in the oxide formed in an ammonia solution including PbO, which is consistent with Ni depletion in the oxide shown in Figs. 1 and 5.

In order to investigate reactions available during the experiment, eight reactions were considered as follows.



Based on thermodynamic data and solubility (MULTEQ, 2008; HSC chemistry database), forward reaction is available for reaction (1) at 315°C assuming that concentrations of nickel and lead ions are  $10^{-6}$  mole and 0.0045 mole, respectively. This reaction can be rewritten as follows by using defect chemistry.



By summing reactions (9) and (10), reaction (11) expressing that Ni at Ni site in the oxide is dissolved leaving Ni vacancy and lead ion reacts with Ni vacancy to be oxidized is obtained.



From reaction (11), Ni as a Ni oxide state can be depleted as shown in Fig. 9 and a strain field in the oxide originating from lattice mismatch can be also generated leading to a degradation of passivity.

However, the backward reaction of reactions (2) and (3) is available indicating that a substitution of lead ion for cations such as Cr and Fe in the oxide is not possible at 315°C. Backward reactions for reactions (4)~(6) describing lead electrodeposition are available. From this, cations in the oxide formed in the leaded aqueous solution can be depleted by lead electrodeposition and moreover, the electrodeposited lead can prevent a formation of

the passive oxide composed of Ni, Cr, Fe and O, especially passive chromium oxide which is formed in the aqueous solution without Pb.

Considering thermodynamics for reactions (7) and (8), lead ion in an aqueous solution and electrodeposited lead are oxidized when a pH at 315°C is larger than 4.46 and a hydrogen partial pressure is as low as the secondary water of NPP, respectively.

### 3.3 Stress corrosion cracking behavior

As shown in Table 2, pH at 315°C increases by adding PbO, which seems to be caused by  $\text{PbO} + \text{H}_2\text{O} = \text{Pb}^{2+} + 2\text{OH}^-$  reaction (Pourbaix, 1966).

Table 3 shows the elongation to rupture and the SCC ratio as a function of the aqueous solution without/with PbO for HTMA Alloy 600. Elongation to rupture and SCC ratio were found from the stress-strain curve and fracture surface observation. Elongation to rupture and SCC ratio can be used as criteria for SCC susceptibility from the fact that yield strength and tensile strength are decreased with the stress corrosion cracking leading to the lower elongation to rupture. The SCC susceptibility was greatly increased up to 0.1M NaOH by adding PbO into the solution. PbO degraded SCC resistance in 10wt% NaOH (2.5M NaOH) where Alloy 600 showed SCC behavior without PbO. However the effect of PbO on SCC in 40wt% NaOH (10M NaOH) was less than that in 0.1M NaOH. Considering that a neutral pH at 315°C is 5.8, HTMA Alloy 600 is susceptible to a PbSCC in a mild caustic solution rather than a strong caustic solution such as 2.5M and 10M NaOH solutions. From the results of 10wt% and 40wt% NaOH solutions, there seems to be a pH range susceptible to PbSCC, which may be closely related to oxide stability such as Ni, Cr, Fe and Pb oxides in a strong caustic solution.

Environment	Elongation to rupture(%)	SCC ratio	pH(315°C) by MULTEQ	Remark
-H <sub>2</sub> O	58	Little	5.8	Neutral
-10,000ppm PbO	30	83	7.9	pH increase
-0.01M Na <sub>2</sub> SO <sub>4</sub> + 0.01M NaHSO <sub>4</sub>	64	16	5.5	Acid
-10,000ppm PbO	40	57	8.7	pH increase
-0.01M Na <sub>2</sub> SO <sub>4</sub>	49	Little	7.5	Mild caustic
-10,000ppm PbO	26	81	8.6	pH increase
-0.1M NaOH (Deaeration)	57	Little	9.9	Caustic: Susceptible to PbSCC
-10,000ppm PbO (Deaeration)	24	78	9.9	
10,000ppm PbO (Non deaeration)	35	48	9.9	
-10wt% NaOH (Deaeration)	55	17	10.4	Strong caustic
-10,000ppm PbO (Deaeration)	33	31	10.4	Susceptible to PbSCC
-40wt% NaOH (Deaeration)	61	Little	10.9	Strong caustic
-10,000ppm PbO (Deaeration)	63	5	10.9	Relatively less susceptible

Table 3. Elongation to rupture and SCC ratio obtained from SSRT test in various aqueous solutions at 315°C

Alloy 690 which consists of 60% Ni, 30% Cr and 10% Fe is not susceptible to stress corrosion cracking in mild caustic solution such as 0.1M NaOH with or without lead while Alloy 690 is very sensitive to stress corrosion cracking in highly caustic solution such as 2.5M NaOH solution, which is more aggravated with Pb (Kim and Kim, 2009). From this it was found that Alloy 690 is not immune to SCC but relatively stronger than Alloy 600.

HTMA Alloy 600 was more susceptible to PbSCC in deaerated solution rather than non-deaerated 0.1M NaOH solution. Pb electrodeposition is not available in non-deaerated solution while Pb is electrodeposited spontaneously in deaerated solution. This indicates that Pb electrodeposition is more important to PbSCC rather than PbO itself. It was also reported that lead ion can be incorporated by occupying a cation site in an oxide producing a metallic dissolution, which could introduce a lattice mismatch leading to a passivity degradation of the oxide and lead could be incorporated into the film as an oxide itself causing the passivity degradation by using the current transient experiment (Kim et al., 2010).

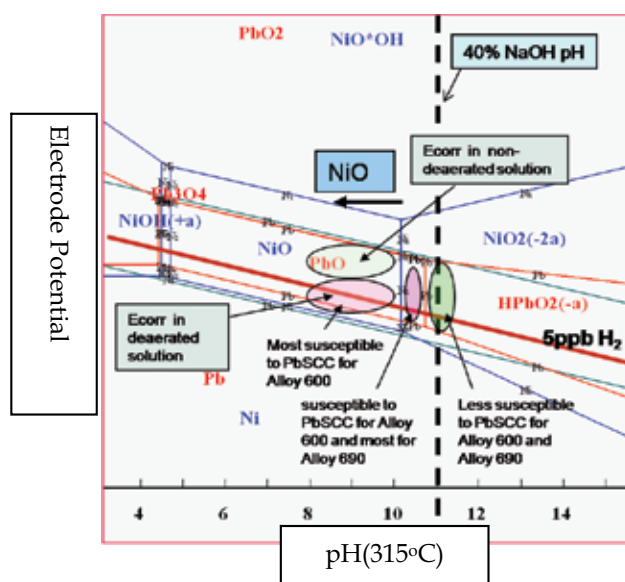


Fig. 9. E-pH diagram at 315°C

From the SSRT and EIS results, it was found that a better passivity improves the SCC resistance. In general, a repassivation of a more passive oxide is faster than that of a less passive oxide in the passive range leading to an SCC resistance. Moreover cracks initiate and propagate through unavoidable breakdowns and alterations of a surface oxide formed naturally on Alloy 600 in an aqueous solution indicating that a passivity is closely related to SCC resistance. Besides passivity, it was reported that the oxide ductility was degraded by lead incorporation into the solution (Lu et al., 2008).

It is notable that Ni among metallic elements which is a major element consisting of Alloy 600 was mainly depleted as shown in Figs. 1 and 5. For this reason, the kinetics of reactions should be considered. Generally, according to the E-pH diagram at a high temperature (HSC chemistry database), the lead contaminants could be reduced and deposited on an

oxide surface as a metallic form, or incorporated into the passive layer as lead ions or a lead oxide, depending on the OCP by the presence of a lead contamination in the secondary-side cooling water of operating NPP.

E-pH diagram at 315°C was shown in Fig. 9. Stable phases of Ni and Pb are also seen. SCC susceptible region for Alloy 600 and Alloy 690 was indicated in the figure.

### 3.4 PbSCC inhibitor

Fig. 10 presents the elongation to rupture as a function of the high temperature pH of leaded solutions without/with NiB for HTMA Alloy 600. An addition of NiB into the solution obviously enhances elongation to rupture.

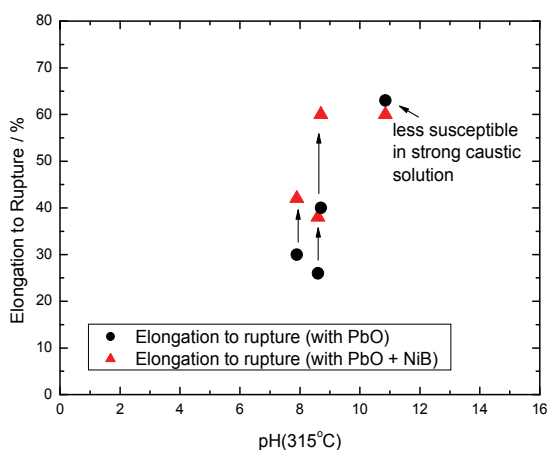


Fig. 10. Elongation to rupture as a function of the pH of leaded solutions without/with NiB for HTMA Alloy 600 (Kim, D.-J. et al., 2010)

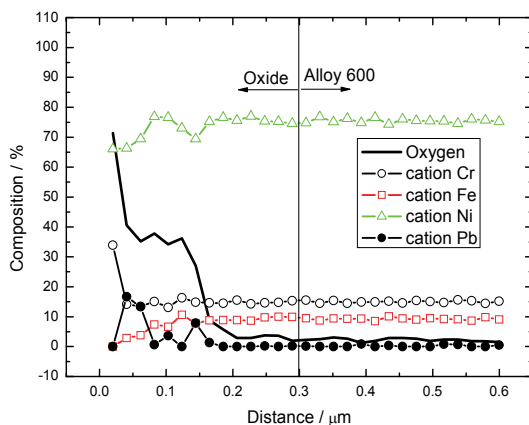


Fig. 11. TEM-EDXS analysis for the in-depth chemical compositions for the surface oxide layer formed on the TT Alloy 600 specimen in leaded 0.1M NaOH solution with NiB at 315°C

Fig. 12 is the XPS results for the specimens tested in the ammonia solution in the presence of PbO and PbO + NiB. Fig. 12 (a) reveals that the lead is incorporated into the oxide layer as a metallic state (136.7 eV) and as a lead oxide (138.9 eV). The lead content in the oxide was significantly decreased by adding NiB to the solution. Fig. 12 (b) is a plot of the XPS intensity against the sputtering time for the metallic lead and lead oxide. The amount of incorporated lead in the oxide was significantly decreased with the sputtering time. It was also found that the amount of incorporated lead was smaller and the lead inclusive layer was thinner in the specimen tested in the solution with NiB. Less incorporation of lead in the oxide led the enhancement of SCC resistance.

In the leaded solution with the NiB inhibitor, the amount of lead in the oxide layer was significantly reduced and the extent of the Ni depletion in the oxide was also decreased as shown in Fig. 11, compared with the results of Fig. 5.

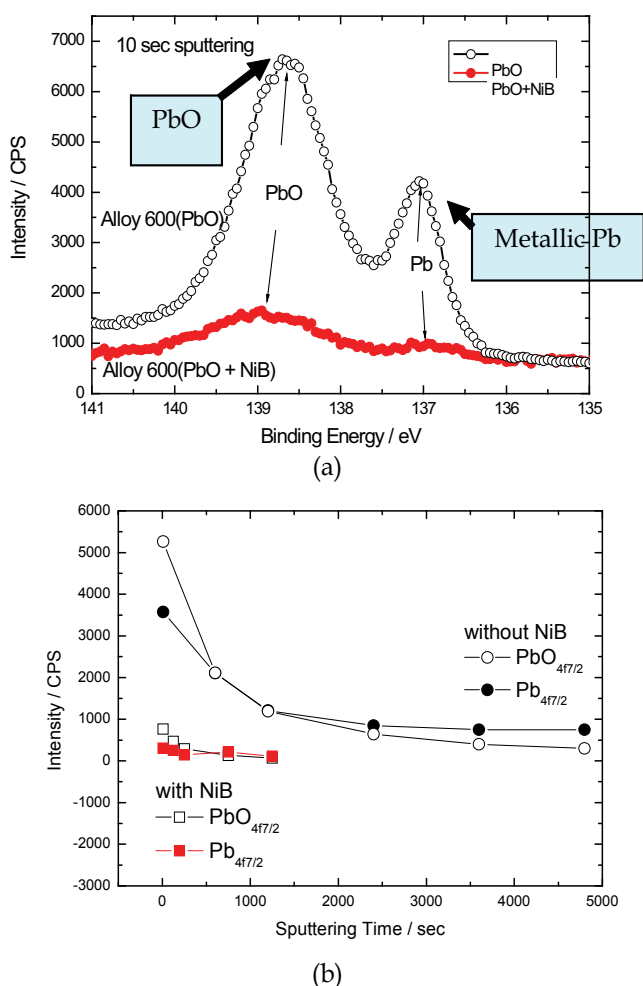


Fig. 12. (a) X-ray photoelectron spectra for surface oxide layer formed in leaded solution without/with NiB inhibitor at 315°C and (b) intensity versus sputter time for PbO (4f7/2) and Pb (4f7/2) (Kim, D.-J. et al., 2010)

It is worthwhile to note that an impedance value obtained in the lead solution with the NiB as shown in Fig. 13 significantly increased, compared with the impedance value obtained in the absence of NiB (Fig. 6). The impedance spectrum showed a clear capacitive arc but the inductive loop which appeared in the lead solution did not appear. The impedance spectrum resembled the spectrum for the reference solution rather than that for the lead solution. It was revealed again that the tendency of SCC resistance was consistent with passivity.

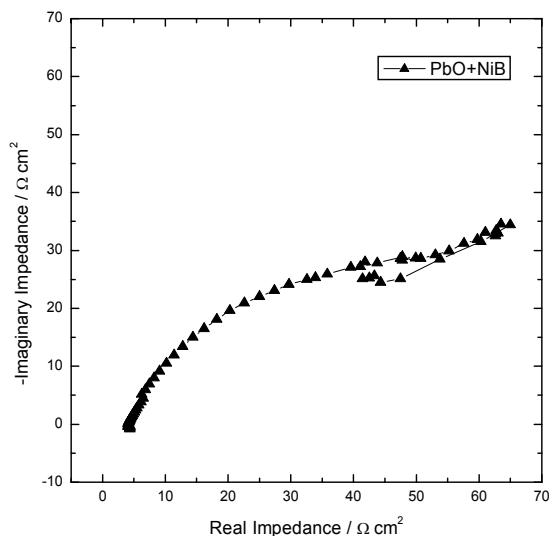


Fig. 13. Nyquist plot obtained from the electrochemical impedance measurements for the TT Alloy 600 immersed in the 0.1M NaOH solution with PbO + NiB at 315°C

From the results of SCC and oxide analysis, it was suggested that a lead incorporation in a surface oxide degrades an oxide passivity, which is related to a SCC susceptibility. By adding NiB into a solution, less incorporation of lead in an oxide retards the oxide degradation significantly leading to an improvement of its SCC resistance.

In Fig. 14, wetting angle obtained for the surface of Alloy 600 as a function of the solution is shown. Wetting angle was decreased as PbO and PbO+NiB were added into a high purity water as a reference solution. According to equation (12), we can consider two limiting cases.

$$\gamma_{SL} + \gamma_{LV} \cos \theta = \gamma_{SV} \quad (12)$$

where  $\gamma_{SL}$ ,  $\gamma_{LV}$ ,  $\gamma_{SV}$  and  $\theta$  represent the surface energy between a solid(Alloy 600) and a liquid(solution), the surface energy between a liquid and a vapor(air), the surface energy between a solid and a vapor and the wetting angle of a droplet between a solid/liquid and a liquid/vapor, respectively.

First, in the case of a complete wetting, the wetting angle is zero and  $\gamma_{SL} + \gamma_{LV} = \gamma_{SV}$ , which means that  $\gamma_{SV}$  is so large that a droplet is completely wetted. Second, in the case of a zero wetting, the wetting angle is 180° and  $\gamma_{SV} + \gamma_{LV} = \gamma_{SL}$ , which means that  $\gamma_{SL}$  is so large that a droplet is not wetted at all. In reference to the zero wetting case, it is expected that a

decrease of the wetting angle indicates a decrease of the surface energy between a solid and a liquid when  $\gamma_{LV}$  and  $\gamma_{SV}$  are not changed significantly by adding additive into a solution. From the result of Fig. 14, PbO is preferentially adsorbed on the Alloy 600 surface when PbO is added into an aqueous solution leading to a lead incorporation in a surface oxide. However, the wetting angle was decreased more when PbO and NiB were added into a solution simultaneously. This indicates that the NiB introduced into a solution competes with the PbO to adsorb on the surface of Alloy 600 and is more preferentially adsorbed on it leading to a lesser incorporation of lead in the oxide as shown in Figs. 11 and 12. As shown in Figs. 1 and 2, the thickness of the oxide layer whose composition was similar to the chemical composition of the oxide layer formed in a solution without NiB was increased by the addition of NiB without PbO. Moreover the addition of NiB into a solution without PbO did not reveal any detrimental effect on the SCC resistance (Yi et al., 2005). Therefore, a fast adsorption of NiB on the Alloy 600 surface at an early stage of an exposure in an aqueous solution can affect an oxide properties and hence its SCC resistance. Inhibitive mechanism of NiB should be clarified more in the future.

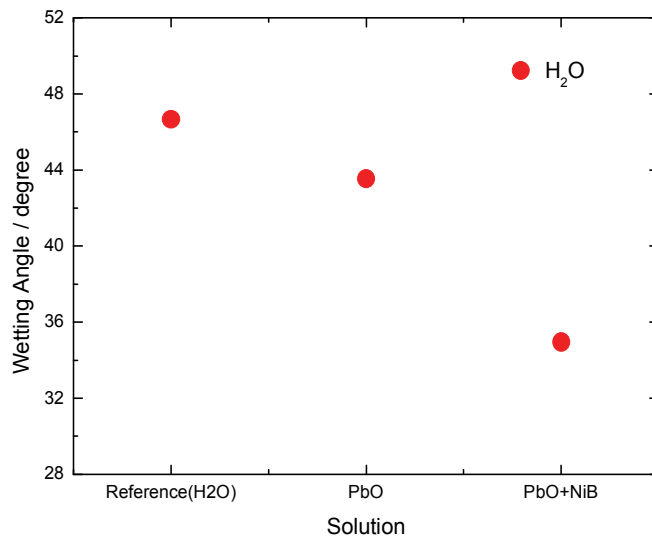


Fig. 14. Wetting angle obtained for Alloy 600 at 315°C as a function of an ammonia solution: (a) without additive (reference solution), (b) with PbO and (c) with PbO and NiB (Kim, D.-J. et al., 2010).

#### 4. Conclusions

The results are summarized as follows.

1. In the unleaded mild caustic solution, a relatively passive duplex oxide layer, i.e., porous nickel-rich outer layer (NiO and Ni(OH)<sub>2</sub>) and dense chromium-rich inner layer (Cr<sub>2</sub>O<sub>3</sub>) was formed while the duplex oxide layer was not observed and cations were



- depleted by lead incorporation in the oxide layer formed in the leaded mild caustic solution.
2. Lead was incorporated into the oxide layer as a metallic state and a lead oxide state. Lead incorporation into the oxide degraded the oxide passivity leading to the SCC susceptibility.
  3. From the thermodynamic considerations supplemented by the experimental results in the high temperature leaded solution, the Ni as a Ni oxide state as well as the Ni as a metallic state can be depleted unlike Cr and Fe. Moreover cations in the oxide can be depleted by the Pb electrodeposition. The Pb incorporation would prevent the passive oxide formation composed of Ni, Cr, Fe and O.
  4. HTMA Alloy 600 was susceptible to a PbSCC in a mild alkaline solution rather than a strong alkaline solution, whereas Alloy 690 was very susceptible to a SCC as well as PbSCC in highly caustic solution.
  5. PbSCC was significantly reduced by adding NiB as an inhibitor, which was consistent with the reduction in an incorporated Pb amount and the increase of electrochemical impedance, accompanied with a significant recovery of the cation depletion. The passivity of the surface oxide was increased in the order of the surface oxide formed in a solution with PbO, PbO+NiB and a reference solution, which was in good agreement with the order of the SCC resistance. It is anticipated that the fast adsorption of NiB on the Alloy 600 surface at an early stage of an exposure in an aqueous solution can affect an oxide properties and hence its SCC resistance.

## 5. Acknowledgement

This work was funded by Korea Ministry of Education, Science and Technology.

## 6. References

- Castano-Marin, M. L.; Gomez-Briceno & D. and Hernandez-Arroyo, F. (1993). *Proc. of 6<sup>th</sup> Int. Symp. on Environmental Degradation of Materials in Nuclear Power Systems-Water Reactors*, p. 189, San Diego, CA, Aug. 1-5.
- Fruzzetti, K. (2005). *Workshop of Effects of Pb and S on the Performance of Secondary Side Tubing of Steam Generators in PWRs*, ANL, IL, May 24-27.
- HSC Chemistry Database, 6.0.  
[Http://www.lasurface.com](http://www.lasurface.com).
- Hwang, S. S.; Kim, H. P. & Lim, Y. S. & Kim, J. S. & Thomas, L. (2007). *Corrosion Science*, Vol. 49, 3797.
- Joint Committee on Power Diffraction Standards (JCPDS) - International Centre for Diffraction Data (ICDD) CD 2001(Card No. 47-1049).
- Joint Committee on Power Diffraction Standards (JCPDS) - International Centre for Diffraction Data (ICDD) CD 2001(Card No. 74-0326).
- Kim, D.-J.; Kim, H. P. (2009). *Proc. of 6<sup>th</sup> CNS Int. Steam Generator Conference*, p. 32, Toronto, Ontario, Nov. 8-11.
- Kim, D.-J.; Kim, H. P. & Hwang, S. S. & Kim, J. S. & Park, J. (2010). *Met. Mater. Int.*, Vol. 16, 259.
- Kim, D.-J.; Kwon, H. C. & Kim, H. P. (2008). *Corrosion Science*, Vol. 50, 1221.

- Kim, D.-J.; Lim, Y. S. & Kwon, H. C. & Hwang, S. S. & Kim, H. P. (2010). *J. of Nanoscience and Nanotechnology*, Vol. 10, 85.
- Kim, U. C.; Kim, K. M. & Lee, E. H. (2005). *J. Nuclear Materials*, Vol. 341, 169.
- Lu, B.; Luo, J. & Lu, Y. (2008). *Workshop on Detection, Avoidance, Mechanisms, Modeling, and Prediction of SCC Initiation in Water-Cooled Nuclear Reactor Plants*, Beaune, Burgundy, France, Sept. 7-12.
- Machet, A.; Galtayreis, A. & Zanna, S. & Klein, L. & Maurice, V. & Jolivet, P. & Foucault, M. & Combrade, P. & Scott, P. & Marcus, P. (2004). *Electrochim. Acta*, Vol. 49, 3957.
- McIntyre, N. S.; Zetaruk, D. G. & Owen, D. (1979). *J. Electrochem. Soc.*, Vol. 126, 750.
- MULTEQ calculation performed at ANL (2008).
- Pourbaix, M. (1966). *Atlas of Electrochemical Equilibria in Aqueous Solutions*, Pergamon press Ltd.
- Rincón, M. E.; Trujillo-Camacho, M. E. & Miranda-Hernández, M. & Cuentas-Gallegos, A. K. & Orozco, G. (2007). *J. Nanoscience and Nanotechnology*, Vol. 7, 1596.
- Robertson, J. (1989). *Corrosion Science*, Vol. 29, 1275.
- Sarver, J. M. (1987). *EPRI Workshop on Intergranular Corrosion and Primary Water Stress Corrosion Cracking Mechanisms*, p. C11/1, NP-5971, EPRI, Palo Alto.
- Staehle, R. W. (2003). *Proc. of 11<sup>th</sup> Int. Symp. on Environmental Degradation of Materials in Nuclear Power Systems-Water Reactors*, p. 381, Stevenson, WA, Aug. 10-14.
- Vaillant, F.; Buisine, D. & Prioux, B. & Gomez Briceno, D. & Castano, L. (1996). *Eurocorr 96*, p. 13/1, Nice.
- Wright, M. D. & Mirzai, M. (1999). *Proc. of 9<sup>th</sup> Int. Symp. on Environmental Degradation of Materials in Nuclear Power Systems-Water Reactors*, p. 657, Newport Beach, CA, Aug. 1-5.
- Yi, Y.; Eom, S. & Kim, H. & Kim, J. (2005). *J. Nucl. Mater.*, Vol. 347, 151.

# Burst and Leak Behaviour of SCC Degraded SG Tubes of PWRs

Seong Sik Hwang, Man Kyo Jung, Hong Pyo Kim and Joung Soo Kim  
*Korea Atomic Energy Research Institute  
Republic of Korea*

## 1. Introduction

Steam generators of Pressurized Water Reactor (PWR) have suffered from many types of corrosion, such as pitting, wastage and stress corrosion cracking (SCC) in the primary and secondary sides (Kim 2003, MacDonald, 1996). Some failure events of steam generator tube have been reported in some nuclear power plants around the world (MacDonald, 1996). In order to prevent the primary coolant from leaking into the secondary side, the tubes are repaired by sleeving or plugging (Benson, 1999). It is important to establish the repair criteria to maintain the plugging ratio within a plugging limit which allows successful plant operation.

In the international steam generator tube integrity program (ISG TIP) supported by the US NRC (Nuclear Regulatory Commission), tasks such as in-service inspection technology development, and studies on steam generator tube degradation modes had been undertaken. As a part of the cooperation work, leak and burst tests were carried out, and the burst behaviour of axial mechanical flaws was studied. Leak rate from archive tubes were measured under different water pressures in order to understand the leak behaviour under operating and accident conditions of PWRs.

## 2. Experimental

### 2.1 Burst pressure measurement of mechanical notched specimens

Various types of axial (longitudinal along the tube) EDM notches were machined on SG tubes of 195 mm long. The tubes were 19.05 mm in outside diameter, and 1.07 mm in thickness as shown in Table 1. They were fabricated from high temperature mill annealed alloy 600, of which the yield strength and ultimate tensile strength were 241 MPa and 655 MPa, respectively. The leak rate and ligament rupture pressure for the part through-wall defects were measured for the tubes at room temperature. The lengths of the part through-wall defects ranged from 5 mm to 62 mm.

Tests with 100 % axial through-wall defects were carried out to measure tube burst pressure at room temperature. The lengths of the 100% through-wall defects ranged from 12 mm to 30 mm. A flexible plastic tube is usually used for the through-wall defect to ensure leak tightness during the pressurization (Cochet, 1991). In this test, however, it was attempted to obtain crack opening displacement (COD) variation during a slow pressurization. Flexible

Tygon™ tubes (bladder) of 175 mm long were used for 100% through-wall tubes in both slow pressurization and fast pressurization.

Number of tests	Tube Dimension, mm	Flaw type	Flaw length, mm	Flaw depth % TW*	Bladder
33	19.05 OD x 1.07 t	EDM notch Axial	5-62	50, 60, 75, 80, 100	With or Without

\*% TW = % through wall penetration depth

Table 1. Information on the tested tubes

To determine the impact of the pressurization rate on the rupture/burst pressure, different pressurization rates were applied for the same types of tube defects. Water leak rates just after the ligament rupture or burst were measured by a balance; water coming out of the failed tube was collected in a plastic container for designated time, and the leak rate was calculated by dividing the amount of water by time. The water flow rate through the tubes and the pressures versus time were recorded on a computer. Evolutions of the crack opening during the pressurization were recorded using a conventional digital camera. The length and depth of the defects of the tubes were measured using eddy current, and the tubes were transferred to the leak and pressure test.

Table

Leak rate tests were performed for the degraded tubes specimens at room-temperature using a high pressure leak-rupture test facility (Fig. 1).

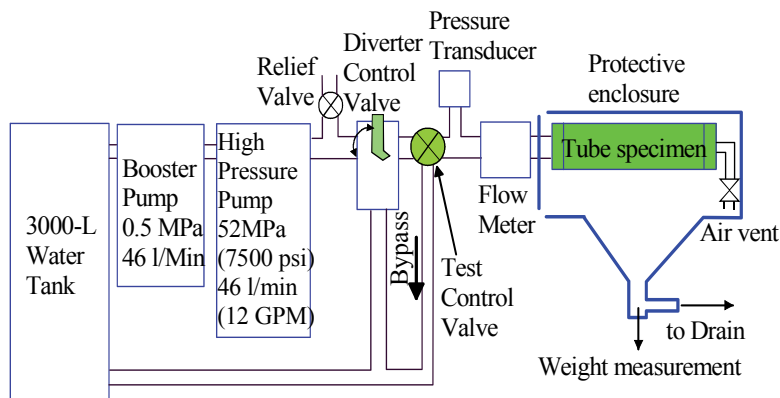


Fig. 1. High pressure leak and burst test facility

## 2.2 Development of SCC tubes

Laboratory induced stress corrosion cracks were developed in steam generator tube specimens using the ANL SCC production facility and the techniques described in reference (Diercks 2000). Two heats of Korean archive alloy 600 tubes (Heat NX 9824, NX 6312, Carbon 0.024 %) were used in the work. The alloy 600 tubings, which have a 19.05 mm outer diameter and a 1.07 mm wall thickness, are mill annealed at high temperature. The tube specimens, which are 356 mm long, were sensitized at 600 °C for 48 hours in a vacuum tube

furnace. In order to avoid any oxidation on the surface of the tubes, the furnace was vacuumed and back filled with helium and hydrogen gas mixture three times. The surface of the tubes was abraded by emery paper # 600 followed by acetone cleaning before being subjected to the SCC development.

The outside diameters (OD) of the tube specimens were exposed to 1 M sodium tetrathionate solution at room temperature and pressurized with nitrogen gas to a pressure of 20.7 MPa. The cracking procedure was stopped when a pressure drop on the tube was observed, indicating that a leak had occurred. The time to form the through wall crack varied from 69 hours to 607 hours depending on the tube. Crack development test conditions and results for each tube are shown in Table 2. The length and depth of the defects of the tubes were checked by the eddy current method, and the tubes were transferred to the leak and pressure test step.

Tube ID	Crack type	SCC Time(hours)	Cursory ECT
SGH001	OD axial	68.8	OD, 95%/5.08mm, 90%/11.43mm
SGH002	"	67.8	Axial indication(1)
SGH005	"	68.8	90%/15.2mm
SGH006	"	68.8	Axial indication(1)
SGH009	"	404	OD, 80%/10.2mm
SGH010	"	607	OD, 85%.5.08mm
SGH012	ID axial	264	ID, 100%. 24mm

(1) Not quantified

-Material: Alloy 600 HTMA ->Sensitized for 48 hrs @ 600 °C

-SCC developed in 1 M Na<sub>2</sub>S<sub>4</sub>O<sub>6</sub> at Room Temp.

Table 2. Laboratory Stress Corrosion Cracking of the Archive Tubes

### 2.3 Large leak rate measurement

Leak rates in the degraded tubes were measured in a room-temperature, high-pressure test facility and a high-temperature, pressure test facility. The room temperature test facility is equipped with a water pressurizing pump, a test specimen section, a control unit and is described in NUREG/CR-6511 (Diercks 1998). In this facility, the first leak from the tube can be detected by eye through the transparent plastic window, and the leak rate at a given pressure can be measured by weighing the water from the leak. The pressure was held at 10.8, 13.8, 17.2, 20.7 and 27.6 MPa for 5 to 10 minutes to determine the variation of the leak rate with the pressure. For some tubes, the burst pressures were determined.

A high temperature pressure test was undertaken to investigate the leak behaviour at the PWR operating temperature of 282 °C. The high-temperature facility consists of a high temperature water reservoir and a test section where the temperature of the specimen and the pressure difference across the tube are controlled. The maximum pressure difference in this test is around 19.3 MPa. Details of this facility are also described in NUREG CR-6511 (Diercks 1998).

During the first stage of the room temperature pressure testing, the pressure at the first leak, the leak rate at certain pressures and the burst pressures were determined. Two specimens,

SGH002 and SGH006, were prepared for this work. In the second stage of the test, 0.7 MPa pressure increments and 4 to 10 minute holds were adapted to obtain the first leak pressure and leak rate changes with time. The pressurization was stopped when a measurable leak rate could be obtained to avoid an unstable burst, which makes the metallography harder. Specimens SGH001, SGH005, SGH009, and SGH010 were used for this analysis.

For the high temperature pressure test, specimens SGH005 and SGH012 were used. The pressure was raised to 8.3 MPa and held for 45 minutes and then increased to 19.0 MPa slowly while checking for an indication of a leak at the muffler at the exit of the test section.

## 2.4 Time dependent leak rate measurement

The inside of the tube was pressurized with water. The water pressure was increased until the tube shows a leakage. The first leak from the tube can be detected visually by the naked eye through a transparent plastic window. The leak rate at a given pressure was measured by weighing the water from the leak. The pressure was held at a certain value for a designated time to measure a leak rate. The water pressure was then increased further while opening the crack. The pressurization was stopped when no increase of the leak rate was recorded. Leak rates were measured under constant pressures at different elapsed times in order to observe a change of the leak rate with time.

## 2.5 Leak rate prediction method

Leak rate based on the prediction model developed by ANL was adapted in order to analyse the leak behaviour of the archive tubes (Majumdar 2000). The equation used in the analysis is:

$$Q = 50.9 \times 106 A (P/\rho)^{0.5} \text{ [l/min]} \quad (1)$$

Where A is the crack opening area in m<sup>2</sup>, P is the pressure difference across the tube wall in MPa, and  $\rho$  is the density of the water in kg/m<sup>3</sup> (1000 kg/m<sup>3</sup> at room temperature, 735 kg/m<sup>3</sup> at 282 °C). Fracture mechanics analyses were done to calculate the crack opening area, using the methods described in Refs (Majumdar 2000, Zahoor 1989). In the case of the Korean tubes that had been heat-treated as part of the process for producing SCC, the yield stress was considered to be the same as the received materials based on a prior experience with heat treatment. Yield stress for a high temperature calculation was estimated to be 10% lower than that at the room temperature (Majumdar 2000). Yield stress of 265.5 MPa and 248.2 MPa for UC4 and YG5,6 respectively was used for the room temperature evaluation. In the case of a high temperature calculation for SGH005, 221.3 MPa was used as the reduced yield stress in the leak rate calculation at 282 °C.

# 3. Results and discussion

## 3.1 Crack opening displacement of axial notches

COD as a function of the applied pressure is important in the modeling of a ligament rupture or the burst pressure in SG tubes. In the preliminary test, the COD increased a little as the pressure increased during the slow pressurization as shown in Fig. 2. When the pressure reached 10 MPa, the flaw began to show a COD increase. The COD corresponding to an applied pressure of 36 MPa was larger than that corresponding to 10 MPa. Whereas the tube integrity was sustained before ligament rupture, a small pressure increase of 1 MPa

caused the tube ligament rupture followed by a burst. Finally, the tube showed a fish-mouth like opening as shown in Fig. 2.

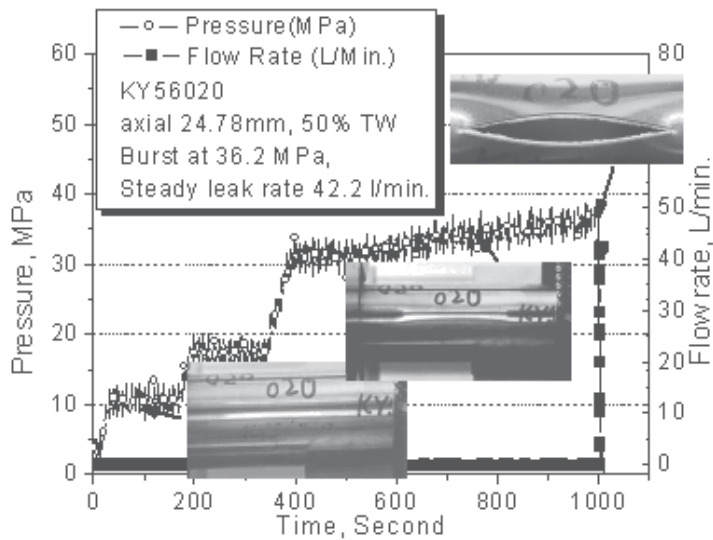


Fig. 2. Crack opening behaviour of a part through-wall flaw

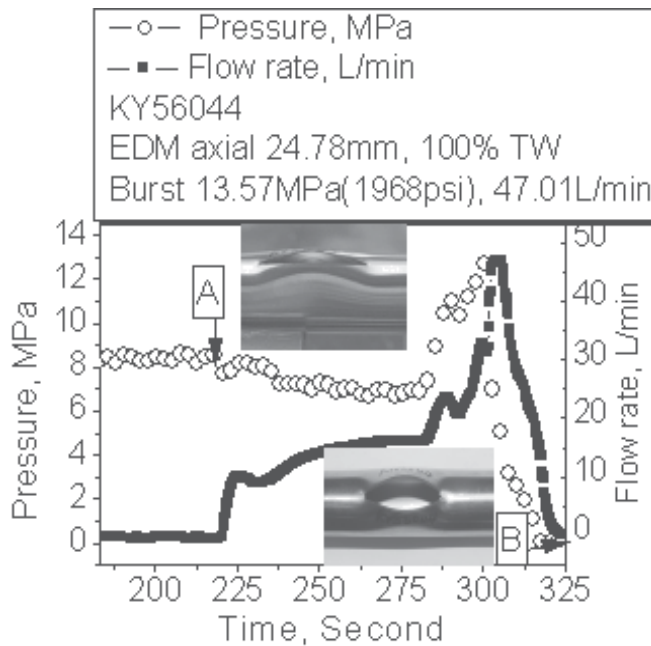


Fig. 3. Crack opening behaviour of a 100% through-wall flaw

Through-wall defect tubes showed a larger COD than that of the part-through-wall defect tubes at the same pressure as shown in Fig. 3. The 175 mm long bladder inserted inside the 25 mm long 100% TW defect tube (KY56044) was perforated at 4.5 MPa, a water jet came out

of the bladder. The bladder extruded out of the defect when the pressure reached at 8.5 MPa. A hole in the bladder was enlarged at a constant pressure, and then the COD of the tube increased for 2 to 3 seconds. There was an extrusion of the bladder throughout the tube opening followed by a tube rupture. The opening was not evaluated quantitatively in this test.

### 3.2 Effect of the defect depth and length on the rupture/ burst pressure

Burst pressures as a function of the defect depth are plotted in Fig. 4. Closed symbols and open symbols are obtained in the present study and acquired from another research group (Cochet, 1991), respectively. Rupture pressures have a linear dependency with defect depth. These results suggest that the rupture pressure of the part through-wall tubes depends rather on the defect depth than on the defect length.

In the case of the 100% through-wall defects, they showed a strong length dependency from about 12 MPa for a 50 mm long defect to 45 MPa for a 7 mm long defect. Fig. 5 shows the rupture pressures as a function of the defect length. Closed symbols were obtained in the present study. Rupture pressure of 50 % TW defect and 75 % TW are around 35 MPa and 20 MPa, respectively regardless of their length from 25 mm up to 62 mm. Short defects below 25 mm, however, showed a dependency with the defect length.

### 3.3 Relationship between the flow rate, defect depth and defect length

Flow rates after the rupture of the part through-wall defect tubes were measured. Defect depths were 50% and 75 % of the wall thickness, and the defect lengths ranged from 25 mm to 62 mm. Regardless of the defect types, the flaws showed a similar flow rate of around 45 l/min, which was the maximum flow capacity of the testing system as shown in Fig. 6.

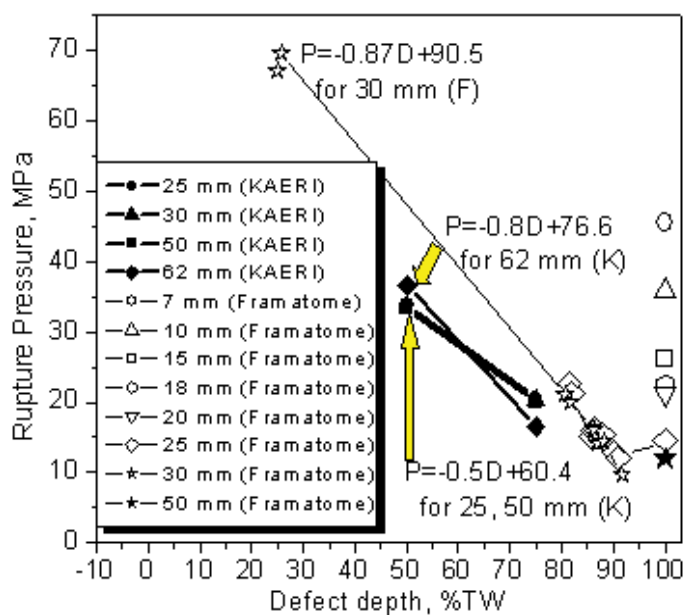


Fig. 4. Effect of the defect depth on the burst pressure



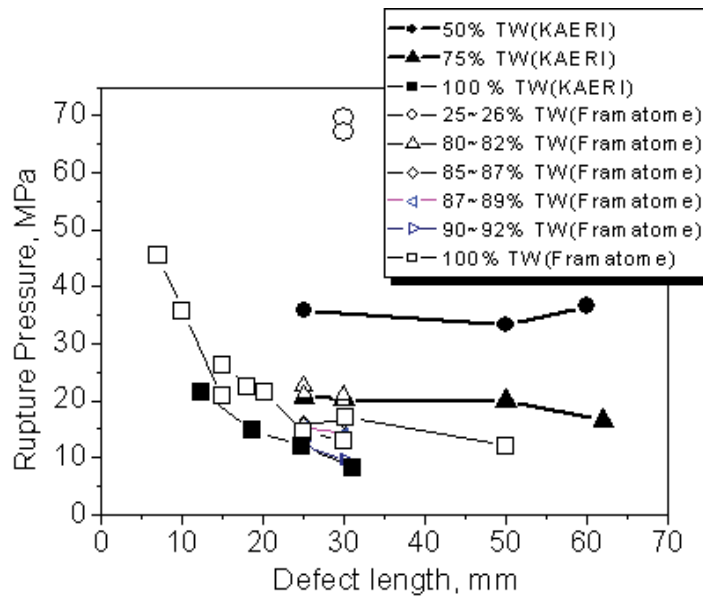


Fig. 5. Effect of the defect length on the burst pressure

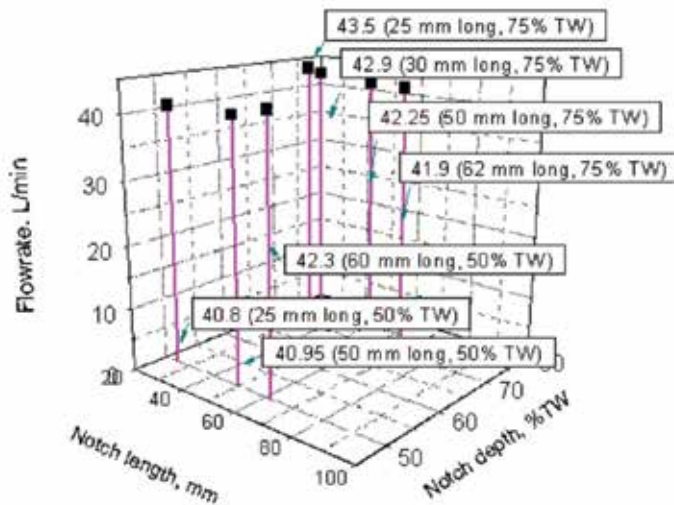


Fig. 6. Relationship among the length, depth and flow rate of the part through-wall defects

### 3.4 Effect of the pressurization rate on the burst pressure of a through-wall defect

A through-wall defected tube showed three stages of rupture behaviour as presented in Fig. 7; flexible plastic tube burst (stage A), the tube hole enlarged (stage B), and finally, the SG tube burst (stage C). The pressure dropped from 6 MPa to 2 MPa when the flexible plastic tube burst. When the internal water pressure increased as in stage B, the flow rate increased. The tube burst occurred at about 9 MPa.

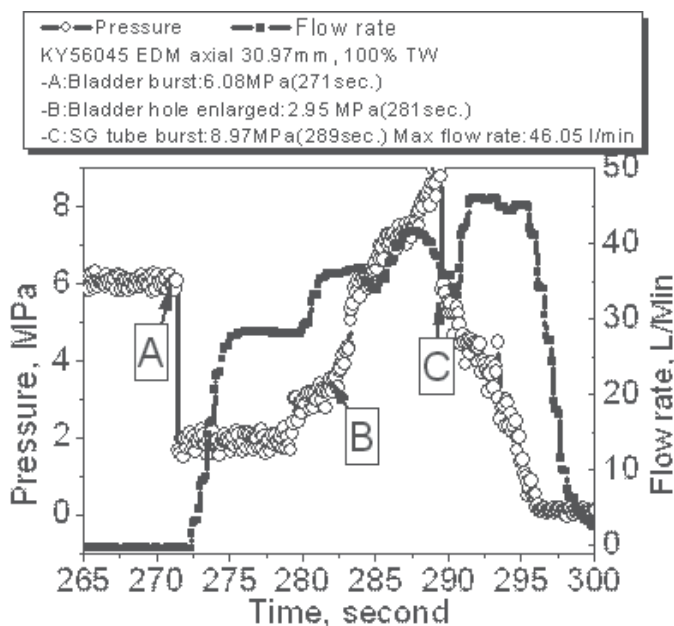


Fig. 7. Burst behaviour of a through-wall defect tube in a slow pressurization

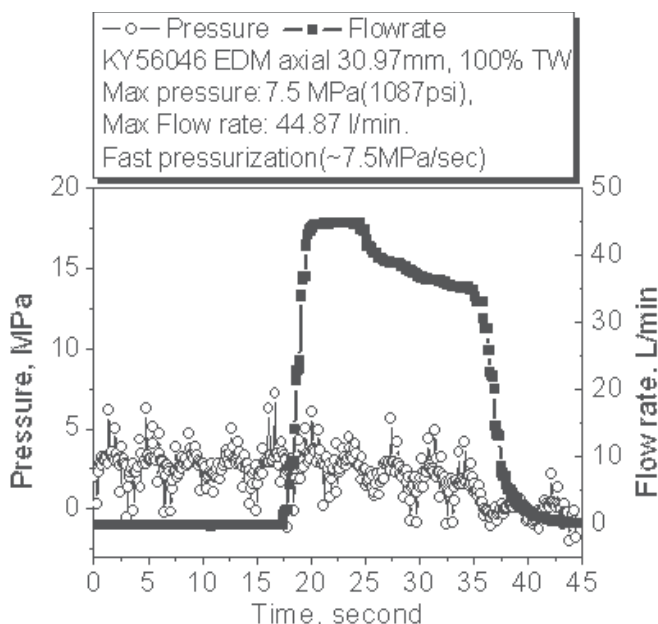


Fig. 8. Burst behaviour of the through-wall defect in a fast pressurization

Fast pressurization led to a different burst behaviour as shown in Fig. 8. The pressurization rate was about 7.5 MPa/sec (1087 psi/second). A pressure fluctuation between 3 MPa and 7 MPa was recorded. Maximum flow rate was achieved 2 seconds after the tube burst. Burst pressure of the tube was about 7.5 MPa, which is smaller than that of a slow pressurization

(9 MPa). It has been reported that there was no burst pressure difference between fast and slow tests without a foil (Keating, 2001). It has also been reported that if a foil reinforcement was used in the fast tests, an average burst pressure increased would be about 25 %. In case of the part through-wall defects, the ligament rupture pressure was reported to increase when the pressurization rate increased (Kasza, 2002). In this test, however, the two tubes were not equipped with a foil. It is considered that the reinforcement effect of the foil was not shown, the tube with the slow pressurization showed a high burst pressure due to the toughness of the bladder itself.

Failure morphologies after the burst of the through-wall defect with a bladder in the two pressurization modes are shown in Fig. 9. The flexible plastic tube extruded out of the SG tube after the burst in the slow pressurization mode, while the plastic tube was torn like a fish mouth in the high pressurization mode. The SG tube failure morphologies, however, are similar. This explains that the flow rates after the SG tube burst are similar at about 45 l/min.

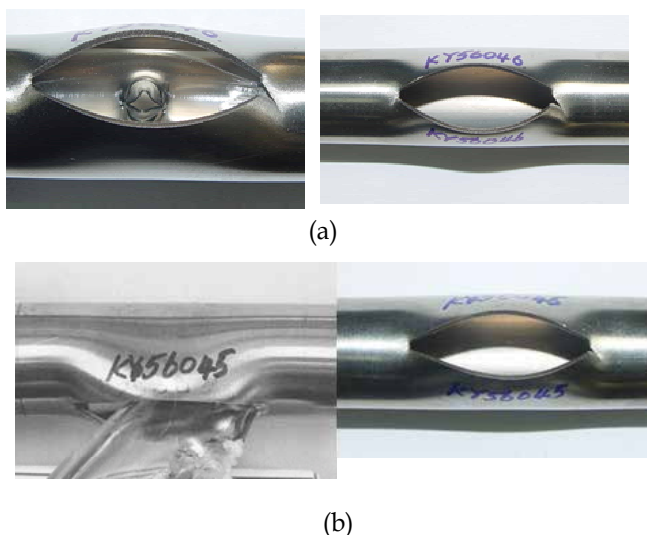


Fig. 9. (a) Fast Pressurization: Fish mouth like failure of the bladder: Burst at 7.5 MPa  
(b) Slow Pressurization: Squeezed out of the bladder Burst at 8.9 MPa

### 3.5 Room temperature pressure test

The first leak was detected at 17.2 and 24.3 MPa for specimens SGH002 and SGH006, respectively. These pressures are similar to those used in the cracking procedure, 20.7 MPa at which it was confirmed that the tube contained a 100 % through wall crack produced by SCC under nitrogen gas pressure. A droplet was formed on specimen SGH002 at 17.2 MPa, but it did not grow any more during a 5 minute hold at that pressure. At 22.0 MPa, the leak rate increased to one drop every 3 seconds. The leak rate was 0.24 l/min at 29.6 MPa and 4.28 liter/min at 34.5 MPa, and the specimen ruptured at 35.9 MPa. Fig. 10 shows the crack of SGH002 after the pressure and leak test done at room temperature. The crack was torn like a fish mouth, which was formed during the rupture at 35.9 MPa, and the length was about 11 mm.

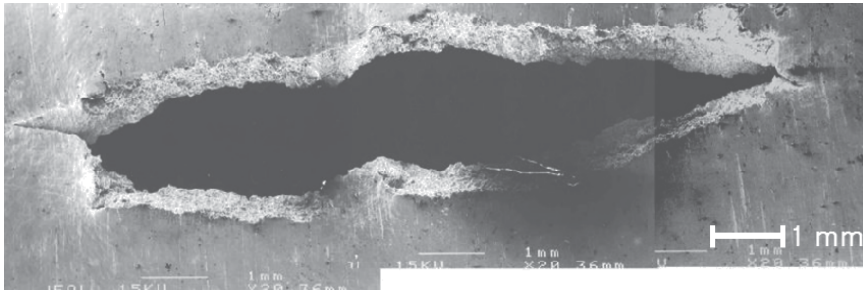


Fig. 10. Crack morphology of SGH002 taken by SEM after the pressure/leak test at room temperature

Specimen SGH006 developed a water spray at 23.4 MPa, which subsequently decreased to a droplet flow with a drop occurring every 4 seconds. It showed a leak rate of 0.27 l/min at 27.6 MPa and 3.87 l/min at 34.5 MPa and ruptured at 39.3 MPa. This tube did not show a leakage at 10.8 MPa and 17.2 MPa.

The pressure test results are summarized in Table 3. Though both tubes had a 100 % through wall penetration, they did not leak at the operating pressure of 10.8 MPa. So, throughwall cracking is not a sufficient criterion for a detectable leakage. On the contrary, the crack opening or tightness is more important for showing a certain amount of the leak rate.

Tube ID	Cursor HCT(Effective crack length, mm)	Leak test RT(4) or 282°C	Leak @10.8 MPa(5)	First leak, MPa	Spray starts MPa	Leak rate 1, l/min	Leak rate 2, l/min	Burst pressure or final leak rate MPa
SGH001	OD, 95%/5.08mm, 90%/11.43mm	RT	No leak	one drop/6sec @25.0	27.4	0.19 @31.7	0.25 @31.7	-
SGH002	Axial indication(3)(10.5mm)	RT	No leak	one drop @17.2	28.3	0.24 @29.7	4.28 @34.5	35.9
SGH005	Before pressurized: 100%/12.7mm After pressurized: 90%/15.24mm	282 °C	No leak	18.6	Leak @18.6, but disappeared after 15 min, No more leak @ 19.0			
SGH005 (1)	After Heat treating (600°C 4 hrs.)(Before RT pressure test) : 100%/15.24mm	RT	Spray @ 0.41 MPa	-	0.23 l/min @10.8	0.32 @17.2	0.31 @19.0	0.43 @20.7
SGH005 (2)	"	RT	Pressurization at 6.9MPa/sec, Leak rate of 44.28 l/min at peak pressure of 34.5 MPa					
SGH006	Axial indication(3)(12.3mm)	RT	No leak	one drop @23.4	23.4	0.27 @27.6	3.87 @34.5	39.3
SGH009	Axial OD, 80%TW/10.16 mm	RT	No leak	one drop @20.7	21.8	0.019 @24.1	0.023 @24.1	0.023 @24.1(7)
SGH010	Axial OD, 85%TW/5.08mm	RT	No leak	one drop @22.8	21.8(6)	0.13 @29.7	0.16 @29.7	0.16 @30.0(7)
SGH012	Axial ID, 100%TW/24mm	282 °C	No leak					
"	"	RT	-	-	atomized spray@8.3	0.020 @8.3	6.99 @28.3	-

Material: Alloy 600 HTMA->Sensitized for 48 hours @ 600 °C

(1) Room temperature pressure test with same tube used at 282 °C(without bladder), (2) Unstable Burst test (with bladder)

(3) Not quantified, (4) RT: Room temperature, (5) Normal operating pressure difference in a PWR

(6) one drop/5 sec, one drop/9sec @ 22.8 MPa, no more drop for 1 min @24.1 MPa, and then one drop/7sec @24.1 MPa, one drop/one sec @24

(7) 10 min interval between the measurements.

Table 3. History of the pressure test for archive tubes

In the second stage of the test, specimens SGH001, SGH009, and SGH010 did not leak at 10.8 MPa, which is the nominal normal operating pressure difference, even after a 5 minute hold time. The first leak pressures of the specimens SGH001, SGH009, and SGH010 were 25.0, 20.7, 22.8 MPa respectively, even though these tubes showed a nitrogen gas leak at 20.7 MPa during crack development. The first leaks were in the form of a single water drop forming every 4 to 8 seconds. The droplet changed into a water jet after the pressure was increased by an additional 2.4 MPa. Leak rates were measurable above the pressure at which an actual jet formed. The initial leak rates for each specimen were 0.19 l/min at 31.7 MPa for SGH001, 0.019 l/min at 24.1 MPa for SGH009, and 0.13 l/min at 29.7 MPa for SGH010. For all three tubes, the leak rates increased with time due to an increase in the crack opening areas at a high pressure, but then they reached a constant leak rate after about 30 minutes.

Fig. 11 shows specimen SGH001 after the pressure test at room temperature. Two or more cracks are linked with each other along the axial direction, and they showed different opening areas.

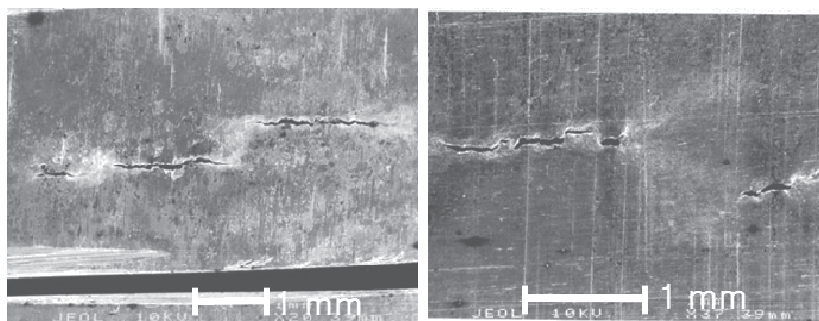


Fig. 11. Flaws on SGH001 after the pressure/leak test at room temperature

Crack length on the inside of the tube is shorter than that on the outside of the tube. It is considered to arise from two factors; one of them is the inside pressurization procedure and the other is the crack development procedure in which the crack is initiated on the outer surface. The effective crack length, which controls the leak rate, is considered as the shorter length on the inner surface. The relationship between the leak rate and crack length is shown in Fig. 12.

The room temperature pressure test for tube SGH005 was carried out after the high temperature pressure test, which is described later in this section. The tube demonstrated a non-measurable leak in the high temperature pressure test. After the high temperature pressure test, where a non-measurable leak was detected, the specimen was heat tinted at 600 °C for 4 hours to simplify the metallography.

The crack seemed to open during the heat tinting, and showed a jet spray at 0.4 MPa, a leak rate of 0.23 l/min at 10.8 MPa and 0.43 l/min at 20.7 MPa. Fig. 13-(b) shows the crack after the room temperature pressure test, the length of the flaw increased a little, but other features such as crack opening do not appear to be very different from that in Fig. 13-(a), which was obtained after the high temperature pressure test. In order to determine the unstable burst pressure of the flaw, SGH005 was pressurized with a pressurization rate of 6.9 MPa/second. Leak rate was 44.28 l/min at the peak pressure of 34.5 MPa. There was no big change in the flaw length even after the unstable burst, whereas the crack opening increased.

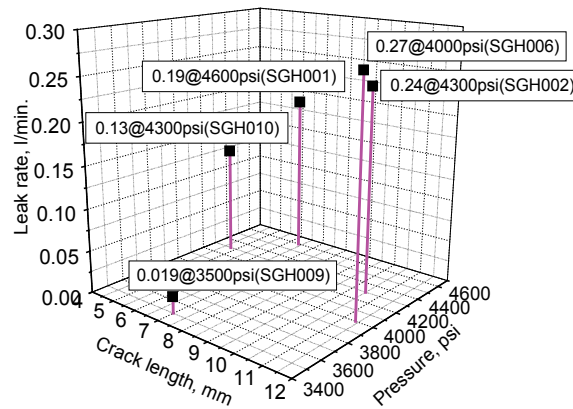


Fig. 12. Relationship between the crack length, pressure and leak rate (1000 psi = 6.9 MPa)

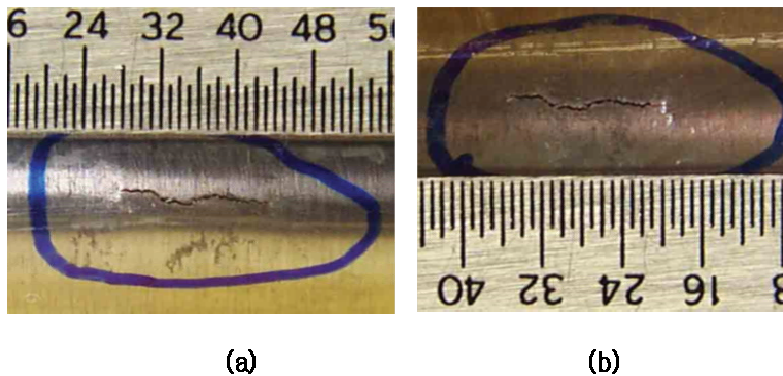


Fig. 13. Flaws on SGH005 after (a) High temperature pressure test, (b) Room temperature pressure test

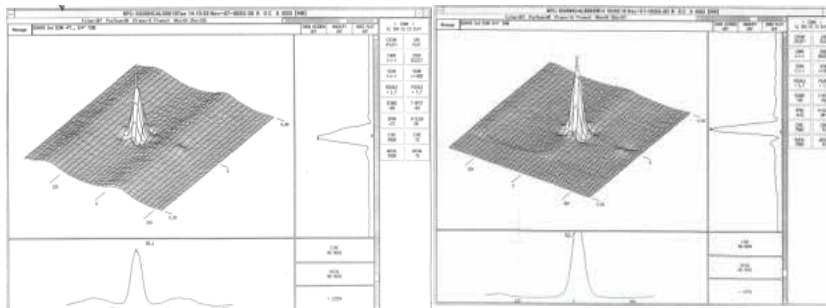


Fig. 14. Eddy current examination for SGH005, (a) before HT pressure test, (b) after HT pressure test



### 3.6 High temperature pressure test

Specimen SGH005, which had been confirmed as a 100 % through wall crack during the crack development, was subjected to the high temperature pressure test first. The tube did not show a leak until the pressure was 18.6 MPa. At the internal pressure of 18.6 MPa, steam was detected at the end of the muffler of the test facility. The leak rate was considered to be as low as 0.1 l/min. The leak, however, stopped after 55 minutes; no further steam was detected even after the pressure increased to the maximum value possible of 19.0 MPa in the facility. After holding it at the maximum pressure for about 10 minutes, the test was stopped and the specimen was cooled down for further testing by using the room temperature test facility.

This behaviour may be interpreted as due to a crack closure effect inside the tube while opening up the outer crack by the internal pressure. ECT (Eddy current test) indicated that the effective length of the crack after the pressure test decreased to 12.7 mm from 15.2 mm, whereas, the EC voltage increased to 99 volts after the pressure test from 30 volts before the pressure test as shown in Fig. 14. These ECT results suggest that a crack closure could have occurred during the pressurizing. However, the ECT results and the leak behaviour could be fortuitous.

SGH 012, which had an inside crack of 23 mm long, showed a similar behaviour at 282 °C. It did not show a leakage at 17.2 MPa for 135 minutes. But it showed a water spray at 8.3 MPa during the room temperature leak test.

### 3.7 Leak rate prediction

This work analyzed three specimens, SGH001, SGH009 and SGH010, which were pressurized to different levels and then the stable leak rates were measured before the final unstable burst.

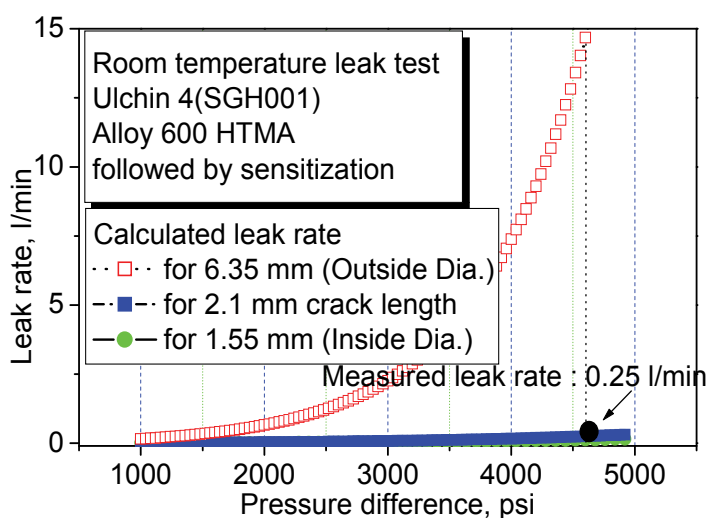


Fig. 15. Comparison of the calculated and measured leak rate for the tube SGH001 (1000 ps i= 6.9 MPa)

Four different pressures were applied to obtain the leak rate from SGH001. The first leak from the tube was recorded at 25.0 MPa in the form of a single water droplet. A leak rate of

that kind of drop is considered as less than 0.01 l/min, the calculated crack length based on the leak rate model described in section 2.3 was about 0.6 mm. A measurable leak rate was obtained at 31.7 MPa, it changed a little with time at that pressure. According to the leak rate model, the calculated crack length was 2.10 mm for the final leak rate of 0.25 l/min as shown in Fig. 15. Crack lengths of the main crack of this tube were 3.85 mm and 1.55 mm outside and inside respectively. The calculated crack length of 2.1 mm was between the measured inside diameter crack length and the outside diameter. From the difference of the crack lengths between the measured and calculated one, it is considered that some of the final leak rate came from the minor cracks. The calculated crack length is also based on a simple rectangular model of the crack shape. The opening of the crack is clearly not going to be as constrained as it would be for a 1.55 mm long rectangular crack. When the pressure reached 31.7 MPa, the calculated leak rate for the 1.55 mm crack was 0.12 l/min. The measured value of 0.25 l/min is close to the calculated value for the 2.10 mm crack.

In the case of SGH009, a leak rate of 0.023 l/min was obtained at 24.1 MPa. The calculated crack length was 1.0 mm, which is longer than the inside crack length and much shorter than the OD crack length. The measured leak rate of 0.023 l/min is for the leak rate line for the 1.0 mm crack length as shown in Fig. 16. This means that the effective length of the flaw in SGH009 is also between the measured inside and outside diameter crack lengths.

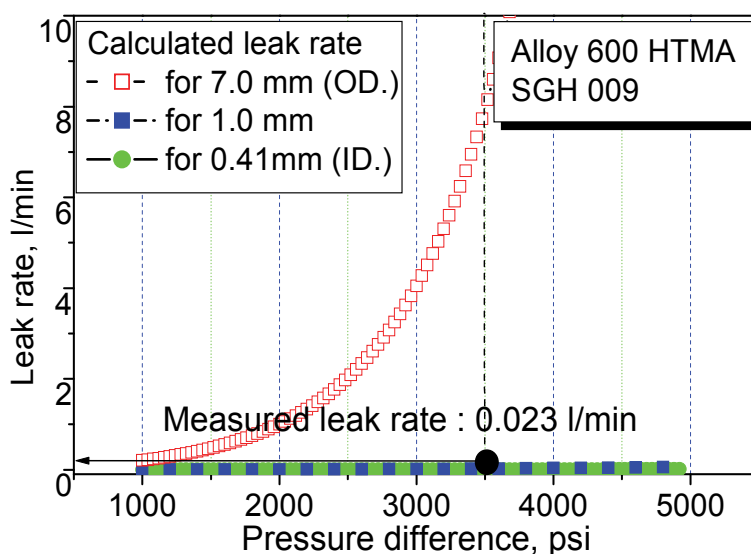


Fig. 16. Comparison of the calculated and measured leak rate for the tube SGH009 (1000 psi = 6.9 MPa)

Fig. 17 shows the relationship between the leak rate and the effective crack length of tube SGH010. Like tube SGH001, this tube showed a time dependent increase of the leak rate. Final leak rate was 0.16 l/min at 29.6 MPa, and this corresponds to an effective crack length of 1.9 mm. The calculated crack length was longer than the measured inside diameter crack length of 1.07 mm. Unlike tube SGH001, both tubes had effective crack lengths significantly greater than the limiting inner diameter length. This may be due to the larger ratio of the outer to inner diameter crack length, which leads to a lessened constraint on the crack opening.



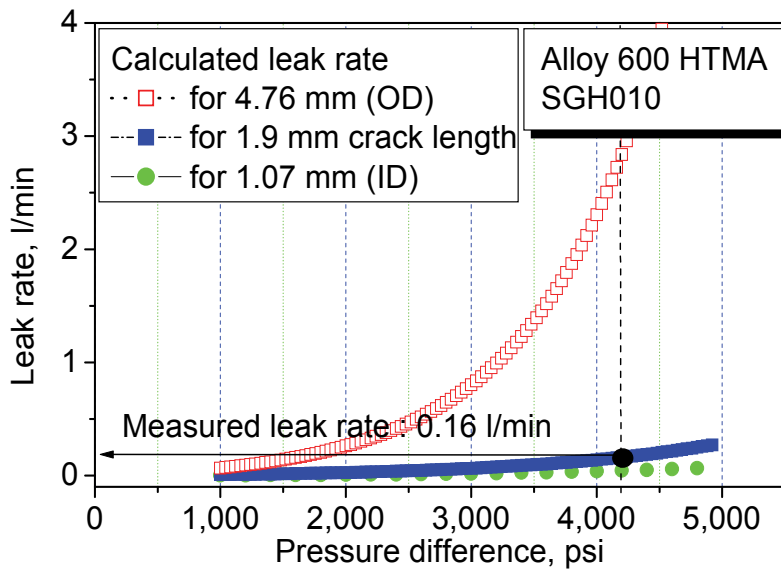


Fig. 17. Comparison of the calculated and measured leak rate for the tube SGH010

### 3.8 Time dependent leak rate evolution of SCC cracks

The measured leak rates were compared with those of the estimated ones based on the leak rate model developed by Argonne National Laboratory (Majumdar 2000). The SCC flaws have a characteristically different flow path through crack surface and showed a different leak behaviour from that of mechanically machined flaws. Several SG tube specimens with various SCCs were tested for the present investigation (Table 4).

Specimen No.	Flaw ID	Flaw type	COA [mm <sup>2</sup> ]	Length [mm]
KY56066	flaw-1	Axial	0.059	3.51
	flaw-2	"	0.038	3.766
	flaw-3	"	2.073	11.1
KY56068	flaw-1	"	0.648	15.04
	flaw-2	"	0.282	7.29
KY56069	flaw-1	Circumferential	0.069	8.586
	flaw-2	"	0.23	7.269
	flaw-3	"	0.027	4.13
KY56070	flaw-1	"	0.123	6.97
	flaw-2	"	0.082	6.02

Table 4. Feature of the cracks developed on the SG tubes

Fig. 18 shows the typical behaviour of the pressure and leakage rate during a water pressurization on a degraded SCC tube. In the case of the KY56065 specimen, the main crack opened at 42 MPa and a leakage began to be recorded. As the pressure increased, the crack opening area also increased. It was considerably torn at 48 MPa, and the water pressure decreased while the flow rate increased. A further increase of the water pressure at the test

time of 670 seconds enabled the crack to open further. Consequently, the leak rate rapidly increased.

Fig. 19 shows the crack features after the burst test. An initial leakage came from the circumferential cracks and a following leakage was originated from the axial ones. This is because the depth and length of the circumferential cracks are much deeper and longer than those of the axial ones respectively. On the other hand, it is also because the hoop stress is two times larger than the axial stress during a water pressurization.

The measured leak rate and an estimated one based on the leak rate model (Majumdar 2000) are shown in Fig. 20. The final measured pressure and leak rate are presented in this figure, and the photos in Fig. 19 were also obtained after a final pressurization at 31 MPa. The measured leak rate of 27.52 l/min at 31 MPa corresponds to an equivalent crack length of 6.7 mm which is calculated from the leak rate model. Then the length of the main crack after the burst was 5 mm long, and there are multiple cracks, whose lengths were 1 mm to 5 mm as shown in Fig. 19. Since the cracks are not singular, it is hard to compare the measured crack length with the estimated one.

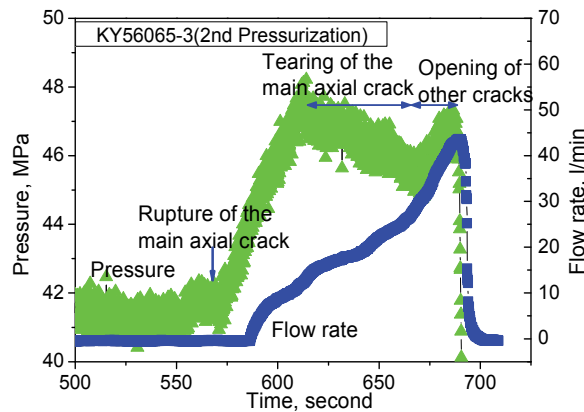


Fig. 18. Leak behaviour for a degraded SCC tube at room temperature

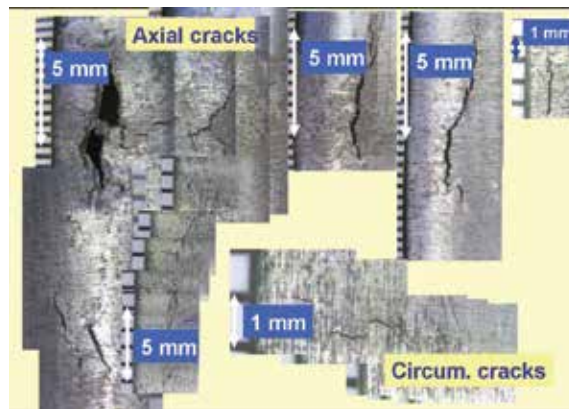


Fig. 19. Feature of the cracks after the burst test of the KY56065 specimen

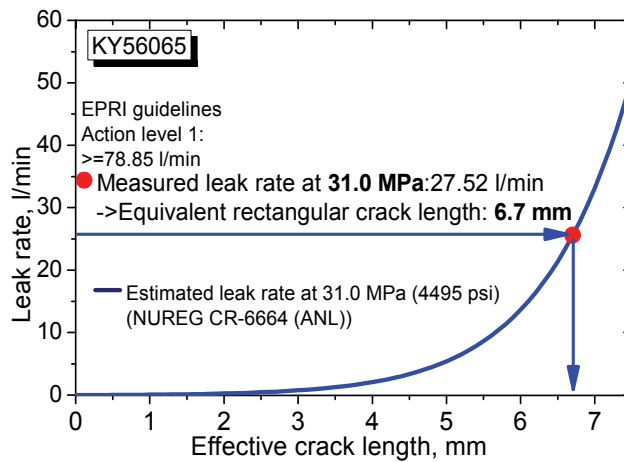


Fig. 20. Comparison on the leak rate measured and estimated based on the leak rate model

The tube showed different leak rates depending on the internal water pressure as depicted in Fig. 21. When considering a pressure difference of 8.5 MPa between the primary and secondary side of the SG tubes, the leak rate of 0.81 l/min at 26 MPa is not that big. On the other hand, the leak rate model estimates a rate of 0.32 l/min for a 6.7 mm long crack at 8.5 MPa. It can be said that multiple cracks of over 5 mm in length on a tube do not reveal the action level 1 (78.85 l/min) of the EPRI leakage guide line (EPRI, 2000).

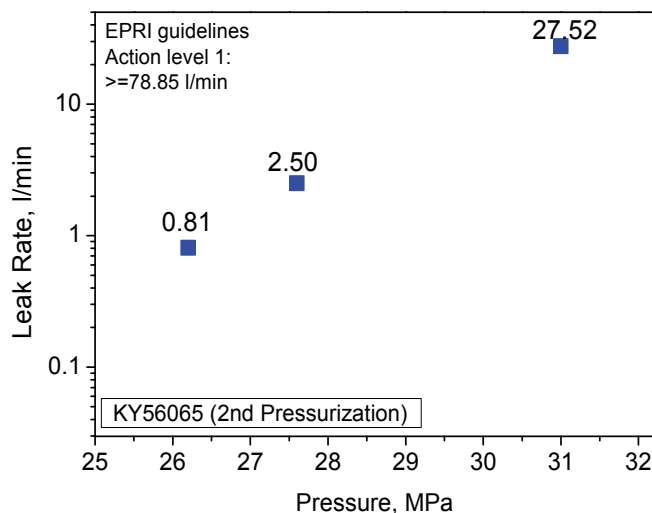


Fig. 21. Dependency of the leak rate on the pressure of a SCC degraded SG tube

The length of the cracks observed in operating steam generators is generally less than 10 mm long, as shown in Fig. 22. Based on the leak rate evaluation from the present work, these cracks might show a negligible leakage even when they are throughwall.

Leak rate from the SCC flaws at a constant pressure showed different behaviours depending on the crack tightness, crack length, or surface morphology of the cracks as shown in Fig. 23. and Fig. 24. A small increase in the leak rate was observed for one specimen (KY56069).

The specimen of KY56069 might have a tight crack, so it did not show a leak increase with the time at a constant pressure. The fact that the type of crack was circumferential seems to be another reason for the leak behaviour. The other specimen, KY56068, however, showed a distinct increase of the leak rate with the time at a constant pressure as shown in Fig. 24. As indicated in Table 4, COA (Crack Opening Area) of the KY56068 is much larger than that of KY56069. Longer crack length of KY56068 also explains the increasing leak rate with time at a constant pressure.

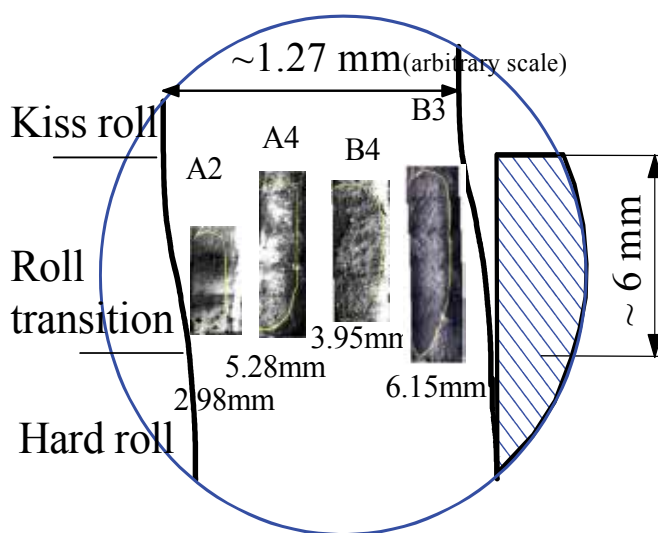


Fig. 22. Feature of the cracks from an operating steam generator

#### 4. Conclusions

While the tube integrity was sustained before the burst, a small pressure increase of 1 MPa caused a tube ligament rupture followed by a burst. For the studied flaw length from 25 mm up to 62 mm, burst pressure of the part through-wall tubes depends rather on the defect depth than on the defect length. Flow rates after a ligament rupture of the part through-wall defect or a burst of the through-wall defect tubes were similar. Burst pressure of a through-wall defect in a fast pressurization was smaller than that of a slow pressurization.

Although all the specimens had 100% throughwall cracks developed under a pressure of 20.7 MPa, none leaked at the plant operating pressure in water. In this test, the outside crack length was at a maximum 17 times longer than the inside crack in a tube. The first leak in the form of a water droplet was detected between 17.2 MPa and 24.8 MPa depending on the flaws. Burst pressure of the through wall crack of 10 mm long was 35.9 to 39.3 MPa. Calculated leak rate for a crack length relatively close to the inside diameter crack length

(which is much smaller than the outer diameter crack length for the cracks in these tests) fits the measured leak rate well.

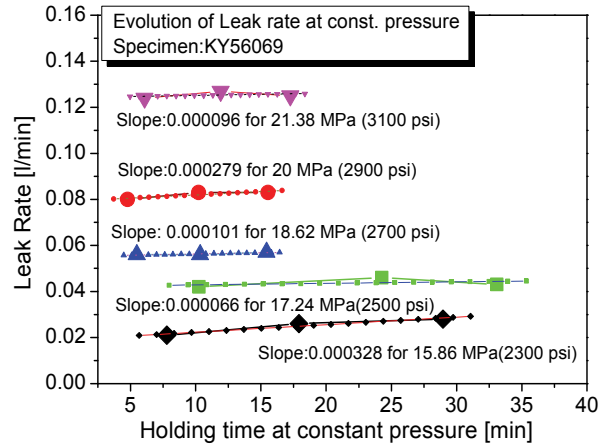


Fig. 23. Leak rate behaviour for the tight corrosion crack at a constant pressure

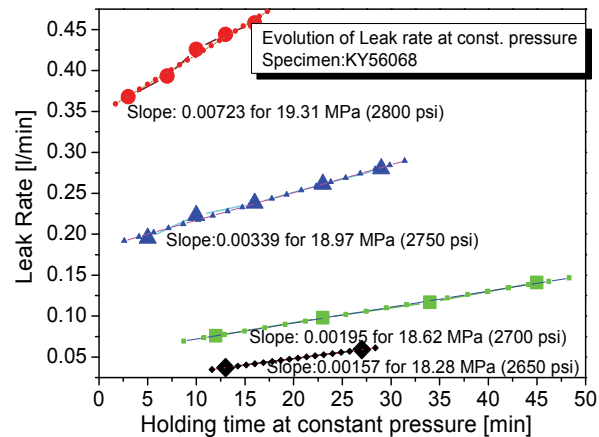


Fig. 24. Leak rate evolution for the large open crack at a constant pressure

SCC crack showed a ligament rupture at the first stage of the pressure test, then a tearing of the main crack and an opening of the crack followed. Measured leakage rate from the SCC flaws agreed reasonably with the estimated value of the leak rate model. Multiple cracks of over 5 mm in length on a tube showed a much lesser leakage rate than the EPRI leakage guidelines, action level 1 (78.85 l/min). The large open and long axial crack showed an increasing leakage rate with the time at a constant pressure.

## 5. Acknowledgement

This work was funded by Korea Ministry of Education, Science and Technology.

## 6. References

- Benson, J., 1999, Steam generator progress report , EPRI TE-106365-R14.
- Cochet, B., 1991, Steam generator tube integrity, EPRI NP-6865L vol. 1.
- Diercks, D.R., Bakhtiari S., et al., 1998, Steam generator tube integrity program-annual report, NUREG/CR-6511, Vol.2, Argonne National Laboratory.
- Diercks, D.R., Bakhtiari, S., et al., 2000, Steam generator tube integrity program-annual report, NUREG/CR-6511, AN Vol.7, ANL-0014, Argonne National Laboratory
- Kim, J.S., Hwang, S.S., et al., 1999, Destructive analysis on pulled tubes from Ulchin unit 1 Korea Atomic Energy Research Institute.
- Kim, J.S, Hwang, S.S., et al., 2003, Destructive analysis on pulled tubes from Ulchin unit 4. Korea Atomic Energy Research Institute.
- MacDonald, P.E., 1996, NUREG/CR-6365, Steam Generator Tube Failures.
- Majumdar, S., Kasza, Ken, et al., 2000, Pressure and leak rate tests and Models for failure of flawed steam generator tubes, NUREG/CR-6664, Argonne National Laboratory.
- Zahoor, A., 1989, Ductile Fracture Handbook, Electric Power Research Institute, Palo Alto, CA.
- EPRI 104788 R2, PWR Primary To Secondary Leak Guidelines-Revision 2, Final Report, April (2000).

# In-situ Monitoring of SCC of Alloy 600 SG Tubing in PWR using EN Analysis

Sung-Woo Kim, Hong-Pyo Kim, Seong-Sik Hwang and Dong-Jin Kim

*Korea Atomic Energy Research Institute  
Republic of Korea*

## 1. Introduction

Nickel based alloys such as Alloy 600 and 690 have been used as the steam generator (SG) tubing materials in a pressurized water reactor (PWR) due to their high corrosion resistance. However, many types of corrosion have occurred in highly caustic environments containing some oxidizing impurities, especially in SG sludge piles, because the highly caustic conditions can be developed in the heated crevices of PWR SG's (Jacko, 1990). Among those impurities, Pb is well known to assist in stress corrosion cracking (SCC) of the SG tubing in the caustic environments (Sakai et al., 1990). Many authors reported on the cracking modes of SCC in Pb-contaminated solutions and the role of Pb on the passive films formed on nickel-based alloys to explain the mechanism of SCC (Hwang et al., 1997; Hwang et al., 1999; Kim et al., 2007; Kim et al., 2008).

Recently, there was an approach to investigate the mechanism by distinguishing between the initiation and propagation stages of Pb-assisted SCC using an electrochemical noise (EN) technique (Kim & Kim, 2009). The EN is defined as a fluctuation of the electrochemical potential or current which is observed experimentally to be associated with localized corrosion processes (Cottis et al., 2001; Stewart et al., 1992). From the analyses of the EN parameters such as the frequency of events, the average charge of events, the noise resistance (Al-Mazeedi & Cottis, 2004; Cottis, 2001; Sanchez-Amyay et al., 2005), and the mean free time-to-failure (Kim & Kim, 2009; Na & Pyun, 2007; Na et al., 20007a, Na et al., 2007b), various types of localized corrosion are distinguishable from each other. Therefore, the EN monitoring technique has become a useful tool for characterizing such localized corrosions as pitting corrosion, crevice corrosion and SCC.

This work is aimed to analyze the EN generated during Pb-assisted SCC of Alloy 600 at high temperature. The EN was measured from C-ring specimens in the highly caustic solution containing oxidizing impurities in two different ways: in a potentiostatic controlled current noise (PCCN) mode, the electrochemical current noise (ECN) was measured from the stressed C-ring specimen by applying an anodic potential. In an uncorrelated three electrode current and potential noise (UCPN) mode, the electrochemical potential noise (EPN) and the ECN were measured simultaneously from the stressed C-ring specimen. Changes in an amplitude and time interval of the ECN and EPN, and variations in power spectral density of the ECN and EPN were analyzed in terms of the initiation and propagation of Pb-assisted SCC of nickel-based alloys in the highly caustic solutions at high temperature.

## 2. Experimental

### 2.1 Preparation of C-ring specimens

Alloy 600 SG tubing (Valinox Heat No. NX8527) with 22.23 mm outer diameter (OD), 1.27 mm thickness was used for this work. The chemical composition of the materials is given in Table 1. The tubing was pilgered by the manufacturer, and heat treated in our laboratory at 920 °C for 15 min in an Ar-filled quartz capsule in a furnace, followed by water quenching, to simulate low-temperature mill-annealing (LTMA). The C-ring specimens were fabricated from the Alloy 600 SG tubing in accordance with the ASTM G38 standard. The OD surface of the specimens was ground by #1000 emery paper, and then cleaned with ethanol and water in sequence. The C-ring specimen was stressed to 150 % of its room temperature yield strength (YS) at the apex using an Alloy 600 bolt and nut.

C	Mn	Si	P	S	Ni	Cr	Ti	Al	Co	Cu	Fe
0.024	0.23	0.13	0.005	<0.001	74.90	15.37	0.28	0.20	0.016	0.009	8.84

Table 1. Chemical composition of the Alloy 600 materials (wt%)

### 2.2 Electrochemical noise measurements

Fig. 1 is a schematic of the C-ring test facility and the EN experiments (Kim & Kim, 2009). The EN measurements were carried out with a Zahner IM6e equipped with a Zahner NProbe. In the PCCN mode, only ECN was recorded between the stressed and unstressed specimens during applying an anodic potential of 100 mV vs. open circuit potential (OCP). No information about the EPN was obtained in the PCCN mode. On the other hand, in the UCPN mode, the EPN of the stressed specimen were recorded relative to a reference electrode simultaneously with the ECN between the stressed and unstressed specimens at OCP.

The reference electrode was an external Ag/AgCl/KCl (0.1 M) electrode, specially designed and constructed for high temperature and pressure applications (Toshin-Kogyo Co., UH type). For reliable measurements of the electrochemical potential, the reference electrode was reassembled and recalibrated frequently during the interruption of the test series. The sample interval and the frequency bandwidth were 0.5 s and 1 mHz ~ 1 Hz, respectively. The power spectral density and the frequency of events were calculated from each set of time records that consisted of 2,048 data points acquired for  $1 \times 10^3$  s.

### 2.3 C-ring immersion tests

In the PCCN mode, the test environment was an aqueous solution of 40 wt% NaOH containing 0.01 wt% PbO (leaded caustic solution). Pb-assisted SCC was accelerated by the potentiostatic method by maintaining the electrochemical potential in the active-passive range for Alloy 600 in caustic environments (Kim. et al., 2005). The C-ring tests in the PCCN mode were performed at 315 °C for 110 h.

In the UCPN mode, the tests were carried out in the leaded caustic solution, and that solution plus 500 ppm CuO. CuO was added to the leaded caustic solution to accelerate Pb-assisted SCC because CuO is a well-known oxidizing species that increases the corrosion potential and promotes Pb-assisted SCC (Jacko, 1990; Kim. et al., 2005). The C-ring tests in UCPN mode were performed at 290 °C for a total accumulated immersion time of 400 h, and



consisted of two phases of immersions in sequence; (a) 278 h in the leaded caustic solution (40 wt% NaOH with 0.01 wt% Pb) and (b) 122 h in that solution plus 500 ppm CuO. The addition of CuO caused an increase of the electrochemical potential by about 150 mV. The surfaces of the specimens were intermittently examined for cracking using an optical stereo-microscopy and scanning electron microscopy (SEM, JEOL JSM-6360).

Prior to the immersion test, the test solution was deaerated with 99.99 % nitrogen gas for 20 h. After the entire immersion test, the specimens were chemically etched with a solution of 2% bromine + 98% methanol, and then examined by SEM equipped with an energy dispersive spectrometer (EDS, Oxford-7582).

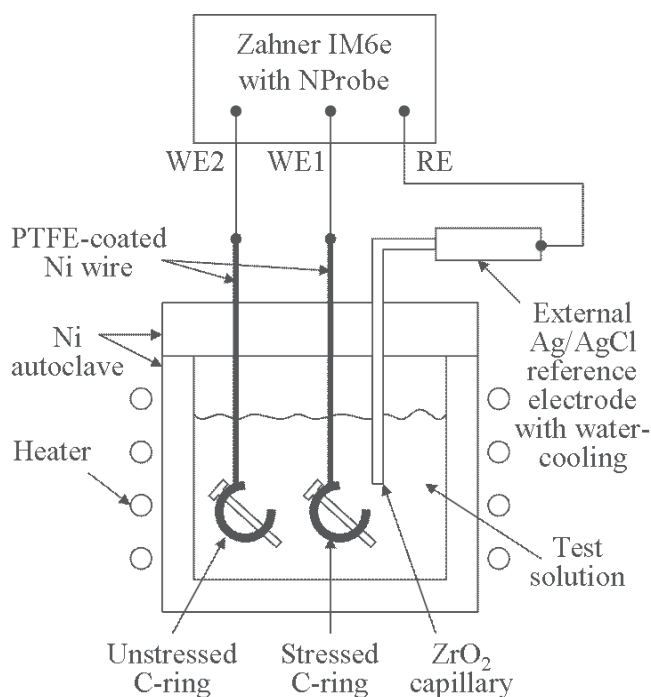


Fig. 1. Schematic of the C-ring test system and the electrochemical noise experiment

### 3. Results and discussion

#### 3.1 Spectral analysis of electrochemical noise in PCCN mode

Fig. 2 gives the time record of the ECN measured from the stressed C-ring specimen in the leaded caustic solution at 315 °C for 110 h by the EN technique in the PCCN mode. There were abrupt changes in the ECN after immersion for  $132 \times 10^3$  s (points B, C, D and E in Fig. 2), which have generally been observed during localized corrosions such as pitting corrosion, crevice corrosion, intergranular corrosion and SCC (Al-Mazeedi & Cottis, 2004; Cottis, 2001; Cottis et al., 2001; Kim & Kim, 2009; Sanchez-Amyay et al., 2005; Stewart et al., 1992). As compared with the ECN at point A, the ECN revealed repetitive current rises followed by fast decay with certain time interval in the time record at points B and C (see the insert in Fig. 2). This means that discrete events of a localized corrosion are occurring

from  $132 \times 10^3$  to  $158 \times 10^3$  s during the immersion in the leaded caustic solution. On the other hand, from  $185 \times 10^3$  to  $240 \times 10^3$  s, the ECN revealed current increases followed by slower decay with longer time interval in the time record at points D and E, indicating the occurrence of a localized corrosion event inducing larger charge passage than that at points B and C.

In order to correlate the changes of the ECN with the cracking stages, the test was interrupted and the surface of the specimen was examined for cracking at accumulated immersion times of 22, 42 and 110 h. After the immersion test in the leaded caustic solution for 22 h, the extensive examination of the surface of the specimen ruled out any cracking. At the accumulated immersion time of 42 h, it turned out that there were many defect sites such as local break-down of the surface oxide film and micro-cracks initiated with depth of one grain boundary or less in the OD surface from the SEM analysis of the C-ring apex as shown in Fig. 3(a). After the entire immersion test for 110 h, one of micro-cracks was propagated as presented in Fig. 3(b). The crack was propagated in an intergranular (IG) mode and the crack mouth and tip were covered by a surface oxide film, which is typical of SCC of Alloy 600 in leaded caustic environments (Hwang et al., 1997; Hwang et al., 1999; Kim et al., 2007; Kim et al., 2008). The chemical composition of the surface film was analyzed with EDS, and summarized in Table 2, along with the chemical composition of the Alloy 600 matrix.

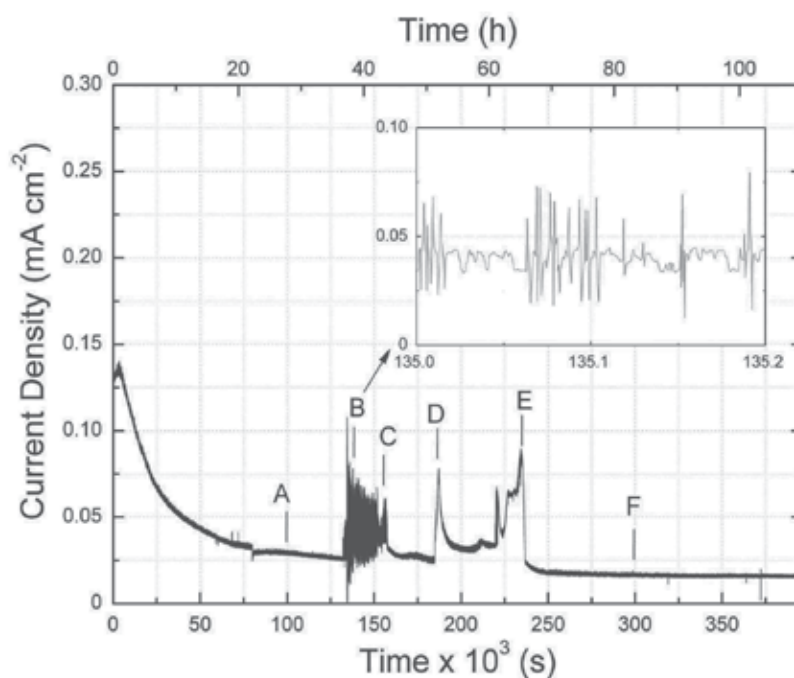


Fig. 2. Time records of the ECN measured in the PCCN mode from the stressed C-ring specimens in a 40 wt% NaOH solution containing 0.01 wt% PbO at 315 °C for 110 h. The test was interrupted and the specimen surface was examined for cracking at accumulated immersion times of 22, 42 and 110 h

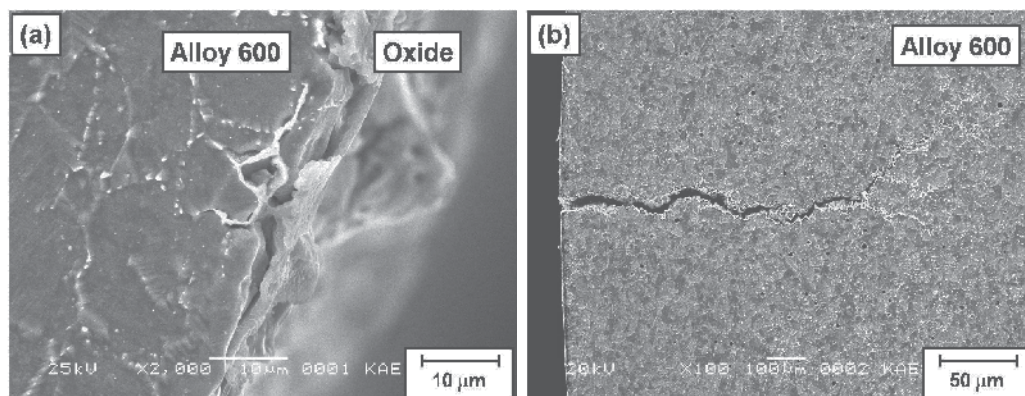


Fig. 3. SEM micrographs of the side surface of the C-ring apex after the accumulated immersion times of (a) 42 h and (b) 110 h in the leaded caustic solution at 315 °C

Position	O	Al	Ti	Cr	Mn	Fe	Ni
Matrix	ND*	0.31	0.18	15.74	0.27	8.35	75.14
Crack mouth	21.61	0.34	0.11	5.96	0.15	2.65	69.18
Crack tip	22.04	0.21	0.15	8.88	0.05	4.10	64.57

\* ND : not detectable

Table 2. Chemical composition of the matrix and the surface film of the crack mouth and tip after a whole immersion test in 40 wt% NaOH solution containing 0.01 wt% PbO at 315 °C for 110 h (wt%)

With the aid of the microscopic analysis, it is easily anticipated that the current rises followed by steeper decay with shorter time interval in the time record of the ECN at points B and C in Fig. 2 are mainly due to the initiation of SCC, whereas the current increases followed by slower decay with longer time interval in the time record at points D and E in Fig. 2 are attributable to its propagation.

Figs. 4(a) and (b) present the plots of the power spectral density (PSD) vs. the frequency calculated from each time record of the ECN by a fast Fourier transform (FFT) algorithm at points A, B and C, and D, E and F, respectively. In Fig. 4(a), it is clearly seen that the PSD of the ECN obtained at points B and C where the initiation of SCC is expected to occur, is higher at whole frequency ranges than that obtained at point A where the general corrosion (the formation of the passive oxide film) occurs on the C-ring surface. Similar behaviors were found in Fig. 4(b), that is, the PSD of the ECN obtained at points D and E where the propagation of SCC is supposed to occur, is higher than that obtained at point F, except the remarkable increase of the PSD at a low frequency limit. The increases of the PSD especially at a low frequency limit in Figs. 4(a) and (b) strongly indicates the increase in the number of localized corrosion events, that is, the initiation and the propagation of Pb-assisted SCC, respectively, as previously reported (Kim & Kim et al., 2009a; Kim & Kim et al., 2009b). Since the type of corrosion can not be reliably distinguished on the basis of the roll-off slope (Cottis, 2001), it will not be considered as indicator of localized corrosions in this work.

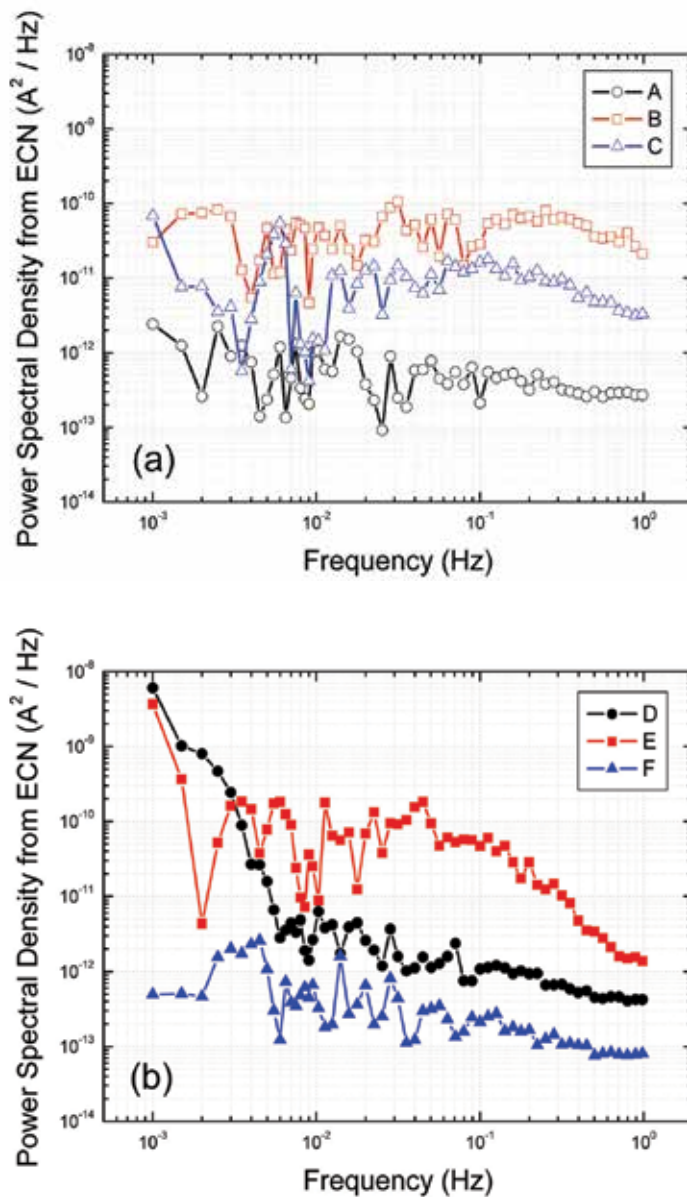


Fig. 4. Plots of the PSD vs. the frequency calculated from each time record of the ECN by the FFT algorithm at points (a) A, B and C, and (b) D, E and F

### 3.2 Spectral analysis of electrochemical noise in UCPN mode

Figs. 5(a) and (b) give typical EPN and ECN recorded from the stressed specimen in the leaded caustic solution for the time period from  $982 \times 10^3$  to  $996 \times 10^3$  s, and for that solution plus CuO for the time period from  $1406 \times 10^3$  to  $1420 \times 10^3$  s, respectively, by the EN measurement in the UCPN mode. There were typical current increases in the ECN concurrent with the potential drops in the EPN at points A, C, D and F, which have also

generally been observed during localized corrosions; the current increase corresponding to the potential decrease means a local break-down of the oxide film resulting in an exposure and local dissolution of the metal surface, whereas the current decrease accompanied by the potential recovery indicates a repair of the surface oxide film (repassivation).

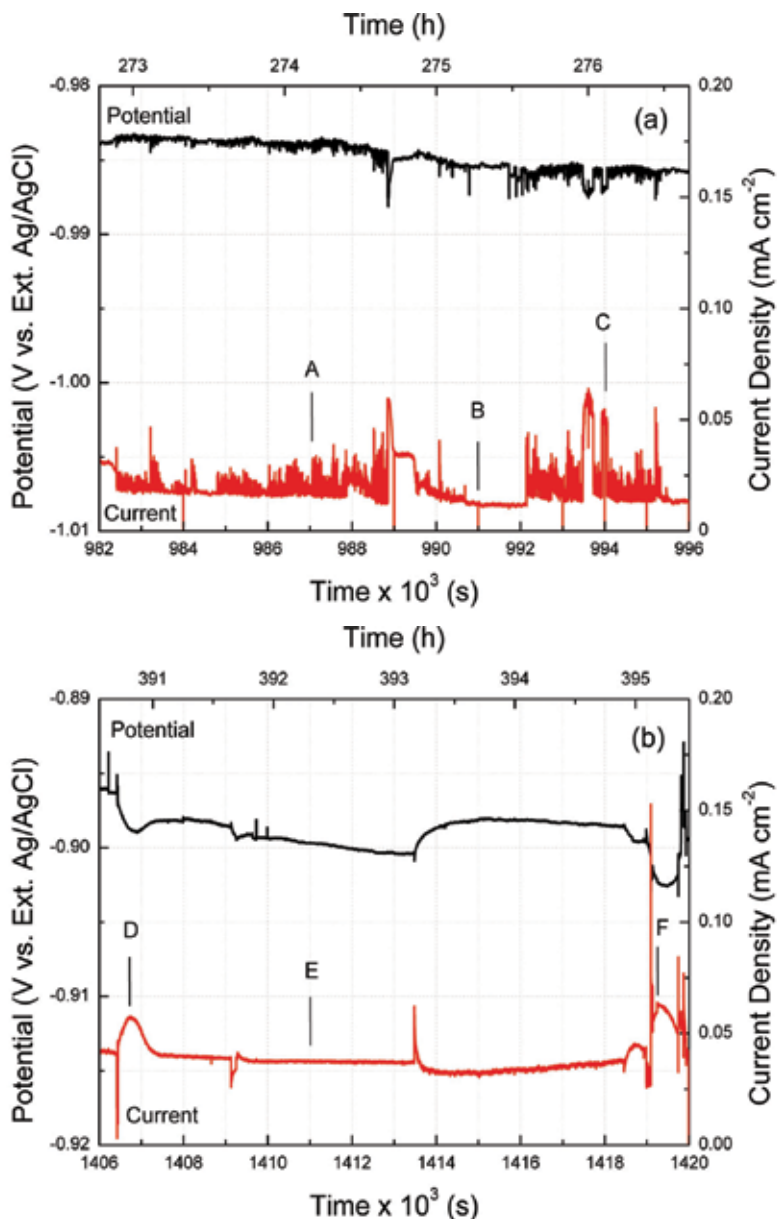


Fig. 5. Time records of the EPN and the ECN recorded in UCPN mode (a) for the leaded caustic solution for the time period from  $980 \times 10^3$  to  $996 \times 10^3$  s, and (b) for that solution plus CuO for the time period from  $1405 \times 10^3$  to  $1421 \times 10^3$  s at 290 °C



The ECN at points A and C in Fig. 5(a) revealed repetitive current increases followed by faster decay with shorter time interval when compared to the ECN at points D and F in Fig. 5(b) exhibiting more localized behavior, that is, current rises followed by slower decay with longer time interval. It is notable that the behavior of the ECN at points A and C recorded in the UCPN mode (Fig. 5(a)) was fairly similar with that of the ECN at points B and C obtained in the PCCN mode (Fig. 2). Also, the ECN at points D and F in the UCPN mode (Fig. 5(b)) resembles the ECN at points D and E in the PCCN mode (Fig. 2) in appearance.

After the immersion test in the leaded caustic solution for 278 h, the surface of the specimen was extensively examined for cracking. From the SEM analysis, the local break-down of the surface oxide film and many defect sites were found on the surface of the stressed specimen (Fig. 6(a)). After the entire immersion test in the leaded caustic solution plus CuO for 400 h, several cracks were propagated in the IG mode (Fig. 6(b)). Consequently, it is strongly suggested that the current increases in the ECN accompanied by the potential drops in the EPN in Fig. 5(a) are mainly due to the initiation of SCC and those changes in the ECN and the EPN in Fig. 5(b) are attributable to its propagation.

Figs. 7(a) and (b) present the plots of the PSD vs. the frequency calculated from each time record of the ECN and the EPN, respectively, by the FFT algorithm at points A, B and C in Fig. 5(a). It is obvious that the PSD of both ECN and EPN at points A and C, where SCC is expected to be initiated in the leaded caustic solution, is higher at whole frequency ranges than that obtained at point B where the general corrosion (the repassivation of the surface oxide film) occurs on the C-ring surface. Similar trends were observed in Figs. 8(a) and (b); the PSD of ECN and EPN at points D and F, where SCC is supposed to be propagated in the leaded caustic solution plus CuO, is higher than that obtained at point E. It is noticeable that the PSD of both ECN and EPN due to the propagation of SCC (Figs. 8(a) and (b)) revealed more dominant increase at a low frequency limit as compared to that PSD due to the initiation of SCC (Figs. 7(a) and (b)), indicating more localized characteristics of the propagation of SCC. The results from the spectral analyses of the ECN and the EPN recorded in the UCPN mode are well coincided with that obtained in the PCCN mode.

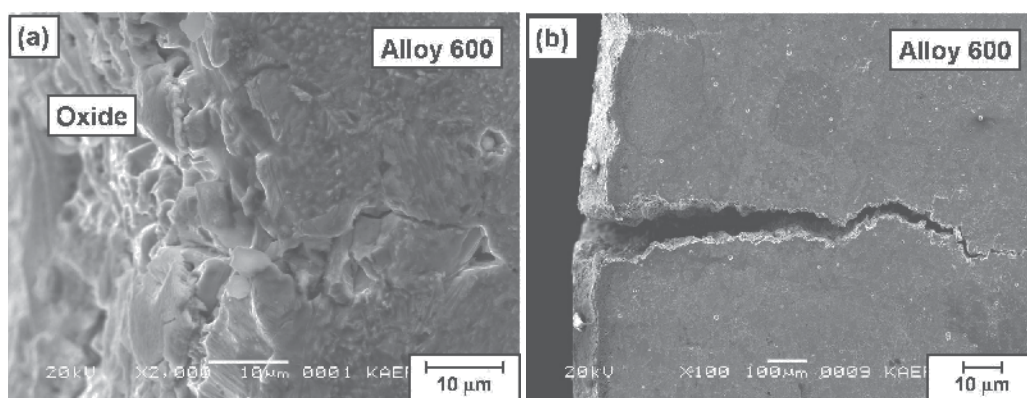


Fig. 6. SEM micrographs of the side surface of the C-ring apex after the accumulated immersion times of (a) 278 h in the leaded caustic solution and (b) 400 h in that solution plus CuO at 290 °C

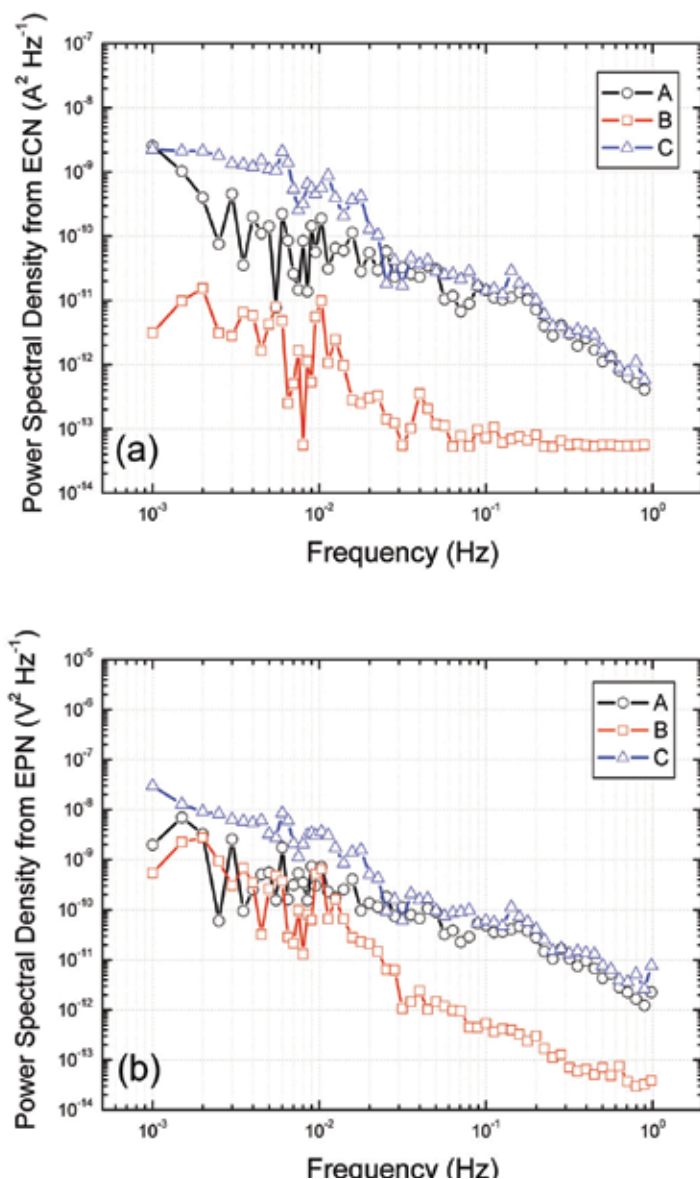


Fig. 7. Plots of the PSD vs. the frequency calculated from each time record of (a) the ECN and (b) the EPN by the FFT algorithm at points A, B and C in Fig. 5(a)

### 3.3 Stochastic analysis of electrochemical noise

To evaluate the stochastic characteristics of the initiation and the propagation of SCC, a shot-noise analysis was employed in this work under the assumption that the ECN concurrent with the EPN is independently produced by the individual event of localized corrosions. Based on the shot-noise theory (Al-Mazeedi & Cottis, 2004; Cottis, 2001; Sanchez-Amyay et al., 2005), the frequency of events  $f_n$  of the localized corrosions is determined from the time record of the EPN as given by,

$$f_n = B^2 / (\Psi_E A) \quad (1)$$

where  $B$  is the Stern-Geary coefficient,  $\Psi_E$  the PSD value of the EPN calculated by averaging several low-frequency points using the FFT algorithm and  $A$  represents the exposed electrode area.

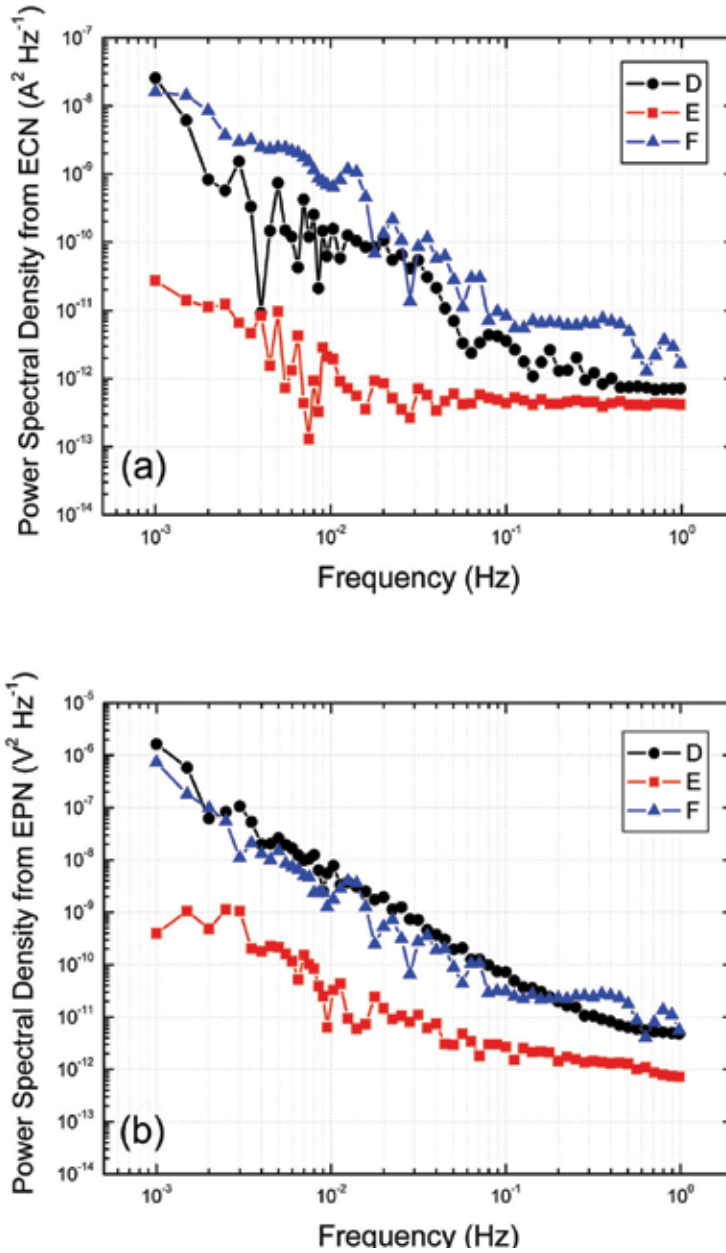


Fig. 8. Plots of the PSD vs. the frequency calculated from each time record of (a) the ECN and (b) the EPN by the FFT algorithm at points D, E and F in Fig. 5(b)



From a set of  $f_n$  calculated from the PSD plots of the EPN according to Eq. (1), the cumulative probability  $F(f_n)$  at each  $f_n$  is determined numerically by a mean rank approximation (Cottis, 2001). In this work, the probability of  $f_n$  for the Pb-assisted SCC was analyzed using the Weibull distribution function, the most commonly used cumulative probability function for predicting a life and failure rate (Na & Pyun, 2007; Na et al., 2007a; Na et al., 2007b). Using the Weibull distribution function, the probability of the mean time-to-failure,  $t_n$ , which corresponds to  $1/f_n$ , is expressed as,

$$\ln\{\ln[1/(1-F(t_n))]\} = m \ln t_n - \ln n \quad (2)$$

where  $m$  and  $n$  are the shape and scale parameters, respectively.

Fig. 9 demonstrates the plots of  $\ln\{\ln[1/(1-F(t_n))]\}$  vs.  $\ln t_n$  calculated from the sets of  $f_n$  at the same time period as Figs. 5(a) and (b). For a comparison, the probability of  $t_n$  obtained from the EN measurement of two identical unstressed Alloy 600 specimens in a 40 wt% NaOH solution without impurities at 290 °C is also plotted. Only general corrosion occurred on the unstressed specimen surface without any cracking. In Fig. 9, it was easily anticipated that the mean time-to-failure  $t_n$  for the localized corrosions such as the initiation and the propagation of SCC shifted to a higher value, analogous to the shift of  $f_n$  to a lower frequency when compared to that for the general corrosion.

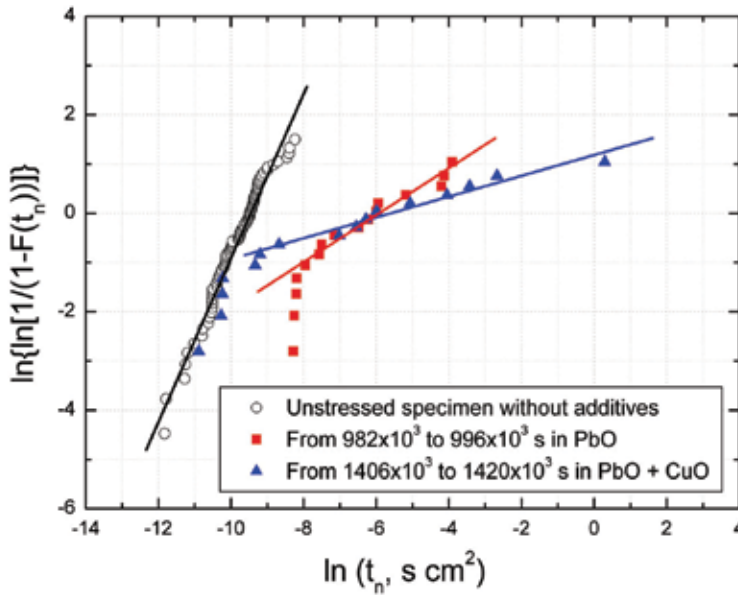


Fig. 9. Plots of  $\ln\{\ln[1/(1-F(t_n))]\}$  vs.  $\ln t_n$  calculated from the sets of  $f_n$  at the same time period as Figs. 5(a) and (b). For a comparison, the probability of  $t_n$  obtained from the EN measurement of two identical unstressed Alloy 600 specimens in a 40 wt% NaOH solution without impurities at 290 °C is also plotted

In previous works (Na & Pyun, 2007; Na et al., 2007a; Na et al., 2007b; Park & Pyun, 2004; Pyun et al., 1993; Pyun et al., 1994), the conditional event generation rate  $r(t)$  of a localized corrosion was introduced as a failure rate using the values of  $m$  and  $n$  as,

$$r(t) = (m/n) t^{m-1} \quad (3)$$

Depending on the corrosion mechanism, the value of  $r(t)$  was regarded as the rate of localized corrosion events such as the pit generation (Pyun et al., 1994), the pit growth (Park & Pyun, 2004) and the propagation of SCC (Na et al., 2007b). There are few reports on the stochastic approach for the localized corrosions of Alloy 600 materials at high temperature in the literature. For stainless steels, Shibata (Shibata, 1990; Shibata, 2007) reviewed the stochastic studies on a passive film break-down triggering the initiation of localized corrosions. He analysed the stochastic characteristics of the local break-down and the repair of the passive film using the Poisson stochastic theory by assuming a completely random occurrence. For the Poisson process, the value of  $m$  in the Weibull probability is unity. In a real situation, however, there is a distortion in the Poisson probability, and hence, a deviation of the value of  $m$  from unity, caused by a difference in many experimental conditions such as the chemistry of the test solution, the applied potential and the interactions between localized events.

On the other hand, Pyun et al. reported that the value of  $m$  increases from 0.7 up to unity with a decreasing applied potential (Pyun et al., 1993) for the pit generation at the surface of Al alloy at room temperature, and the value of  $m$  decreases from 0.4 to 0.1 with the addition of  $\text{SO}_4^{2-}$  and  $\text{MoO}_4^{2-}$  ions in a 0.1 M NaCl solution (Na et al., 2007a) and with the addition of  $\text{SO}_4^{2-}$ ,  $\text{NO}_3^-$  and  $\text{PO}_4^{3-}$  ions in a 1M HCl solution (Na & Pyun, 2007) for the pit initiation at the surface of pure Al at room temperature. Interestingly, they also reported that the value of  $m$  is 0.33 for the SCC propagation of Alloy 600 in a neutral solution containing PbO at room temperature (Na et al., 2007b).

In our previous works (Kim & Kim, 2009a; Na et al., 2007a; Na et al., 2007b), it was reported that the shape parameter  $m$  of the Weibull distribution can be regarded as an indicator of types of corrosion. In the present work, the value of  $m$  determined from Fig. 9 by a linear curve fitting method were 1.46 for the general corrosion on the unstressed specimen in the caustic solution without any oxidizing impurities, 0.47 for the initiation of SCC on the stressed specimen in the leaded caustic solution, and 0.21 for its propagation in the leaded caustic solution plus CuO. The values of  $m$  in this work revealed good agreement with those values previous reported for each stage of the Pb-assisted SCC (Kim & Kim, 2009a).

#### 4. Conclusions

From the microscopic and the EN analyses of Alloy 600 SG tube materials in the leaded caustic solution environment at high temperature, it is strongly suggested that the repetitive current rises followed by steeper decay with shorter time interval in the time record of the ECN measured in the PCCN mode are mainly due to the initiation of SCC, whereas the current increases followed by slower decay with longer time interval are attributable to its propagation.

From the spectral analysis of the ECN, the PSD increased more remarkably at low frequency limit for the propagation of SCC as compared to that for the initiation of SCC. Similar trends were observed in both ECN and EPN measured in the UCPN mode in the caustic solution environments with various oxidizing impurities. In addition, from the stochastic analysis of the EPN obtained in the UCPN mode, it was found the shape parameter of the Weibull distribution of the mean time-to-failure for the initiation of SCC is clearly distinguishable from that parameter for the propagation of SCC as well as for the general corrosion.

## 5. Acknowledgement

This work was funded by Korea Ministry of Education, Science and Technology.

## 6. References

- Al-Mazeedi, H.A.A. & Cottis, R.A. (2004). A practical evaluation of electrochemical noise parameters as indicators of corrosion type, *Electrochim. Acta*, Vol. 49, p. 2787
- Cottis, R.A. (2001). Interpretation of electrochemical noise data, *Corrosion*, Vol. 57, p. 265
- Cottis, R.A. ; Al-Awadhi, M.A.A.; Al-Mazeedi H. & Turgoose, S. (2001). Measures for the detection of localized corrosion with electrochemical noise, *Electrochim. Acta*, Vol. 46, p. 3665
- Hwang, S.S.; Kim, U.C. & Park, Y .S. (1997). The effects of Pb on the passive film of Ni-base alloy in high temperature water, *J. Nucl. Mater.*, Vol. 246, p. 77
- Hwang, S.S. ; Kim, H.P.; Lee, D.H.; Kim, U.C. & Kim, J.S. (1999). The mode of stress corrosion cracking in Ni-base alloys in high temperature water containing lead, *J. Nucl. Mater.*, Vol. 275, p. 28
- Jacko, R.J. (1990). *Corrosion Evaluation of Thermally Treated Alloy 600 Tubing in Primary and Faulted Secondary Water Environments*, EPRI NP-6721, Pittsburgh, Pennsylvania
- Kim, D.J. Kim; Kwon, H.C & Kim, H.P. (2008). Effects of the solution temperature and the pH on the electrochemical properties of the surface oxide films formed on Alloy 600, *Corros. Sci.*, Vol. 50, p. 1221
- Kim, H.P.; Hwang, S.S.; Kim, J.S. & Hwang, J.H. (2007). Stress corrosion cracking of steam generator tubing materials in lead containing solution, *Proc. of the 13th Int. Conf. on Environmental Degradation of Materials in Nuclear Power Systems*, Whistler, Canada, Aug. 19-23, 2007
- Kim, S.W. & Kim, H.P. (2009a). Electrochemical noise analysis of PbSCC of Alloy 600 SG tube in caustic environments at high temperature, *Corros. Sci.*, Vol. 51, p. 191
- Kim, S.W. & Kim, H.P. (2009b). Interpretation of electrochemical noise parameters as indicators of initiation and propagation of SCC of an Alloy 600 SG tube at high temperatures, *Nuclear Engineering and Technology*, Vol. 41, p. 1315
- Kim, U.C.; Kim, K.M. & Lee, E.H. (2005). Effects of chemical compounds on the stress corrosion cracking of steam generator tubing materials in a caustic solution, *J. Nucl. Mater.*, Vol. 341, p. 169
- Na, K.H. & Pyun, S.I. (2007). Effects of sulphate, nitrate and phosphate on pit initiation of pure aluminium in HCl-based solution, *Corros. Sci.*, Vol. 49, p. 2663
- Na, K.H.; Pyun, S.I. & Kim, H.P. (2007a). Analysis of electrochemical noise obtained from pure aluminium in neutral chloride and alkaline solutions, *Corros. Sci.*, Vol. 49, p. 220
- Na, K.H.; Pyun, S.I. & Kim, H.P. (2007b). Effects of NiB, PbO, and TiO<sub>2</sub> on SCC of sensitized Inconel Alloy 600 in RT-tetrathionate solution, *J. Electrochem. Soc.*, Vol. 154, p. C349
- Park, J.J. & Pyun, S.I. (2004). Stochastic approach to the pit growth kinetics of Inconel alloy 600 in Cl<sup>-</sup> ion-containing thiosulphate solution at temperatures 25-150 °C by analysis of the potentiostatic current transients, *Corros. Sci.*, Vol. 46, p. 285
- Pyun, S.I.; Lee, E.J. & Kim, C.H. (1993). Stochastic approach to analysis of pitting corrosion of anodic oxide film on Al-1wt.%Si-0.5wt.%Cu alloy, *Surf. Coat. Tech.*, Vol. 62, p. 480

- Pyun, S.I.; Lee, E.J. & Han, G.S. (1994). Localized corrosion of sputtered Al-1wt.%Si-0.5wt.%Cu alloy thin film, *Thin Solid Films*, Vol. 239, p. 74
- Sakai, T.; Okabayashi, S.; Aoki, K.; Matsumoto, K. & Kishi, Y. (1990). A study of oxide thin film of Alloy 600 in high temperature water containing lead, *Corrosion/90*, paper no. 520, NACE, Houston
- Sanchez-Amyay, J.M.; Cottis, R.A. & Botana, F.J. (2005) Shot noise and statistical parameters for the estimation of corrosion mechanisms, *Corros. Sci.*, Vol. 47, p. 3280
- Shibata, T. (1990). Stochastic studies of passivity breakdown, *Corros. Sci.*, Vol. 31, p. 413
- Shibata, T. (2007). Passivity breakdown and stress corrosion cracking of stainless steel, *Corros. Sci.*, Vol. 49, p. 20
- Stewart, J.; Wells, D.B.; Scott, P.M. & Williams, D. E. (1992). Electrochemical noise measurements of stress corrosion cracking of sensitised austenitic stainless steel in high-purity oxygenated water at 288 °C, *Corros. Sci.*, Vol. 33, p. 73

# Effect of Long-Term Thermal Influence on Mechanical Properties of Welded Joints for Carbon Steels used in Power Engineering

Zilvinas Bazaras and Boris Timofeev

<sup>1</sup>*Kaunas University of Technology,*

<sup>2</sup>*Saint Petersburg State Polytechnic University*

<sup>1</sup>*Lithuania*

<sup>2</sup>*Russia*

## 1. Introduction

Carbon steels widely used in power engineering for manufacture of different types of equipment. A lot of part of WWER and RBMK equipments is produced from 22K steel (Timofeev, 1982) or its foreign analogs (Vaseneva, 1990). For example, the case of steam generator PGV-440, cases of separator and also the pipe-lines of the large diameter for NPP with RBMK reactors. Thus for manufacturing the equipment were used as the forgings and the plates or sheets from this steel of various methods of melt – open hearth furnace, vacuum arc and electro-slag re-melting. Separate semi-products of this equipment was joined using welding – MAW (manual arc welding), SAW (submerged arc welding) and ESW (electro-slag welding).

## 2. Information

### Case of PGV-440 steam generator of NPP with WWER-440 reactors

Steam generator case (Zherebenkov, 1979) consists of two central shells (having a thickness of 135 mm) and two end shells (having a thickness of 78 mm) to which the nozzles Du-250, Du-500, Du-700, Du-1100 and some small nozzles and unions and also two bottoms (with thickness 84 mm) are welded. The case design is given in Fig.1. Plane billets of bottoms and shells of steam generators were produced using electro-slag welding of two plates of 22K steel with the use of Sv-10Mn2 wire and AN-8M flux. During edge preparation the edges of plates to be welded were subjected to ultrasonic inspection. Stamped bottoms after heat treatment were also tested using various inspection procedures. Shells were joined (using submerged arc welding with Sv-08A wire under AN-348A flux) with three circumferential welds. The welding up of nozzles which are displaced relatively the steam generator axis is carried out manually with the use of electrodes of the type YONI-13/55.

Thus steel type 22K (OHF, ESM or VAM) and three method of welding can be used at manufacture of PGV-440 steam generator.

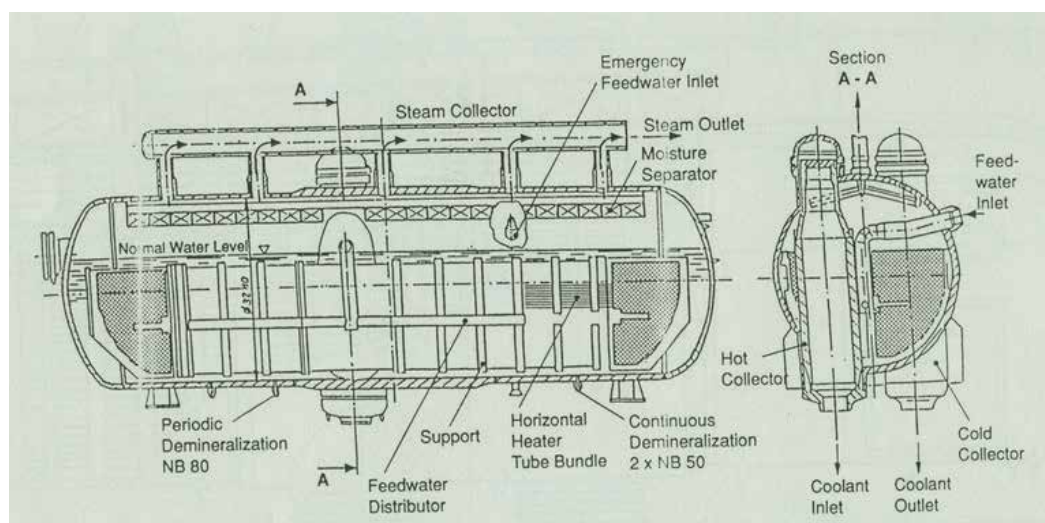


Fig. 1. Sketch of PGV-440 steam generator case

### Separator drum of NPP with RBMK-1000 reactors

The design of separator drum of steam (Kashirin, 2004) is a vessel with the following geometrical dimensions: outer diameter – 2300 mm, length – 30480 mm, wall thickness – 105 mm. Sketch of design is presented in Fig.2.

Separators are manufactured from two semi-vessels, each of which consists of some sections. The section includes bottom (thickness – 115 mm) and shells (thickness – 105 mm) or only shells. Each of these elements are assembled from two clad plates, which (in the form of half-cylinders) are joined with longitudinal welds produced by electroslag welding (wire Sv-10Mn2, flux AN-8M). The different number of 22K steel heats (from 30 to 40) is used because one heat (2-4 ingots) may be used for different components of pressure vessel. Post-welding heat treatment is carried out on the following regime: normalization at  $930 \pm 10^\circ\text{C}$  exposure for 2.5 hours, cooling in air. Welding of shells with each other and a shell with a bottom using circumferential welds is produced by submerged arc welding (SAW) using Sv-08A wire and AN-348A flux. After welding up circumferential welds the tempering is carried out at  $630 \pm 10^\circ\text{C}$ , exposure for 4 hours and cooling in air. Welding up of shells to nozzles is performed with manual arc welding (MAW) with the use of the type YONI-13/55 electrode and then the whole pressure vessel is subjected to tempering at  $630 \pm 10^\circ\text{C}$  (heating rate –  $80^\circ\text{C}/\text{min}$ ) for a time of 11 hours.

Separator drum case consists of 20 shells and 2 bottoms. Each shell is assembled from two components welded (“semi-troughs”) together with two longitudinal welds. There is a man-hole in the separator case (Fig.3) numerous nozzles are welded in the case wall. Sketches of units of connecting nozzles to separator case are given in Fig.3.

It follows from Fig.3 that the largest holes (diameter 470 mm) in separator case wall are from 24 nozzles of down-comer pipe-lines, from a man-hole – diameter 400 mm, from nozzles of steam rejection – diameter 297 mm. Besides there are other nozzles with smaller holes including nozzles of steam-water service lines – diameter 76 mm. All these numerous nozzles are located in the separator case in the distance from longitudinal welds.

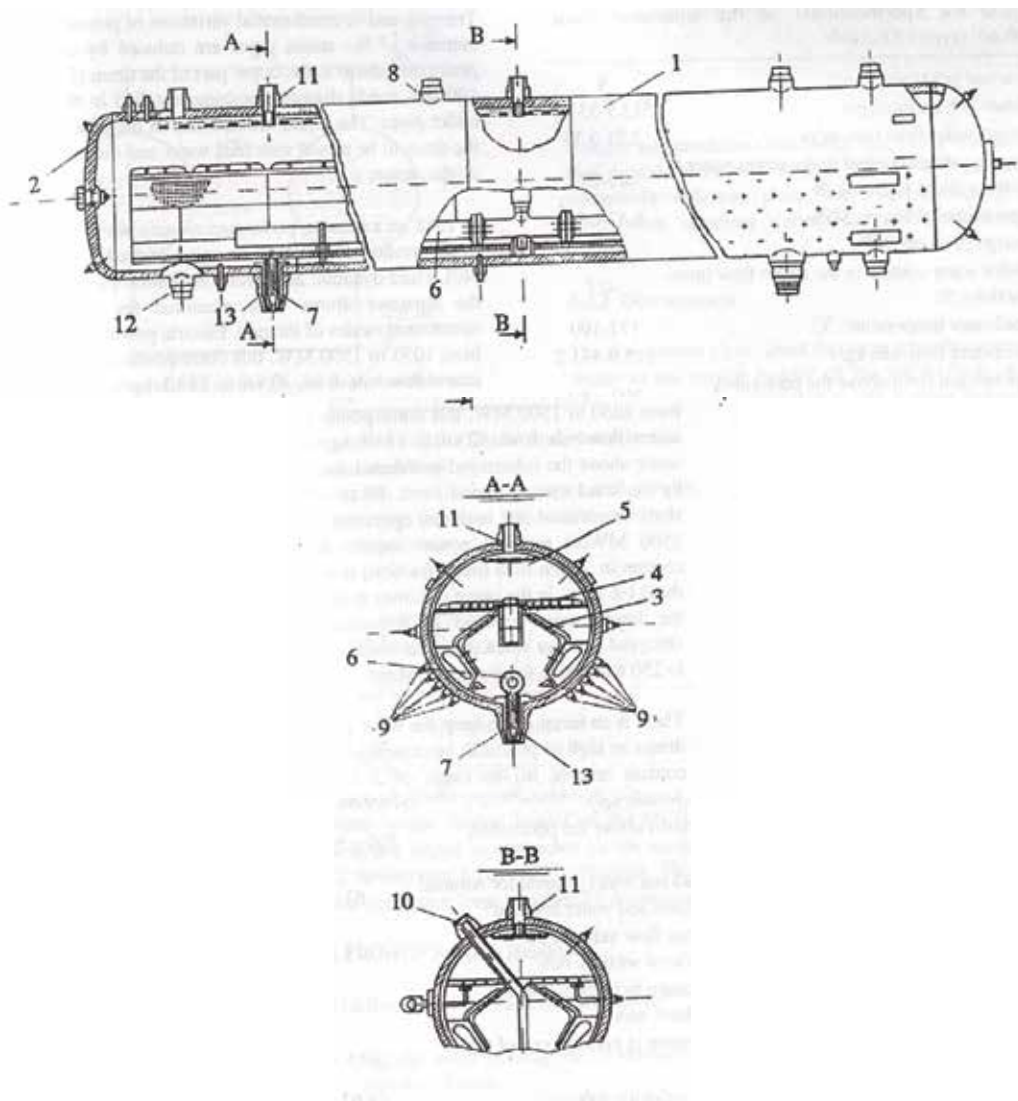


Fig. 2. Sketch of separator drum: 1 – vessel case; 2 – bottom; 3 – plate receiving water and steam flow; 4 – perforated plate in water; 5 – upper perforated plate; 6 – distribution collector of potable water; 7 – nozzle for water rejection; 8 – nozzle for steam line; 9 – nozzle of steam-water piping; 10 – nozzle of feed water; 11 – nozzle in steam zone; 12 – nozzle in water zone; 13 – nozzle of down-comers

In connection with numerous holes in the steam separator case these zone are stress concentrators. Increased stresses are acting in them (above the yield stress) conditioned both by concentration and stiffness variation. The accumulation of fatigue damage is possible in stress concentration zones, which may cause both the nucleation of cracks and their development in the process of operation. As stated above the rules of nuclear power engineering design do not permit holes in the regions of longitudinal and circumferential welds of vessel nozzles. At the same time the connection of nozzles to the case is performed

with welding and namely in this unit the maximum stresses are acting during operation and this results in the necessity to carry out low cycle fatigue investigations not only for base metal but also for weld metal.

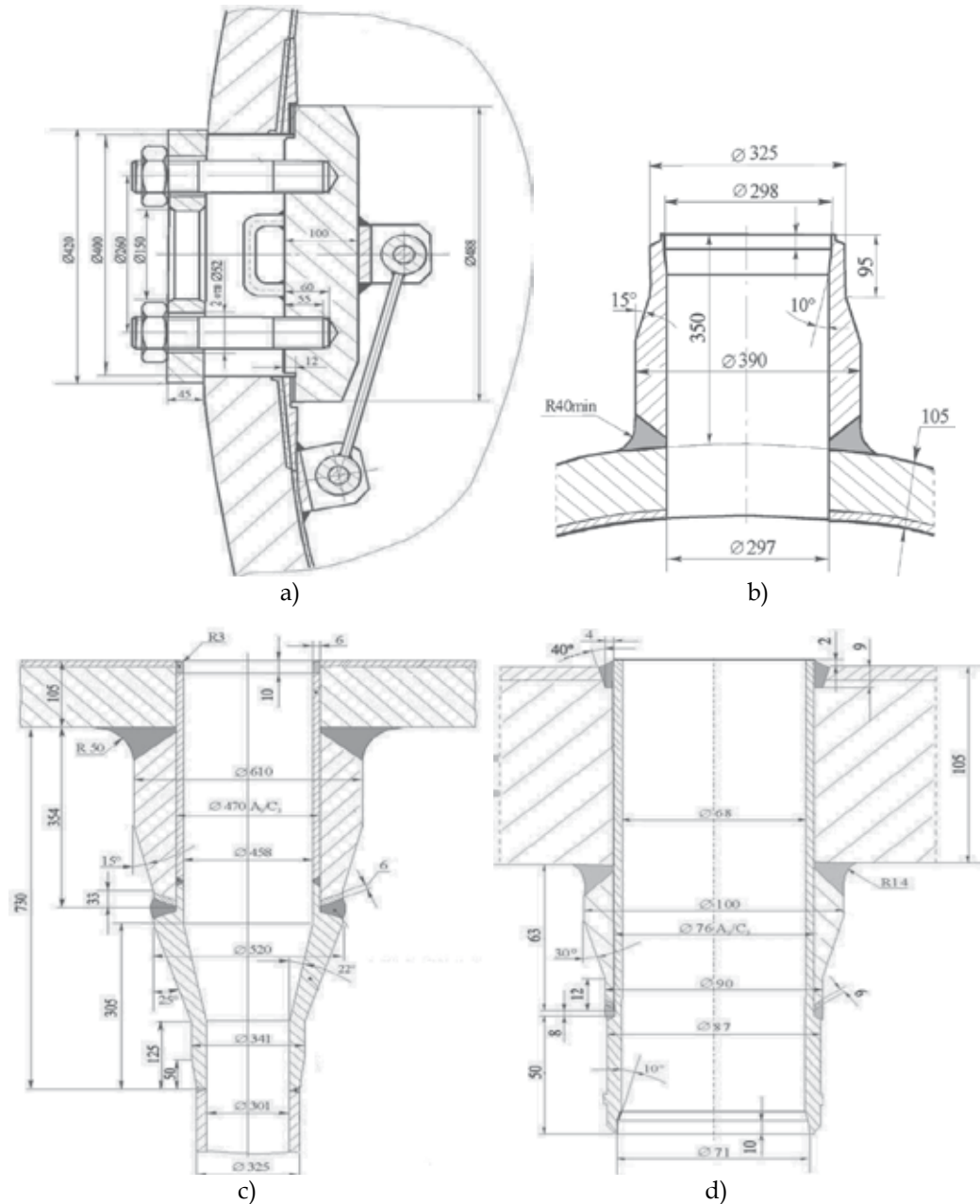


Fig. 3. Sketches of units of connecting various nozzles with steam separator case: a – man-hole; b – nozzles of steam rejection; c – nozzle of down-comer; d – nozzle of steam-water of service lines



## 2.1 Steam headers of NPP with RBMK-1000 reactors

Collectors are manufactured from 5-7 shells having a diameter of 900 mm (wall thickness – 60-70 mm) and two bottoms (wall thickness – 70-80 mm). The type 22K steel clad with EI-898 (Sv-08Cr18Ni10Mn2Nb) steel is used for the manufacture of collectors. A shell consists of two semi-shells connected with each other using Sv-10Mn2 wire and AN-8M flux. Welding up of nozzles to a collector case is performed manually with YONI-13/55 electrodes.

Headers in-take (Fig.4) and pumping (Fig.5) are made from 5-7 shells (diameter – 900 mm, wall thickness – 70 mm in pumping and wall thickness – 60 mm in-take) and two bottoms (wall thickness 80 mm and 70 mm, respectively for i-take and pumping collectors). The type 22K steel was used for the manufacture of collectors, clad by EI-898 steel. Each shell consisted of two semi-shells, connected with each other by electro-slag welds produced using Sv-10Mn2 wire and AN-8M flux. Welding of nozzles to collector is performed manually with YONI-13/55 electrodes.

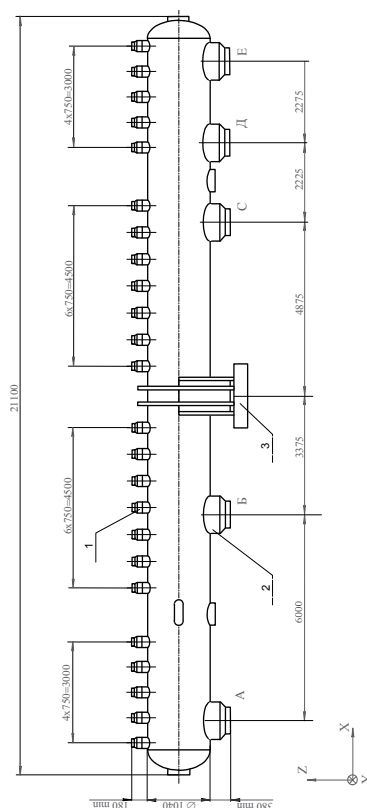


Fig. 4. Sketch of header in-take: 1 – nozzle DN300 to joint with down-comer; 2 – nozzle DN750 to joint with pipe-lines in-take; 3 – central stopper

The design service life of header is 25 years. Geometrical sizes are : diameter 800 mm, length – 21500 mm, wall thickness – 70 (60) mm. Coolant temperature – 290°C, working pressure – 9.1 MPa. For in-take and 7 MPa for pumping collectors, working environment – water of high purity.

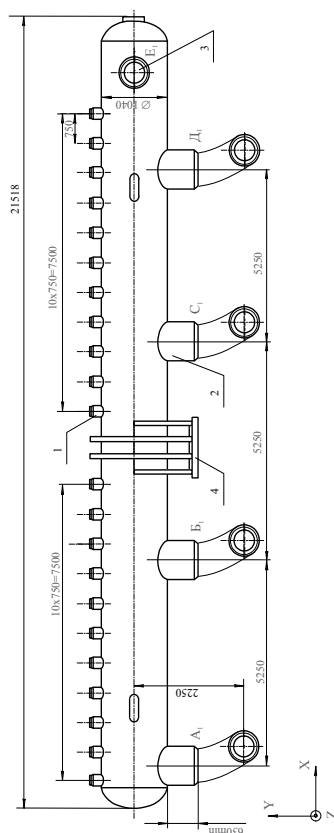


Fig. 5. Sketch of header pumping: 1 - nozzle DN300 to joint RGK; 2 - nozzle DN750 and elbow to joint with pipe-line pumping; 3 - nozzle DN750 to joint with unit between headers in-take and pumping; 4 - central stopper

Requirements for chemical composition and properties of 22K steel used for manufacture of in-take and pumping collectors are presented in Specification TU 24-1-11-427-67. The statistical treatment of certificate data presented in Certificates on the product was carried out. The results of statistical treatment are given below.

## 2.2 Pipe-lines Du-800 with RBMK-1000 reactors

Tube units of MFCC circuit in-take pipes (diameter - 836 mm, wall thickness - 42 mm) and pumping pipes (diameter - 848 mm, wall thickness - 48 mm) Du-800 (Fig.6). Tube units of the main circulating suction pipes ( $\varnothing 838 \times 42$  mm) and pressure pipes ( $\varnothing 848 \times 48$  mm) are made from Du-800 tubes. The main elements of tube units are semi-shells and half-cylinders from 22K steel of the first generation, for which chemical composition and mechanical properties are defined separately. The semi-shells, which are joined with each other using SAW (Sv-08A wire, AN-348A flux) were used for straight section of Du-800 pipe-lines. The elbow sections of Du-800 pipe-line the half-cylinders were used which were also joined with each other by SAW with same welding materials (Sv-08A wire, An-348A flux). For Du-800 pipe-lines of the second generation the French carbon steel Creselso-330E and Japanese 19MN5 steel were used instead of 22K steel.

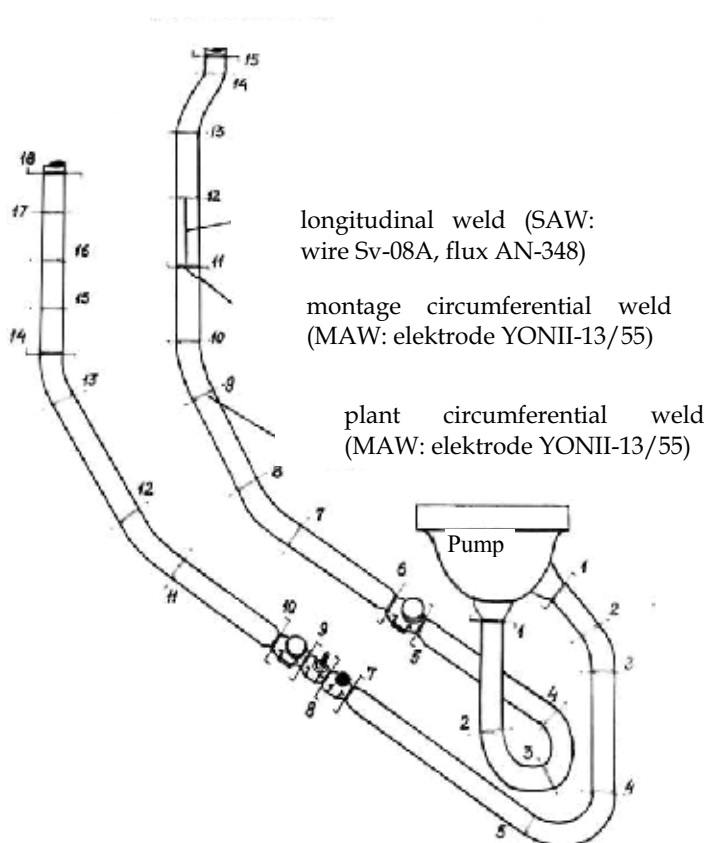


Fig. 6. Sketch of MFCC Du-800

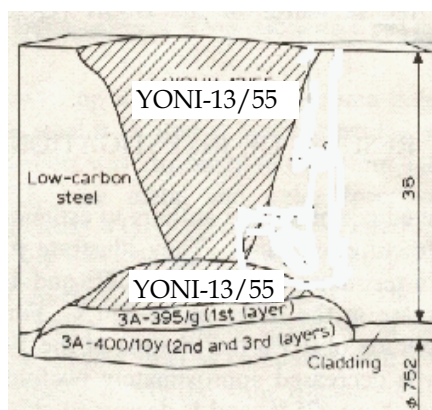


Fig. 7. Sketch of circumferential weld joint

Tube units of the main circulating suction pipes ( $\varnothing 838 \times 42 \text{ mm}$ ) and pressure pipes ( $\varnothing 848 \times 48 \text{ mm}$ ) are made from Du-800 tubes. The main elements of tube units are semi-shells and half-cylinders from 22K steel of the first generation, for which chemical composition

and mechanical properties are defined separately. The semi-shells, which are joined with each other using SAW (Sv-08A wire, AN-348A flux) were used for straight section of Du-800 pipe-lines. The elbow sections of Du-800 pipe-line the half-cylinders were used which were also joined with each other by SAW with same welding materials (Sv-08A wire, An-348A flux). For Du-800 pipe-lines of the second generation the French carbon steel Creselso-330E and Japanese 19MN5 steel were used instead of 22K steel.

Tube blocks are made from separate units consisting of two semi-elbows Ø836x42 mm and Ø848x48 mm connected with each other with longitudinal weld (SAW Sv-08A wire, AN-348M flux). Separated units are connected with circumferential welds, produced by manual welding with YONI-13/55 electrodes. The type 22K steel clad from the inside with EI-898 (Sv-08Cr18Ni10Mn2Nb) steel (thickness -6 mm) was used for the manufacture of tube units.

### 2.3 Operating conditions of steam generated systems

The design service life of steam generated systems is 25-30 years. The main factors working in the equipment at operation are:

- elevated temperature is,
- working pressure,
- working environment (water + saturated steam).

The main operating conditions during the design service life are determined by the chief designer of NPP with RBMK-1000 reactors – Research and Development Institute of Power Engineering (RDIPE). The calculated loading regimes of multiple forced circulation circuit (MFCC) are defined for various operating conditions, namely, for normal operating conditions (NOC), breakdown of normal operating conditions and hydraulic tests (HT). They are given in Table 1.

N	Operating conditions	Number of regimes
<b>1. Normal of operating conditions</b>		
1	Normal calculation regime (285°C)	-
2	Planning start (from 40 to 285°C)	300
3	Planning shut down (from 285 to 40°C)	300
4	Cooling with rate 60°C/h (from 285 to 100°C)	100
5	Heating with rate 30°C/h (from 100 to 285°C)	120
6	Operating regime A3 (from 285 to 250°C)	200
7	Normal heating (from 250 to 285°C)	200
<b>2. Break down of normal operating conditions</b>		
8	Cooling with rate 120°C/h (from 285 to 100°C)	20
<b>3. Hydraulic tests</b>		
9	Hydraulic tests during operation	100

Table 1. Calculation loading regimes for MFCC circuit

In total, more than 1000 loading cycles of MFCC are possible during the project service life of NPP with RBMK reactors and this leads to the necessity of studying cyclic strength of

materials from which the separator was manufactured. By this, it is necessary to study fatigue resistance of both base metal and weld metal.

General operation condition of equipment of all generated systems is presented in Table 2.

Equipment	Type of steel	Type of melt	Semi-product	Pressure, MPa	Temperature, °C
SG	22K	OHF, ESM, VAM	Plate, forging	5.7	273
Separator	22K	OHF	Plate	7.6	260-275
Header	22K	OHF	plate	8.5	260-275
MFCC	22K, Crezelsko-330, 19MN5	OHF	Sheet Tube Tube	8.5	285

Table 2. General operation condition of equipment

### 3. Investigated materials

Melting of steel of the given mark (22K) from metallic charge is a task of open hearth process. The composition of metallic charge may vary from 100% pig iron to 100% steel return; in this case the pig iron component may be in liquid and solid state. Materials: ore, pitch, oxygen and fuel. Melted metal is cast. The low part of ingot (zone with negative chemical heterogeneity) and sink head (zone of positive segregation with increased content of sulphur, phosphorus and carbon) are removed and we have open-hearth furnace steel (Zherebenkov, 1980).

Metal of electroslag melting is obtained by melting of bars (rods) of open-hearth melting in the electrical conductive slag. Electroslag process takes place in copper mould cooled by water. Slag is formed at the expense of melting of the flux AHF-6 ( $\text{CaF}_2 + \text{Al}_2\text{O}_3$ ). Metal is obtained of more pure especially on the content of gases because the process of rod metal melting takes place in the protective slag system. Metal of vacuum arc melting is practically formed under the same conditions like the electroslag process. Vacuum is used instead of slag protection and the process itself- electric arc. This makes possible to obtain more pure metal. Steel of special melting methods has more dense uniform oriented structure, containing minimum number of non-metallic inclusions. It is well known that with using melting it is possible to obtain more refined metal containing sulphides less by 40-50%, the number of oxide inclusions and silicates less by 1.5 times as compared with the steel of the same type of open-hearth melting. Ductility and fatigue strength of steel (of these melting for products manufacture the macrostructure of zone with increased etching ability must be limited in sizes and mainly depends on metal crystallization and sulphur content in it. It is necessary to take into account the fact that in ingots from 22K steel of usual melting the off-axis inhomogeneity take place. In some ingots the sources of this inhomogeneity are sulphides "whiskers" which reach considerable sizes. In the process of operation the presence of such defects may result in metal delaminating or plate cracking.

In VAR and ESR due to the oriented crystallization and uniform sulphur distribution across the whole section the "whiskers" are absent, therefore the production of components and

welded joints of pressure vessels with wall thickness equal to 120 mm and more is carried out only from steel of special melting method. The content of gas in metal of special procedures of melting is considerably lower than by the open hearth melting. As concerns density, homogeneity and absence of internal defects the vacuum-arc steel exceeds greatly electroslag, open-hearth and electric furnace steels. Structure and properties of steel depend not only on metallurgical effect of melting but also on a possible variation of its chemical composition within the limits of values permissible in Specification.

The chemical composition of investigated materials is presented in Fig.8. Statistical treatment was applied for more than 200 heats of sheets (plates) which were used at manufacture the steam generator cases.

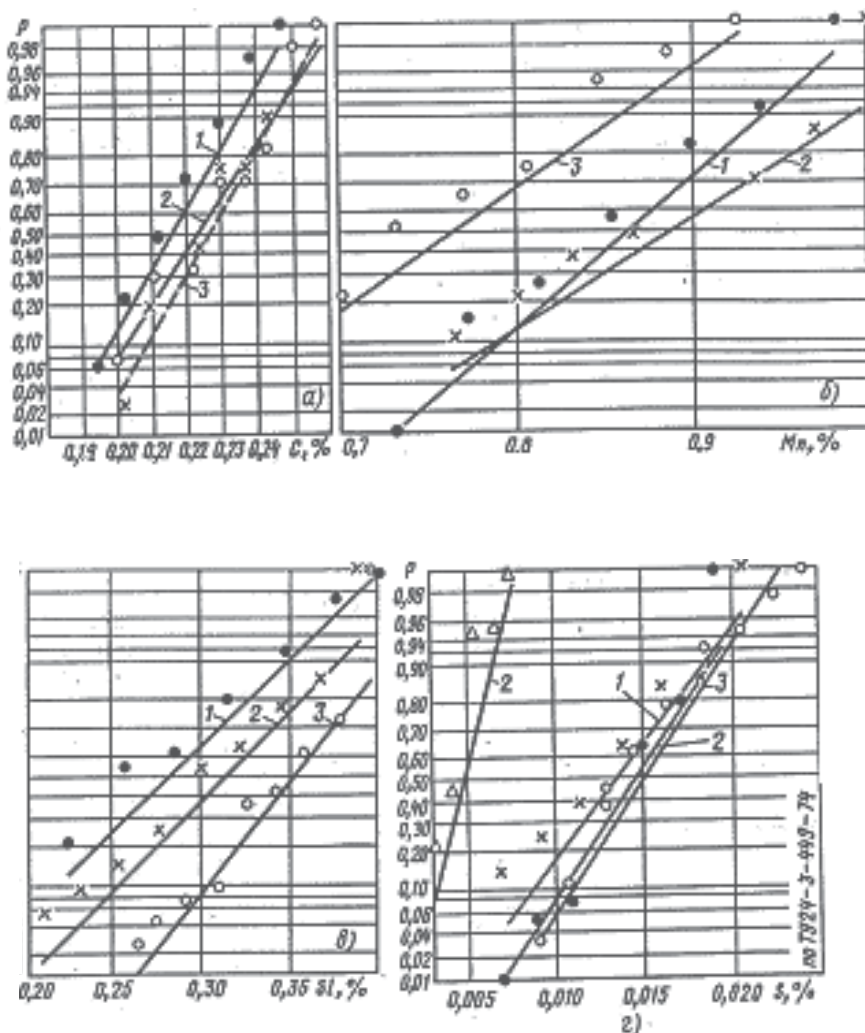


Fig. 8. Distribution of basic elements of 22K steel for various melting methods: ● - OHF; x - VAR; o - ESM (Δ - in ladle).

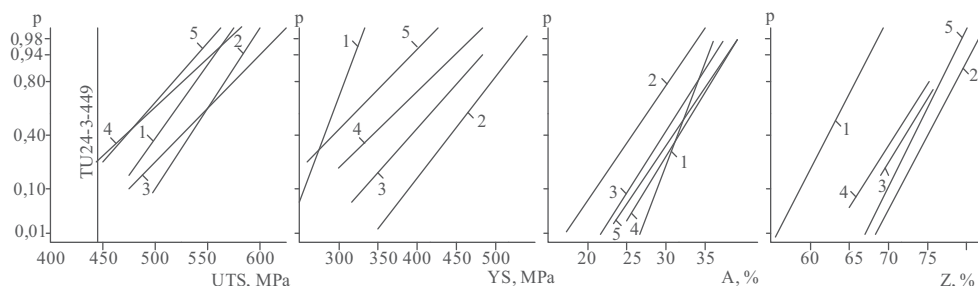


Fig. 9. Distribution of mechanical properties for welded joints of PGV-440 steam generator case: 1 – base metal (22K steel); 2 and 3 – weld metal produced by MAW using YONII-13/45 and YONII-13/55 electrodes; 4 – weld metal produced by SAW using welding wire Sv-08A; 5 – weld metal produced by ESW using welding wire Sv-10Mn2

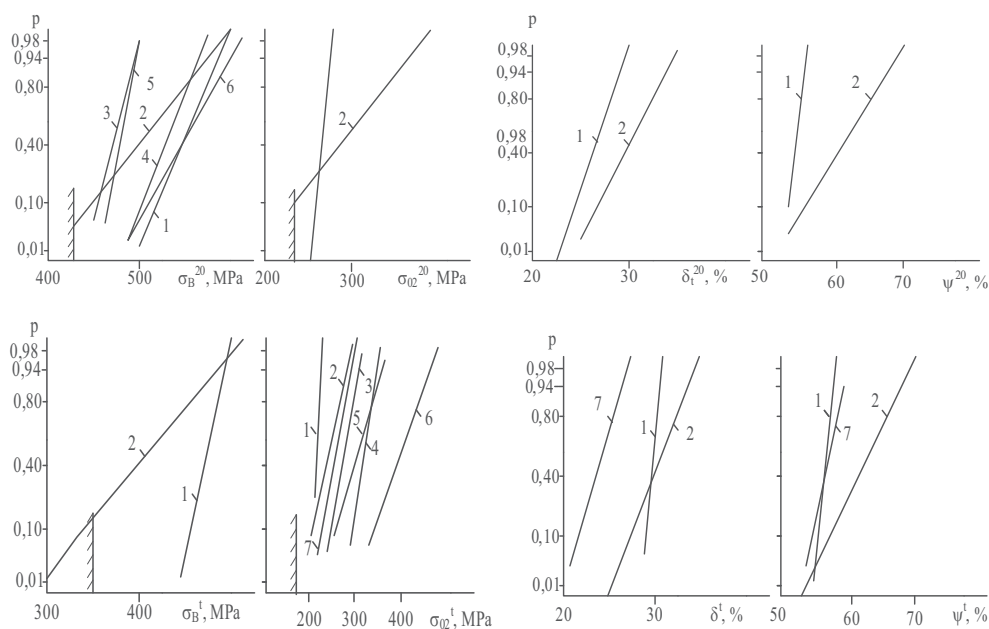


Fig. 10. Distribution of mechanical properties for welded joints on statistical analysis of manufactured RBMK units at room and elevated temperatures: 1 – base metal Crezelso 330E; 2 – base metal 22K; 3 – weld metal (SAW wire Sv-08A); 4 – weld metal (SAW wire SF-2); 5 – weld metal (MAW electrode YONII-13/55); 6 – weld metal (MAW electrode ETNA-52HR), 7 – base metal (22K) at 270°C

In Russia eleven power units with RBMK-1000 reactors are being operated at a present time. Four of them (1 and 2 power units of Sosnovy Bor and Kursk NPP) refer to power units of the first generation for which the design service life completed or will complete in the nearest time. Practically all these power units were manufactured on the same technology with the use of same materials delivered on the unitary documentation. Their operating conditions are practically identical. Thus for the elements of multiple forced circulating

circuit (MFCC) namely for steam separators, suction and pressure collectors and Du-800 pipe-lines the carbon steel 22K clad with stainless steel of the type EI-898 (08Cr18Ni10Mn2Nb) and delivered on specification TU24-1-11-427-67 was used. About 30 – 40 steel heats of different melting methods (open-hearth furnace, electroslag and vacuum arc) in the form of rolled plate of different thickness (105 and 115 mm) are used for the manufacture of one separator drum vessel. Approximately the same number of heats but with less thickness of rolled plates (60-80 mm) are used for each collector and with the thickness of rolled sheets from 38 to 48 mm – for tube units. A large bulk of information (more than 500 heats) on properties and chemical composition of MFCC was of interest in view of statistical assessment. The statistical treatment for each equipment element on four power units as a whole was performed and the comparison of properties for different products was carried out.

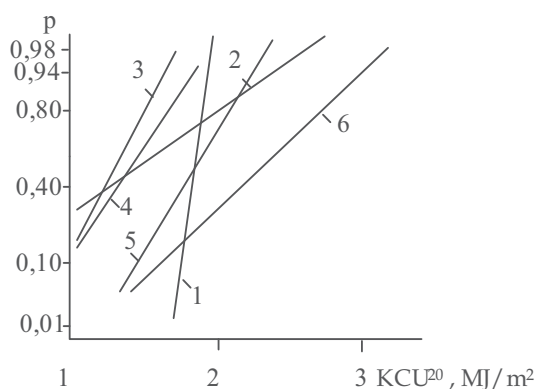


Fig. 11. Distribution of impact strength (KCU) for welded joints on statistical analysis of manufactured RBMK units at room temperature (conventional sign the same as Fig.10)

Separators ( $\varnothing 2300 \times 105$  mm, length - 30,5 m) are manufactured from two semi-vessels, each of which consists of some sections [1]. The section includes bottom (thickness – 115 mm) and shells (thickness – 105 mm) or only shells. Each of these elements are assembled from two clad plates, which (in the form of half-cylinders) are joined with longitudinal welds produced by electroslag welding (wire Sv-10Cr2, flux AN-8M). The different number of 22K steel heats (from 30 to 40) is used because one heat (2-4 ingots) may be used for different components of pressure vessel. Post-welding heat treatment is carried out on the following regime: normalization at  $930 \pm 10^\circ\text{C}$  exposure for 2.5 hours, cooling in air. Welding of shells with each other and a shell with a bottom using circumferential welds is produced by submerged arc welding (SAW) using Sv-08A wire and AN-348A flux. After welding up circumferential welds the tempering is carried out at  $630 \pm 10^\circ\text{C}$ , exposure for 4 hours and cooling in air. Welding up of shells to nozzles is performed with manual arc welding (MAW) with the use of the type YONII-13/55 electrode and then the whole pressure vessel is subjected to tempering at  $630 \pm 10^\circ\text{C}$  (heating rate –  $80^\circ\text{C}/\text{min}$ ) for a time of 11 hours.

Collectors are manufactured from 5-7 shells having a diameter of 900 mm (wall thickness – 60-70 mm) and two bottoms (wall thickness – 70-80 mm). The type 22K steel clad with EI-898 steel is used for the manufacture of collectors. A shell consists of two semi-shells connected with each other using Sv-10Mn2 wire and AN-8M flux. Welding up of nozzles to a collector case is performed manually with YONII-13/55 electrodes.



Tube units of the main circulating suction pipes ( $\varnothing 838 \times 42 \text{ mm}$ ) and pressure pipes ( $\varnothing 848 \times 48 \text{ mm}$ ) are made from Du-800 tubes. The main elements of tube units are semi-shells and half-cylinders from 22K steel of the first generation, for which chemical composition and mechanical properties are defined separately. The semi-shells, which are joined with each other using SAW (Sv-08A wire, AN-348A flux) were used for straight section of Du-800 pipe-lines. The elbow sections of Du-800 pipe-line the half-cylinders were used which were also joined with each other by SAW with same welding materials (Sv-08A wire, An-348A flux). For Du-800 pipe-lines of the second generation the French carbon steel Creselso-330E and Japanese 19MN5 steel were used instead of 22K steel.

Earlier as applied to PGV-440 steam generator cases, made from 22K steel the statistical analysis of mechanical properties was performed. There is one publication for components of NPP equipment with RBMK reactors, where the limited information presented. The statistical treatment in more representative volume of data was carried out in this work and the results are given in Tables 3 and 4 only for steam separator (SD) and in Figures 12-15 for tube units and steam separators in comparison with the recommendations of documentation. In this case the law of normal distribution was accepted for the statistical treatment of 22K steel mechanical properties on the certificate data of corresponding product.

Number of SD	Content of elements, %							
	C	Si	Mn	S	P	Cr	Ni	Cu
SD-1	0,21	0,32	0,86	0,012	0,013	0,17	0,26	0,23
SD-2	0,23	0,32	0,86	0,012	0,013	0,17	0,26	0,24
SD-3	0,22	0,31	0,87	0,011	0,013	0,16	0,25	0,22
SD-4	0,22	0,29	0,85	0,011	0,013	0,15	0,25	0,22
SD-5	0,22	0,30	0,86	0,011	0,013	0,18	0,25	0,23
SD-6	0,23	0,30	0,85	0,013	0,012	0,18	0,25	0,22
SD-7	0,22	0,30	0,82	0,013	0,012	0,18	0,23	0,21
SD-8	0,21	0,28	0,82	0,012	0,013	0,19	0,23	0,20
SD-9	0,22	0,29	0,87	0,013	0,013	0,21	0,23	0,20
SD-10	0,22	0,30	0,87	0,015	0,013	0,20	0,23	0,19
SD-11	0,22	0,30	0,88	0,013	0,013	0,21	0,22	0,19
SD-12	0,225	0,32	0,86	0,012	0,013	0,17	0,26	0,23
SD-18	0,22	0,31	0,86	0,012	0,011	0,20	0,24	0,20
SD-19	0,22	0,31	0,85	0,012	0,012	0,21	0,23	0,21
SD-20	0,23	0,32	0,86	0,014	0,013	0,19	0,19	0,18
SD-23	0,22	0,33	0,84	0,015	0,014	0,17	0,18	0,18
TU	0,19- 0,26	0,20- 0,40	0,75- 1,0	$\leq 0,030$	$\leq 0,030$	$\leq 0,40$	$\leq 0,30$	$\leq 0,30$

Table 3. Chemical composition of 22K steel for steam separator of NPP units with RBMK-1000 reactors of the first generation

As can be seen from the presented in Figs.12 and 13 data the strength properties (average values, dispersion) at room temperature for the metal of separator and tube units does not practically differ and the values (UTS and YS) required on documentation (Specification TU24-1-11-427-67) are provided with a high degree of reliability (more than 99%). As

concerns the ductility characteristics the results in view of meeting requirements of documentation appeared somewhat different. The differential curves for elongation (A) and impact strength (KCU) at 20°C confirm this idea.

Number of SD	At 20°C				At 350°C
	UTS MPa	YS MPa	A %	KCU J/cm <sup>2</sup>	YS MPa
SD-1	534	354	25,5	176	249
SD-2	537	342	25,1	175	244
SD-3	528	335	25,7	184	238
SD-4	526	340	25,2	186	244
SD-5	523	337	27,5	183	249
SD-6	535	349	24,6	169	246
SD-7	520	328	25,4	174	245
SD-8	515	319	25,1	170	238
SD-9	528	346	27,4	180	248
SD-10	530	347	29,9	158	262
SD-11	533	343	29,7	177	251
SD-12	525	343	32,1	149	254
SD-18	523	304	31,5	144	254
SD-19	507	309	31,4	157	237
SD-20	518	316	31,8	170	234
SD-23	511	321	32,1	176	232

Table 4. Mechanical properties of steam separator

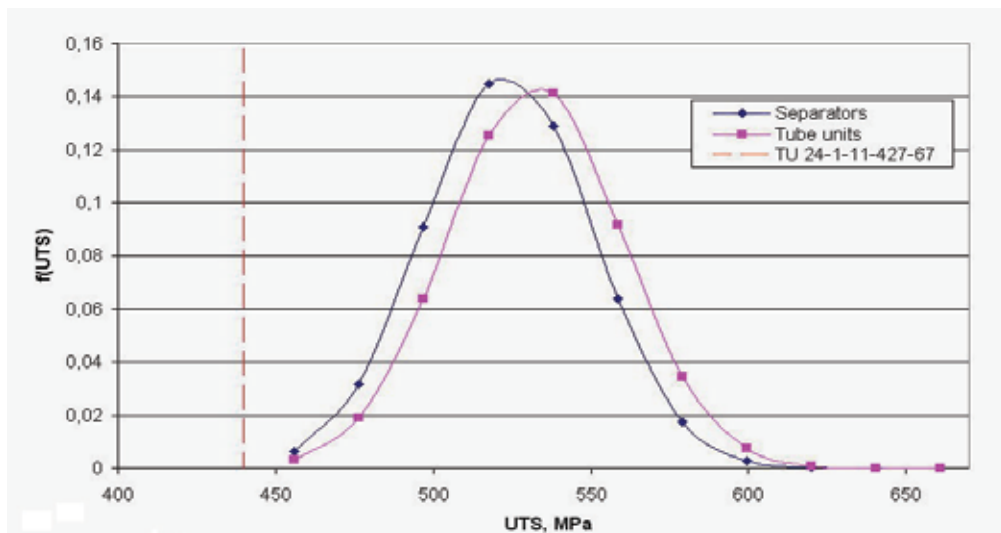


Fig. 12. Comparison of theoretical curve of ultimate tensile strength distribution at 20°C for separators and tube units with requirements of specification TU 24-1-11-427-67

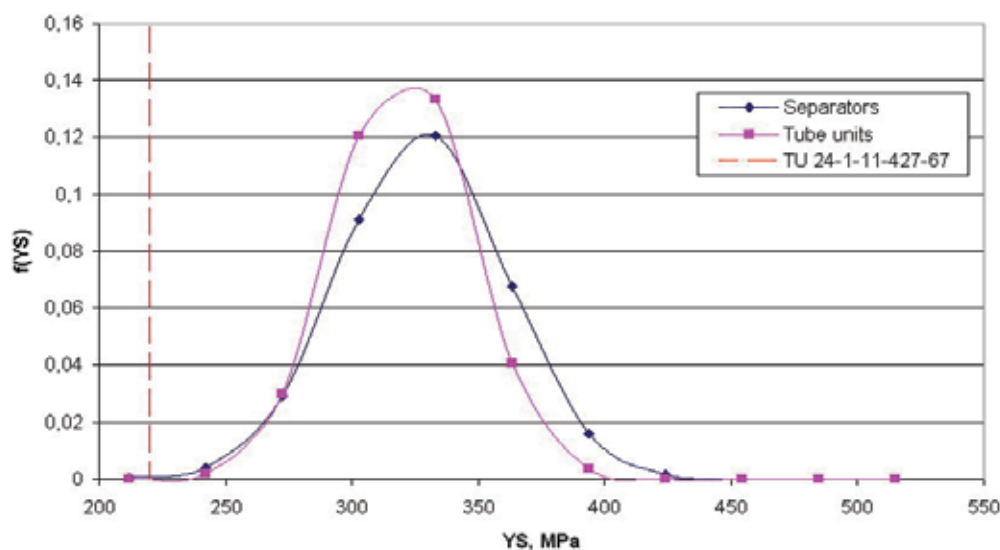


Fig. 13. Comparison of theoretical curve of yield strength at 20°C for separators and tube units with requirements of specification TU 24-1-11-427-67

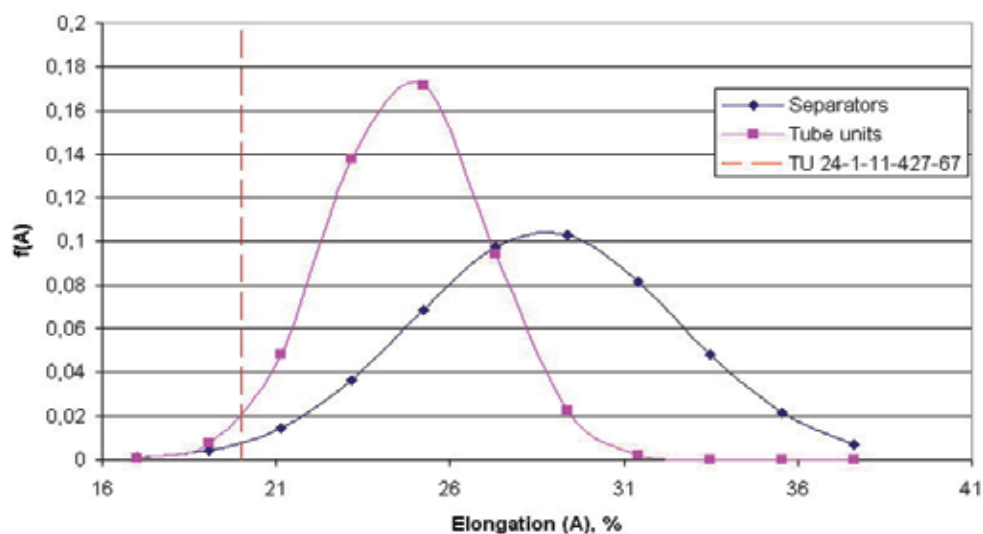


Fig. 14. Comparison of theoretical curve of elongation distribution at 20°C for separators and tube units with requirements of specification TU 24-1-11-427-67

The characteristics presented in Figs. 14 and 15 reflect in a higher degree the ductile properties of material at room temperature. The relative elongation and impact strength on Manager specimens rather relates to qualitative characteristic and usually are not used by the conduction of strength calculations. At the same time we may note that  $A$  and  $KCU$  for material of tube units are a few not so good than for steel of the same separator type, and the theoretical curves of distribution of these characteristics confirm it. The same may be said about the value of yield strength at elevated temperature.

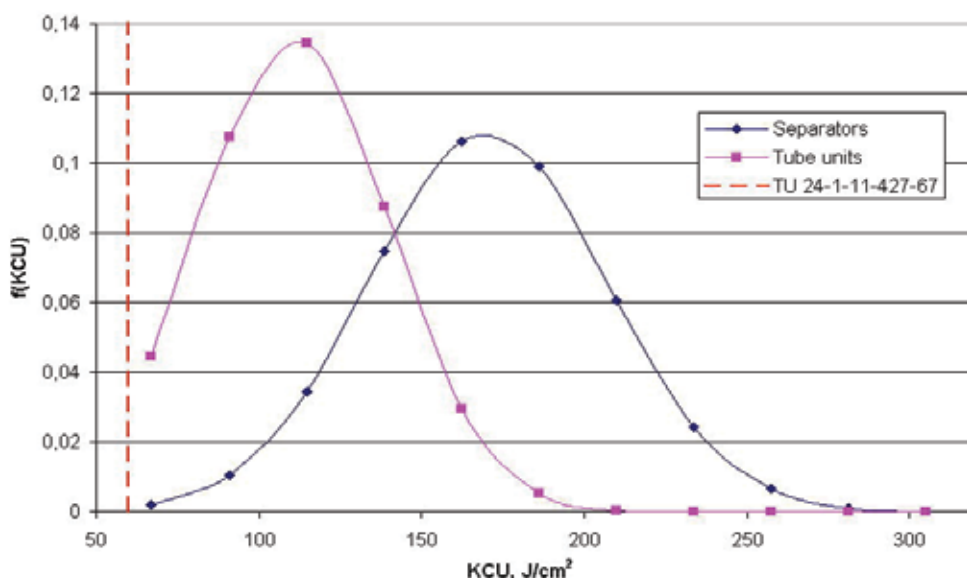


Fig. 15. Comparison of theoretical curve of impact strength at 20°C for separators and tube units with requirements of specification TU 24-1-11-427-67

#### 4. Requirements for stability of properties during operation

In accordance with item 7.6.3 (PNAE G-7-008-89, 1990) the inspection of equipment mechanical properties is carried out using destructive and non-destructive techniques. It shall be performed out not rarely than at interval of 100000 hrs of operation for NPP with water-cooled and water-moderated reactors (WWER) and water-graphite reactors (RBMK), and at intervals of 50000 hrs for fast reactors with liquid metal coolant (BN). This order of assessment of actual properties of material in the process of operation was introduced in the regulations of NPP works for the purpose of safety provision. This requirement was associated with the necessity to obtain valid information about material ageing in the NPP equipment operation and on the base of this information to estimate the change of strength margin coefficient used in design with regard to variations of initial mechanical properties of materials. It is possible to assess various methods using surveillance specimens, part of materials removed from the inner surface of equipment (RPV, SG and other large cases) or a part of the piping. For RPV as a rule the variation of mechanical properties are examined with the use of surveillance specimens which are tested not less than six times during the calculated design lifetime of reactor.

By the development of the first normative documents for NPP arrangement and safe operation of other equipment and piping of NPP PNAE G-7-008-89 the regulation about a periodical inspection of steel mechanical properties on the base of test results of specimens removed from pipe-lines was introduced. It makes possible to follow the actual state of pipe-lines and variation of mechanical properties of base metal and welded joints under the influence of real operating conditions (elevated temperature, pressure, corrosive medium) by all regimes. It is natural to suggest that due to the operation influence (static and cyclic loads, a prolonged effect of elevated temperatures and coolant) the degradation of material mechanical properties is possible. Of course in accordance with (PNAE G-7-002-86, 1989)

these factors should be taken into consideration in the condition by calculations. The values of the mechanical properties of NPP materials during the whole designed lifetime is estimated by definite requirements which are presented in Table 5.

BASE Material	Part of welded joint	At 20°C				At 350°C				T <sub>KO</sub> , °C
		UT MPa	YS, MPa	A,%	Z,%	UTS MPa	YS, MPa	A,%	Z,%	
22K	Base metal	430	215	18	40	392	177	18	40	+40
	SAW Sv-08A	353	196	20	55	314	176	13	50	0
	MAW									
	YONIL- 13/45	353	216	20	55	314	176	20	55	+20
	YONIL- 13/55	431	255	20	50	372	216	18	50	+30
	ESW Sv-10Mn2	372	216	16	50	=	196	-	-	+40

Table 5. Requirements of mechanical properties for NPP equipment materials

At a present time a great experience has been accumulated on the determination of ageing processes under conditions of NPP pipe-lines operation which has shown that the steel mechanical properties variations of pipe-lines are small and are within the limits of measurement accuracy. Such results might be expected for operation conditions of pipe-lines in light water pressurized reactors thanks to:

- steady structure equilibrium of structural steels used for pipe-lines which should provide a relative stability of steel structure and properties during operation;
- a low level of membrane stresses (margins  $n_{0.2}=1.5$  and  $n_B=2.6$ ) assuring the operation of the main metal mass in the elastic area;
- in principle the steels considered are cyclically stable and this makes the processes of cyclic hardening insignificant.

The aim of this presentation is as follows:

- generalization of experimental results and analysis their stability;
- determination of a possible decrease of inspection scope of mechanical properties under NPP conditions up to a complete or partial cancellation, decrease or cancellation of metal removal from real pipe-lines considering the fact that the removal of specimens from real pipe-lines did not promote the increase of pipe-lines quality and reliability because the repair process results in the increase of defective pipe-lines welds which are performed under assembling conditions with radiation influence

Based on the operation conditions by the conduction of strength calculations of equipment it is necessary to take into account the variation of properties due to the action of the main damaging factors during the designed service life (30 years). They are:

- structural changes and degradation of material properties caused by a prolonged influence of elevated temperatures;
- generation of cracks caused by low cycle loads by a combined action of cyclic (including thermal cycles) and static loads;

- embrittlement of material and welded joints due to the influence of static and cyclic loads;
- corrosion damage due to a prolonged effect of coolant.

Ageing is defined as the metal state variations which may take place in the course of time under external influences or without them. The ageing by heat treatment, a prolonged temperature influence, by strain aging, under operational and thermo-mechanical influences, etc. are distinguished. As ageing occurs, as a rule, mechanical properties of metal are degraded. Taking into account an obligatory execution of the item 7.6.3 PNAE G-7-008-89 a lot of tests of specimens removed from piping after operation 100000 hrs were carried out in our country and also other countries and large number of data were accumulated. Nevertheless the published information about the effect of operational factors on material mechanical properties is quite limited. The first publication was devoted to the investigations performed for the main circulating piping from stainless steel intended for units 3 and 4 of Novo-Voronezh NPP (Gaponov, 1989). Such results for piping made from carbon steels appeared later and are presented in (Timofeev, 2004). The information accumulated for the last 15 years on the investigation of the state of base metal and welded joints after a prolonged operation (100000 hrs and more) makes possible to analyze the variation of strength and ductility characteristics. Besides there are some publications (Timofeev, 2009) and (Petrov, 2004) ) about thermal ageing of RPV steels and their welded joints. This paper presents the analysis for carbon steel and their welded joints mainly as applied to operation conditions of NPP.

## 5. Thermal ageing

The first results for piping made from carbon steels appeared later and they are presented (Gaponov, 1989) and (Beznosikov, 1995). The information accumulated for the last 15 years on the investigation of the state of base metal and welded joints after a prolonged operation (100000 hrs and more) makes possible to analyze the variation of strength and ductility characteristics. The mechanical properties of carbon steels of the type 20 and 22K and their welded joints produced using manual arc welding (MAW) with covered electrode after a prolonged (100000 hours) influence of operation temperatures up to 290°C practically do not change. This tendency for base metal is confirmed up to 200000 hours, i.e. to the designed service life of piping (30 years) makes possible to correct item 7.6.3 "Rules of arrangement and safe operation of equipment and piping of NPP" as concerns the inspection periodicity of mechanical properties with destructive techniques at the NPP in the period of planned maintenance repair. As the degradation of mechanical properties of carbon steel is practically absent during the designed service life was recommends to carry out inspection after 200000 hrs of operation and not 100000 hrs and the basis for this conclusion was presented. On the base of earlier performed investigations (Karzov, 1993) we can mention a high stability of strength and ductile properties of this steel at 20°C independent of temperature and a prolonged thermal exposure. In this case the level of mechanical properties after thermal exposures does not decrease below the normative requirements for the initial period of operation. At the same time it should be noted the insignificant decrease of impact strength of steel by Menage specimens tests after the exposure during 10000 hrs at the thermal temperature 450°C if we compare with value according to the normative requirements. The critical transition temperature of 22K steel is also nearly stable after thermal ageing at studied temperatures (except 340°C) on the duration 100000 hrs.

A section of Du-800 piping was cut out from Sosnovyj Bor NPP, operated under the influence of elevated temperatures and pressure for nearly 30 years, in order to assess the mechanical properties variation of piping material after a prolonged operation. Specimens were made from base metal (22K steel) of the removed from piping (0828x38 mm) element and tested by one-fold tension. Fig.16 presents the summarized results which make possible to judge about the relation between actual properties of materials with the requirements on the values of characteristics specified by the technical normative documentation and it was accepted to conduct strength calculations by the chief designer of the power plant. In this case the actual values in as-produced condition are accepted with regard for their distribution according to the investigation data in (Timofeev, 2004) after 100000 hours of operation - data of NPP reports for various power units and after 30-year period of operation - test results of specimens removed from the piping of unit 1 Sosnovyj Bor NPP (Karzov, 1999).

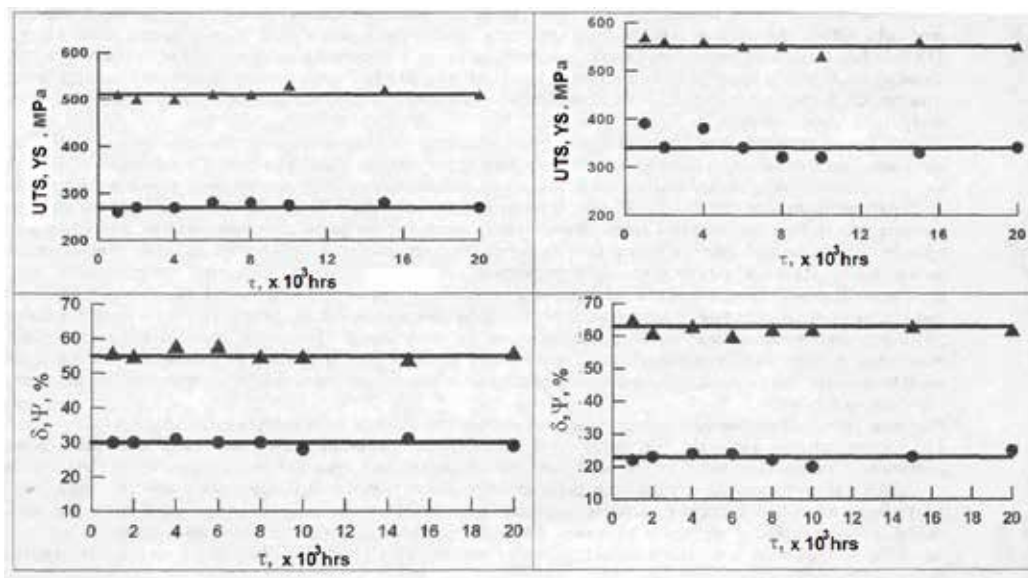


Fig. 16. Variation of mechanical properties for 22K steel (left) and its weld metal (right) produced by MAW electrode YONII-13/45 at room temperature for different time of thermal ageing

As follows from Fig.16 the variations of mechanical properties of both base metal and weld metal during the designed operation time of pipe-lines made from carbon steels as related to these materials in as-produced condition (before operation) practically do not occur and thus margins of static strength accepted at the project stage are retained. This conclusion may be drawn for margins of cyclic strength because the values of material reduction of area independent of the thermal ageing duration is actually at the same level as in as-produced condition.

The obtained experimental data for 22K steel show that after the operation time (30 years) the mechanical properties are appreciably higher than required by the documentation TU-24-3-449-74. And this is the evidence for the fact that a prolonged heating of 22K steel within

the range of operation temperatures and operating pressure does not result in an appreciable degradation of properties.

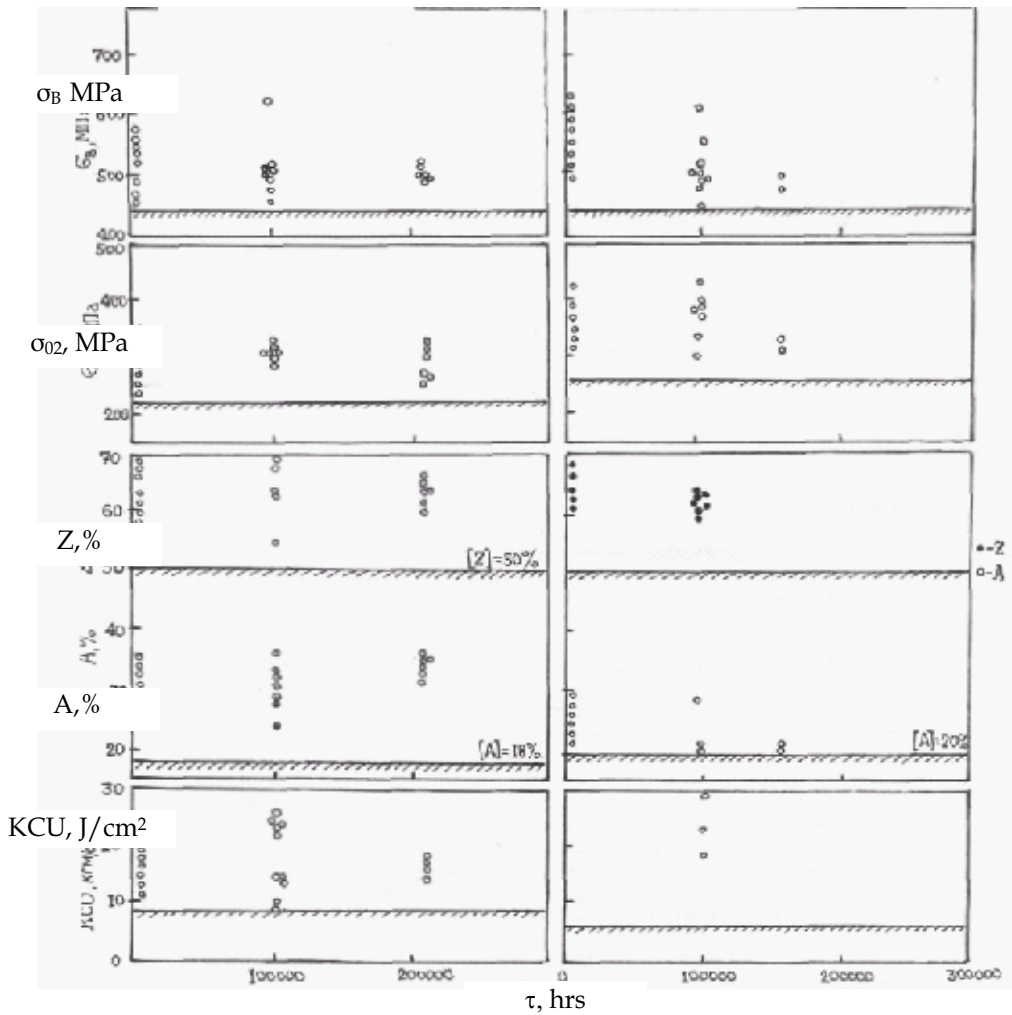


Fig. 17. Summarized data of effect of thermal ageing on mechanical properties of welded joints for carbon steel type 22K

## 6. Strain ageing

The equipment and pipe-lines of NPP manufactured in carbon steel are operated at elevated temperatures up to 360°C that lay within the temperature range of dynamic strain ageing which manifests itself in strength properties improvement and plastic properties deterioration under single loading (Karzov, 1993). The variation of mechanical and fatigue properties of steels in the temperature range from 20 to 400°C can be attributed to different reasons, including carbon and nitrogen atomic hardening around screw dislocations, strain



ageing due to internodes carbon and nitrogen atoms, and also to dislocation precipitation of carbide and nitride particles.

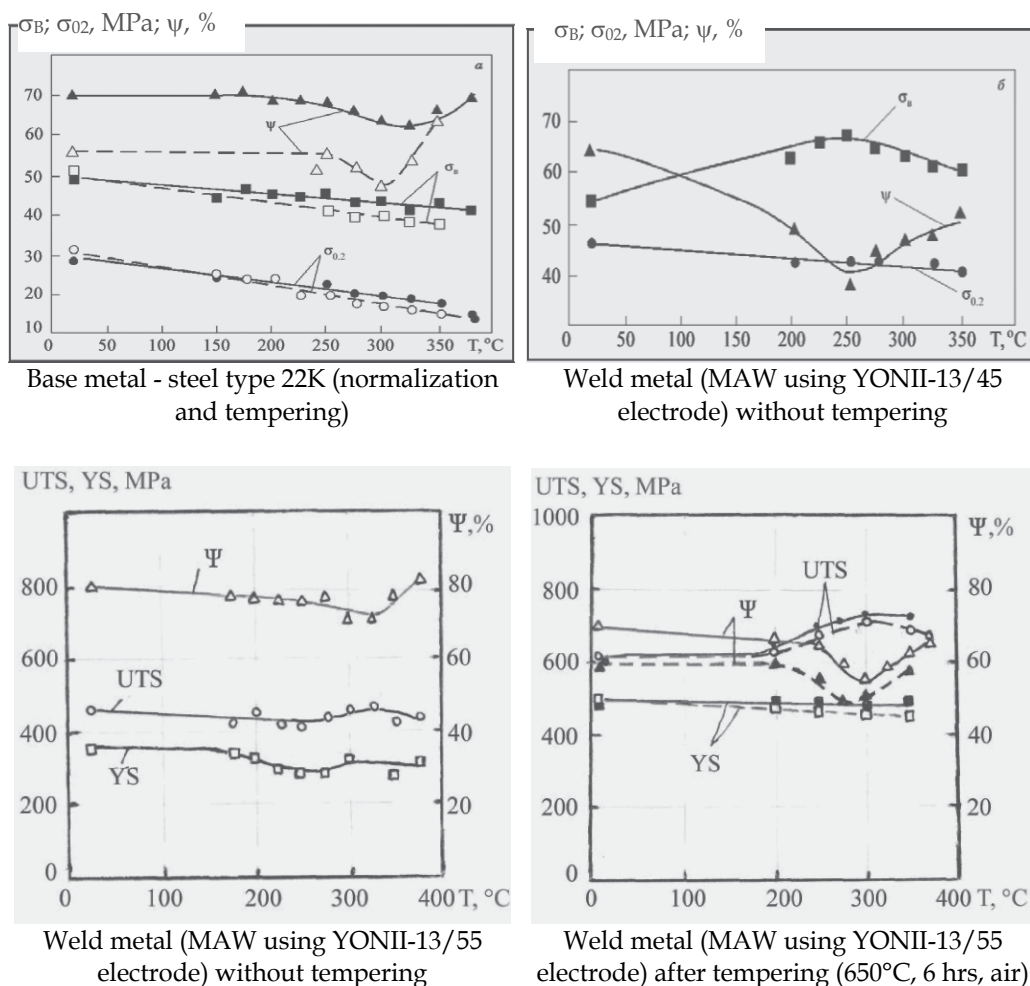


Fig. 18. Variation of mechanical properties for base and weld metal of 22K welded joints in BOL ( $\tau = 0$ ) and EOL ( $\tau = 30$  years)

From these assumptions it is noted in Ref. [9] that the effect of mechanical and fatigue properties variation must be most evident in welded joints since high heating temperatures in welding and subsequent fast cooling enhance super saturation and ageing. Some investigations carried out in our country during 1970 are devoted to this problem. The variation of mechanical properties in the temperature range from 20°C up to 400°C was investigated for different materials (base metal and welds, Fig 18) under single tension at the strain rate of  $150 \times 10^{-4} \text{ s}^{-1}$  (the rate applied in low-cycle fatigue tests). It has been established that strain ageing shows up most vividly in reduction of area Z (Daunene, 1975) and (Daunis, 1982).

## 7. Low cycle fatigue

Experimental results of low cycle fatigue tests for low carbon steel of grade 22K are shown in Fig. 19. Here data of 22K steel after various procedures (melting in open-hearth furnace, electro-slag and vacuum-arc re-melting) is presented. These data were received for forging, sheet rolling and a pipe at room and elevated temperatures. The thickness of semi-products is changed from 38 to 120 mm. All experimental points are located in a fairly narrow scatter band and, therefore, can be referred to a single general population. This fact enabled us to construct a mean-square relation (solid line 4) and bound areas of the 95% confidence interval (dashed lines 2 and 3) for the entire array of experimental data. The mean-square relation is described by the formula  $\log \varepsilon_a = 1.29154 - 0.45116 \log N$ . Comparison of this relation and the lower envelope of the common data array at 20°C with the design curve of fatigue for carbon steels (line 1) shows that the values of safety factors  $n_o=2$  and  $n_N=10$  by the lower envelope (line 3) are provided for the base metal (Timofeev, 2005).

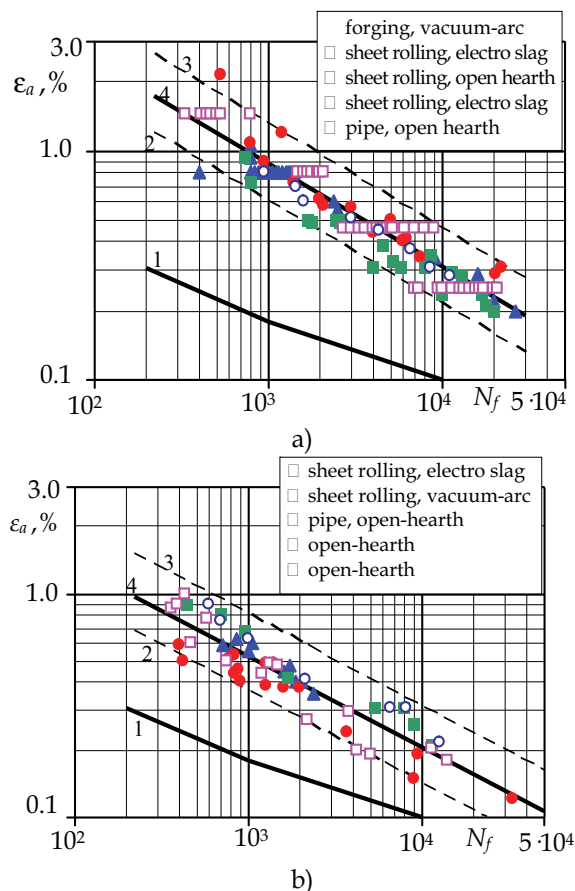


Fig. 19. Low-cycle fatigue curves of 22K steel of different melting: a – at room temperature; b – at 350°C temperature. Dots – experimental data for different heats of steel; 1 – Reference curve for low alloyed steel; 2 and 3 – data falling outside the 5 and 95% tolerance bounds for steel at 20°C; 4 – mean square dependence for the scatter band for steel at 20°C

## 8. Conclusion

The generalization of experimental investigation results performed in our country and devoted to the effect of thermal ageing at 250-350°C on mechanical properties of carbon steel and its welds has shown that variation of structure, strength and ductility characteristics, practically, does not occur during the 30-years service life. There are only some deviations from the general tendency, however they are small and always within the limits of the accuracy of characteristic measurement on the accepted determination procedure.

A prolonged operation experience of carbon steels in the composition of equipment of the LWR confirmed the absence of variation of mechanical characteristics of the carbon steel. Some decreasing of reduction of area materials is observed because some of them (weld metal without tempering) have sensitivity to strain ageing.

## 9. References

- Beznosikov S.A., Mjasnjankin A.I., Veselovsky V.F., Timofeev B.T., Filchagin Yu. (1995). Assessment of State of Properties for Base Metal and Welds of NPP Pipe-Lines after Prolonged Operation. *Proceedings of Workshop "Ageing of NPP Component Materials"*, St-Petersburg, 28 February-2 March 1995, p.221-232.
- Dauniene S.A., Karzov G.P., Timofeev B.T., Timofeeva A. (1975). Experimental Assessment of Sensitivity of Weld Metal to Strain Ageing. *Sudostroitel'naja Promyshlennost*, serja "Svarka", issue 20, p. 17-21.
- Daunys M.A., Dauniene S.A., Timofeev B. (1982). Properties of Welded Joints at Strain Ageing during Low Cycle Fatigue. *Svarochnoe Proizvodstvo*, No. 12, 1982, p. 12-14.
- Gaponov, A. (1989). The State of the Du-500 Piping of the WWER Main Circulating Circuit after 100000 hrs Operation. *Teploenergetika*, No.1, p.43-44.
- Karzov G.P., Timofeev B. (1999). Assessment of Degradation of Mechanical Properties of Steels and Weldments for Pressure Vessels and Piping. *Proceedings of the Joint EC – IAEA Specialists Meeting on NDT "Methods for Monitoring Degradation"*. 10-12 March 1999, Petten, p.94-103.
- Karzov G.P., Timofeev B.T., Filchagin Yu.G. The Influence of Prolonged Exposure to Operating Temperatures and Strain Aging on the Material Properties of Nuclear Power Plant Reactor Vessels and Piping. *International Journal of Pressure Vessel and Piping*. Volume 53, No.2, 1993, p.195-216.
- Kashirin V., Krasnov A., etc. (2004). Problems and their Solution by the Substantiation of a Possible Service Life Extension of Steam Separators and Collectors of Unit 1 Sosnovy Bor NPP. *Proceedings of Int. Conf. "Channel reactors: Problems and Solution"*, Moscow, 8p.
- Petrov V.A., Timofeev B.T., Shalygin A.S. (2004). Influence of Prolonged Operation Time on Mechanical Properties of NPP Piping Welded Joints from Carbon Steels. *Proceedings of the Tenth Workshop "Provision on Safety and Economy of Power Engineering Equipment"*. 23-26 November 2004, St. Petersburg, p.175-180.
- PNAE G-7-002-86. *Strength Calculations Norms for Nuclear Power Plant Equipment and Piping*. Energoatomizdat, Moscow, 1989, 525p.
- PNAE G-7-008-89. *Regulations of the NPP Equipment Installation and Piping Safe Operation*. Energoatomizdat, Moscow, 1990, 168p.

- Timofeev B.T., Shalygin A. (2004). Assessment of Variation of Properties for Welded Joints of Piping from Carbon Steels during Design Lifetime. *Voprosy Materialovedeniya*, No.3(39), p.54-61.
- Timofeev B., Bazaras Z. (2005). Cyclic Strength of the Equipment of Nuclear power Plants Made of 22K Steel. Cyclic Strength of the Equipment of Nuclear power Plants Made of 22K Steel. *International Journal Materials Science*, 2005, vol.41, No.5, p.680-685.
- Timofeev, B. (2009). Thermal Ageing of Russian RPV Materials Used for NPP with LWR. *Proceeding of the 15 Int. Conf. "Building Services > Mechanical and Building Industry Days"*. 15-16 October 2009, Debrecen, Hungary. Mechanical Engineering Section, p.55-66.
- Timofeev, B.; Zhrebentkov, A.; Chernaenko, T. (1982). *Statistical Approach to Estimation Quality and Properties of Welded Joints*. Leningrad, LDNTP, 23p.
- Vaseneva, N.; Generalova, S.; Timofeev, B.; Chernaenko, T. (1990). Properties of Steel and Welded Joints of Pipe-Lines of Circuit MFCC for NPP with RBMK Reactors of First and Second Generations. *Sudostroitel'naya promyshlennost*, Issue Number 9 "Welding", p.29-34.
- Zhrebentkov A., Timofeev B., Chernaenko T.. (1979). Dispersion of Mechanical Properties of Welded Joints from the Type 22K Steel. *Scientific-Technical Collection "Problems of Shipbuilding"*. Ser. Welding, issue 28, 1979, p.56-59.
- Zhrebentkov A.; Sobolev Yu.; Timofeev B.; Zemzin V. (1980). Comparative Assessment of Properties and Composition of the Used in Power Mechanical Engineering 22K Steel Depending on Melting Method. *Energomashinostroenie*, No.11, 1980, p.20-23.

# Primary to Secondary Leakage at PSB-VVER Test Facility, Simulated by CATHARE 2 Code

Luben Sabotinov and Patrick Chevrier  
*Institut de Radioprotection et de Sûreté Nucléaire (IRSN)*  
France

## 1. Introduction

The current analysis was carried out in the framework of the international PHARE project on code assessment and validation with participation of IRSN-France, GRS-Germany, NRI-Czech republic and EREC-Russia. Overall objectives of this project are utilization and transferring of methodologies for computer codes validation using available experimental data of VVER test facility.

The experiment “Primary to Secondary Leakage” (PRISE) was performed by EREC at PSB-VVER test facility. It replicates an accident on VVER-1000 with an equivalent diameter of 100 mm for the leak size, which corresponds to a break size of 1.4%. The initial event of the experiment is a leakage from primary to secondary side as a result of a cover break of a hot steam generator collector. This test provides the data required to perform an analysis with the thermal-hydraulic computer code CATHARE: initial and boundary conditions, transient scenario, experimental results.

## 2. PSB-VVER test facility

The PSB-VVER facility is a large-scale integral test facility, which structure is similar to that of the primary circuit of VVER-1000 nuclear power plant (NPP). It is scaled 1:1 in height and 1:300 in volume and power.

The facility consists of a reactor model, four loops, four steam generators, a pressurizer (PRZ) and an emergency core cooling system (ECCS). The reactor model comprises five elements: lower plenum (LP), core simulator (CS), external core bypass (BP), upper plenum (UP) and external downcomer (DC). Each loop includes a circulation pump (MCP), a steam generator (SG), and hot and cold legs (HL and CL). Special lines (primary to secondary leakage system) connect the upper part of SG #4 headers to the steam generator secondary side, which allows simulation of both hot and cold SG collectors break. MCPs are installed on CLs. They can operate in two-phase flow and have a motor speed control system (Melikhov et al., 2003).

The PRZ is a vessel, connected to one of the loop HL through a surge line. It operates similarly to the reference NPP one, controlling primary pressure. It is equipped with a relief valve, a spray line for pressure decrease and an electrical heater – installed in the vessel lower part – for pressure increase. In this scenario, PRZ is connected to loop #2.

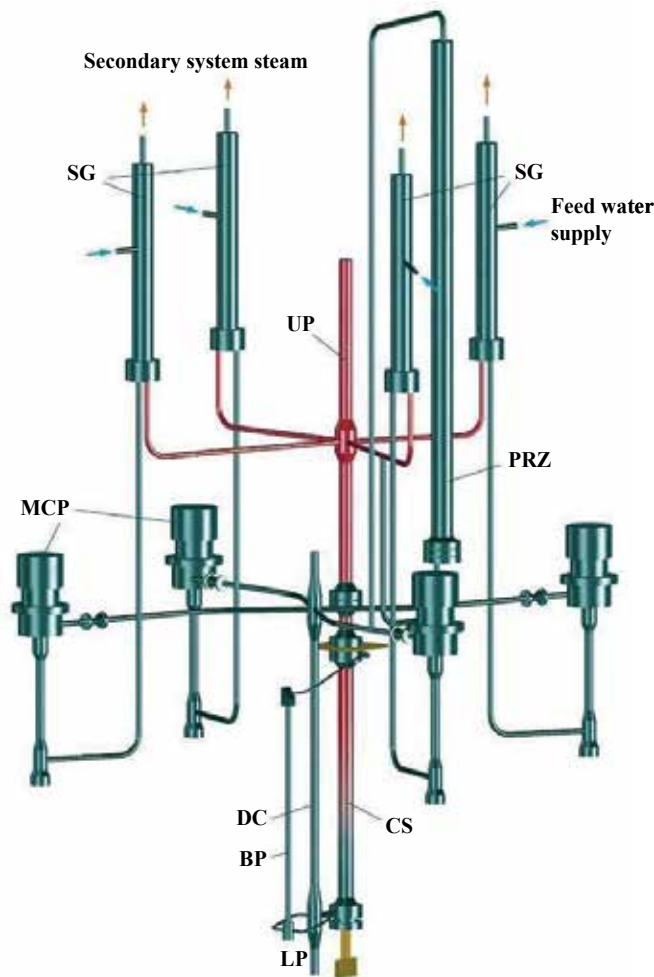


Fig. 1. General view of PSB-VVER facility

ECCS of the facility includes three subsystems: a passive system, a high pressure active system (HPSI) and a low pressure active system (LPSI). The passive system consists of four hydroaccumulators (ACCUs) connected in pairs to the downcomer inlet chamber and to the upper plenum outlet chamber. Both active ECCS are simulated by a proper delivery of cold water into hot and cold legs of loops #1, #3 and #4, from a feed water system.

The core simulator is a bundle of 168 fuel rods (FRs) and one central non-heated tube, placed in a regular hexagonal channel. These FRs are electric resistance heating rods, with a uniform power profile along the height. FRs and central tube are grouped along a triangular lattice. Along bundle height, 17 spacer grids are welded to the central tube. The bypass connects the lower plenum with the upper plenum. Its walls are heated directly by electric power supplies.

Heat is removed from primary circuit using steam generators. Each SG consists of a vertical vessel with two vertical headers inside (hot and cold collectors), interconnected with 34 helical tubes. Thus, the heat-exchanging surface of SG model is a slightly inclined helical bundle of 34 tubes.

Secondary circuit of the facility is designed as an open loop. Feed water is supplied to steam generators through annular header. Flow rate of feed water is regulated with control valves. Steam from each SG flows through steam discharge lines to a common header and then to a special process condenser. An atmospheric steam dump system (ADS) is connected to each SG.

The test facility is equipped with advanced data acquisition and process control systems. The latter controls the experiment on PSB-VVER facility.

### 3. CATHARE 2 computer code

CATHARE (Code for Analysis of Thermal-Hydraulics during an Accident of Reactor and safety Evaluation) is an advanced, two-fluid, thermal-hydraulic code. It is developed in France by the French Atomic Energy Commission (CEA), Electricité de France (EDF), Areva NP and IRSN.

CATHARE is designed to perform best-estimate calculations of accidents in pressurized water reactor, including VVER. Specific modules have also been implemented to allow modeling of other reactors like boiling water reactors or gas cooled reactors. CATHARE is limited to transients during which no severe damage occurs to fuel rods; more precisely, fuel ballooning and clad rupture are assumed not to have major effect on water flow in the reactor core. Its range of application covers all loss-of-coolant accident (LOCA), all degraded operating conditions in steam generators secondary systems, following ruptures or system malfunctions (Barre & Bestion, 1995).

CATHARE has a modular structure with five main modules: 1D axial module for pipes, tubes or channels where velocity has a preferential direction; 0D volume module for vessels or plenums where fluid is not channeled in a preferential direction of flow and where inertial forces are negligible compared with gravity; 3D module; boundary condition module; double-ended break module. Each 0D module is divided in two sub-volumes. Any kind of hydraulic circuit may be represented by a set of modules, which are connected by junctions. Hydraulic elements (axial, volume and 3D modules) can be connected to multi-layer walls. The heat exchange between one primary and several secondary circuits, via heat exchangers, can be calculated. Other gadget sub-modules are available to represent local changes to standard thermal hydraulic equations: hydroaccumulator; valve; 0D pump, using homologous curves of head and torque; break; heat and/or mass sources; heat and/or mass sinks; etc.

These modules allow to take into account any two-phase flow behavior. Thus, mechanical and thermal non-equilibrium, as well as all flow and heat transfer regimes, are described: stratified and co- or counter-current flow; critical flow and heat flux; reflooding; natural and forced convection; subcooled and saturated nucleate boiling; film boiling and condensation; etc. In particular, a flooding counter-current flow limitation (CCFL) is modelled (Sabotinov, 1997).

Two-phase flows are described using a two-fluid six-equation model. These equations represent conservation of mass, energy and momentum, for separate processing of liquid and steam. The presence of one to four non-condensable gases can be taken into account by one to four additional transport equations. This system of equation is closed by a complete set of momentum, mass and energy transfer laws for exchange at liquid/steam interfaces or at walls. Specific models are also available to represent fuel rods thermomechanics, core neutronics, reflooding, etc. (Bazin & Pellissier, 2006).

The mass and energy balance equations are of primary form whereas the momentum equations are of secondary form. The six main variables are pressure, liquid enthalpy, gas enthalpy, void fraction, liquid velocity and gas velocity and, if it exists, up to four non-condensable mass fraction. In 0D modules, two energy and mass balance equations are written for each sub-volume (inertia is neglected). The main variables (except velocity) are then calculated for each sub-volume, as well as the separation level elevation between the two sub-volumes. In 3D modules, the momentum equation is written in all three directions. The numerical choices are finite volume discretisation with structured mesh, first order discretisation in space and time, staggered spatial mesh and donor cell principle. Time discretisation is fully implicit (semi-implicit for 3D) and enables solution stability to be achieved over a broad range of time step values. The maximum time step is up to the user and depends on the problem being solved. A non-linear system is thus obtained, solved using the Newton-Raphson iterative method.

## 4. Test specification

### 4.1 Facility configuration

The pressurizer is connected to loop #2. Two lines of HPSI are connected to the cold legs of loops #3 and #4. Two lines of LPSI are connected to the hot and cold legs of loops #3 and #4. The two other active ECCS lines are disconnected. All ACCUs are enabled: ACCUs #1 and #3 are connected to the UP outlet chamber while ACCUs #2 and #4 are connected to the DC inlet chamber.

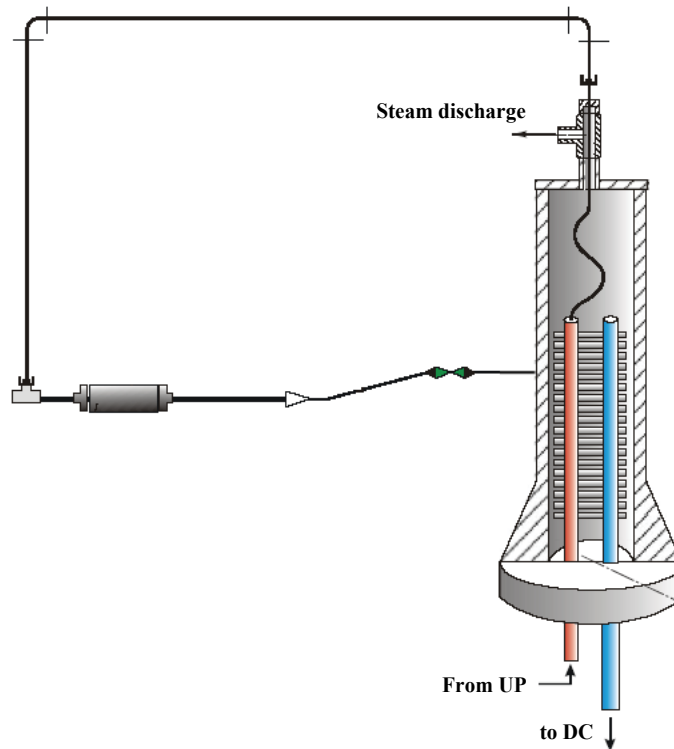


Fig. 2. Primary to secondary leakage system



Level in SGs under steady-state conditions is maintained by means of pulsed supply of feed water with a temperature of about 220°C. Atmospheric steam dumping systems are connected to each SG. In each ADS line, a throttle of 50 mm long by 12.1 mm inner diameter is installed. The opening/closing of ADS are set to 7.16/6.28 MPa.

The leakage simulation system connects the top of the SG #4 hot header to the steam generator secondary side (figure 2). In this connecting branch, a throttle of 56 mm long by 5.8 mm inner diameter is installed.

#### 4.2 Initial conditions

Initial conditions of the experiment (Elkin et al., 2005) with respective results of the steady-state calculation by CATHARE are presented in table 1.

Parameters	Experiment	Calculation
Primary circuit		
Core simulator power, kW	1507	1507
Bypass power, kW	15.0	15.0
Loop-1 flow rate, kg/s	10.45	10.45
Loop-2 flow rate, kg/s	10.41	10.41
Loop-3 flow rate, kg/s	10.39	10.39
Loop-4 flow rate, kg/s	10.15	10.15
Pressure at CS outlet, MPa	15.74	15.65
Coolant temperature at DC inlet, °C	280	281
Coolant temperature at UP inlet, °C	291	288
Collapsed level in PRZ, m	6.71	6.69
Secondary circuit		
Pressure in SG-1, MPa	6.28	6.32
Pressure in SG-2, MPa	6.30	6.32
Pressure in SG-3, MPa	6.33	6.31
Pressure in SG-4, MPa	6.29	6.32
Collapsed level in SG-1, m	1.70	1.70
Collapsed level in SG-2, m	1.71	1.71
Collapsed level in SG-3, m	1.70	1.70
Collapsed level in SG-4, m	1.69	1.69
Hydroaccumulators		
Pressure in ACCU-1, MPa	5.88	5.88
Pressure in ACCU-2, MPa	5.87	5.87
Pressure in ACCU-3, MPa	5.87	5.87
Pressure in ACCU-4, MPa	5.90	5.90
Collapsed level in ACCU-1, m	4.84	4.84
Collapsed level in ACCU-2, m	4.84	4.84
Collapsed level in ACCU-3, m	4.84	4.84
Collapsed level in ACCU-4, m	4.86	4.86

Table 1. Initial conditions

### 4.3 Boundary conditions and scenario

The experiment starts with the opening of an isolation valve in the break line.

PRZ heater power is regulated depending on the pressure in UP according to a specified law. When collapsed level in PRZ reaches 2.33 m, its heater power is switched off.

When the level of affected steam generator (SG #4) reaches 1.77 m, a signal is given to close the valve of the steam discharge line of this SG – and then to isolate it from intact SGs – with a delay of 2 s. The valve is completely closed in 11.3 s.

When the pressure in UP reaches 13.7 MPa, a scram signal is simulated, which leads to four actions. Firstly, core and bypass power start to reduce, according to a specified law, with a delay of 5.6 s. Secondly, a command to close the feed water valve of SG #4 – and then to stop feed water supply to this SG – is given with a delay of 4.6 s. The valve is completely closed in 2 s. Thirdly, level in intact SGs is maintained at 1.67 m by operation of emergency feed water pumps. These pumps are actuated with a delay of 2 s. The temperature of emergency feed water is 150°C, and the maximum flow rate is 67 g/s. Fourthly, the valve that controls steam removal from SGs is closed in 16.6 s.

When the difference between the saturated temperature of primary circuit and the maximal coolant temperature in hot legs of primary loops reaches 10°C, a signal to stop MCPs is given with a delay of 17 s. MCPs are completely stopped in 232 s.

The opening/closing of ADS are set to 7.16/6.28 MPa. ADS in SG #1, #2 and #3 operates according to pressure in SG #2 secondary side, while ADS in SG #4 operates according to pressure in SG #4 secondary side. After the first opening of ADS in affected steam generator (SG #4) a seizure is simulated and then this ADS remains in fully open position until the end of the transient.

When the UP pressure drops below 10.8 MPa, cooling water from HPSI is supplied to the cold leg of loops #3 and #4 with a delay of 1 s. HPSI flow rate is regulated depending on the pressure in UP, according to a specified law.

On decreasing the primary pressure below the set point of ACCUs actuation (5.9 MPa), they start to supply water to the primary circuit. When the level in ACCU falls down to 0.45 m, they are isolated from primary circuit by closing a valve.

When the UP pressure drops below 2.5 MPa, cooling water from LPSI is supplied to the cold and hot legs of loops #3 and #4. LPSI flow rate is regulated depending on the pressure in UP, according to a specified law.

When the total volume of water injected into primary circuit through HPSI and LPSI reaches 0.33 m<sup>3</sup>, a signal to stop HPSI and LPSI injections is given with a delay of 10 s (simulation of water tank emptying).

The experiment is terminated when the maximal FR cladding temperature reaches 300°C.

## 5. Transient calculation

### 5.1 Modeling of PSB facility by Cathare 2

An input data deck (IDD) for LOCA calculations of PSB-VVER test facility has been developed for the code version CATHARE 2 V2.5\_1. It is based on IDD of PSB-VVER developed for the version CATARE 2 V1.3\_1 for natural circulation calculation system (Melikhov et al., 2004). The geometrical information of the test facility is checked against the information provided by EREC in the framework of an OECD project. The basic IDD has been modified for the specific initial and boundary conditions of the PRISE experiment.

Nodalization scheme of the primary circuit includes four loops. The core vessel is modeled by a lower plenum, an average core channel, with 21 axial segments (168 fuel rods), a core bypass, an upper plenum and an external downcomer. The models of the LP, UP and DC consist of volume and axial elements connected by junctions.

The pressurizer consists of a volume with internal wall, modeling the heaters. It is connected to loop #2.

For the SGs modeling, a multitube approach is applied as for PACTEL experimental facility (Sabotinov, 1993), (Sabotinov, 2005). The 34 heat exchange tubes of each SG are presented as 3 axial elements, located at different horizontal elevations (high, middle and low tube bundles). Each axial element is divided into 26 segments.

The SG secondary side is presented by a recirculation model. It consists of one axial and one volume element, connected to the steam discharge lines. The latter also consist of volume and axial elements, with a unique pressure boundary condition at the outlet. Each SG feed water is modeled by a source.

HPSI and LPSI are modeled by sources, connected to the hot and cold legs of loop #3 and #4. Each ACCU is modeled by an accu gadget: ACCUs #1 and #3 are connected to UP, while ACCUs #2 and #4 are connected to DC.

Each ADS is represented by a sink gadget, connected to the steam discharge line of the SG.

The primary to secondary leak is modeled by a pressure boundary condition with sonic blocking at the top of the hot collector of SG #4 in the primary side, and a source in the secondary side.

The CATHARE model of PSB-VVER primary circuit is presented in figure 3. Loop #1 is not represented.

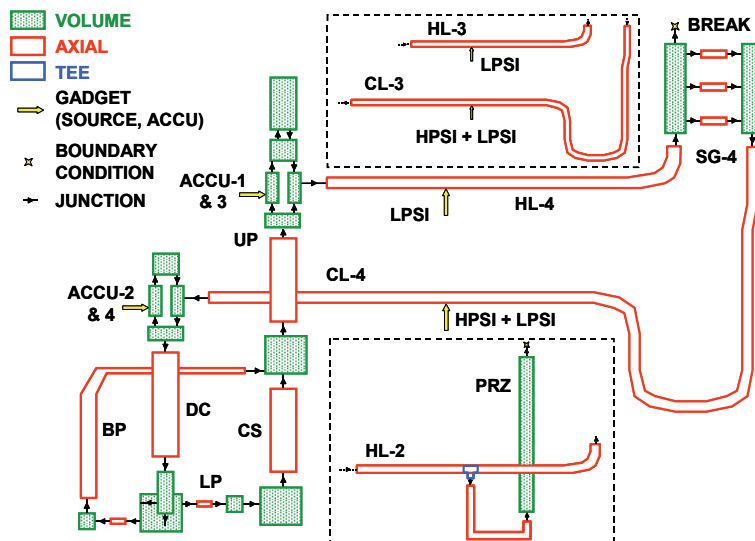


Fig. 3. CATHARE model for primary circuit

The primary circuit nodalization consists of 55 hydraulic modules (28 axial, 24 volume and 3 boundary condition elements) for a total scalar meshes number of 1279. The secondary circuit nodalization consists of 30 hydraulic modules (16 axial, 13 volume and 1 boundary condition elements) for a total scalar meshes number of 488.

### 5.2 Steady state calculation

In order to achieve nominal conditions the following regulators are used in the IDD: regulation of primary flow rates in the 4 loops by MCPs speed variation; regulation of the SGs level by source of water; regulation of the equilibrium between steam and feed water flow rates; regulation of the nominal PRZ level by source of water; regulation of primary side pressure by the PRZ heaters.

The steady state has been calculated for 3000 s. The last 500 s, the regulators were switched off in order to check that the parameters remain constant. Values of main parameters, obtained at the end of the steady state, are presented in table 1, where they are compared with experimental initial parameters (Elkin et al., 2005).

### 5.3 Transient calculation results

The calculation is carried out until the maximal FR cladding temperature reaches 300°C. This happened at  $t = 12645$  s. The calculation took 4 hours and 30 minutes on PC bi-processor Intel with 3.6 GHz under Windows XP operating systems.

A large number of sensitivity calculations have been performed, regarding different modeling and CATHARE options:

- different modeling of the primary to secondary leak;
- variation of the hydraulic resistance of the break line in order to evaluate the break flow and the primary pressure;
- variation of the discharge coefficient of the atmospheric steam dump system (ADS) in order to predict correct secondary pressure evolution of SG #4;
- with and without CCFL model between core and upper plenum with sensitivity study on the CCFL parameters to evaluate the influence on the core cooling;
- modeling of the SG level regulation with constant or impulse feed water supplies (negligible effect);
- different heat loss coefficients in the SG for better prediction of the SG secondary pressures.

The steady state provides the initial conditions of the transient. A comparison of calculated and experimental (Elkin et al., 2005) times of occurrence of main events is presented in table 2.

Event		Time (s)	
		Experiment	Calculation
1	Leakage opening	0	0
2	Signal for steam line closing in SG-4 (SG-4 level > 1.77 m)	4.3	4.0
3	Beginning of steam line closing in SG-4 (event #2 + 2 s)	6.3	6.0
4	Complete steam line closing in SG-4 (event #3 + 11.3 s)	17.6	17.2
5	Scram signal, begin of intact SGs isolation (press. in UP < 13.7 MPa)	26.9	21.8
6	Actuation of emergency feed water pumps (event #5 + 2 s)	28.9	23.8
7	Beginning of feed water closing in SG-4 (event #5 + 4.6 s)	31.5	26.4

	Event	Time (s)	
		Experiment	Calculation
8	Switching off of PRZ heaters (PRZ collapsed level < 2.33 m)	32.0	27.8
9	Start of core and bypass power reduction (event #5 + 5.6)	32.5	27.4
10	Opening and seizure ADS of SG-4 ADS (press. in SG-4 > 7.16 MPa)	32.5	25.3
11	Complete feed water closing in SG-4 (event #7 + 2 s)	33.5	28.4
12	Stopping of SG-1, 2 and 3 steam discharge (event #5 + 16.6 s)	43.5	38.4
13	PRZ emptying	50.0	42.6
14	Pressure in UP < 10.8 MPa	62.0	54.0
15	Start of HPSI injection (event #14 + 1 s)	63.0	55.5
16	Primary coolant reaches a subcooling of 10°C	66.5	63.5
17	Start of MCPs coast down (event #16 + 17 s)	83.6	80.6
18	Complete switching off of MCPs (event #17 + 232 s)	289	313
19	Start of ACCU-1 injection	617	635
	Start of ACCU-2 injection	617	636
	Start of ACCU-3 injection	617	637
	Start of ACCU-4 injection (primary pressure < ACCU pressure)	617	627
20	Pressure in the primary side is lower than in the secondary one	416	444
21	Volume of water injected in primary circuit by HPSI > 0.33 m <sup>3</sup>	888	861
22	Stop of HPSI injection (event #21 + 10 s)	898	872
23	Stop of ACCU-1 injection	4600	6108
	Stop of ACCU-2 injection	4675	6105
	Stop of ACCU-3 injection	4615	6109
	Stop of ACCU-4 injection (ACCU level < 0.45 m)	4620	6110
24	Start of the first bundle heat up	8521	-
25	First loop seal clearing	8635	-
26	Start of the second bundle heat up	12208	12400
27	Stop of experiment	12425	12645

Table 2. Chronology of main events

The leak flow is very specific in PRISE compared to leakages from primary or secondary circuit to the ambient atmosphere. Secondary pressure is higher than atmospheric pressure,

so the ratio between the pressure at break upstream and downstream is lower in the first case. Thus, in PRISE, critical flow is observed at the very beginning of the accident, whereas the sonic flow remains a long period of time in case of a leakage to atmosphere.

Due to the leak, the primary pressure is decreasing (figure 4), which leads to the actuation of the scram signal at 21.8 s (UP pressure < 13.7 MPa).

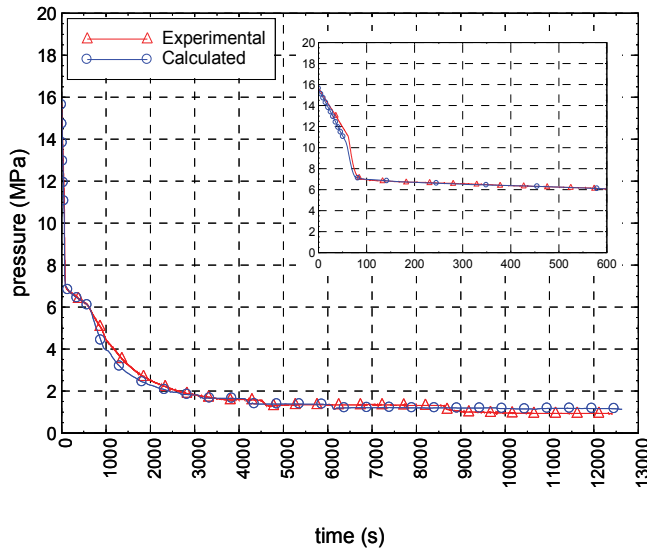


Fig. 4. Pressure in the UP (hot leg connection area)

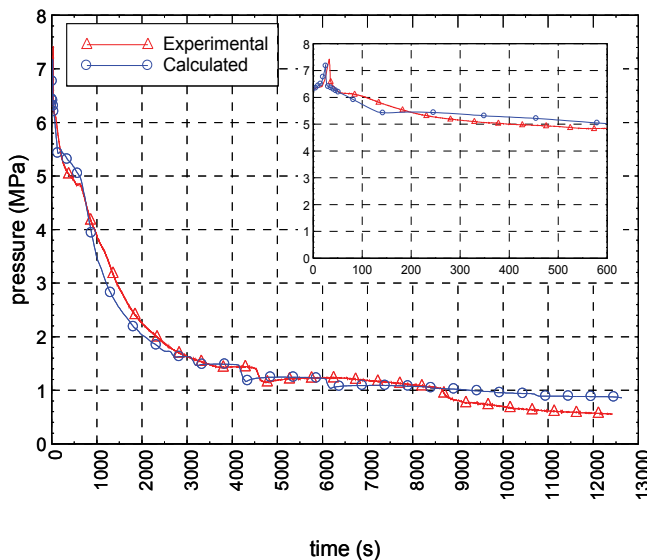


Fig. 5. SG-4 secondary pressure

The power in the core simulator and bypass heaters starts to decrease according to the specified law with a delay of 5.6 s after the scram signal. On the secondary side, the valve

that controls steam removal from steam generators begins to close. Feed water supplies of intact SGs are switched to the emergency feed water, with a delay of 2 s, while feed water supply to broken SG is closed.

The pressure and the water level in the broken SG (SG #4) rapidly increase from 6.31 to 7.16 MPa. So that the signal for steam line closing, due to SG high level ( $> 1.77$  m), is given at 4.0 s (4.3 s in the experiment). Complete steam line closure occurs at 17.2 s. (17.6 s measured).

At 25.3 s, the pressure in the broken steam generator (SG #4) reaches 7.16 MPa (figure 5), then opening and seizure of ADS in open position occurs.

In the intact SGs, the pressure also increases but do not reaches the set point for ADS opening (figure 6).

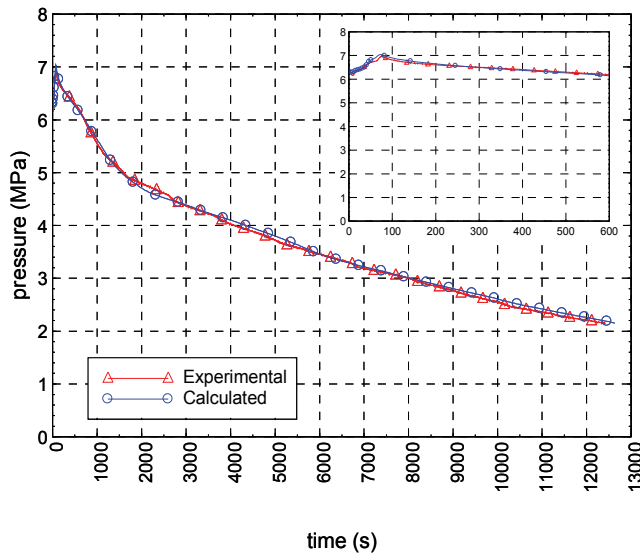


Fig. 6. SG-2 secondary pressure

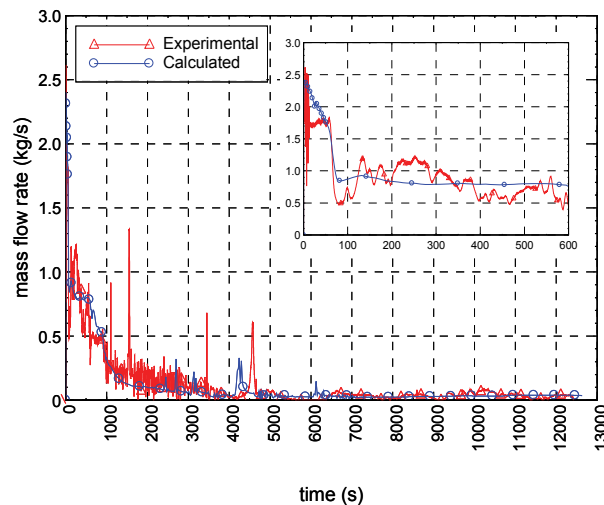


Fig. 7. Break line flow rate

The calculated leak flow reaches the maximal value of 2.4 kg/s at the very beginning of the transient (figure 7). It can be compared with the experimental value of 2.6 kg/s.

According to EREC specialists, one shall consider that the two-phase flow rate measurements must be used with care, comparing them with the calculated mass ejected through the break. More reliable is the comparison of the rejected masses (figure 8).

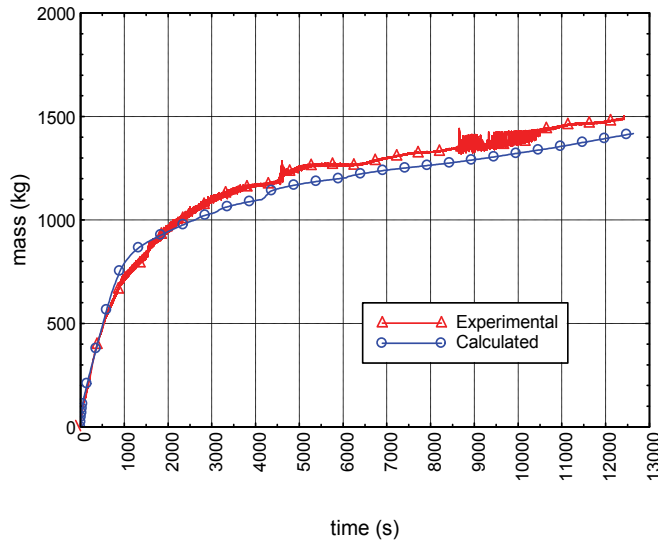


Fig. 8. Mass of coolant ejected through the break

The pressurizer level rapidly decreases due to the leak from primary circuit. Pressurizer heaters are switched off at 27.8 s. (PRZ level < 2.33 m). The PRZ is completely empty at 42.6 s (50 s in the test).

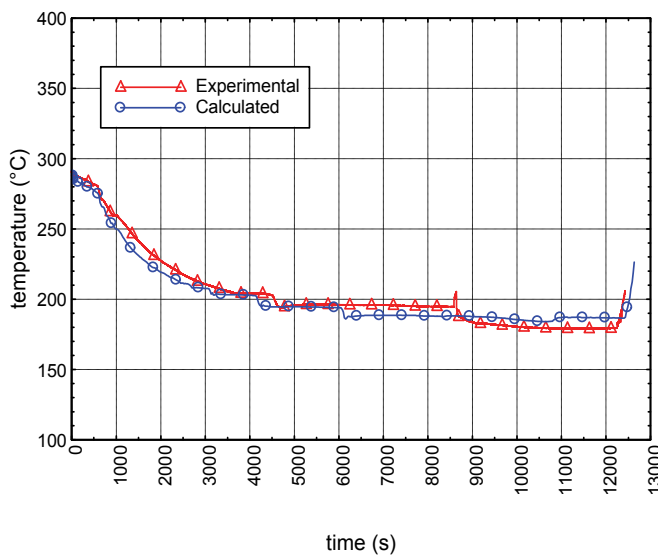


Fig. 9. Coolant temperature in the UP lower part



At 63.5 s (66.5 s in the experiment) the primary coolant reaches a sub-cooling of 10°C and the main circulation pumps starts coast down, with a delay of 17 s, according to a specified law. The coolant temperature in the upper plenum lower part – at core outlet – is shown in figure 9. After pressure in primary circuit decreases below 10.8 MPa at 54 s, HPSI pumps start to inject water into the cold legs of loops #3 and #4. The injection lasts until 861 s (888 s in the experiment) when the storage tank is empty (0.33 m<sup>3</sup>). The LPSI does not start because the tank is already empty when reaching the actuation set point of 2.5 MPa.

Further decrease of primary pressure causes hydroaccumulators injection at 627-635 s (primary pressure < ACCU pressure set point). The ACCU injection is sufficient to compensate the loss of the coolant through the break. The primary mass inventory stabilizes until the end of ACCU injection (injection stops when the ACCU level decreases below 0.45 m). The behavior of ACCU #1 is shown in figure 10.

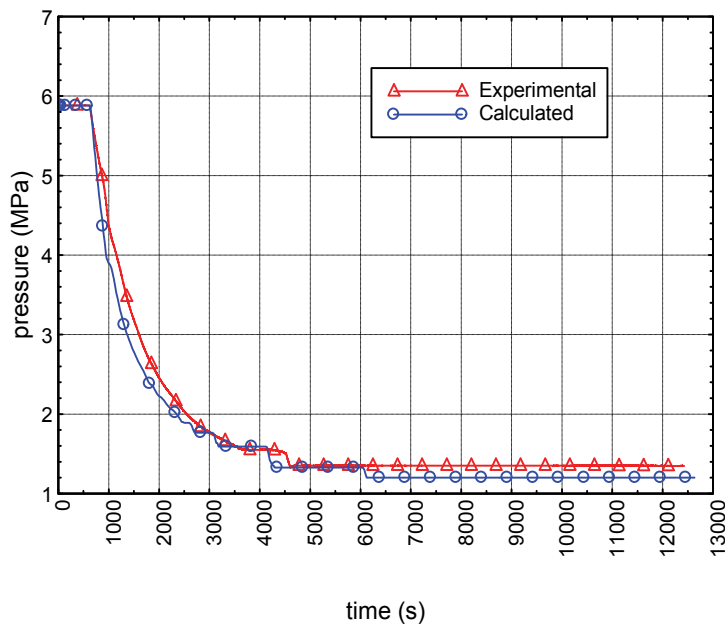


Fig. 10. Pressure in ACCU-1

At 444 s (416 s in the experiment) the pressure in the primary side decreases below the secondary pressure in SG #1, #2 and #3. The heat exchange between primary and secondary circuit is different in the intact and broken steam generators. In the broken SG, heat is transferred from the primary side to the SG and then released through ADS, whereas in the intact SGs, reversed heat flow occurs and they are cooled down by the primary side and the heat losses.

After the stop of ACCUs injection, primary mass inventory continually decreases, core void fraction increases and finally heat up of the upper part of the fuel bundle occurs. Figure 11 shows the bounding fuel cladding temperature in the core: i.e. at each time step, the maximum fuel cladding temperature in the whole core is considered.

In the experiment, a small core heat up ( $t = 270^{\circ}\text{C}$ ) can be observed at 8638 s, which is not predicted by CATHARE code. The second fuel simulator heat up is rather well predicted by

CATHARE. It starts at 12400 s in the calculation (12208 s in the experiment). The experiment and the calculation finish when the fuel cladding temperature reaches 300°C. The differential pressure in the core is represented in figure 12.

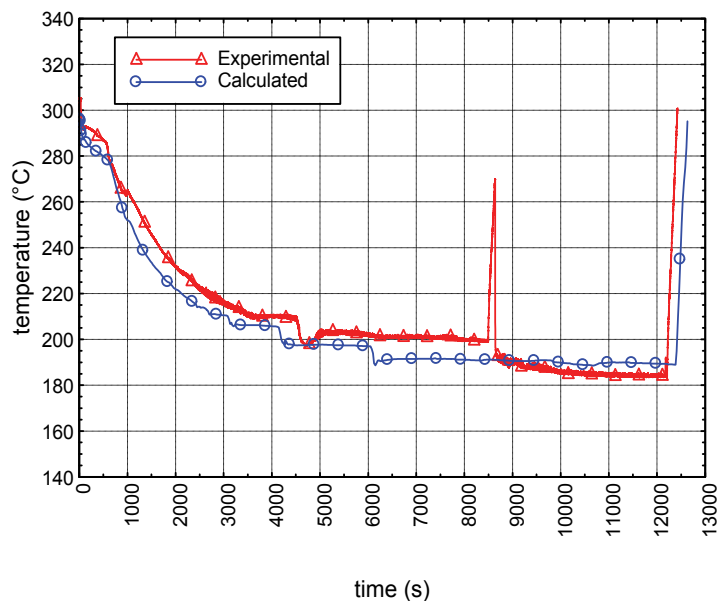


Fig. 11. Bounding fuel cladding temperature

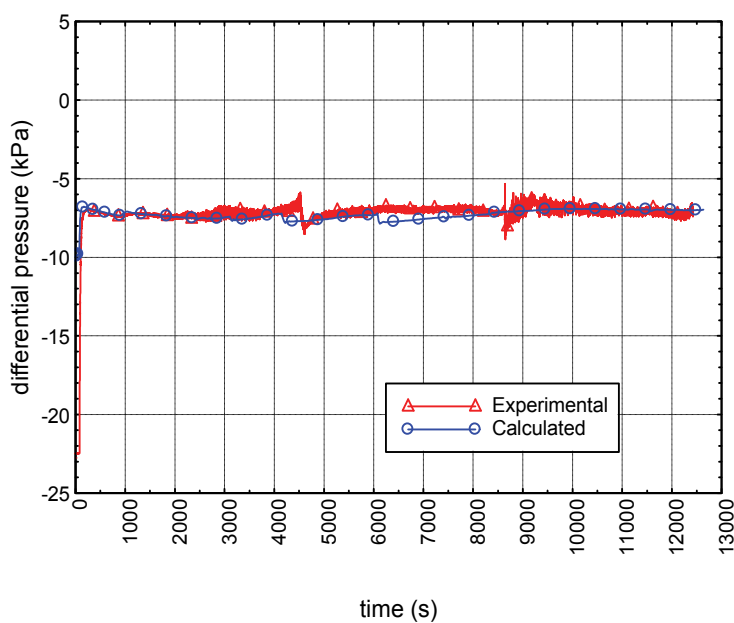


Fig. 12. Differential pressure in core

Differential pressure in the upper plenum is shown in figures 13 and 14.

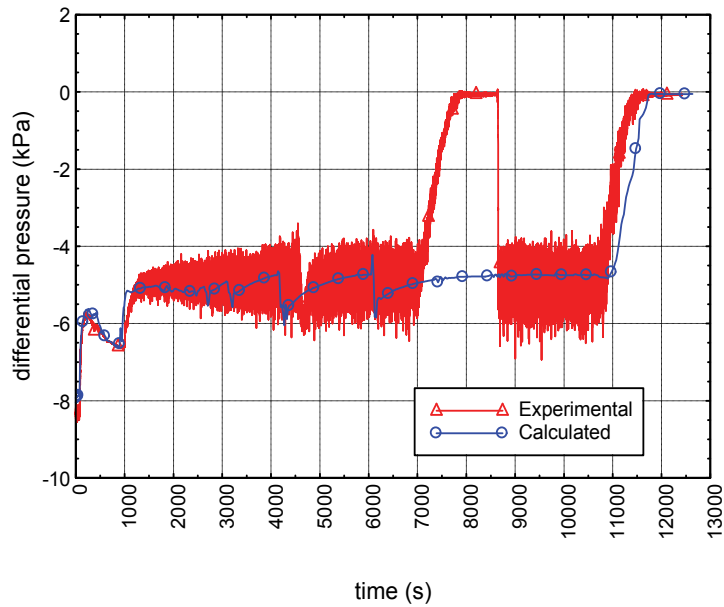


Fig. 13. Differential pressure in the UP lower part

Figures 15 and 16 illustrate respectively the calculated fuel cladding temperature and void fraction in the core as function of time and axial position.

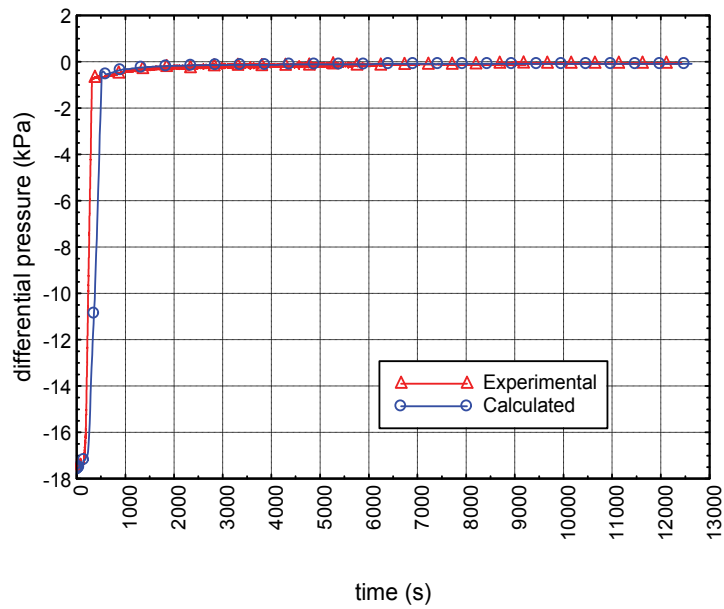


Fig. 14. Differential pressure in the UP upper part

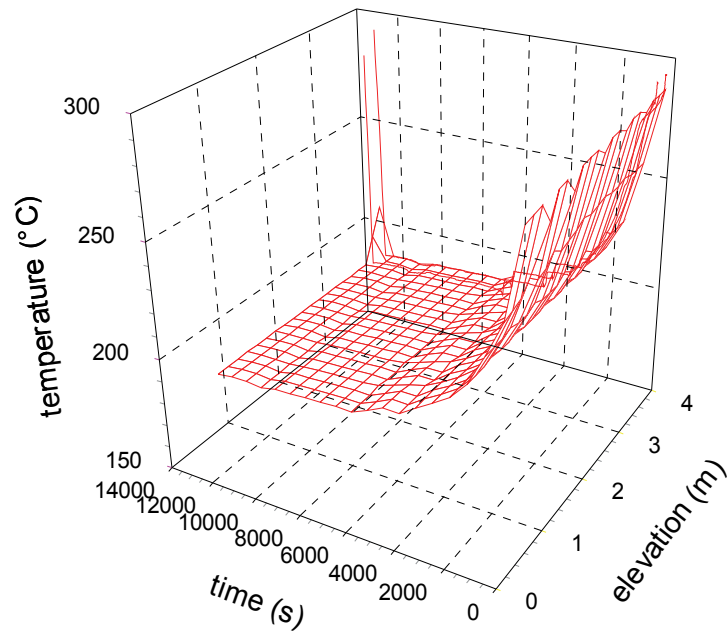


Fig. 15. Fuel cladding temperature

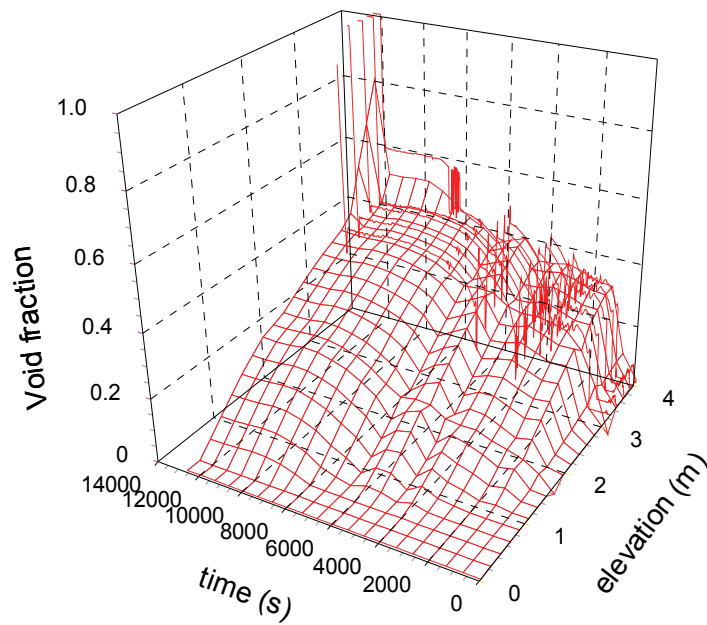


Fig. 16. Void fraction in the core

## 6. Conclusion

Comparison between calculated and experimental results shows good prediction of the basic physical phenomena and parameters such as primary and secondary pressures, temperatures, loop flows, etc.

Discrepancies appear in some differential pressures and loop seal clearance is delayed. Some overprediction of primary mass inventory can be observed.

The final core heat up is in good agreement with the experiment.

## 7. Acronyms

ACCU	Hydroaccumulator
ADS	Atmospheric Steam Dump System
BP	Core Bypass
CCFL	Counter-Current Flow Limitation
CL	Cold Leg
CS	Core Simulator
DC	Downcomer
ECCS	Emergency Core Cooling System
FR	Fuel Rod
HL	Hot Leg
HPSI	High Pressure Safety Injection
IDD	Input Data Deck
LOCA	Loss of Coolant Accident
LP	Lower Plenum
LPSI	Low Pressure Safety Injection
MCP	Main Circulation Pump
NPP	Nuclear Power Plant
PRISE	Primary to Secondary Leakage
PRZ	Pressurizer
PSB	Polnomasshtabnyi Stend Besopasnosti (Fullscale Safety Mock-up)
PWR	Pressurized Water Reactor
SG	Steam Generator
UP	Upper Plenum
VVER	Vodo-Vodianoii Energeticheskii Reaktor (Russian designed PWR)

## 8. References

- Melikhov, O. et al. (2003). Report about PSB-VVER Description (including measurement system), *OECD PSB-VVER Project*, PSB-03, Electrogorsk, Russia
- Barre, F. & Bestion, D. (1995). Validation of the CATHARE System Code for Nuclear Reactor Thermalhydraulics, *CEA STR/LML/EM/95-347*, Grenoble, France
- Sabotinov, L. (1997). Calculation of the Hydroaccumulator Line Break of VVER-1000. CCFL Modeling, *20th CUC meeting*

- Bazin, P. & Pellissier, M. (2006). CATHARE 2 V2.5\_1: Description of the Base Revision 6.1 Physical Laws used in the 1D, 0D and 3D Modules, *CEA SSTH/LDAS/EM/2005-038*, Grenoble, France
- Elkin, I. et al. (2005). Experimental Data Report Test 4, *OECD PSB-VVER Project*, PSB-08, Electrogorsk, Russia
- Melikhov, O. et al. (2004). Analysis of the Natural Circulation Test at the PSB VVER Test Facility with CATHARE V1.3L Code, *Cathare-Neptune Int. Seminar*
- Sabotinov, L. & Laugier, E. (1993). ISP-33 Post-Test Analysis, *CTC meeting*
- Sabotinov, L. et al. (2005). Analyses of PACTEL Experiments, *ECC project IMPAM-VVER*, FIKS-CT-2001-00196

# Reliability of Degraded Steam Generator Tubes

Leon Cizelj and Guy Roussel

<sup>1</sup>*"Jožef Stefan" Institute,*

<sup>2</sup>*Vinçotte Nuclear Safety*

<sup>1</sup>*Slovenia*

<sup>2</sup>*Belgium*

## 1. Introduction

Steam generators in the second generation nuclear power plants with pressurized water and CANDU reactors were in most cases of the shell-and-tube type. The reactor coolant passes through the tubes at the primary side and boils water on the outside of the tubes (secondary shell side) to make steam.

Typical dimensions of the tubes are the diameter of about one inch or less and the tube wall thickness of about 1 mm. A few thousand tubes with shape of inverted letter U were installed in a typical steam generator. The dominant choice of material was Ni-Cr-Fe alloy Inconel 600. After some years of operation the first degradations were detected. Degradations were caused by a variety of mechanisms and were not limited to Inconel 600. A good review of designs, materials and degradation mechanisms was given in (Shah and MacDonald 1993).

Replacements of steam generators solved the degradation problem mainly by the choice of different tubing material (IAEA 2008). A large number of original steam generators are still in operation and some of them may operate without replacement until the final shutdown of the plants. Consequently, the degradation of the steam generator tubes is still in the focus of research and maintenance activities. Recent examples include (Lee, Park et al. 2010), (Revankar, Wolf et al. 2009), (Hur, Choi et al. 2010), (Pagan, Duan et al. 2009) and (Pandey, Datla et al. 2009).

Our main purpose is a critical compilation of the past work in the field of probabilistic assessment of steam generator degradation and maintenance strategies. The probabilistic apparatus already proposed to serve in specific cases has been consolidated and generalized to accommodate a wide range of mechanistic and empirical models describing the tube failure modes.

### 1.1 Safety consequences of degradations

Steam generator tubes are exposed to thermal and mechanical loads combined with aggressive environmental conditions. Rather severe corrosion damage resulting in through wall flaws has been, among others, reported in tubes made of Inconel 600 (Shah and MacDonald 1993).

Through-wall flaws in ductile pressurized components may at appropriate conditions lead to detectable leaks long before the structural integrity of the component is challenged.

Through-wall leaks should in most cases be interpreted as a reliable call for a corrective action (repair or replacement). However, in some specific cases continued operation with controlled leaks within the safety, legal, economical or other constraints might be acceptable. The Inconel 600 mill annealed (MA) steam generator tubes in pressurized water reactors may serve as a good example of allowable continued operation with limited leakage. The tubes confine radioactivity from neutron activation or fission products to the primary coolant during normal operation. However, the primary reactor coolant is at a higher pressure than the secondary coolant, so any leakage through defects in the tubes is from the primary to the secondary side, and rupture of the steam generator tubing can result in release of radioactivity to the environment outside the reactor containment through the pressure relief valves in the secondary system.

Steam generator tubing represents a large part of the reactor coolant pressure boundary, which represents the second of three consecutive safety barriers preventing the release of the radioactive materials to the environment. The integrity of the reactor coolant boundary and therefore also of the steam generator tubes is therefore considered a paramount safety goal (Murphy 2007). Two potential failure modes of the tubes have received special attention (IAEA 1997):

- i. single or multiple tube rupture and
- ii. excessive primary-to-secondary leakage without tube rupture.

A sufficient safety margin against tube rupture used to be the basis for a variety of maintenance strategies, which were developed to maintain a suitable level of plant safety and reliability (see (Shah and MacDonald 1993) for more details). This topic will not be pursued further here. It will merely be noted that some of the maintenance strategies justified sufficient margin also for the tubes with through-wall flaws. Consequently, several through-wall flaws may remain in operation and potentially contribute to the total primary-to-secondary leak rate. Cases with up to 2000 flaws within a single steam generator have been reported to operate successfully (Cuvelliez and Roussel 1995).

## 1.2 Inspection and repair strategies

Traditionally, the steam generators were declared operable following a successful completion of the surveillance program. The surveillance program required periodic tube inspections. The inspection of tubes was typically performed using eddy current probes in intervals between 12 and 40 months. The required sample of the inspection depended on the number of defects found and ranged from 3 to 100% of the tubes. The tubes with damage exceeding the repair criteria, typically 40% reduction in the tube wall thickness, were required to be repaired (Murphy 2007). Repair typically included plugging or sleeving of the tube (Shah and MacDonald 1993). The aim was to preserve the integrity of the tube, both in terms of appropriate margins against tube rupture and leakage in normal and anticipated accidental conditions.

Significant degradation problems could result in increasing number of plugged tubes that could severely reduce the performance of the steam generators. At the same time, the eddy current errors and defect growth rates sometimes exceeded those allowed by the tube repair criteria. This motivated the regulators to move towards performance based requirements to ensure the integrity of the steam generators. These allowed for the use of defect specific inspection and repair strategies, which were supported by experimental and analytical findings. Probabilistic assessment became a frequent part of the analytical efforts to quantify



the success of inspection and repair strategies in terms of tube failure probability. The probabilistic assessment techniques are discussed in detail in the following sections. The overview of the performance based requirements in USA is given in (Murphy 2007).

### 1.3 Outline of this chapter

Section 2 (Probabilistic modelling) outlines the consolidated and generalized probabilistic apparatus already proposed to serve in specific cases and generalized in this section to accommodate a wide range of mechanistic and empirical models describing the tube failure modes. Section 3 (Numerical examples) provides illustrative and practical examples demonstrating and illustrating the performance of the generalized probabilistic apparatus. Section 4 (Information content of successful sampling inspections) investigates the inspection situation typical for replacement steam generators, where the inspection of a small random sample selected from all tubes reveals no defects. The probability of having certain number of defective tubes in the uninspected part of steam generator is discussed.

## 2. Probabilistic modelling

### 2.1 Basic assumptions

The following basic assumptions are used in the sections below:

- the defect size as measured by the non-destructive examination technique can be used to describe failure behaviour.
- The reliability and sizing accuracy of the non-destructive examination technique can be quantified.
- The repair of the defects with measured size exceeding allowable size is perfect. In other words, repair restores the virgin state of the tube or removes the tube from operation.
- There is a potential to predict the growth of the degradation in the period until the next inspection.
- There is exactly one crack per tube.
- The parameters governing the tube failure are statistically independent.

### 2.2 Failure integral

Let us assume that the failure behaviour of the damaged tube can be described using  $n$  random variables  $\vec{x} = (x_1, \dots, x_n)$  and a failure function  $g(\vec{x})$ . Further, let the failure function be defined so that  $g(\vec{x}) < 0$  indicates the failure of the damaged tube. The probability of failure  $P_f$  of the population of tubes is then defined as (Madsen and Krenk 1986):

$$P_f = \int_{g(\vec{x}) < 0} f(\vec{x}) d\vec{x} \quad (1)$$

Now, the probability that  $j$  tubes will fail within a steam generator with total of  $N$  tubes may be estimated using:

$$p(j) = \frac{(N P_f)^j}{j!} e^{-N P_f} \quad (2)$$

The probabilities that one or more tubes will fail are therefore given as:

$$P(j = 1) = N P_f e^{-N P_f} \quad (3)$$

$$P(j \geq 1) = 1 - e^{-N P_f} \quad (4)$$

### 2.3 Examples of failure functions

Examples of failure functions given in this section are based on specific types of defects found in steam generator tubes with respective defect specific maintenance strategies:

- Axial cracks in tube expansion transitions just above the tube sheet. The cracking resulted from primary water stress corrosion (cracks initiated at the tube inner surface) driven by substantial residual stresses in expansion transition zones (Fig. 1.). Only the tube rupture was considered as possible failure mode here. Special inspection techniques were developed to reliably and accurately measure the crack length. The tubes with measured crack length exceeding predefined repair limit were repaired. The leaks through safely short cracks were experimentally determined to be rather insignificant and also easily detectable (Esteban, Bolaños et al. 1990; Flesch and Cochet 1990).
- Outside diameter stress corrosion cracking under the tube support plates. The widely accepted root cause were aggressive impurities, which accumulated in the crevices between the tubes and tube support plates. These caused rather large network of intergranular cracks initiated at the outside tube surface. Some of the damaged tubes were pulled from the steam generators and served to establish empirical correlations between the defect size indicated by the inspection equipment on one side and the burst pressure and leak rate on the other side (see for example (Dvoršek, Cizelj et al. 1998) and the references therein).

Further examples of models, which may be used in the definition of the failure function for various degradation processes have been proposed in the literature. Recent examples include for example (Revankar and Riznic 2009), (Kim, Oh et al. 2010), (Hui and Li 2010), (Kim, Jin et al. 2008) and (Hwang, Namgung et al. 2008).

#### 2.3.1 Axial cracks in expansion transition zones: tube rupture

Primary water stress corrosion cracking was one of the first degradation mechanisms which were tackled by the defect specific inspection and repair strategy (Hernalsteen 1993). In most cases it resulted in axial cracks, mainly driven by the residual stresses caused by the expansion process during the manufacturing of the steam generators.

Consider a long pressurized tube which is fixed into a drilled tubesheet by the means of expansion (Fig. 1.). The tube contains an axial through wall crack with length  $2a$ . The failure mode of concern is the unstable (ductile) propagation of the crack leading to tube rupture. Leak through the tube is not the concern. Nevertheless, the reader is referred to (Revankar, Wolf et al. 2009) for a recent review of available leak rate models through cracks in steam generator tubing.

The nuclear steam generator tubes are typically made of ductile Ni based alloys. A limit load model may therefore be appropriate:

$$g(\vec{x}) = \sigma_f - m_F \sigma_\phi \quad (5)$$

$\sigma_f$  represents the flow stress,  $\sigma_\phi$  is the pressure induced hoop stress and  $m_F$  the so called bulging factor (Erdogan 1976):

$$m_F = 0.614 + 0.386 e^{-2.25 \frac{a}{\sqrt{Rt}}} + 0.866 \frac{a}{\sqrt{Rt}} \quad (6)$$

$a$  represents the crack half length at the end of inspection cycle.  $R$  and  $t$  are the mean radius of the tube ( $R_{out} - t/2$ ) and the tube wall thickness. The bulging factor essentially accounts for bending stresses at the crack lips, which bulge towards shape similar to fish mouth with increasing pressure or crack length.

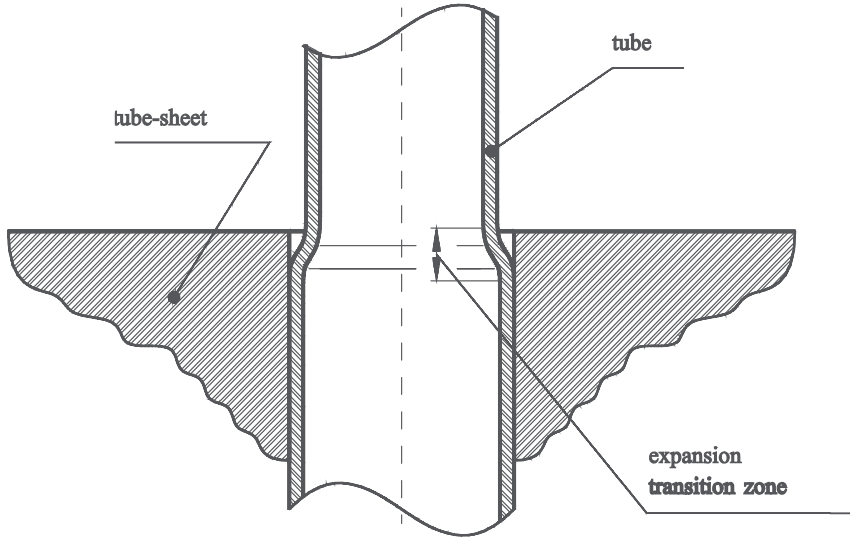


Fig. 1. A tube expanded into a tube sheet: expansion transition zone

The flow stress  $\sigma_f$  is defined by the yield strength  $\sigma_y$  and ultimate tensile stress  $\sigma_M$  of tube material and may be adjusted for operating temperature ( $\delta_T$ ), if the  $\sigma_y$  and  $\sigma_M$  were obtained at a different temperature:

$$\sigma_f = \kappa (\sigma_y + \sigma_M) \delta_T \quad (7)$$

$\kappa$  is an experimentally determined constant which describes the degree of strain hardening behaviour of the tube material. Typical value for ductile metals in question is about 0.5. The hoop stress  $\sigma_\phi$  represents the crack driving membrane stress perpendicular to the direction of the crack, which is governed by the pressure difference  $\Delta p$ :

$$\sigma_\phi = \Delta p \left( \frac{R}{t} - \frac{1}{2} \right) \quad (8)$$

Numerical values of the random variables indicated in eqs. (5) to (8) are detailed in Table 1.

### 2.3.2 ODSCC under tube support plates: tube rupture

The ODSCC under tube support plates resulted in complex networks of intergranular cracks. The characterization of the crack networks by the non-destructive examination was not

sufficient to support a mechanistic model of stable and unstable crack growth. The failure assessment was therefore based on an empirical relation between the defect size as measured by the non-destructive examination method and the experimentally determined tube rupture pressures (EPRI 1993).

The failure function for the evaluation of failure probabilities was formulated as (Dvoršek, Cizelj et al. 1998):

$$g(\Delta p, \Delta p_f, a) = \Delta p - \Delta p_f(a) \quad (9)$$

$\Delta p$  represents the loading expressed as the pressure difference across the tube wall. The highest pressure differences in the PWR NPP are typically caused by the accidents involving loss of secondary coolant system. The  $\Delta p_f(a)$  denotes the burst pressure of the tube containing a defect of size  $a$ . This is given by an empirical relation (EPRI 1993) as :

$$\Delta p_f(a) = A + B \cdot \log_{10}(a) + \varepsilon \quad (10)$$

$A$  and  $B$  are proprietary coefficients obtained by regression analysis of tube burst pressures measured on degraded tubes pulled from operating steam generators (EPRI 1993). At present, they are assumed constant.  $\varepsilon$  models the random error of the regression model.

The defect size is the direct reading from the measurement by the appropriately calibrated bobbin coil probes (eddy current technique). The result of the inspection, which is assumed to indicate the defect size, is the amplitude of the signal (measured in Volts) obtained from the bobbin coil. As a very general reference, the signal amplitude indicates the volume of the lost material in the sense that its value depends on the crack length, crack depth and crack opening.

### 2.3.3 ODSCC under tube support plates: excessive leakage

The extent and complex morphology of the ODSCC also required verification that the leaking through all defects will remain within statutory limitations. The assessment of the leakage was again based on an empirical relation between the defect size as measured by the non-destructive examination method and the experimentally determined leak rates at assumed fixed pressure differences (EPRI 1993). The failure function was formulated by (Cizelj, Hauer et al. 1998) and (Cizelj and Roussel 2003):

$$g(Q_{MAX}, Q_T) = Q_{MAX} - Q_T \quad (11)$$

$Q_{MAX}$  represents the statutory leak rate limit which is not to be exceeded during all design basis events.  $Q_T$  is the total leak rate through all  $n$  defects:

$$Q_T = \sum_i^n Q_i(a_i) = \sum_i^l Q_i(a_i)|_{P_i > 0} + \sum_{j=1}^{n-l} Q_j(a_j)|_{P_j = 0} \quad (12)$$

The leak rates through the individual defects  $Q_i(a_i)$  depend on the defect size  $a_i$  and operational parameters:

$$Q_i(a_i) = \begin{cases} Q(a_i, \Delta p, T, \dots), & P_i(a_i) > 0 \\ 0, & P_i(a_i) = 0 \end{cases} \quad (13)$$

The operational parameters (pressure difference  $\Delta p$ , temperature  $T$  etc.) are for simplicity assumed constant over all defects considered. The individual leak rates are defined as an empirical function (EPRI 1993):

$$\log(Q_i) = b_0 + b_1 \cdot \log(a_i) + \varepsilon \quad (14)$$

$b_0$  and  $b_1$  are proprietary coefficients obtained by regression analysis of tube leaks measured on degraded tubes pulled from operating steam generators (EPRI 1993). At present, they are assumed constant.  $\varepsilon$  models the random error of the regression model. The probability that a particular defect of size  $a_i$  is leaking is also given by an empirical function (EPRI 1993):

$$P(a_i) = \frac{1}{1 - \exp[-(\eta_0 + \eta_1 \cdot \log(a_i)) + z \cdot \sigma_n]} \quad (15)$$

$\eta_0$ ,  $\eta_1$  and  $z \cdot \sigma_n$  are proprietary coefficients obtained by regression analysis of tube leaks measured on degraded tubes pulled from operating steam generators (EPRI 1993).  $z \cdot \sigma_n$  models the random error of the regression model. Recent research may enable future use of more mechanistic leak rate models (Hwang, Kim et al. 2005).

## 2.4 Size of the defects

In the field situations the information about the defect sizes comes from non-destructive examinations. It is therefore reasonable to reconstruct the distribution of actual defect sizes from the measured data. In this attempt, we assume a joint probability density of measured ( $m$ ) and actual defect sizes ( $a$ ) denoted by  $p_{A,M}(a, m)$ . The density of measured defect sizes  $p_M(m)$  is then given by (Barnier, Pitner et al. 1992):

$$p_M(m) = \int_0^{\infty} p_{M|A}(m|a) p_A(a) da \quad (16)$$

Please note that the Bayes' theorem requires that

$$p_{A,M}(a, m) = p_{M|A}(m|a) p_A(a), \quad p_M(m) = \int_0^{\infty} p_{A,M}(a, m) da \text{ and } p_M(a) = \int_0^{\infty} p_{A,M}(a, m) dm \quad (17)$$

Further, we may safely assume that not all defects are detected during the inspection. Let the probability that a defect of actual size  $a$  is detected be denoted as  $P_{OD}(a)$ . Then, the conditional probability density  $p_{A|D}(a)$  that a defect of size  $a$  is detected is given as:

$$p_{A|D}(a) = \frac{p_A(a) P_{OD}(a)}{\int_0^{\infty} p_A(\acute{a}) P_{OD}(\acute{a}) d\acute{a}} \quad (18)$$

Equation (5) may now be combined with eq. (16) to yield:

$$p_M(m) = \frac{\int_0^{\infty} p_{M|A}(m|a) p_A(a) P_{OD}(a) da}{\int_0^{\infty} p_A(\acute{a}) P_{OD}(\acute{a}) d\acute{a}} \quad (19)$$

Distribution of  $p_A(a)$  may be estimated by inverting eq. (16). A useful numerical procedure has been proposed by (Barnier, Pitner et al. 1992). It requires a selection of functional form of

$p_A(a)$ . Then,  $p_M(m)$  is calculated using eq. (16), which depends on the unknown parameters of  $p_A(a)$ . These can be determined by fitting the calculated values of  $p_M(m)$  to the empirical distribution of measured defect sizes by using for example minimization of  $\chi^2$ .

## 2.5 Repair of the defects

Typically, the defects exceeding certain size, denoted repair limit  $L$ , need to be repaired. The defect of size  $a$  will therefore exceed the repair limit with probability:

$$P_L(a) = \frac{1}{\eta} P_{OD}(a) \int_L^{\infty} p_{M|A}(m|a) dm (1 - \varepsilon_L) \quad (20)$$

$1/\eta$  represents the fraction of inspected tubes. A residual repair unreliability  $\varepsilon_L$  is provided to account for rare events like human error. The fraction of repaired defects is then given as:

$$\int_0^{\infty} p_A(a) P_L(a) da \quad (21)$$

Similarly, the probability that a defect of size  $a$  will not be repaired is given by:

$$p_A(a)(1 - P_L(a)) \quad (22)$$

## 2.6 Growth of the defects

The growth of the defects can be rather efficiently estimated from the successive inspections. A careful statistical analysis of inspection records may also provide a reasonable indication of measurement errors (Cizelj and Dvoršek 1999). The obvious drawback of such an approach is the need to rely entirely on historic data and operational conditions already observed. Since this approach is rather straightforward, it is not pursued further here.

Mechanistic models of crack growth, if available, may provide predictions for a wide range of operational conditions. As an example, the asymmetric crack growth law proposed for axial stress corrosion cracks in expansion transitions of steam generator tubes (Cizelj, Mavko et al. 1995) is given below.

The growth rate of a stress corrosion crack is given as (Cizelj, Mavko et al. 1995):

$$\dot{a}_{\pm a} = \left( \frac{da}{dt} \right)_{\pm a} = C_{\pm a} (K_{\pm a} - K_{ISCC})^m \quad (23)$$

Please note that the crack growth rate is different for both crack tips ( $\pm a$ , Fig. 2). The growth of the crack is accompanied by the moving center point, as indicated in Fig. 2. The stress intensity factors  $K_{\pm a}$  are to be estimated from the quite irregular stress field indicated in Fig. 2. A rather simple procedure for stress calculations appropriate for reliability calculations is proposed in (Cizelj 1994). Material properties  $C_{\pm a}$ ,  $K_{ISCC}$  and  $m$  are taken from literature (Scott 1991) and detailed in Table 2. The proportionality constant  $C_{\pm a}$  is reported to be about 6 times higher in cold worked than in virgin material (Cassagne, Combrade et al. 1992).

The operational and residual stresses in are, together with stress intensity factors of both crack tips  $K_{\pm a}$ , analysed in detail in (Cizelj 1994).

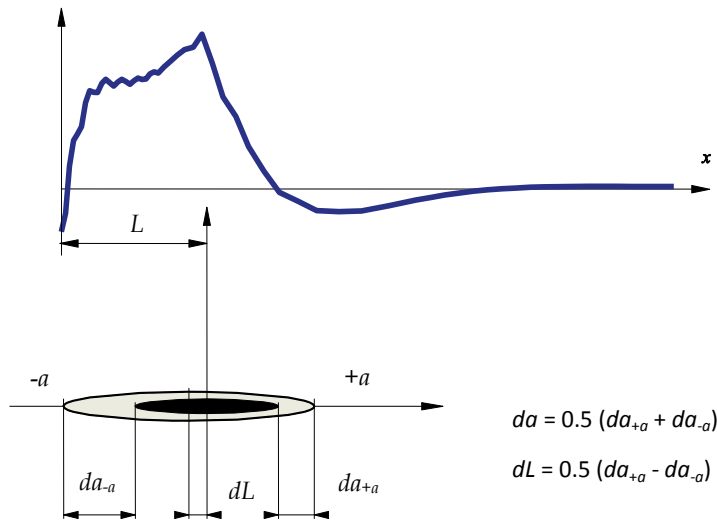


Fig. 2. Residual hoop stress in an expanded tube and asymmetric crack propagation. Reprinted from International Journal of Pressure Vessels and Piping, Vol. 63, L. Cizelj, B. Mavko, H. Riesch-Oppermann, A. Brücker-Foit, Propagation of stress corrosion cracks in steam generator tubes, p. 35, Copyright (1995), with permission from Elsevier

## 2.7 Numerical solutions of the failure integral

The basic numerical methods implemented to evaluate the numerical examples are briefly outlined in this section for completeness. These are the direct Monte Carlo (DMC) simulation and the First- and Second Order Reliability Methods (FORM and SORM). The reader is referred for example to (Madsen and Krenk 1986) for a more rigorous description. Other numerical methods have been proposed in addition to the DMC, FORM and SORM and are implemented in computational tools such as for example ZERBERUS (Cizelj and Riesch-Oppermann 1992), COMPROMIS (Pitner, Riffard et al. 1993), PFMAD (Beardsmore, Stone et al. 2010), PROBANS (Det Norske Veritas 2010) and ANL/CANTIA (Revankar, Wolf et al. 2009). Some of them also include useful fracture mechanics models.

Direct Monte Carlo corresponds to a sequence of numerical experiments. The failure function in eq. (1) is evaluated for  $n$  realisations of the random vector  $\vec{x}$ . Let  $n_f$  denote the number of realisations with  $g(\vec{x}) < 0$ . The estimator of the  $P_f$  is then given as:

$$P_f = \frac{n_f}{n} \quad (24)$$

The standard error of the estimator in eq. (24) is given as:

$$s = \sqrt{\frac{P_f(1 - P_f)}{n}} \quad (25)$$

Large number of repeated evaluations of failure function may be required for a reasonably small standard error. Less computationally intensive methods are available when dealing with complex failure functions that may only be evaluated using significant computational resources. Such methods on the one hand include Monte Carlo methods with variance

reduction sampling, such as for example latin hypercube sampling. On the other hand, approximate methods such as First- and Second Order Reliability Method (FORM and SORM, respectively) may offer reasonably accurate results with low computational intensity. The First Order Reliability Methods (FORM) relies on the closed form solution of the failure integral in the case of standard normal variables and linear failure function, given as:

$$P_f = \Phi(-\beta) \quad (26)$$

$\Phi$  being the cumulative standard normal distribution and  $\beta$  the reliability index:

$$\beta = \frac{g_u(\vec{u}^*) - \vec{a} \cdot \vec{u}^*}{|\vec{a}|} \quad (27)$$

Reliability index is the minimum distance between the origin of space of standard normal variables and the failure surface. The point on the failure surface with the minimum distance to the origin is called the design point  $\vec{u}^*$ . Please note that  $\vec{a} = \text{grad}(g_u(\vec{u}^*))$ . For non-linear failure functions, the linearization of the failure function in the design point provides an approximate value of the failure probability:

$$P_f \approx \Phi(-\beta) \quad (28)$$

The non-normal basic variables are to be transformed from the physical  $\vec{x}$  to the normal  $\vec{u}$  space. The transformation of stochastically independent basic variables is given as

$$U_i = \Phi^{-1}(F_i(X_i)) \quad (29)$$

Its inverse is defined as:

$$X_i = F^{-1}(\Phi(U_i)) \quad (30)$$

The inverse transformation (eq. (31)) is also used to transform the failure function. The sensitivity of the failure probability to the scatter of basic variables is expressed as:

$$\frac{\partial \beta}{\partial u_i} = \frac{u_i^*}{|\vec{u}|} \quad (31)$$

The Second Order Reliability Method (SORM) may improve the accuracy of the FORM by approximating the failure function in the design point by a quadratic hypersurface, which preserves the main curvatures  $\kappa_i$  of the failure function. The failure probability is given:

$$P_f \approx S_1 + S_2 + S_3 \quad (32)$$

$$S_1 = \Phi(-\beta) \prod_{i=1}^{n-1} (1 - \beta \kappa_i)^{-0.5} \quad (33)$$

$$S_2 = [\beta \Phi(-\beta) - \varphi(\beta)] \left[ \prod_{i=1}^{n-1} (1 - \beta \kappa_i)^{-0.5} - \prod_{i=1}^{n-1} (1 - (\beta + 1) \kappa_i)^{-0.5} \right] \quad (34)$$



$$S_3 = (\beta + 1)[\beta\Phi(-\beta) - \varphi(\beta)] \left[ \prod_{i=1}^{n-1} (1 - \beta \kappa_i)^{-0.5} - \operatorname{Re} \left( \prod_{i=1}^{n-1} (1 - (\beta + i) \kappa_i)^{-0.5} \right) \right] \quad (35)$$

Re represents the real part of the complex argument and  $i$  the imaginary unit.  $\varphi$  is standard normal probability density function. The applicability and reasonable accuracy of FORM and SORM in the reliability analyses of the cracked steam generator tubing has been confirmed in (Cizelj, Mavko et al. 1994).

### 3. Numerical examples

Three numerical examples are provided to illustrate the results obtained using the probabilistic model outlined in section 2. All three numerical examples are based on the data obtained from regular inspections of steam generators in operating nuclear power plants at Krško, Slovenia and Doel, Belgium. All nuclear power plants mentioned in the examples have already replaced the steam generators.

#### 3.1 Axial SCC in expansion transitions

This numerical example is based on the crack population detected in the nuclear power plant at Krško, Slovenia. The data on the geometry and material of the tubing is outlined, together with assumed distributions, in Table 1. The pressure difference  $\Delta p$  acting on the steam generator tubes corresponds to the maximal pressure difference mentioned in the plant safety analysis report and is representative for a limiting hypothetical accident “feedwater line break”. The failure probabilities reported in this section are therefore conditional given that the feedwater line break has already occurred.

The distribution of actual crack lengths was described using the lognormal distribution with shape and scale parameters of 0.532 and 1.627, respectively. This was obtained using the measured crack length distribution (Krško SG #1, 1992, (Cizelj 1994)) and the procedure outlined in eqs. (16) through (19). Random measurement error with normal distribution with 0 mean and standard deviation of 0.75 mm and detection probability  $P_{OD}(a) = (1 - e^{-0.9a}) (1 - \varepsilon_{OD})$  were assumed. Possible systematic errors were not considered in this analysis. The residual non-detection and non-repair probabilities were assumed at  $\varepsilon_{OD} = \varepsilon_L = 10^{-4}$ .

All results presented in this section were obtained using the FORM and SORM as implemented in the code ZERBERUS (Cizelj and Riesch-Oppermann 1992). The stochastic parameters of the crack growth law (eq. (23)) are given in Table 2.

Basic variable	Distribution		Unit
	Type	Parameters	
$R_{out}$	normal	$\mu=9.525, \sigma=0.0254$	mm
$t$	normal	$\mu=1.0922, \sigma=0.039$	mm
$\kappa$	normal	$\mu=0.545, \sigma=0.03$	-
$\delta_T$	normal	$\mu=0.928, \sigma=0.003$	-
$\sigma_Y$	normal	$\mu=362., \sigma=34.$	MPa
$\sigma_M$	normal	$\mu=713., \sigma=25.$	MPa

Table 1. Geometry and material data (Krško steam generator No. 1)

The resulting failure probabilities at different repair limits and time intervals between consecutive inspections are depicted in Fig. 3. The repair assumes that the detected cracks with measured lengths exceeding the repair limit are repaired. Beneficial effects of lower repair limit and shorter time between inspections are clearly shown. The plateau of all four curves below repair limit of approximately 13 mm is caused by the residual non-detection and non-repair limits  $\varepsilon_{OD} = \varepsilon_L = 10^{-4}$ .

An optimal repair limit is however clearly noted and varies from about 11 mm (15 months between inspections) and 13 mm (6 months between inspections). In the particular case studied, the gain of more frequent inspections may be seen as rather insignificant.

Basic variable	Distribution		Unit	Comments
	Type	Parameters		
$C_a$	normal	$\mu=2.8 \cdot 10^{-11}$ , $\sigma=1.0 \cdot 10^{-12}$	m/s	Assumed
$K_{ISCC}$	normal	$\mu=9.0$ , $\sigma=0.3$	MPa m <sup>1/2</sup>	Assumed
$m$	normal	$\mu=1.16$ , $\sigma=0.03$	-	Assumed

Table 2. Values of crack growth parameters in eq. (23)

The variables with the strongest influence on the failure probability are the exponent  $m$  in the crack growth law (eq. (23)), the wall thickness of the tube  $t$  and the flow stress factor  $\kappa$  (eq. (7)).

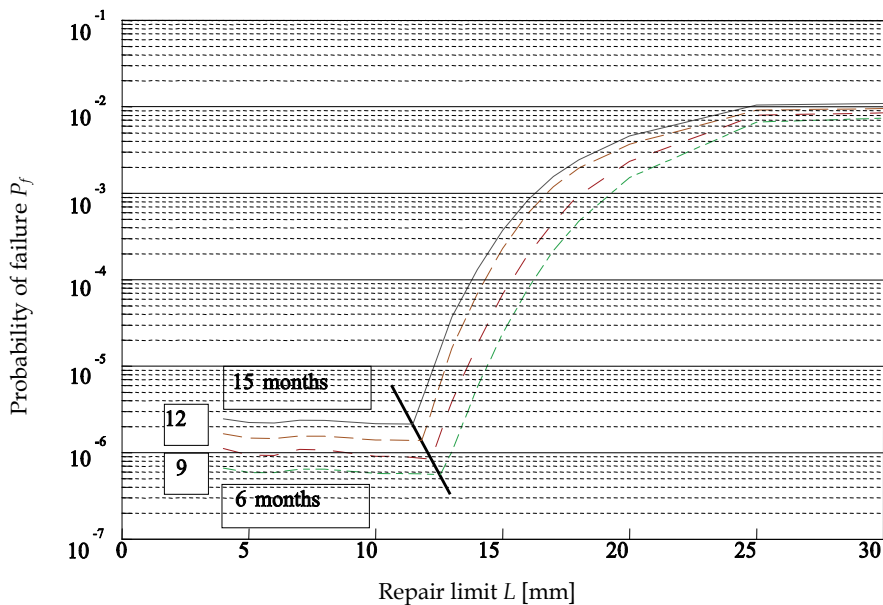


Fig. 3. Probability of failure  $P_f$  as a function of repair limit  $L$  and time between two consecutive inspections. Reprinted from Journal of pressure vessel technology, Vol. 118, L. Cizelj, B. Mavko, and P. Vencelj, Reliability of steam generator tubes with axial cracks, p. 441, Copyright (1996), with permission from ASME

The dependence of the failure probability on the number of repaired cracked tubes is depicted in Fig. 4. Please note that the failure probability is interpreted as probability of tube

failure (eq. (4)). 841 cracks were detected in the SG #1 in Krško NPP in 1992. The probability of tube failure is constant for repair limits below approximately 12 mm. At the same time, the number of cracks to be repaired (tubes to be plugged) is increasing very fast with decreased repair limit. The repair limit of 12 mm is therefore seen as an optimal choice preserving the most tubes in operation without sacrificing reliability and safety of the plant.

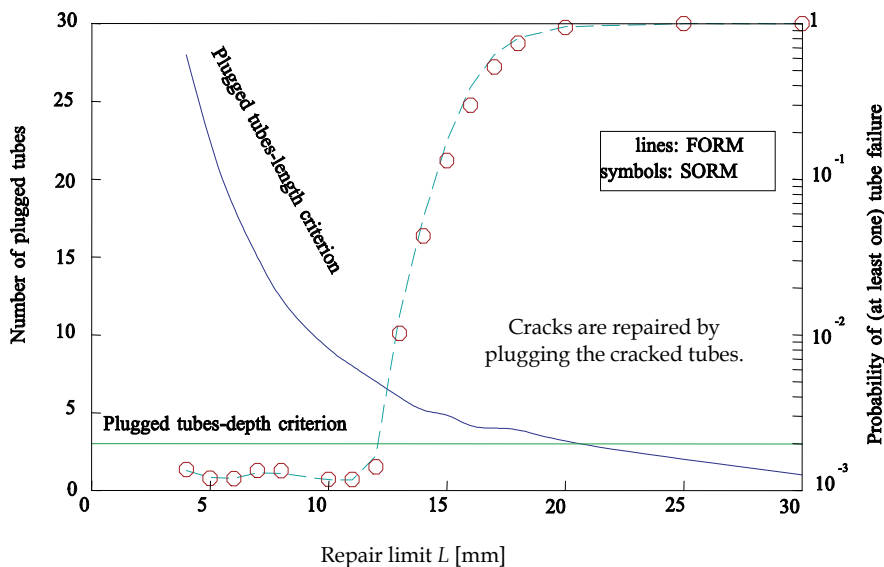


Fig. 4. Failure probability and the number of repaired tubes

The success of the traditional defect depth repair limit (40% loss of tube wall) is indicated assuming a poor correlation between the measurements of defect depth and defect length. The traditional repair strategy could therefore result in a moderate number of repaired tubes at the cost of a certain steam generator tube rupture following the feedwater line break.

### 3.2 Tube burst due to the ODSCC at tube support plates

Defect sizes as obtained from 5 consecutive (100%) bobbin coil inspections of one steam generator at the Krško NPP are shown in Fig. 5. The distributions remained fairly stable over the years in all cases analysed in this section. The tail of the measured sizes obtained during In-Service Inspection (ISI) 5 is getting fat as compared to the older data. The lognormal distribution was considered to provide reasonable fit (Dvoršek, Cizelj et al. 1998). We should note here that the number of defect sizes detected has grown from 261 in the first to over 2000 in the last inspection. Although the change in the number of tubes does not directly influence the calculation of failure probability (eq. (1)), it significantly influences the single SGTR probability (eq. (2)).

Distributions of defect growth depicted in Fig. 6 were obtained directly from each pair of two consecutive measurements available. The number of available data points grew from 80 in the first inspection to over 1300 in the last. Reasonably stable distribution of positive growth was observed over all years, tending to get a more fat distribution tail in ISI 5.

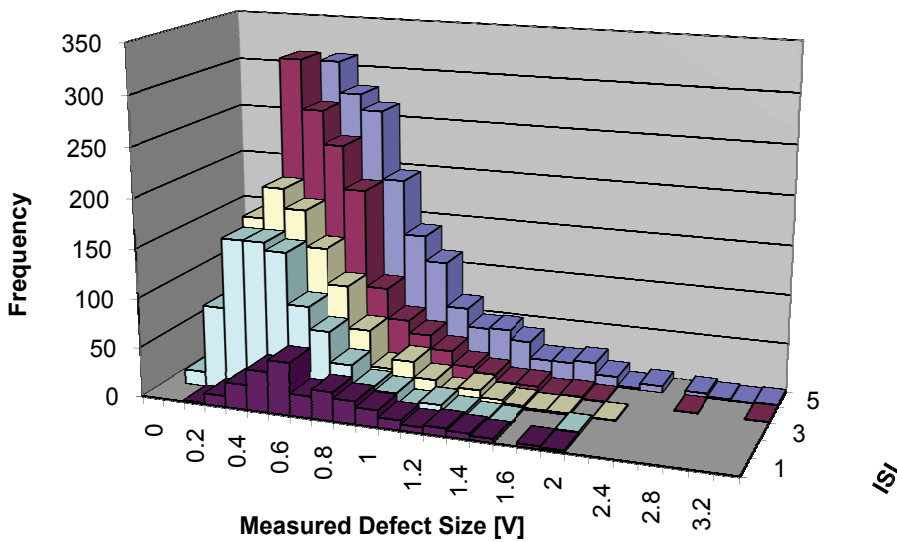


Fig. 5. History of defect sizes

Only the data points exhibiting positive growth were used to directly fit the distributions of measured defect growth, which is consistent with routine analyses of Krško ODSCC at tube support plates. Reasonable fits were provided by either lognormal or gamma distributions. Lognormal distributions were used in subsequent calculations since they are known to cause larger failure probabilities than gamma distribution.

The negative growth is attributed to the measurement error. The data on the negative growth may therefore be directly used to infer the stochastic properties of the measurement error (Cizelj and Dvoršek 1999).

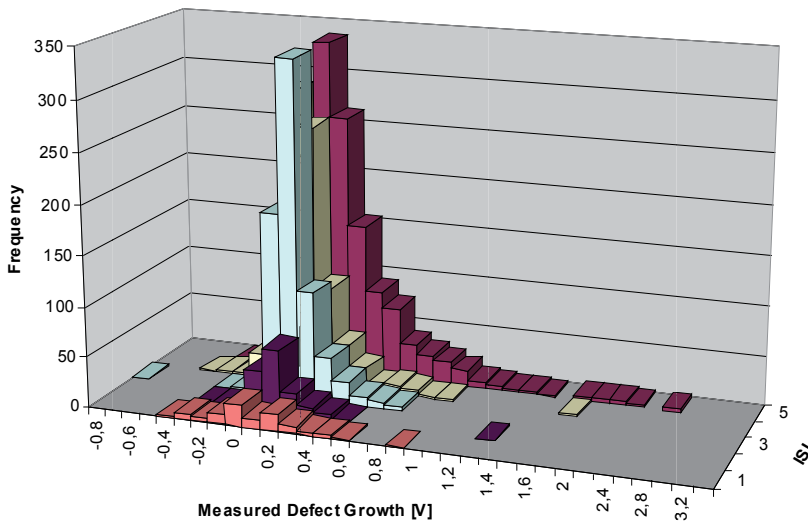


Fig. 6. Defect growth

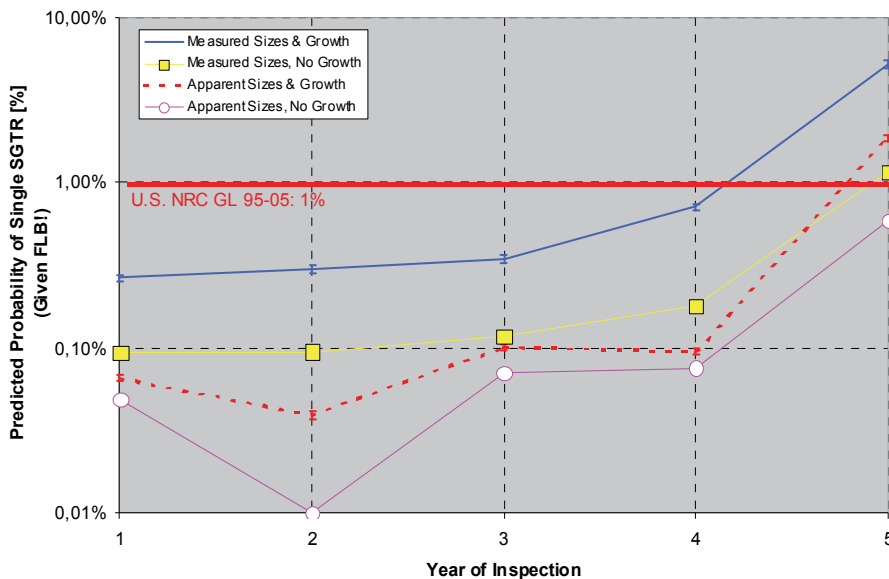


Fig. 7. Failure probabilities with time and different assumptions on measurement errors and defect growth

To estimate the tube rupture probability a postulated Feedwater Line Break (FLB) accident was assumed with differential pressure of 195.6 bar (2850 psi).

In this section we present the single tube rupture probabilities. The estimated probability of multiple tube rupture was in all cases at least two orders of magnitude lower than for the single tube rupture probability. Thus, the multiple tube rupture event was not considered to be of particular importance at this time.

The absolute values of the single tube rupture probabilities are depicted in Fig. 7 as a function of time. In addition, impact of different assumptions on the defect sizes and defect growth on the single tube rupture probability is given, exhibiting a considerable impact of about one order of magnitude. All of them are however depicted without tube repair. It is clear from Fig. 7 that all of the tube rupture probabilities except in the year 5 were estimated to be less than 1%, which is in agreement with U.S. NRC requirements [10] (Nuclear Regulatory Commission 1995). In the year 5, a repair of a moderate number of tubes would be required to stay below 1%.

The estimated single tube rupture probabilities are conditional, given a postulated FLB accident.

### 3.3 Leakage through ODSCC at tube support plates

Two numerical examples were chosen to illustrate the performance of the proposed probabilistic approach. They are based on the inspection data obtained from Slovenian Krško and Belgian Doel-4 steam generator tubes (3/4 inch tubes made of Inconel 600 Mill Annealed) in (Cizelj and Roussel 2003).

In operation, the defect size is generally a time dependent variable. In this analysis, two points in time are of concern and fully define the defect size: (1) beginning (BOC) and (2)

end (EOC) of the cycle between two consecutive inspections. Thus, the prediction of the EOC defects sizes includes stochastic combination of BOC defect sizes and defect growth.

The distribution of defect sizes in the Krško plant at the BOC is given in Fig. 8. In the calculations, empirical and fitted lognormal distributions of defect sizes at BOC were used. The differences between failure probabilities obtained with different defect size distributions were comparable to the statistical noise of the Monte Carlo simulation. Nevertheless, the empirical distribution consistently leads to higher values of the probability of exceeding the allowable leak rate and was therefore selected as representative input data model for subsequent analysis. The total number of defects detected was 492.

Allowances for defect growth (with 52,6 % of defects exhibiting nonnegative growth, compare Fig. 6) and measurement errors were also provided and yielded the defect size at EOC.

Fig. 9 depicts probability of excessive leakage as a function of allowable total leak rate. Three different curves are given to illustrate the effect of defect progression: BOC (no defect progression), EOC with 52,6% of defects exhibiting growth (which is consistent with field observations in Krško) and EOC with 100% of defects exhibiting growth. The Krško specific growth rate is used in the analysis and is shown to contribute less than one order of magnitude.

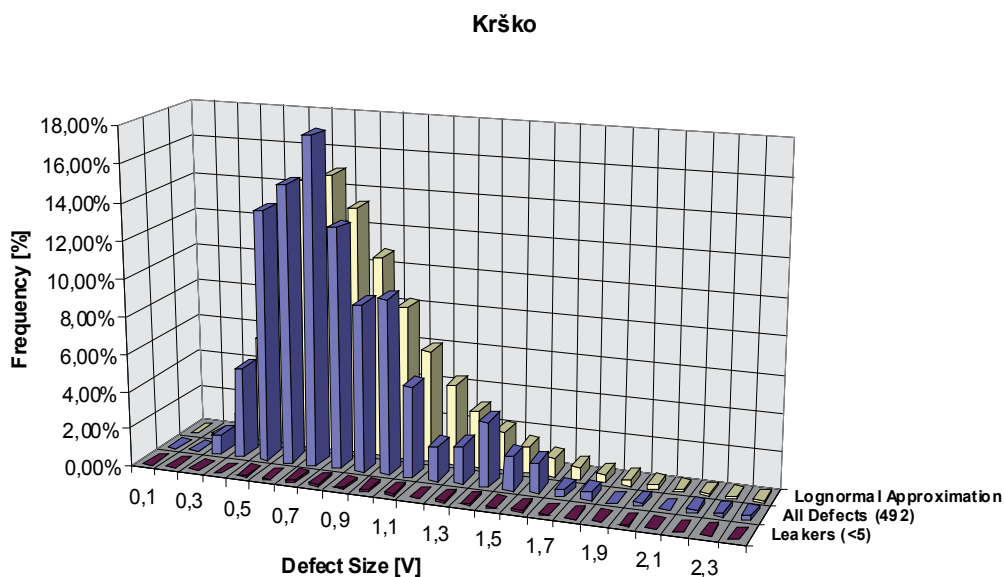


Fig. 8. Distribution of BOC defect sizes-Krško plant. Reprinted from Nuclear Engineering and Design, Vol. 185, L. Cizelj, I. Hauer, G. Roussel, C. Cuveliez, Probabilistic assessment of excessive leakage through steam generator tubes degraded by secondary side corrosion, p. 347, Copyright (1998), with permission from Elsevier

The statistical standard error of Monte Carlo simulations is represented by error bars in Fig. 9. It is in the order of 0.1% and is considered to have negligible influence on the quality of results presented here. Further, simulations revealed that only about 5 (1%) out of 492 potential leakers would really leak given assumed model (recall eqs. (13) and (15)) and postulated hypothetical accidental conditions - steam line break.

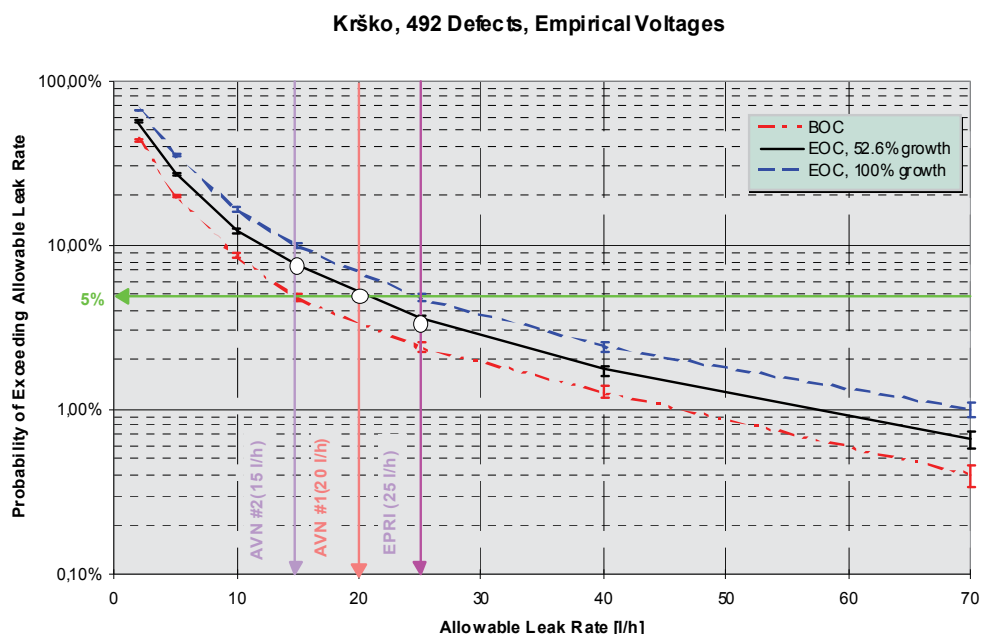


Fig. 9. Probability of Exceeding Allowable Leak Rates - Krško plant. Reprinted from Nuclear Engineering and Design, Vol. 185, L. Cizelj, I. Hauer, G. Roussel, C. Cuvellez, Probabilistic assessment of excessive leakage through steam generator tubes degraded by secondary side corrosion, p. 347, Copyright (1998), with permission from Elsevier

The labels AVN#1, AVN#2 and EPRI denote empirical estimators aiming to predict the value of the total leak rate at or exceeding the cumulative probability of 95%. The AVN#1 and AVN#2 estimators were proposed in (Cuvellez and Roussel 1995) as alternatives to the proposal by EPRI (EPRI 1993). The properties of all three estimators are analyzed in detail in (Cizelj, Hauer et al. 1998). For the purpose of this section, they are considered as empirical estimators of the 5% failure probability and are used to validate the probabilistic results.

The results of the three estimators are visualized by vertical lines at appropriate values of total leak rates (Fig. 9). Thus, for EPRI estimator, the failure probability is defined by the intersection of curves denoted by EOC, 52,6% growth and EPRI (25 l/h). Its value is about 3.5%. The AVN estimators #1 and #2 tend to 5 and 11%, respectively.

The distribution of defect sizes from Belgian Doel-4 plant is given in Fig. 10. The number of defects detected is 1960 (significantly more than in Krško). The size of defects is rather large with a maximum of 18.9 V. It should be however noted that Belgian inspection standards differ from EPRI standards. Appropriate correlation between “Belgian” and “EPRI” bobbin coil signal amplitudes was implemented to generate input data. This may be an additional source of uncertainties, which was not further investigated (Cizelj and Roussel 2003).

The presence of large defects is due to the use of a specific repair criterion allowing defects of about 10V to remain in service. The distribution of defects shown in Fig. 10 is the raw distribution as given by the bobbin coil. Also, a fit of lognormal distribution to the empirical distribution is depicted in Fig. 10. No defect progression was considered in the calculations.

The subpopulation of tube leakers in Fig. 10 illustrates the sample distribution of defects with  $P_i(a_i) > 0$  (eq. (15)). The simulations revealed that approximately 330 (17%) defects would leak in this particular case. It is clearly shown in Fig. 10 that larger defects tend to leak more frequently, which is in accordance with eq. (15).

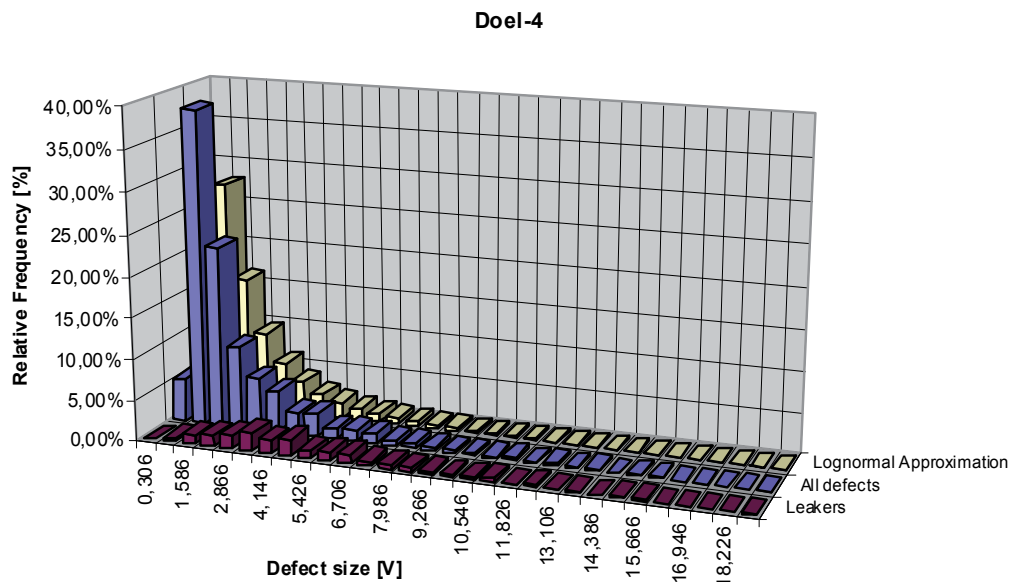


Fig. 10. Distribution of BOC defect sizes - Doel-4 plant. Reprinted from Nuclear Engineering and Design, Vol. 185, L. Cizelj, I. Hauer, G. Roussel, C. Cuveliez, Probabilistic assessment of excessive leakage through steam generator tubes degraded by secondary side corrosion, p. 347, Copyright (1998), with permission from Elsevier

The probability of excessive leakage is depicted in Fig. 11 as a function of allowable total leak rate. Results obtained by two different input distributions of defect sizes are shown. The histogram of all defects shown in Fig. 10 served as the empirical distribution. On the other hand, the lognormal distribution was fitted to the raw inspection data. The rather large difference between both curves is caused by two facts:

- lognormal distribution explicitly allows for rare events. In other words, it allows for occurrences of large defects, which exceed the measured maximum of 18.9 V.
- the probability of leakage eq. (15) is approaching 1 as the defect size is approaching 20 V. Thus, the uncertainties in the leak rate model are not dominant in this region which increases the sensitivity to the input data as compared to the Krško case.

Again, the results of three estimators are comparatively depicted in Fig. 11. All of them rely on empirical distributions of the defect sizes, which suggests the comparison with probabilities of excessive leakage obtained from empirical distribution. The results of two estimators appear to be slightly conservative (EPRI 1.8%, AVN#1 3.5%) while AVN#2 tends to the expected 5%. On the other hand, if the lognormal distribution is used, EPRI estimator seems to be realistic (leading to failure probability of 6%) while the AVN estimators lead to failure probabilities exceeding 10% (AVN#1 11%, AVN#2 16%).



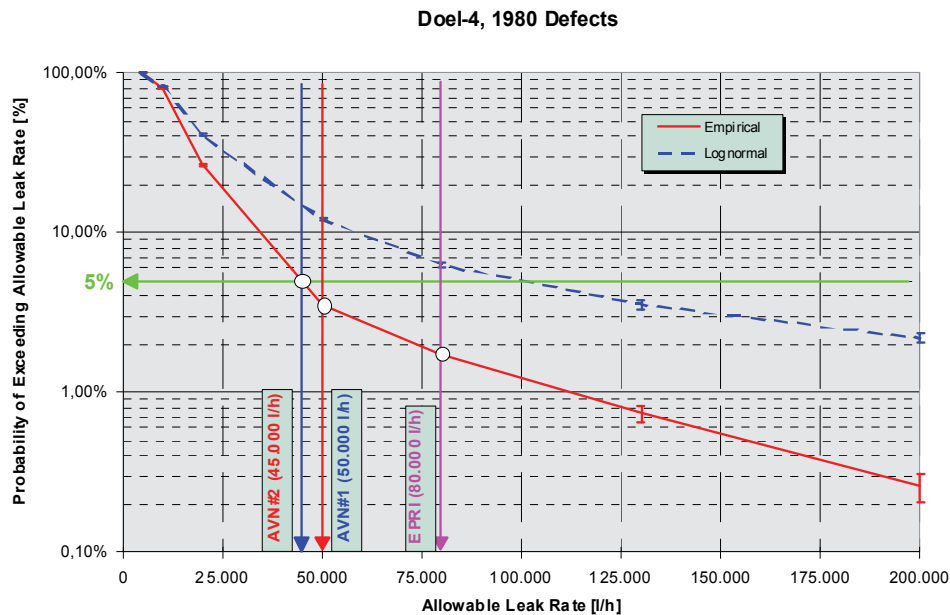


Fig. 11. Probability of exceeding allowable leak rates – Doel-4 plant. Reprinted from Nuclear Engineering and Design, Vol. 185, L. Cizelj, I. Hauer, G. Roussel, C. Cuvellez, Probabilistic assessment of excessive leakage through steam generator tubes degraded by secondary side corrosion, p. 347, Copyright (1998), with permission from Elsevier

#### 4. Information content of successful sampling inspections

In replaced steam generators, the in-service inspection may be performed within a rather limited sample of tubes. Since the main objective of the in-service inspection is to provide reasonable insurance of tubing integrity, the information gained about a limited sample of steam generator tubes must be used to make predictions about the entire population.

The case where the inspection of a small sample selected randomly from the population of all tubes showed exactly zero defects is investigated in this section. In particular, the probability of having certain number of defective tubes in the finite population in the case of zero defects found is discussed. To this end, some closed-form solutions derived using the Bayesian probability theory in (Roussel and Cizelj 2007) are used. The main assumptions made in (Roussel and Cizelj 2007) were:

1. all steam generators perform in a like manner;
2. only one flaw may affect a steam generator tube;
3. the samples are selected on a random basis;
4. the probability of detection for flaws with size larger than the detection threshold is 1.

##### 4.1 Basic relations

Consider multiple  $N$  units of the same type. It is expected that there are a few defective units present. Before inspection, however, there is no known reason to distinguish between different units as far as their individual plausibility to be defective is concerned.

Random sampling of  $n$  units from the lot may be considered as a random drawing without replacement of  $n$  units. Put  $S_n$  the number of defective units in a random sample of size  $n$ . The case where  $n=N$  means that the sampling without replacement has been performed until all units have been drawn and hence  $S_N$  is the number of defective units contained in the lot.

In the case where the lot is known to include  $k$  defective tubes, the probability of  $l$  defective units among any random sample of size  $n$  follows the hypergeometric distribution and is given by

$$P(S_n = l | S_N = k) = h(l, n, k, N) = \frac{\binom{k}{l} \binom{N-k}{n-l}}{\binom{N}{n}} \quad (36)$$

In the case where the composition of the population is unknown, the probability of  $l$  defective tubes among any random sample of size  $n$  is given by the mixture of hypergeometric probabilities by application of the rule of total probabilities:

$$P(S_n = l) = \sum_{k=1}^{N-n+l} P(S_n = l | S_N = k) P(S_N = k) = \sum_{k=1}^{N-n+l} h(l, n, k, N) P(S_N = k) \quad (37)$$

In the Bayesian approach, the prior belief about the probability of  $k$  is quantified by a probability distribution, the prior distribution of  $k$ , i.e.,  $P(S_N = k)$ . Data  $l$  are then collected, and the likelihood function  $h(l, n, k, N)$  is constructed. Finally, the posterior distribution  $P(S_N = k | S_n = l)$  is constructed, by combining the prior distribution  $P(S_N = k)$  and the likelihood function  $h(l, n, k, N)$ :

$$P(S_N = k | S_n = l) = \frac{P(S_n = l | S_N = k) P(S_N = k)}{P(S_n = l)} \quad (38)$$

And finally,

$$P(S_N = k | S_n = l) = \frac{h(l, n, k, N) P(S_N = k)}{\sum_{k'=1}^{N-n+l} h(l, n, k', N) P(S_N = k')} \quad (39)$$

The posterior distribution (eq. (39)) shows the updated belief about the values of the probability that accounts for the observed data. The summation in the denominator ensures that the right hand side of the equation is properly scaled. In any case, it is just a constant that is independent of the values of the parameter  $k$ .

#### 4.2 Prior and posterior distributions

The choice of the prior distribution of defective tubes  $P(S_N = k)$  is subjective. In the following, a few examples of prior distributions are discussed. They share a very useful feature: a closed-form posterior density.

In absence of any information it may be useful to consider a non-informative uniform prior distribution:

$$P(S_N = k) = \frac{1}{N+1} \quad 0 \leq k \leq N \quad (40)$$

This leads to the closed form posterior in the form of:

$$P(S_N = k | S_n = 0) = \frac{1+n}{1+N} h(0, n, k, N) \quad (41)$$

We may also assume that the number of defective tubes in the finite population follows the binomial distribution with expected number of defective tubes being  $pN$ :

$$P(S_N = k) = \binom{N}{k} p^k (1-p)^{N-k} \quad 0 \leq k \leq N \quad (42)$$

This in turn leads to the closed form posterior in the form of:

$$P(S_N = k | S_n = 0) = \binom{N-n}{k} p^k (1-p)^{N-n-k} h(0, n, k, N) \quad (43)$$

Further details on derivation and properties of the above posterior distributions are given in (Cizelj and Roussel 2003).

### 4.3 Numerical example

Predicting the results of measurements is the forward problem. The inverse problem consists of using the actual results of measurements to infer the values of the parameters that characterize the system. The main characteristic of the inverse problem is that it does not have a unique solution. Because of this, in the inverse problem, a priori information about the model parameters is needed. In this case, inferring the number of defective tubes in the whole population from the results of an inspection of a random sample is an inverse problem. In the probabilistic formulation of the inverse problem, a priori information about the probability distribution of the system parameters is needed.

The choice of the particular prior in Bayesian analysis is usually interpreted as the knowledge or belief the analyst has about the investigated problem. Now, let us examine two rather extreme states of knowledge assumed by our imaginary analyst:

1. The material and design improvements made in the replacement steam generators are believed to be so efficient that active degradation processes are extremely unlikely. At the same time it is acknowledged that rare events might occur. Our prior information about the condition of the tubes then appears described correctly with a binomial distribution associated with a low value of the probability  $p$ .
2. On the other hand, we may acknowledge the material and design improvements made in the replacement steam generators. At the same time, we are convinced that the nature is more imaginative than the most experienced engineers. Then, our belief may well be that no knowledge about the condition of the tubes exists prior to the inspection. In such situation, the uniform distribution may appear to be a well-suited distribution.

At the first glance, it might appear that the binomial distribution expresses more information about the actual proportion of defective tubes in the steam generators than the uniform distribution. However, comparing eqs. (42) and (43) reveals that the posterior in eq. (43) is identical to the prior (eq. (42)) we would have postulated for any subset of  $N-n$  tubes in the population. Otherwise stated, the data collected during the in-service inspection of the first sample ( $n$ ) tells us nothing at all about the unsampled tubes ( $N-n$ ). Indeed, the choice of a binomial prior introduces a strong belief that there is a limited and rather well

characterized subpopulation of defective tubes. Since we do not find any defective tubes during the inspection of the sample  $n$ , the entire defective subpopulation must have survived the inspection and remains in the uninspected set of the tubes.

The explanation of the uniform prior requires numerical example. The steam generator contains  $N=10,000$  tubes in all subsequent discussions. The definition of the relative sample size always refers to  $N$ . For example, a 10% sample would consist of  $n=1000$  tubes.

Let us reiterate that the choice of uniform prior introduces the a-priori belief that any number of defective tubes is equally probable. This results in the posterior density (eq. (41)) of the number of defective tubes left in uninspected tubes, given the random sample of size  $n$  revealed zero defective tubes. Posterior densities for selected inspection samples are plotted together with the prior density in Fig. 12.

The non-informative uniform prior has a value of about  $10^{-4}$ , which is independent of the number of defective tubes in the steam generator. Now, assume that inspection of a small (0,5%) random sample has been performed without finding any defects. Our information about the uninspected tubes improved drastically: The probability of having small number of defects increased for about two orders of magnitude. At the same time, although not shown in Fig. 12, the probability of having large number of defects in the uninspected part of the steam generator also decreased significantly. The expected number of defective tubes, which was 5000 for the uniform prior, decreased to 191 (yellow dots in Fig. 12).

Further increases in sample size are shown to increase the knowledge about the uninspected part of the population significantly. Inspecting the 20% random sample (without finding any defects) results in expected number of remaining defects at about 4 and in very fast decrease of probability of having larger numbers of defects.

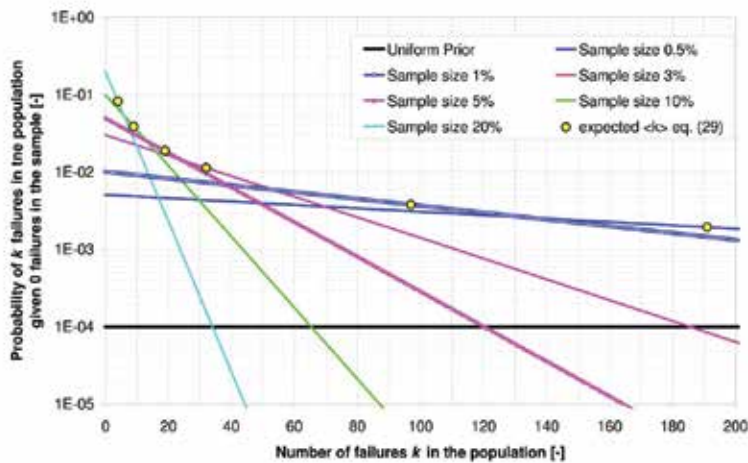


Fig. 12. Posteriors with different sample sizes. Uniform prior and 0 defects in the sample. Reprinted from Journal of pressure vessel technology, Vol. 129, Guy Roussel and Leon Cizelj, Propagation of stress corrosion cracks in steam generator tubes, p. 109, Copyright (1996), with permission from ASME

Expected number of defective tubes in the uninspected part of the population is plotted as a function of the sample size in Fig. 13. In addition, the 90% and 99% confidence curves are

plotted based on the expected number of degraded tubes and its variance defined in (Cizelj and Roussel 2003). Without inspection, the expected number of defects is 5000. It diminishes fast with increasing inspection sample. 3% inspection is shown to give 90% confidence, that there are less than 80 defective tubes left undetected. Similarly, 20% inspection is shown to give 99% confidence, that there are fewer than 11 defective tubes left undetected.

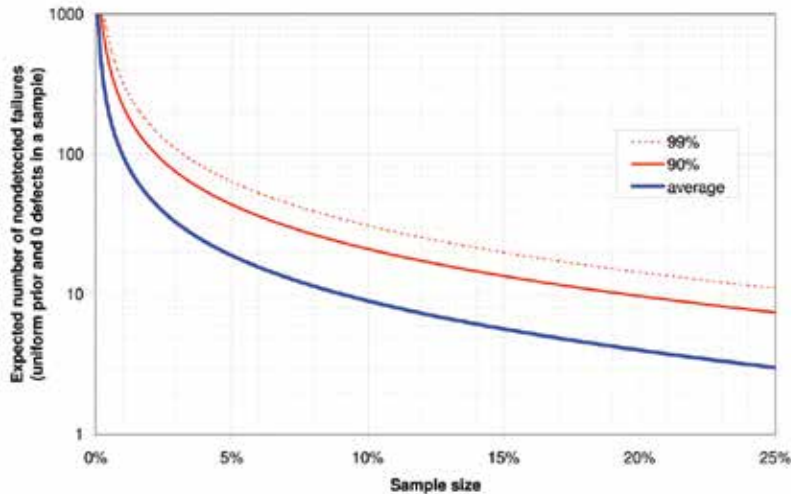


Fig. 13. Expected number of undetected defective tubes. Uniform prior and 0 defects in the sample. Reprinted from Journal of pressure vessel technology, Vol. 129, Guy Roussel and Leon Cizelj, Propagation of stress corrosion cracks in steam generator tubes, p. 109, Copyright (1996), with permission from ASME

The confidence to be placed in the results of the sampling inspection therefore depends mainly on the knowledge about the defective tubes existing prior to the inspection. As a rough practical guide, sampling inspection will only improve our knowledge about the defective subpopulation if we had very poor or no knowledge about it prior to the inspection. The sampling inspection (with uniform prior) may therefore be trusted as long as no defects are detected. With first failures detected, however, other inspection approaches might give more reliable results. This will be one of the topics of future investigations.

## 5. Summary

A critical compilation of the past work in the field of probabilistic assessment of degradation and maintenance strategies for degraded steam generator tubes was performed. The probabilistic apparatus previously proposed to serve in specific cases has been consolidated and generalized to accommodate a wide range of mechanistic and empirical models describing the tube failure modes. Realistic numerical examples provided illustrative and practical demonstration of the generalized probabilistic apparatus. Results include tube rupture probabilities, excessive tube leakage probabilities and comparisons of different maintenance approaches in probabilistic terms.

The basis for determining the size of the small random samples of tubes to be inspected in replacement steam generators is revisited. It is assumed that the probability of finding a

defective tube in a random sample is exceedingly small. A procedure to estimate the maximum number of defective tubes left in the steam generator after no defective tubes have been detected in the randomly selected inspection sample is proposed.

The confidence to be placed in the results of the sampling inspection has been found to depend mainly on the knowledge about the defective tubes existing prior to the inspection. As a rough practical guide, sampling inspection will only improve our knowledge about the defective subpopulation if we had very poor or no knowledge about it prior to the inspection.

The future work is expected to be focused mainly on the mechanistic models describing the rupture and leakage properties of various defects found in steam generator tubes. This will improve the predictive capabilities of the probabilistic framework described here.

## 6. References

- Barnier, M., P. Pitner, et al. (1992). Estimation of crack size distribution from in-service inspection data for the calculation of the failure probabilities. *Safety and reliability* 92. Copenhagen, Denmark: 527-538.
- Beardsmore, D., K. Stone, et al. (2010). Advanced probabilistic fracture mechanics using the R6 procedure. *ASME Pressure Vessels & Piping Conference*. Bellevue, Washington, USA, ASME: PVP2010-25942.
- Cassagne, T. B., P. Combrade, et al. (1992). The influence of mechanical and environmental parameters on the crack growth behaviour of alloy 600 in PWR primary water. *12th Scandinavian corrosion congress & Eurocorr*. Espoo, Finland: 55-67.
- Cizelj, L. (1994). On the estimation of the steam generator maintenance efficiency by the means of probabilistic fracture mechanics. Karlsruhe, Germany, Kernforschungszentrum Karlsruhe.
- Cizelj, L. and T. Dvoršek (1999). The relative impact of sizing errors on steam generator tube failure probability. *Third International Conference on Steam Generators and Heat Exchangers*, Toronto, Ontario, Canada, Canadian Nuclear Society.
- Cizelj, L., I. Hauer, et al. (1998). Probabilistic assessment of excessive leakage through steam generator tubes degraded by secondary side corrosion. *Nuclear Engineering and Design* 185(2-3): 347-359.
- Cizelj, L., B. Mavko, et al. (1994). Application of 1st and 2nd-Order Reliability Methods in the Safety Assessment of Cracked Steam-Generator Tubing. *Nuclear Engineering and Design* 147(3): 359-368.
- Cizelj, L., B. Mavko, et al. (1995). Propagation of Stress-Corrosion Cracks in Steam-Generator Tubes. *International Journal of Pressure Vessels and Piping* 63(1): 35-43.
- Cizelj, L. and H. Riesch-Oppermann (1992). ZERBERUS the code for reliability analysis of crack containing structures, Kernforschungszentrum Karlsruhe.
- Cizelj, L. and G. Roussel (2003). Probabilistic evaluation of leak rates through multiple defects: the case of nuclear steam generators. *Fatigue & Fracture of Engineering Materials & Structures* 26(11): 1069-1079.
- Cuvelliez, C. and G. Roussel (1995). Assessment of the Leak Tightness Integrity of the Steam Generator Affected by ODS-CC at Tube Support Plates. *CNRA/CNSI Workshop on Steam Generator Tube Integrity in Nuclear Power Plants* (NUREG/CP-0154), Oak Brook, Illinois, USA.

- Det Norske Veritas (2010). Probabilistic analysis - PROBAN, <http://www.dnv.com/services/software/products/safeti/safetiqlra/proban.asp>.
- Dvoršek, T., L. Cizelj, et al. (1998). Safety and availability of steam generator tubes affected by secondary side corrosion. *Nuclear Engineering and Design* 185(1): 11-21.
- EPRI (1993). Outside Diameter Stress Corrosion Cracking (ODSCC) of Steam Generator Tubing at Tube Support Plates-A Database for Alternate Repair Limits Vol. 2: 3/4 Inch Diameter Tubing. Palo Alto, Ca., USA, Electric Power Research Institute. EPRI TR-100407, Rev. 1.
- Erdogan, F. (1976). Ductile fracture theories for pressurised pipes and containers. *International Journal of Pressure Vessels and Piping* 4(4): 253-283.
- Esteban, A., M. F. Bolaños, et al. (1990). A plugging criterion for steam generator tubes based on leak-before-break. *International Journal of Pressure Vessels and Piping* 43(1-3): 181-186.
- Flesch, B. and B. Cochet (1990). Leak-before-break in steam generator tubes. *International Journal of Pressure Vessels and Piping* 43(1-3): 165-179.
- Hernalsteen, P. (1993). PWSCC in the tube expansion zone - an overview. *Nuclear Engineering and Design* 143(2-3): 131-142.
- Hui, H. and P. Li (2010). Plastic limit load analysis for steam generator tubes with local wall-thinning. *Nuclear Engineering and Design In Press*, 240(10): 2512-2520.
- Hur, D. H., M. S. Choi, et al. (2010). A case study on detection and sizing of defects in steam generator tubes using eddy current testing. *Nuclear Engineering and Design* 240(1): 204-208.
- Hwang, S. S., H. P. Kim, et al. (2005). Leak behavior of SCC degraded steam generator tubings of nuclear power plant. *Nuclear Engineering and Design* 235(23): 2477-2484.
- Hwang, S. S., C. Namgung, et al. (2008). Rupture pressure of wear degraded alloy 600 steam generator tubings. *Journal of Nuclear Materials* 373(1-3): 71-74.
- IAEA (1997). Assessment and management of ageing of major nuclear power plant components important to safety : steam generators. *IAEA-TECDOC-981*. Vienna, IAEA.
- IAEA (2008). Heavy component replacement in nuclear power plants: experience and guidelines. *IAEA Nuclear energy series*. NP-T-3.2.
- Kim, H.-S., T.-E. Jin, et al. (2008). Restraining effect of support plates on the limit loads for circumferential cracks in the steam generator tube. *Nuclear Engineering and Design* 238(1): 135-142.
- Kim, N.-H., C.-S. Oh, et al. (2010). A method to predict failure pressures of steam generator tubes with multiple through-wall cracks. *Engineering Fracture Mechanics* 77(5): 842-855.
- Lee, J. B., J. H. Park, et al. (2010). Evaluation of ECT reliability for axial ODSCC in steam generator tubes. *International Journal of Pressure Vessels and Piping* 87(1): 46-51.
- Madsen, H. O. and K. Krenk (1986). *Methods of structural safety*, Englewood Cliffs : Prentice-Hall.
- Murphy, E. (2007). New requirements for ensuring steam generator tube integrity in pressurized water reactors in the united states. *Structural mechanics in reactor technology*. Toronto, Ontario, Canada, SMiRT. O-03/1.

- Nuclear Regulatory Commission (1995). Voltage-Based Repair Criteria for Westinghouse Steam Generator Tubes Affected by Outside Diameter Stress Corrosion Cracking. Rockville, Md., USA. *Generic Letter* 95-05.
- Pagan, S., X. Duan, et al. (2009). Characterization and structural integrity tests of ex-service steam generator tubes at Ontario Power Generation. *Nuclear Engineering and Design* 239(3): 477-483.
- Pandey, M. D., S. Datla, et al. (2009). The estimation of lifetime distribution of Alloy 800 steam generator tubing. *Nuclear Engineering and Design* 239(10): 1862-1869.
- Pitner, P., T. Riffard, et al. (1993). Application of probabilistic fracture mechanics to optimize the maintenance of PWR steam generator tubes. *Nuclear Engineering and Design* 142(1): 89-100.
- Revankar, S. T. and J. R. Riznic (2009). Assessment of steam generator tube flaw size and leak rate models. *Nuclear Technology* 167(1): 157-168.
- Revankar, S. T., B. Wolf, et al. (2009). ANL/CANTIA code for steam generator tube integrity assessment. *6th CNS International steam generator conference*. Toronto, Ontario, Canada, Canadian nuclear society.
- Revankar, S. T., B. Wolf, et al. (2009). Crack leak rate models for steam generator tube integrity assessment *6th CNS International steam generator conference*. Toronto, Ontario, Canada, Canadian nuclear society.
- Roussel, G. and L. Cizelj (2007). Reliability of sampling inspection schemes applied to replacement steam generators. *Journal of Pressure Vessel Technology-Transactions of the Asme* 129(1): 109-117.
- Scott, P. M. (1991). An analysis of primary water stress corrosion cracking in PWR steam generators. *NEA-CSNI-UNIPED Specialist meeting on operating experience with steam generators*. Brussels, Belgium.
- Shah, V. N. and P. E. MacDonald (1993). Ageing and life extension of major light water reactor components. Amsterdam, Elsevier.



## **Part 2**

### **Nondestructive Evaluation and Diagnostics**



# The Development of Eddy Current Technique for WWER Steam Generators Inspection

Valentin Uchanin and Vladimir Najda

*Karpenko Physico-Mechanical Institute of National Academy of Sciences,  
Paton Electric Welding Institute, design bureau,  
Ukraine*

## 1. Introduction

Safety and efficiency of nuclear power plants (NPP) are dependent of the technical state of heat exchanger tubes installed in steam generators (SG). The majority of Russian and Ukrainian WWER type NPP units as well as NPP in Czech Republic (Temelin) and Bulgaria (Kozloduy) are equipped by PGV-1000 type SG. These NPP units were introduced into service from 1982 to 2004. Decommissioning dates (or dates of life time prolongation) are planned from 2012 to 2034 (Balitskii et al., 2005). SG heat exchanger tubes create a barrier between the radioactive primary and secondary water circuits and are one of the most critical component in NPP due different type defects and damages initiated during in-service life (Neklyudov et al., 2006; Mytrofanov et al., 2008). The in-service defects appear along the full tube length and in the zone of the tubes mounting to collector desk. Therefore, the complex diagnostics of heat exchanger tubes based on the trustworthy results of nondestructive testing is the question of great importance (IAEA-TECDOC-981, 1997; IAEA-EBP-VVER-11, 1998; IAEA-TECDOC-1400, 2004).

## 2. State of the art

The routine examinations of SG tubes along the full length are executed by eddy current (EC) method which has many advantages in comparison with methods based on other physical phenomena. Different type internal EC probes for SG tubes inspection are developed. The most known are bobbin, rotational and array EC probe (Alferink & Meier, 1996; Amedro et al., 1983; Werner et al., 1987; Clark, 1993; Cecco et al., 1996; Herka et al., 1999; Krajcovic & Plasek, 2006). Each type of EC probe has advantages and limitations shortly analyzed in Table 1. At the present time the largest amount of SG tube inspections are executed by the internal bobbin type probes application. The main reasons of such choice are high inspection speed, lowest price, large flaw detection experience and established tradition. Particularly, the bobbin type EC probes are only one type of probes applied at Ukrainian NPP for full length tube inspection (Mytrofanov et al., 2008; Uchanin, 2009).

For inspection data interpretation many theoretical and experimental investigations were carried out (Ida, 1986; Pichenot et al., 2004). In another investigations special algorithms, based on feature extraction, neural network, etc, were proposed (Wong et al., 1995; Song et al., 2003; Sabbagh et al., 2008; Nam et al., 2009). But the mentioned results were obtained

mostly for SG tubes of another types then used at WWER type NPP. Thus for appreciable understanding of the results obtained during PGV-1000 type SG tube inspection the subsequent signal response investigation are steel needed. And reliable detection and the quantification of defects is still difficult task.

Next actual question of EC probe application is the passing ability across full tube length. This problem is especially significant for SG tubes of WWER type NPP because of considerable tube geometry disturbances and clogging by deposits.

	<i>Advantages</i>	<i>Disadvantages</i>
<i>Bobbin probe</i>	1) High sensitivity to axial cracks. 2) High inspection speed. 3) Determination of defect location in axial direction. 4) Determining defect depth and length. 5) High reliability and durability. 6) Comparatively low price.	1) Low sensitivity to circumferential cracks. 2) Unrecognizing and false interpretation when several defects are situated with the same axial location.
<i>Rotating probe</i>	1) High sensitivity to cracks of different orientation. 2) Crack orientation determination. 3) Length and depth of crack determination. 4) Determination of defect location in axial direction. 5) Good inspection results visualization.	1) Low inspection speed. 2) Comparatively low reliability and durability. 3) Comparatively low passing ability. 4) High price.
<i>Array probe</i>	1) High sensitivity to cracks of different orientation. 2) High inspection speed. 3) Crack orientation determination. 4) Determination of flaw location in axial direction. 5) Determination of defect parameter.	1) Very high price. 2) Comparatively low reliability and durability. 3) Comparatively low passing ability.

Table 1. Comparative analysis of different type EC probe features.

The next key component important for SG reliability and life-time growth is considered to be the junction points in which tubes are mounted to the collector wall (Balitskii et al., 2005). PGV-1000 SG operating experience shows that the collector material is exposed to stress corrosion, which leads to stress corrosion cracking of collector wall between tube holes (Melechov & Pochmurskij, 2003). Thus, the task is to detect cracks in the collector wall, which are developed mainly from the tube holes. For detection of this crack through tube wall it is possible to use more complicated low frequency EC technique. For such inspection only totally automatic inspection due the influence of radioactive environment can be offered.

SG tubes have 16.0 mm in diameter with 1.5 mm wall thickness and are fabricated of nonmagnetic stainless steel 08X18N10T (AISI 321). The collector wall is fabricated of low-

alloy pearlitic ferromagnetic steel 10GN2MFA with a wall thickness of 171 mm. The inner surface of collectors is plated by 07H25N13 steel cladding. The tube ends are flared in the collector wall and welded to the cladding steel layer. There are 119 vertical and 110 horizontal rows of tube inlet holes accessible from the inner surface of the collector. Thus, the total number of inlet holes is more than 11000. The placement of inlet holes from the collector side and some dimensions are shown in Fig. 1.

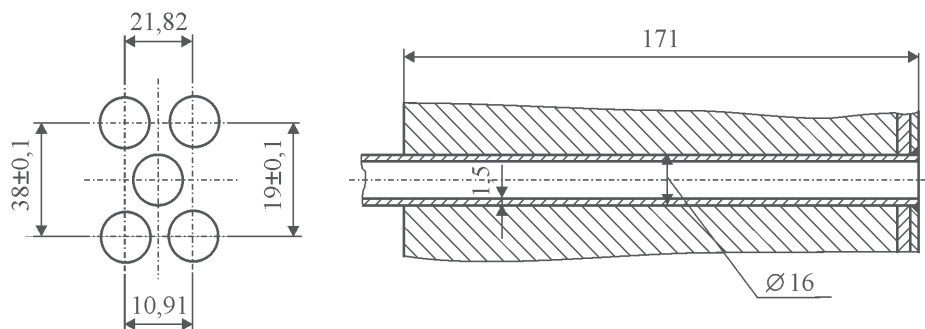


Fig. 1. The scheme of inlet holes placement on the inner surface of collector (left) and heat exchanger tube mounted in collector wall (right).

### 3. The investigation and development of eddy current bobbin probes for SG heat exchanger tubes inspection

#### 3.1 Model based eddy current bobbin probe defect signal response analysis

A differential type bobbin EC probe consists of two opposite connected identical coils. Because of such connection differential bobbin probes are insensitive to gradual changes of tube wall thickness and temperature. Due this feature differential bobbin EC probes are used for defect detection only. The computational model (Fig. 2) deals with a differential bobbin EC probe placed in a tube of stainless 08X18N10T steel, which corresponds to the heat exchanger SG tubes. The 08X18N10T steel specific conductivity was specified to be 1.2 MSm/m. The geometric parameters of the investigated EC probe (internal  $r_1$  and external  $r_2$  radii, length  $l_0$ , the number of turns  $w$ , and the base of placement of the windings  $l_b$ ) can be changed in process of calculations, and, hence, we succeed in optimizing their choice for a specific object and inspection conditions. The defect is located in the tube so that its midpoint corresponds to  $X$  coordinate zero point. The EC probe signal responses were determined by the volume integral method application (Dunbar, 1985; Sabbagh et al, 2008). There were calculated the changes in the real  $X_D$  and imaginary  $R_D$  components of the EC probe impedance  $Z_D$  as well as signal response amplitude  $Mod Z_D$  at operational frequency 100 kHz in the course of EC probe scanning along the tube (the  $X$  coordinate was varied by 1 mm within the range  $\pm 10$  mm) from cracks of different length  $l_{cr}$ , located symmetrically with respect to the  $X$  coordinate zero point (Fig. 2). The computations were performed for the differential EC probe in which internal  $r_1$ , external  $r_2$  radii and winding length  $l_0$  equal to 4.7; 5.1 and 1.6 mm respectively. The number of turns of the coil windings is  $w = 60$ . The inductance of each coil winding in the absence of tested object is equal to 5.5  $\mu$ H, which corresponds with the measured inductance of a real EC probe with the same parameters. The differentially connected coils are separated with distance  $l_b = 3.0$  mm. The crack depth

remained unchanged and was taken equal to 0.5 mm, and crack width (opening) was 0.2 mm. To reach high calculation accuracy, we chose the number of cells in the crack volume over width, length and depth equal to 8, 32 and 16 cells respectively (Uchanin, 2009).

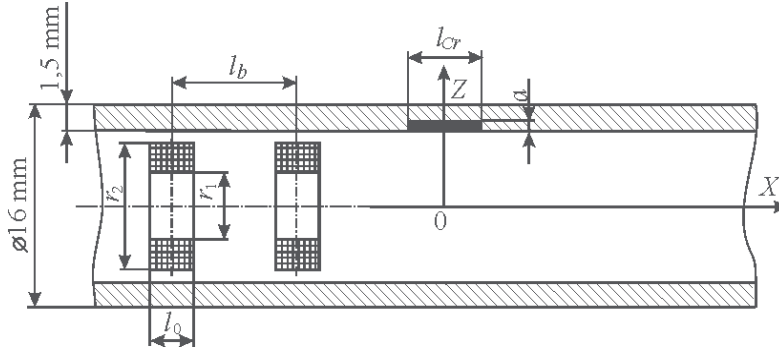


Fig. 2. The dimensions and relative position of the bobbin type EC probe and crack in the tested heat exchanger tube.

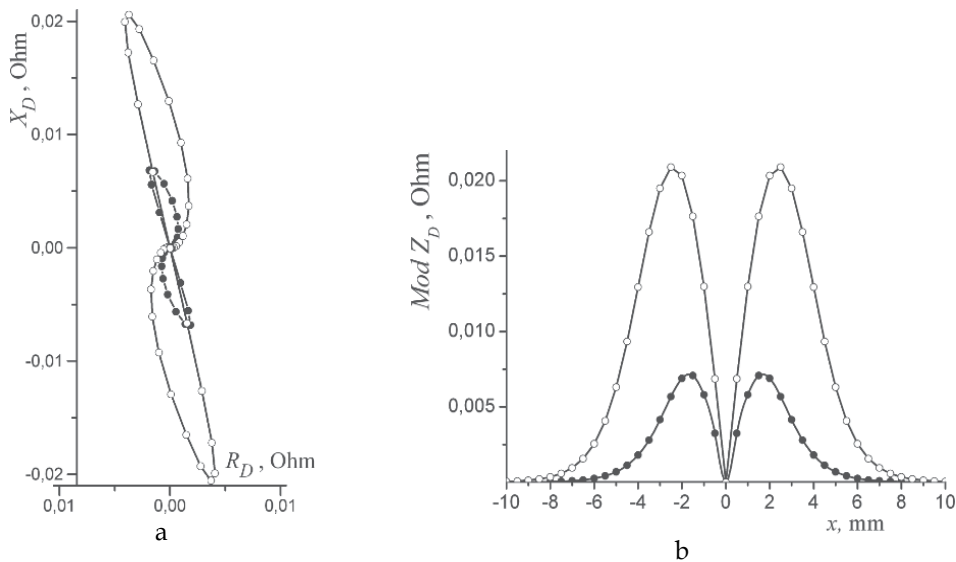


Fig. 3. EC probe signal response scanning hodographs (a) and amplitude distributions (b) for transverse (●) and longitudinal (○) cracks with length  $l_{cr} = 5.0$  mm.

It was established (Fig. 3) that the scanning hodographs and distributions of the EC probe signal amplitude for longitudinal and transverse cracks are similar. The EC probe signal response obtained from a longitudinal crack is approximately thrice as larger against the signal response for transverse crack of the same size. It was noticed that the EC probe begins to “sense” a transverse crack at a distance of 5–6 mm from its center and a longitudinal crack at 7–8 mm. If the EC probe is located symmetrically with respect to the defect the signals responses of separated coil are equal and the output EC probe signal response is equal to zero, which was expected for the differential connection of windings. In addition, it is

necessary to notice that for internal surface (with respect to the EC probe) crack, the imaginary component of the signal response at the operational frequency 100 kHz is four to five times greater than the real component.

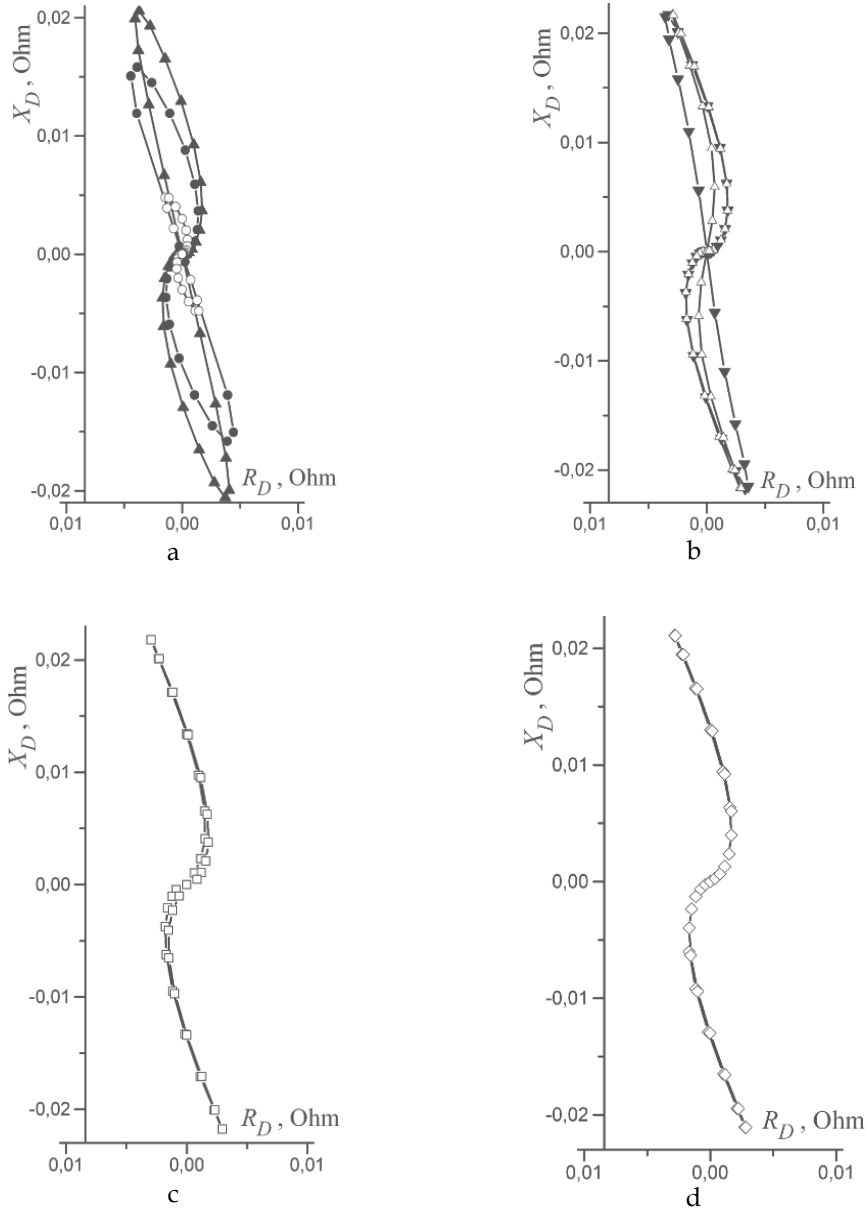


Fig. 4. EC probe signal response scanning hodographs for longitudinal cracks of different length  $l_{cr}$ : a - 1.0 ( $\circ$ ), 3.0 ( $\bullet$ ) and 5.0 mm ( $\blacktriangle$ ); b - 6.0 ( $\blacktriangledown$ ) and 8.0 mm ( $\triangle$ ); c - 10.0 mm ( $\square$ ); d - 12.0 mm ( $\diamond$ ).

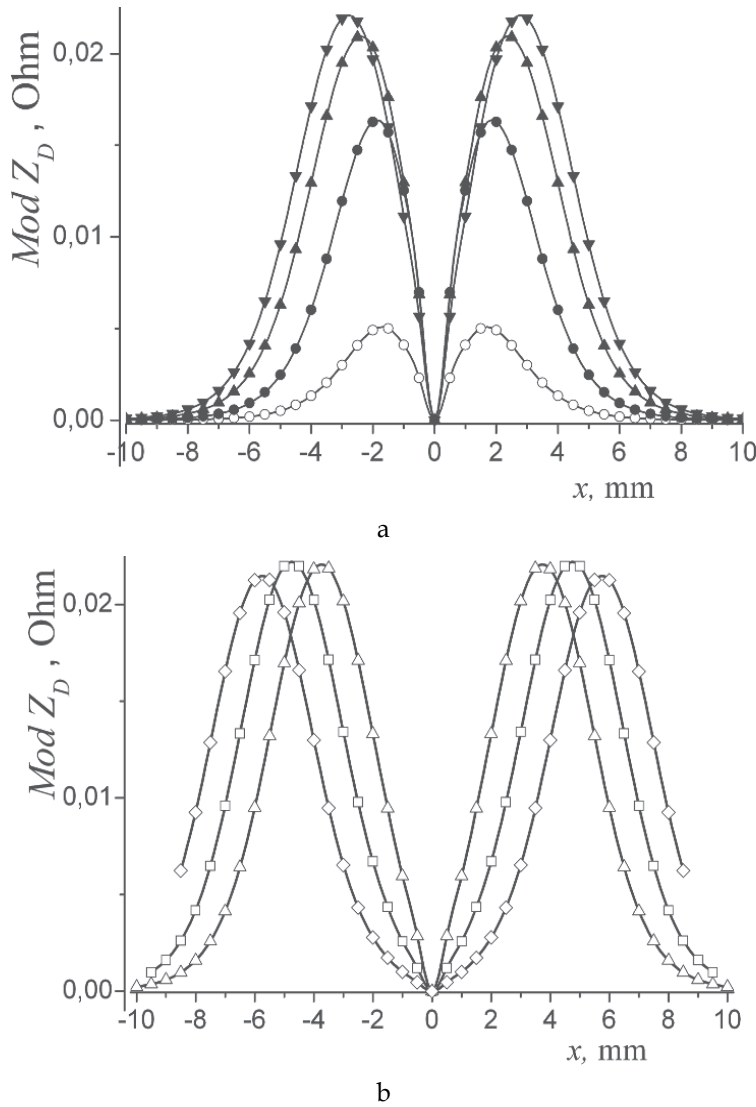


Fig. 5. Signal response amplitude distributions for longitudinal cracks of different length  $l_{cr}$  : a – 1.0 ( $\circ$ ), 3.0 ( $\bullet$ ), 5.0 ( $\blacktriangle$ ) and 6.0 mm ( $\blacktriangledown$ ); b – 8.0 ( $\Delta$ ), 10.0 ( $\square$ ) and 12.0 mm ( $\diamond$ ).

The signal response hodographs (Fig. 4) have a characteristic ansiform shape, which is well known from experimental investigations (Alferink & Meier, 1996). It is possible to observe here certain differences for cracks of different length. The hodographs of short cracks ( $l_{cr} < 5$  mm, Fig. 4a) have a figure-of-eight shape with characteristic rounded part, which begins from the zero point, when the EC probe does not sense the crack yet, and continue to the point of maximum signal response amplitude, and nearly linear part, which connects the points of maximum signal amplitude. In the linear part, the signal response amplitude changes most significantly per unit of change in the X coordinate and this is reflected in a greater distance between these points. For a crack length  $l_{cr} = 6$  mm (Fig. 4b), the linear part



of hodograph begins to bend and with further increase in the length come nearer towards its rounded part (Fig. 4c). For long cracks ( $l_{cr} > 10$  mm), the parts of increase and decrease in the signal amplitude and the corresponding points on hodographs are coincided. (Fig. 4d). These features of the EC probe signal response formation for cracks of different length have a physical interpretation and can be explained by the simultaneous influence of the beginning and the end of a crack on the EC probe coils for short cracks. For some values of the defect length, the phenomena indicated above are confirmed in some investigations (Pichenot et al., 2004; Bisiaux et al., 2006).

It was established (Fig. 4 and 5) that the signal response amplitude from a longitudinal crack depends on its length for cracks not longer than 6 mm. We observe here inessential changes in the signal phase, which are manifested in a slight turn of the hodograph in the complex plane. Under the subsequent crack length increase the amplitude and slope of hodograph of EC probe signal response remain practically invariable. Note that, for short longitudinal (1 mm) and transverse cracks, the coordinates of maxima correspond to the base  $l_b = 3.0$  mm of the coil windings placement. The amplitude distribution of EC probe signal response for cracks of length more 1 mm depends on their length (Fig. 5). Hence, knowing the signal distribution, we can determine crack lengths. It should be noted that, in determining the length of long cracks from the Z coordinates, where the signal amplitude is greater than the threshold of operation of the flaw detector, we can obtain a significant error whose sign and value depend on the assigned threshold of sensitivity. More exact results can be obtained if, for this purpose, the coordinates of maximum values of the amplitude distributions of signals will be used. From Fig. 6 we can see that the distance  $l_{Max}$  between coordinates of maximum amplitude correlate with crack length  $l_{cr}$  very good. Insignificant data scattering can be explained by discrete choice of crack length in calculations.

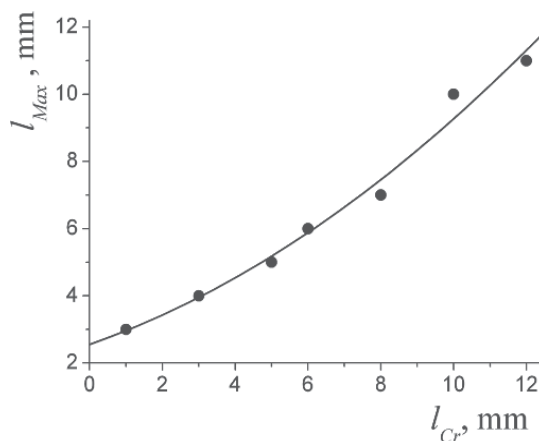


Fig. 6. Influence the crack length  $l_{cr}$  on the distance  $l_{Max}$  between maxima points of longitudinal cracks signal response distribution.

So, we have studied the distribution of the signal responses of internal bobbin EC probes for cracks of different orientation and length in the SG heat exchangers tubes. Some specific features of hodographs and signal amplitudes for cracks of different length were established. The results obtained can be used for the interpretation of the EC probe signal responses and adjustment of the inspection procedures.

The result of inspection must contain not only the information about the presence of defect, though it is also very important. The main task is to predict the subsequent operating time without tube leakage, when defect during its growth reach the opposite surface of tube, independently of internal or outer tube surface was damaged from the beginning. Such estimation can be carried out, when the parameters of detected defects will be evaluated with the fracture mechanic approaches. Such parameter as "metal loss" or defect volume very often is applied in practice (Neklyudov et al., 2006). But for small opening fatigue crack the tube damage and safety are not accompanied by loss of material. To our opinion the residual tube thickness is the better operability criterion to make decision about tube plugging. It is clear, the residual thickness can be obtained from the defect depth measurement results independently of the tube surface the defect was initiated. Therefore the defect depth and residual thickness very often are estimated in percent of tube thickness. The defect width and length also influence the tube durability and availability, but don't have priority importance for estimation of leakage possibility.

To analyze the problems in inspection results interpretation the signal response amplitude and phase in dependence of defect parameters were investigated. In contrast to previous investigations, when the signal response distribution was calculated, the dependence of signal response parameters in specified points defined during the scanning along the tested tube (for example in the point of maximum signal amplitude) must be the main point of interest. That is why, for next calculations the absolute type EC probe it is convenient to apply, because the signal response maximum for defect will be correspond the zero point of  $X$  coordinate ( $x = 0$  in Fig. 2). Hereupon the probe winding parameters were selected the same as in previous calculations.

The changes of the EC probe signal response amplitude  $Mod Z_D$  and phase  $\varphi$  at operational frequency 100 kHz for longitudinal cracks on internal tube surface, when probe is situated in zero point ( $x = 0$ ), in dependence of depth  $a$ , width (opening)  $c$  and length  $l_{cr}$  were defined (Fig. 7-9). The signal response amplitudes were balanced and normalized in respect to signal response of EC probe situated in defect-free zone of tube.

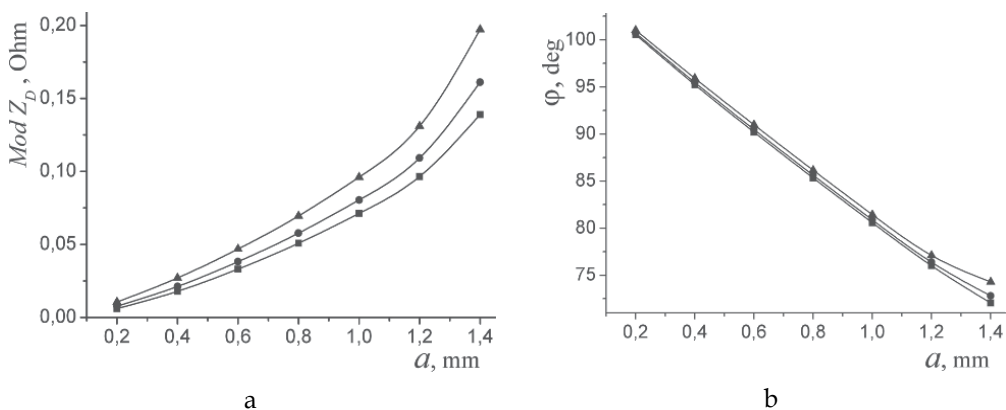


Fig. 7. Influence of crack depth  $a$  on the amplitude  $Mod Z_D$  (a) and phase  $\varphi$  (b) for longitudinal 6 mm long crack with width 0.1 mm (■); 0.2 mm (●) and 0.4 mm (▲).

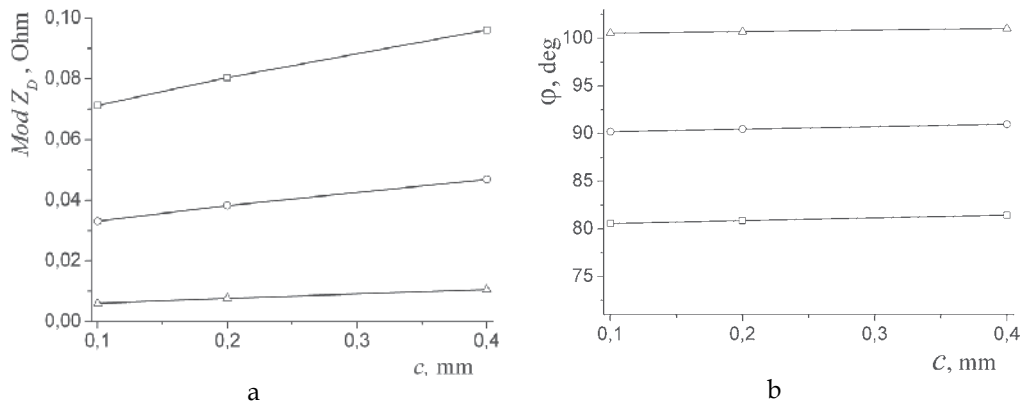


Fig. 8. Influence of crack width  $c$  on the amplitude  $Mod Z_D$  (a) and phase  $\varphi$  (b) for longitudinal 6.0 mm long crack with depth 0.2 mm ( $\Delta$ ); 0.6 mm ( $\circ$ ) and 1.0 mm ( $\square$ ).

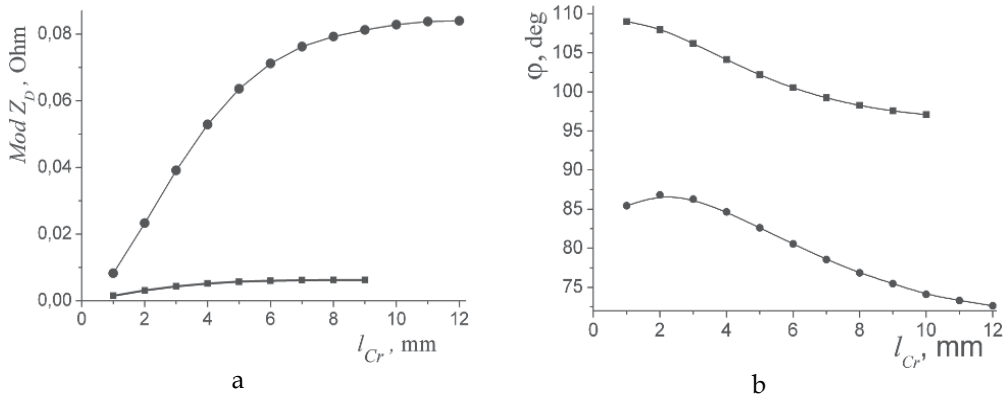


Fig. 9. Influence of crack length  $l_{cr}$  on the amplitude  $Mod Z_D$  (a) and phase  $\varphi$  (b) for longitudinal crack with depth 0.2 mm ( $\blacksquare$ ) and 1.0 mm ( $\bullet$ ).

Presented results show strong amplitude-depth and phase-depth EC probe defect signal response dependence. In our case, the amplitude is increased more than to one order and phase is changed more than 30 degrees, when crack depth is changed from 0.2 mm to 1.4 mm. The dependence of signal response amplitude becomes stronger with the crack depth growth. It is especially noticed, when crack depth is more than 1.2 mm, what is fitted with experimental results (Alferink & Meier, 1996). The amplitude-depth dependence (Fig. 7a) coincides with experimental results obtained for artificial electro-erosion defects and introduced stress corrosion cracks in tubes identical to our calculation mode (Krajcovic & Plasek, 2006).

As we can see on Fig. 7b the phase-depth curves for cracks with different width are very close each other to draw a conclusion about the invariant property of phase relatively the crack width changes. This conclusion is confirmed by dependences on Fig. 8b, where it was shown that crack depth weakly influence the signal response phase. As it was mentioned before, similar conclusion it is impossible to say about the signal response amplitude.

It is necessary to emphasize, that the phase is not the invariant parameter relatively the crack length, when the crack depth it is needed to be defined, especially for short cracks. Such influence of crack length to signal response phase is low in comparison with the crack depth influence. At least, two defects with 0.2 mm and 1.4 mm depths can be differentiated by phase measurements even for high difference in crack length (Fig. 9b). More accurate algorithm for crack length estimation can be established from the signal response distribution (see Fig. 5) (Uchanin, 2009). In this case, for crack depth estimation it is possible to use the phase-depth dependences obtained for previously defined crack length.

Let us consider the signal response features for local defects with different depths originated from internal and outer tube surfaces. Calculations were carried out for absolute type EC probe (with only one winding) moved along X axis (Fig. 2). It was considered local corrosion (like pitting) defect simulated by 1 mm diameter circular hole with flat bottom. Depths of holes were increased from 0.3 mm to through wall condition, when 1.5 mm depth was reached. As in previous calculations, EC probe signals were balanced relatively EC probe signal for unflawed tube. Operational frequency was 100 kHz as in previous investigations. On next figures the EC probe signal response scanning hodographs in complex plane for different depth holes situated on internal (fig. 10a) and external (fig. 10b) tube surfaces were plotted.

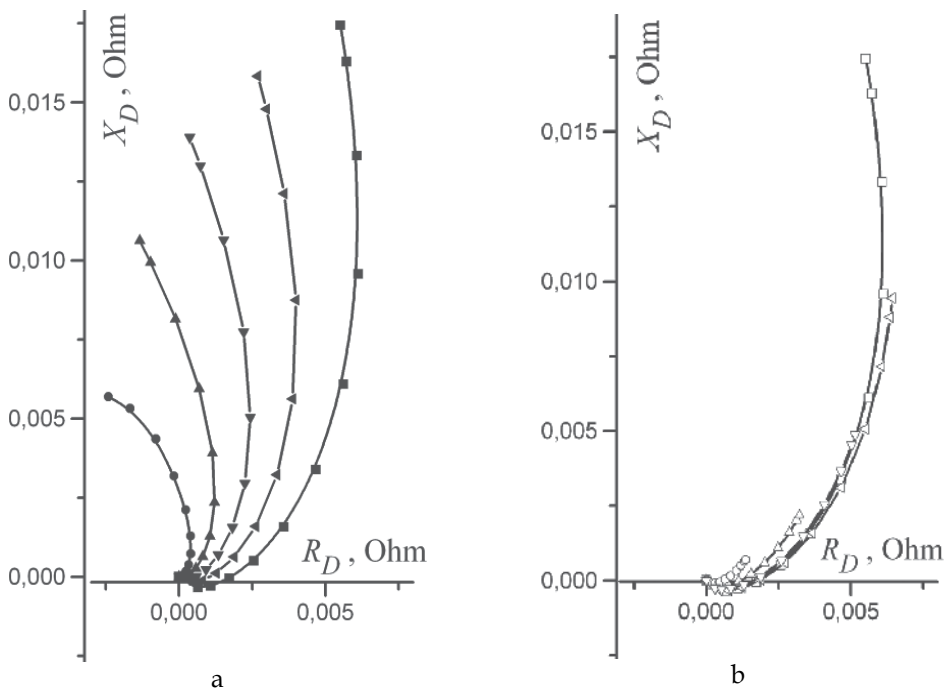


Fig. 10. EC probe scanning hodographs for holes situated on internal (a) and external (b) tube surfaces for hole depth 0.3 mm (● and ○); 0.6 mm (▲ and △); 0.9 mm (▼ and ▽); 1.2 mm (◄ and ▷) and 1.5 mm (■ and □).

It can be noticed, that depth of the hole for internal and external defects influences the hodographs pattern. For any tube surface the defect depth growth lead to amplitude growth and the hodograph rotation. The amplitude changes for subsurface defects on external tube

surface are more considerable than amplitude changes for surface defect on internal tube surface. It seems that the hodograph rotation and phase changes are stronger for surface defects in comparison with such changes for defects on external tube surface. Such feeling is wrong and this statement was confirmed, when more scrupulous analyze was done. When depth of surface defect is increased from 0.3 mm to 1.5 mm, the phase of signal response in the points of amplitude maximum is changed on  $32.4^\circ$  from  $104.8^\circ$  to  $72.4^\circ$  (Fig. 10a). The same growth of the depth for subsurface defect rotate the hodographs in counterclockwise direction and phase is changed on  $45^\circ$  from  $26.9^\circ$  to  $72.4^\circ$  (Fig. 10b).

This conclusion is confirmed by next diagrams (Fig. 11), whereon the amplitude and phase in the points of EC probe maximum amplitudes in dependence versus the defect depth independently of the tube surface the defects were originated are presented. Black marks correspond with the surface defects on the internal tube surface and the white marks are fitted with defects on outer tube surface.

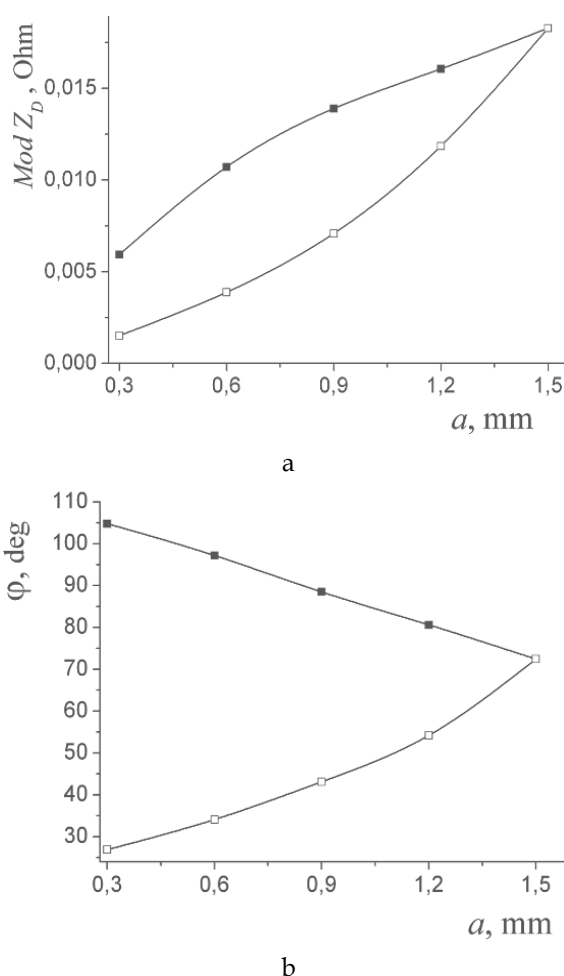


Fig. 11. Influence of defect depth  $a$  on the EC probe signal response amplitude (a) and phase (b) for holes situated on internal (■) and external (□) tube surfaces.

Depth-amplitude diagram on Fig. 11a show, that the same amplitude can be corresponded with two different defects, situated on different tube surfaces. Thereby, the signal amplitude doesn't give the possibility for recognition of defects situated on different tube surfaces. Such recognition can be obtained by phase measurements. The depth-phase diagrams similar to presented on Fig. 11b are widely used in practice for defect depth estimations. It is important to notice, that such diagrams must to be obtained for specified EC probe, selected operational frequency and tube material. Very often this requirement is violated in practice, because of the difficulties in producing the reference standard set with different size defects needed for precise eddy current inspection equipment calibration.

### **3.2 The development of bobbin probe with enhanced breakage resistance and tube passing ability**

Unfortunately, low passing ability is the characteristic feature of tubes mounted in overwhelming majority of WWER type NPP. This circumstance is the root cause of considerable reduction of quantity of tubes, inspected by one bobbin probe, due rapid wear and cable breakage. To improve the bobbin probe breakage resistance and passing ability some new technical judgment were proposed (Mozhuchin et al., 2002; Najda et al., 2002).

Conventional bobbin probes for SG tube inspection consist of eddy current coils and long cables (such long as tube length) for connection with eddy current device. All cables are protected by tubular flexible sheath. Probes are moved along the tube by special push-puller system. During in-service life these cables are repeatedly wound on special drum for probes carrying purposes. For electronic noise suppression cables are executed to be coaxial. The weak point of conventional EC probe is the point of the connection of coil wires to the cable. Therefore the coil wires lost contact with cable during the windings on the drum. To prevent the probe damage the internal wires and cables must be longer than the tubular sheath. In conventional probes this difference is insufficient even when wires are produced to have wave like form (see for example Amedro et al., 1983). So, these probes have low operational reliability and resource, because the inspection technology provides multiple "winding - unwinding" cycles, when the inspected tubes are changed. The average lifetime of these probes is limited by 300 - 400 tube inspections. Despite the high price all damaged probes are throwing away because are not repairable due radionuclide contamination.

One of proposed probe (Najda et al., 2002) has inspection head 1 with EC coils and electrical connector 2, which are mounted on opposite sides of flexible tubular sheath 3 (Fig. 12). Tubular sheath can be executed in cylindrical helix form 4. Probe coils 5 are electrically connected to connector 2 by the cables 5 located inside the tubular sheath 3. The cables 5 are executed in the form of at least one pair of essentially straight sections, which alternate with sections, where cables have the form of cylindrical spiral springs with the adjacent turns in initial part. Cables 6 and 7 may be closely wound around the common axis 8 and 9 forming a common helix diameter (Fig. 12b). In alternative embodiment cables 10 and 11 can be wound in spirals around parallel axes 12 and 13 (Fig. 12c). The spiral sections of one cable are shifted relatively the spiral sections of second cable to some distance 14 and situated near its rectilinear sections. The alternative embodiment of proposed invention with most compact version of cable laying is presented in Fig. 12d. Here straight sections of each cable are situated inside a cylindrical spiral springs areas of second cable.

In the initial state the tubular sheath 3 of EC probe is straightened and the spiral spring turns 6 and 7 are compressed and fitted each other. When tubular sheath is wound on the

drum the possible cable length deficit is compensated by the spiral springs stretching. So during the multiple “winding - unwinding” cycles the cables are not displaced relative to the tubular sheath and not damaged.

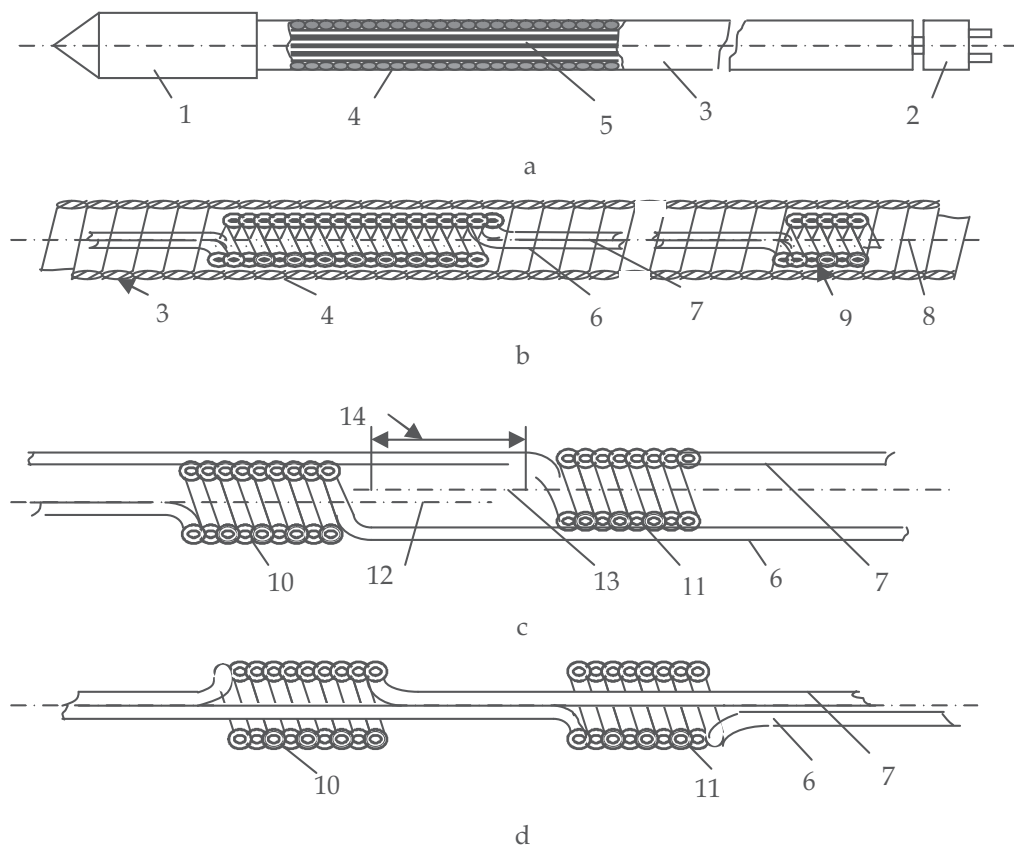


Fig. 12. Eddy current probe with improved resistance: a – general arrangement; b, c and d – alternative embodiments with different cable laying.

The next step in EC probe improvements was the increase the possibility to pass through bended zones of SG heat exchanger tubes. To solve this problem the new construction (Fig. 13) of EC probe was proposed (Mozhuchin et al., 2002). Improved EC probe is supplied by spiral 4 mounted to inspection head 1. Close to inspection head section 6 of spiral 4 is executed with clearance between spiral turns. The length of this section  $L$  is equal to  $2-15 d$ , where  $d$  – spiral diameter. The rest section of spiral 4 can be executed with contacting turns. Section 6 can be executed with changing cross-section area of spiral turns. In this case the spiral thickness monotonously increases from the head 1 toward the connector 2. In Fig. 13a and Fig. 13b alternative embodiments of presented improvement are presented. Spiral profile in section 6 can be produce to be constant in outer (Fig. 13a) or internal (Fig. 13b) spiral diameters. The embodiment on Fig. 13b is more technological. Thus, in all cases the part at the front end of the spiral section 6 is made with weakened bending resistance for better tube passing ability.

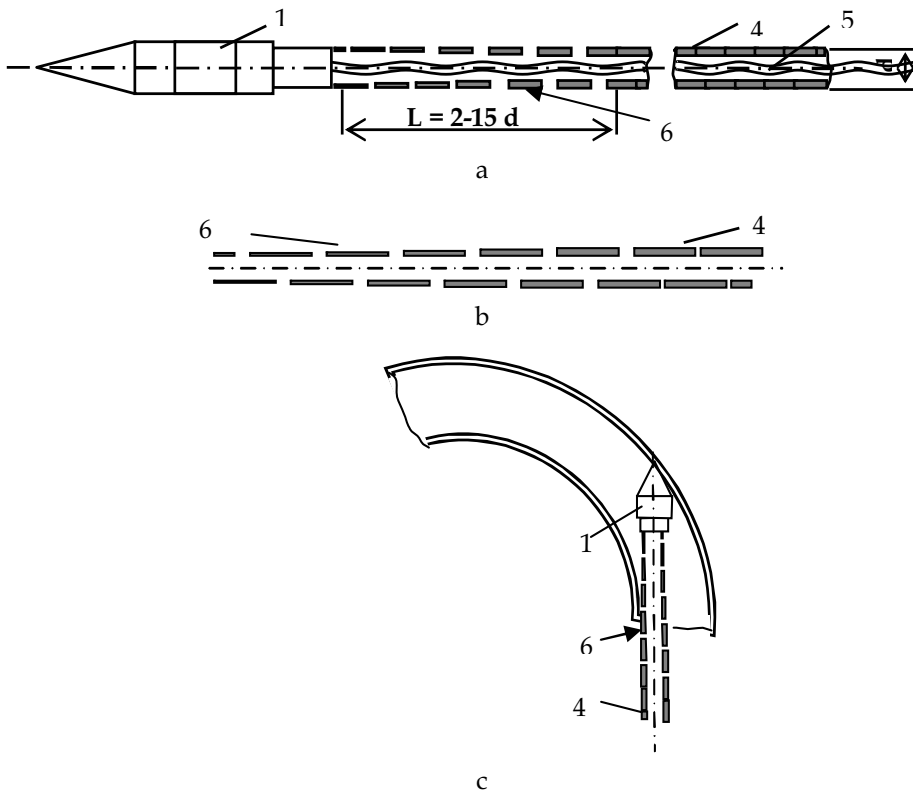


Fig. 13. Different embodiments of eddy current probe with improved passing ability (a, b) and eddy current probe in bended part of tube (c).



Fig. 14. EC probes for heat exchanger tube inspection.

The increased resistance and passing ability of improved EC probes (Fig. 14) was confirmed by in-service inspection of PGV type SG on Zaporizhia NPP. The quantity of tubes tested by one improved probe was increased more than 5 times in relation to conventional EC probes.



#### 4. The development of automated system for eddy current inspection of collector wall cracking.

The defect detection in NPP collector wall must be executed in conditions of high level of radiation and pollution. So, full automation of inspection operations it is assumed to be applied. In addition, for EC probe protection the protective cover, which reduce the EC probe sensitivity also it is needed. In addition the defect detection in collector wall can be executed only through the heat exchanger tube wall.

The block diagram of developed automated system for inspection of collectors is shown in Fig. 15. The system includes a manipulator, unit for servo drive controlling, TV positioning unit, remote operator working place, industrial computer and eddy current flaw detector device with rotary scanner for superimposed EC probe rotation (Najda et al., 2008).

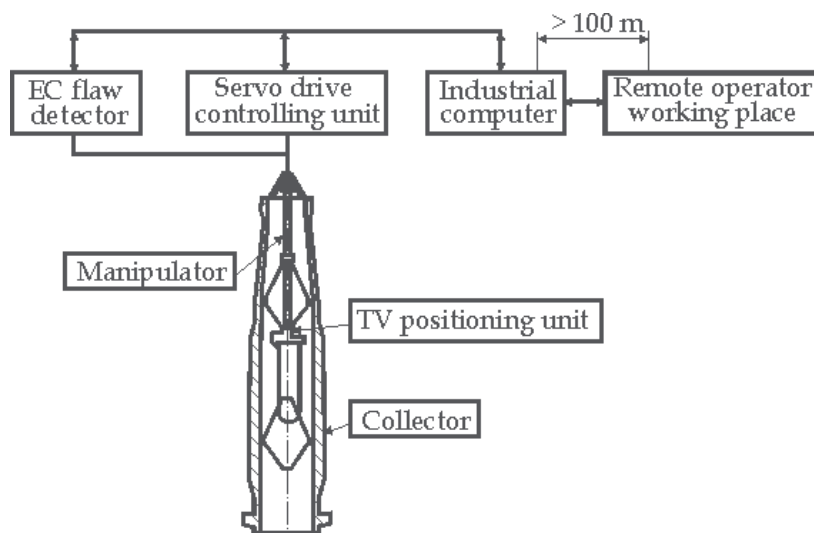


Fig. 15. The generalized scheme of the automated EC system for collector wall inspection.

As the inspection part of the automated EC system it is supposed to use the EC flaw detector Elotest N320 developed by Rohmann GmbH (Germany), which provides the necessary facilities needed for automated system creation, in particular:

- Remote control via Ethernet channel, which allows flaw device managing from remote computer;
- The ability to record and store device settings and obtained inspection signal responses needed for database creation;
- Representation of signal responses in X-Y, X-t, Y-t or C-Scan form, which provides advanced visual and programmed signal responses analysis;
- The possibility to realize the two-frequency signal processing and filtering by software mode application for better suppression of disturbing factors influence;
- Open data transfer protocol for creation of the software based on specific parameters of the inspected object.

The manipulator (Fig. 16a) is intended for EC probe displacement in the vertical, azimuthal and radial directions (Fig. 16b) for introduction to the collector inlet holes (Fig. 1a). The manipulator can be operated in automatic mode on defined inspection map and in manual

mode. A specific feature of the developed manipulator is a mechanism for coaxial connection of inspection head to inlet holes, which in the initial state have the deviation from concentricity and parallelism.

To scan the inner surface of tubes in the collector wall zone special rotary scanner was designed (Fig. 16c), which provides the tube internal surface scanning by helical trajectory with speed to 3000 rpm needed for dynamic mode of signal processing. In contrast to some other inspection systems, the developed scanner was supplied with the protective stainless steel cover to prevent the EC probe radioactive contamination.

The unit for servo drives controlling was intended to receive the commands from remote operator working place, to control the signal formation for manipulator and to transfer the information about the current servo drive parameters to operator working place.

Positioning unit is used to define the presence of plug in the inlet hole, as well as for centring of the inspection head with EC probe in inlet hole of inspected tube. The positioning unit operation is based on the processing of television images and the application of the pattern recognition algorithms. As a result of television information processing unit make a decision about the presence of plug in the heat exchanger tube, form a signal about possible displacement in the vertical and horizontal planes for servo drive controlling.

The automated operator working place is intended to manage the system, to organize the interaction of the operator interface with the system, to display and store the inspection results and to analyse the collector wall technical condition.



a



b



c

Fig. 16. The manipulator (a), mechanism for inspection head displacement (b) and rotary scanner with EC inspection head (c).

For better noise suppression the two-frequency mode for EC probe excitation (12 and 60 kHz) in combination with signal filtering in dynamic mode were applied. The defect signal response after amplification and processing can be presented in the complex plane in the form of the hodograph with characteristic amplitude (pick-to-pick distance) and phase (hodograph orientation). By the signal response amplitude and phase analysis the detected defects can be classified and defect parameters, in particular its depth, can be estimated. The sensitivity threshold for collector inspection is adjusted to be equivalent to artificial defect with depth 1.0 mm and width (opening) 0.3 mm. To simulate the defects with different depth two types of reference standards (Fig. 17) with artificial like crack defects were proposed (Najda et al., 2008; Uchanin et al., 2009).

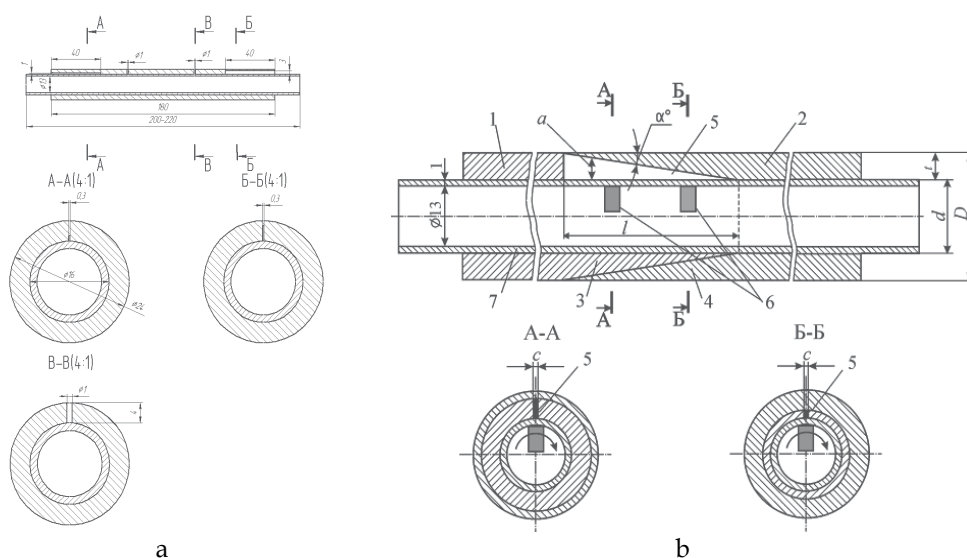


Fig. 17. Reference standard for 1 mm and 3 mm flaw depths simulation (a) and combined reference standard for different depth defects simulation in dynamical mode.

Reference standard on Fig. 17a is easier in producing, but can simulate cracks with 1 mm and 3 mm depth only. Combined reference standard (Fig. 17b) can be applied only in dynamic mode, when EC probe signal response from conical junction of two parts 1, 2 with length  $l$  during EC probe 6 rotation is suppressed. Crack signal response is simulated by longitudinal cut 5 in conical part 1. The defect depth can be chosen by change of EC probe location.

To detect the cracks in collector wall throw the tube wall and the protective cover special superimposed small size multidifferential type EC probes (specified as Leotest MDF) were developed in Leotest-Medium Center (Lviv, Ukraine). This type EC probes were investigated in many known European scientific organizations, such as Otto-von-Guericke University (Magdeburg), Fraunhofer Institute for non-destructive testing (Saarbrücken), Kontroll Technik GmbH (Schwarmstedt) at alias (Uchanin et al., 2002; Uchanin, 2006; Uchanin et al., 2006; Mook et al., 2007; Uchanin, 2009). The main task for developed EC probe is to detect 1.0 mm depth defect throw 1.5 mm tube wall thickness plus 1 mm protective cover thickness. The signal response for 1 mm depth defect in complex plane on EC device screen is presented on Fig. 18.

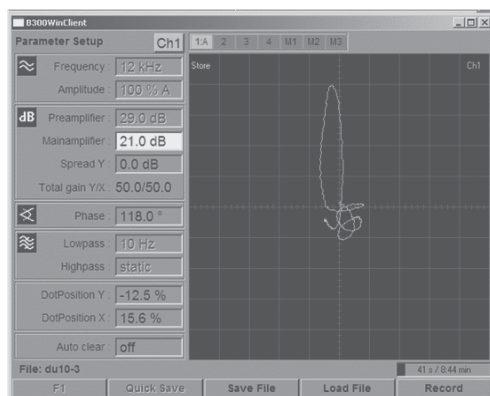


Fig. 18. Complex plane signal response obtained for 1 mm depth defect in reference standard (Fig. 17a).

Presented signal responses (Fig. 18) confirm good sensitivity and low noise level of developed EC system, when defect detection is performed through the heat exchanger tube wall.

## 5. Conclusion

In this chapter the results of bobbin type EC probe signal response investigation are presented. The specific features of signal response distribution for cracks of different orientation, length and depth are analyzed. The inspection procedure for defect parameters estimation is discussed. The results obtained were used for bobbin type EC probe optimization and can be applied for inspection data interpretation.

The results of new EC bobbin probes development also are presented. For better tube passing ability special structural arrangements of EC probe constructions were proposed. It is especially important for examination of WWER type SG tubes because of inconvenient geometry and/or clogging.

The automatic EC system for detection of cracks in collector wall with rotary low frequency superimposed EC probe is presented. The developed automatic system consists of rotary scanner with EC head, EC flaw detector device, manipulator supplied with TV positioning unit for controlling the inspection head introduction to inlet holes, industrial computer for tested data collection and remote operator working place. The performance of developed low frequency superimposed EC probe confirms good sensitivity of developed EC system.

## 6. References

- Alferink, R. & Meier, J. (1996). Detection and quantification of axial crack in heat exchanger tubes. *Insight*, Vol. 38, No 10, pp. 711-714. ISSN 1354-2575.
- Amedro, A., Audemard, B. & De Mull, R. (1983). Eddy current inspection probe for non-destructive inspection of tubes with a probe body having an outer coiled spring sheath and an inner plastic material sheath. US patent № 4413231, G01N27/72.
- Balitskii, A., Makhnenko, O., Balitskii, O., Grabovskii, V., Zaverbnyi, D. & Timofeev, B. (2005). *Strength of Materials and Durability of Structural Elements of Nuclear Power*

- Plant: Handbook* (in Ukrainian), Vol. 8, Akademperiodika, ISBN: 966-360-035-7, Kyiv, Ukraine.
- Bisiaux, B., Pichenot, G., Prémel, D., Reboud, C. & Lesselier, D. (2006). Simulation of 3D Eddy Current testing of Tubes with external Probes: Modeling Approach and Experimental Validations, *Proceedings of 9-th Europ. Conf. on NDT*. www.ndt.net. Paper We.2.3.1. Berlin, Germany.
- Cecco, V., Sharp, F. & Marini, L. (1996). Differential transmit-receive eddy current probe incorporating bracelets of multi-coil units. US patent № 5506503, G01N27/90.
- Clark, W. (1993). Multiple-element eddy current probes for enhanced inspection. *Materials Evaluation*, № 6, pp. 794-802, ISSN: 0025-3327.
- Dunbar, W.S. (1985). The Volume Integral Method of Eddy Current Modeling. *J. Nondestructive Evaluation*, Vol. 5, № 1, pp. 9-14, ISSN: 0195-9298.
- Herka, M.; Kubis, S., Ilencik, K. & Krajcovic, R. (1999). Degradation monitoring of steam generator tubes of VVER 440 NPP using eddy current technique, *Proceedings of Joint EC-IDEA Meeting "NDT Methods for Monitoring Degradation"*. pp. 215-220, Petten, Netherlands.
- Hofler, J. (1999). Additional Steam Generator Eddy Current Inspection Techniques, *Proceedings of Joint EC-IDEA Meeting "NDT Methods for Monitoring Degradation"*. pp. 31-37, Petten, Netherlands.
- IAEA-TECDOC-981. (1997). Assessment and management of ageing of major nuclear power plant components important to safety: Steam generators. International atomic energy agency. Vienna, Austria, 173 p.
- IAEA-EBP-WWER-11. (1998). Methodology for qualification of in-service inspection systems for WWER nuclear power plants. International atomic energy agency. Vienna, Austria, 21 p.
- IAEA-TECDOC-1400. (2004). Improvement of in-service inspection in nuclear power plants. International atomic energy agency. Vienna, Austria, 38 p.
- Ida, N. (1986). Computer modeling of eddy current field, In: *Nondestructive testing handbook*, 2nd ed. by R. McMaster & P.McIntire, Vol. 4, pp. 561-590, American Society for Nondestructive Testing, ISBN: 0-931403-01-4, USA.
- Krajcovic, R. & Plasek, J. (2006). Eddy Current Inspection of WWER Steam Generator Tubes - Sensitivity of Bobbin Probe Technique. *Proceedings of 9-th Europ. Conf. on NDT* (www.ndt.net). - Index Th.3.1.4. Berlin, Germany.
- Laube, U., Grigoriev, M. & Lovchev, V. (2006). In-service Inspection of Russian VVER Nuclear Power Plants, *Proceedings of 9-th Europ. Conf. on NDT*. (www.ndt.net). Paper P166. Berlin, Germany.
- Melechov, R. & Pochmurskij, V. (2003). *Constructional materials of power equipment* (in Ukrainian), Naukova dumka, ISBN: 966-00-0150-9, Kyiv, Ukraine
- Mook, G., Hesse, J. & Uchanin, V. (2007). Deep Penetrating Eddy Currents and Probes. *Materials Testing*, Vol. 49, №5. pp. 258-264.
- Mozhuchin, A., Kovbasenko, O., Pyshnyj, V., Lobanov, O. & Najda, V. (2002). The probe for inspection of long curved tubes (in Ukrainian). Ukrainian patent № 50074, G01N27/90.
- Mytrofanov, A.; Neklyudov, I. & Ozhygov, L. (2008). In-service defects in the heat exchanger tubes of steam generators at nuclear power plants. *Material Science*, Vol. 44, No. 4, pp. 589-593, ISSN: 1068-820X.

- Najda, V., Pyshnyj, V., Moszhuchin, A., Kovbasenko, O., Chizhenko, V. & Lobanov, O. (2002). The probe for non-destructive inspection of tube metal state and method for of its realization (in Ukrainian). Ukrainian patent № 50073, G01N27/90.
- Najda, V., Uchanin, V., Moszhuchin, A., Gogulia, O. & Gulko, V. (2008). The development of system for automated eddy current inspection of nuclear power plants collectors (in Russian). *Technical diagnostic and nondestructive testing*, No. 3, pp. 21–24, ISSN: 0235-3474.
- Nam Jo. & Hyang-Beom Lee. (2009). A novel feature extraction for eddy current testing of steam generator tubes. *NDT&E International*, Vol. 42, pp. 658–663, ISSN: 0963-8695.
- Neklyudov, I., Azhazha, V., Ozhygov, L., Mytrofanov, A.; Krajniuk, Je. & Lisna, V. (2006). Atlas of the operational defects in steam generator heat exchanger tubes of power units of NPP with VVER type reactors (in Ukrainian), In: *The problems of life-time and safety of constructions, buildings and machines*, Ed. B. Paton, pp. 157–160, Paton electric welding institute, ISBN 966-8872-04-5, Kyiv.
- Pichenot, G., Buvat, F., Maillot, V. & Voillaume, H. (2004). Eddy Current Modelling for Nondestructive Testing. *Proceedings of 16 World Conf. for NDT* (www.ndt.net). Montreal, Canada.
- Sabbagh, H., Murphy, R., Sabbagh, E. & Alrin, J. (2008). Application of model based inversion to eddy current NDT of heat exchanger tubing. *Materials Evaluation*, № 7, pp. 764–774, ISSN: 0025-3327.
- Song, S., Kim, Y., Kim, E. & Choi, Y. (2003). Model-based interpretation of experimental eddy current signals obtained from steam generator tubes by bobin probe. *Insight*, Vol. 45, No 5, pp. 337–343, ISSN 1354-2575.
- Uchanin, V., Mook, G. & Stepinski, T. (2002). The investigation of deep penetrating high resolution EC probes for subsurface flaw detection and sizing. *Proceedings of the 8 European Conf. on NDT* (www.ndt.net). Barselona.
- Uchanin, V. (2006). Eddy current multidifferential probes and their application (in Russian). *Technical diagnostic and nondestructive testing*, No. 3, pp. 34–41, ISSN: 0235-3474.
- Uchanin, V., Lutcenko, G. & Nikonenko, A. (2006). Automated Eddy Current System for Flaw Detection and Sizing during In-service Stainless Steel Tube Inspection, *Proceedings of 9 European Conf. on NDT*. (www.ndt.net). Berlin.
- Uchanin, V. (2009). Analysis of the signals of the internal coaxial eddy current converter for flaw of pipes of steam generators. *Material Science*, Vol. 45, No. 3, pp. 448–452, ISSN: 1068-820X.
- Uchanin, V., Najda, V., Kirichenko, I. & Gogulia, J. (2009). The reference standard for adjustment, calibration and certification of eddy current flaw detectors (in Ukrainian). Ukrainian patent № 2008 10692, G01N27/90.
- Werner, R., Bernus, L. & Jacob, H. (1987). Development of multi-channel eddy current examination system for automated inspection of steam generator tubing, *Proceedings of Europ. Conf. on NDT*. Vol. 4, pp. 2572–2580. London.
- Wong, B., & Tan, K. (1995). Software developed to analyse the signals from the eddy current inspection of heat exchanger tubes. *Insight*, Vol. 37, No 2, pp. 87–92, ISSN:1354-2575.

# Detection of Magnetic Phase in the Steam Generator Tubes of NPP

Duck-Gun Park, Kwon-Sang Ryu and Derac Son  
*KAERI, KRISS, Hannam Univiersity  
Korea*

## 1. Introduction

Steam generator tube (SGT) in nuclear power plant is a boundary between primary side and secondary side, whose integrity is one of the most critical factors to nuclear safety (Roberts, 1981). The SGT is made of nickel based Inconel alloy, which is composed of 75% Ni, 16.5%Cr and 8.15%Fe. Inconel alloy has very little magnetic response due to its austenitic nickel base, and the domain walls move relatively unimpeded through the material. The SGT are continuously exposed to harsh environmental conditions including high temperatures, pressures, fluid flow rates and material interactions resulting in various types of degradation mechanism such as corrosion, pitting, denting and inter granular attack. Multifrequency eddy current inspection techniques are currently among the most widespread techniques for the rapid inspection of SGT in nuclear power industry. Although the eddy current test (ECT) technique is adopted widespread in the nuclear industry (Bakhtiari, 1999), it has the limitation to size the flaw accurately because the eddy current measure the impedance signified by the conductivity change associated with the volumetric change of flaws, where the permeability of flaw is considered unity. The EC test currently applied in the nonferrous materials having relative permeability 1 such as Inconel alloy because the magnetic permeability of magnetic materials severely limits the depth of penetration of induced eddy currents. Furthermore, the small magnetic phase having permeability variation inherent in SGT can cause spurious EC test results (Park et al., 2010). It is well known that some part of SGT change as a magnetic phase known as permeability variation clusters (PVC) under the conditions of high pressure and temperature which is the operating environments of nuclear power plant. The relative permeability of the magnetic phase is greater than 1, and with a number of ferromagnetic metals, a value of several thousand can be reached. Internal stresses caused by drawing, straightening, or similar work on the material, can give rise to severe fluctuations in the permeability (Takahashi, 2004). These fluctuations would always cause interference with the test signals. In order to eliminate this interference effect during testing, the ferromagnetic test piece is magnetized by a suitable device such as magnetized ECT probe. Recently, to eliminate ECT signal fluctuation, the magnetized probe with the built-in permanent magnet is being used in the SG tube inspection, because a strong magnetic field of this probe reduces the variation of magnetic permeability, which gains S/N ratio. If we can separate magnetic phase (MP) selectively from the flaws using magnetic sensor, the reliability of EC in SGT inspection will



be greatly enhanced. This book begins with the introduction of steam generator, the creation mechanism of MP, the simulation, design and application of new probe which detect the MP. In section 2 we present a brief recapitulation of the steam generator and the material properties of Inconel alloy, and ECT data containing the PVC obtained from nuclear power plant was analyzed, and also the hysteresis loop of PVC which is extracted from retired Kori-1 SG were measured. In section 3 we introduced the principle of new probe which separate the defects and MP, and the design of new probe in order to detect the MP and defects of SGT. In section 4 we performed electromagnetic analysis of MP using finite element simulation, and the results are compared with the experimental one which is obtained from our new probe.

## 2. Steam generator in pressurized water reactor

### 2.1 Overview of steam generator

Steam generator (SG) is the heat exchanger used to convert water into steam by using heat produced in a nuclear reactor core. The SGs also have an important safety role because they constitute one of the primary barriers between the radioactive and non-radioactive sides of the plant as the primary coolant becomes radioactive from its exposure to the core (Roberts, 1981). The function of the steam generator is to transfer the heat from the reactor cooling system to the secondary side of the tubes which contain feedwater. In commercial power plants SGs can measure up to 21 m in height and weigh as much as 800 tons. The layout of pressurized water reactor (PWR) components, and the structure of SG is shown in Fig. 1. Generally, 2~4 sets of SG were installed in the each nuclear power plant. Each SG can contain anywhere from 3,000 to 16,000 tubes, each about 20 mm in diameter. The coolant (treated water), which is maintained at high pressure to prevent boiling, is pumped through the nuclear reactor core. Heat transfer takes place between the reactor core and the

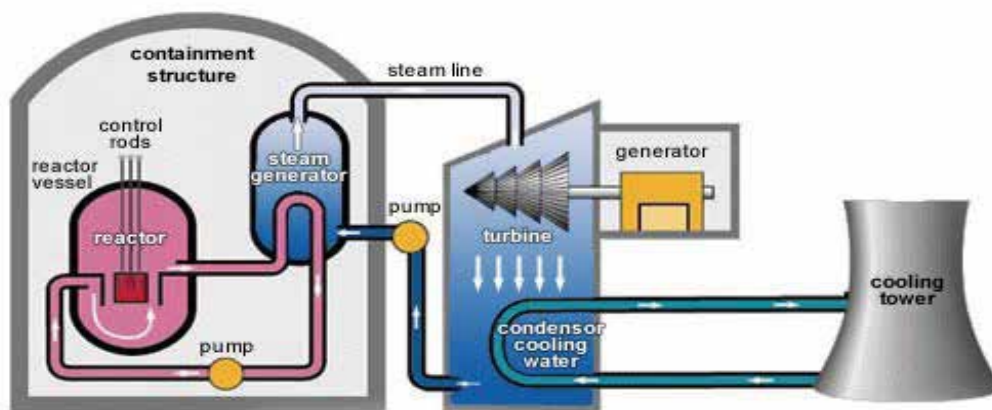


Fig. 1. The layout of pressurized water reactor (PWR) components, and structure of SG

circulating water and the coolant is then pumped through the primary tube side of the SG by coolant pumps before returning to the reactor core. This is referred to as the primary loop. As the feedwater passes the tube, it picks up heat and eventually gets converted to steam. That water flowing through the SG boils water on the shell side to produce steam in



the secondary loop that is delivered to the turbines to make electricity. The steam is subsequently condensed via cooled water from the tertiary loop and returned to the SG to be heated once again. The tertiary cooling water may be recirculated to cooling towers where it sheds waste heat before returning to condense more steam. Once through tertiary cooling may otherwise be provided by a river, lake, or ocean. This primary, secondary, tertiary cooling scheme is the most common way to extract usable energy from a controlled nuclear reaction. For this reason, the integrity of the tubing is essential in minimizing the leakage of water between the two sides of the plant. There is the potential that, if a tube bursts while a plant is operating, contaminated steam could escape directly to the secondary cooling loop. Radioactive releases can occur early in the event until the SG with the broken tube is isolated. Release paths include - air ejector exhaust and turbine driven emergency feed water pump exhaust normally; releases from the SG power operated relief valves may occur.

## 2.2 The degradation of SG and material specification

Two of the most important factors affecting a tube's vulnerability to degradation are the tube material and the tube's heat treatment. The two types of tube material being used in the PWR are Alloy 600 and Alloy 690 (Harrod et al., 2001). The chemical compositions of these materials are given in table 1. The two types of heat treatment applied to these materials for improving their mechanical and corrosion properties are mill annealing and thermal treatment. The SG tubes are either mill-annealed Alloy 600, thermally treated Alloy 600, or thermally treated Alloy 690. During the early-to-mid 1970s all plants, except one, had mill-annealed Alloy 600 steam generator tubes. The extensive tube degradation at PWRs with mill-annealed Alloy 600 SG tubes has resulted in tube leaks, tube ruptures, and midcycle SG tube inspections. This degradation also led to the replacement of mill-annealed Alloy 600 SGs at a number of plants and contributed to the permanent shutdown of other plants. There are known SGT damage mechanisms such as outer diameter stress corrosion cracking (ODSCC), pitting, volumetric changes, primary water stress corrosion cracking (PWSCC), and inter granular attack (IAG) (Okimura et al., 2006). The structure of SG and degradation mechanism is shown in Fig. 2. The dominant cause of tube degradation of Alloy 600 SGT was tube thinning. The cause of thinning is known as corrosion; therefore water chemistry flowing around them is treated as importantly. All plants have their water chemistry control programs virtually to eliminate the problem of tube thinning. After tube thinning, tube denting became a primary concern in the mid to late-1970s. Denting results from the corrosion of the carbon steel support plates and the buildup of corrosion product in the crevices between tubes and the tube support plates. Stress corrosion cracking (SCC) has primarily occurred at plants with mill-annealed Alloy 600 SGTs.

In the late 1970s, Alloy 600 tubes were subjected to a high-temperature treatment to improve the tube's resistance to corrosion. This thermal treatment process was first used on tubes installed in replacement SGs put into service in the early 1980s. Although no significant degradation problems have been observed in plants with thermally treated Alloy 600 SGTs, plants which replaced their SGs since 1989 have primarily used tubes fabricated from thermally treated Alloy 690, which is believed to be even more corrosion resistant than thermally treated Alloy 600. Traditional tube repair criteria are based on a minimum wall thickness requirement (USNRC, 2006). Typically, the tube wall thickness may be degraded by up to 40% of the initial wall thickness before the tube must be repaired. This allows an adequate margin against leakage and bursting. This criteria can be overly conservative for localized flaws such as short stress corrosion cracks. As a result, use of the 40% through-

wall repair criteria may result in tubes being unnecessarily removed from service even though they would continue to satisfy the existing regulatory guidance for adequate structural and leakage integrity. Most of the newer steam generators, including all of the replacement steam generators, have features which make the tubes less susceptible to corrosion-related damage. These include using stainless steel tube support plates to minimize the likelihood of denting and new fabrication techniques to minimize mechanical stress on tubes.

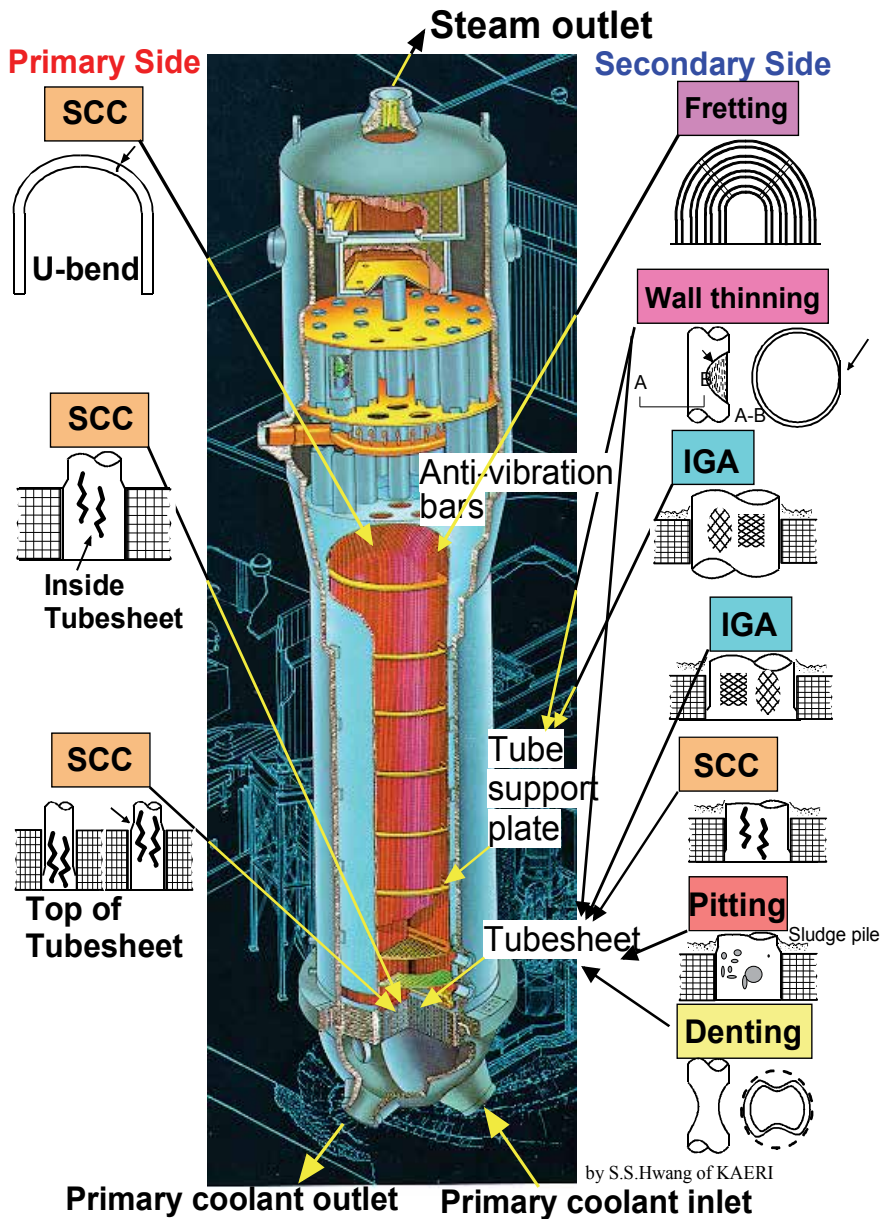


Fig. 2. The structure of SG and degradation mechanism

Material	Composition, wt%							
	Fe	Ni	Cr	C	Mn	Si	Al	Ti
I-600	8	72	15	.03	.2	.1	.2	.25
I-690	10	58	30	.02	.2	.1	.2	.25

Table 1. Chemical compositions (wt%) of Inconel 600 and Inconel 690

### 2.3 The inspection of SG

Since traditional inspection techniques only partially identified and precisely measured the size of cracks. The procedure performing comprehensive tube examinations must use appropriate inspection techniques and equipment capable of reliably detecting degradation, which is given in the code and standard (EPRI, 2010). The industry has since developed better methods of detecting cracks before tube integrity is potentially impaired. However, there continue to be challenges including precisely measuring crack size. Thus during scheduled maintenance outages or shutdowns, some or all of the steam generator tubes are inspected by ECT. Since the early days of commercial nuclear power, plant staffs at all plants have monitored the integrity of the SGTs using ECT during the normally scheduled refueling outages. If there is a thinning above a preset criterion or indications of abnormalities in the tubes, the tubes would be plugged or sleeved. Plugs prevent water from flowing through the tube. Sleeves may be used in those cases where defects or thinning might be present close to the tube sheet. Electric power research institute (EPRI) in US has supported industry efforts to improve steam generator reliability. A number of utilities have replaced their original steam generators. It is expected that during the 40 year initial operating license period, a plant may have to replace steam generators once. Excellent chemistry control on the secondary side of the steam generator is required. The ECT is the conventional method for inservice inspection (ISI) of SG tubing that is exposed to corrosive, high-pressure, and temperature environments. This nondestructive evaluation (NDE) method has advanced significantly over the years in all areas associated with probe design, instrumentation, and computer-aided data analysis (Sakamoto, 1993).

### 2.4 The problem of ECT

Although the EC technique is adopted widespread in the nuclear industry, it has the limitation like size the flaw accurately because the EC signal behavior depends on the total volume of flaw. Furthermore, PVC such as the build-up of magnetite ( $\text{Fe}_3\text{O}_4$ ) and MP on the secondary side of the SG tubing has no direct effect on the tube integrity but it causes spurious EC test results (Kim et al., 2004). The relative permeability of the PVC is greater than 1, and with a number of ferromagnetic metals, a value of several thousand can be reached. Internal stresses caused by drawing, straightening or similar works on the material, creates the MP in the SG tube, which can give rise to several fluctuations in the permeability (Takahashi et al., 2004). These fluctuations would always cause interference with the test signals. Recently, to eliminate EC signal fluctuation, the magbias probe which the built-in permanent magnet being installed in the probe is used in the SG tube inspection, because of strong magnetic field of this probe reduces the variation of magnetic permeability, which gains S/N ratio (Song, 2006). However, the magbias ECT probe could not saturate strong PVC having large permeability, and the strong magnetic field of magnetized ECT probe amplifies the EC signal with noise by the interaction of magnetic field of ECT probe and

induced currents of probe coil. In this study, ECT data containing the PVC obtained from nuclear power plant was analyzed, and also the hysteresis loop of PVC which is extracted from retired Kori-1 SG were measured.

#### 2.4.1 ECT signal fluctuation due to PVC (magnetic phase)

Fig. 3 shows inspection results by using the conventional probe and magbias probes. These signals are extracted from ECT data which is recorded as PVC signal by ECT examiner. The tubes were inspected by bobbin and motorized rotating probe coil (MRPC) probe with and without magnetized unit. The Fig.3 (a,b,c) represent the results of conventional bobbin and MRPC probe and Fig.3 (d,e,f) represent that of magbias probe. The MRPC probe consists of

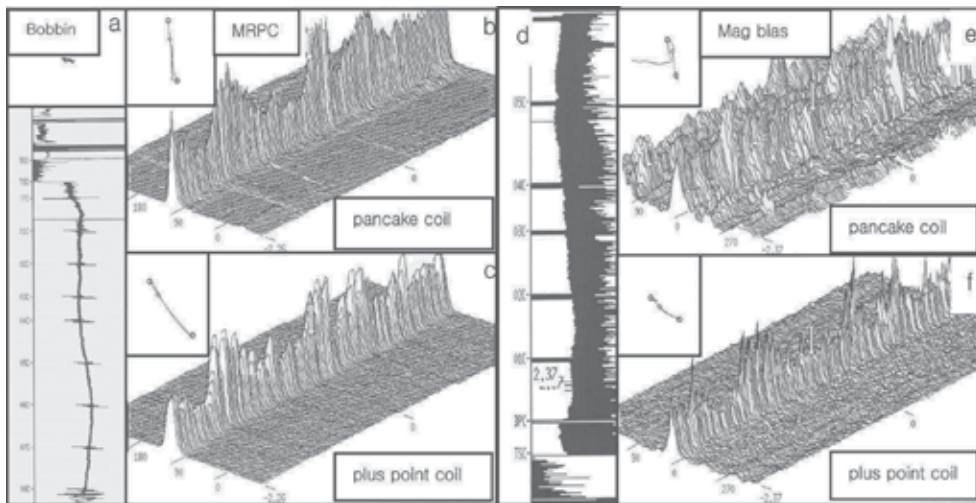


Fig. 3. The signal from (a) bobbin probe, (b) pancake coil (c) Plus point coil, and (d), (e), (f) represent the corresponding signals by magbias probe

three types of coils: two pancake and a +point. The pancake coils consist of two different diameters: 2.0 mm and 2.9 mm. The larger diameter pancake coil is to improve penetration depth of the signal to outside surface. Field experience shows that pancake coil has better sensitivity to volumetric defects whereas +point coil has better sensitivity to crack like defect (USNRC, 1996). Prior inspection of SG tube by bobbin probe indicates continuous distribution of PVC signal up to 1 m (Fig.3 (a, d)). However the PVC signal was not eliminated by magbias probe as shown in the left side of Fig. 3 (d, e, f), and the S/N ratio was reduced which is contrary to our expectation. The magnetized probe was introduced to saturate the ferromagnetic nature of PVC, but the saturation field depends on various factors such as demagnetization coefficient of the PVC. If the magnetic field of magnetized probe could not saturate the PVC, then the distortion of the ECT signals increases by the interaction of the magnetic field of magbias probe and PVC, which results low S/N ratio. The noise level by the +point coil was significantly decreased by the use of magbias probe. The data of the inspected tube shows the indication of long and narrow axial defects in bobbin and MRPC data. However, reevaluated results by magnetized probe shows that the data obtained from pancake coil covered with noise like signal and the data from plus point coil shows sharp ridge of mountain. The peak distribution obtained from pancake coil

considerably decreased and that from plus point coil disappeared by using the magnetized coil. The S/N ratio obtained from the bobbin and pancake of MRPC probe considerably decreased by using the magnbias probe, which suggests the flaw is constituted as a volumetric defect.

#### 2.4.2 Confirmation of MP in SG

The samples for PVC in SG tube were extracted from retired SGT of Kori-1 NPP in Korea. Fig. 4 shows a permanent magnet attached on the fragment of SGT containing the PVC, which means that some parts of SG tube transformed as a MP. In order to investigate the magnetic properties of this PVC, the fragment was machined as rectangular type of 2 x 2 mm samples for measuring hysteresis loop using VSM. To confirm the mechanism of MP by deformation in Inconel alloy 600, the tensile tests were conducted in the room temperature and 600°C. The deformed area of tensile tested specimen was cut as a slice with 2 mm length for VSM measurement, and deformation rate was measured at each slice.

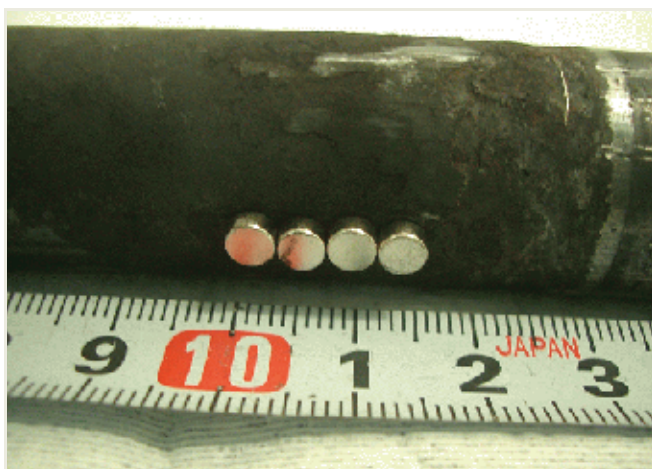


Fig. 4. The picture showing the substance of magnetic phase (PVC) in the SG tube. The sample was extracted from the retired SG tube of Kori-1 NPP

Fig. 5 shows the typical hysteresis loop of a fragment of PVC parts of SGT. The loop show different configuration for part by part of fragment. Although the sample is extracted from the same fragment, the magnetic moment and the coercivity shows different value with respect to sample position in the fragment. The onset of ferromagnetism in the high Cr and low Ni steels was associated with the formation of ferrite during sensitization. However, in higher nickel contents alloy such as Inconel 600, no ferrite formed and sensitization occurred without an increase in magnetic induction (Bain et al., 1993). For still higher Ni content in alloys, Curie temperature decrease rapidly with an increase in Cr content (Chevenard, 1934). Takahashi et al (Takahashi et al., 2004) proposed that the creation of MP in Inconel Alloy 600 is related with the decrease of Curie temperature by Cr depletion, however the permeability increase is less than 1.2 although the Cr content decreased from 17 to 14 wt% by depletion. These values are too small to form the hysteresis loop observed in Fig. 5. In order to identify the mechanism of PVC in the retired Kori-1 SG tube, the changes of hysteresis loop by deformation of Inconel 600 alloy were investigated.

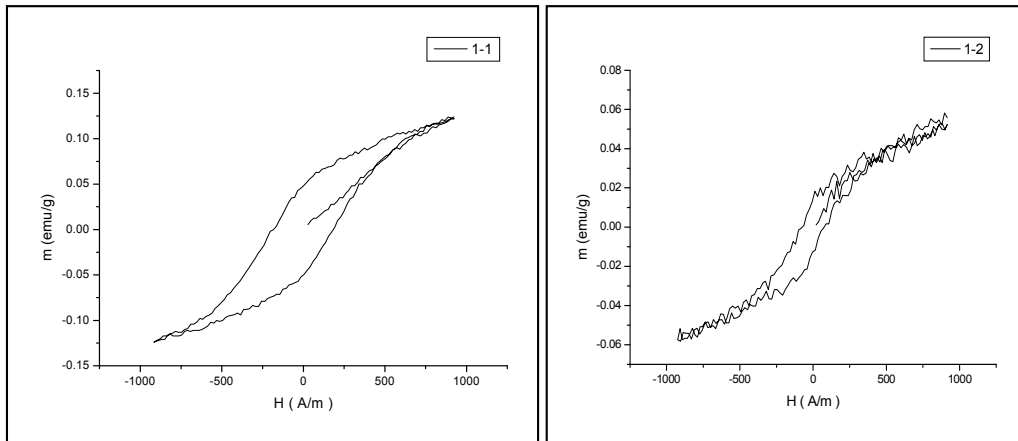


Fig. 5. The hysteresis loop in the fragment of PVC parts of Kori-1 retired SG tube

Fig. 6 show the change of hysteresis loop for the specimen which are deformed at room temperature and 600 °C. The hysteresis was not appeared in the annealed specimen at high temperature and tensile specimen tested at room temperature, but it was appeared in the tensile specimen tested at high temperature. The hysteresis of the specimen in the Fig. 6(b) cannot be explained as a Cr depletion, because it was not appeared in the undeformed specimen at high temperature. Therefore the MP can be created under the high temperature and pressure conditions, which is correspond to the stress corrosion cracking in the SG tube in the NPP (Bruemmer et al., 1981).

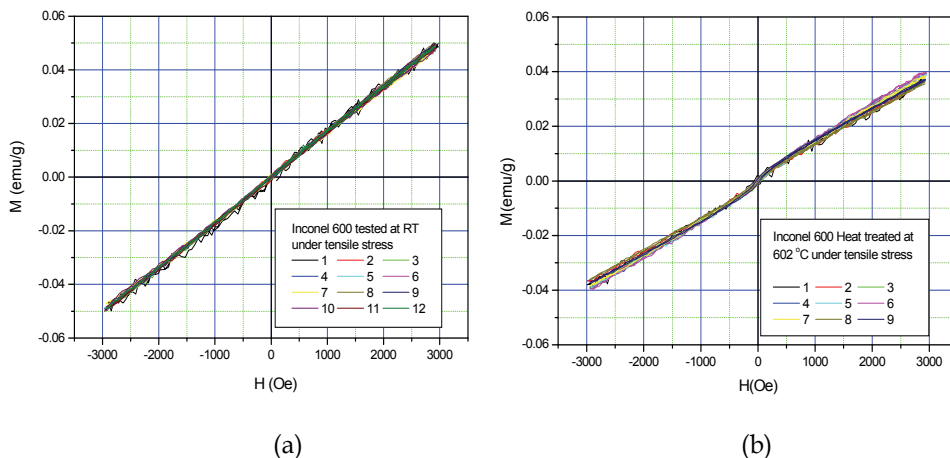


Fig. 6. The hysteresis loop of the tensile tested specimen at room temperature (a), and tensile tested at high temperature (b)

### 3. Design and construction of sensor for MP measurement

Fig. 7 shows physical principle of ECT. When we measure impedance from applied voltage and current, there exist certain phase shift due to the resistance and inductance of coil as



shown in Fig. 7 (a). The phase will be changed by a defect as shown in Fig. 7(b). If we measure this phase, we could measure defects, and this is basic principle of ECT. But if there is defect in ferromagnetic material as shown in Fig. 7(d), we could not distinguish non-magnetic specimen without defect (Fig. 7(a)) and ferromagnetic specimen with defect. This is a critical problem, may be happen, flows generated in PVC of SGT.

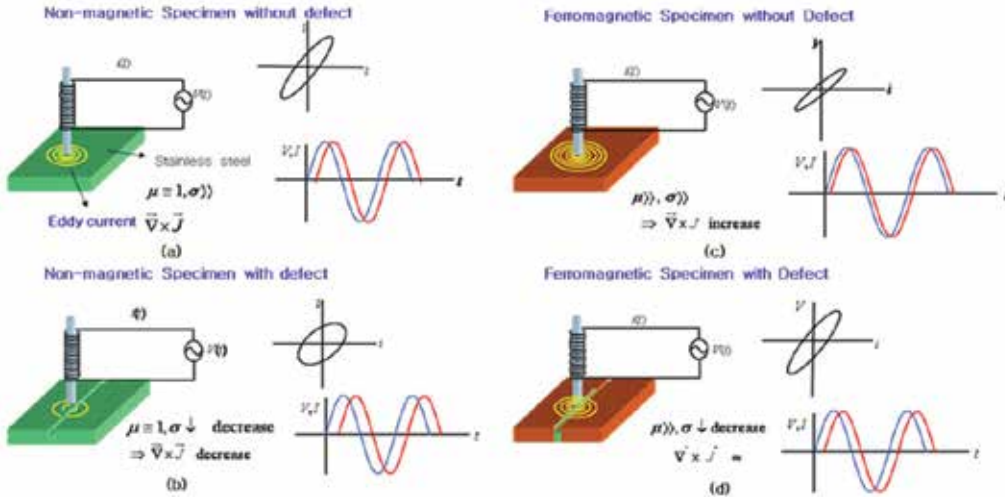


Fig. 7. Phase relationship between voltage and current of EC probe; (a) non-magnetic specimen without defect, (b) non-magnetic specimen with defect, (c) ferromagnetic specimen without defect, and (d) ferromagnetic specimen with defect

### 3.1 Fabrication of sensor

Fig. 8 shows the principle of the new probe which separates the defects and MP. U-shape of yoke was employed to magnetize test specimen and induced voltage from B-coil is proportional to the permeability of the specimen. To reduce lift-off effect, H-coil was used. The H-coil was connected to B-coil in series opposition. Fig. 9(a) shows dimension of the yoke and Fig. 9(b) shows photograph of the sensing yoke wound magnetizing coil, B-coil, and H-coil. As yoke material, 0.15 mm thickness of non-oriented silicon steel was used, and epoxy molded in vacuum. Using the thin gauged laminated core, we can magnetize yoke up to 10 kHz.

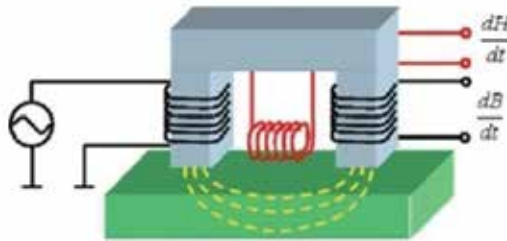


Fig. 8. Structure of the permeability sensor

Schematic diagram of the sensor electronics for signal processing is shown in Fig. 10. To measure amplitude variation and phase shift of induced voltage due to the magnetic reluctance change caused by the presence of magnetic phase and defects in the steam generator tube, two phase lock-in amplifier was employed, because magnetic permeability increase inductance of primary winding and phase angle between primary current and  $B$ -coil voltage will be increase, and vice versa in case of defects. To distinguish directions of

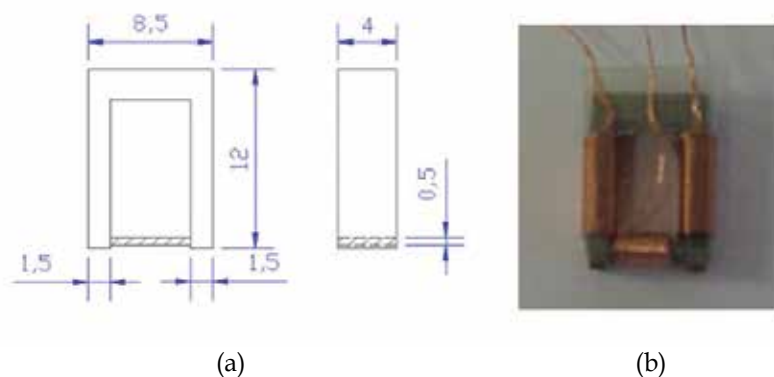


Fig. 9. Dimension (a) and photograph (b) of U-shape sensing yoke

longitudinal and transverse defects, we have made two sensors and put into the probe with perpendicular each other. 4-channel analog signals (2-channel analog signal per sensor  $\times$  2 sensors) are converted to the digital signal using 4-channel input 16 bit ADC (Analog to Digital Converter), and the digital signals are transmitted to the personal computer through the RS232C interface using 8 bit embedded microcontroller. Fig. 11 shows photograph of front side and rear side of completed sensor. Diameter and length of the sensor were 16 mm and 200 mm respectively. Left hand side of front view of the probe, we can see two sensors one for longitudinal defect and the other for transverse defect. Fig. 12 shows developed scanning system and data acquisition software. Scanning of the sensor through the steam generator tube was controlled by stepping motor and motor controller, and software was programmed using LabVIEW (Son et al., 2009).

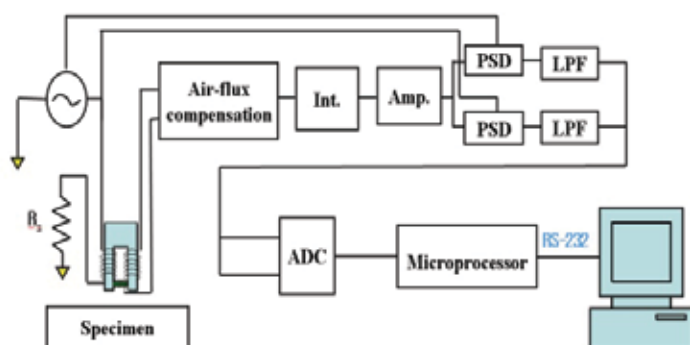


Fig. 10. Schematic diagram of the sensor system





Fig. 11. Photograph of the new probe, front side (above) and rear side (bottom)

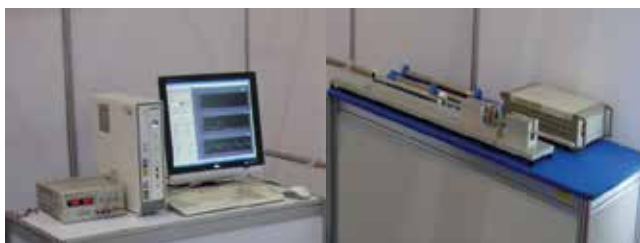


Fig. 12. Photograph of the completed measuring system data acquisition software in PC and probe scanning system

### 3.2 Design of reference specimen

For the testing of the developed sensor for the defect detection of SG tube, we have made a reference specimen (RS) which consists of four kinds of artificial defects; defects located inside of tube, defects located outside of tube, and defects with and without ferromagnetic material. Fig.13 shows schematic diagram of constructed RS using Alloy600 in this work. The defects were machined with electrical discharge machining (EDM) method. Defects number 1, 2, 7, and 8 are located inside of tube and empty defect, and defects number 3, 4, 5, and 6 are located outside of tube are filled with ferromagnetic material in empty defects to demonstrate magnetic phase. Table 2 shows the dimension of the machined defects. Width and length of defects were fixed as 0.2 mm and 5 mm respectively, but depth of the defects was changed from 20% of the tube thickness (0.22 mm) to 80% of the tube thickness with step of 20%.

### 3.3 Experimental results

Fig. 14 shows the experimental results obtained by scanning of developed sensor using the reference specimen of Fig. 13. Here  $L_x$  means output voltage of in phase signal from longitudinal sensor,  $L_y$  output voltage of out of phase signal from longitudinal sensor,  $T_x$  output voltage of in phase signal from transverse sensor,  $T_y$  output voltage of out of phase signal from transverse sensor. From Fig. 14, we can see longitudinal sensor is sensitive to the longitudinal defects and signal amplitude is proportional to the defect size, and signals for MP (number 3,4,5,6,) are bigger than normal defects(number 1,2,7,8). Sign of x- and y-component signals are the same in case of MP but opposite in case of normal defects. For the case of transverse defects and MPs, sensor output voltage signals for the transverse reference specimen are shown in Fig. 15. Transverse sensor is sensitive to the transverse defects and MPs but not sensitive to the longitudinal defects and MPs. Signs of x- and y-component signals for the MPs and normal defects are the same as longitudinal defects. From Fig. 14 and Fig. 15, we can see that developed U-shape yoke sensor for SGT could detect not only MPs but also normal defects, and also distinguish longitudinal and transverse defects which are impossible with conventional bobbin type ECT.

Longitudinal and transverse defects				
Def.#	W	L	D	Remarks
1	0.2	5.00	0.213 (20 %)	Internal defects
2	0.2	5.00	0.427 (40 %)	
3	0.2	5.00	0.213 (20 %)	
4	0.2	5.00	0.427 (40 %)	External defects PVC(1018)
5	0.2	5.00	0.639 (60 %)	
6	0.2	5.00	0.852 (80 %)	
7	0.2	5.00	0.639 (60 %)	Internal defects
8	0.2	5.00	0.852 (80 %)	

Table 2. Dimension of defects in designed reference specimen

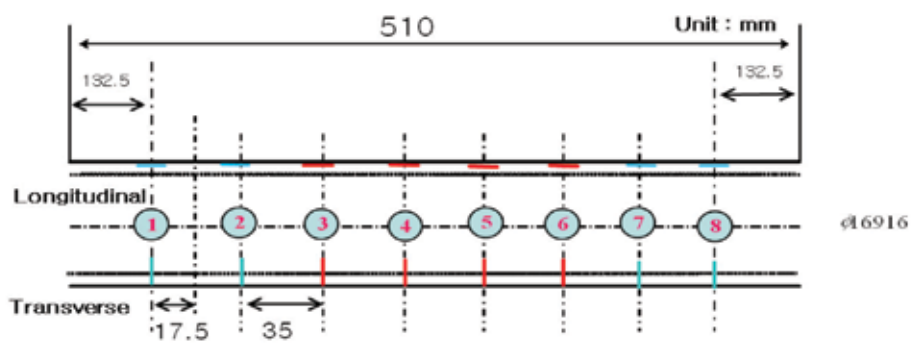


Fig. 13. Schematic diagram of reference specimen for the verification of developed sensor

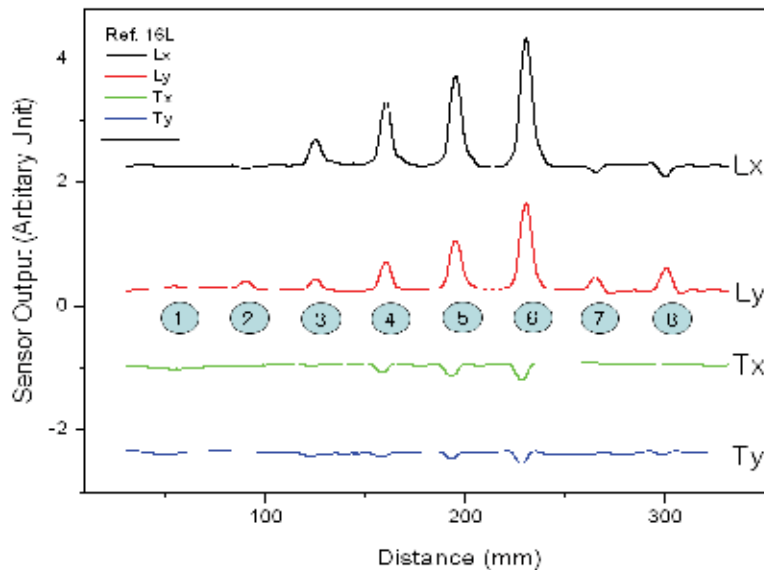


Fig. 14. Sensor output voltage signals from the longitudinal and transverse sensor for the longitudinal reference specimen

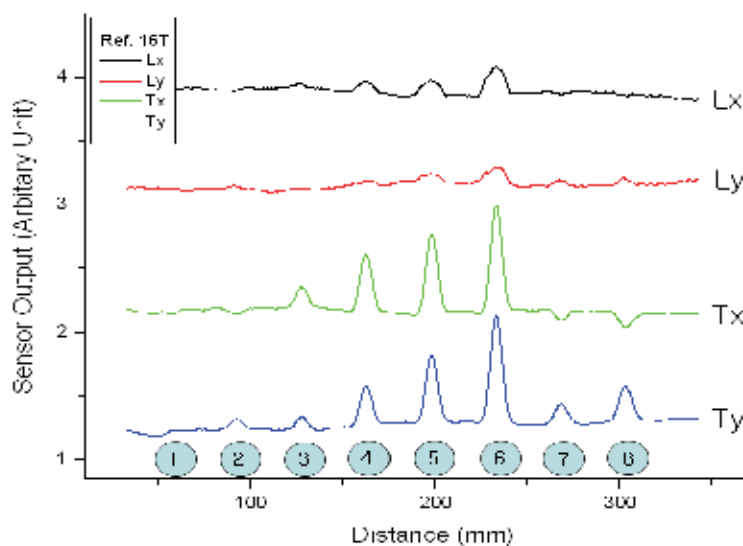


Fig. 15. Sensor output voltage signals from the longitudinal and transverse sensor for the transverse reference specimen

## 4. Magnetic field simulation

### 4.1 Manufacture of reference specimen

Fig. 16 (a) and (b) are the diagrams of the RS for testing a new designed sensor and simulating a magnetic field for longitudinal and circumferential MPs and defects. The inner diameter, the outer diameter, and the length of RS are 16.916 mm $\phi$ , 19.05 mm $\phi$ , and 440 mm, respectively. As shown Fig. 16 (a), the numbers 1, 2, 3, and 4 are longitudinal magnetic phase (LMPs) in the outer wall, while 5 and 6 are longitudinal defects (LDs) in the inner one (Ryu et al., 2010). As shown Fig. 16 (b), the numbers 1, 2, 3, and 4 are circumferential magnetic phases (CMPs) in outer wall, 5 and 6 are circumferential defects (CDs) in inner one (Ryu et al., 2010). The AISI 1810 steel was used to simulate the MPs. Magnetic properties were measured by hysteresis remagraph (Magnet-Physik), and conductivity was measured by using 4-point probe method (Janezic, 2004). The maximum permeability, coercivity, remanence, and conductivity of this steel are  $9.80 \times 10^{-4}$  H/m, 0.44 kA/m, 0.83 T, and  $6.0 \times 10^5$  S/m, respectively. Table 3 and 4 show the dimension and position of MPs and defects in the RS. The shape of MPs and defects is a hexahedron. The length and width of MPs and defects are the same, and the depth is deeper as the number increases.

The appearance of defects with outside ferrite sludge transforms the flow of magnetic flux because the EC is changed by the permeability of defects. Fig. 17 is a schematic diagram of the RS with outside ferrite sludge. The numbers 1, 2, 3, and 4 are inner defects, 5, 6, 7, and 8 are outer defects, 9, 10, 11 are inner defects, and 12 is penetration with outside ferrite sludge (Ryu et al., 2009). Table 5 shows the dimension and position of defects. Fig. 18 is a schematic diagram of the RS with nickel sleeving. The numbers 1, 2, 3, and 4 are inner defects with nickel sleeving. The thickness of nickel sleeving is 250  $\mu$ m (Ryu et al., 2009). Table 6 shows the dimension of the artificial defects. The length and width are the same, only the depth is different.

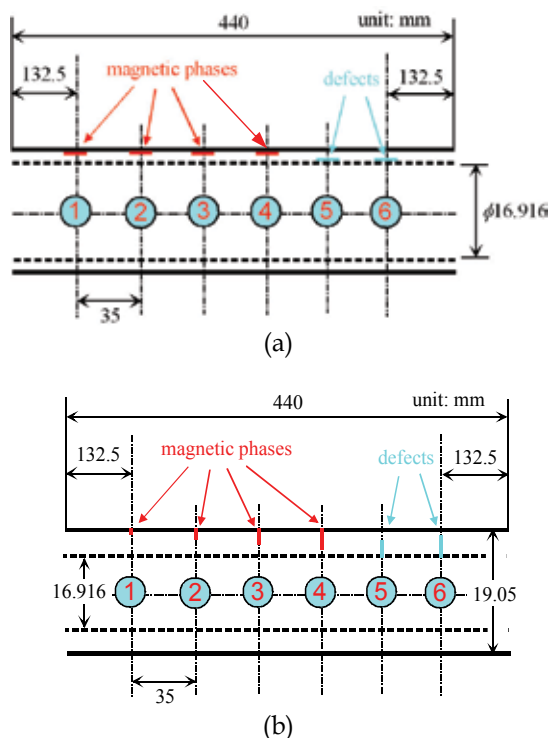


Fig. 16. Schematics of the RS for simulation of MPs and defects. (a) The numbers 1, 2, 3, and 4 are LMPs in the outer wall, while 5 and 6 are LDs in the inner one. (b) The numbers 1, 2, 3, and 4 are CMPs in the outer wall, while 5 and 6 are CDs in the inner one

Defect type	Defect No.	$L$ (mm)	$W$ (mm)	$D$ (mm)
Outer defect (Insertion of MP)	1	5.00	0.20	0.213 (20%)
	2	5.00	0.20	0.427 (40%)
	3	5.00	0.20	0.639 (60%)
	4	5.00	0.20	0.852 (80%)
Inner defect	5	5.00	0.20	0.639 (60%)
	6	5.00	0.20	0.852 (80%)

Table 3. The dimension of the LMPs and LDs in the RS

Defect type	Defect No.	$L$ (mm)	$W$ (mm)	$D$ (mm)
Outer defect (Insertion of MP)	1	5.00	0.20	0.213 (20%)
	2	5.00	0.20	0.427 (40%)
	3	5.00	0.20	0.639 (60%)
	4	5.00	0.20	0.852 (80%)
Inner defect	5	5.00	0.20	0.639 (60%)
	6	5.00	0.20	0.852 (80%)

Table 4. The dimension of the CMPs and CDs in the RS

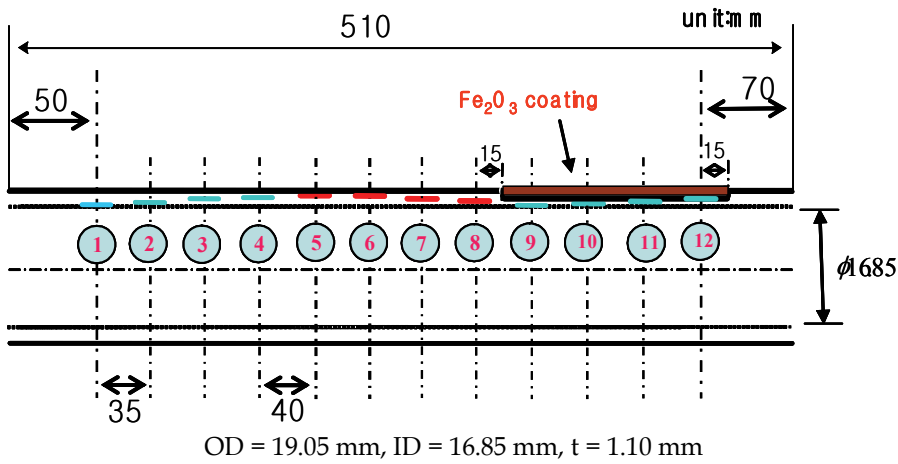


Fig. 17. Schematic diagram of RS. The number 1, 2, 3, and 4 are inner defects, 5, 6, 7, and 8 are outer defects, 9, 10, 11 are inner defects, and 12 is penetration with outside ferrite sludge

Defect type	Defect No.	L (mm)	W (mm)	D (mm)
Inner defect	1	10.00	0.20	0.22
	2	10.00	0.20	0.44
	3	10.00	0.20	0.66
	4	10.00	0.20	0.88
Outer defect	5	10.00	0.20	0.22
	6	10.00	0.20	0.44
	7	10.00	0.20	0.66
	8	10.00	0.20	0.88
Inner defect (30% cutting) + Fe <sub>2</sub> O <sub>3</sub> coating	9	10.00	0.20	0.22
	10	10.00	0.20	0.44
	11	10.00	0.20	0.66
	12	10.00	0.20	penetration

Table 5. Dimension of defects with and without outside ferrite sludge

Defect No.	Width (mm)	Length (mm)	Depth (mm)	Note
1	0.20	10.00	0.25	Inner defect
2	0.20	10.00	0.51	
3	0.20	10.00	0.76	
4	0.20	10.00	1.02	

Table 6. Dimension of defects in designed RS sleeved by nickel

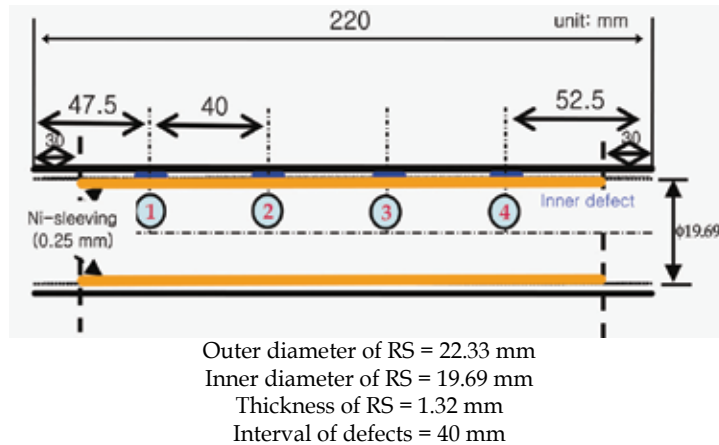


Fig. 18. Schematic diagram of RS with nickel sleeving. The numbers 1, 2, 3, and 4 are inner defects in nickel sleeving

#### 4.2 Magnetic field simulation

The Ansoft Maxwell V12 3D software was used for calculating the reactance change caused by the presence of MPs and defects (Ansoft Corp., 2009). The U-type probe, which has two kinds of coils perpendicularly stands on the Inconel tube including the MPs and defects. The solver for the FEM was the eddy current. The magnetic potential applied to the magnetizing coil was 10 A turn, the frequency was 10 kHz. Fig. 19 shows the mesh configuration for simulating the reactance change of (a) LMPs and LDs, and (b) CMPs and CDs. The mesh size of LMPs and LDs was about 280,000 tetrahedra, and one of CMPs and

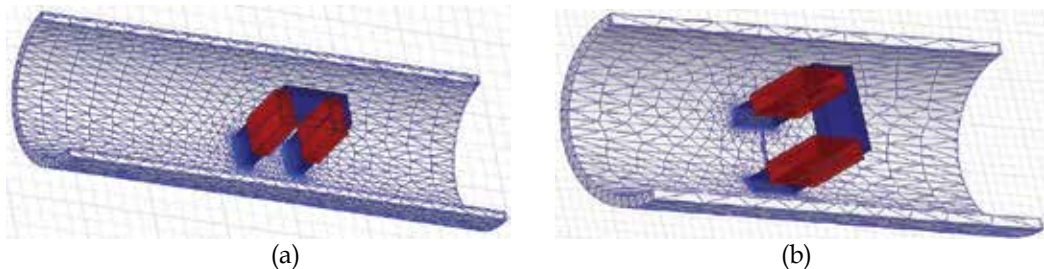


Fig. 19. Mesh configuration for simulating the reactance change of (a) LMPs and LDs, (b) CMPs and CDs

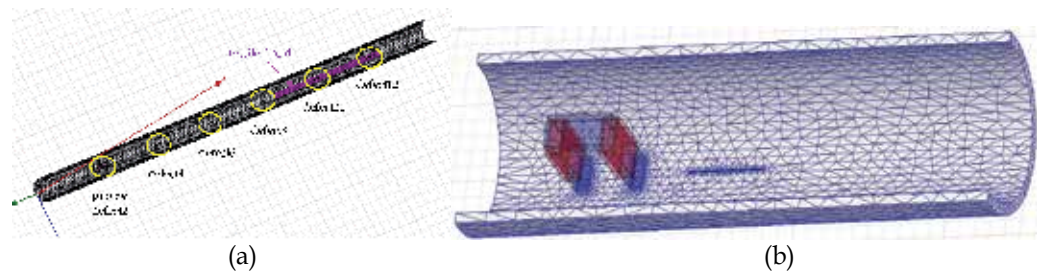


Fig. 20. (a) FEM model with outside ferrite sludge and (b) mesh configuration for simulating the reactance

CDs was about 260,000 tetrahedra. Fig. 20 shows (a) the FEM model, and (b) the mesh configuration of the defect with outside ferrite sludge. The size of the mesh was 291,000 tetrahedra. Figure 21 shows (a) the FEM model for LDs in Inconel tube with nickel sleeving, and (b) the mesh configuration of the defect sleeved by nickel. The solver of FEM was eddy current, the number of mesh was 364,000 tetrahedra.

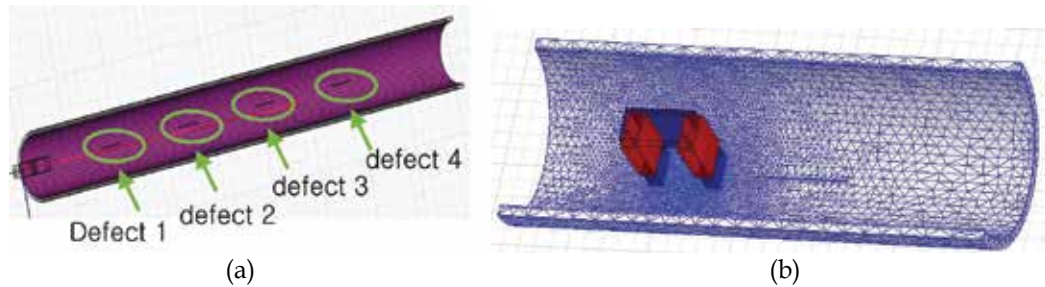


Fig. 21. (a) FEM model for LDs in Alloy600 tube with nickel sleeving, and (b) mesh configuration of the defect with nickel sleeving for simulation

### 4.3 Results and discussions

The calculated results by the FEM for LMPs and LDs are shown in Fig. 22(a), and sensor output is shown in Fig. 22(b). As shown in Fig. 22, the reactance amplitude increases with increasing depth of the inner LMP and outer LD (Ryu, 2010). The symbols are the reactance simulated by FEM, and the solid line, without symbols, is the reactance measured of the fabricated sensor (Son, 2009). The amplitude of signals at the LMPs and LDs increase with deepening depth, but the phase of signals is the opposite. So the new sensor can distinguish the LMPs and LDs produced in SGT.

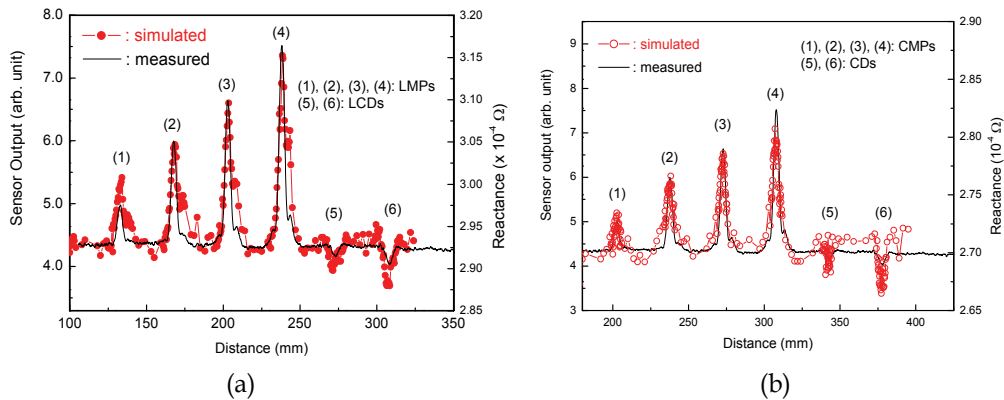


Fig. 22. Reactance simulated by FEM and output measured by manufactured sensor for (a) LMPs and LDs, (b) CMPs and CDs. The numbers 1, 2, 3, and 4 are LMPs, 5 and 6 are LDs at (a), and the numbers 1, 2, 3, and 4 are CMPs, 5 and 6 are CDs at (b)

The results calculated by the FEM and the in-phase  $x$ -output of sensor for CMPs and CDs are shown in Fig. 22(b). As shown in figure 22(b), the reactance amplitude increases with increasing depth of the outer CMP and inner CD (Ryu, 2010). The symbols are the reactance



simulated by FEM, the solid line, without symbols, indicates the reactance change measured of the fabricated sensor. The amplitude of signals at the CMPs and CDs increase with depth, but the phase of signals is opposite each other. So the new sensor can measure CMPs and CDs, and also distinguish the CMPs and CDs produced in SGT by phase.

The result simulated by FEM and the output measured by fabricated sensor for RS with and without outside ferrite sludge are shown in Fig. 23(a). The reactance amplitude increases with increasing depth of the inner and outer defect (Ryu, 2009). It jumps when there is outside ferrite sludge because the reactance is affected by the permeability of the ferrite sludge. Also, it increases with increasing depth, and is much stronger for passed through defect. The measured signal at the *B*-sensing coil is composed of a resistance (real part) and a reactance (imaginary part). Using this, we calculated the reactance of the *B*-sensing coil. The solid line, without symbols, indicated the reactance measured (Ryu, 2009). Fig. 23(b) shows the output of fabricated sensor and the calculated reactance for defects in Alloy tube with nickel sleeving. As shown in Fig. 23(b), the reactance amplitude increases with deepening depth of defect (Ryu, 2009). The defect 1 was not measured, because the distance from the end of the specimen to defect 1 is very short. The measured signal at *B*-sensing coil is composed of resistance (real part) and reactance (imaginary part), we calculated the reactance of *B*-sensing coil. The reactance amplitude calculated for the defect present in the reference Alloy 600 tube is well agreeable with the results measured by the fabricated probe.

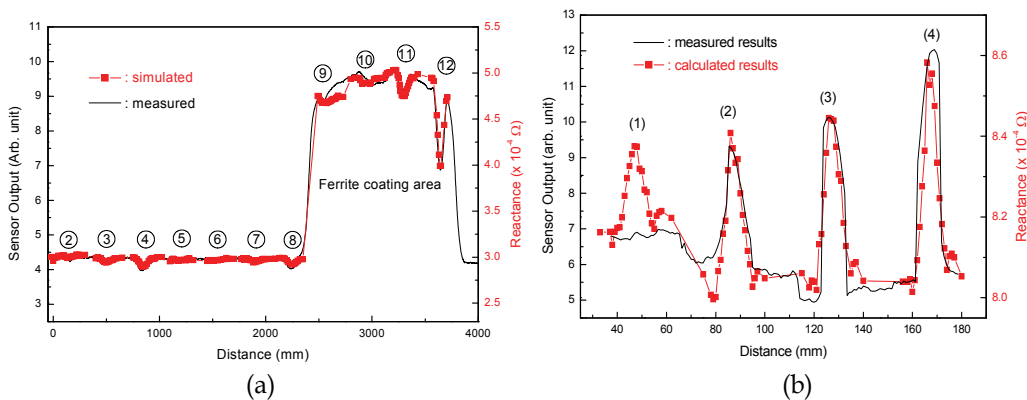


Fig. 23. Reactance simulated by FEM and output measured by manufactured sensor for (a) with and without outside ferrite sludge, (b) with nickel sleeving. The numbers from 2 to 8 are LMPs, from 9 to 12 LMPs with outside ferrite sludge at (a), and the numbers 1, 2, 3, and 4 are LMPs with nickel sleeving at (b)

## 5. Conclusion

The degradation and materials specification of SGT were reviewed, and the limitation of ECT was designated. The effects of magnetic phase on ECT signal were analyzed using the inspection data of NPP. The large coercivity and clear hysteresis loops of PVC which is extracted from the retired SG tubes of Kori-1 NNP are cannot be explained as a decrease of Curie temperature by Cr depletion. The hysteresis loop which is observed in the tensile tested specimen at high temperature suggests that the MP created in the SG tube is related with stress corrosion cracking. To separate the MP and defect using one sensor, new kind of



probe which measure permeability change of the specimen was developed. Using the new probe and RS which has MP and normal defect, we could measure and distinguish not only MP but also normal defect, and also distinguish longitudinal and transverse defects which are impossible with conventional bobbin type ECT probe. The reactance change of various MPs and defects was calculated by FEM simulation, and the results were compared with measured value by new probe. The reactance increased with increasing depth of the LMPs, CMPs, LDs and CDs, but the phase of signals at the MPs and defects are the opposite. The reactance increased with increasing depth of the defect with and without outside ferrite sludge. But it jumps when there is outside ferrite sludge, and is much stronger for passed through defect. The reactance increased with deepening the depth of the defect with nickel sleeving. The reactance calculated for the MPs and defects in the Alloy600 tube agrees with the result measured by the sensor. So the new sensor can distinguish the MPs and defects produced in SGT by phase change.

## 6. References

- Ansoft Corp.; (2009), <http://www.ansoft.com>.
- Bain, E. C. Aborn, R. H. & Rutherford, J. J. (1933). *Trans. ASM*. Vol. 21, (Month & Year ) 481.
- Bakhtiari, S. (1999). Advanced Eddy Current NDE for Steam Generator Tubing, ANL/ET/CP-98667
- Bruemmer, S.M.; Charlot, L.A. & Henager, C.H. (1988). *Corrosion*, 782
- Chevenard, P. (1934). *C.R. Acad. Sci*. Vol. 198, pp.1144.
- EPRI; (2010), 2010 Portfolio PWR Steam Generator Management Program Overview 41.01.02
- Hwang, S.S.; Kim, H.P. Kim, J.S. (2003). Corrosion degradation of steam generators in Korea, *Proc. Of SMiRt 17*, Czech Republic (Agu. 17-22), Prague.
- Harrod, D.L. Gold, R.E. & Jacko, R.J. (2001). Alloy Optimization for PWR Steam Generator Heat-Transfer Tubing, *JOM Journal of the Minerals, Metals and Materials Society*, Vol. 53, No.7, (July 2001), pp.14-17
- Jackson, L.R. & Russel, H.W. (1938). *Instruments*. Vol. 11, pp.280
- Janezic, M. D.; (2004). DC Conductivity Measurements of Metals, *NIST Technical Note*, 1531.
- Kim, Y. H. Song, S. J. Heo, J. S. Lee, H. B. & Song, M. H. (2004). *Key Engineering Materials*. Vol. 555, pp. 270-273,
- Okimura, K. Hori, N. Mukai, M. Masumoto, K. Kamo, K. & Kurokawa, M. (2006). Mitsubishi Heavy Industries Technical Review. Vol. 43, No. 4, (Dec. 2006).
- Park, D.G. Ryu, K.S. Son, D. & Cheong, Y.M. (2010). Effects of magnetic phase on the ECT signal in the SG tubes, *IEEE-Trans. Mag*. Vol. 46, No. 2, (Feb. 2010), pp.560-562.
- Roberts, J.T. A. (1981 ). *Structural Materials in Nuclear Power Systems*, Plenum Press, New York,
- Ryu, K. S. Son, D. Park, D. G. Jung, J. K. & Kim, Y. I. (2009). Reactance simulation for the defects in steam generator tube with outside ferrite sludge, *J. Appl. Phys.*, Vol. 105, No. 7, (March 2009), pp. 07E712-1 (3 pages).
- Ryu, K. S. Son, D. Park, D. G. & Jung, J. K. (2009). Reactance change at defect in inconel tube with nickel sleeving, *IEEE Trans. Magn*, Vol. 45, No.6, ( June2009, pp. 2733-2735
- Ryu, K. S. Son, D. Park, D. G. Jung, J. K. & Kim, Y. I. (2010). Magnetic field simulation of magnetic phase detection sensor for steam generator tube in nuclear power plants. *J. Appl. Phys*, Vol. 107, No.9, (May 2010), pp.09E704-1 (3 pages).

- Sakamoto, T.; (1993) *Journal of the Japanese Society for Non-destructive Inspection*. Vol.42, No. 9
- Son, D., Joung, W., Park, D., Ryu, K., (2009). *J. of Magnetism*. Vol. 14, No. 2, pp. 97.
- Son, D. Joung, W. Park, D. G. Ryu, K. S. (2009). Magnetic sensor for the defect detection of steam generator tube with outside ferrite sldge, *IEEE Trans on Magnetism*. Vol. 45, No. 6, (June 2009), pp. 2724-2726.
- Son, D. Joung, W. I. Park, D. G. Ryu, K. S. (2009). *J. of Magnetism*, Vol. 14, No. 2, pp.90.
- Song, S. C. Lee, Y.T. Jung, H.S. & Shin, Y.K. (2006). *J. Kor. Soc. NDT*. Vol. 26, No. 3, pp.174.
- Strauss, B. Schotty, H. & Hinnueber, J. (1930). *Z. Anorg. Allg. Chem.* Vol.18, No.1, (March 1930), pp. 309-324.
- Takahashi, S. Sato, Y. Kamada, Y. Abe, T. (2004). Study of chromium depletion by magnetic method in Ni-based alloys, *J. Magn. Magn. Mater.* Vol. 269, No.2, (Feb 2004), pp. 139-149.
- Takahashi, S. Sato, H. Kamada, Y. Ara, K. & Kikuchi, H. (2004). A new magnetic NDE method in inconel 600 alloy, *International Journal of Applied Electromagnetics and Mechanics*, Vol. 19, No. 1-4, (April 2004), pp.3-8.
- USNRC; (2006) NEI97-06, Related documents and other resources, <http://www.nrc.gov>
- USNRC; (1996), Steam Generator Tube Failures, NUREG/CR-6365

# Optical Methods for On-line Quality Assurance of Welding Processes in Nuclear Steam Generators

Adolfo Cobo, Jesús M<sup>a</sup> Mirapeix, David Solana<sup>1</sup>,  
Alfonso Álvarez-de-Miranda<sup>1</sup>, Pilar-Beatriz García-Allende,  
Olga M<sup>a</sup> Conde and José Miguel López-Higuera  
*Photonics Engineering Group at the University of Cantabria,*  
*<sup>1</sup>Equipos Nucleares, S.A. (ENSA)*  
*Spain*

## 1. Introduction

The manufacturing of steam generators relies heavily in many different processes of welding, involving a wide range of materials, welding procedures and requirements. Quality assurance is of paramount importance in these processes, and in the case of the nuclear industry, even more rigorous quality control procedures, according to the nuclear safety regulatory rules and customer specifications, are required.

The currently accepted procedure for quality control is based on the rigorous control of the welding parameters, such as the heat input, welding speed, material geometry, surface preparation and cleanness, etc. However, it is known that the physics involved in these processes is extremely complex, and the efforts aimed at developing a reliable formulation of the relationships between the process parameters and a defect-free welding seam have mostly failed (Wu et al., 1997), with only some success in the prediction of stress and distortion of the joined piece (Dong, 2005).

For that reason, quality assurance in welding processes is typically performed by means of procedure trials, where the suitable welding parameters are established and used later in production. However, as there is no guarantee that a free-defect welding is always achieved, non-destructive testing (NDT) techniques are routinely applied in different stages of the manufacturing process. These techniques (liquid penetrant, magnetic-particle, ultrasonic, X-Ray, Eddy current testing ...) are quite effective to validate the quality of the welds, but most of them are difficult to automate, require complex procedures and take a significant amount of the production time.

Although *off-line* NDT procedures can not be avoided in those critical applications, there is still a great interest in the possibility of *on-line* monitoring and control of the welding process. This approach allows the early repair (or even the real-time correction) of defects, resulting in a reduction of the manufacturing time and costs.

This paper deals with one particular approach for on-line sensing, namely, the spectroscopic detection and processing of the light generated by the process itself. A great deal of information about the real-time behaviour of the welding process can be extracted through

the analysis of the spectroscopic signal, including the detection and classification of defects. This approach is valid in all processes in which thermal plasmas are generated, for example, arc and laser welding in the keyhole regime, which have strong optical emission in the visible range. In this work, the proposed technique has been validated for the arc welding process and several alloys.

The field trials, performed in the production facilities of Equipos Nucleares, S.A. (ENSA), have been focused on one particular process: the tube-to-tubesheet welding in large steam generators for the nuclear industry. This is a particularly demanding process in terms of quality control due to the huge number of tubes involved and the severe consequences of difficult-to-detect defects like small porosities. Although the current production methods result in rare occurrences of such defects, their detection at late stages of the manufacturing process (for example, during the high-pressure hydraulic test of the finished steam generator) requires time consuming reworks. Many welding procedures in the manufacturing of components for the nuclear industry can also benefit from on-line monitoring. Figure 1 shows a sector of a large steam generator's tubesheet with more than 10,000 tubes to be welded as part of the manufacturing process.



Fig. 1. Tubesheet of a steam generator for the nuclear industry

In the next section, a brief introduction to the different approaches for on-line monitoring of the welding processes is presented. Section 3 provides details about the fundamentals of the plasma emission spectroscopy. Different methods to adapt the spectroscopic approach for welding diagnosis are also proposed, with the aim of real-time defect detection capabilities. The implementation of the sensor system is discussed in section 4, in particular, different solutions to the non-invasive capture of light in a production environment are provided.

Section 5 presents the results obtained with the different sensor implementations and spectroscopic processing techniques that have been tested in field trials for the monitoring of the tube-to-tubesheet welding process of large steam generators for nuclear power plants. Finally, some conclusions and future lines of work are discussed.

## 2. On-line monitoring of the welding processes

The importance of on-line monitoring of the welding processes has been recognised long time ago, even if off-line NDT procedures can not be avoided. Several technologies have been proposed and investigated for this task, with different level of success and commercial adoption. For example, today is very common for automated welding procedures to be guided by seam tracking devices. They are usually based on the projection of a laser line on the workpiece, while a video camera take an image of the surface profile to guide the trajectory of the torch or the laser beam (Bae et al., 2002). Voltage sensors to automatically adjust the current in arc welding processes are also routinely used. Although these approaches help to improving the quality, there is no real assessment of the resulting quality and the presence of defects in the weld seam. For this task, other approaches have been investigated but not widely adopted in production so far.

One possibility is the capacitive sensing between the welding nozzle and the workpiece, which has been investigated in (Li et al., 1996) for the laser welding process in the keyhole regime. This measurement is expected to give a constant value for a uniform seam with constant parameters, and any deviation can be attributed to a potential defect. This technique has demonstrated a detection rate over 95% of common defects like poor penetration, hole formation (as small as 0.1mm), miss-tracking, etc. However, as one single variable is provided and processed, this method makes it difficult to classify and distinguish defects.

Acoustic detection gives also real time information about the process. It has been proved that the arc and laser welding produces acoustic emission in the audible and ultrasonic ranges that can be correlated with the onset of defects (Wang & Zhao, 2001). As with the previous technique, it is however difficult to discriminate among different defects, although a statistical analysis applied to the spectra of sound has demonstrated some success in predicting the weld quality (Gu & Duley, 1996).

Thermography is also a powerful monitoring technique. It offers advantages over classical artificial vision systems in the visible range, as there is a more direct estimation of the temperature distribution over the workpiece, which is clearly a magnitude directly related to the welding quality. A particular case is the single-point temperature measurement, which is a robust approach when used in a production environment, although with limited capabilities (Wikle et al., 2001). Thermographic imaging (2D) is a better method which provides spatial and temporal resolution (Cobo et al., 2007), but the availability of robust infrared cameras for the industrial environment is still limited.

Plasma optical spectroscopy has also proven to be a promising solution. It extracts rich information about the process from the strong optical emission of the thermal plasma generated by the process. Some of the advantages of this technique are the following:

- The optical spectrum includes a continuum of radiation and emission lines from the atomic species found in the plasma. Both of them (specially the emission lines) offer information about the plasma and therefore about the welding process. As the intensity of the lines is related to the level of participation of the chemical elements (and their

ions) in the plasma, and many lines from several elements are typically found even in a short wavelength range, it is possible to derive detailed information about the behaviour of the process.

- The sensor can be a simple non-invasive optical fibre located at a distance from the arc or beam, while the optoelectronic instrumentation can be dozens of metres away in a controlled environment. The instrumentation of a monitoring system comprises a spectrometer and a processing unit. With the proper optics, the end of the optical fibre can be placed also far away from the pool and protected from fumes or projections.
- Due to the strong light emission from the plasma, a simple and inexpensive CCD (Charge Coupled Device)-based spectrometer can be used to provide high-speed and real-time analysis of the welding quality.
- The optical fibre is intrinsically immune to the strong electromagnetic interferences (EMI) associated with the welding process.
- It does not require any modification of the procedure setup.

However, this approach is not free of drawbacks. One is that the classical processing technique of the acquired spectra is the determination of the electronic temperature of the plasma ( $T_e$ ). This involves a series of steps, including the identification and characterization of the emission lines, which require significant processing power. On the other hand, the relationship between  $T_e$  (and other spectroscopic variables) with the resulting quality is not clear in many cases, and always difficult to model, nevertheless.

For that reasons, the works presented in this chapter try to optimize the spectroscopic approach for real-time quality monitoring, including the evaluation of more efficient processing techniques and exhaustive experimental works to improve the detection and classification of defects. Next section introduces the fundamentals of the proposed spectroscopic method and different approaches of spectroscopic analysis.

### 3. Spectroscopic methods for on-line welding monitoring

The plasma emission optical spectroscopy is based on the wavelength-resolved analysis of the light generated by the thermal plasma, which is naturally produced by some welding procedures such as arc and laser welding. The “hardware” of the sensor system is simple: it comprises an optical fibre to capture the plasma emission from the process, and a remote spectrometer to obtain spectral-resolved information. The captured spectrum is then processed to obtain relevant information. The common approach when using plasma spectroscopy in a welding sensor and monitoring system is to calculate the plasma electronic temperature  $T_e$ , as it is known that there is a correlation between the resulting profiles of this parameter and the quality of their associated welds (Poueyo-Verwaerde et al., 1993). Figure 2 shows the processing steps needed with this “classical” approach of spectroscopic analysis.

Determination of  $T_e$  is typically carried out by means of the information associated with two different atomic emission lines, of the same element in the same ionization stage

$$T_e = \frac{E_m(2) - E_m(1)}{k \ln \left[ \frac{I(1)A(2)g_m(2)\lambda(1)}{I(2)A(1)g_m(1)\lambda(2)} \right]} \quad (1)$$

where  $E_m$  is the upper level energy,  $g_m$  the statistical weight,  $A$  the transition probability,  $\lambda$  the wavelength,  $I$  the emission line relative intensity and  $\kappa$  the Boltzmann constant.

Equation (1) is a simplification of the so-called Boltzmann-plot, which allows the use of several emission lines for the Te calculation process

$$\ln\left(\frac{I_{mn}\lambda_{mn}}{A_{mn}g_m}\right) = \ln\left(\frac{hcN}{Z}\right) - \frac{E_m}{kT_e} \quad (2)$$

where  $h$  is the Planck's constant,  $c$  is the light velocity,  $N$  the population density of the state  $m$  and  $Z$  the partition function. The representation of the left-hand side of Equation (2) versus  $E_m$  has a slope inversely proportional to  $T_e$ . Equation (2) is derived from the Boltzmann equation

$$N_m = \frac{N}{Z} g_m \exp\left(\frac{-E_m}{kT_e}\right) \quad (3)$$

and the expression that relates the intensity of a given emission line  $I_{mn}$  to the population density of the upper level  $N_m$ ,

$$I_{mn} = N_m A_{mn} h \nu_{mn} \quad (4)$$

The use of Equation (3) is valid when the plasma is in the state known as Local Thermodynamic Equilibrium (LTE) (Griem, 19643). The condition for LTE is satisfied when

$$N_e \geq 1.6 \times 10^{12} T_e^{1/2} (\Delta E)^3 \quad (5)$$

where  $N_e$  is the plasma electronic density and  $\Delta E$  the largest energy gap in the atomic energy level system.

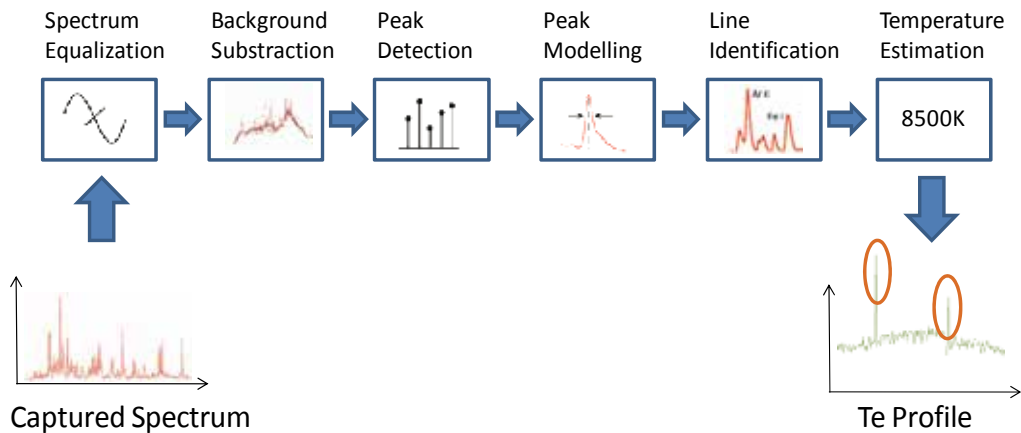


Fig. 2. Classical spectroscopic processing chain to obtain the profile of electronic temperature for a weld seam, from which defect formation can be estimated

Using either a pair of lines or a wider set to calculate the Boltzmann-plot, it is necessary to select and identify the lines for a specific element, and measure their centre wavelength, spectral width and intensity. This is not an easy task due to the presence of noise, overlapping lines, and calibration issues of the spectrometer, which could result in the

wrong identification of the atomic element or appreciable errors in the estimation of the light intensity emission. Furthermore, iterative techniques like Levenberg-Marquardt (Robinson et al., 1998) are typically used for peak characterization. However, their high computational cost makes these solutions unsuitable for a real-time monitoring and control system (Ancona et al., 2001).

### 3.1 Efficient estimation of the electronic temperature of the plasma

One possibility is the non-recursive and time-efficient analysis of the lineshape. For this task, the linear phase operator (LPO), a sub-pixel technique, has been proposed (Mirapeix et al., 2006). Figure 3 (left) shows a captured spectrum for a TIG (Tungsten Inert Gas) welding in which several elements (Iron, Manganese...) have been identified in real time.

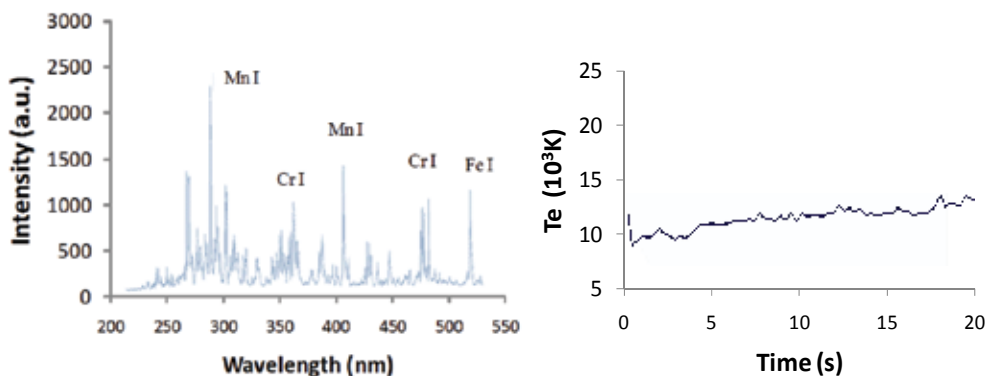


Fig. 3. Spectrum of a TIG welding in which the emission lines of some of the steel constituents and shielding gas have been identified and measured in real time (left). Calculation of the electronic temperature of the plasma ( $T_e$ ) for the case of a seam without defects (right)

Once the electronic temperature is calculated, a complete “profile” for the entire seam can be obtained. Both the absolute value and the relative variations of  $T_e$  give information about the process. For a welding seam with constant parameters,  $T_e$  is expected to be within a particular range of values; and any unexpected variation can be attributed to a perturbation of the process, and hence to a potential defect. Several statistical analysis techniques have been proposed to detect in real time any possible defect (Ancona et al., 2004) (Bebiano & Alfaro, 2009). Fig. 3 (right) shows an example of a temperature profile for a correct weld seam with nominal parameters.

In the following sub-sections, several techniques for automatic and real-time defect detection are explored. They try to substitute the estimation of the electronic temperature for a simpler spectroscopic variable, or even to correlate directly the captured (raw) spectra with the occurrence of defects. The aim is the real-time identification of defects with a simple and efficient technique that can be implemented in a real production environment, in particular, for the manufacturing of large steam generator for nuclear power plants.

### 3.2 Spectroscopic analysis based on the background radiation

The background radiation (continuum) is usually ignored or removed from the captured spectrum. It is generated by recombination processes of free electrons and ions, and by the



Bremsstrahlung effect, and does not offer specific information about particular atomic species. However, it can be helpful to simplify the calculation of Te or to detect defects. For example, an alternative method to compute Te is the line-to-continuum ratio method (Bastiaans & Mangold, 1985). In this case, Te is calculated using the relation between a single emission line intensity (integrated over the line profile)  $\varepsilon_l$  and the intensity of the adjacent background radiation (non-integrated)  $I_c$ :

$$\frac{\varepsilon_l}{I_c}(\lambda) = 2.0052 \times 10^{-5} \frac{A_{mn} g_m}{Z_i} \frac{1}{T_e \zeta} \exp\left(\frac{E_i - E_m}{kT_e}\right) \frac{\lambda}{\Delta\lambda} \quad (6)$$

where  $Z_i$  is the ion partition function,  $\zeta$  the free-bound continuum correction,  $E_i$  the ionization potential and  $\Delta\lambda$  the wavelength bandwidth. Although the calculation of Te is not straightforward and an iterative method is required, the ratio  $\varepsilon_l/I_c$  can be directly used as the monitoring signal, given that there is a direct relation between this quotient and Te. If only this ratio is to be determined, this method is easy to implement as the selected emission line does not need to be identified.

However, it has been demonstrated that not all emission lines are good candidates to infer information about the welding process (Mirapeix et al., 2008). For that reason, a previous process of line selection using the Sequential Floating Forward Selection (SFFS) algorithm is proposed (García-Allende et al., 2009). This algorithm is widely applied to reduce the dimensionality, i.e., the number of wavelengths, of spectral data prior to their interpretation (Ferry et al., 1994). In this case, previously capture spectra are labelled according to their associated defects, and the optimum spectral band in terms of defect classification is obtained by the algorithm. These wavelengths are then used as the spectroscopic monitoring signal for the process. Fig. 4 shows how the processing steps are reduced with this approach.

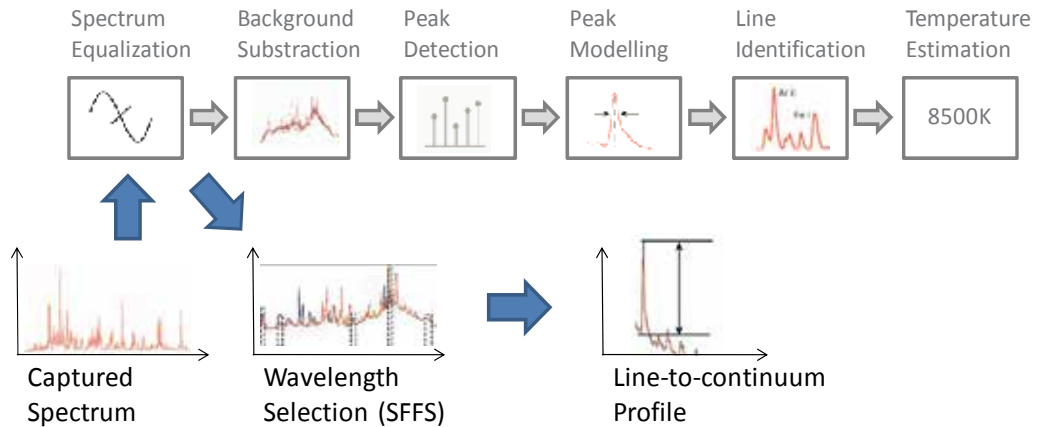


Fig. 4. Spectroscopic processing using SFFS for line selection and line-to-continuum as the monitoring variable

Once the optimum emission lines are selected *a priori*, the monitoring task involves the measurement of the emitted light at that particular wavelength with respect to the surrounding background level. Any variation of this ratio for a constant parameters welding can be analyzed and related to a particular defect.

Another possibility for defect detection is the analysis of the shape of the continuum radiation. It has been demonstrated that this background radiation has a wavelength of maximum emission, and this wavelength is fairly stable for a defect-free, constant-parameters welding process. Thus, the real-time tracking of this wavelength can be an indicator of defect formation.

The implementation of this solution is quite simple, as the only processing requirement is the extraction of the plasma background signal from the acquired spectra. Two different alternatives have been explored in this regard. An initial approach has been carried out by means of a smoothing algorithm, which was already implemented in (Mirapeix et al., 2006) to perform the background subtraction stage. The only parameter to take into account is the size (in spectral bands) of the moving window. Modelling of the plasma background has also been attempted by means of a low-pass filter. A frequential analysis of the welding spectra was initially conducted to remove the contribution of the emission lines. After the filtering process, the resulting background signal is modelled as a blackbody radiation via the Planck function:

$$B_{\lambda}(T) = \frac{2hc^2}{\lambda^5} \frac{1}{\left( e^{\frac{hc}{kT\lambda}} - 1 \right)} \quad (7)$$

where  $T$  is the temperature that has to be previously obtained by means of

$$\lambda_{max} = \frac{2.9 \cdot 10^6}{T} \quad (8)$$

where  $\lambda_{max}$  is the wavelength associated with the maximum intensity of the plasma spectrum after the filtering process. Processing needs with this approach are much simplified, as can be seen in Figure 5 with respect to the classical approach of  $T_e$  estimation (Mirapeix et al., 2008).

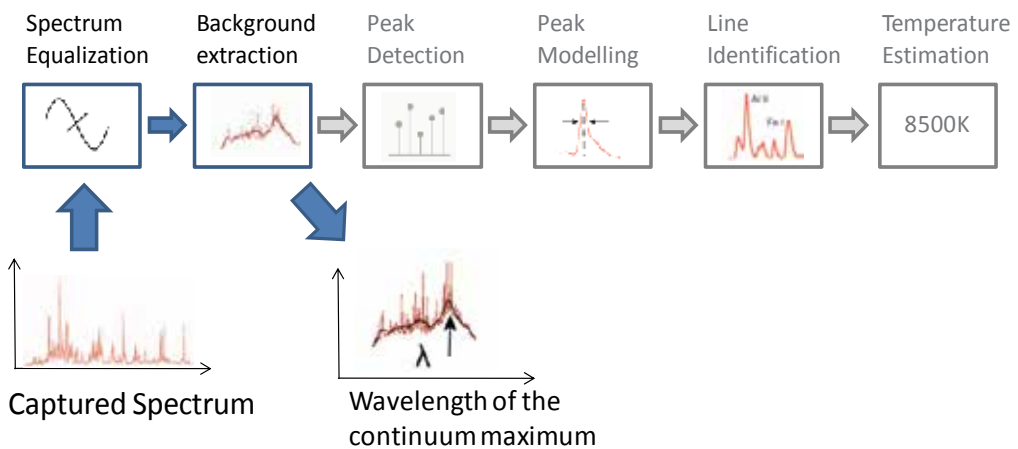


Fig. 5. Spectroscopic processing using the estimation of the wavelength of maximum radiation in the background signal

The results obtained in field trials with these two continuum-based methods are presented in section 5.

### 3.3 Defect detection through the RMS spectroscopic signal

Another alternative has been explored to avoid the use of the plasma emission lines. The plasma RMS (Root Mean Square) signal is determined by considering the spectral intensity of the plasma spectra over a specific spectral window, thus being directly related to the process heat input and behaviour (Mirapeix et al., 2010). This approach is directly related to other based on the use of photodiodes for process monitoring (Park et al., 2001).

The processing scheme required for this option is very simple (see Figure 6), it may allow fast implementations independently of the particular process and material to be welded, and the obtained results show that there is a good correlation between it and the quality events identified on the seams.

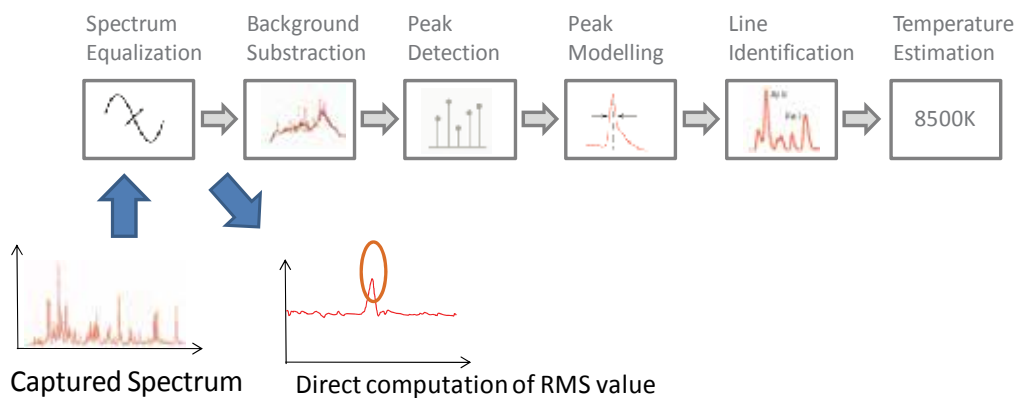


Fig. 6. RMS spectroscopic signal as a defect indicator

### 3.4 Direct defect detection by means of artificial neural networks

Finally, we propose another processing technique based on the use of artificial neural networks (ANN) to achieve classification of defects from the raw spectra captured by the spectrometer. This approach is an interesting solution due to the lack of a suitable mathematical model of the welding process and when abundant experimental data is available from the specific welding process to train the network.

However, the amount of information to process by the ANN, considering a real-time system, could be a mayor drawback. For example, a typical spectroscopic system consists of 2048 wavelengths (number of pixels of the spectrometer's CCD used), with an average of 50 spectra captured per second. For this reason, it would be desirable to reduce the number of wavelengths to process, which can be done taken into account that not all the spectral lines offer relevant information about the process.

Two techniques are proposed for the task of reducing the amount of spectral information that feeds the ANN. The first one is the Principal Component Analysis (PCA), which performs redundancy removal and data compression simultaneously (Workman & Springsteen, 1998). Performing data compression implies reducing the number of required components, as much as possible, without losing relevant information. This is accomplished by the expression of the captured spectra in a different vectorial basis which is obtained in

such a way that the new basis vectors are those directions of the data containing the most relevant information. The result of the process is a smaller data set including most of the information. Selecting a set of about 15 values, a compression rate of 99% is achieved without significant loss of defect detection capabilities (Mirapeix et al., 2007).

The second technique is the Sequential Floating Forward Selection (SFFS) algorithm already mentioned. One important advantage of SFFS is that the output of this algorithm is a selection of the most discriminant wavelengths, as opposed to PCA, which gives a set of discriminant features that cannot be associated with any particular spectral band. For this reason, by applying SFFS to an experimental set of data from the same welding process, it is possible to automatically select a reduced number of optimum wavelengths to monitor for defect detection. Experiments confirm that the selected wavelengths are those of the significant elements of the material to be welded or those of the shielding gas. In the case of TIG welding of steel with Argon gas, for example, selected wavelengths are typically the emission lines of Iron, Manganese and Argon. It has been demonstrated that the defect-detection and classification capabilities are not significantly reduced even when only 10 wavelengths are supplied to the ANN (García-Allende et al., 2008).

The proposed architecture for the ANN is a multilayer feed-forward network with a back-propagation learning algorithm. Its main performance metrics is (apart from computation efficiency for real time applications) the classification error, that is, its ability to give the correct defect indication for a given spectrum at its input. During the training stage, spectra of correct welds and all the possible defects have to be supplied to the neural network. In this step the network iteratively adjusts its parameters (weights and biases) in order to produce an output that matches the expected results. Several experiments have been realized to determine the appropriate number of hidden layers, the number of neurons or processing elements and the topology. ANN topologies with one and two hidden layers and with a number of neurons in each layer from 30 to 50 have been tested. The neurons in all layers have a log-sigmoid transfer function. Figure 7 shows the proposed architecture for an ANN, with five outputs that signal a correct welding or four possible situations: slight lack of penetration, severe lack of penetration, reduction of shielding gas flow and low welding current. The capability of this approach to detect these defects has been tested experimentally in the laboratory on TIG welding of steel plates. A better performance than the analysis of the electronic temperature profiles for defect detection has been found (García-Allende et al., 2009a).

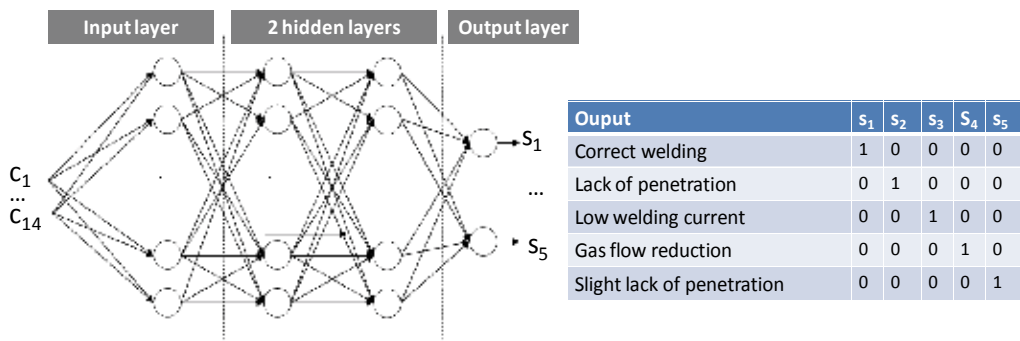


Fig. 7. Architecture of a ANN to classify between four possible welding conditions that lead to defect formation

In summary, several techniques of spectroscopic analysis offer the possibility of real-time automatic quality assurance of the welding process. In the next section, the implementation of these techniques in a spectroscopic sensor system able to work in a real industrial production environment is addressed.

#### 4. Spectroscopic sensor implementation for production environments

A spectroscopic sensor, as described above, needs a CCD spectrometer and a processing unit that can be placed far away from the welding point, thanks to the light transmission capabilities of the optical fibre. The generic architecture of a spectroscopic sensor system is shown in Figure 8.

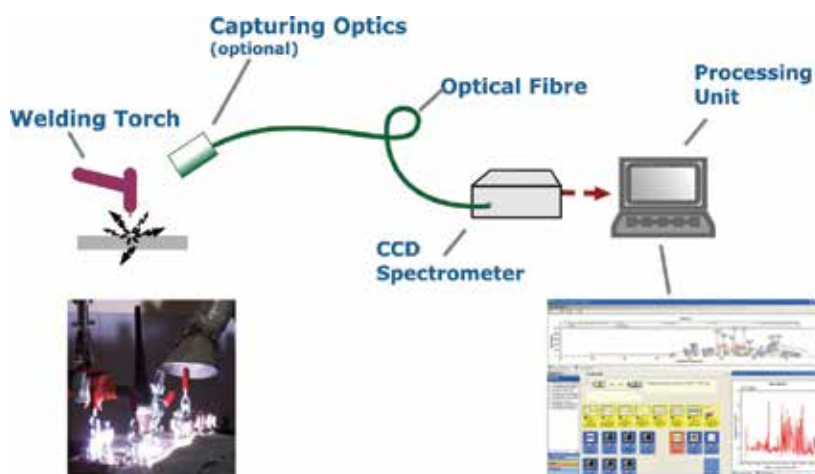


Fig. 8. Spectroscopic sensor architecture

However, one end of the optical fibre must be located close to the generated plasma, and this can be challenging in a real industrial scenario, due to reliability issues, heat, projections, fumes, accessibility of the process and workplace configuration. In laser welding this can be solved by using the optical port usually available at the laser head. In this case, the plasma emission is co-axially captured from the plume through the focusing lens of the laser beam. For arc welding, two non-intrusive solutions for the capture of light have been proposed. The first one is suitable for TIG and MIG torchs, and it is based on the embedding of the bare optical fibre tip in one of the shielding gas nozzle exits. The gas flow has a cooling effect upon the fibre, also preventing possible weld pool projections from interfering with the light capturing process. It has been demonstrated that, although the fibre suffers some external deterioration due to the welding process, the fibre core remains unaffected, and the fibre effectively collects the light even after 100 welding tests (total welding time of 800 seconds). Measurements of the fibre transmission after several welding processes have shown the appearance of some wavelength-dependent losses in the UV region due to the intense plasma radiation. However, although special solarization-resistant fibres could be used to avoid this phenomenon, the effect of these losses is not especially relevant, as the fibres employed in our tests have proved to be suitable for plasma spectroscopic analysis. Figure 9 shows a photograph of one embedded fibre tip in a TIG welding torch and a microscope view of the fibre's end before and after intensive welding trials (Mirapeix et al., 2007a).



Fig. 9. Optical fibre embedded in a TIG welding torch (left), and view of the fibre's end before and after more than 100 welding trials

The second approach has been developed specifically for orbital TIG welding of tubes to the tubesheet of steam generators. In this case, the welding torch includes a complex mechanism to automatically perform the orbital weld seam over the tube's perimeter. The entire mechanism is enclosed in a protective shield with the shielding gas, being difficult to collect the light from the moving arc with the optical fibre. The proposed solution is depicted in Figure 10. Two cosine correctors are placed at the end of two optical fibres (silica fibres with a core diameter of  $600\mu\text{m}$ ), which are attached to the welding torch through two holes in the steel case. The cosine corrector, whose diffusing material is Spectralon, is a spectroradiometric optics designed to collect light over  $180^\circ$ , which is of special interest given the moving arc. The light from the two fibres is combined with an optical 2x1 coupler and sent to the CCD spectrometer. Although this optical setup results in some variation of the overall collected light intensity when the electrode moves along the circular path, the relative nature of the spectroscopic processing approach does not affect to the capability of defect detection (Cobo et al., 2007a).

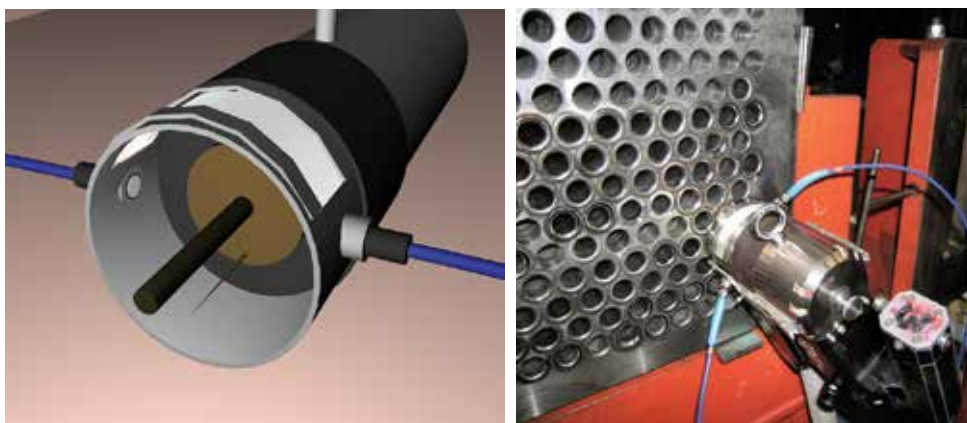


Fig. 10. Optical setup for efficient and non-invasive light capturing in the orbital TIG welding of tubes

In the next section, the results in field trials in a production environment of the proposed spectroscopic sensor system with the different processing approaches mentioned above are presented.



## 5. Field trials in the manufacturing process of steam generators

The above proposed techniques have been tested in the welding trials and qualification of large steam generators for nuclear power plants, in particular, for monitoring and real time defect detection in the tube-to-tubesheet TIG welding process in the facilities of the company ENSA (Equipos Nucleares S.A.) in Maliaño, Spain. The INCONEL-690 tubesheet cladding mock-ups include tubes with a diameter of 19.2 mm and a thickness of 1 mm. The welding system is formed by a Model 227 Power Supply (Arc Machines Inc.) attached to a Model 96 Tube-to-tubesheet automated weld head, designed to perform the required orbital welds, as described above. The welding current was pulsed at 50Hz with a maximum of 60A. Argon and Helium were used as shielding gases, with a mixture of 40% and 60% respectively. The electrode is made of tungsten, and the total duration of the welding process for each tube is about 30 seconds.

The light capturing optics consists of two optical fibres (Ocean Optics P600-UV-VIS, 4 metres long) with cosine correctors, an optical coupler, and a CCD spectrometer (Ocean Optics USB2000) with 2048 pixels and a resolution of about 0.2 nm in the range from 195 to 530nm (blue-green zone of the visible spectrum).

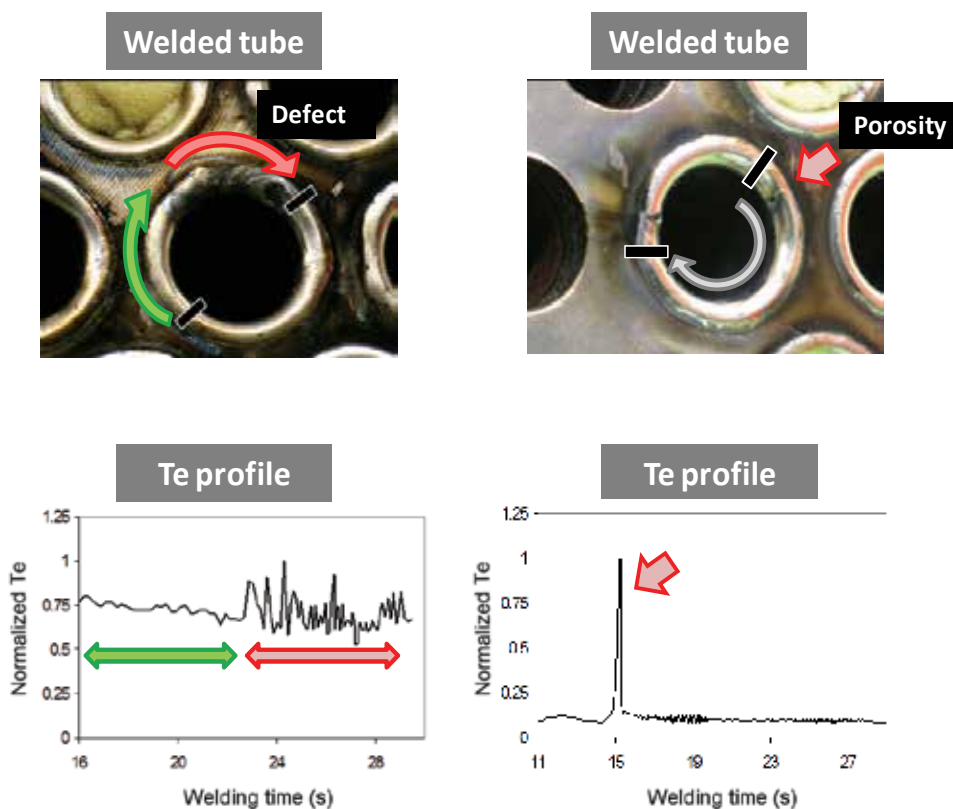


Fig. 11. Detection of defects by means of the Te profile. Left: defective weld seam due to shielding gas shortage. Right: small porosities

Due to the rare occurrence of real defects during the manufacturing process, deliberate change of process parameters and perturbations have been produced in weld test coupons

to simulate defects, like porosities and lack of penetration. The formation of defects has been validated by means of PT (Penetrant Testing) procedures.

The results from the application of the different spectroscopic processing techniques described above are presented in the rest of this section.

### 5.1 Defect detection using the real-time estimation of the electronic temperature of the plasma

The spectroscopic processing technique described in section 3.1 has been tested in a production environment with the aim of automatically detect and classify defects occurring during the orbital welding of INCONEL-690 tubes. The example spectrum and the electronic temperature profile of a defect-free weld seam already shown in Figure 3 correspond to these experiments. The initial and final parts of the seam have been removed because welding current is not constant at these points. It can be seen that the value (around 12,000K) is fairly stable, an indication of a correct welding.

In Figure 11, two defects with their corresponding temperature profile are shown. To the left, a shortage of the shielding gas starts in the middle of the seam, producing a defective welding, which is clearly visible in the Te profile. To the right, one point of the tube's edge has been deliberately contaminated, resulting in a small area of porosities. The Te profile shows a clear indication of this defect.

### 5.2 Defect detection by means of the optical background radiation

As described in section 3.2, the background radiation (continuum) of the plasma emission can be analysed to obtain warnings of defect formation. The tracking of the wavelength of maximum emission of the background radiation has also been applied to the tube-to-tubesheet welding process. In Figure 12, a weld seam is shown with a deliberate defect: the operator produced a perturbation in the shielding gas by blowing into the welding torch head at  $t \approx 24$  sec. It can be seen a sudden perturbation of the wavelength of maximum background radiation, while its value is stable when no defects are being produced. The constant variation of the wavelength (with negative slope) shown in Figure 12 has not been observed in other experiments with different welding processes, and a possible explanation is that the orbital welding produces variations in the global light intensity captured along the weld seam. This method, not being relative like the Te estimation, is more affected by this problem.

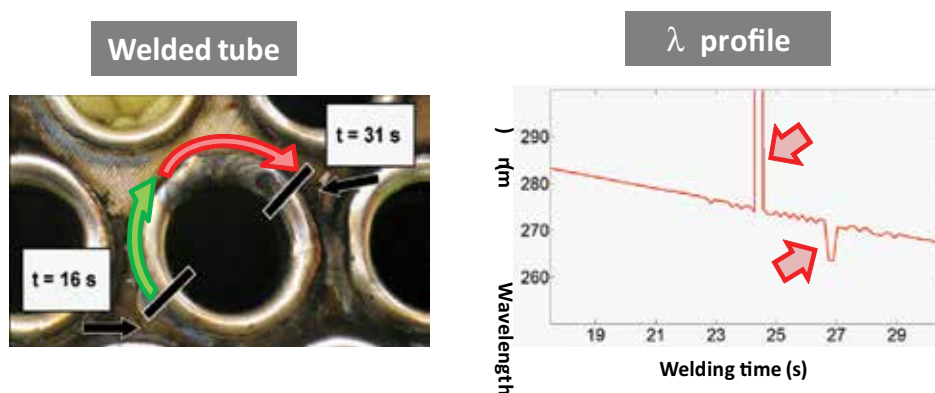


Fig. 12. The tracking of the shape of the background radiation allows detecting defects like perturbation in the shielding gas



The line-to-continuum method, already presented in section 3.2, is a relative method that also takes into account the background radiation. Figure 13 shows one of the experiments in which porosity was formed. The upper graph shows the line-to-continuum ratio for the spectral band of 404.14nm, corresponding to the neutral species Mn I, and previously selected by the SFFS algorithm as a significant wavelength. However, the zone with the porosity (red box) shows no clear indication of the defect. The lower graph, however, corresponds to the wavelength of 422.84nm (ion Fe II) and shows a clear indication of the defect. For that reason, it is important to have previous experimental data to determine the best wavelengths for a particular defect.

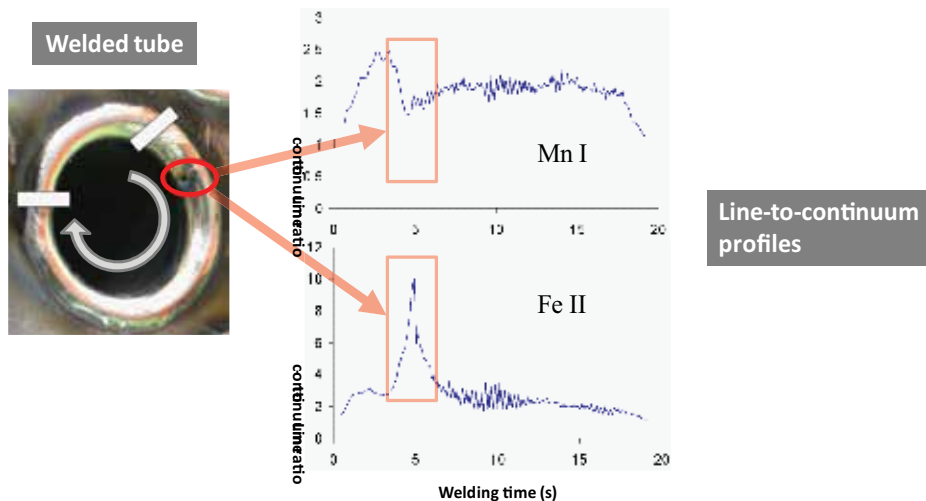


Fig. 13. Tracking of the line-to-continuum ratio for two selected wavelengths

### 5.3 RMS spectroscopic signal as a defect indicator

The real-time calculation of the Root Mean Square (RMS) of the captured spectrum is related to the process behaviour and the heat input, as explained in section 3.3. The capability of this technique to detect common defects has also been tested in field trials for the same welding process (Mirapeix et al., 2010).

In Figure 14, the resulting RMS profile for a defective weld seam is shown. To the left, a welded tube with a porosity (produced by including contamination in the tube-to-tubesheet interface) is shown. The RMS profile shows a sharp peak associated with this porosity. In addition, the rest of the profile shows periodic perturbations that also indicate that the contamination was also present at that section. In Figure 14 (right), a defect was simulated by disturbing the protection gas flow, thus provoking a clear defective section in the welded tube. There is a correlation between the correct seam (highlighted in green) of the analyzed section and the defective area (red), and their corresponding plasma RMS signals. While the former has an associated plasma RMS profile without perturbations, the latter shows rapid variations of the signal indicating the occurrence of a defect.

These experiments confirm that all the spectroscopic processing techniques are able to detect typical defects found in the TIG welding process of tubes for steam generators. Although the field trials have been limited to welding of INCONEL alloys, in-lab experiments with steel plates offer the same performance. In fact, one important advantage of the spectroscopic

method is that it is quite independent of the material and the process parameters, provided that the material to be welded is known and appropriate emission lines are selected *a priori*.

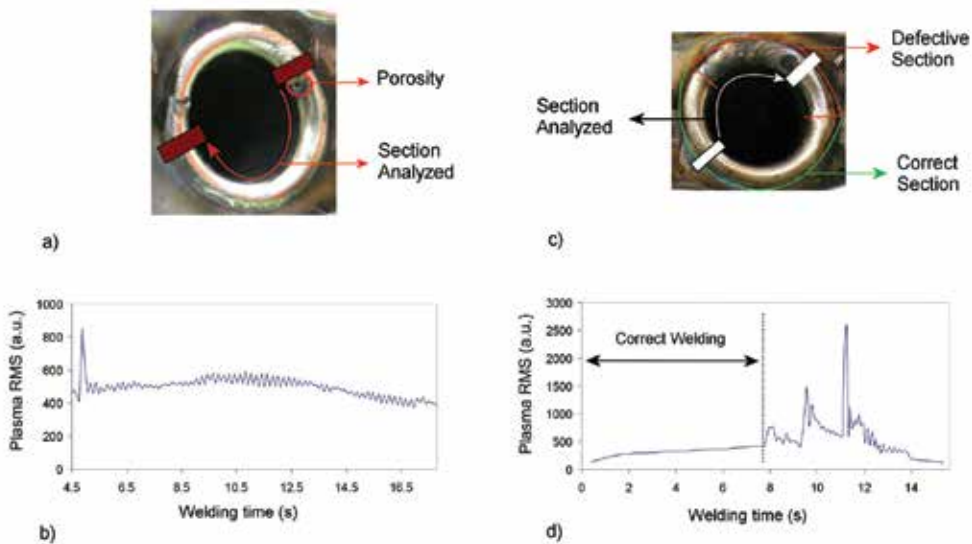


Fig. 14. The real-time calculation of the RMS value of the entire spectrum is able to detect some defects that other methods have trouble with

## 6. Conclusions and future works

An optical spectroscopic method for the monitoring of welding processes has been presented. It is based on the capture of the light emitted by thermal plasmas, which is characteristic of the arc and laser welding process. The spectroscopic analysis of the captured light provides rich information about the process behaviour, allowing to detect the occurrence of defects in the weld seam. Such a sensor system consists of an optical fibre to collect the light, a CCD spectrometer and a processing unit.

If the monitoring is to be performed in real-time, an important challenge for this approach is how to deal with the amount of generated data, because a typical scenario involves the capture of dozens of spectra per second, each one with thousands of spectral bands. For this reason, several spectroscopic processing techniques that try to optimize the real-time operation and defect-detection capabilities have been presented: an efficient computation of the electronic temperature profile, the analysis of the background radiation, the calculation of the RMS value of the spectrum, and the use of artificial neural networks (ANN) to automatically detect and classify defects from the captured spectra.

Those techniques have been validated in the manufacturing of large steam generators for nuclear power plants, in particular, the tube-to-tubesheet welding process. A solution for non-invasive capture of light in the orbital TIG welding process has been proposed, and the capabilities of each technique to detect typical defects in this process have been discussed. Up to some extent, all these methods were able not only to detect defects but to discriminate between them, a capability much needed if the monitoring system is to be extended not only to monitor but to control the process. With this approach, some defects could be prevented in real-time.

The later represent the main research line for future works: the use of ANN and other techniques to improve the classification of defects in this application and the investigation of ways to control the welding process in real-time once a possible defect is being generated.

## 7. Acknowledgment

The authors want to thank to J.J. Valdiande, F. Linares and F. Gómez-Estefanía for their valuable contributions to this work.

## 8. References

- Ancona, A.; Lugara, P.M.; Otonelli, F.; Catalano, I.M. (2004), A sensing torch for on-line monitoring of the gas tungsten arc welding process of steel pipes, *Meas. Sci. Tech.*, 15, 2412-2418, 0095-7023.
- Ancona, A.; Spagnolo, V.; Lugara, P.M.; Ferrara, M. (2001), Optical sensor for real-time monitoring of CO<sub>2</sub> laser welding process, *Applied Optics*, Vol. 40, N. 33, pp. 6019-6025, 0003-6935.
- Bae, K.-Y.; Lee, T.-H.; Ahn, K.-C. (2002), An optical sensing system for seam tracking and weld pool control in gas metal arc welding of steel pipe, *Journal of Materials Processing Technology*, 120 (1-3), pp. 458-465, 0924-0136.
- Bastiaans, G. J.; Mangold, R. A. (1985) The calculation of electron density and temperature in Ar spectroscopic plasmas from continuum and line spectra, *Spectrochim. Acta Part B Atomic Spectroscopy*, 40B 885-92, 0584-8547.
- Bebiano, D.; Alfaro, S. C. A. (2009), A Weld Defects Detection System Based on a Spectrometer, *Sensor*, 9, 2851-2861, 1424-8220.
- Cobo, A.; Mirapeix, J.; Conde, O.M.; García-Allende, P.B.; Madruga, F.J.; López-Higuera, J.M. (2007), Arc welding process control based on back face thermography: Application to the manufacturing of nuclear steam generators, *Proceedings of the of SPIE - The International Society for Optical Engineering*, v 6541, 2007, Thermosense XXIX, 0819466638, April, 2007, SPIE, Orlando (USA).
- Cobo, A.; Mirapeix, J.; Linares, F.; Piney, J. A.; Solana, D.; López-Higuera, J. M. (2007a), Spectroscopic Sensor System for Quality Assurance of the Tube-To-Tubesheet Welding Process in Nuclear Steam Generators, *IEEE Sensors Journal*, Vol. 7, No. 9, pp. 1219-1224,
- Dong, P. (2005) Residual stresses and distortions in welded structures: A perspective for engineering applications, *Science and Technology of Welding and Joining*, 10 (4), pp. 389-398, 1362-1718.
- Ferri, F.; Pudil, P.; Hatef, M.; Kittler, J. (1994), *Comparative study of techniques for large-scale feature selection. Pattern Recognition in Practice IV: Multiple Paradigms, Comparative Studies, and Hybrid Systems*; Gelsema, E.S. (Ed.), Kananl, L.N. (Ed.), Eds.; Elsevier Science: New York, ISBN 0444818928, NY, USA.
- García-Allende, P.B.; Mirapeix, J.; Conde, O.; Cobo, A.; López-Higuera, J.M. (2009), Defect detection in arc-welding processes by means of the line-to-continuum method and feature selection, *Sensors*, Vol. 9, No. 10, pp. 7753-7770, 1424-8220.
- García-Allende, P.B.; Mirapeix, J.; Conde, O.; Cobo, A.; López-Higuera, J.M. (2008), Arc-welding quality assurance by means of embedded fiber sensor and spectral

- processing combining feature selection and neural networks, *Sensors*, 8(10), 6496-6506, 1424-8220.
- García-Allende, P.B.; Mirapeix, J.; Conde, O.; Cobo, A.; López-Higuera, J.M. (2009a), Spectral processing technique based on feature selection and artificial neural networks for arc-welding quality monitoring, *NDT&E International*, 42, 56-63, 0963-8695.
- Griem, H. R. (1963), Validity of local thermal equilibrium in plasma spectroscopy, *Phys. Rev.*, Vol. 131, pp. 1170-6, 1050-2947.
- Gu, H.; Duley, W.W. (1996), Statistical approach to acoustic monitoring of laser welding, *J Phys D*, 29 556-60, 0022-3727.
- Li, L.; Brookfield, D.J.; Steen, W.M. (1996), Plasma charge sensor for in-process, non-contact monitoring of the laser welding process, *Measurement Science & Technology*, 7, pp. 615-26, 0957-0233.
- Mirapeix, J.; Cobo, A.; Fernández, S.; Cardoso, R.; López-Higuera, J.M. (2008), Spectroscopic analysis of the plasma continuum radiation for on-line arc-welding defect detection, *Journal of Physics D: Applied Physics*, Vol. 41, No. 13, 0022-3727.
- Mirapeix, J.; Cobo, A.; García-Allende, P.B.; Conde, O.; López-Higuera, J.M. (2010), Use of the plasma RMS signal for on-line welding quality monitoring, *Proceedings of the SPIE Photonics Europe*, Brussels, Belgium.
- Mirapeix, J.; Cobo, A.; Quintela, A.; López-Higuera, J.M. (2007a) , Embedded spectroscopic fiber sensor for on-line arc-welding analysis, *Applied Optics*, Vol. 46, No. 16, pp. 3125-3220, 1559-128X.
- Mirapeix, J.; García-Allende, P.B.; Cobo, A.; Conde, O.M.; López-Higuera, J.M. (2007), Real-time arc-welding defect detection and classification with principal component analysis and artificial neural networks, *NDT&E International*, 40, 315-323, 0963-8695.
- Mirapeix, JM; Cobo, A.; Jaúregui, C.; López-Higuera, J.M. (2006), Fast algorithm for spectral processing with application to on-line welding quality assurance, *Meas. Sci. Technol.* 17 2623, 0095-7023.
- Park, h.; Rhee, S.; Kim, D. (2001), Fuzzy pattern recognition based system for monitoring laser weld quality, *Measurement Science and Technology*, Vol. 12, N. 8, pp. 1318-1324, 0957-0233.
- Poueyo-Verwaerde, A.; Fabbro, R.; Deshors, G.; De Frutos, A.M.; Orza, J.M. (1993), Experimental study of laser-induced plasma in welding conditions with continuous CO<sub>2</sub>, *Journal of Applied Physics*, 74 (9), pp. 5773-5780, 0021-8979.
- Robinson, AW; Gardner, P; Stampfl, APJ; Martin R and Nyberg, G (1998), Error analysis in the fitting of photoemission lineshapes using the Levenberg-Marquardt method, *Journal of Electron Spectroscopy and Related Phenomena* 94 97-105, 0368-2048.
- Wang, Y.; Zhao, P. (2001), Noncontact acoustic analysis monitoring of plasma arc welding, *International Journal of Pressure Vessels and Piping*, 78, 43-47, 0308-0161.
- Wikle III, H.C.; Kottilingam, S.; Zee, R.H.; Chin, B.A. (2001), Infrared sensing techniques for penetration depth control of the submerged arc welding process, *Journal of Materials Processing Technology*, 113, 228-33, 0924-0136.
- Workman Jr., J.; Springsteen, A.W. (1998) *Applied Spectroscopy: A compact reference for Practitioners*, London Academia Press Limited, ISBN 0127640703, London.
- Wu, C.S.; Ushio M. & Tanaka M. (1997), Analysis of the TIG welding arc behaviour, *Computational Materials Science*, Vol. 7, pp. 308-14, 0927-0256.

## **Part 3**

### **Heat Transfer and Coolant Flow Processes**



# Countercurrent Flow in a PWR Hot Leg under Reflux Condensation

Noritoshi Minami<sup>1</sup>, Michio Murase<sup>2</sup> and Akio Tomiyama<sup>3</sup>

<sup>1</sup>*The Kansai Electric Power Company, Inc.,*

<sup>2</sup>*Institute of Nuclear Safety System, Inc.,*

<sup>3</sup>*Graduate School of Engineering, Kobe University  
Japan*

## 1. Introduction

Nuclear power plants periodically shut down for plant maintenance and refueling. During a pressurized water reactor (PWR) plant outage, decay heat is removed by residual heat removal (RHR) systems. The reactor coolant level temporarily needs to be kept around the middle of the primary loop to inspect the steam generator (SG) tubes and so on. This operation is called “mid-loop operation”. In some plants, a loss of RHR event occurred during the mid-loop operation (USNRC, 1987, USNRC, 1990). Probabilistic safety assessment (PSA) studies under plant shutdown conditions have been performed and they confirmed that the loss of RHR cooling during the mid-loop operation is a relatively high risk event for PWR plants. One of the effective methods to cool the reactor core in this event is reflux condensation, in which water condensed in a SG flows into the reactor core through a hot leg and cools down the reactor core as shown in **Fig. 1**. In the reflux condensation, steam generated in the core and water condensed in the SG form a countercurrent flow in the hot leg. This phenomenon limits water into the reactor vessel and affects the performance of core cooling.

System computer codes, as typified by RELAP, employ a simplified model to a certain extent to calculate efficiency, however, the hot leg consists of a horizontal section, elbow, and inclined section. Hence it is unclear whether the countercurrent flow in the hot leg can be well predicted or not. To improve reliability of the transient analysis, we need to understand and model the countercurrent flow in the hot leg.

A number of experiments have been made about the countercurrent flow in the hot leg (Richter et al., 1978, Ohnuki, 1986, Ohnuki et al., 1988, Mayinger et al., 1993, Wongwises, 1996, Navarro, 2005), observations of detailed flow patterns in the hot leg, however, have not been reported. On the other hand, numerical simulations are a realistic way to evaluate the flow, because it is difficult to check the flow pattern in the actual PWR hot leg. Few examples of numerical simulations have been reported, however.

Our objectives in this study were to clarify the flow pattern and dominant factors of the countercurrent flow and to develop the flow model which improves the reliability of the transient analysis. At first, we carried out air-water experiments with a scale model of the actual PWR hot leg. We used two types of small scale PWR hot legs. One was a 1/5th scale

rectangular duct (Minami et al., 2008a), and the other was a 1/15th scale circular pipe (Minami et al., 2010a). Then we carried out numerical simulations of these small scale experiments to investigate flow pattern and CCFL characteristics (Minami et al., 2008b and 2010b). We used a three-dimensional two-fluid model to evaluate the capability of predicting countercurrent flow in the hot leg.

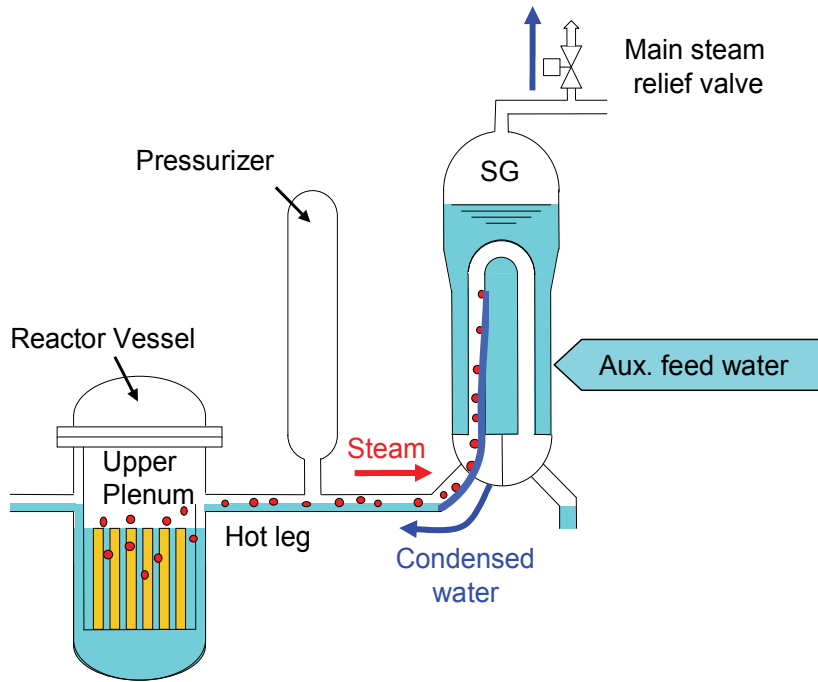


Fig. 1. Schematic view of reflux condensation

## 2. Experiments

The gas-liquid two-phase flow is complex because the gas-liquid interface takes various geometric configurations and it changes with time. It is, therefore, important to grasp the interfacial behavior. Hence we carried out air-water experiments with a rectangular duct. We chose the rectangular duct because observing the countercurrent flow and following the interface are easy in this duct. Then we carried out experiments with a circular pipe having a configuration geometrically similar to the actual hot leg.

### 2.1 Experimental setup

**Figure 2** shows schematic view of the experimental setup. It consists of the upper tank, which corresponds to the inlet plenum of the SG, the hot leg, the lower tank, which corresponds to the upper plenum of the reactor vessel, the reservoir, and the air and water supply systems. Tap water at room temperature is pumped to the upper tank through a flow meter. Air is supplied from a compressor and flows into the lower tank through a regulator and a flow meter. When CCFL occurs in the hot leg, some of the water overflows the upper tank and drains into the reservoir.



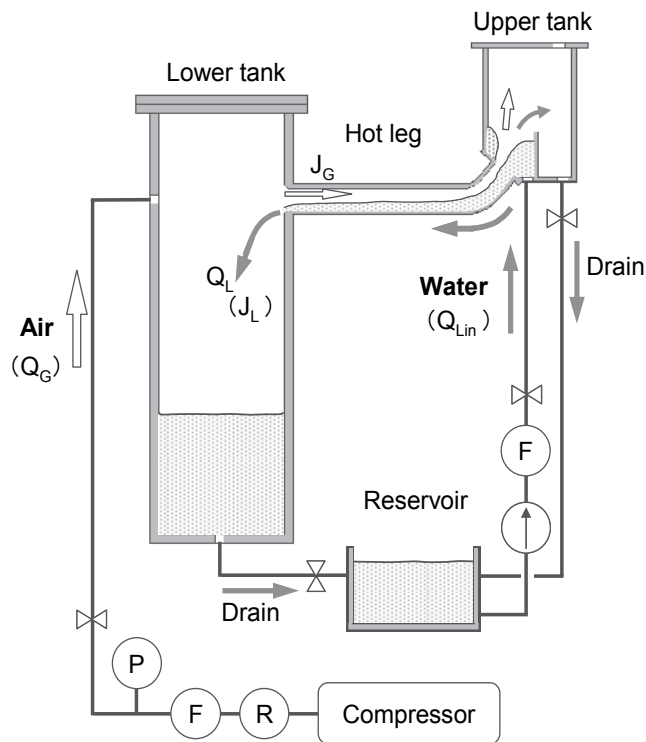


Fig. 2. Schematic view of experimental setup

### 2.1.1 1/5-scale rectangular duct

Figure 3 shows the test section of the 1/5-scale rectangular duct, which is made of transparent acrylic resin to allow easy observation of countercurrent flow. The height is about 1/5th that of the pipe diameter of an actual PWR hot leg. The inclination of the inclined pipe is  $50^\circ$ .

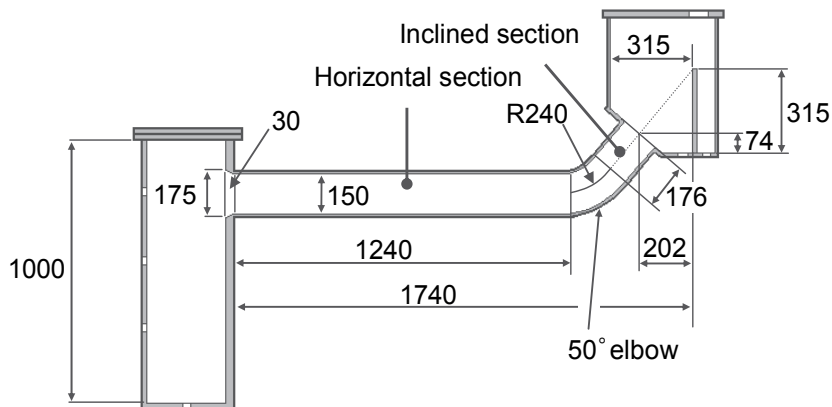


Fig. 3. Test section of 1/5th rectangular duct (unit: mm)



## 2.3 Experimental results of 1/5th rectangular duct

### 2.3.1 Flow patterns

Flow patterns could be classified into the following three regimes.

#### (A) Stratified flow

At low  $J_G$ , the gas and liquid phase was stratified in all sections of the hot leg. Few waves were observed in the horizontal section. **Figures 5-7** show typical images of the stratified flows in the horizontal, elbow and inclined sections, respectively. Injected water formed a thin water film at the bottom of the flow channel and sped up in the inclined and elbow sections. Water slowed down in the horizontal section and a hydraulic jump occurred due to the transition from supercritical flow to subcritical flow. The onset of a hydraulic jump in the flow channel depended on  $Q_{Lin}$  and  $J_G$ . At high  $J_G$ , the hydraulic jump appeared near the elbow. Under the stratified condition in this study, the hydraulic jump always appeared.

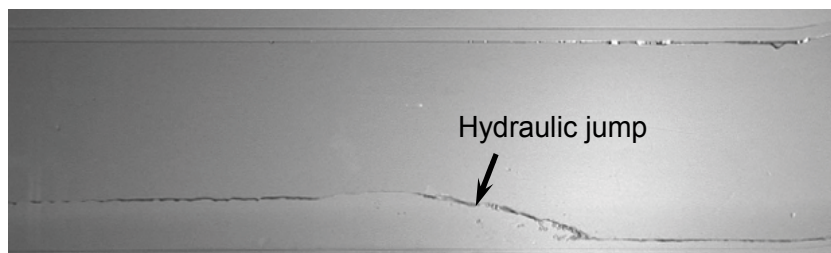


Fig. 5. Typical image of stratified flow in the horizontal section ( $Q_{Lin}=5$  l/min,  $J_G=4.3$  m/s)

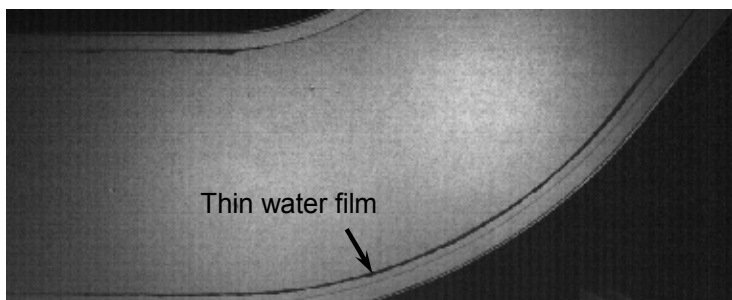


Fig. 6. Typical image of stratified flow in the elbow section ( $Q_{Lin}=5$  l/min,  $J_G=4.3$  m/s)

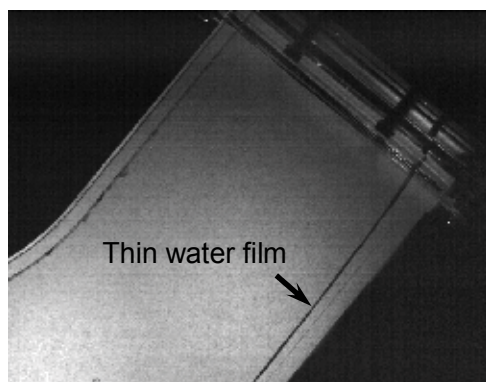


Fig. 7. Typical image of stratified flow in the inclined section ( $Q_{Lin}=5$  l/min,  $J_G=4.3$  m/s)

### (B) Wavy flow

As  $J_G$  increased, the gas-liquid interface started to ruffle, and the flow pattern transitioned from stratified to wavy flow.

**Figures 8(I) and (II)** show images of wavy flows in the horizontal section. The onset point of wave depended on  $Q_{Lin}$ . At low  $Q_{Lin}$ , the wave appeared near the air inlet, then grew up and transferred toward the elbow section, as shown in Fig. 8(I). On the other hand, at high  $Q_{Lin}$ , an unstable interface formed in the horizontal section near the elbow, and disturbance wave occurred there, as shown in Fig. 8(II). Under the condition that the wavy flow formed in the horizontal section, the wavy flow also formed in the elbow section due to inflow of wave generated in the horizontal section. In the bottom region, a circulation flow of water with bubble and droplet formed. In the upper region of the elbow, it was stratified flow with a thin water film (in other words, the wavy flow was not observed in the inclined section).

**Figure 9** shows the typical image of wavy flows in the elbow section.

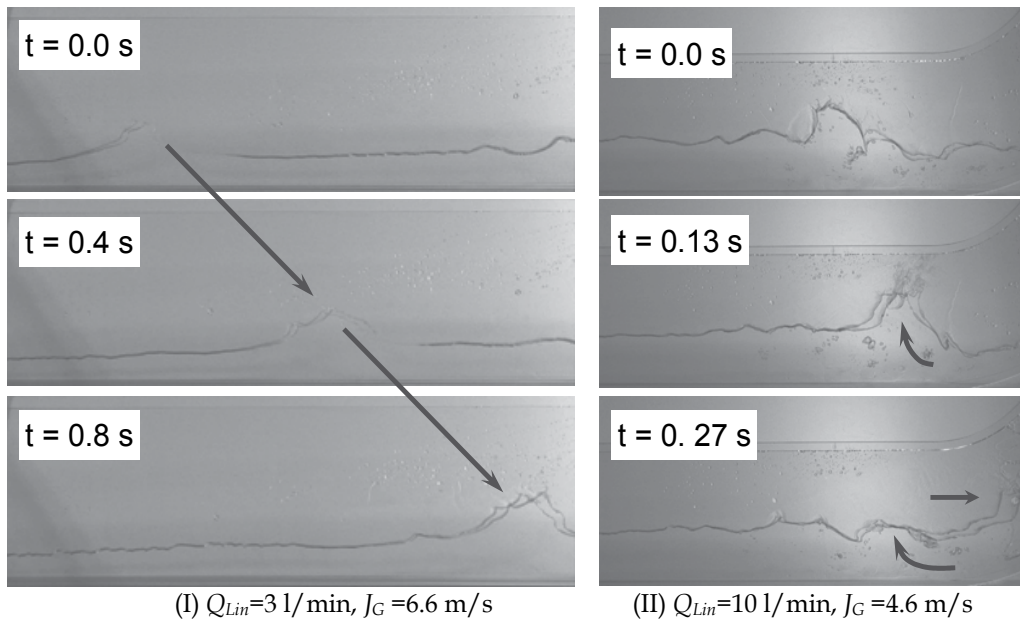


Fig. 8. Typical images of wavy flow in the horizontal section

### (C) Wavy-mist flow

With further increase in  $J_G$ , air velocity became high near the wave peak which finally broke up. Some injected water returned to the upper tank which overflowed. This flow pattern is referred to as wavy-mist flow. **Figure 10** shows a typical image of wavy-mist flow in the horizontal section. For wavy-mist flow, mist occurred at the elbow side while wavy flow occurred at the lower tank side. In the elbow and inclined sections, the wavy-mist flow also formed due to inflow of mist generated in the horizontal section. **Figures 11 and 12** show typical images of wavy-mist flow in the elbow and inclined sections, respectively. A circulation flow with large disturbance waves formed in the liquid phase when the large wave occurred in the horizontal section. The circulation flow with large disturbance waves involved bubbles in the water flow.

When  $J_G$  was more than 10.8 m/s, zero water penetration with no flow to the lower tank was achieved. At that time wavy-mist flow formed near the elbow, while wavy flow formed near the lower tank. In addition, a liquid phase leading edge moved to the elbow side with the increase in the air velocity. **Figure 13** shows a typical image.

When  $J_G$  was more than 21.3 m/s, no water was in the horizontal section, as shown in **Fig. 14**.

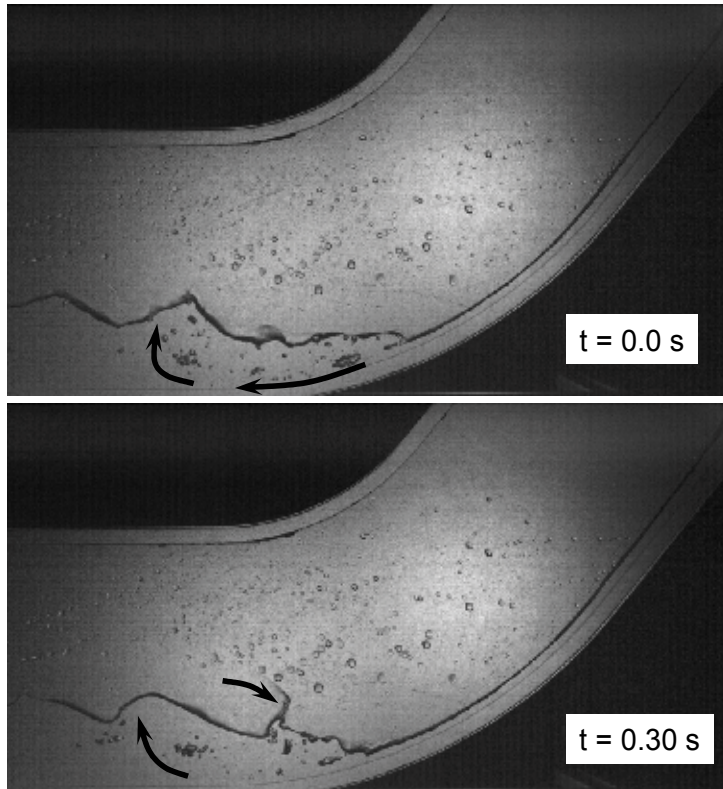


Fig. 9. Typical images of wavy flow in the elbow section ( $Q_{Lin}=5$  l/min,  $J_G=6.3$  m/s)

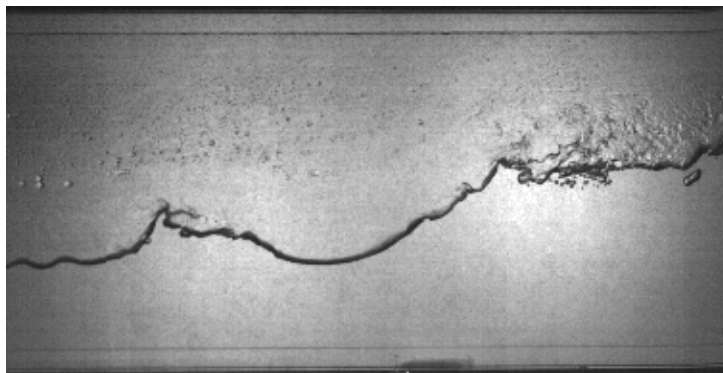


Fig. 10. Typical image of wavy-mist flow in the horizontal section ( $Q_{Lin}=5$  l/min,  $J_G=9.0$  m/s)



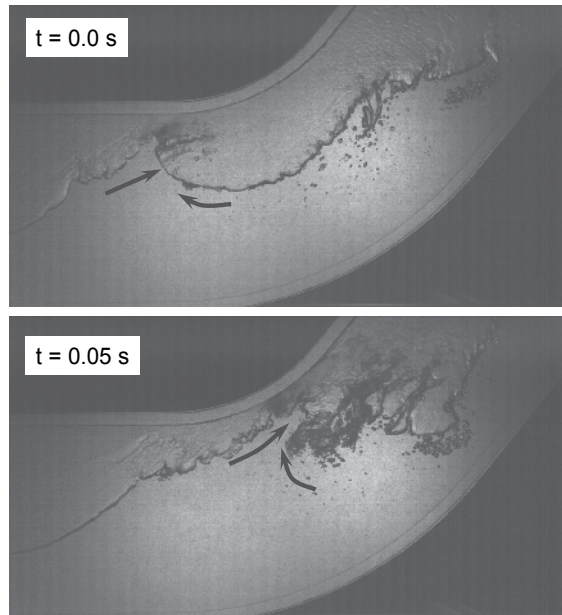


Fig. 11. Typical images of wavy-mist flow in the elbow section ( $Q_{Lin}=5 \text{ l/min}$ ,  $J_G=9.0 \text{ m/s}$ )

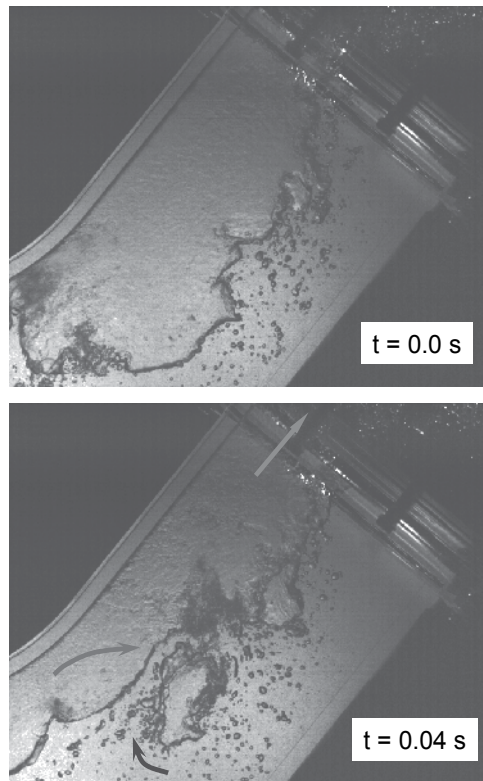


Fig. 12. Typical images of wavy-mist flow in the inclined section ( $Q_{Lin}=5 \text{ l/min}$ ,  $J_G=9.0 \text{ m/s}$ )

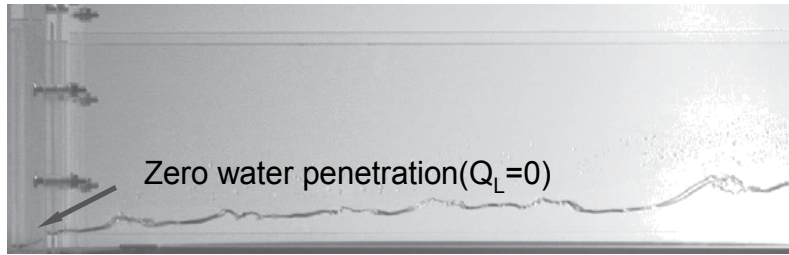


Fig. 13. Typical image of zero water penetration in the horizontal section ( $Q_{Lin}=5$  l/min,  $J_G=10.8$  m/s)

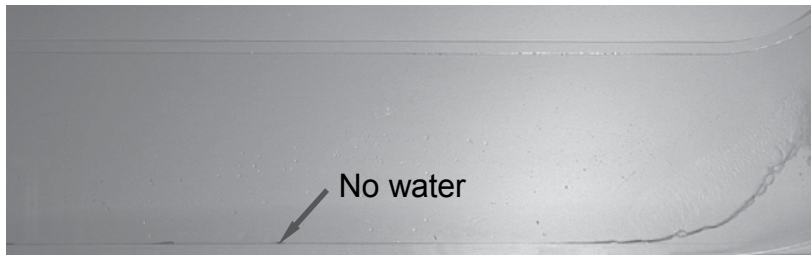


Fig. 14. Typical image of dry condition in the horizontal section ( $Q_{Lin}=5$  l/min,  $J_G=21.3$  m/s)

### 2.3.2 Flow pattern map

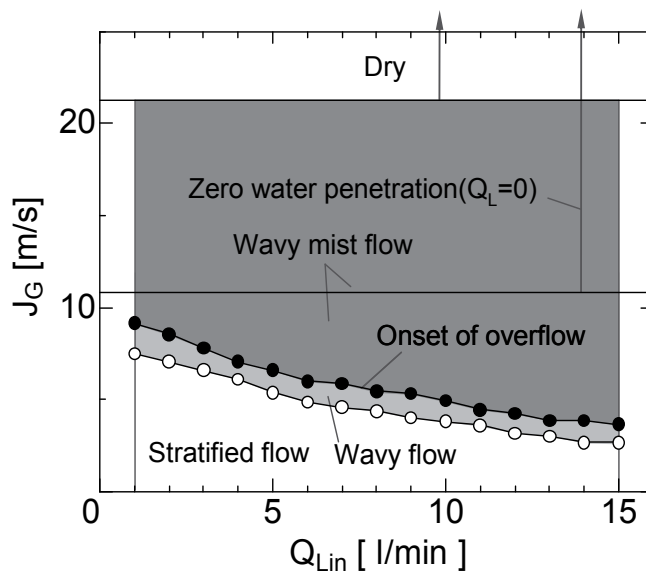
Figure 15 shows the flow pattern maps in the horizontal, elbow and inclined sections, respectively. In the horizontal section, as  $J_G$  increased for a given  $Q_{Lin}$ , the flow pattern changed from stratified flow to wavy flow, and then wavy to wavy-mist flow. After transition to wavy-mist flow, water flow into the lower tank through the horizontal section started to be restricted. Further increase in  $J_G$  caused zero water penetration at  $J_G=10.8$  m/s and finally no water was present in the horizontal section for  $J_G>21.3$  m/s. Flow pattern transition from stratified flow to wavy flow and wavy to wavy-mist flow occurred at low  $J_G$  condition when  $Q_{Lin}$  was large. This was because higher  $Q_{Lin}$  led to a large water depth and narrow air flow area, and local air velocity increased. On the other hand,  $J_G$  at the transition to zero water penetration did not depend on  $Q_{Lin}$ .

In the elbow section, as  $J_G$  increased, the transition to wavy flow began due to the intrusion of wavy flow generated in the horizontal section. Therefore,  $J_G$  at the transition was almost the same as that in the horizontal section. Further increase in  $J_G$  caused flow pattern transition to wavy-mist flow due to droplets breaking from the peaks of the waves.

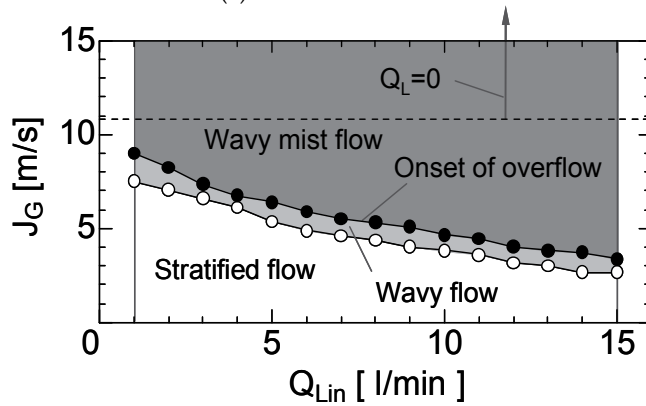
In the inclined section, when water accumulated in the upper tank and overflow occurred, the flow pattern changed from stratified flow to wavy-mist flow without the appearance of wavy flow. Flow patterns in the elbow and inclined sections were strongly affected by those in the horizontal section.

### 2.3.3 CCFL characteristics

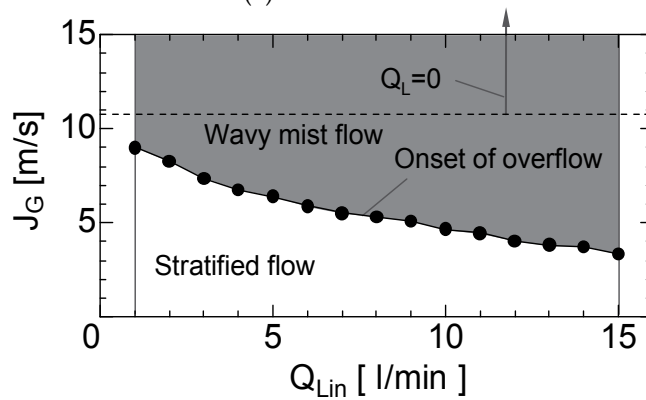
Figure 16 plots experimental results for the relationship between  $J_G^{*0.5}$  and  $J_L^{*0.5}$ . In this figure, the duct height of this study was used for  $D$  in Eq. (2). There was a linear relationship between  $J_G^{*0.5}$  and  $J_L^{*0.5}$ . CCFL characteristics did not depend on  $Q_{Lin}$ , and CCFL constants were  $m=0.67$  and  $C=0.56$  in Eq. (1).



(a) Horizontal section



(b) Elbow section



(c) Inclined section

Fig. 15. Flow pattern maps



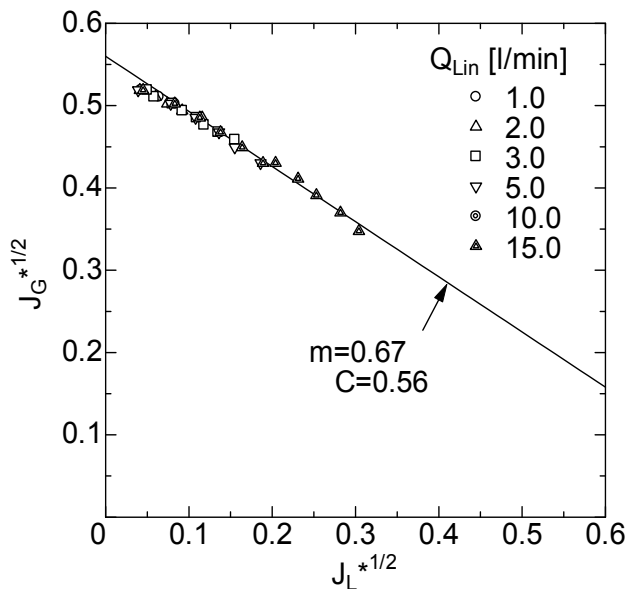


Fig. 16. CCFL characteristics

### 2.3.4 Relationship between CCFL characteristics and flow pattern transition

Figure 17 shows the relationship between CCFL characteristics and flow pattern transitions. The flow pattern transitioned from stratified to wavy flow and wavy to wavy-mist flow showed a linear relationship. The transition line from wavy flow to wavy-mist flow agreed well with the CCFL correlation.

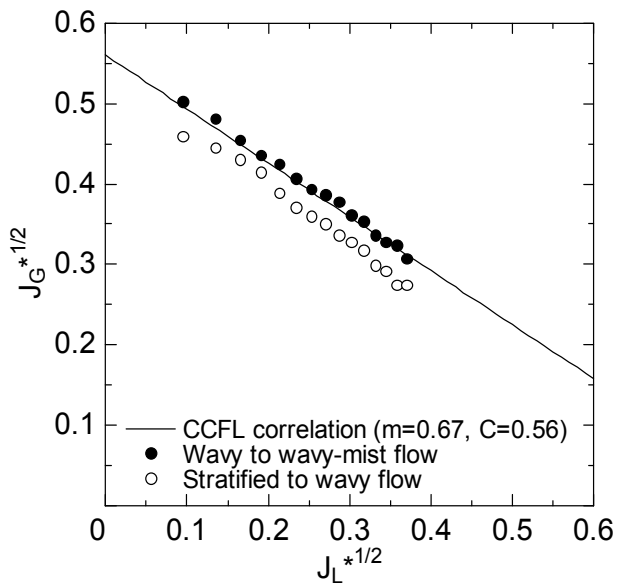


Fig. 17. Relationship between CCFL and flow pattern transitions

## 2.4 Experimental results of 1/15th circular pipe

### 2.4.1 Flow patterns

Flow patterns could be classified into the following four regimes.

#### (A) Stratified flow

At low  $J_G$ , the gas and liquid phases were separated in all sections of the hot leg as shown in **Fig. 18**. In this regime, supplied water was not limited and all the water flowed into the lower tank. The hydraulic jump observed in the rectangular test was not observed. This should be considered due to the water not being enough acceleration to achieve supercritical flow.

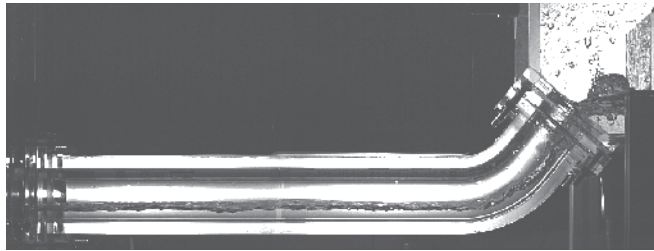


Fig. 18. Stratified flow  $Q_{Lin}=20$  l/min,  $J_G=4.3$  m/s (increasing  $J_G$ )

#### (B) Wavy(+) flow

As  $J_G$  increased, the supplied water accumulated in the upper tank and covered the junction of the hot leg and the upper tank. The air penetrated the liquid phase intermittently. Hence the gas-liquid interface fluctuated at the junction, and some of the supplied water flowed back into the reservoir, that is, CCFL took place at the upper end of the inclined section. In this condition, waves that formed in all sections of the hot leg were caused by this fluctuation. Taking the direction from the upper tank to the lower tank as the positive direction, then the sign of the wave velocity is positive. This flow pattern is referred to as wavy(+) flow. A typical image of this condition is shown in **Fig. 19**.

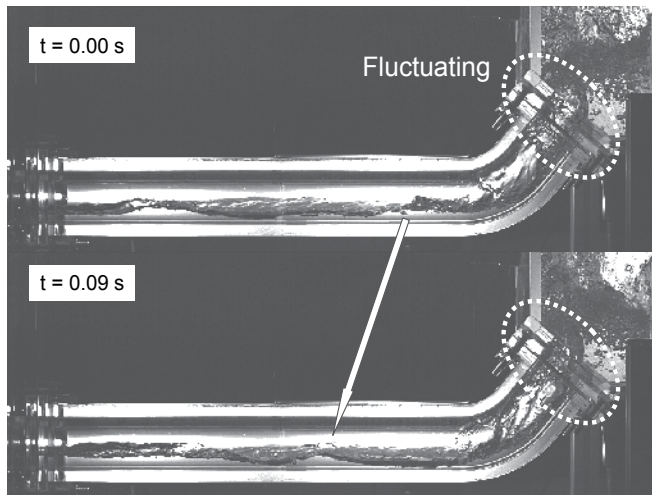


Fig. 19. Wavy(+) flow  $Q_{Lin}=20$  l/min,  $J_G=4.8$  m/s (increasing  $J_G$ )

### (C) Wavy(-) flow

Further increase in  $J_G$  caused flow disturbance in the hot leg. When wave height was high, the flow pattern in the horizontal section immediately changed to wavy flow with a negative wave velocity. This flow pattern is referred to as wavy(-) flow. **Figure 20** shows a typical image. A mist occurred in the elbow side in the horizontal section. In the elbow and inclined section, annular-mist flow, in which the liquid phase reached the upper wall of the pipe and entrained upward, was observed. This was due to the intrusion of the waves with breaking of droplets generated in the horizontal section. Circulation of water with bubbles and droplets was formed. The flow in the elbow and the inclined section strongly fluctuated.

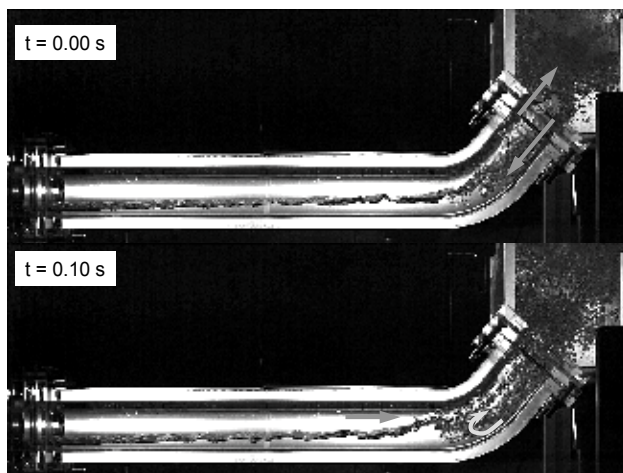


Fig. 20. Wavy(-) flow  $Q_{Lin}=20$  l/min,  $J_G=6.5$  m/s (increasing  $J_G$ )

### (D) Oscillatory flow

As  $J_G$  decreased from the negative wavy flow condition, the injected air did not penetrate the liquid phase in the upper tank and oscillatory flow (**Fig. 21**) was observed. The flow patterns in the elbow and the inclined section were also oscillatory flow.

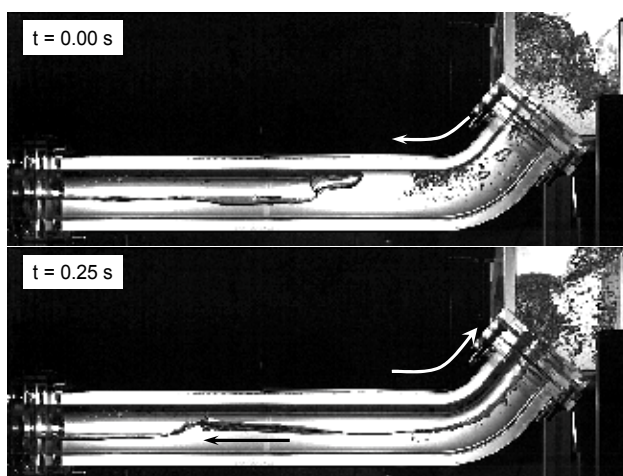


Fig. 21. Oscillatory flow  $Q_{Lin}=20$  l/min,  $J_G=0.65$  m/s (decreasing  $J_G$ )

### 2.4.2 Flow pattern map

Flow pattern maps obtained by increasing  $J_G$  and decreasing  $J_G$  are shown in **Figs. 22(a)** and **(b)**, respectively. There was a large difference in the two maps. When  $Q_{Lin}$  was high ( $\geq 15$  l/min), the junction of the hot leg and the upper tank was covered with the air-water mixture as  $J_G$  increased. Thus the flow pattern transitioned from stratified flow to wavy(+) flow. Further increase in  $J_G$  caused the flow pattern transition to wavy(-) flow in the horizontal section. On the other hand, when  $Q_{Lin}$  was low ( $< 15$  l/min), air and water were separated at the junction of the hot leg and the upper tank. Hence the stratified flow was kept for  $J_G < 8$  m/s. At  $J_G = 8$  m/s, the flow pattern directly transitioned from stratified flow to wavy(-) flow in the horizontal section and to annular-mist flow in the elbow and inclined section.

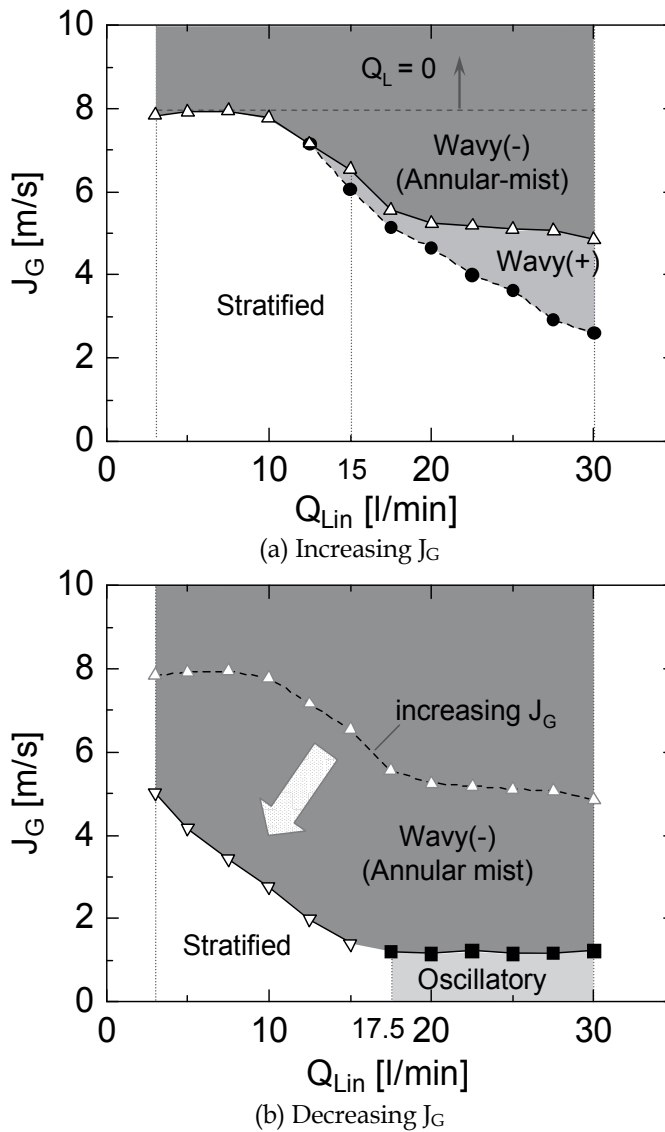


Fig. 22. Flow pattern maps

In this condition, water ceased to flow into the lower tank. The flow pattern transition to annular-mist flow took place simultaneously with the flow pattern transition to wavy(-) flow in the horizontal section. This was due to the intrusion of waves generated in the horizontal section into the elbow. Flow patterns in the elbow and the inclined section were, therefore, strongly affected by those in the horizontal section. The transition from wavy(-) to stratified flows when decreasing  $J_G$  took place at a lower  $J_G$  than the transition from stratified to wavy flows when increasing  $J_G$ . That is, there was a hysteresis in the flow pattern transition. In the case of  $Q_{Lin} \geq 17.5$  l/min, the flow pattern in the whole hot leg transitioned to oscillatory flow as  $J_G$  decreased. It should be noted that (a) the amount of water accumulation in the upper tank has nothing to do with the hysteresis appearing in the hot leg, and (b) the same kind of hysteresis in flow patterns has also been observed in countercurrent flows in a vertical pipe (Hewitt & Wallis, 1963).

### 2.4.3 CCFL characteristics

**Figure 23(a)** shows the CCFL characteristics at  $Q_{Lin} = 10, 20$  and  $30$  l/min. The CCFL characteristics obtained by increasing  $J_G^*$  differed from those obtained by decreasing  $J_G^*$ . In the case of  $Q_{Lin} = 20$  l/min (as the base case), as  $J_G$  gradually increased, CCFL first occurred at the upper end of the inclined section and the flow pattern transitioned to wavy(+) flow. As  $J_G^*$  increased, the flow pattern in the horizontal section transitioned from wavy(+) to wavy(-) flows. In this condition, CCFL occurred in the horizontal section. When this transition occurred,  $J_L^*$  decreased abruptly by a slight increase in  $J_G^*$ . When the water height was high due to overlapping of these waves, waves were pushed back toward the upward direction (Fig. 23(b)), and the flow pattern transitioned to wavy(-) flow.

When  $J_G^*$  decreased, the flow remained as wavy(-) flow. When the flow pattern in the horizontal section was wavy(-) flow, CCFL characteristics showed a linear relationship. Though the values of  $J_G^{*1/2}$  in Figs. 23(a)(I) and (II) were the same, the flow in (II) was more restricted than that in (I). This was due to the difference in the flow pattern in the horizontal section. Hence, the CCFL characteristics were closely related with the flow patterns.

In the case of  $Q_{Lin} = 10$  l/min, as  $J_G$  increased, the flow pattern in the horizontal section suddenly transitioned from stratified to wavy flow. A typical image of this transition is shown in Fig. 23(c). This transition was due to the wave generated in the gas inlet. In this case, wavy(+) flow did not appear because the water did not cover the junction at any  $J_G$ . After this transition, no water flowed into the lower tank at  $J_G^{*1/2} = 0.62$ . The CCFL characteristics obtained by decreasing  $J_G$  agreed well with those in the case of  $Q_{Lin} = 20$  l/min.

In the case of  $Q_{Lin} = 30$  l/min, the junction of the hot leg and the upper tank was covered with the supplied water at  $J_G^{*1/2} = 0$ . For  $J_G^{*1/2} \geq 0.3$ , CCFL took place at the upper end of the inclined section, for which the CCFL characteristics followed the linear relationship between  $J_G^{*1/2}$  and  $J_L^{*1/2}$ .  $J_G^{*1/2}$  was decreased from 0.6 to 0.2, the flow pattern in the horizontal section was wavy(-) flow and the CCFL characteristics agreed well with those in the case of  $Q_{Lin} = 20$ . For  $J_G^* < 0.2$ , the flow pattern in the horizontal section transitioned from wavy(-) to oscillatory flow, and the CCFL characteristics at  $J_G^{*1/2} = 0.16$  disagreed with the Wallis correlation.

The CCFL characteristics obtained by increasing  $J_G$  depended on  $Q_{Lin}$ . This was because CCFL at the junction was affected by the water level in the upper tank which depends on  $Q_{Lin}$ . It should be noted that the water level in the upper tank might relate to the dimensions of the inlet plenum of the upper tank. On the other hand, the CCFL characteristics obtained

by decreasing  $J_G$  did not depend on  $Q_{Lin}$ . This was because CCFL occurred at the horizontal section and it depended not on  $Q_{Lin}$  but on  $J_L$ .

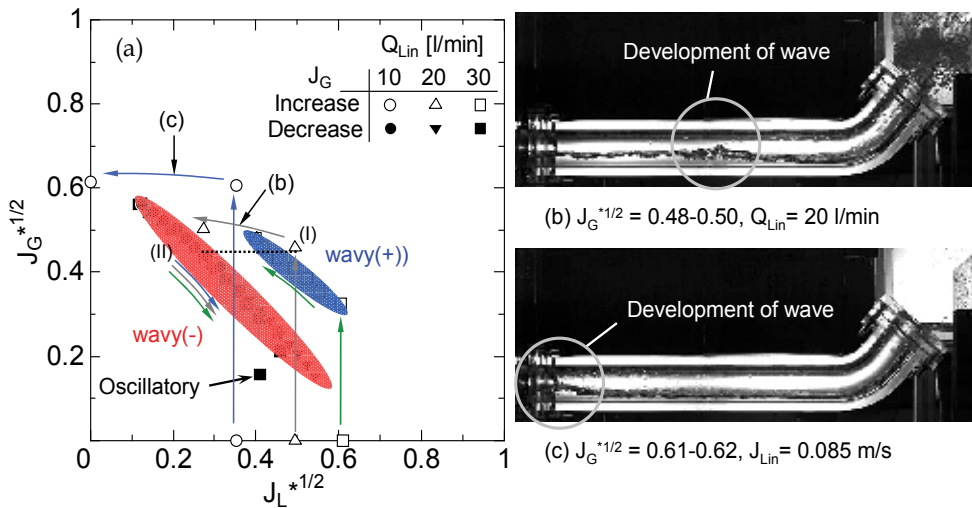


Fig. 23. Relationship between CCFL characteristics and flow patterns

**Figure 24** shows CCFL characteristics in the case with decreasing  $J_G$ . The boundary between wavy(-) flow and stratified flow agreed well with the CCFL characteristics. This result indicated that CCFL characteristics were closely related with the flow patterns in the hot leg and that the onset of deflooding or the flow pattern transition line agreed with the CCFL line.

Figure 24 also compares CCFL data in the literature (Ohnuki, 1986, Mayinger et al., 1993) and the present study. Ohnuki (1986) examined the countercurrent flow using air-water and saturated steam-water systems with a 0.6 m length 45° inclined pipe and a 0.3 m length horizontal pipe with the inner diameter of 0.051 m, and a 0.6 m length 45° inclined pipe and a 0.4 m length horizontal pipe with the inner diameter of 0.076 m, in order to investigate the effects of length-to-diameter ratio in the horizontal pipe, the shape of the upper exit of the inclined riser, and the length of the inclined riser. Mayinger (1993) used a full-scale apparatus simulating the hot leg. Test conditions in these studies are summarized in Table 1. Though all the hot legs were of different sizes and fluid properties, these data were very close together.

	Inner diameter[m]	Length of the horizontal section [m]	Angle of elbow [deg]	Working fluid
This study	0.050	0.43	50	Air-water
Mayinger et al.(1993)	0.75	7.20	50	Steam-water
Ohnuki (1986)	(1) 0.051	0.30	45	Air-water
	(2) 0.051	0.30	45	Steam-water
	(3) 0.076	0.40	45	Air-water
	(4) 0.076	0.40	45	Steam-water

Table 1. Test conditions

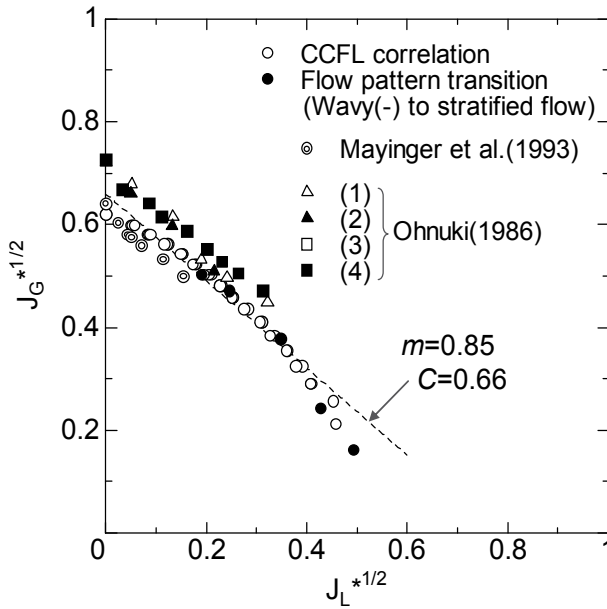


Fig. 24. Comparison with previous CCFL data

### 3. Numerical calculations

We carried out three-dimensional calculations of the scale model of the PWR hot legs mentioned in section 2 to examine the feasibility of predicting these complicated flow patterns and CCFL characteristics in the hot leg using a standard two-fluid model.

#### 3.1 Numerical method

In numerical calculations, we adopted the two-fluid model and the  $k-\varepsilon$  model in the CFD code, FLUENT6.3.26. Correlations for interfacial friction coefficients are required when applying the code to a two-phase flow of concern. The interfacial friction force  $F_i$  in the momentum equation is defined by:

$$F_i = \frac{1}{2} C_D a_i \rho_G |u_r| u_r, \quad (3)$$

where  $u_r$  is the relative velocity between the gas and liquid phases, and  $a_i$  is the interfacial area concentration. The interfacial friction coefficient,  $C_D a_i$ , applicable to three-dimensional simulations has not been established. We therefore tested various combinations of correlations developed for a one-dimensional two-fluid model. Then we selected a combination of correlations which gave the best agreement with the experiments. The resulting combination is given by

$$C_D a_i = \min \left[ (C_D a_i)_B, \max \{ (C_D a_i)_S, (C_D a_i)_A \} \right], \quad (4)$$

$$(C_D a_i)_B = 2\alpha(1-\alpha)g / V_{Gf}^2, \quad (5)$$

$$(C_D a_i)_S = 9.8(1 - \alpha)^3 \left( \frac{4.5\alpha}{D_h} \right), \quad (6)$$

$$(C_D a_i)_A = 0.02 \{1 + 75(1 - \alpha)\} \alpha^{0.5} / D_h, \quad (7)$$

where  $\alpha$  is the void fraction,  $V_{GJ}$  is the drift velocity of the gas phase and  $D_h$  is the hydraulic diameter. Equations (5), (6) and (7) are for low (Minato et al., 2000), intermediate (Ishii & Mishima, 1984) and high (Wallis, 1969) void fraction regions, respectively. The drift velocity is given by (Kataoka et al., 1987):

$$V_{GJ} = \{1.4 - 0.4 \exp(-10\alpha)\} (D_h^*)^{0.125} \left\{ \frac{g\sigma(\rho_L - \rho_G)}{\rho_L^2} \right\}^{1/4} \quad (8)$$

where

$$D_h^* = D_h \left\{ \frac{g(\rho_L - \rho_G)}{\sigma} \right\}^{1/2}, \quad (9)$$

and  $\sigma$  is the surface tension. The following simplified form of Eq. (8) was used in the present simulations:

$$V_{GJ} = 1.4 (D_h^*)^{0.125} \left\{ \frac{g\sigma(\rho_L - \rho_G)}{\rho_L^2} \right\}^{1/4}. \quad (10)$$

### 3.2 Computational grid

We carried out three-dimensional simulations using a computational domain including the lower and upper tanks to avoid uncertainties in the inlet and outlet boundary conditions and to accurately evaluate the wall friction.

#### 3.2.1 1/5th-scale rectangular duct

**Figure 25** shows the computational grid. Air was supplied into the lower tank through the air-inlet pipe at a constant velocity. Water was supplied from the bottom of the upper tank at a constant velocity.  $J_L$  was calculated from the increasing rate of the mass of water in the lower tank. When CCFL occurred in the hot leg, some water overflowed the upper tank and flowed out through the mixture outlet. The pressure at the mixture outlet was set constant. The hot leg was a rectangular cross section (10 mm wide and 150 mm high). The height was about 1/5th of the pipe diameter of an actual PWR hot leg. The inclination of the inclined pipe was 50°. The geometry was the same as the experiment for the rectangular duct. Hence the total number of cells was about 140,000.

#### 3.2.2 1/15th-scale circular pipe

**Figure 26** shows the computational grid. The size was the same as that of the 1/15-scale model. Air was supplied into the lower tank through the air-inlet pipe at a constant velocity. Water was supplied from the bottom of the upper tank at a constant velocity. Unlike the tests, water was supplied from all over the bottom to minimize external influence.





**Figure 27** shows the predicted flow pattern after achieving the quasi-steady state. Flooding occurred in the hot leg. The liquid phase dropped from the upper tank and accumulated near the elbow in the horizontal section. Then the wave formed and was blown up to the upper tank. The predicted flow pattern could reproduce the wavy-mist flow in the experiments. To predict the flow pattern in the experiment, it is important to simulate the hot leg including the upper tank and the lower tank faithfully.

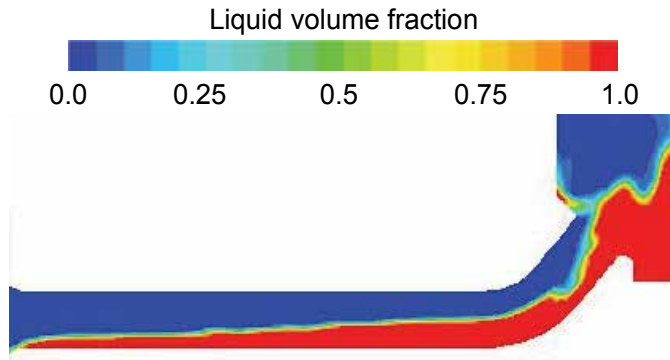


Fig. 27. Predicted flow pattern ( $Q_{Lin} = 36$  l/min,  $J_G = 9.5$  m/s)

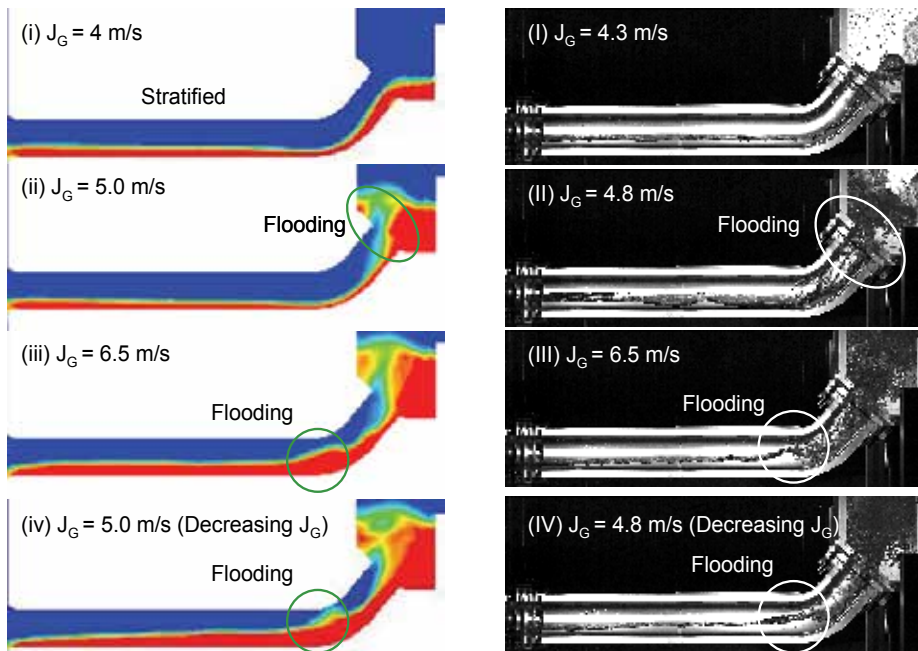


Fig. 28. Comparison between the predicted and measured flow patterns ( $Q_{Lin} = 20$  l/min)

### 3.3.2 1/15th-scale circular pipe

**Figure 28** compares predicted and measured flow patterns at  $Q_{Lin} = 20$  l/min. In the simulation, at low  $J_G$ , a stratified flow was calculated in all sections of the hot leg as shown

in (i). As  $J_G$  increased, fluctuation of flow took place at the junction of the hot leg and the upper tank as shown in (ii). At  $J_G = 6.5$  m/s as shown in (iii), the flow pattern near the elbow in the horizontal section was a wavy flow, whereas it was a wavy-mist flow in the elbow and the inclined section. When we decreased  $J_G$  from 6.5 m/s, the flow pattern remained unchanged even though  $J_G$  was the same as in (ii). These flow behaviors were almost the same as the observed flow patterns as shown in (I) to (IV).

**Figure 29** shows a comparison between calculated and measured CCFL characteristics at  $Q_{Lin} = 10, 20$  and  $30$  l/min. At  $Q_{Lin} = 10, 20$  l/min, the calculated CCFL characteristics agreed well with the measured data. On the other hand, at  $Q_{Lin} = 30$  l/min,  $J_L^*$  in the simulation resulted in underestimation of  $J_L^*$  in the test at low  $J_G^*$ . This was due to a large difference between the measured and the predicted flow patterns at the junction of the hot leg and the upper tank. In the simulation, the flow was calm, whereas the flow fluctuated at the junction as shown for the measured data (Fig. 29(b)).

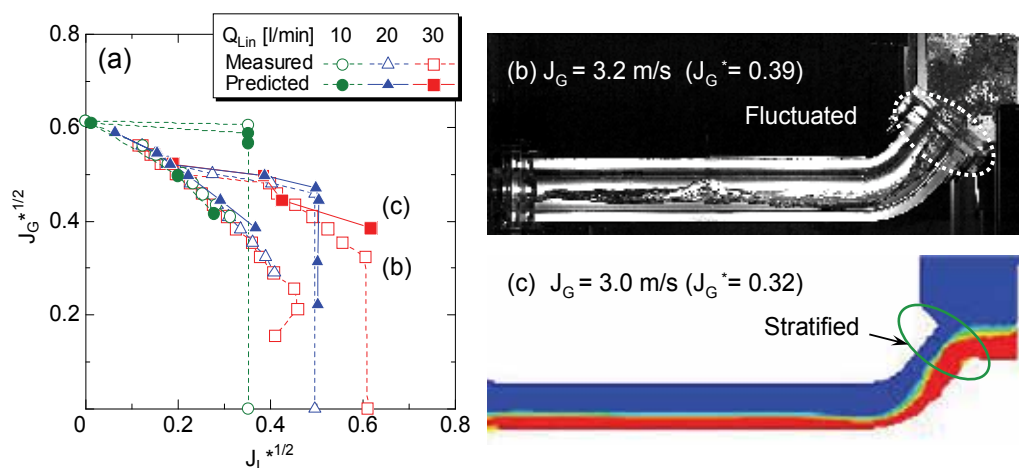


Fig. 29. Comparison between the calculated and measured CCFL data.

## 4. Conclusions

The objectives of this study were to clarify the flow patterns and dominant factors of countercurrent flow and to develop the flow model which improves the reliability of transient analysis. Results of experiments and numerical simulations for countercurrent flow in a PWR hot leg under reflux condensation were summarized, and the following conclusions were obtained.

- The effects of gas and water flow rate on the flow patterns in the hot leg were clarified. Flow patterns in the elbow and the inclined section were strongly affected by those in the horizontal section.
- The flow patterns were closely related to the CCFL characteristics.
- The calculation results of scale model experiments agreed well with the measured data using an appropriate set of correlations for interfacial friction coefficient.

The combination of calculation model and interfacial friction coefficients used in this study can predict the countercurrent flow in a hot leg qualitatively and quantitatively.

## 5. References

- Hewitt, G. F. & Wallis, G. B. (1963). ASME Multi-phase Flow Symposium, 62, Philadelphia, PA.
- Ishii, M. & Mishima, K. (1984). Two-Fluid Model and Hydro-dynamic Constitutive Relations. *Nuclear Engineering and Design*, Vol. 82, 107-126.
- Kataoka, Y. H. Suzuki & Murase, M (1987). Drift-Flux Parameters for Upward Gas Flow in Stagnant Liquid. *Journal of Nuclear Science and Technology*, Vol. 24 (7), 580-586.
- Mayinger, F.; Weiss P. & Wolfert, K. (1993). Two-phase flow phenomena in full-scale reactor geometry. *Nuclear Engineering and Design*, Vol. 145, pp. 47-61.
- Minami, N.; Nishiwaki, D.; Kataoka, H.; Tomiyama, A.; Hosokawa, S. & Murase, M. (2008a). Countercurrent Gas-Liquid Flow in a Rectangular Channel Simulating a PWR Hot Leg (1) Flow Pattern and CCFL Characteristics. *Japanese J. of Multiphase Flow*, Vol. 22, (4), pp. 403-412. (in Japanese)
- Minami, N.; Murase, M.; Nishiwaki, D. & Tomiyama, A. (2008b). Countercurrent Gas-Liquid Flow in a Rectangular Channel Simulating a PWR Hot Leg (2) Analytical Evaluation of Countercurrent Flow Limitation. *Japanese J. of Multiphase Flow*, Vol. 22(4), pp. 413-422 (in Japanese).
- Minami, N.; Nishiwaki, D.; Nariai, T.; Tomiyama, A. & Murase, M. (2010a). Countercurrent Gas-Liquid Flow in a PWR Hot Leg under Reflux Cooling (I), Air-Water Test for 1/15-Scale Model of a PWR Hot Leg, *Journal of Nuclear Science and Technology*, 47 [2], pp. 142-148.
- Minami, N.; Murase, M. & Tomiyama, A. (2010b). Countercurrent Gas-Liquid Flow in a PWR Hot Leg under Reflux Cooling (II), Numerical Simulation for 1/15-Scale Air-Water Tests. *Journal of Nuclear Science and Technology*, 47 [2] pp. 149-155.
- Minato, A.; Takamori, T. & Ishida, N. (2000). An Extended Two-Fluid Model for Interface Behavior in Gas-Liquid Two-Phase Flow. *Proc. of 8th Int. Conf. on Nuclear Engineering*, No. 8045 Baltimore, MD.
- Navarro, M. A. (2005). Study of countercurrent flow limitation in a horizontal pipe connected to an inclined one. *Nuclear Engineering and Design*, Vol. 235, 1139-1148.
- Ohnuki, A. (1986). Experimental Study of Counter-Current Two-Phase Flow in Horizontal Tube connected to an Inclined Riser. *Journal of Nuclear Science Technology*, Vol. 23 (3), pp. 219-232.
- Ohnuki, A.; Adachi, H. & Murao, Y. (1988). Scale Effects on Countercurrent Gas-Liquid Flow in a Horizontal Tube Connected to an Inclined Riser. *Nuclear Engineering and Design*, Vol. 107, pp. 283-294.
- Richter, H. J., et al., (1978), Deentrainment and Countercurrent Air-water Flow in a Model PWR Hot-leg, NRC-0193-9.
- USNRC, (1987). *Loss of Residual Heat Removal System, Diablo Canyon, Unit 2 on April 10, 1987*, NUREG-1269, U. S. Nuclear Regulatory Commission.
- USNRC, (1990). *Loss of Vital AC Power and the Residual Heat Removal System during Mid-Loop Operations at Vogtle Unit 1 on March 20, 1990*, NUREG-1410, U. S. Nuclear Regulatory Commission.
- Wallis, G. B. (1969). *One-dimensional Two-phase Flow*, McGraw-Hill, New York.
- Wongwises, S. (1996). Two-phase countercurrent flow in a model of a pressurized water reactor hot leg. *Nuclear Engineering and Design*, Vol. 166, pp. 121-133.

# Evaluation of Non-condensable Gas Recirculation Flow in Steam Generator U-tubes during Reflux Condensation

Michio Murase<sup>1</sup>, Takashi Nagae<sup>2</sup> and Noritoshi Minami<sup>2</sup>

<sup>1</sup>*Institute of Nuclear Safety System, Incorporated,*

<sup>2</sup>*The Kansai Electric Power Company, Inc.  
Japan*

## 1. Introduction

Under mid-loop operation during a PWR (pressurized water reactor) plant outage, reflux condensation in the SG (steam generator) U-tubes can be one of the major heat removal mechanisms in a hypothetical loss-of-RHR (residual heat removal systems) event. In mid-loop operation, the reactor coolant level is kept around the hot leg nozzle center and non-condensable gas (air or nitrogen) is present in the reactor coolant system (RCS). Such non-condensable gases are well known to accumulate on the condensation heat transfer surface and consequently inhibit steam from condensing. Therefore, in order to evaluate the effectiveness of reflux condensation in the SG U-tubes, the condensation heat transfer characteristics in the presence of a non-condensable gas must be clarified.

In the riser section of the SG U-tubes, the steam and non-condensable gas mixture and liquid condensate form countercurrent flow. A model for the influence of non-condensable gas on condensation was developed by Nithianandan et al. (1986) for the RELAP5/MOD2 code, based on an analogy between mass and heat transfers. However, the model was not well validated for countercurrent flow conditions while the condensation heat transfer coefficients in the presence of a non-condensable gas have been measured in many experiments, they have been measured very few times in countercurrent flow. Moon et al. (2000) measured the condensation heat transfer coefficients of steam-air mixtures in countercurrent flow, and proposed an empirical correlation as a degradation factor to the heat transfer coefficient of pure steam. Meanwhile Chun et al. (2001) placed a condenser tube bundle in a water pool and improved the empirical correlation by Moon et al. (2000). However, the correlations are limited to turbulent conditions of gas flow and when applied to laminar flow conditions, they overestimate the heat transfer coefficient.

Therefore, in our study, we carried out condensation heat transfer experiments in the presence of a non-condensable gas in a collaborative study at Purdue University (Vierow et al., 2003) and derived an empirical correlation mainly for laminar flow (Nagae et al., 2005). Moreover we conducted additional condensation heat transfer experiments, especially at high flow rates of a non-condensable gas, and improved the empirical correlation for turbulent flow conditions (Nagae et al., 2007a). In this article, we summarize the major results.

Using the BETHSY facility, which was a scale-model of a three-loop PWR, Noel & Deruaz (1994) and Noel & Dumont (1997) conducted reflux condensation tests. Different flow patterns were observed in the 34 U-tubes in the tests 7.2c with nitrogen injection (Noel & Deruaz, 1994), but were not observed in the tests 10.2 with helium injection (Noel & Dumont, 1997). In the test 7.2c-1.3 for example, an active condensation zone developed in the up-flow side of 21 U-tubes (active U-tubes), but nitrogen reverse flow from the outlet plenum to the inlet plenum occurred in some U-tubes (passive U-tubes).

In our study, we calculated steady-state flow patterns in U-tubes for the BETHSY tests 7.2c by one-dimensional analyses (Murase & Nagae, 2005) using a parallel channel model and the old correlation for condensation heat transfer coefficients by Nagae et al. (2005). In the steam-nitrogen mixture, density head is higher in the cold-side of active U-tubes than in the hot-side. In the region of low steam flow rates with small friction loss, the pressure becomes higher in the outlet plenum than in the inlet plenum, and nitrogen flows from the outlet plenum to the inlet plenum in passive U-tubes. About 10 solutions with different numbers of active U-tubes were obtained in our calculations. Using the assumption that the flow might be most stable in the case with the maximum nitrogen recirculation flow rate, we could obtain a unique solution for the number of active U-tubes, and the estimated number of active U-tubes agreed well with the BETHSY test results.

We also calculated different flow patterns in U-tubes (Nagae et al., 2007b) observed in the reflux condensation tests 7.2c by the BETHSY facility using the RELAP5/MOD3.2 code (The RELAP5 Development Team, 1995), where the improved correlation by Nagae et al. (2007a) for condensation heat transfer coefficients were applied. With modification of the equation for the interfacial and wall friction coefficients, nitrogen reverse flow was successfully calculated by RELAP5/MOD3.2, where SG U-tubes were modeled with two parallel flow channels. There were many solutions with different numbers of active U-tubes with condensation and the predicted number of active U-tubes agreed rather well with the measured values based on the assumption that the flow might be most stable in the case with the maximum nitrogen recirculation flow rate. In the calculations, however, the validity of the assumption has not been confirmed. Therefore, using RELAP5/MOD3.2 we calculated using three flow channels in order to change the flow area of active and passive U-tubes rather smoothly, and we evaluated the number of active U-tubes without the assumption (Minami et al., 2008). The ratio of active U-tubes calculated with three flow channels gave a good prediction of the ratio of active U-tubes. The results indicate the validity of the assumption that flow with the maximum nitrogen recirculation flow rate may be most stable and appear most probably among different numbers of active U-tubes. In this article, we also summarize the methods to predict the ratio of active U-tubes.

## 2. Heat transfer in the presence of non-condensable gas

In order to evaluate reflux condensation heat transfer characteristics in SG U-tubes in the presence of a non-condensable gas, experiments were conducted for condensation heat transfer of steam-air mixture under countercurrent flow in a vertical tube having an inside diameter of 19.3 mm and with pressure range from 0.1 to 0.4 MPa (Nagae et al., 2005 & 2007a).

## 2.1 Measurement methods

The design and manufacture of the experimental facility, experimental measurements, and data processing were done at Purdue University (Vierow et al., 2003). Figure 1 shows the experimental setup. Its main component was a vertical, double-pipe heat exchanger made of Type 304 stainless steel (SUS 304). The inner tube was the heat transfer tube with an inside diameter of 19.3 mm, wall thickness of 3.04 mm and a heat transfer length of 1.8 m. The mixture of steam and air flowed into the tube from the lower plenum. The coolant water flowed along the outer surface of the heat transfer tube.

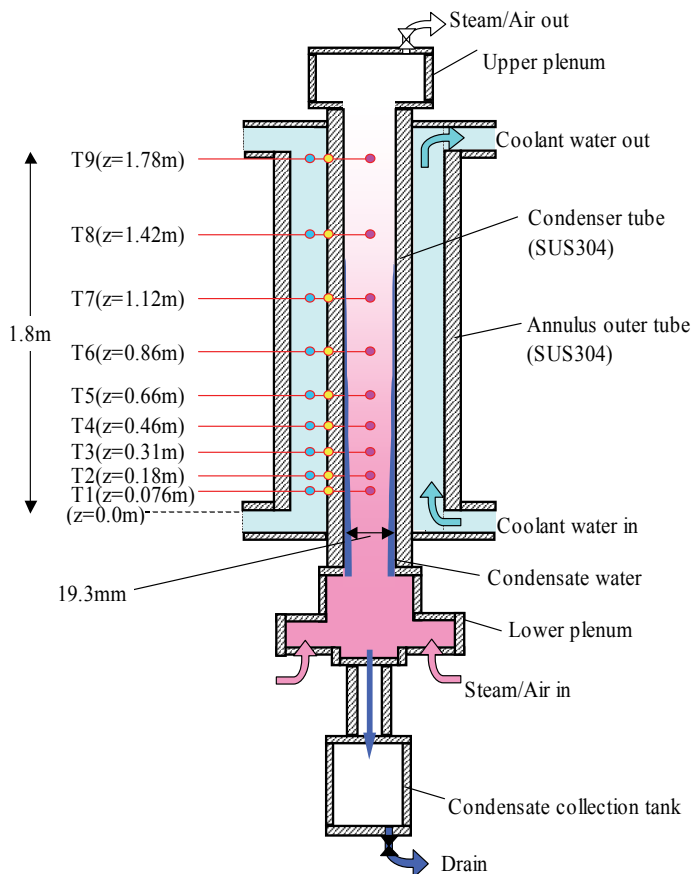


Fig. 1. Experimental setup (Vierow et al., 2003)

To obtain the condensation heat transfer coefficient under steady state conditions, the steam-air mixture temperature, outer wall temperature of the heat transfer tube, and coolant water bulk temperature were measured at nine elevations along the experimental section. The experimental conditions are listed in Table 1. The pressure, inlet steam mass flow rate, and air mass flow rate at the inlet of the test section were varied to examine their influence on the condensation heat transfer coefficient. The pressure and steam flow rate were selected based on the values presumed in the loss-of-RHR event during mid-loop operation. One objective of the experiment was to obtain a database under laminar and turbulent flow conditions.

Pressure (MPa)	0.1	0.2	0.4
Inlet conditions			
Steam mass flow rate (g/s)	0.49-1.9	1.1-1.9	0.48-1.9
Air mass flow rate (g/s)	0.03-0.18	0.06-0.5	0.06-0.8
Reynolds number of mixture	2900-10000	6500-10000	3100-9500
Measured regions			
Steam mass flow rate (g/s)	0.00031-1.9	0.00039-1.9	0.00020-1.9
Partial pressure ratio, $P_{steam}/P_{air}$	0.027-120	0.012-47	0.0054-49
Reynolds number of mixture	73-10000	210-10000	210-9500

Table 1. Experimental conditions

In the experiment, the temperature of the steam-air mixture,  $T_g$ , and the outer wall temperature of the heat transfer tube,  $T_{w,o}$ , were measured, and the heat flux at the inner surface of the heat transfer tube,  $q''$ , and the overall heat transfer coefficient,  $K$ , were defined by the following equations:

$$q'' = K(T_g - T_{w,o}) \quad (1)$$

$$\frac{1}{K} = \frac{r_{w,i} \ln(r_{w,o}/r_{w,i})}{\lambda_w} + \frac{1}{h_c} \quad (2)$$

where  $r_{w,i}$  is the inner radius of the heat transfer tube,  $r_{w,o}$  is the radius of the thermocouple location to measure outer wall temperature of the heat transfer tube,  $\lambda_w$  is the thermal conductivity of the heat transfer tube, and  $h_c$  is the condensation heat transfer coefficient. The first term on the right hand side of Eq. (2) can be calculated from the dimensions and physical properties of the heat transfer tube. Accordingly, the condensation heat transfer coefficient,  $h_c$ , can be calculated once the heat flux is known.

From the coolant temperature variation, the mean heat flux  $q''$  between the measured sections in Eq. (1) can be calculated. Since the coolant temperature variation is small in the downstream region of the heat transfer tube, where both the condensation rate and measurement accuracy are low, the mean heat flux between the measured sections is calculated from the temperature variation of the steam-air mixture. Temperature measurements provide the local saturation pressure, and the steam mass flow rate can be calculated from the partial pressure of steam,  $P_{steam}(T_g)$ , assuming a Gibbs-Dalton mixture of steam and an ideal non-condensable gas. Then the local heat flux can be obtained (for details, see Nagae et al., 2005 & 2007a).

In Eq. (2), the condensation heat transfer coefficient consists of the heat transfer coefficient of the liquid film,  $h_f$ , and the heat transfer coefficient at the gas-liquid interface,  $h_i$ , which are separately evaluated in this study, because they are different heat transfer mechanisms. When the effects of the liquid film subcooling and the liquid film thickness on the gas-liquid interface area can be neglected, the condensation heat transfer coefficient is expressed by:

$$\frac{1}{h_c} = \frac{1}{h_f} + \frac{1}{h_i} \quad (3)$$



According to the calculations, the subcool enthalpy of the liquid film is about 3% of the condensation enthalpy, and the gas-liquid interface area is about 99% of the inner surface area of the heat transfer tube under the experimental conditions. In Eq. (3), the heat transfer coefficient of the liquid film,  $h_f$ , can be calculated by Nusselt's film condensation theory or an empirical correlation for a turbulent film such as the correlation modified by McAdams (1954), which we use in this study. Then, the interfacial heat transfer coefficient,  $h_i$ , is obtained from the measured condensation heat transfer coefficient,  $h_c$ .

## 2.2 Interfacial heat transfer coefficients

Important parameters for the interfacial heat transfer coefficients,  $h_i$ , are properties of a non-condensable gas and gas velocity. The effects of a non-condensable gas were evaluated by Nagae et al. (2005), and mass flow ratio of ( $W_{steam} / W_{air}$ ) and pressure ratio of ( $P_{steam} / P_{air}$ ) gave similar results. In the transient analysis, mass flow rates sometimes fluctuate and pressures are more stable than mass flow rates. Therefore the pressure ratio of ( $P_{steam} / P_{air}$ ) is adopted in this study. As for gas velocity, steam Reynolds number gave better results than steam-air mixture Reynolds number for limited data (Nagae et al., 2005). However, steam Reynolds number is not suitable for the additional data (Nagae et al., 2007a). Therefore, the empirical correlation for the interfacial heat transfer coefficient was reevaluated using the Reynolds number of the steam-air mixture,  $Re_g$ . The same function of ( $P_{steam} / P_{air}$ )<sup>0.75</sup> for laminar flow (Nagae et al., 2005) is used for turbulent flow, and the constants  $a$  and exponent  $b$  for  $Re_g$  are determined by the least mean square method. The modified empirical correlation by Nagae et al. (2007a) is as follows:

$$Nu_i = \frac{h_i d_{w,i}}{\lambda_g} = 120 \left( \frac{P_{steam}}{P_{air}} \right)^{0.75} \max(1.0, a Re_g^b) \quad (4)$$

with  $Re_g = \frac{j_g d_{w,i}}{\nu_g} \leq 10,000$ ,  $a = 0.0035$ ,  $b = 0.8$ ,

where  $j_g$  is the superficial velocity of the steam-air mixture and  $\nu_g$  is the viscosity of the steam-air mixture. In order to apply Eq. (4) to the transient analysis codes, where empirical correlations are often used beyond their application limits, the following limits are suggested:

$$Nu_i = \frac{h_i d_{w,i}}{\lambda_g} \geq 4.36, \quad 0.0054 \leq \frac{P_{steam}}{P_{air}} \leq 120, \quad Re_g = \frac{j_g d_{w,i}}{\nu_g} \leq 10,000, \quad (5)$$

where the lower limit of the Nusselt number corresponds to the heat transfer of a gas laminar flow without steam condensation and gives about  $h_f = 7 \text{ W/m}^2\text{K}$ . Other limits are the measured region listed in Table 1.

Figure 2 compares the interfacial heat transfer coefficients calculated by Eq. (4) with measured values (Nagae et al., 2005 & 2007a). The calculated results agreed well with the data in a wide range of heat transfer coefficients. In the region of large heat transfer coefficients, however, the points were scattered because the measured values scattered near the entrance of the experimental section due to a small increase in the cooling water temperature.

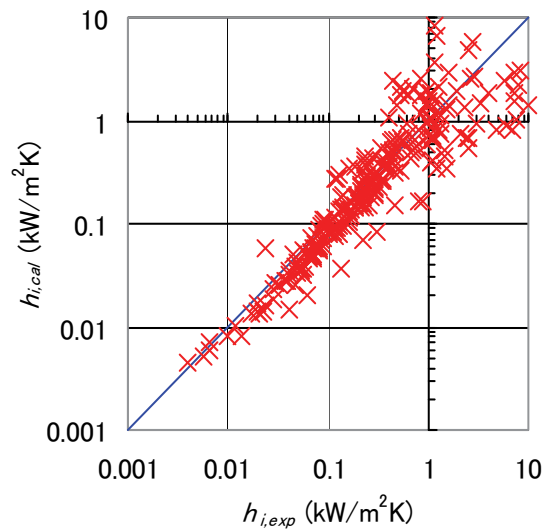


Fig. 2. Comparison of interfacial heat transfer coefficients,  $h_{i,cal}$ , calculated by Eq. (4) with data,  $h_{i,exp}$

### 2.3 Experimental analyses by RELAP5/MOD3.2 with modified correlation

Figure 3 shows the nodalization scheme of RELAP5/MOD3.2 for calculations of the condensation heat transfer experiments shown in Fig. 1. The nodalization scheme contains 125 control volumes, 7 junctions, and a valve and heat structure. Both the steam-air mixture and coolant were injected at constant flow rates upward into the heat transfer tube and along the outer surface of the tube, respectively. In the calculation, this behavior is simulated using a volume and a junction to specify flow, pressure and temperature conditions. Volumes act as infinite sources or sinks and represent boundary conditions. Volume 100 is connected to Pipe 110, which represents the lower plenum with a junction. Junction 115 connects Pipe 110 with the inlet of Pipe 140, which represents the inlet pipe and measurement section. Junction 141 connects the outlet of Pipe 140 with Pipe 142, which represents the upper plenum. Valve 175 is used to regulate the venting of the residual steam-air mixture to the atmosphere. Junction 159 connects Pipes 156 and 160 that simulate a condensate water line and a collection tank. Volumes 200 and 280 are connected to Pipe 240, which represents the coolant water line, with Junctions 210 and 270, respectively. Heat structure 140 with 55 sub-volumes is used to represent the heat transferred from the steam-air mixture to the coolant through the heat transfer tube.

Figure 4 shows the axial temperature profiles (Nagae et al., 2007a). Using the default model correlation by Nithianandan et al. (1986) gave much higher mixture temperatures especially for a high pressure condition. It seemed that the default vapor-diffusion model through the non-condensable gas layer underestimated heat transfer coefficients especially for high pressures. On the other hand, the temperature distribution of the steam-air mixture calculated by RELAP5/MOD3.2 with the modified correlation agreed well with the data. The calculations overestimated the outer surface temperatures of the tube near the inlet in all cases. The reason might be the high heat transfer coefficient outside the heat transfer tube near the inlet due to the entrance effect in the experiments.

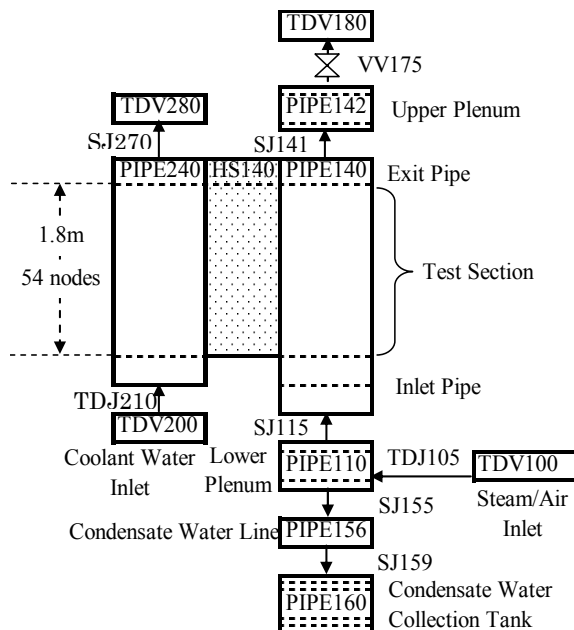


Fig. 3. Nodalization for calculations using RELAP5/MOD3.2

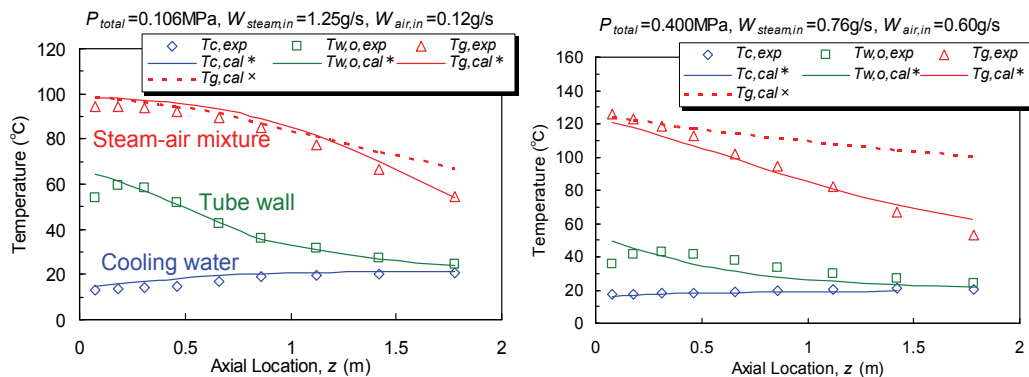


Fig. 4. Comparison of axial temperatures (exp: measured data; cal\*: RELAP5-modified correlation; calx: RELAP5-default model correlation)

### 3. Steady-state calculations of BETHSY tests 7.2c

In order to evaluate the mechanism of different flow patterns observed in the BETHSY tests 7.2c (Noel & Deruaz, 1994), steady-state calculations were conducted using a parallel channel model (Murase & Nagae, 2005; Nagae et al., 2007b).

#### 3.1 Reflux tests in BETHSY facility

The BETHSY facility is a scale-model of a three-loop 900 MWe PWR with the full height and 1/100 of the volume, flow rate and power level. Each SG has 34 U-tubes with the inner diameter of 19.68 mm and the average length of 19.45 m.

The conditions and major results of the reflux tests 7.2c (Noel & Deruaz, 1994) are listed in Table 2. In the tests, one loop was used and the other two loops were isolated. The power in the core was constant at about 98 kW, which simulated about 0.33 % of the rated power and generated the steam flow rate of 47 g/s (1.38 g/s/U-tube). The secondary-side pressure of the SG was constant at 0.2 MPa. A test was started with pure steam, and nitrogen was injected gradually into the vertical part of the hot leg upstream of the SG inlet plenum. The injected nitrogen flowed into the U-tubes and accumulated in the SG outlet plenum and the cold leg, which was sealed with coolant water in the crossover leg. The primary pressure increased gradually during injection of nitrogen, and reached a constant value after the termination of the injection. Table 2 shows the primary pressure and the number of active U-tubes at a steady state after the termination of the nitrogen injection. The temperatures in the inlet of the 34 U-tubes were measured, and it seemed that U-tubes with a temperature close to the inlet plenum temperature and U-tubes with a temperature close to the outlet plenum temperature would be evaluated as active U-tubes with steam condensation and passive U-tubes with a nitrogen reverse flow, respectively.

	Test conditions				Results	
Test No.	$Q_{core}$ (kW)	$P_2$ (MPa)	Gas	$M_{NG}$ (kg)	$P_1$ (MPa)	$N_{act}$
7.2c-1.1	97.0	0.2	None	0.0	0.23	34
7.2c-1.2	98.5	0.2	N <sub>2</sub>	0.32	0.38	24
7.2c-1.3	98.5	0.2	N <sub>2</sub>	0.65	0.55	21
7.2c-1.4	99	0.2	N <sub>2</sub>	1.08	0.78	19

Table 2. Test conditions and major results of the BETHSY tests 7.2c (Noel & Deruaz, 1994);  $M_{NG}$ : mass of injected nitrogen;  $N_{act}$ : number of active U-tubes;  $P_1$  and  $P_2$ : pressure of primary and secondary loops, respectively;  $Q_{core}$ : core power

### 3.2 Calculation model

In this study, we did calculations for the steady state after the termination of the nitrogen injection in the tests 7.2c, where different flow patterns appeared. Flow patterns in U-tubes are illustrated in Fig. 5. We assumed that there were active U-tubes with steam condensation and passive U-tubes with a nitrogen reverse flow, and the one-dimensional flow in the axial direction was calculated accordingly. In the calculation of thermal-hydraulics in a single U-tube, the temperature distribution of the steam-nitrogen mixture and the pressure drop between the inlet and outlet plenums were calculated while varying the steam flow rate or nitrogen flow rate as a parameter. In the calculation of thermal-hydraulics in parallel U-tubes, the number of active U-tubes was fixed at one value, the temperature distributions and the pressure drops in active and passive U-tubes were calculated varying the nitrogen recirculation flow rate as a parameter, and the solution with the same pressure drop between active and passive U-tubes was obtained.

The pressure drop between the inlet and outlet plenums could be expressed by the equation:

$$P_{in} - P_{out} = \frac{\zeta_{in}}{2} (\rho_m |j_m| j_m)_{in} + \int_0^L \rho_m \left( \frac{f}{2d_i} |j_m| j_m + g \right) dz + \frac{\zeta_{out}}{2} (\rho_m |j_m| j_m)_{out} \quad (6)$$

where  $\rho_m$  and  $j_m$  are the density and superficial velocity of the steam-nitrogen mixture, respectively.  $j_m$  and  $dz$  are positive in the region of  $0 < z < L/2$ , but negative in the region of

$L/2 < z < L$ , where  $L$  is the length of the U-tube. Inlet pressure loss coefficient of  $\zeta_{in} = 0.5$  without curvature at the corner and outlet pressure loss coefficient of  $\zeta_{out} = 1.0$  for sudden expansion were used. The friction loss coefficient,  $f$ , for an annular flow by Wallis (1969) was used.

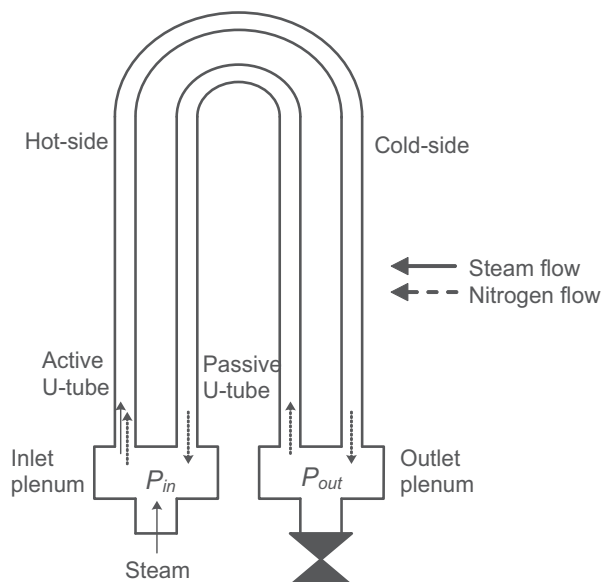


Fig. 5. Calculation model of flow patterns in U-tubes

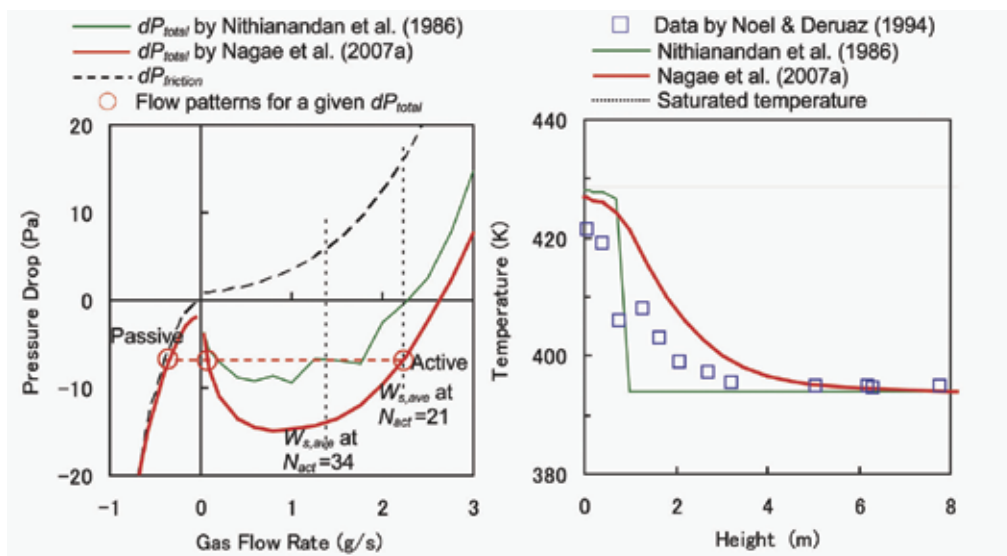
The density of the steam-nitrogen mixture,  $\rho_m$ , was a function of the pressure and temperature. Steam pressure could be calculated by applying Dalton's law and ideal gas law to nitrogen. The temperature of the steam-nitrogen mixture was calculated from the steam partial pressure by assuming a saturated state of steam. The steam flow rate could be calculated by the heat transfer equations, where the heat transfer coefficient outside the U-tube was calculated by the maximum value of the laminar flow heat transfer at low superheating and the pool nucleate-boiling heat transfer by Kutateladze at high superheating, and the condensation heat transfer coefficient was calculated using Eqs. (3) and (4) (for details, see Nagae et al., 2007b).

### 3.3 Pressure drop and axial temperature distribution

Figure 6 (a) shows calculated pressure drop in a single U-tube for the test 7.2c-1.3. Positive and negative gas flow rates represent those of steam and nitrogen, respectively. It should be noted that Fig. 6 (a) shows an example of pressure drop characteristics; the actual pressure drop changed depending on the number of active U-tubes and nitrogen recirculation flow rate. Friction loss,  $dP_{friction}$ , in the figure included inlet and outlet pressure losses in Eq. (6) and the difference between the total pressure drop,  $dP_{total}$ , and friction loss was the term of density head. Because density head was larger in the cold-side than in the hot-side, the pressure drop between inlet and outlet plenums became negative in the region of low flow rates with small friction loss. Correlations of the condensation heat transfer coefficient affected temperature and density head. The calculated pressure drop using the correlation

by Nithianandan et al. (1986) did not change smoothly, which may be due to the rapid change of heat transfer coefficients from turbulent flow to laminar flow. However, its effect was several Pa and small compared with the differential pressures in the hot-side and cold-side of about 400 Pa.

In the test 7.2c-1.3, the average steam flow rate per U-tube was  $W_{s,ave}=1.38$  g/s and the steam flow rate per U-tube in the case of 21 active U-tubes ( $N_{act}=21$ ; see Table 2) became 2.24 g/s. In the U-tube bundle, the pressure drop of each U-tube became equal, and three patterns (three open circles in Fig. 6 (a)), active U-tubes, passive U-tubes and U-tubes with low steam flow rate, may appear for a given pressure drop. However, it is well known that the flow pattern with a negative pressure drop gradient is unstable and may not appear in parallel channels (Ozawa, 1999). Therefore, in this study, we considered active U-tubes and passive U-tubes in the following calculations.



(a) Calculated pressure drop (test 7.2c-1.3) (b) Axial temperature distribution ( $N_{act} = 21$ )

Fig. 6. Results of steady-state calculations ( $N_{act}$ : number of active U-tubes)

Figure 6 (b) compares measured and calculated temperatures of steam-nitrogen mixture in active U-tubes. In the calculations, the measured number of active U-tubes,  $N_{act}=21$ , was used. Changing the nitrogen recirculation flow rate as a parameter, we calculated pressure drops of active and passive U-tubes, and a solution with the same pressure drops between the active and passive U-tubes was obtained.

In the calculation using the correlation by Nithianandan et al. (1986), as shown in Fig. 6 (a), the pressure drop was nearly zero at  $N_{act}=21$  and the nitrogen reverse flow rate in the passive U-tube was quite low. Therefore, almost pure steam entered the active U-tube and the temperature of the mixture decreased rapidly due to steam condensation. On the other hand, in the calculation using the correlation by Nagae et al. (2007a), the nitrogen reverse flow rate in the passive U-tube was large, condensation heat transfer coefficients became low due to the non-condensable gas, and the temperature of the mixture decreased gradually. The temperatures calculated using the correlation by Nagae et al. (2007a) were overestimated, but showed good agreement with the trend of the measured temperatures.

### 3.4 Prediction of number of active U-tubes

Under the countercurrent gas-liquid flow in vertical parallel channels between upper and lower plenums, where gas is supplied to the lower plenum and liquid is supplied to the upper plenum, the pressure drop between the upper and lower plenums has a similar trend to the pressure drop shown in Fig. 6 (a), and gas up-flow and liquid down-flow appear in parallel channels (Wallis et al., 1981; Murase & Suzuki, 1986). In this case, the flow pattern with the minimum pressure drop is the most stable among several flow patterns and appears most easily (Murase & Suzuki, 1986). In the vertical parallel channels, however, the gas flow rate and the pressure drop are positive, which are different from those in the U-tubes shown in Fig. 6 (a) where the pressure drop was negative. In the long U-tubes, the steam flow rate generated by decay heat was low compared with the large heat transfer area. Therefore, we assumed that the flow might be most stable in the case with the maximum nitrogen recirculation flow rate, and the predicted number of active U-tubes using the assumption agreed well with the BETHSY test results (Murase & Nagae, 2005).

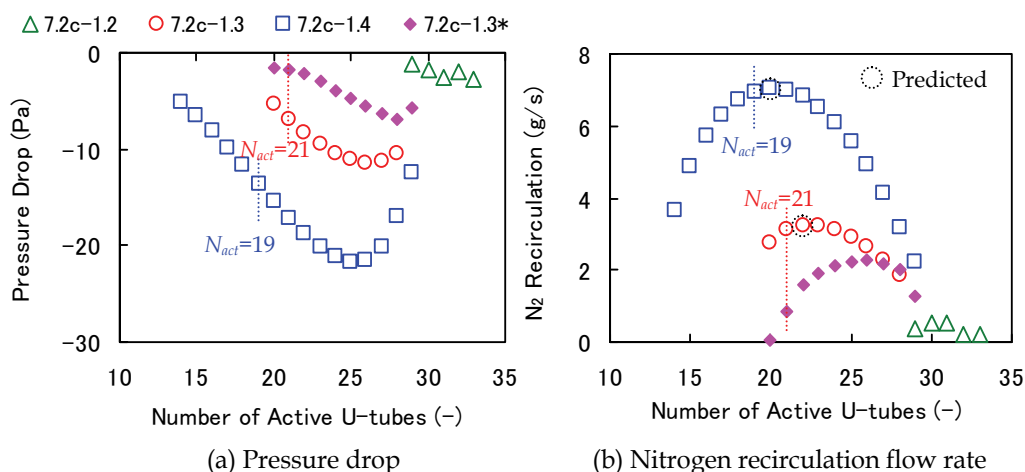


Fig. 7. Results calculated for 34 U-tubes;  $N_{act}$ : number of active U-tubes observed by Noel & Deruaz (1994); \*condensation heat transfer correlation by Nithianandan et al. (1986); others: condensation heat transfer correlation by Nagae et al. (2007a)

Figure 7 shows calculated pressure drop and nitrogen recirculation flow rate (Nagae et al., 2007b). As the injected mass of nitrogen increased, nitrogen recirculation flow rate increased and the pressure difference between the inlet and outlet plenums (absolute value of the pressure drop of U-tubes) became large. By assuming that the flow might be most stable in the case with the maximum nitrogen recirculation flow rate, the predicted numbers of active U-tubes agreed well with the measured values except for 7.2c-1.2. In order to predict the number of active U-tubes,  $N_{act}=24$  in 7.2c-1.2, an accurate pressure drop calculation is required. In the case of 7.2c-1.4, the predicted number of active U-tubes was 20 for the measured value of  $N_{act}=19$ . The differences of calculated temperatures in the cases of  $N_{act}=18$  to 20 were small and less than 2 K. Figure 7 (b) also shows that the condensation heat transfer correlation was important to predict the number of active U-tubes, because the pressure drop between the inlet and outlet plenums was very small as shown in Fig. 7 (a).

## 4. Transient calculations using RELAP5/MOD3.2

### 4.1 Calculation model and conditions

In the transient calculations of the BETHSY tests 7.2c, RELAP5/MOD3.2 was used (Nagae et al., 2007b; Minami et al., 2008), where the correlation of condensation heat transfer was modified using Eq. (4). In the transient analyses, SG U-tubes are generally modeled by a single flow channel, but they must be modeled by multiple flow channels for the calculation of the nitrogen reverse flow from the outlet plenum to the inlet plenum, so we modeled SG U-tubes by two or three flow channels.

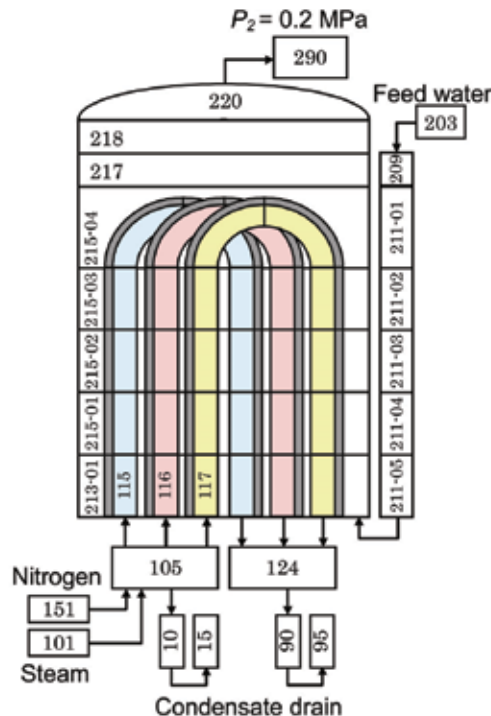


Fig. 8. Nodalization for calculations by RELAP5/MOD3.2

Figure 8 shows the nodalization scheme of the SG of the BETHSY tests with three flow channels, Volumes 115, 116 and 117. In the case of two flow channels, Volumes 115 and 116 were used. The nodalization used for these calculations included control volumes, junctions and heat structures. Volume 101 simulated the steam flow rate generated in the core. Volume 151 simulated the nitrogen flow injected into the hot leg. Volumes 10 and 15, and 90 and 95 were connected to the inlet plenum and the outlet plenum, respectively, in order to drain the condensate water, since the change in free volume would affect the calculations. The water level in the secondary side of the SG was kept constant by feed water from Volume 203. The pressure in the secondary side was kept at 0.2 MPa. The inner diameter of U-tubes was 19.68 mm, and the length of U-tubes was 17.98, 19.45 or 20.92 m. In Fig. 8, the average length of 19.45 m was used for the three flow channels, Volumes 115, 116 and 117, because the difference of pressure drops calculated for 17.98, 19.45 and 20.92 m was smaller than 1 Pa (Murase & Nagae, 2005).



The volume of the inlet and outlet plenums is about 0.035 m<sup>3</sup> in the BETHSY facility (Bazin, 1988), but is about 0.05 m<sup>3</sup> in the same scale model of a Japanese typical PWR plant. The volume of the inlet and outlet plenums does not directly affect thermal-hydraulic behavior, but the important parameter is the gas volume in the outlet plenum and cross-over leg, which affects the partial pressure of nitrogen there. According to the calculation by Murase & Nagae (2005) using the one-dimensional parallel channel model, the gas volume of the outlet plenum was about 0.02 m<sup>3</sup>, which was obtained from the mass of injected nitrogen and measured pressure of the primary loop in the BETHSY tests. Therefore, we used the volume of 0.02 m<sup>3</sup> for the base case or 0.05 m<sup>3</sup> for a parameter calculation to evaluate its effect.

#### 4.2 Modification of calculation equation

At first, a transient calculation was conducted using two flow channels with the flow area ratio of 21:13. Both flow channels were active in test 7.2c-1.1 without nitrogen injection, and the gas flow rate ratio and heat transfer ratio between Volumes 115 and 116 were almost the same as their flow area ratio (i.e. number ratio of U-tubes). After nitrogen injection, the calculated gas flow rates and heat transfer rates in Volumes 115 and 116 repeated out-of-phase oscillations and nitrogen reverse flow was not calculated. Moreover, the calculated steam velocities in the test 7.2c-1.1 were different by about 0.5 % between Volumes 115 and 116, which was small as a calculated result but large as a calculation error. We found that the gas-liquid interfacial friction forces between Volumes 115 and 116 were different by about 5%. Therefore, we checked calculation equations of the interfacial friction force. In RELAP5, the node and junction method, where pressure is defined at the center of each volume and velocity is defined at each junction, is used. And in the calculation of pressure drop between volumes, the following weighting factor is used for calculations of the interfacial friction force and the wall friction force.

$$\frac{A_j(j)}{A_v(i)} \cdot \frac{0.5L_v(i)}{0.5L_v(i) + 0.5L_v(k)} + \frac{A_j(j)}{A_v(k)} \cdot \frac{0.5L_v(k)}{0.5L_v(i) + 0.5L_v(k)} \quad (7)$$

where  $A_j$  is flow area of a junction,  $A_v$  is flow area of a volume,  $L_v$  is length of a volume, and (i) and (k) show the upstream and downstream volumes of the junction, respectively. It is not clear why the flow area ratio ( $A_j / A_v$ ) is used in Eq. (7), but it is clear that Eq. (7) gives different forces for the U-tube volumes because flow areas of the junctions  $A_j$  (j) for Volumes 115 and 116 are 21:13. Therefore, Nagae et al. (2007b) modified Eq. (7) to:

$$\left[ \frac{D_j(j)}{D_v(i)} \right]^2 \cdot \frac{0.5L_v(i)}{0.5L_v(i) + 0.5L_v(k)} + \left[ \frac{D_j(j)}{D_v(k)} \right]^2 \cdot \frac{0.5L_v(k)}{0.5L_v(i) + 0.5L_v(k)} \quad (8)$$

where  $D_j$  is the hydraulic diameter of a junction and  $D_v$  is the hydraulic diameter of a volume. We used Eq. (8) to minimize the modification of Eq. (7) and to keep  $(A_j / A_v) = (D_j / D_v)^2$  for a circular tube because its effects on the other configurations are not clear.

In the case of 17:17, for example, the interfacial friction force and the wall friction force of the inlet plenum should be about 0.13 % of those of the U-tube inlet section. However, the first term of Eq. (7) gave about 13.5 % of the second term of Eq. (7). This meant that Eq. (7) gave large interfacial force and wall friction force. The first term of Eq. (8) gave about 0.01 % of the second term of Eq. (8), which was smaller than 0.13 % mentioned above. However, its effect on the calculated values of the interfacial force and wall friction force was negligibly small.

### 4.3 Transient calculations with two flow channels

Figure 9 shows the calculated gas flow rate at the inlet of SG U-tubes and pressure at the SG inlet plenum (Nagae et al., 2007b), where Eq. (8) was used for calculations of the interfacial friction force and wall friction force. In the two flow channels, their number of U-tubes are 21 and 13 for Volumes 115 and 116, respectively. The volume of inlet and outlet plenums is 0.02 or 0.05 m<sup>3</sup>.

The gas flow rate ratio between Volumes 115 and 116 were the same as their flow area ratio (i.e. number ratio of U-tubes) of 21:13. After nitrogen injection, the pressure drop became negative, and the gas flow rate of Volume 115 increased. On the other hand, the gas flow rate of Volume 116 became negative (reverse flow). Nitrogen flowed from the outlet plenum to the inlet plenum in Volume 116 and recirculated into Volume 115. Two flow channels separated into active U-tubes (Volume 115) and passive U-tubes (Volume 116) in the calculations. Special thermal-hydraulic models and input data were not used for Volumes 115 and 116, and it seemed that the calculated results approached the more stable solution due to some disturbance in the calculation. In tests 7.2c-1.3 and 7.2c-1.4, Volume 115 and Volume 116 remained active and passive, respectively. As the injected nitrogen increased, the gas flow rate of Volume 115 increased because nitrogen reverse flow increased in Volume 116 and recirculated into Volume 115. The heat transfer rate in passive U-tubes was only about 0.3% of the whole heat transfer rate.

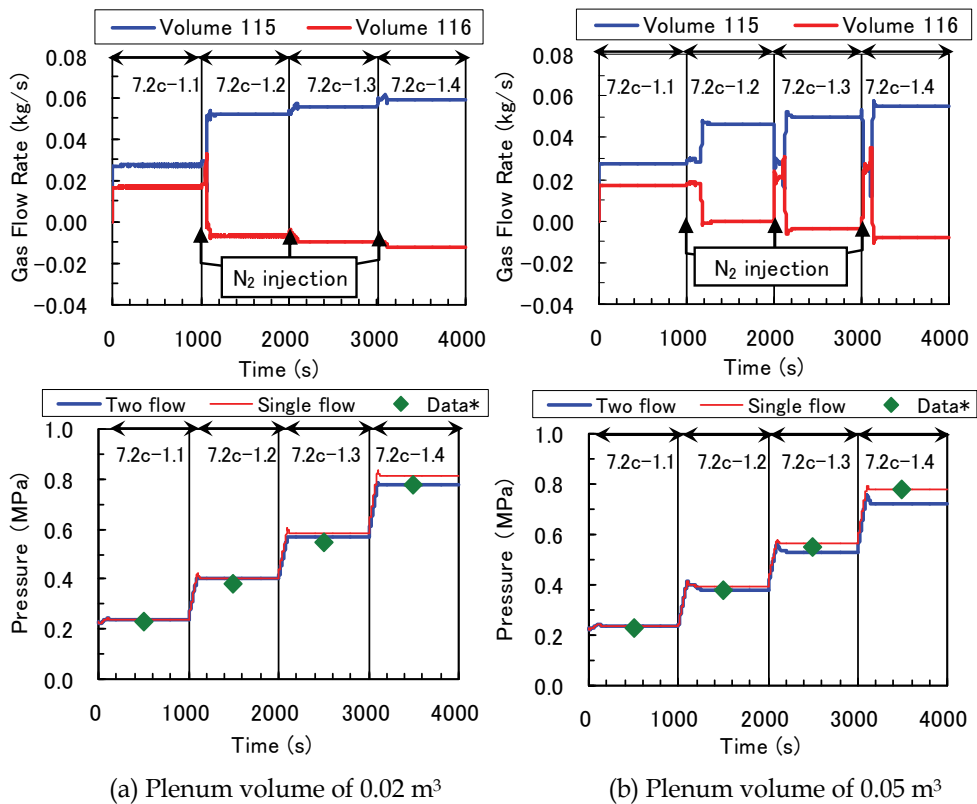


Fig. 9. Results calculated by RELAP5/MOD3.2 using two flow channels with 21 and 13 U-tubes; \*Data: Noel & Deruaz (1994)

The calculated results were similar between the plenum volumes of 0.02 and 0.05 m<sup>3</sup>, except for the behavior during the nitrogen injection and the pressure at the SG inlet plenum. The nitrogen reverse flow continued in the case with the plenum volume of 0.02 m<sup>3</sup>, but terminated during the nitrogen injection in the case with the plenum volume of 0.05 m<sup>3</sup>. Pressures calculated with the two flow channels were a little lower than those calculated with the single flow channel, but the differences were small because the steam condensation zone was much shorter than the U-tube length and the inlet and outlet plenum volume was small, and the calculated pressures of both cases agreed well with the measured values. Figure 9 results indicated that the volume of the SG inlet and outlet plenums with non-condensable gas affected the pressure at the SG inlet plenum and stability of the calculations.

Figure 10 shows the nitrogen recirculation flow rate and the SG inlet plenum pressure versus the number of active U-tubes as the calculation parameter (Nagae et al., 2007b).

In the steady state calculations, assuming that the flow might be most stable in the case with the maximum nitrogen flow rate, a unique solution for the number of active U-tubes could be obtained, and the estimated number of active U-tubes agreed well with observed results except 7.2c-1.2, as shown in Fig. 7 (b). Therefore, similar calculations were performed using RELAP5/MOD3.2. Figure 10 (a) shows nitrogen recirculation flow rates calculated changing the flow area ratio of U-tube Volumes 115 and 116. In the calculations, the flow area ratio of U-tubes changed from 17:17 to 33:1. In the calculations, active U-tubes with condensation and passive U-tubes with the nitrogen reverse flow appeared even in the calculations for 7.2c-1.2, and the horizontal axis in Fig. 10 shows the number of active U-tubes as calculated results. In the case of the plenum volume of 0.02 m<sup>3</sup>, active U-tubes appeared in the flow channel with large flow area in all calculations and the nitrogen reverse flow was calculated in the region of  $N_{act} \geq 17$ . The results underestimated the number of active U-tubes with the maximum nitrogen recirculation flow rate, but they agreed well with the measured value within a difference of two U-tubes. In the case of the plenum volume of 0.05 m<sup>3</sup>, the nitrogen reverse flow was not calculated in the region of  $N_{act} \leq 20$  for 7.2c-1.2, but it was calculated in the region of  $N_{act} \geq 17$  for 7.2c-1.3. For 7.2c-1.4, the flow channel with the larger flow area became the nitrogen reverse flow in cases of 19:15 and 18:16. The results overestimated the number of active U-tubes with the maximum nitrogen recirculation flow rate, but they agreed rather well with the measured value within a difference of 4 U-tubes. Compared with the steady-state analyses shown in Fig. 7 (b), solutions were obtained over a wide range of flow conditions.

Figure 10 (b) shows the calculated pressure at the SG inlet plenum. The number of active U-tubes, 34, shows the calculated pressure with a single flow channel, which was overestimated. As discussed in Fig. 9, the calculations with two flow channels and the inlet and outlet plenum volume of 0.05 m<sup>3</sup> underestimated the primary loop pressure, especially for 7.2c-1.4. Figure 10 (b) results indicated that the flow area ratios of U-tubes in the two flow channels model and the number of active U-tubes did not greatly affect the calculated primary loop pressure. On the other hand, the gas volume in the outlet plenum, which had an uncertainty in this study, affected the calculated primary loop pressure, and the calculations with two flow channels and the inlet and outlet plenum volume of 0.02 m<sup>3</sup> agreed well with the data.

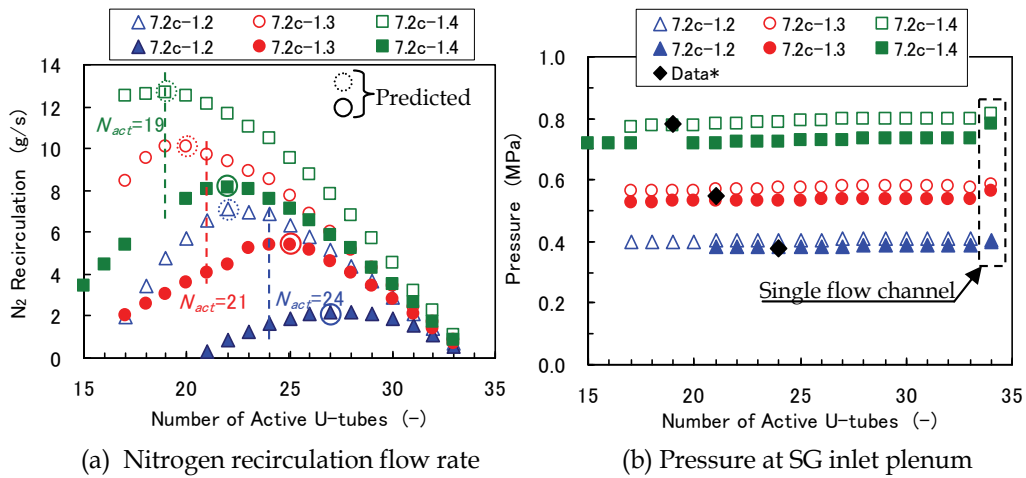


Fig. 10. Effects of number of active U-tubes as calculation parameter; open: plenum volume of 0.02 m³; closed: plenum volume of 0.05 m³;  $N_{act}$ : observed number of active U-tubes\*; \*Data: Noel & Deruaz (1994)

## 5. Transient calculations with three flow channels

In the calculations with two flow channels, we needed to perform many calculations and to assume that flow may be most stable in the case with maximum nitrogen flow rate in order to predict the number of active U-tubes. However, the assumption has not been well validated. Therefore, we did calculations using three flow channels of U-tubes in order to change the flow areas of active and passive U-tubes rather smoothly (Minami et al., 2008). We expected that the number of active U-tubes could be predicted without the assumption.

### 5.1 Calculation conditions

The nodalization scheme of the SG of the BETHSY tests is shown in Fig. 8. U-tubes were modeled by three flow channels, Volumes 115, 116 and 117. The calculation parameters were the plenum volume and the flow area ratio of the three flow channels. The volume of inlet and outlet plenums was 0.02 or 0.05 m³. The flow area ratio of the three flow channels was 55, 30 and 15%, 45, 35 and 20%, 45, 30 and 25% or 40, 35 and 25%. In the case of 55, 30 and 15% for example, the possible number ratios of active U-tubes were 100, 85, 70, 55, 45, 30 and 15%.

### 5.2 Transient behavior

Figure 11 shows gas flow rate at the U-tube inlet in three flow channels with the flow area ratios of 55, 30 and 15% (Minami et al., 2008). In the case of the plenum volume of 0.02 m³, after nitrogen injection, Volume 116 with the 30% flow area changed to nitrogen reverse flow in test 7.2c-1.2 and Volume 117 with the 15% flow area changed to nitrogen reverse flow in test 7.2c-1.3. On the other hand, in the case of the plenum volume of 0.05 m³, Volume 117 with the 15% flow area changed to nitrogen reverse flow after nitrogen injection and continued the same flow pattern. As shown in Fig. 11, the gas volume in the SG outlet plenum affected the transient behavior because nitrogen accumulated in the volume.

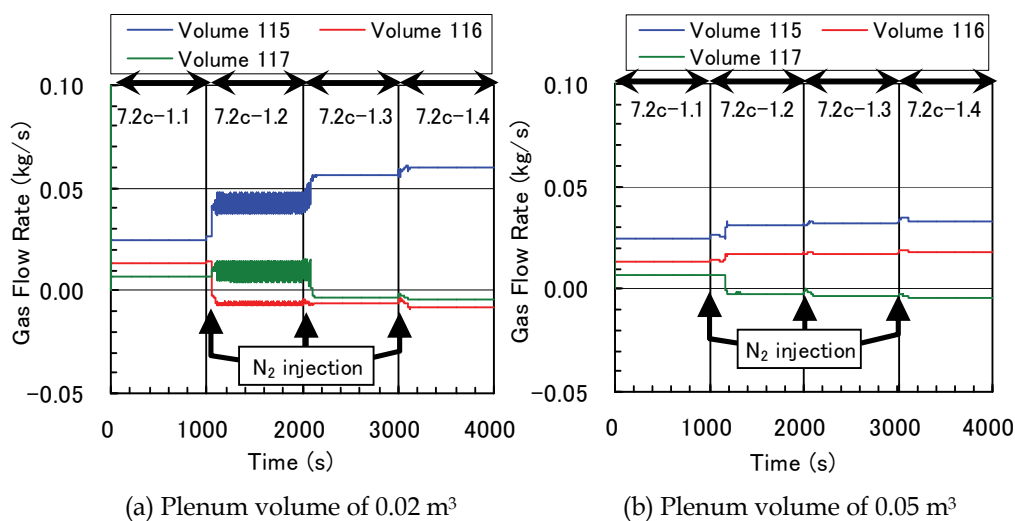


Fig. 11. Gas flow rate at U-tube inlet calculated by RELAP5/MOD3.2 using three flow channels with flow area ratios of 55, 30 and 15%

### 5.3 Number ratio of active U-tubes

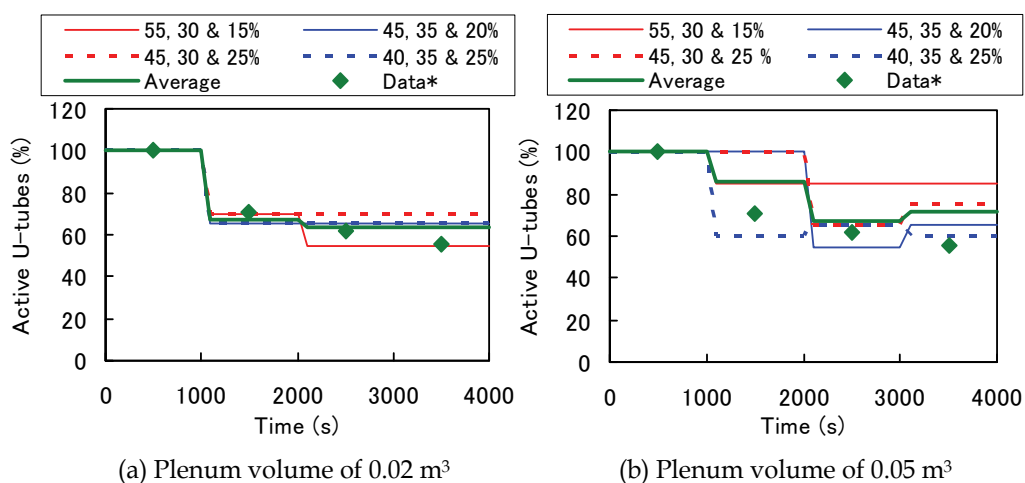


Fig. 12. Ratio of active U-tubes calculated with three flow channels

Figure 12 shows the ratio of the calculated active U-tubes (Minami et al., 2008). The calculation parameter was the flow area ratio set of U-tubes, which were 55, 30 and 15%, 45, 35 and 20%, 45, 30 and 25% or 40, 35 and 25%. In the case of the plenum volume of 0.02 m<sup>3</sup>, only Volume 116 with the medium flow area changed to nitrogen reverse flow, except for the flow area ratio set of 55, 30 and 15% shown in Fig. 11 (a), and the ratio of active U-tubes agreed with each other and with the data. Against our expectation, however, once the flow pattern changed from active flow to nitrogen reverse flow, the nitrogen reverse flow rarely returned to active flow and other channels rarely changed to nitrogen reverse flow. In the case of the plenum volume of 0.05 m<sup>3</sup>, all Volumes 115, 116 and 117 became nitrogen reverse

flow depending on the flow area ratio, and the calculated ratios of active U-tubes were scattered. The average ratios of active U-tubes were overestimated, which was similar to calculations with two flow channels shown in Fig. 10 (a), but agreed rather well with the data.

In the calculations with three flow channels, the assumption to decide the most stable state was not needed.

## 5.4 Discussion

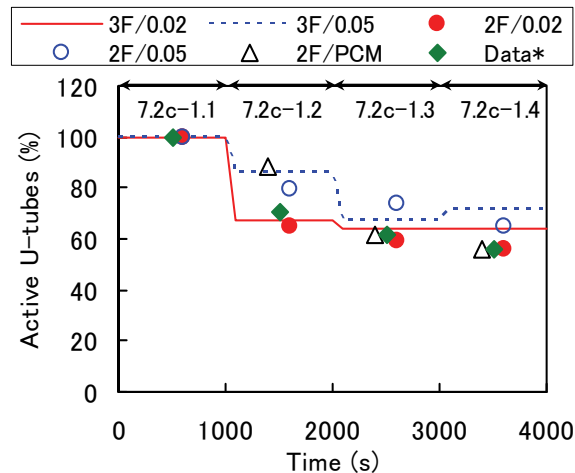


Fig. 13. Comparison of predicted ratio of active U-tubes; 2F & 3F: two and three flow channels, respectively; 0.02 & 0.05: plenum volume ( $\text{m}^3$ ); PCM: parallel channel model (c.f. Fig. 7 (b)); \*Data: Noel & Deruaz (1994)

Figure 13 compares the ratio of active U-tubes predicted using three flow channels with that using two flow channels. The predicted ratios of active U-tubes agreed well with the data in the case with the plenum volume of  $0.02 \text{ m}^3$ , but were overestimated in the case with the plenum volume of  $0.05 \text{ m}^3$ . However, both cases of  $0.02$  and  $0.05 \text{ m}^3$  agreed well between two and three flow channels.

In the three flow channel calculations, the assumption that flow was most stable in the case with maximum nitrogen flow rate was not used. Three flow channel calculations without the assumption gave similar results to two flow channel calculations using the assumption as shown in Fig. 13. This meant that the assumption that flow was most stable in the case with the maximum nitrogen flow rate was valid.

## 6. Concluding remarks

In this study, condensation heat transfer of a steam-air mixture was measured using a vertical tube with the inner diameter of  $19.3 \text{ mm}$ , and an empirical correlation of condensation heat transfer coefficients for reflux condensation was derived. The correlation was incorporated into the transient analysis code RELAP5/MOD3.2 and the temperature distributions of the steam-air mixture calculated by the code for reflux condensation tests were shown to agree well with the measured results.

Different flow patterns in U-tubes observed in the reflux condensation tests 7.2c with nitrogen injection, done using the BETHSY facility with 34 U-tubes, were calculated with two flow channels of active and passive U-tubes using a parallel channel model for steady-states and RELAP5/MOD3.2 for transient calculations. In the region of low steam flow rates, the pressure in the outlet plenum became higher than the pressure in the inlet plenum due to density head of gases, and a nitrogen reverse flow occurred, which was successfully calculated by RELAP5/MOD3.2. There were many solutions with different numbers of active U-tubes with steam condensation and the predicted number of active U-tubes agreed well with the measured values based on the assumption that the flow might be most stable in the case with the maximum nitrogen recirculation flow rate. Without the assumption of the most stable state, the calculations with three flow channels gave good prediction of the ratio of active U-tubes.

By using the proposed method (one-dimensional parallel-channel calculations), the ratio of active and passive U-tubes can be predicted even for an actual steam generator with about 3,000 U-tubes. However, it should be noted that the method can not identify the location of active U-tubes. In order to do that, three-dimensional calculations are required to evaluate the inertia effect of a steam flow into the SG inlet plenum.

## 7. References

- Bazin, P. (1988). *BETHSY: DATA BASE note SETH/LES/87-28*, Centre D'etudes Nucleaires De Grenoble, Grenoble, France.
- Chun, M. H.; Won, K. W. & Chu, I. C. (2001). An Experimental Investigation of Reflux Condensation Phenomena in Multiple U-tubes with and without Non-Condensable Gas, *Proceedings of 2001 ASME Int. Mechanical Eng. Congress and Exposition*, HTD-Vol. 369-2, pp. 194-196, New York, NY, November 2001, American Society of Mechanical Engineers, New York.
- McAdams, W. H. (1954). *Heat Transfer*, 3rd ed., McGraw-Hill, New York.
- Minami, N.; Chikusa, T. & Murase, M. (2008). RELAP5 Analyses of Thermal-Hydraulic Behavior in Steam Generator U-tubes during Reflux Condensation, *Nuclear Technology*, Vol. 164, pp. 265-277.
- Moon, Y. M.; No, H. C.; Park, H. S. & Bang, Y. S. (2000). *Assessment of RELAP5/MOD3.2 for Reflux Condensation Experiments*, NUREG/IA-0181, U. S. Nuclear Regulatory Commission, Washington, DC.
- Murase, M. & Nagae, T. (2005). Analysis of Non-condensable Gas Recirculation in Steam Generator U-tubes during Reflux Cooling, *Japanese J. of Multiphase Flow*, Vol. 19, No. 2, pp. 136-143. [in Japanese]
- Murase, M. & Suzuki, H. (1986). Countercurrent Gas/Liquid Flow in Parallel Channels Simulating a Boiling Water Reactor Core, *Nuclear Engineering and Design*, Vol. 95, pp. 79-89.
- Nagae, T.; Murase, M.; Wu, T. & Vierow, K. (2005). Evaluation of Reflux Condensation Heat Transfer of Steam-Air Mixtures under Gas-Liquid Countercurrent Flow in a Vertical Tube, *J. Nucl. Sci. Tech.*, Vol. 42, No. 1, pp. 50-57.
- Nagae, T.; Murase, M.; Chikusa, T.; Vierow, K. & Wu, T. (2007a). Reflux Condensation Heat Transfer of Steam-Air Mixtures under Turbulent Flow Conditions in a Vertical Tube, *J. Nucl. Sci. Tech.*, Vol. 44, No. 2, pp. 171-182.

- Nagae, T.; Chikusa, T.; Murase, M. & Minami, N. (2007b). Analysis of Noncondensable Gas Recirculation Flow in Steam Generator U-tubes during Reflux Condensation using RELAP5, *J. Nucl. Sci. Tech.*, Vol. 44, No. 11, pp. 1395-1406.
- Nithianandan, C. K.; Morgan, C. D.; Shah, N. H. & Miller, F. R. (1986). RELAP5/MOD2 Model for Surface Condensation in the Presence of Noncondensable Gases, *Proceedings of 8<sup>th</sup> Int. Heat Transfer Conf.*, Vol. 4, pp. 1627-1633, San Francisco, USA, August 1986.
- Noel, B. & Deruaz, R. (1994). Reflux condenser mode with non-condensable gas: assessment of Cathare against Bethsy test 7.2c, *Nuclear Engineering and Design*, Vol. 149, pp. 291-298.
- Noel, B. & Dumont, D. (1997). Effect of Non-Condensable Gas on Steam Generator Condensation Heat Transfer: BETHSY Test 10.2, *Proceedings of 5<sup>th</sup> Int. Conf. on Nuclear Eng.*, ICONE5-2536, Nice, France, May 1997.
- Ozawa, M. (1999). Flow instability problems in steam-generating tubes, *Steam power engineering: thermal and hydraulic design principles*, Ishigai, S. Ed., pp. 323-385, Cambridge University Press, Cambridge.
- The RELAP5 Development Team (1995). RELAP5/MOD3 Code Manual, NUREG/CR-5535, INEL-95/0174, Vo. 2, Idaho National Engineering Laboratory, Idaho Falls, ID.
- Vierow, K.; Nagae, T. & Wu, T. (2003). Experimental investigation of reflux condensation heat transfer in PWR steam generator tubes in the presence of non-condensable gases, *Proceedings of The 10<sup>th</sup> Int. Topical Meeting on Nuclear Thermal Hydraulics*, Seoul, Korea, October 2003.
- Wallis, G. B. (1969). *One-dimensional Two-phase Flow*, McGraw Hill, New York.
- Wallis, G. B., et al. (1981). Countercurrent Gas-Liquid Flow in Parallel Vertical Tubes, *Int. J. of Multiphase Flow*, Vol. 7, pp. 1-19.



# Coolant Channel Module CCM. An Universally Applicable Thermal-Hydraulic Drift-Flux Based Separate-Region Mixture-Fluid Model

Alois Hoeld

*Retired from GRS, Garching/Munich  
Bernaysstr. 16A, D-80937 Munich  
F.R. of Germany*

## 1. Introduction

The development of LWR Nuclear Power Plants (NPP) and the question after their safety behaviour have enhanced the need for adequate theoretical descriptions of these plants. Thus thermal-hydraulic models and, based on them, effective computer codes played already very early an important role within the field of NPP safety research. The models and codes should have the potential to describe the steady state and transient behaviour of characteristic key parameters of a single- or two-phase fluid flowing along the corresponding loops of such a plant and thus also along any type of heated or non-heated coolant channels.

Obviously many discussions have and will continue to take place among experts as to which type of theoretical approach should be chosen for the correct description of thermal-hydraulic two-phase problems when looking at the wide range of applications. Very comprehensive reviews and critical discussions of different possible methods have been published already very early in the book of Ishii (1990), in the workshop presentations of Wulff (1987) and by Banerjee and Yadigaroglu (1990). Due to the presence of discontinuities in the first principle of mass conservation in a two-phase flow model, caused at the transition from single- to two-phase flow and vice versa, it turns out that the direct solution of the basic conservation equations for mixture fluid along such a coolant channel gets very complicated. What is thus the most appropriate way to deal with such a special thermal-hydraulic problem?

With the introduction of the '**Separate-Phase Model**' concept it could already very early a very successful way be shown how to avoid upcoming difficulties in finding solution methods to treat such a two-phase flow situation under the assumption of separating the two-phases of such a mixture-flow completely from each other. This yields a system of 4-, 5- or sometimes even 6-equations defined by splitting each of the conservation equations into two so-called 'field equations'. Hence, compared to the four independent parameters characterising the mixture fluid, the separate-phase systems demand a much higher number of additional variables and special assumptions. This has the consequence that an enormous

amount of CPU-time has to be expended for the solution of the resulting sets of differential and analytical equations in a computer code. It is clear that, based on such assumptions, the interfacial relations both between each phase and the (heated or cooled) wall but also between each of the two phases are completely rearranged, raising the difficult question of how to describe in a realistic way the direct heat input into and between the phases and the movement resp. the friction of the phases between them. This problem is solved in such an approach by introducing corresponding exchange (=closure) terms between the equations based on special transfer (= closure) laws. Since they can, however, not be based on fundamental laws or at least on experimental measurements this approach requires a significant effort to find a correct formulation of the exchange terms between the phases. It must therefore be recognised that the quality of these basic equations (and especially their boundary conditions) will be intimately related to the (rather artificial and possibly speculative) assumptions adopted if comparing them with the original conservation laws of the 3-equation system and their constitutive equations as well. The problem of a correct description of the interfacial reaction between the phases and the wall remains. Hence, very often no consistency between different models due to their underlying assumptions can be stated. Another problem arises from the fact that special methods have to be foreseen to describe the moving boiling or mixture level boundaries (or at least to estimate their 'condensed' levels) in such a mixture fluid (see, for example, the 'Level Tracking' method in TRAC). Additionally, these methods show often deficiencies in describing extreme situations such as the treatment of single- and two-phase flow at the ceasing of natural circulation, the power situations if decreasing to zero etc. The codes are sometimes very inflexible, especially if they have to provide to a very complex physical system also elements which belong not to the usual class of 'thermal-hydraulic coolant channels'. These can, for example, be nuclear kinetic considerations, heat transfer out of a fuel rod or through a tube wall, pressure build-up within a compartment, time delay during the movement of an enthalpy front along a downcomer, natural circulation along a closed loop, parallel channels, inner loops etc.

Despite of these difficulties the 'Separate-Phase Models' have become increasingly fashionable and dominant in the last decades of thermal-hydraulics as demonstrated by the widely-used codes TRAC (Lilles et al., 1988, US-NRC, 2001a), CATHENA (Hanna, 1998), RELAP (US-NRC, 2001b, Shultz, 2003), CATHARE (Bestion, 1990), ATHLET (Burwell et al., 1989, Austregesilo et al., 2003, Lerchl et al., 2009).

Several reasons can be named why this method is preferred by many authors and users:

- Advantages due the unique formulation of the up to 6 basic partial differential eqs. which allows then also to apply a unique mathematical solution method,
- the possibility to circumvent discontinuities (Wulff, 1987) in simulating the transitions from single- to two-phase flow and vice versa, thus avoiding difficulties in describing the movement of phase boundaries along a coolant channel,
- avoiding the very difficult direct theoretical treatment of a mixture-fluid approach,
- allowing establishing within the resulting 'modular' codes the necessary set of solution equations (ODE-s and constitutive equations in dependence of corresponding perturbation parameters) by combining them by means of an adequate input data set, i.e. outside of the code, with the advantage that the user does not need to be familiar with the construction of digital codes.

- giving the possibility to assume further-on that, in the case of two-phase flow situations, the water-phase can adopt temperatures below, the steam phase above saturation conditions. This means, the model can also take care of 'thermal-hydraulic non-equilibrium' situations, an important advantage for the application of this class of codes (as this is for example the case if cold water is injected into a steam dome or steam into a sub-cooled water plenum etc.).

It is on the other hand clear that as an alternative for the description of two-phase phenomena by splitting them into different phases the direct solution of the basic equations of a **mixture-fluid technique** could be regarded as a very appropriate approach, provided that despite of the above mentioned difficulties an exact solution can be found. This direct method could therefore be seen as a real counterpart to the currently preferred and dominant 'separate-phase models'.

However, in the past the difficulties in the direct treatment of a 'mixture-fluid approach' have been responsible for the fact that only approximate and very simplified solutions for special situations could be provided, thus demanding severe restrictions in their field of application. As pointed-out by (Fabric, 1996) in the early seventies such simplified 'homogenous equilibrium models (HEM-s)' have been derived under the assumption of a homogeneous fluid, a mixture where water and steam phase are assumed to move with the same velocity, i.e. the slip remains equal to 1 and the relative and thus also drift velocities equal to 0. Since for most purposes this is too far from reality, it is obvious that such simplified 'homogeneous' approaches (see for example Dunn, 1998) could only be applied to special cases, for example where the speed of the calculation has to be enhanced in order to be usefully applied in comprehensive two-phase flow studies. Their shortcomings are mainly responsible for the seemingly widespread misunderstanding of the quality of 'mixture-fluid' models, their poor image and the subsequent unfair treatment of this class of models.

Zuber et al. (1965) and Wulff (1987) proposed already very early a concept called (a bit imprecisely) '**drift-flux model**' which has been continuously expanded according to the rising demands in reactor safety research. In fact it is a 'four-equation non-homogeneous non-equilibrium two-phase flow model' with mass-, energy- and momentum balances for the mixture and a separate mass balance for the vapour phase based on a specially developed 'drift-flux theory'. It has been successfully applied in a number of post-calculations of reactor transients (with up to ten times real-times simulation speed) including BWR instability simulations with large power and flow oscillations.

At the Gesellschaft für Anlagen- und Reaktorsicherheit (GRS) at Garching/Munich very early activities have been started too to develop thermal-hydraulic models and digital codes which have the potential to describe in a detailed way the overall transient and accidental behaviour of fluids flowing along the core but also the main components of different Nuclear Power Plants (NPP) types. For one of these components, namely the natural circulation U-tube steam generator together with its main steam system, an own theoretical model has been derived. The resulting digital code UTSG (Hoeld, 1978) could be used both in a stand-alone way but also as part of more comprehensive transient codes, such as the thermal-hydraulic GRS system code ATHLET (Burwell et al., Austregesilo, 2003) with an high level simulation language GCSM (General Control Simulation Module) to take care of the balance-of-plant (BOP) actions. Based on the experience of many years of application both at the GRS and a number of other institutes in different countries but also due to the

rising demands coming from the safety-related research studies this UTSG theory and code has been continuously extended, yielding finally a very satisfactory and mature code version UTSG-2 (Hoeld, 1990a).

During the research work for the development of the code UTSG-2 it arose finally the idea to establish an own basic element which is able to simulate the thermal-hydraulic mixture-fluid situation within any type of cooled or heated channel in an as general as possible way, having the aim to be applicable for any modular construction of complex thermal-hydraulic assemblies of pipes and junctions. Thereby, as described in detail in this paper, in contrast to the above mentioned class of 'separate-phase' modular codes instead of separating the phases of a mixture fluid within the entire coolant channel an alternative theoretical approach has been chosen, differing both in its form of application but also in its theoretical background. To circumvent the above mentioned difficulties due to discontinuities resulting from the spatial discretization of a coolant channel, resulting eventually in nodes with a transition from single- to two-phase flow and vice versa, a special and unique concept has been derived assuming that a (basic) coolant channel (BC) should be subdivided into a number of sub-channels (SC-s) with the imposition that each of these SC-s can consist of only two types of flow regimes, an SC with just a single-phase fluid, containing exclusively either sub-cooled water (setting  $L_{\text{FTYPE}}=1$ ) or superheated steam ( $L_{\text{FTYPE}}=2$ ), or an SC with a two-phase mixture ( $L_{\text{FTYPE}}=0$ ). The theoretical considerations of this '**separate-region approach**' (within the class of mixture-fluid models) can then be restricted to only these two regimes. Hence, for each SC type, the 'classical' 3 conservation equations for mass, energy and momentum can be treated in a direct way. In case of a sub-channel with mixture flow these basic equations have to be supported by a drift flux correlation yielding an additional relation for the appearing fourth variable, namely the steam mass flow. This can, eventually, be achieved by any two-phase correlation (for example also a slip correlation). But, to take care also of stagnant or counter-current flow situations, an effective drift-flux correlation seems to be more effective. For separate-phase models no such direct experimentally based correlations are available. It has to be noted that, different to the 'drift-flux model' where a 4-th mass balance equation for the vapour phase is introduced, the fundamental mixture-fluid equations are based on an adequate drift-flux correlation in an analytical form.

It is obvious that this procedure has, however, the consequence that varying SC entrance and outlet boundaries have to be considered too. As demonstrated in this paper an adequate way to solve this essential problem could be found and a corresponding procedure been established.

As a result of these theoretical considerations an universally applicable 1D thermal-hydraulic drift-flux based separate-region coolant channel module (and code) CCM could be constructed. Its aim is to make it possible to calculate automatically the steady state and transient behaviour of all characteristic parameters of a single- and two-phase fluid within the entire coolant channel. It represents thus a valuable tool for the establishment of complex codes and can contribute even in the case of complex thermal-hydraulic systems which may consist of a number of different types of (basic) coolant channels to the overall set of equations by determining automatically the different differential and constitutive equations needed for each of these sub- and thus basic channels.

To check the performance and validity of the code package CCM, to verify and validate it (see Hoeld, 1978, 1990b, 2002a, 2007a, 2007b) the digital code UTSG-2 has been extended to a new version, called UTSG-3. It is based, similarly as in the previous code UTSG-2, on the

same U-tube, main steam and downcomer (with feedwater injection) system layout, but now, among other essential improvements, the three characteristic channel elements of the code UTSG-2 (i.e. the primary and secondary side of the heat exchange region and the riser region) have been replaced by adequate CCM modules. Naturally, during the application of UTSG-3 and thus CCM both codes have been continuously expanded to a now very mature form (Hoeld, 1998b, 1999, 2000).

It is obvious that such a theoretical 'separate-region' approach can disclose a new way in describing thermal-hydraulic problems, regarding the resulting 'mixture-fluid' technique as a very appropriate way to circumvent the uncertainties apparent from the separation of the phases in a mixture flow. The starting equations are the direct consequence of the original fundamental physical laws for the conservation of mass, energy and momentum, supported by well-tested heat transfer and single- and two-phase friction correlation packages (and thus avoiding also the sometimes very speculative derivation of the 'closure' terms). In a very comprehensive study by (Hoeld, 2004b) a variety of arguments for the here presented type of approach is given, some of which will be discussed in the conclusions presented in chapter 6.

The very successful application of the code combination UTSG-3/CCM demonstrates the ability to find an exact and direct solution for the basic equations of a 'non-homogeneous drift-flux based thermal-hydraulic mixture-fluid coolant channel model'. The theoretical background of CCM will be described in very detail in the following chapters.

For the establishment of the corresponding (digital) module CCM, based on this theoretical model and written in double-precision (with its single-precision version CCMS) very specific methods had to be achieved, thereby taking into account the following points:

- The code should be easily applicable, demanding only a limited amount of easily available input data. It should also be able to simulate the thermal-hydraulic mixture-fluid situation along any cooled or heated channel in as general a way as possible. It should thus be able to describe any modular construction of complex thermal-hydraulic assemblies of pipes and junctions. Such an universally applicable tool can then be taken for calculating the steady state and transient behaviour of all the characteristic parameters of each of the appearing coolant channels and thus be a valuable element for the construction of complex computer codes. It should yield as output all the necessary time-derivatives and constitutive parameters of the coolant channels required for the establishment of an overall thermal-hydraulic code.
- It was the intention of CCM that it should act as a complete system in its own right, requiring only BC- (and not SC-) related, and thus easily available input parameters (geometry data, initial and boundary conditions, parameters resulting from the integration etc.). The partitioning of BC-s into SC-s is done at the begin of each recursion or time-step automatically within CCM, so no special actions are required of the user.
- Knowing now the characteristic parameters at all SC nodes (within a BC) then the single- and two-phase parameters at all node boundaries of the entire BC can be determined, but also also the corresponding time-derivatives of the averaged parameters over these nodes. This yields a final set of ODE-s and constitutive equations.
- The quality of such a model is very much dependent on the method by which the problem of the varying SC entrance and outlet boundaries can be solved, especially if they cross BC node boundaries during their movement along a channel. Hence, on the

basis of the 'Leibniz' rule (see eq.(29)), special measures had to be developed which allow the characterisation of their transient behaviour in deriving own differential equations.

- For the support of the nodalized differential equations along different SC-s a 'quadratic polygon approximation' procedure (PAX) was constructed in order to interrelate the mean nodal with the nodal boundary functions. Additionally, due to the possibility of varying SC entrance and outlet boundaries, nodal entrance gradients are also required from the PAX procedure too (See section 3.3).
- Several correlation packages such as, for example, packages for the thermodynamic properties of water and steam, heat transfer coefficients, drift flux correlations and single- and two-phase friction coefficients had to be established and implemented (See sections 2.2.1 to 2.2.4).
- In order to be able to describe also thermodynamic non-equilibrium situations it can be assumed that each phase is described by an own with each other interacting BC. Then, in the model the possibility of a variable cross flow area along the entire channel had to be considered as well.

Within the CCM procedure two further aspects play an important role. These are, however, not essential for the development of mixture-fluid models but can help enormously to enhance the computational speed and applicability of the resulting code in simulating a complex net of coolant pipes:

- Solution of energy and mass balance equations during each intermediate time step independently from momentum balance considerations in order to avoid the heavy CPU-time consuming solution of stiff equations (See section 3.5).
- This allows then also the introduction of an 'open' and 'closed channel' concept (see section 3.11), a special method which can be very helpful in describing complex physical systems with eventually inner loops, as this can be done for example if simulating a 3D compartment by parallel channels (Jewer et al., 2005).

The application of a direct mixture-fluid technique follows a long tradition of research efforts. Ishii (1990), a pioneer of two-fluid modelling, states with respect to the application of effective drift-flux correlation packages in thermal-hydraulic models: 'In view of the limited data base presently available and difficulties associated with detailed measurements in two-phase flow, an advanced mixture-fluid model is probably the most reliable and accurate tool for standard two-phase flow problems'. There is no new knowledge available to indicate that this view is invalid.

Generally, the mixture-fluid approach is in line with (Fabric, 1996) who names three strong points arguing in favour of this type of drift-flux based mixture-fluid models:

- They are supported by a wealth of test data,
  - they do not require unknown or untested closure relations concerning mass, energy and momentum exchange between phases (thus influencing the reliability of the codes),
  - they are much simpler to apply,
- and, it can be added,
- discontinuities during phase changes can be avoided by deriving special solution procedures for the simulation of the movement of these phase boundaries,
  - the possibility to circumvent a set of 'stiff' ODE-s saves an enormous amount of CPU time which means that the other parts of the code can be treated in much more detail.

A first version of the module CCM has already been presented in October 2005 at the NURETH-11 conference at Avignon (Hoeld, 2005), a corresponding detailed version published then in (Hoeld, 2007a). Due to the rising experiences in applying this module it has been continuously adapted during the last years resulting in the here presented final form.

The theoretical model and module CCM has the potential to be extended, in a second phase, to a 'porous' coolant channel model too, porous at each node boundary, i.e. to the more detailed case where coolant mass (water, steam and/or water/steam mixtures) is exchanged also at nodal boundaries between neighbouring channels (and not only at BC entrance or outlet).

Parallel to this paper in a second article within this 'Open Access Book' a detailed description of the last status of the resulting 'Natural-circulation U-tube Steam Generator' Code UTSG-3 (including main steam and feedwater systems) is given by (Hoeld, 2011). It demonstrates the ability to apply the 'Coolant Channel Module CCM' as an important element in a complex system of loops and branches in a successful way.

## 2. Thermal-hydraulic drift-flux based mixture fluid approach

### 2.1 Thermal-hydraulic conservation equations

Thermal-hydraulic single-phase or mixture-fluid models for coolant channels or, as presented here, for each of the sub-channels are generally based on a number of fundamental physical laws, i.e. on genuine conservation equations for mass, energy and momentum. They are supported by adequate constitutive equations (packages for thermodynamic and transport properties of water and steam, for heat transfer coefficients, for drift flux, for single- and two-phase friction coefficients etc.). Thereby second-order terms (representing, for example, dissipation in flow direction, drag and gravitational work) are frequently found to be quantitatively insignificant (Wulff, 1987) and will thus not be taken into account.

In view of possible applications as an element in complex thermal-hydraulic ensembles outside of CCM eventually a fourth and fifth conservation law has to be considered too. The equation for volume balance makes it possible to calculate for example the transient behaviour of the overall system pressure. Together with the local pressure differences then the absolute pressure profile along the BC can be determined. The fifth physical law is based on the (trivial) fact that the sum of all pressure decrease terms along a closed loop must be zero. It is the basis for the treatment of the thermal-hydraulics of a channel according on 'the closed channel concept'. If thus such a channel acts as a part of a closed loop (with given fixed BC entrance and outlet pressure terms) then the necessary entrance mass flow term has been determined in order to fulfil the demand from momentum balance.

#### 2.1.1 Mass balance (for both single- and two-phase flow)

$$\frac{\partial}{\partial t} \{A[(1-\alpha)\rho_w + \alpha\rho_s]\} + \frac{\partial}{\partial z} G = 0 \quad (1)$$

containing the density terms  $\rho_w$  and  $\rho_s$  for sub-cooled or saturated water and saturated or superheated steam, the void fraction  $\alpha$  and the cross flow area  $A$  which can eventually be changing along the coolant channel. It determines, after a nodalization, the total mass flow  $G=G_w+G_s$  at node outlet in dependence of its node entrance value.

### 2.1.2 Energy balance (for both single- and two-phase flow)

$$\frac{\partial}{\partial t} \{A[(1-\alpha)\rho_w h_w + \alpha\rho_s h_s - P]\} + \frac{\partial}{\partial z} [G_w h_w + G_s h_s] = q_L = U q_F = A q \quad (2)$$

containing the enthalpy terms  $h_w$  and  $h_s$  for sub-cooled or saturated water and saturated or superheated steam. As boundary values either the 'linear power  $q_L$ ', the 'heat flux  $q_F$ ' along the heated (or cooled) tube wall (with its perimeter  $U_{TW}$ ) or the local 'power density term  $q$ ' are demanded to be known (See also sections 2.2.4 and 3.5). They are assumed to be directed into the coolant (then having a positive sign).

After an appropriate finite-difference nodalization procedure (see chapter 3.2) it follow in the transient case (as demonstrated in the sections 3.7 to 3.9) then differential equations

- for the mean nodal enthalpies ( $h_{WMn}$ ,  $h_{SMn}$ ) of either sub-cooled water (if  $L_{FTYPE}=1$ ) or superheated steam ( $L_{FTYPE}=2$ ) in the case of a single-phase flow situation and thus, by applying water/steam tables, corresponding coolant temperature terms ( $T_{WMn}$ ,  $T_{SMn}$ ) too, or, at two-phase flow conditions ( $L_{FTYPE}=0$ ), for the mean nodal void fraction  $\alpha_{Mn}$  over each node  $n$

and

- at the transition from single- to two-phase (and vice versa) for the boiling boundary  $z_{BB}$  (if  $\alpha=0$ ) or, if  $\alpha=1$ , the mixture (or dry-out) level  $z_{ML}$  (section 3.9). Thereby it can be taken advantage of the fact that at these positions either the coolant enthalpy or temperature are limited by its saturation enthalpy or temperature ( $h_w = h'$  or  $h_s = h''$  and  $T_w = T_s = T_{SAT}$  or  $T_s = T_{SAT}$ ) or the void fraction becomes equal to 1 (or 0).

### 2.1.3 Momentum balance (for both single- and two-phase flow)

$$\frac{\partial}{\partial t} (G_F) + \left( \frac{\partial P}{\partial z} \right) = \left( \frac{\partial P}{\partial z} \right)_A + \left( \frac{\partial P}{\partial z} \right)_S + \left( \frac{\partial P}{\partial z} \right)_F + \left( \frac{\partial P}{\partial z} \right)_X \quad (3)$$

describing either the pressure differences (at steady state) or (in the transient case) the change in the total mass flux ( $G_F = G/A$ ) along a channel.

The general pressure gradient ( $\frac{\partial P}{\partial z}$ ) can be determined in dependence of

- the mass acceleration

$$\left( \frac{\partial P}{\partial z} \right)_A = - \frac{\partial}{\partial z} [(G_{FW} v_w + G_{FS} v_s)] \quad (4)$$

with  $v_s$  and  $v_w$  denoting steam and water velocities given by the eqs.(9) and (10),

- the static head

$$\left( \frac{\partial P}{\partial z} \right)_S = - \cos(\Phi_{ZG}) g_c [\alpha\rho_s + (1-\alpha)\rho_w] \quad (5)$$

with  $\Phi_{ZG}$  representing the angle between upwards and flow direction, i.e.,

$\cos(\Phi_{ZG}) = \pm z_{EL}/z_L$  and  $z_L$  denoting the length,  $z_{EL}$  the relative elevation height with a positive sign at upwards flow)

- the single- and/or two-phase friction term

$$\left( \frac{\partial P}{\partial z} \right)_F = - f_R \frac{G_F |G_F|}{2 d_{HW} \rho} \quad (6)$$



with a friction factor derived from corresponding constitutive equations (section 2.2.2) and finally

- the direct perturbations  $(\partial P / \partial z)_x$  from outside, arising either by starting an external pump or considering a pressure adjustment due to mass exchange between parallel channel.

## 2.2 Constitutive equations

For the exact description of the steady state and transient behaviour of single- or two-phase fluids there are needed, besides the conservation equations, a number of mostly empirical constitutive relations. Naturally, any effective correlation package can be used for this purpose. A number of such correlations have been developed at the GRS and thoroughly tested, showing very satisfactory results.

### 2.2.1 Thermodynamic and transport properties of water and steam

The different thermodynamic and transport properties for water and steam demanded by the conservation and constitutive equations have to be determined by applying adequate water/steam tables. This is, for light-water systems, realized in the code package MPP (Hoeld, 1996). It yields the wanted values such as the saturation temperature  $T_{SAT}$ , densities ( $\rho'$ ,  $\rho''$ ), enthalpies ( $h'$ ,  $h''$ ) for saturated water and steam with respect to their local pressure (P) and corresponding densities ( $\rho$ ) and enthalpies (h) for sub-cooled water or superheated steam (index W and S) again with respect to their independent local parameters T and P (but also h and P).

For the solution of the conservation equations also time-derivatives of these thermodynamic properties which respect to their independent local parameters are demanded. They get, for example for the case of an enthalpy term h, the form

$$\begin{aligned} \frac{d}{dt} h(z,t) &= \frac{d}{dt} h[T(z,t), P(z,t)] = \left( \frac{\partial h}{\partial T} \right) \frac{d}{dt} T_{Mn}(t) + \left( \frac{\partial h}{\partial P} \right)_{Mn} \frac{d}{dt} P_{Mn}(t) \\ &= h^T \frac{d}{dt} T_{Mn}(z,t) + h^P \frac{d}{dt} P_{Mn}(z,t) \end{aligned} \quad (7)$$

Hence the thermodynamic water/steam tables should provide also the derivatives ( $T_{SAT}^P$ ,  $\rho'^P$ ,  $\rho''^P$ ,  $h'^P$ ,  $h''^P$ ) for saturated water and saturated steam but also the partial derivatives ( $\rho^T$ ,  $\rho^P$ ,  $c_p = h^T$ ,  $h^P$ ) for subcooled water or superheated steam with respect to their independent parameters T and P (but also h and P). Additionally, corresponding thermodynamic transport properties such as 'dynamic viscosity' and 'thermal heat conductivity' (and thus the 'Prantl number') are asked from some constitutive equations too as this can be stated, for example, for the code packages MPPWS and MPPETA (Hoeld, 1996). All of them have been derived on the basis of tables given by (Schmidt and Grigull, 1982) and (Haar et al., 1988). Obviously, the CCM method is also applicable for other coolant systems (heavy water, gas) if adequate thermodynamic tables for this type of fluids are available.

### 2.2.2 Single- and two-phase friction factors

In the case of **single-phase flow** with regard to equation (6) the friction factor  $f_R$  will, as recommended by (Moody, 1994), be set equal to the Darcy-Weisbach single-phase friction factor  $f_{DW}$  being represented by

$$f_R = f_{DW} = \frac{1}{\xi^2} \quad (\text{at single-phase flow}) \quad (8)$$

with the parameter  $\xi$  depending on the Reynolds number  $Re = G d_H / (A \eta)$  and the relative roughness  $\varepsilon_{TW} / d_H$  of the wall surface. The factor  $\xi$  can be approximated by the relation

$$\begin{aligned} \xi &= 2 \log_{10} \left( \frac{d_H}{\varepsilon_{TW}} \right) + 1.14 \quad \text{if } Re > Re_{CTB} = 441.19 \left( \frac{d_H}{\varepsilon_{TW}} \right)^{1.1772} \\ &= -2 \log_{10} \left( 2.51 \frac{\xi}{Re} + \frac{\varepsilon_{TW}}{3.71 d_H} \right) \quad \text{if } Re \leq Re_{CTB} \end{aligned} \quad (9)$$

For **two-phase flow** conditions this factor can be extended to

$$f_R = f_{DW} \Phi_{2PF}^2 \quad (\text{at two-phase flow}) \quad (10)$$

with the single-phase part  $f_{DW}$  to be determined under the assumption that the fluid moves with the total mass flow  $G$  (= 100 % liquid flow). The two-phase multiplier  $\Phi_{2PF}^2$  (dependent only on steam quality and pressure) is given by (Martinelli-Nelson, 1948) as measured curves. A possible attempt to describe these curves analytically could, as proposed by (Hoeld, 1990a, 2004a), be given by the approximation function

$$\Phi_{2PF}^2 = \exp \frac{f_1 X}{\sqrt{1 + f_2 X + f_3 X^2}} \rightarrow \frac{\rho'}{\rho''} \frac{(f_{WD})_S}{(f_{WD})_W} \quad \text{if } X \rightarrow 1 \quad (11)$$

with the factors

$$\begin{aligned} f_1 &= 44.216 + 0.7428 \cdot 10^{-6} P \\ f_2 &= 12.645 + 4.9841 \cdot 10^{-6} P \\ f_3 &= 17.975 + 25.7440 \cdot 10^{-6} P \end{aligned} \quad (P \text{ in Pa}) \quad (12)$$

For the special case of a steam quality  $X$  nearing 1 the friction term has to approach the single-phase steam friction factor  $(f_{DW})_S$ . Thus the two-phase multiplier has, as shown above, to be corrected in an appropriate way (for example, by changing the curve after a maximum of  $X$  at about 0.8).

### 2.2.3 Drift flux correlation

In the case of two-phase flow, the three conservation equations (1), (2) and (3) demanding four independent variables ( $G$ ,  $\alpha$ ,  $P$  and  $G_S$ ) have to be completed by an additional two-phase relation in order to obtain an adequate representation of the needed fourth variable  $G_S$ . This can be achieved by any two-phase correlation, e.g. also a slip correlation. However, to take care of stagnant or counter-current flow situations too an effective drift-flux correlation seemed here to be more appropriate, correlations which can be seen as a 'bridge' between  $G_S$  and  $\alpha$ .

For this purpose an own drift-flux correlation package has been established, named MDS (Hoeld, 2001 and 2002a). It is based on the result of a very comprehensive study (Hoeld et al., 1992) and (Hoeld, 1994) comparing different slip (6) and drift-flux (3) correlations with each other and also with a number (5) of available experimental data in order to check their validity over a wide range of application. Besides them, it had to be found which of them is

most suited for incorporation into the MDS package and thus CCM code. Due to different requirements in the application of CCM it turned out that the drift-flux correlation package in the form of the 'flooding-based full-range' Sonnenburg correlation (1989) should be preferred. This correlation combines the common drift-flux procedure being formulated by (Zuber-Findlay, 1965) and expanded by (Ishii-Mishima, 1980) and (Ishii, 1990) etc. with the modern envelope theory. The correlation in the final package MDS had to be rearranged in such a way that also the special cases of  $\alpha \rightarrow 0$  or  $\alpha \rightarrow 1$  (where its absolute values but also their gradients are demanded by CCM) could be treated. Additionally, an inverse form had to be installed and considerations with respect to a possible entrainment be included.

For the case of a vertical channel this correlation can be represented as

$$v_D = 1.5 v_{WLM} C_0 C_{VD} [(1+C_{VD}^2)^{3/2} - (1.5+C_{VD}^2) C_{VD}] \quad (13)$$

with  $v_D \rightarrow v_{D0} = \frac{9}{16} C_0 v_{WLM}$  if  $\alpha \rightarrow 0$

where the coefficient  $C_{VD}$  is given by

$$C_{VD} = \frac{2}{3} \frac{v_{SLIM}}{v_{WLM}} \frac{1 - C_0 \alpha}{C_0 \alpha} \quad (14)$$

The resulting package MDS yields in combination with an adequate correlation for the phase distribution parameter  $C_0$  relations for the limit velocities  $v_{SLIM}$  and  $v_{WLM}$  and thus (independently of the total mass flow  $G$ ) for the drift velocity  $v_D$  in relation to the void fraction  $\alpha$ . All of them are dependent on the given 'system pressure  $P$ ', the 'hydraulic diameter  $d_{HW}$ ' (with respect to the wetted surface  $A_{WSF}$ ) and its inclination angle  $\Phi_{ZG}$ , on specifications about the geometry type ( $L_{GTYPE}$ ) and, for low void fractions, the information whether the channel is heated or not.

The drift flux theory can be expressed (by a now already on  $G$  dependent) steam mass flow term

$$G_S = \frac{\rho'^{1/2}}{\rho'} \frac{\alpha}{C_{CC}} (C_0 G + A \rho' v_D) = A G_{FS} \quad (15)$$

with the coefficient

$$C_{CC} = 1 - (1 - \frac{\rho'^{1/2}}{\rho'}) \alpha C_0 \rightarrow 1 \text{ if } \alpha \rightarrow 0 \text{ and } \rightarrow \frac{\rho'^{1/2}}{\rho'} \text{ if } \alpha \rightarrow 1 \quad (16)$$

by considering the definition equations of the velocities for steam, water and drift

$$v_D = (1 - \alpha C_0) v_S - (1 - \alpha) C_0 v_W \quad (17)$$

$$v_S = \frac{G_S}{A \alpha \rho'^{1/2}} \quad \text{with } G_S = G - G_W = XG \quad (18)$$

$$v_W = \frac{G_W}{A(1 - \alpha) \rho'} \quad \text{with } G_W = (1 - X)G \quad (19)$$

By means of this drift-flux correlation now the fourth variable is determined too. Then also all other characteristic two-phase parameters can be derived starting from their definition equations. Their interrelations are shown, for example, in the tables of (Hoeld, 2001 and 2002a). Such two-phase parameters could be the phase distribution parameter  $C_0$ , the water mass flow  $G_W$ , drift, water, steam and relative velocities  $v_D$ ,  $v_W$ ,  $v_S$  and  $v_R$  and eventually the steam quality  $X$ . Especially the determination of the steam mass flow gradient

$$\begin{aligned} G_S^{(\alpha)} \rightarrow G_{S0}^{(\alpha)} &= \frac{\rho''}{\rho'} (C_{00} G + A \rho' v_{D0}) = A \rho' v_{S0} \quad \text{or} = 0 \quad \text{if } \alpha \rightarrow 0 \text{ and } L_{HEATD} = 0 \text{ or } 1 \\ \rightarrow G_{S1}^{(\alpha)} &= A \frac{\rho''}{\rho'} (1 + C_{01}^{(\alpha)}) (G - \rho' v_{SLIM}) = A \rho' v_{W1} \quad \text{if } \alpha \rightarrow 1 \end{aligned} \quad (20)$$

will play (as shown, for example, in eq.(70)) an important part, if looking to the special situation that the entrance or outlet position of a SC is crossing a BC node boundary ( $\alpha \rightarrow 0$  or  $\rightarrow 1$ ). This possibility makes the drift-flux package MDS to an indispensable part in the nodalization procedure of the mixture-fluid mass and energy balance.

The solution of the basic (algebraic) set of steady state equations demands the steam mass flow term  $G_S$  as the independent variable, and not the void fraction  $\alpha$ . The same is the case after an injection of a two-phase mixture coming from a 'porous' channel or an abrupt change in steam mass flux  $G_{FS}$  (as this takes place after a change in total mass flow or in the cross flow area of a following BC). Then the total and the steam mass flows  $G$  and  $G_S$  have to be taken as the basis for further two-phase considerations. The void fraction  $\alpha$  and other two-phase parameters ( $v_D$ ,  $C_0$ ) can then to be determined from an inverse (INV) form of this drift-flux correlation (with  $G_S$  now as input):

$$\alpha = f_{\text{DRIFT}}^{(\text{INV})} (G_S \text{ or } v_D, G, P, \frac{Z_{EL}}{Z_L}, d_{HW}, \dots) \quad (21)$$

As shown in (Hoeld, 2002a) counter-current flow (CCF) along the entire void fraction range can be stated if the signs of the gradients of the  $G_S$ - $\alpha$  curve at  $\alpha = 0$  and  $\alpha = 1$  are opposite, i.e. if the total mass flux  $G_F$  lies within certain lower and upper limits

$$\begin{aligned} \text{If } G_{FCL} \leq G_F = \frac{G}{A} \leq G_{FCU} \quad \text{then CCF} \\ (\text{with } G_{FCL} = -\frac{9}{16} \rho' v_{W LIM} \text{ and } G_{FCU} = \rho'' v_{S LIM}) \end{aligned} \quad (22)$$

Besides vertical up- or downwards, co-, stagnant or even counter-current two-phase flow situations (along channels of different geometry types such as rod bundles, rectangular ducts, round pipes etc.) the drift-flux correlations must have the potential to describe also two-phase flow situations through inclined or even horizontal channels in order to make the theoretical model as generally applicable as possible.

Usually correlations and thus also the drift-flux theory are based on steady state measurements. During transient calculations the correlation can thus be used only in a pseudo-stationary way, i.e., a change in void fraction results in an immediate change in drift velocity and thus in all the other characteristic two-phase parameters. There exist, however, physical phenomena (interactions of melt with water, condensation shocks, water and steam

hammer) where the delay between relative velocity and void fraction has a special importance, also if this delay lays within a range of 0.01 to 0.1 s. In the 'drift flux model' this is taken care by the fourth mass balance equation for the steam, in the separate-phase models by the (time-dependent) exchange term within the mass balance equations for the two phases water and steam. To cover thus in this approach also such transient phenomena the drift-flux considerations can be extended by providing the drift velocity  $v_D$  with respect to the void fraction with a corresponding time-delay function of 1-st order. Then the original (pseudo-steady state) drift velocity parameter  $v_D = v_{DPSE}$  has to be expanded to its transient counter-part

$$v_D = v_{DPSE} - (v_{DPSE} - v_{DB}) \exp\left(-\frac{t - t_B}{\Theta_{VDT}}\right) \quad (23)$$

with  $v_{DB} = v_D$  at the begin of a time interval  $t = t_B$ . All the other two-phase parameters are then calculated accordingly. The disadvantage of not directly knowing the time coefficient  $\Theta_{VDT}$  is outweighed by the advantage of having a direct and controlled input coefficient, avoiding thus the uncertainties of the sometimes very complex separate-phase theory. There exist different possibilities to determine indirectly this coefficient, either from similar theoretical considerations as performed to establish the exchange terms, from experience or from adequate parameter studies.

## 2.2.4 Heat transfer coefficients

As input to the energy balance eq.(2) the linear power value  $q_L$  (or the corresponding heat flux  $q_F$  along the perimeter  $U_{TW}$ ) are demanded. They describe the heat transferred into or out of the coolant channel), i.e. from a heated or cooled surface (for example from or into a U-tube wall or out of the casing of a fuel rod). These terms (but also the local surface temperature  $T_{TW}$  of the channel wall) can be determined by solving an adequate Fourier heat conduction equation with its boundary condition

$$q_F = \alpha_{TW} (T_{TW} - T) = \frac{q_L}{U} = \frac{A}{U} q \quad (24)$$

This is, for example, demonstrated for the case of heat conduction through a U-tube wall in (Hoeld, 2002b, 2011).

Hence, a method how to get the necessary heat transfer coefficients  $\alpha_{TW}$  at different flow regimes within a coolant channel had to be established. In connection with the development of the UTSG code (and thus also of CCM) an own very comprehensive heat transfer coefficient package, called HETRAC (Hoeld 1988a), has been established. It combines, for example, especially for this purpose chosen HTC correlations for each possible flow situation within LWR-s and steam generators (i.e., into or out of heated or cooled tube walls or fuel elements) in a very effective way. Thereby adequate correlations for the cases of sub-cooled water, sub-cooled and nucleate boiling, onset of critical heat flux, transient or instable film boiling, stable film boiling, onset of superheating and superheated steam for different geometry constellations and over a wide range of input parameters (pressures, total and steam mass flows, coolant temperatures, wall temperatures or heat fluxes etc.) had to be selected. The package describes not only heat transfer from wall to the different phases but also between these phases.

This classic method is different to the 'separate-phase' models where it must be assumed that the heat is transferred both directly from the wall to each of the two possible phases but also exchanged between them. There arises then the question how the corresponding heat transfer coefficients for each phase should look like.

### 3. Coolant channel module CCM

#### 3.1 Channel geometry and finite-difference nodalization

The theoretical considerations take advantage of the fact that, as sketched in fig.1, a 'basic' coolant channel (BC) can, according to their flow regimes (characterized by the logical  $L_{FTYPE}$

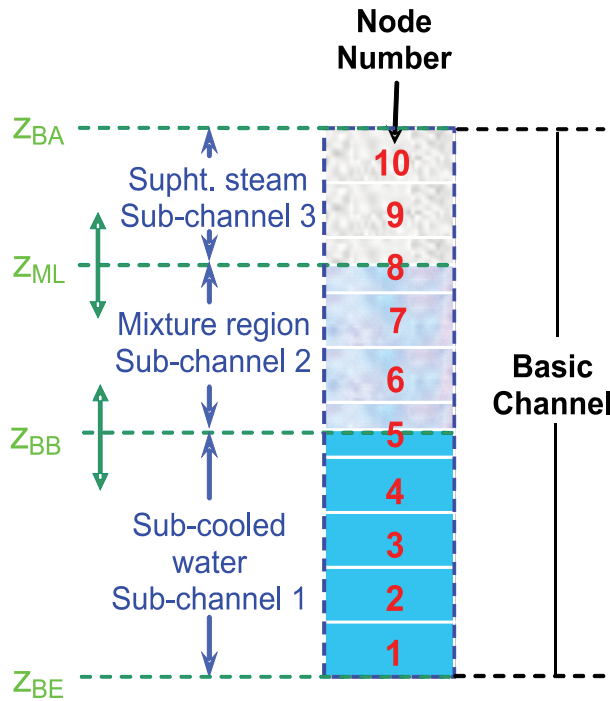


Fig. 1. Subdivision of a 'basic channel' into 'sub-channels' according to their flow regimes. Discretization of BC and SC-s

= 0, 1 or 2), be subdivided into a number ( $N_{SCT}$ ) of sub-channels (SC-s), with the consequence of having variable entrance and outlet positions.

The BC with its total length  $Z_{BT} = Z_{BA} - Z_{BE}$  can then, for discretization purposes, be subdivided into a number of (not necessarily equidistant)  $N_{BT}$  nodes. Their nodal positions are  $Z_{BE}$ ,  $Z_{Bk}$  (with  $k=1, N_{BT}$ ), the elevation heights  $Z_{ELBE}$ ,  $Z_{ELk}$ , the nodal length  $\Delta Z_{Bk} = Z_{Bk} - Z_{Bk-1}$ , nodal elevations  $\Delta z_{ELBk} = Z_{ELBk} - Z_{ELBk-1}$ , locally varying cross flow and average areas  $A_{Bk}$  and  $A_{BMk} = 0.5(A_{Bk} + A_{Bk-1})$  with the slopes  $A_{Bk}^z = (A_{Bk} - A_{Bk-1}) / \Delta z_{Bk}$  and corresponding nodal volumes  $V_{BMk} = \Delta z_{Bk} A_{BMk}$ . All of them can be assumed to be known from input.

As a consequence, each of the sub-channels (SC-s) is then subdivided too, now into a number of  $N_{CT}$  SC nodes with geometry data being identical to the corresponding BC values, except, of course, at their entrance and outlet positions. The SC entrance position  $Z_{CE}$

and their function  $f_{CE}$  are either identical with the BC entrance values  $z_{BE}$  and  $f_{BE}$  or equal to the outlet values of the SC before. The SC outlet position ( $z_{CA}$ ) is either limited by the BC outlet ( $z_{BA}$ ) or characterized by the fact that the corresponding outlet function has reached an upper or lower limit ( $f_{LIMCA}$ ), with the term representing either a function at the boiling boundary or a mixture level. Such a function follows from the given BC limit values and will, in the case of single-phase flow, be equal to the saturation temperature  $T_{SATCA}$  or saturation enthalpies ( $h'$  or  $h''$  if  $L_{FTYPE}=1$  or 2), in the case of two-phase flow ( $L_{FTYPE}=0$ ) equal to a void fraction of  $\alpha = 1$  or  $0$ . The moving SC inlet and outlet positions  $z_{CE}$  and  $z_{CA}$  can (together with their corresponding BC nodes  $N_{BCE}$  and  $N_{BCA} = N_{BCE} + N_{CT}$ ) be determined according to the conditions ( $z_{BNk-1} \leq z_{CE} < z_{BNk}$  at  $k = N_{BCE}$ ) and ( $z_{BNk-1} \leq z_{CA} < z_{BNk}$  at  $k = N_{BCA}$ ). Then also the total number of SC nodes ( $N_{CT} = N_{BCA} - N_{BCE}$ ) is given, the connection between  $n$  and  $k$  ( $n = k - N_{BCE}$  with  $n=1, N_{CT}$ ), the corresponding positions ( $z_{Nn}$ ,  $z_{ELCE}$ ,  $z_{ELNn}$ ), their lengths ( $\Delta z_{Nn} = z_{Nn} - z_{Nn-1}$ ), elevations ( $\Delta z_{ELNn} = z_{ELNn} - z_{ELNn-1}$ ), and volumes ( $V_{Mn} = z_{Nn} A_{Mn}$ ) and nodal boundary and mean nodal flow areas ( $A_{Nn}$ ,  $A_{Mn}$ ) with

$$A_{Nn} = A_{Nn-1} + A_{Bk}^z \frac{\Delta z_{Nn}}{\Delta z_{Bk}}$$

$$A_{Mn} = 0.5(A_{Nn} + A_{Nn-1}) = A_{Nn-1} + 0.5 A_{Bk}^z \frac{\Delta z_{Nn}}{\Delta z_{Bk}} \quad (n=1, N_{CT}, k=n + N_{BCE}) \quad (25)$$

Hence, also their time-derivatives and that of the nodal volumes can be ascertained from the relations above.

### 3.2 Spatial discretization of PDE-s of 1-st order (Modified finite element method)

Based on this nodalization the spatial discretization of the fundamental eqs.(1) to (3) can be performed by means of a 'modified finite element method'. This means that if a partial differential equation (PDE) of 1-st order having the general form with respect to a general solution function  $f(z,t)$

$$\frac{\partial}{\partial t} f(z,t) + \frac{\partial}{\partial z} H[f(z,t)] = R[f(z,t)] \quad (26)$$

is integrated over the length of a SC node three types of discretization elements can be expected:

- Integrating a function  $f(z,t)$  over a SC node  $n$  yields the nodal mean function values  $f_{Mn}$

$$\int_{z_{Nn-1}(t)}^{z_{Nn}(t)} R[f(z,t)] dz = \Delta z_{Nn}(t) R[f_{Mn}(t)] \quad (n=1, N_{CT}) \quad (27)$$

- integrating over the gradient of the function yields to a difference of functions values at their node boundaries

$$\int_{z_{Nn-1}(t)}^{z_{Nn}(t)} \frac{\partial}{\partial z} H[f(z,t)] dz = H[f_{Nn}(t)] - H[f_{Nn-1}(t)] \quad (n=1, N_{CT}) \quad (28)$$

- and finally the integration over a time-derivative of a function (by applying the 'Leibniz' rule)

$$\int_{z_{Nn-1}(t)}^{z_{Nn}(t)} \frac{\partial}{\partial t} f(z,t) dz = \Delta z_{Nn}(t) \frac{d}{dt} f_{Mn}(t) - [f_{Nn}(t) - f_{Mn}(t)] \frac{d}{dt} z_{Nn}(t) - [f_{Mn}(t) - f_{Nn-1}(t)] \frac{d}{dt} z_{Nn-1}(t) \quad (n=1, N_{CT}) \quad (29)$$

This last rule plays in the case of the here presented 'separate-region' mixture-fluid approach an outstanding part, allowing determining the movement of SC boundaries within a BC in a direct way, i.e., yielding time-derivatives of parameters which represent either a boiling boundary or a mixture level. This procedure differs considerably from some of the 'separate-phase methods' where, as already pointed out, very often only the collapsed levels of a mixture fluid can be calculated.

### 3.3 Quadratic polygon approximation procedure PAX

Looking at the above described three different types of possible discretization elements it is obvious that appropriate methods had to be developed which can help to establish relations between such mean nodal ( $f_{Mn}$ ) and node boundary ( $f_{Nn}$ ) function values after a discretization procedure.

In the 'separate-phase' models mostly a method is applied (called 'upwind or donor cell differencing scheme') where the mean parameter values are shifted (in flow direction) to the node boundaries.

This is not possible for the mixture-fluid approach of CCM. There, as can be seen from the relations of the sections 3.7 to 3.9, not only the absolute nodal SC boundary or mean function values are demanded but as well also their nodal slopes and thus, if the length of the SC nodes tends to zero, gradients. For this purpose a special 'quadratic polygon approximation' procedure, named 'PAX', had to be developed. It plays an outstanding part in the development of 'mixture-fluid models'. In particular, the difficult task of how to take care of the varying SC boundaries (eventually crossing BC node boundaries) in an appropriate and exact way had to be solved.

#### 3.3.1 Establishment of an adequate approximation function

The PAX procedure is based on the assumption that the solution function  $f(z)$  of a PDE is split into a number of  $N_{CT}$  nodal SC functions  $f_n(z,t)$ . Each of them being approximated by a specially constructed quadratic polygon

$$f_{Nn} = f_{Nn-1} + a_{Nn} \Delta z_{Nn} + b_{Nn} \Delta z_{Nn}^2 \quad (n=1, N_{CT}) \quad (30)$$

Their nodal mean functions  $f_{Mn}$  (for all SC nodes) will thus have the form

$$f_{Mn} = \frac{1}{\Delta z_{Nn}(t)} \int_{z_{Nn-1}(t)}^{z_{Nn}(t)} f(z,t) dz = f_{Nn-1} + \frac{1}{2} a_{Nn} \Delta z_{Nn} + \frac{1}{3} b_{Nn} \Delta z_{Nn}^2 \quad (n=1, N_{CT}) \quad (31)$$

the corresponding nodal slopes of either the mean nodal or the nodal boundary functions

$$f_{Nn}^{(s)} = \frac{(f_{Nn} - f_{Nn-1})}{\Delta z_{Nn}} = a_{Nn} + b_{Nn} \Delta z_{Nn} \rightarrow f_{CEI}^{(z)} \text{ (at } n=1) \text{ or } \rightarrow f_{Nn-1}^{(z)} \text{ (at } n=N_{CT}>1) \text{ if } \Delta z_{Nn} \rightarrow 0 \quad (32)$$



$$f_{Mn}^{(s)} = 2 \frac{(f_{Mn} - f_{Nn-1})}{\Delta z_{Nn}} = a_{Nn} + \frac{2}{3} b_{Nn} \Delta z_{Nn} \rightarrow f_{CEI}^{(z)} \text{ (at } n=1) \text{ or } \rightarrow f_{Nn-1}^{(z)} \text{ (at } n=N_{CT}>1) \text{ if } \Delta z_{Nn} \rightarrow 0 \quad (33)$$

and, finally, their nodal gradients (needed for the case that during a transient the length of a node tends to zero)

$$f_{Nn}^{(z)} = \left( \frac{\partial f}{\partial z} \right)_{Nn} = a_{Nn} + 2 b_{Nn} \Delta z_{Nn} = 4 f_{Nn}^{(s)} - 3 f_{Mn}^{(s)} = \frac{2}{\Delta z_{Nn}} (2f_{Nn} - 3f_{Mn} + f_{Nn-1}) \quad (n=1, N_{CT}) \quad (34)$$

Thereby the approximation functions have to fulfil the following requirements:

- The node entrance functions ( $f_{Nn-1}$ ) must be either equal to the SC entrance function ( $f_{Nn-1} = f_{CE}$ ) (if  $n=1$ ) or to the node outlet function of the node before (if  $n > 1$ ). This is obviously not demanded for the gradients of the nodal entrance functions (except for the last node at  $n = N_{CT}$ ).

$$f_{Nn-1}^{(z)} = a_{Nn} = \text{either } f_{CE}^{(z)} = f_{CEI}^{(z)} \text{ or } = f_{Nn}^{(z)} \text{ (of the node before)} \quad (n = N_{CT} \text{ if } N_{CT}=1 \text{ or } > 1) \\ = \frac{1}{2} (3 f_{Mn}^{(s)} - f_{Nn}^{(z)}) = \frac{2}{\Delta z_{Nn}} (3f_{Mn} - f_{Nn} - 2f_{Nn-1}) \rightarrow f_{Mn}^{(s)} = f_{Mn-1}^{(s)} \text{ if } \Delta z_{Nn} \rightarrow 0 \quad (35) \\ (n=1, N_{CT}-1 \text{ if } N_{CT} > 1)$$

- The mean function values  $f_{Mn}$  over all SC nodes have to be preserved (otherwise the balance equations could be hurt).
- With the objective to guarantee stable behaviours of the approximated functions (for example by excluding 'saw tooth-like' behaviour) it will, in an additional assumption, be demanded that the outlet gradients of the first  $N_{CT}-1$  nodes should be set equal to the slopes between their neighbour mean function values. The entrance gradient of the last node ( $n = N_{CT}$ ) should be either equal to the outlet gradient of the node before (if  $n = N_{CT} > 1$ ) or equal to a given SC input gradient (for the special case  $n = N_{CT}=1$ ). Thus

$$f_{Nn}^{(z)} = 2 \frac{f_{Mn+1} - f_{Mn}}{\Delta z_{Nn+1} + \Delta z_{Nn}} \quad (n=1, N_{CT}-1, \text{ if } N_{CT}>1) \quad (36)$$

$$f_{Nn-1}^{(z)} = f_{CE}^{(z)} = f_{CEI}^{(z)} \quad (n = N_{CT}=1) \\ = \frac{2}{\Delta z_{Nn}} (2f_{Nn} - 3f_{Mn} + f_{Nn-1}) \rightarrow f_{Nn-1}^{(z)} \text{ if } \Delta z_{CA} \rightarrow 0 \quad (n = N_{CT}, \text{ if } N_{CT} > 1) \quad (37)$$

This means, the corresponding approximation function reaches not only over the node  $n$  but its next higher one ( $n+1$ ) has to be considered too (except, of course, for the last node). This assumption makes the PAX procedure very effective (and stable). It helps to smooth the curve, guarantees that the gradients at the upper or lower SC boundary do not show abrupt changes if these boundaries cross a BC node boundary and has the effect that perturbations at channel entrance do not directly affect corresponding parameters of the upper BC nodes.

For the special case of a SC having shrunk to a single node ( $n=N_{CT}=1$ ) the quadratic approximation demands (instead of the now not available term  $f_{Mn}$ ) as an additional input to PAX the gradient  $f_{CEI}^{(z)}$  at SC entrance. It represents thereby the gradient of either the coolant temperature  $T_{CEI}^{(z)}$  or void fraction  $\alpha_{CEI}^{(z)}$  (in case of single- or two-phase flow entrance conditions). If this parameter is not directly available it can, for example, be estimated by combining the mass and energy balance equations at SC entrance in an adequate way (See Hoeld, 2005). This procedure allows to take care not only of SC-s consisting of only one single node but also of situations where during a transient either the first or last SC of a BC starts to disappear or to be created anew (i.e.  $z_{CA} \rightarrow z_{BE}$  or  $z_{CE} \rightarrow z_{BA}$ ), since now the nodal mean value  $f_{Mn}$  at  $n = N_{CT}$  (for both  $N_{CT} = 1$  or  $> 1$ ) is no longer or not yet known.

### 3.3.2 Resulting nodal parameters due to PAX

In order to be able to determine the nodal approximation coefficients  $f_{Nn-1}$ ,  $a_{Nn}$  and  $b_{Nn}$  of eq.(30) (and, in turn, then also all other characteristic functions of the PAX procedure), it must, in dependence of the available input data, be distinguished between a steady and a transient case.

The **steady state** part of the basic equations consists of a set of non-linear algebraic equations (as presented later-on in the sections 3.7 and 3.8). It can be expected that as input to PAX the following data are available:

- SC entrance ( $z_{CE}$ ) and node positions ( $z_{Nn}$ ) (and thus also the SC outlet boundary position  $z_{CA}$  as explained in section 3.9) determining then in PAX the number of SC nodes ( $N_{CT}$ ),
- the nodal function limit values  $f_{LIMNn}$  (usually saturation temperature values at single-phase flow resp.  $f_{LIMNn} = 1$  or  $=0$  at mixture flow conditions),
- the SC entrance function  $f_{N0} = f_{CE}$  and (at least for the special case  $n=N_{CT}=1$ ) its gradient  $f_{CEI}^{(z)}$  and
- the nodal boundary functions  $f_{Nn}$  ( $n=1, N_{CT}$ ) with  $f_{CA} = f_{Nn}$  at  $n = N_{CT}$  and  $f_{CA} = f_{LIMCA}$  if  $z_{CA} < z_{BA}$ .

These inputs act within the PAX procedure as basic points of the polygon approximation curves, yielding then the nodal mean function values  $f_{Mn}$  (at  $n=1, N_{CT}$ ) which are needed as initial values for the transient case. Hence, after rearranging eqs. (30) and (31) it follows (including the special case of  $N_{CT} = 1$ )

$$\begin{aligned}
 f_{Mn} &= \frac{(\Delta z_{Nn+1} + \Delta z_{Nn})(2f_{Nn} + f_{Nn-1}) - \Delta z_{Nn} f_{Mn+1}}{3\Delta z_{Nn+1} + 2\Delta z_{Nn}} \\
 &= \frac{1}{3} (f_{CA} + 2f_{CE}) + \frac{1}{6} \Delta z_{CA} f_{CEI}^{(z)} \quad (n = N_{CT} = 1) \\
 &= \frac{1}{3} (f_{CA} + 2f_{Nn-1}) + \frac{1}{6} \frac{\Delta z_{Nn-1}}{\Delta z_{CA} + \Delta z_{Nn-1}} (f_{CA} - f_{Nn-2}) \quad (n = N_{CT} > 1) \quad (38)
 \end{aligned}$$

In the **transient case** the discretization of the PDE-s yields (for each SC) a set of  $N_{CT}$  ordinary differential equations (ODE-s) (as to be shown again in the sections 3.7, 3.8 and 3.9).

From their integration it follow then

- the SC outlet position  $z_{CA}(=z_{Nn}) < \text{or} = z_{BA}$  (at  $n=N_{CT}$ ) and thus also the total number  $N_{CT}$  of SC nodes

and either

- if  $z_{CA}=z_{BA}$  (i.e. if the now known SC outlet position is identical with the BC outlet) the mean nodal function values  $f_{Mn}$  for all  $N_{CT}$  nodes ( $n=1, N_{CT}$ )

or

- if  $z_{CA} < z_{BA}$  (i.e., if this SC outlet position moves within the BC) the mean nodal function values  $f_{Mn}$  of only  $N_{CT}-1$  nodes ( $n=1, N_{CT}-1$ ), but now, instead of the missing last SC mean node function  $f_{Mn}$ , knowing that the outlet function  $f_{Nn}$  must be equal to  $f_{CA} = f_{LIMCA}$  at  $z_{Nn} = z_{CA}$ .

Knowing now  $N_{CT}$  these nodal input function values can then be taken (together with its input parameter  $f_{CE}$  and the nodal positions  $z_{BE}$  and  $z_{Bn}$  at  $n=1, N_{CT}$ ) as basic points for the PAX procedure yielding, after rearranging the eqs.(30) to (34) in an adequate way, the other characteristic nodal function parameters of the SC.

Hence, it follows for the special situation of a SC being the last one within the BC (i.e., if  $z_{CA} = z_{BA}$ )

$$\begin{aligned} f_{Nn} &= \frac{1}{2} (3f_{Mn} - f_{Nn-1}) + \frac{1}{2} \frac{\Delta z_{Nn}}{\Delta z_{Nn+1} + \Delta z_{Nn}} (f_{Mn+1} - f_{Mn}) \quad (n=1, N_{CT}-1 \text{ with } N_{CT} > 1 \text{ if } z_{CA} = z_{BA}) \\ &= 3f_{Mn} - 2f_{CE} - \frac{1}{2} \Delta z_{CA} f_{CE}^{(z)} \quad (n = N_{CT} = 1 \text{ if } z_{CA} = z_{BA}) \\ &= f_{CA} = 2(f_{Mn} - f_{Mn-1}) + f_{Nn-2} \quad (n = N_{CT} > 1 \text{ if } z_{CA} = z_{BA}) \end{aligned} \quad (39)$$

resp. for the case  $z_{CA} < z_{BA}$

$$\begin{aligned} f_{Nn} &= \frac{1}{2} (3f_{Mn} - f_{Nn-1}) + \frac{1}{2} \frac{\Delta z_{Nn}}{\Delta z_{Nn+1} + \Delta z_{Nn}} (f_{Mn+1} - f_{Mn}) \quad (n=1, N_{CT}-2 \text{ with } N_{CT} > 2 \text{ if } z_{CA} < z_{BA}) \\ &= \frac{1}{2} (3f_{Mn} - f_{Nn-1}) + \frac{1}{4} \frac{\Delta z_{Nn}}{\Delta z_{Nn+1} + \Delta z_{Nn}} (f_{LIMCA} - f_{Nn-1}) \quad (n=N_{CT}-1 \text{ with } N_{CT} > 1 \text{ if } z_{CA} < z_{BA}) \\ &= f_{CA} = f_{LIMCA} \quad (n = N_{CT} \text{ if } z_{CA} < z_{BA}) \end{aligned} \quad (40)$$

The last mean nodal function value  $f_{Mn}$  (at  $n=N_{CT}$ ) is for the case  $z_{CA} < z_{BA}$  not yet determined (but needed). It follows if rearranging eq.(44) and replacing there  $f_{CA}$  by  $f_{LIMCA}$

$$\begin{aligned} f_{Mn} &= \frac{1}{3} (f_{LIMCA} + 2f_{CE}) + \frac{1}{6} \Delta z_{CA} f_{CE}^{(z)} \quad (n = N_{CT} = 1 \text{ if } z_{CA} < z_{BA}) \\ &= f_{Mn-1} + \frac{1}{2} (f_{LIMCA} - f_{Nn-2}) = \frac{1}{3} (f_{LIMCA} + 2f_{Nn-1}) + \frac{1}{6} \frac{\Delta z_{Nn-1}}{\Delta z_{CA} + \Delta z_{Nn-1}} (f_{LIMCA} - f_{Nn-2}) \quad (41) \\ &\quad (n = N_{CT} > 1 \text{ if } z_{CA} < z_{BA}) \end{aligned}$$

The corresponding time-derivative which is needed for the determination of the SC boundary time-derivative (see section 3.9) follows (for the case  $z_{CA} < z_{BA}$ ) by differentiating the relation above

$$\frac{d}{dt} f_{Mn} = f_{PXCA}^t + f_{PXCA}^z \frac{d}{dt} z_{CA} \quad (n = N_{CT} \text{ if } z_{CA} < z_{BA}) \quad (42)$$

yielding the coefficients

$$\begin{aligned}
f_{PXC}^t &= \frac{1}{3} \left( \frac{d}{dt} f_{LIMCA} + 2 \frac{d}{dt} f_{CE} \right) - \frac{1}{6} \left( f_{CE}^{(z)} \frac{d}{dt} z_{CE} - \Delta z_{CA} \frac{d}{dt} f_{CE}^{(z)} \right) \quad (n = N_{CT} = 1 \text{ if } z_{CA} = z_{BA}) \\
&= \frac{d}{dt} f_{Mn-1} + \frac{1}{2} \frac{d}{dt} f_{LIMCA} - \frac{1}{2} \frac{d}{dt} f_{Nn-2} \quad (n = N_{CT} > 1 \text{ if } z_{CA} < z_{BA}) \\
f_{PXC}^z &= \frac{1}{6} f_{CE}^{(z)} \quad \text{or} \quad = 0 \quad (n = N_{CT} = 1 \text{ or } > 1 \text{ if } z_{CA} < z_{BA}) \quad (43)
\end{aligned}$$

The differentials  $\frac{d}{dt} f_{Mn-1}$ ,  $\frac{d}{dt} z_{CA}$ ,  $\frac{d}{dt} f_{LIMCA}$  are directly available from CCM and, if  $N_{CT}=2$ , the term  $\frac{d}{dt} f_{Nn-2} = \frac{d}{dt} f_{CE}$  from input. For the case that a SC contains more than two nodes only their corresponding mean values are known, the needed term  $\frac{d}{dt} f_{Nn-2}$  has thus to be estimated by establishing the time-derivatives of all the boundary functions at the nodes below  $N_{CT} < 2$ . These can be derived in an iterative way by differentiating eq.(40)

$$\begin{aligned}
\frac{d}{dt} f_{Nn} &= \frac{d}{dt} f_{CE} \quad (n = 0) \\
&= \frac{d}{dt} f_{CA} = \frac{d}{dt} f_{LIMCA} \quad (n = N_{CT} \text{ if } z_{CA} < z_{BA}) \\
&= \frac{d}{dt} f_{CA} = 2 \left( \frac{d}{dt} f_{Mn} - \frac{d}{dt} f_{Mn-1} \right) + \frac{d}{dt} f_{Nn-2} \quad (n = N_{CT} > 1 \text{ if } z_{CA} = z_{BA}) \\
&= \frac{d}{dt} f_{Mn} + \frac{1}{2} \left( \frac{d}{dt} f_{Mn+1} - \frac{d}{dt} f_{Nn-1} \right) \\
&\quad + \frac{1}{2} \frac{\Delta z_{Nn+1}}{\Delta z_{Nn+1} + \Delta z_{Nn}} \left[ \frac{d}{dt} f_{Mn} - \frac{d}{dt} f_{Mn+1} - \frac{f_{Mn+1} - f_{Mn}}{\Delta z_{Nn+1} + \Delta z_{Nn}} \frac{d}{dt} z_{Nn-1} \right] \quad (44) \\
&\quad (n=1, N_{CT}-2 \text{ and } N_{CT} > 2 \text{ if } z_{CA} < z_{BA}) \text{ or } (n=1, N_{CT}-1 \text{ and } N_{CT} > 1 \text{ if } z_{CA} = z_{BA})
\end{aligned}$$

with

$$\begin{aligned}
\frac{d}{dt} f_{Nn-1} &= \frac{3}{2} \frac{d}{dt} f_{Mn-1} - \frac{1}{2} \frac{d}{dt} f_{Nn-2} + \frac{1}{4} \frac{\Delta z_{Nn-1}}{\Delta z_{CA} + \Delta z_{Nn-1}} \left[ \frac{d}{dt} f_{LIMCA} - \frac{d}{dt} f_{Nn-2} - \frac{f_{LIMCA} - f_{Nn-2}}{\Delta z_{CA} + \Delta z_{Nn-1}} \Delta z_{CA} \right] \quad (45) \\
&\quad (n = N_{CT} > 1 \text{ if } z_{CA} < z_{BA})
\end{aligned}$$

This term follows after differentiating eq.(44). It plays an important role for the propagation of perturbations below the last node.

The differentials  $\frac{d}{dt} f_{Mn}$  (at  $n = N_{CT}$  if  $z_{CA} = z_{BA}$ ) or  $\frac{d}{dt} z_{CA}$  (at  $n = N_{CT}$  if  $z_{CA} < z_{BA}$ ) can only be established if they are combined with corresponding expressions being derived within the mixture-fluid model (See chapters 3.7 and 3.8). They will then be added to the overall set of ODE-s.

Finally, with regard to the eqs.(32) and (33) the slopes, gradients and approximation coefficients can be determined.

### 3.3.3 Code package PAX

Based on the above established set of equations the subroutine PAX could be installed. It is derived with respect to the (automatic) calculation of the nodal mean or nodal boundary values (for a steady state or transient situation). It allows also determining the gradients and slopes at SC entrance and outlet (and thus also outlet values characterizing the entrance parameters of an eventually subsequent SC). Additionally, contributions needed for the determination of the time-derivatives of the boiling boundary or mixture level can be gained (See later-on the eqs.(87) and (88)).

Before incorporating the subroutine into the overall coolant channel module the validity of the presented PAX procedure has been thoroughly tested. With the help of a special driver code (PAXDRI) different characteristic and extreme cases have been calculated.

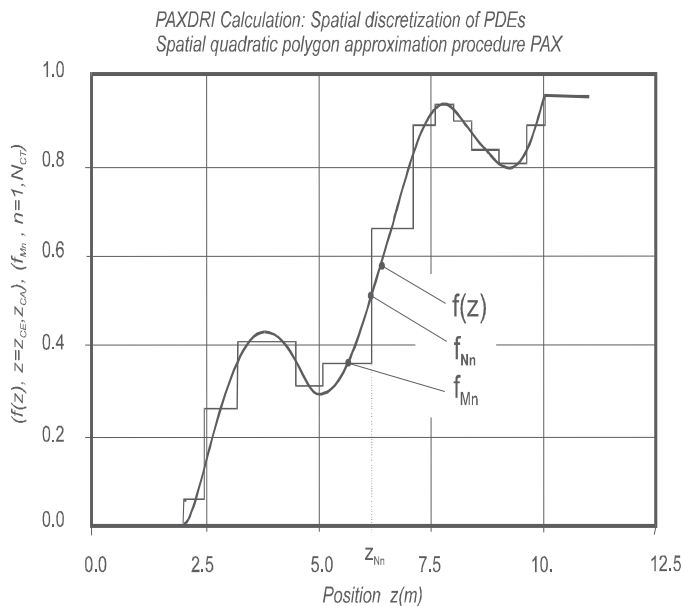


Fig. 2. Approximation function  $f(z)$  along a SC for both steady state and transient conditions after applying PAX (Example)

The resulting curves of such a characteristic example are plotted in fig.2. It presents an approximation curve of an artificially constructed void fraction distribution  $f(z) = \alpha(z)$  along a SC with two-phase flow both in a steady state but also transient situation. Both curves (on the basis of  $f_{Mn}$  and  $f_{Nn}$ ) should be (and are) identical.

### 3.4 Needed input parameters

#### 3.4.1 Initial conditions

For the start of the transient calculations corresponding steady state parameters will be taken as initial conditions.

#### 3.4.2 Boundary conditions

For steady state and especially for transient calculations the following input parameters are expected to be known (as boundary conditions), all of them being restricted to only (easily available) BC values (They will then, within CCM, be automatically translated into the corresponding SC values):

- Power profile along the entire BC. This means that the nodal heat flux terms  $q_{FBE}$  and  $q_{FBk}$  (at BC entrance and each node  $k=1, N_{BT}$ ) are wanted, known either directly from input, calculated from corresponding power density input values  $q_{BE}$  and  $q_{Bk}$  or from

$q_{BE}$  and the nodal power terms  $Q_{Bk} = 0.5 \cdot (q_{Bk} + q_{Bk-1}) \Delta z_{Bk}$ . These values can be also achieved (on the basis of given nodal wall temperature values) by solving the appropriate 'Fourier heat conduction eq.' taking into account the heat transfer boundary condition of eq.(24) (see sections 2.2.4 and 3.5). This can, for example, be done by applying an own heat conduction module as demonstrated by (Hoeld, 2002b, 2004a and 2011).

- For normalization purposes at steady state conditions then, as an additional parameter, the total nominal (steady state) heat power  $Q_{NOM,0}$  is asked.
- Channel entrance temperature  $T_{BEIN}$  (or enthalpy  $h_{BEIN}$ )
- System pressure  $P_{SYS}$  and its time-derivative ( $dP_{SYS}/dt$ ), situated at a fixed position either along the BC (entrance, outlet) or even outside of the ensemble. Due to the fast pressure wave propagation the local pressure time-derivatives can then be set equal to the change in system pressure (as described in section 3.6).
- Total mass flow  $G_{BEIN}$  at BC entrance together with pressure terms at BC entrance  $P_{BEIN}$  and outlet  $P_{BAIN}$ . These three parameters are needed for steady state considerations (partially used for normalization purposes). In the transient case only two of them are demanded as input, the third one will be determined automatically by the model. These allows then to distinguish between the situation of an 'open' or 'closed channel' concept as this will be explained in more detail in section 3.11.
- Steam mass flow  $G_{SBEIN}$  at BC entrance ( $=0$  or  $= G_{BEIN}$  at single- or  $0 < G_{SBEIN} < G_{BEIN}$  at two-phase flow conditions). The corresponding entrance void fraction  $\alpha_{BE}$  will then be determined automatically within the code by applying the inverse drift-flux correlation (see eq.(21)).

Eventually needed time-derivatives of such entrance functions can either be expected to be known directly from input or be estimated from their absolute values.

By choosing adequate boundary conditions then also thermal-hydraulic conditions of other situations can be simulated, such as, for example, that of several channel assemblies (nuclear power plants, test loops etc.) which can consist of a complex web of pipes and branches (represented by different BC-s, all of them distinguished by their key numbers KEYBC). Even if the ensemble consists of inner loops (for example in case of parallel channels) the case can be treated in an adequate way according to the concept of a 'closed' channel (see section 3.6.2).

### 3.4.3 Solution vector resulting from the integration procedure

The characteristic steady state parameters are determined in a direct way, i.e. calculated according to the non-linear set of equations for the SC-s (being presented in the chapters 3.7, 3.8 and 3.9), combined to BC parameters and then send again back to the main (= calling) program. However, since the constitutive equations demand parameters (coolant temperatures, void fractions, pressures, etc.) which are the result of these calculations a recursive procedure in combination with and controlled by the main program has to be applied until a certain convergence in these parameters can be stated.

For the transient case, as a result of the integration (performed within the calling program and thus outside of CCM) the solution parameters of the set of ODE-s are transferred after each intermediate time step to CCM. These are (as described in detail also in chapter 4) mainly the mean nodal SC and thus BC coolant temperatures, mean nodal void fractions and the resulting boiling or superheating boundaries. These last two parameters allow then to subdivide the BC into SC-s yielding the corresponding constitutive parameters and the total and nodal length ( $z_{Nn}$  and  $\Delta z_{Nn}$ ) of these SC-s and thus also their total number ( $N_{CT}$ ) of

SC nodes. The needed SC (and thus BC) time-derivatives are then determined in CCM (as described in the sections 3.7, 3.8 and 3.9) and then transmitted again to the calling program where the integration for the next time step takes place.

### 3.5 BC (and thus also SC) power profile

The power terms ( $Q_{Bk}$ ) into or out of a BC node  $k$  (with corresponding positive or negative signs) can, together with a linear power term or power density term at BC entrance, be expected to be either known from input (e.g., in the case of a heated loop) or from the solution of a Fourier heat conduction equation (in connection with the energy balance equation). From this BC power profile obeying to the relation

$$\begin{aligned} Q_{Bk} &= \frac{1}{2} \Delta Z_{Bk} (q_{LBk} + q_{LBk-1}) = \frac{1}{2} \Delta Z_{Bk} (U_{Bk} q_{FBk} + U_{Bk-1} q_{FBk-1}) \\ &= \frac{1}{2} \Delta Z_{Bk} (A_{Bk} q_{Bk} + A_{Bk-1} q_{Bk-1}) \text{ and thus } q_{LB} = \frac{2Q_{Bk}}{\Delta Z_{Bk}} - q_{LBk-1} \quad (k=1, N_{BT}) \end{aligned} \quad (46)$$

the corresponding SC nodal terms ( $q_{LNn}$ ,  $Q_{Mn}$  and  $q_{Nn}$ ) can be determined. They are usually equal to the corresponding BC terms, except for the SC entrance (if  $z_{CE} > z_{BE}$ ) or outlet (if  $z_{CA} < z_{BA}$ ). Hence, if assuming linear behaviour of the linear nodal power terms within the corresponding BC nodes it follows for the 'linear SC power' term

$$\begin{aligned} q_{LNn} (=q_{LCE}) &= q_{LBE} (=input) \text{ or } = (q_{LCA}) \text{ of the last node of the SC before} \quad (n=0 \text{ if } z_{CE} = \text{or} > z_{BE}) \\ &= q_{LBk} \quad (n=1, N_{CT} \text{ and } k=n+N_{BCE} \text{ if } L_{FTYPE}=2) \\ &= q_{LBk} \quad (n=1, N_{CT-1} \text{ and, if } z_{CA} = z_{BA}, n= N_{CT} \text{ with } k=n+N_{BCE}) \\ &= q_{LBk-1} + (q_{LBk} - q_{LBk-1}) \frac{\Delta Z_{CA}}{\Delta Z_{Bk}} \quad (n=N_{CT} \text{ and } k=N_{BCA} \text{ if } z_{CA} < z_{BA}) \end{aligned} \quad (47)$$

for the 'total power term' into the node  $n$

$$\begin{aligned} Q_{Mn} &= Q_{Bk} \text{ or } = Q_{Bk} - (Q_{MCA}) \text{ of last node of the SC before} \quad (n=1 \text{ with } k=1+N_{BCE} \text{ if } z_{CE} = \text{or} > z_{BE}) \\ &= Q_{Bk} \quad (n=1, N_{CT} \text{ and } k=n+N_{BCE} \text{ if } L_{FTYPE}=2) \\ &= \frac{1}{2} \Delta Z_{Nn} (q_{LNn} + q_{LNn-1}) = Q_{Bk} \quad (n=2, N_{CT-1} \text{ and, if } z_{CA} = z_{BA}, n= N_{CT} \text{ with } k=n+N_{BCE}) \\ &= Q_{MCA} = \Delta Z_{CA} [q_{LBk-1} + \frac{1}{2} (q_{LBk} - q_{LBk-1}) \frac{\Delta Z_{CA}}{\Delta Z_{Bk}}] \quad (n=N_{CT} \text{ and } k=N_{BCA} \text{ if } z_{CA} < z_{BA}) \end{aligned} \quad (48)$$

and finally for the 'mean nodal' and 'nodal boundary power density' terms ( $q_{Mn}$  and  $q_{Nn}$ ), being independent of  $\Delta Z_{Nn}$  and thus also valid for the case  $\Delta Z_{Nn} \rightarrow 0$  (as demanded later-on by the eqs.(52) and (69))

$$\begin{aligned} q_{Mn} &= \frac{Q_{Mn}}{\Delta Z_{Nn}} = \frac{1}{2 A_{Mn}} (q_{LNn-1} + q_{LNn}) \quad (n=1, N_{CT}) \\ q_{Nn} &= q_{CE} = q_{BE} \text{ or } = (q_{CA}) \text{ of the last node of the SC before} \quad (n=0 \text{ if } z_{CE} = \text{or} > z_{BE}) \\ &= 2q_{Mn} - q_{Nn-1} \quad (n=1, N_{CT}) \end{aligned} \quad (49)$$

The SC length  $z_{CA}$  (and thus the length of its last node  $\Delta z_{CA}$ ) are (for the case  $z_{CA,0} < z_{BA}$ ) only in the transient case known (as a result of the integration procedure). For steady state conditions the term  $Q_{MCA,0}$  follows from energy balance considerations (eqs.(61) and (80)). Then, in a reverse manner,  $\Delta z_{CA,0}$  can be calculated from eq.(86) (See section 3.10).

In special (and very seldom) situations the assumption of linearity within such a BC node may not any longer be suited. This is, for example, the case if a very steep increase or decrease in heat transfer within a BC can be expected (for example at the onset of sub-cooled boiling or at dry-out conditions of the two-phase mixture). Corresponding corrections have then to be foreseen, for example, by a denser nodalization, i.e. further subdividing the corresponding CCM node length into more 'HTC' nodes.

### 3.6 Decoupling of mass and energy balance from momentum balance equations

Treating the conservation equations in a direct way produces due to elements with fast pressure wave propagation (and thus being responsible for very small time constants) a set of 'stiff' ODE-s with the consequence that their solution turns out to be enormously CPU-time consuming. To avoid this costly procedure the CCM has been developed with the aim to decouple the mass and energy from their momentum balance equations. This can be achieved by determining the thermodynamic properties of water and steam in the energy and mass balance equations on the basis of an estimated pressure profile  $P(z,t)$ . Thereby the pressure difference terms from a recursive (or a prior computational time step) will be added to an eventually time-varying system pressure  $P_{SYS}(t)$ , known from boundary conditions. After having solved the two conservation equations for mass and energy (now separately from and not simultaneously with the momentum balance) the different nodal pressure gradient terms can (by the then following momentum balance considerations) be determined according to the eqs.(4), (5) and (6).

For the time-derivatives it can additionally be assumed that according to the fast (acoustical) pressure wave propagation along a coolant channel all the local pressure time-derivatives can be set equal to a given external system pressure time-derivative, i.e.,

$$\frac{d}{dt} P(z,t) \cong \frac{d}{dt} P_{SYS} \quad (50)$$

By applying the above explained 'intelligent' (since physically justified) simplification in CCM the small, practically negligible, error in establishing the thermodynamic properties on the basis of such an estimated pressure profile can be outweighed by the enormous benefit substantiated by two facts:

- The very time-consuming solution of stiff equations can be avoided,
- the calculation of the mass flow distribution into different channels resulting from pressure balance considerations can, in a recursive way, be adapted already within each integration time step, i.e. there is no need to solve the entire set of differential equations for this purpose (See 'closed channel' concept in section 3.11).

### 3.7 Thermal-hydraulics of a SC with single-phase flow ( $L_{FTYPE} > 0$ )

The spatial integration of the two PDE-s of the conservation eqs.(1) and (2) over the (single-phase) SC nodes  $n$  (by taking into account the rules from section 3.2, the relations from the eqs.(7) and (50) and the possibility of locally changing nodal cross flow areas along the BC) yields for the transient case



- a relation for the total nodal mass flow

$$\begin{aligned} G_{Nn} &= G_{Nn-1} - V_{Mn}(\rho_{Mn}^T \frac{d}{dt} T_{Mn} + \rho_{Mn}^P \frac{d}{dt} P_{SYS}) + (\rho_{Nn} - \rho_{Mn}) A_{Nn} \frac{d}{dt} z_{Nn} + \\ &\quad + (\rho_{Mn} - \rho_{Nn-1}) A_{Nn-1} \frac{d}{dt} z_{Nn-1} \\ &= G_{Nn-1} - G_{ITn} - G_{IPn} + G_{IZn} \quad (n=1, N_{CT}), L_{FTYPE} > 0 \end{aligned} \quad (51)$$

and

- the time-derivatives for the mean nodal coolant temperatures (if eliminating the term  $G_{Nn}$  in the resulting equation by inserting from the equation above):

$$\begin{aligned} \frac{d}{dt} T_{Mn} &= T_{Tn}^t + T_{TCA}^z \frac{d}{dt} z_{Nn} \\ (n=1, N_{CT} \text{ and } z_{CA}=z_{BA}) \text{ or } (n=1, N_{CT}-1 \text{ and } z_{CA} < z_{BA}), L_{FTYPE} > 0 \end{aligned} \quad (52)$$

with the abbreviations

$$T_{Tn}^t = \frac{q_{Mn} - \frac{G_{Nn-1}}{A_{Mn}} h_{Nn}^{(s)} + q_{Pn}}{\rho_{Mn} h_{Mn}^T C_{TMn}} + T_{TCE}^z \frac{d}{dt} z_{Nn-1} \quad (53)$$

$$T_{TCE}^z = \frac{1}{2} [T_{Mn}^{(s)} - 2(1 - \frac{\rho_{CE}}{\rho_{Mn}}) T_{Nn}^{(s)}] \frac{A_{CE}}{A_{Mn} C_{TMn}} \quad \text{or} \quad = 0 \quad (n=1 \text{ or } > 1), L_{FTYPE} > 0 \quad (54)$$

$$\begin{aligned} T_{TCA}^z &= 0 \quad \text{or} \quad = \frac{1}{2} \frac{A_{Nn}}{A_{Mn} C_{TMn}} T_{Nn}^{(s)} \\ (n < N_{CT} \text{ or } = N_{CT} \text{ if } z_{CA} < z_{BA} \text{ or } = z_{BA}), L_{FTYPE} > 0 \end{aligned} \quad (55)$$

and the coefficients

$$q_{Pn} = [1 - \rho_{Mn} h_{Mn}^P + \rho_{Mn}^P (h_{Nn} - h_{Mn})] \frac{d}{dt} P_{SYS} \quad (56)$$

$$q_{Zn} = \frac{1}{2A_{Mn}} \{A_{Nn} \rho_{Mn} h_{Nn}^{(s)} \frac{d}{dt} z_{Nn} + A_{Nn-1} [\rho_{Mn} h_{Mn}^{(s)} - 2(\rho_{Mn} - \rho_{Nn-1}) h_{Nn}^{(s)}] \frac{d}{dt} z_{Nn-1}\} \quad (57)$$

$$C_{TMn} = 1 - \frac{\rho_{Mn}^T}{\rho_{Mn}} \frac{h_{Nn} - h_{Mn}}{h_{Mn}^T} = 1 - \frac{\rho_{Mn}^T}{\rho_{Mn}} (T_{Nn} - T_{Mn}) \quad (58)$$

$$\begin{aligned} T_{TCE}^z &= \frac{1}{2} [T_{Mn}^{(s)} - 2(1 - \frac{\rho_{CE}}{\rho_{Mn}}) T_{Nn}^{(s)}] \frac{A_{CE}}{A_{Mn} C_{TMn}} \quad \text{or} \quad = 0 \\ &\quad (\text{if } n=1 \text{ and } z_{CE} > z_{BE} \text{ or } = z_{BE}), L_{FTYPE} > 0 \end{aligned} \quad (59)$$

It can be expected that at the begin of each (intermediate) time step the mean nodal coolant temperature values  $T_{Mn}$  are known, either from steady state considerations (at the begin of

the transient calculations) or as a result of the integration procedure. Hence the parameters needed in the relations above can be determined too. From the PAX procedure it follows the SC nodal terms  $T_{Nn}$ ,  $T_{Nn}^{(s)}$  and  $T_{Mn}^{(s)}$  and, demanded for the case that  $\Delta z_{Nn} \rightarrow 0$ , their gradients. Finally, by considering the water/steam tables (Hoeld, 1996), also their nodal enthalpies are fixed.

If, in the transient case, the SC nodal boundary temperature does not reach along the entire BC its limit value ( $T_{LIMNn}=T_{SATNn}$ ) the total number of SC nodes is given as  $N_{CT}=N_{BT}-N_{BCE}$  and  $z_{Nn}$  (at  $n=N_{CT}$ )  $=z_{CA}=z_{BT}$ . Otherwise, if this limit is (at node  $n$ ) reached, then  $N_{CT}=n$ ,  $T_{Nn}=T_{SATNn}$  with  $z_{CA} (< z_{BT})$  resulting from the integration. Then, from the procedure above also the time-derivative of the boiling boundary moving within this channel can be derived (as this will be discussed in section 3.9).

The **steady state** part of the total nodal mass flow (characterized by the index 0) follows from the basic non-linear algebraic equation (resulting from setting in eq. (51) the time-derivative equal to 0)

$$G_{Nn,0} = G_{CA,0} = G_{CE,0} = G_{BA,0} = G_{BE,0} \quad (n=1, N_{CT}), L_{FTYPE} > 0 \quad (60)$$

Replacing in eq.(52)  $Q_{Mn,0}$  by  $Q_{BK,0}$  (if  $n > 1$ ), since  $N_{CT}$  is not yet known, yields the steady state nodal enthalpy terms

$$h_{Nn,0} = h_{Nn-1,0} + \frac{Q_{Mn,0}}{G_{BE,0}} \leq h'_{Nn,0} \text{ or } \geq h''_{Nn,0} \quad (\text{with } h_{Nn-1,0} = h_{CE,0} \text{ at } n=1) \quad (61)$$

(if  $L_{FTYPE} = 1$  or  $= 2$  at  $n = 1, N_{BT}-N_{BCE}$ )

Regarding the restrictions above the total number  $N_{CT}$  of SC nodes for the steady state is then also fixed with

$$N_{CT} = n < N_{BT} - N_{BCE} \text{ and } z_{CA,0} (=z_{Nn,0}) < z_{BA} \quad (\text{if } h_{Nn,0} = h'_{Nn,0} \text{ and } L_{FTYPE} = 1)$$

$$N_{CT} = N_{BT} - N_{BCE} \text{ and } z_{CA,0} = z_{BA} \quad (\text{if } h_{Nn,0} < h'_{Nn,0} \text{ and } L_{FTYPE} = 1) \text{ or } (\text{if } L_{FTYPE} = 2) \quad (62)$$

Finally, according to eq.(51), the nodal power term for the last SC node is given as

$$Q_{MCA,0} = Q_{Mn,0} = (h'_{CA,0} - h_{Nn-1,0}) G_{BE,0} \quad (\text{if } n = N_{CT} < N_{BCA} \text{ and } L_{FTYPE} = 1)$$

$$= (h_{Nn-1,0} - h''_{CA,0}) G_{BE,0} \quad (\text{if } n = N_{CT} < N_{BCA} \text{ and } L_{FTYPE} = 2) \quad (63)$$

From the resulting steady state enthalpy values  $h_{Nn,0}$  at their node boundaries follow then (from the thermodynamic water/steam tables) the corresponding coolant temperature values  $T_{Nn,0}$  (with  $T_{Nn,0} = T_{SATNn,0}$  if  $n = N_{CT}$  and  $z_{CA} < z_{BA}$ ) and by applying the PAX procedure (according to section 3.3) their mean nodal temperature and enthalpy values  $T_{Mn,0}$  and  $h_{Mn,0}$  (acting as start values for the transient calculations). It has to be noted that, due to the non-linearity of the basic steady state equations, this procedure has to be done in a recursive way. It can additionally be stated that both the steady state and transient two-phase mass flow parameters get the trivial form

$$G_{SNn} = G_{SNn,0} = 0 \text{ resp. } G_{WNn} = G_{CE} \text{ and } G_{WNn,0} = G_{BE,0} \quad (n=1, N_{CT}, \text{ if } L_{FTYPE} = 1)$$

$$G_{SNn} = G_{CE} \text{ and } G_{SNn,0} = G_{BE,0} \text{ resp. } G_{WNn} = G_{WNn,0} = 0 \quad (n=1, N_{CT}, \text{ if } L_{FTYPE} = 2) \quad (64)$$

and

$$\frac{d}{dt} \alpha_{Mn} = 0 \quad \text{and} \quad \alpha_{Nn} = \alpha_{Nn,0} = \alpha_{Mn,0} = X_{Nn} = X_{Nn,0} = 0 \quad \text{or} = 1 \quad (65)$$

(n=1, N<sub>CT</sub>, if L<sub>FTYPE</sub> = 1 or = 2)

### 3.8 Thermal-hydraulics of a SC with two-phase flow (L<sub>FTYPE</sub> = 0)

Similar as in the section before, the spatial integration of the two PDE-s of the conservation eqs.(1) and (2) now over the (mixture-phase) SC nodes n (by taking into account the rules from section 3.2, the relations from the eqs.(7) and (50) and the possibility of locally changing nodal cross flow areas along the BC) yields for the transient case

- the total nodal mass flow terms

$$G_{Nn} = G_{Nn-1} + V_{Mn} (\rho' - \rho'')_{Mn} \left( \frac{d}{dt} \alpha_{Mn} - \alpha_{GPn}^t - \alpha_{GZn}^t \right) = G_{Nn-1} + G_{2An} - G_{2Pn} - G_{2Zn} \quad (66)$$

(n=1, N<sub>CT</sub>, L<sub>FTYPE</sub> = 0)

by introducing (if neglecting thereby the small differences between mean and nodal saturation thermodynamic values) the coefficients

$$\alpha_{GPn}^t = \left( \frac{1}{(\rho' - \rho'')} \right)_{Mn} [(1 - \alpha) \rho'^P + \alpha \rho''^P]_{Mn} \frac{d}{dt} P_{SYS} \quad (67)$$

$$\alpha_{GZn}^t = \frac{1}{2} \frac{A_{CE}}{A_{Mn}} \alpha_{Mn}^{(s)} \frac{d}{dt} z_{CE} \quad (n = 1 \text{ and } z_{CE} > z_{BE})$$

$$= 0 \quad (1 < n < N_{CT})$$

$$a \quad = \frac{A_{CA}}{A_{Mn}} \left( \alpha_{CA}^{(s)} - \frac{1}{2} \alpha_{Mn}^{(s)} \right) \frac{d}{dt} z_{CA} \quad (n = N_{CT}, N_{CT} > 1 \text{ and } z_{CA} < z_{BA}) \quad (68)$$

and

- the mean nodal void fraction time-derivatives

$$\frac{d}{dt} \alpha_{Mn} = \alpha_{ASn}^t - \alpha_{APn}^t + \alpha_{CA}^z \frac{d}{dt} z_{Nn} + \alpha_{CE}^z \frac{d}{dt} z_{Nn-1} = \alpha_{An}^t + \alpha_{AZn}^t \quad (69)$$

(n=1, N<sub>CT</sub> and z<sub>CA</sub>=z<sub>BA</sub>) or (n=1, N<sub>CT</sub>-1, N<sub>CT</sub>>1 and z<sub>CA</sub><z<sub>BA</sub>), L<sub>FTYPE</sub>=0

with the coefficients

$$\alpha_{ASn}^t = \alpha_{AQn}^t - \alpha_{AGn}^t = \frac{1}{\rho_{Mn}''} \left( \frac{q_{Mn}}{h_{SWMn}} - \frac{G_{SNn}^{(s)}}{A_{Mn}} \right) \quad (70)$$

$$\alpha_{APn}^t = \frac{1}{(\rho_{Mn}''/h_{SW})_{Mn}} [(1 - \alpha) \rho' h'^P + \alpha (\rho' h''^P + \rho'' h_{SW}) - 1]_{Mn} \frac{d}{dt} P_{SYS} \quad (71)$$

$$\alpha_{AZn}^t = \alpha_{GZn}^t \quad (72)$$

$$G_{SNn}^{(s)} = \frac{\Delta G_{SNn}}{\Delta z_{Nn}} \rightarrow G_{SNn}^{(z)} = G_{SNn}^{(\alpha)} \alpha_{Nn}^{(z)} \quad \text{if } \alpha_{Nn} \rightarrow \alpha_{CE} = 0 \text{ (at } n=1) \quad (73)$$

or  $\alpha_{Nn} \rightarrow \alpha_{CA} = 1 \text{ (at } n=N_{CT})$

It can again be expected that at the begin of each (intermediate) time step the mean nodal void fraction values  $\alpha_{Mn}$  are known, either from steady state considerations (at the begin of the transient calculations) or as a result of the integration procedure. Hence the parameters needed in the relations above can be determined too. From the PAX procedure it follow their nodal boundary void fraction terms  $\alpha_{Nn}$  together with their gradients  $\alpha_{Nn}^{(z)}$  and  $\alpha_{Mn}^{(z)}$ . The slopes  $\alpha_{Nn}^{(s)}$  and  $\alpha_{Mn}^{(s)}$  can be established from their definition equations and thus, as shown both in section 2.2.3 but also in the tables given by Hoeld (2001 and 2002a), all the other characteristic two-phase parameters (such as steam, water or relative velocities etc). It has again to be noted that, due to the non-linearity of the basic equation, this procedure has to be done in a recursive way.

If, in the transient case, the SC nodal boundary void fraction  $\alpha_{Nn}$  does not reach along the entire BC its limit value ( $\alpha_{LIMNn}=1$  or 0) the total number of SC nodes is given as  $N_{CT}=N_{BT}-N_{BCE}$  and  $z_{Nn}$  (at  $n=N_{CT}$ ) =  $z_{CA}=z_{BT}$ . Otherwise, if this limit is reached (at node  $n$ ), then  $N_{CT} = n$ ,  $\alpha_{Nn}=1$  (or =0) with  $z_{CA} (< z_{BT})$  resulting from the integration. Then, from the procedure above also the time-derivative of the boiling boundary moving within this channel can be derived (as this will be discussed in section 3.9).

Hence it follows for the steam mass flow gradients

$$G_{SNn}^{(\alpha)} = A_{CE} v_{S0} \rho_{Nn}^{//} \quad \text{with } v_{S0} = v_S \text{ (at } \alpha_{Nn} = 0) \text{ (} n=1 \text{ and } \alpha_{Nn} \rightarrow \alpha_{CE} = 0)$$

$$= A_{CA} v_{W1} \rho_{Nn}^{/} \quad \text{with } v_{W1} = v_W \text{ (at } \alpha_{Nn} = 1) \text{ (} n=N_{CT}-1 \text{ and } \alpha_{Nn} \rightarrow \alpha_{CA} = 1) \quad (74)$$

The term  $\frac{d}{dt} \alpha_{Mn}$  can be eliminated in eq.(66) if inserting from eq.(69) yielding a relation between  $G_{SNn}$  and  $G_{Nn}$

$$G_{Nn} + \left( \frac{\rho'}{\rho^{//}} - 1 \right)_{Mn} G_{SNn} = G_{Xn} \quad (n=1, N_{CT}, L_{FTYPE}=0) \quad (75)$$

with the 'auxiliary' mass flow term  $G_{Xn}$  referring only to values known from the node below

$$G_{Xn} = G_{Nn-1} + \left( \frac{\rho'}{\rho^{//}} - 1 \right)_{Mn} G_{SNn-1} + V_{Mn} (\rho' - \rho'')_{Mn} (\alpha_{AQn}^t - \alpha_{APn}^t - \alpha_{GPh}^t) \quad (76)$$

(n=1,  $N_{CT}$ ,  $L_{FTYPE}=0$ )

A similar relation to  $G_{Nn}$  can be established from the drift flux correlation (eq.(18)). Thereby it has been taken advantage of the fact that the needed drift velocity  $v_{DNn}$  and the phase distribution parameter  $C_{0Nn}$  can be determined independently from the total mass flow  $G_{Nn}$  (and thus before this term is known). Hence, combining the eqs.(75) and (18) results in

$$G_{Nn} = \frac{G_{Xn} - (A \alpha_{VD} \rho' C_{DC})_{Nn}}{1 + (\alpha C_0 C_{DC})_{Nn}} \quad (n=1, N_{CT}) \quad (77)$$

with the coefficient

$$C_{DCNn} = \left( \frac{\rho'}{\rho''} - 1 \right)_{Mn} \left( \frac{\rho''}{\rho' C_{GC}} \right)_{Nn} \quad (78)$$

From the drift flux correlation package (Hoeld et al., 1992 and Hoeld, 1994, see also the eqs.(13) and (18)) follow then all the other characteristic two-phase parameters, e.g. the nodal steam mass flow  $G_{SNn}$  and, eventually,  $\alpha_{Nn}^{(z)}$  and, according to eq.(74), also the slope  $G_{SNn}^{(s)}$ . Then, finally, from the eqs.(69) (but also (66)) the mean nodal void fraction time-derivative  $\frac{d}{dt} \alpha_{Mn}$  can be derived, needed for the next integration step. Obviously, at mixture flow the mean nodal temperature and enthalpy terms are equal to their saturation values

$$T_{Mn} = T_{SAT}(P_{Mn}) \text{ resp. } h_{Mn} = h'(P_{Mn}) \text{ or } h''(P_{Mn}) \quad (n = 1, N_{CT} \text{ and } L_{FTYPE} = 0) \quad (79)$$

and are thus only dependent on the local resp. system pressure value.

From mass conservation considerations it is obvious that at a transient situation and in the case of a transition from one BC into another obviously only the mass flow terms remain unchanged, not the void fractions.

Setting in the eqs.(66) and (69) the time-derivatives equal to 0, one obtains relations for the **steady state case**. For the total mass flow parameters  $G_{Nn,0} = G_{BE,0}$  a similar relation as already given for the single-phase flow in eq.(60) is valid. The nodal steam mass flow gets the form

$$G_{SNn,0} = G_{SNn-1,0} + \frac{Q_{Mn,0}}{h_{SWMn,0}} \leq G_{BE,0} \quad (n = 1, N_{BT} - N_{BCE} \text{ and } L_{FTYPE} = 0) \quad (80)$$

Regarding the restrictions above the total number  $N_{CT}$  of SC nodes is fixed in the steady state case with

$$\begin{aligned} N_{CT} = n < N_{BT} - N_{BCE} & \text{ and } z_{CA,0}(=z_{Nn,0}) < z_{BA} & (\text{if } G_{SNn,0} = G_{BE,0} \text{ and } L_{FTYPE} = 0) \\ N_{CT} = N_{BT} - N_{BCE} & \text{ and } z_{CA,0} = z_{BA} & (\text{if } G_{SNn,0} < G_{BE,0} \text{ and } L_{FTYPE} = 0) \end{aligned} \quad (81)$$

The steady state nodal steam quality parameters are given as

$$X_{Nn,0} = \frac{G_{SMn,0}}{G_{Nn,0}} \quad (n = 1, N_{CT} \text{ if } L_{FTYPE} = 0) \quad (82)$$

the corresponding nodal boundary void fraction values  $\alpha_{Nn,0}$  by applying the inverse drift-flux correlation (eq.(21)). The corresponding mean nodal void fraction values  $\alpha_{Mn,0}$  can be determined by applying the PAX procedure, parameters which are needed as starting values for the transient calculation.

Then from eq.(80) it follows for the case  $N_{CT} < N_{BT} - N_{BCE}$  the corresponding nodal power for the last SC node

$$Q_{MCA,0} = Q_{Mn,0} = (G_{Nn,0} - G_{SNn-1,0}) h_{SWNn,0} \quad (n = N_{CT} < N_{BCA} \text{ if } L_{FTYPE} = 0) \quad (83)$$

### 3.9 SC boundaries

The SC entrance position  $z_{CE}$  ( $= z_{Nn}$  at  $n=0$ ) is either equal to the BC entrance  $z_{BE}$  (for the first SC within the BC) or equal to the SC outlet boundary of the SC before.

In the **steady state** case the SC outlet boundary ( $=$  boiling boundary  $z_{BB,0}$  or mixture level  $z_{ML,0}$ ) can be represented as

$$\begin{aligned} z_{CA,0} &= z_{BA} & (n = N_{CT} \text{ and } z_{CA,0} = z_{BA}) \\ &= z_{Nn-1} + \Delta z_{CA,0} & (n = N_{CT} \text{ and } z_{CA,0} < z_{BA}) \end{aligned} \quad (84)$$

The (steady state) term  $N_{CT}$  is already determined in the eqs.(62) or (81), the corresponding nodal power  $Q_{MCA,0}$  given by the eqs.(63) or (80). Hence after rearranging eq.(32) one gets an algebraic quadratic equation with respect to  $\Delta z_{CA,0}$

$$\begin{aligned} Q_{MCA,0} = Q_{Mn,0} = \Delta z_{CA,0} \left[ q_{LBk-1} + \frac{1}{2} \frac{q_{LBk,0} - q_{LBk-1,0}}{\Delta z_{Bk}} \Delta z_{CA,0} \right] \\ (n = N_{CT} \text{ and } k = N_{BCA} \text{ if } N_{CT} < N_{BCA}) \end{aligned} \quad (85)$$

yielding finally as solution

$$\begin{aligned} \Delta z_{CA,0} &= \Delta z_{Bk} & (n = N_{CT} \text{ and } k = N_{BCA} \text{ if } N_{CT} = N_{BT}) \\ &= \Delta z_{Bk} \frac{q_{LBk-1,0}}{q_{LBk-1,0} - q_{LBk,0}} \left[ 1 - \sqrt{1 - 2 \left( 1 - \frac{q_{LBk,0}}{q_{LBk-1,0}} \right) \frac{Q_{CMA,0}}{\Delta z_{Bk} q_{LBk-1,0}}} \right] \\ & & (k = N_{BCA} \text{ if } N_{CT} < N_{BT}) \\ \rightarrow \frac{Q_{MCA,0}}{q_{LBk-1,0}} \left[ 1 + \frac{1}{2} \left( 1 - \frac{q_{LBk,0}}{q_{LBk-1,0}} \right) \frac{Q_{CMA,0}}{\Delta z_{Bk} q_{LBk-1,0}} \right] & \text{ if } q_{LBk,0} \rightarrow q_{LBk-1,0} \end{aligned} \quad (86)$$

From the relations in section 3.5 then also the other steady state power terms can be determined.

In the **transient case** the outlet boundary  $z_{CA}$  ( $=$ boiling boundary or mixture level) follows, as already pointed-out, directly from the integration procedure. Then also  $\Delta z_{CA}$  and  $N_{CT}$  are fixed. This SC outlet boundary  $z_{CA}$  can move along the entire BC and thus also cross BC node boundaries. A SC can even shrink to a single node ( $N_{CT}=1$ ), start to disappear or to be created anew. This means that in PAX the slope in the vicinity of such a boundary is replaced by a gradient.

The mean nodal coolant temperature or, if  $L_{FTYPE}=0$ , void fraction of the last SC node is interrelated by the PAX procedure with the locally varying SC outlet boundary  $z_{CA}$ . Hence, in a transient situation the time-derivative of only one of these parameters is demanded, after the integration then the second one follows from the PAX procedure.

If combining (in the case of single-phase flow) the eqs.(42) and (52), the wanted relation for the SC boundary time derivative can be expressed by

$$\frac{d}{dt} z_{CA} = \frac{d}{dt} z_{BB} = \frac{T_{PXCA}^t - T_{ICA}^t}{T_{ICA}^z - T_{PXCA}^z} \text{ or } = 0 \quad (n = N_{CT}, z_{CA} < z_{BA} \text{ or } z_{CA} = z_{BA} \text{ if } L_{FTYPE} > 0) \quad (87)$$

and, if considering the eqs. (42) and (69), for the case of mixture flow

$$\frac{d}{dt} z_{CA} = \frac{d}{dt} z_{ML} = \frac{\alpha_{PXCA}^t - \alpha_{ACA}^t}{\alpha_{ACA}^z - \alpha_{PXCA}^z} \text{ or } = 0 \quad (n = N_{CT}, z_{CA} < z_{BA} \text{ or } z_{CA} = z_{BA} \text{ if } L_{FTYPE} = 0) \quad (88)$$

If  $z_{CA} < z_{BA}$ , the corresponding time-derivatives  $\frac{d}{dt} T_{Mn}$  or  $\frac{d}{dt} \alpha_{Mn}$  of the last SC node (at  $n=N_{CT}$ ) follow then by inserting the terms above into the eqs.(52) or (69). After the integration procedure then the SC outlet boundary  $z_{CA}$  (= boiling boundary  $z_{BB}$  or mixture level  $z_{ML}$ ) and thus also the total number  $N_{CT}$  of SC nodes is given.

In these considerations it is excluded that a BC node can contain more than one moving boundary. Hence a SC with  $N_{CT}=1$  can only appear at BC entrance ( $z_{CE} = z_{BE}$ ) or BC outlet ( $z_{CA} = z_{BA}$ ). For such a special case either the temperature slope ( $T_{CE}^z$ ) resp. (at mixture fluid conditions) the term  $\alpha_{CE}^z$  at SC entrance are needed as input to the PAX procedure (see section 3.3.1).

### 3.10 Pressure profile along the SC (and thus also BC)

After having solved the mass and energy balance equations separately (and not simultaneously) with the momentum balance the now exact nodal SC and BC pressure difference terms ( $\Delta P_{Nn} = P_{Nn} - P_{Nn-1}$  and  $\Delta P_{BNn}$ ) can (for both single- or two-phase flow situations) be determined by discretizing the momentum balance eq.(3) and integrating over the corresponding SC nodes. The total BC pressure difference  $\Delta P_{BT} = P_{BA} - P_{BE}$  between BC outlet and entrance follows then from the relation

$$\Delta P_{BT} = \Delta P_{PBT} - \Delta P_{GBT} \quad (89)$$

(with  $\Delta P_{GBT,0} = 0$  at steady state conditions)

with

$$\Delta P_{PBT} = \Delta P_{SBT} + \Delta P_{ABT} + \Delta P_{XBT} + \Delta P_{FBT} + \Delta P_{DBT} \quad (90)$$

(with  $\Delta P_{PBT,0} = \Delta P_{BTIN,0}$  at steady state conditions)

comprising terms from static head ( $\Delta P_{SBT}$ ), mass acceleration ( $\Delta P_{ABT}$ ), wall friction ( $\Delta P_{FBT}$ ) and external pressure accelerations ( $\Delta P_{XBT}$ , pump or other perturbations from outside) and (in the transient case) the pressure difference term  $\Delta P_{GBT}$  which takes care of the time-dependent changes in total mass flux along a BC (caused by the direct influence of changing nodal mass fluxes) having the form

$$\begin{aligned} \Delta P_{GBT} &= \int_0^{z_{BT}} \frac{d}{dt} G_{FB}(z,t) dz = z_{BT} \frac{d}{dt} G_{FBMT} \quad \text{at transient conditions} \\ &= 0 \quad \text{at steady state} \end{aligned} \quad (91)$$

Thereby the 'fictive' mean mass flux term  $G_{FBMT}$  (averaged over the entire BC) has been introduced which can be represented as

$$\begin{aligned} G_{FBMT} &= \frac{1}{z_{BT}} \int_0^{z_{BT}} G_{FB}(z,t) dz \\ &\cong \frac{1}{z_{BT}} \sum_{n=1}^{N_{SCT}} \sum_{n=1}^{N_{CT}} \Delta z_{Nn} G_{FBMn} = \frac{1}{2} \frac{1}{z_{BT}} \sum_{k=1}^{N_{BT}} \frac{\Delta z_{Bk}}{A_{BMk}} (G_{Bk} + G_{Bk-1}) \end{aligned} \quad (92)$$

Its time derivative can be estimated as

$$\begin{aligned} \frac{d}{dt} G_{FBMT} &\cong \frac{G_{FBMT} - G_{FBMTB}}{\Delta t} \\ &\rightarrow \left( \frac{d}{dt} G_{FBMT} \right)_{at \ t=tB} \text{ if } \Delta t = t - t_B \rightarrow 0 \text{ (Index B = begin of time-step)} \end{aligned} \quad (93)$$

Regarding, however, the friction correlations, there arises the problem how to consider correctly contributions from spacers, tube bends, abrupt changes in cross sections etc. as well. The entire friction pressure decrease ( $\Delta P_{FBT}$ ) along a BC can thus never be described solely by analytical expressions in a satisfactory manner. To minimize these uncertainties a further friction term will be included into these considerations having the form

$$\Delta P_{DBT} = (f_{FMP,0} - 1) \Delta P_{FBT} + \Delta P_{FADD} \quad (94)$$

This means that eq.(90) is either supplemented with an additive term (index FADD) or the friction parts are provided with a multiplicative factor  $f_{FMP,0}$ . Which of them should prevail can be governed from outside by an input coefficient  $\varepsilon_{DPZ} = \varepsilon_{DPZI}$ . Thereby, the additive part will be assumed to be proportional to the square of the total coolant mass flow (e.g., at BC entrance)

$$\Delta P_{FADD} = -f_{ADD,0} z_{BT} \left( \frac{G_F |G_F|}{2\rho d_{HW}} \right)_{BE} \quad (95)$$

At steady state conditions the total BC pressure difference term ( $\Delta P_{BT,0}$ ) is known from input ( $\Delta P_{BT,0} = \Delta P_{BTIN}$ ). Since  $\Delta P_{GBT,0} = 0$ , the steady state total additional term  $\Delta P_{DBT,0}$  results from eq.(90). If defining the additive steady state friction pressure difference  $\Delta P_{FADD,0}$  to be the  $(1 - \varepsilon_{DPZ})$ -th part of the total additional pressure difference term then

$$\Delta P_{FADD,0} = (1 - \varepsilon_{DPZ}) \Delta P_{DBT,0} \quad (96)$$

The corresponding additive friction factor  $f_{ADD,0}$  follows then directly from eq.(95), the multiplicative one  $f_{FMP,0}$  from the combination of the eqs.(94) and (96)

$$f_{FMP,0} = 1 + \varepsilon_{DPZ} \frac{\Delta P_{DBT,0}}{\Delta P_{FBT,0}} \quad (97)$$

There arises the question how the validity of both friction factors can be expanded to transient situations too. This can, for example, be done by assuming that they should remain time-independent. Then, finally, the wanted nodal pressure decrease terms can be determined for both steady state but also transient situations. By adding now the resulting nodal BC pressure difference terms to the (time-varying) system pressure  $P_{SYS}(t)$  (given from outside as boundary condition with respect to a certain position (in- or outside of the BC)) then finally also the absolute nodal pressure profile  $P_{Bk}$  along the BC can be established (needed at the begin of the next time step for the determination of the constitutive equations).

### 3.11 BC entrance mass flow ('Open and closed channel concept')

As to be seen from the sections above in order to be able to calculate the characteristic nodal and total single- and two-phase parameters along a BC the BC entrance mass flow must be



known. This term is for the steady state case given by input ( $G_{BE} = G_{BEIN}$ ), together with the two pressure entrance and outlet values ( $P_{BE} = P_{BEIN}$ ,  $P_{BA} = P_{BAIN}$ ). In the transient situation it can, however, be expected that for the normal case of an 'open' channel besides the entrance mass flow only one of these two pressure terms is known from input, either at BC entrance or outlet. The missing one follows then from the calculation of the pressure decrease parts.

Such a procedure can not be applied without problems if the channels are part of a complex set of closed loops, loops consisting of more than one coolant channel (and not driven by an outside source, such as a pump). Then the mass flow terms (and especially entrance term of at least one of the channel) has to be adjusted to the fact that the sum of the entire pressure decrease terms along such a closed circuit must be zero. Usually, in the common thermal-hydraulic codes (see for example the 'separate-phase' approaches) this problem is handled by solving the three (or more) fundamental equations for the entire complex system simultaneously, a procedure which affords very often immense computational times and costs. In the here applied module (based on a separate treatment of momentum from mass and energy balance) a more elegant method could be found by introducing an additional aspect into the theory of CCM. It allows, different to other approaches, taking care of this situation by solving this problem by means of a 'closed channel concept' (in contrast to the usual 'open channel' method).

Choosing for this purpose a characteristic 'closed' channel within such a complex loop it can be expected that its pressure difference term  $\Delta P_{BT} = \Delta P_{BA} - \Delta P_{BE}$  over this channel is fix (= negative sum of all the other decrease terms of the remaining channels which can be calculated by the usual methods). Thus also the outlet and entrance BC pressure values ( $P_{BAIN}$ ,  $\Delta P_{BEIN}$ ) are now also available as inputs to CCM. Since, according to eq.(91), then also the term  $\Delta P_{PBT}$  is known, it follows from eq.(95) the 'closed channel concept criterion'

$$z_{BT} \frac{d}{dt} G_{FBMT} = \Delta P_{GBT} = \Delta P_{PBT} - \Delta P_{BTIN} \quad (\text{at 'closed channel' conditions}) \quad (98)$$

This means that for this purpose the total mass flow along a BC (and thus also at its entrance) must be adapted in such a way that the above for the 'closed channel' concept essential criterion remains valid at each time step, i.e., that the actual time derivative of the mean mass flux  $G_{FBMT}$  averaged over the channel must, as recommended by eq.(92), agree in a satisfactory manner with the required one from the equation above.

There exist, obviously, different methods how to deal with this complicated problem. One of them could be to determine the entrance mass flow  $G_{BE}$  by changing this value in a recursive way until the resulting term  $\frac{d}{dt} G_{FBMT}$  agrees with the criterion above.

Another possibility is to find a relation between the time-derivatives of the mean and certain local mass flux values (e.g., at BC entrance), i.e., to establish for example a relation between the terms  $\frac{d}{dt} G_{FBMT}$  and  $\frac{d}{dt} G_{FBE}$ . Then the wanted mass flow time-derivative at BC entrance can be determined directly from eq.(98). One practicable method to establish such a relation could follow if considering that a change of the mass flux is propagating along the channel so fast that the time derivative of its mean values could be set (in a first step) almost equal to the time-derivative at its entrance value. This term can, eventually, be provided with a form factor which can be adapted by an adequate recursion procedure until the condition of eq.(98) is fulfilled. The so won entrance mass flow is then governing the mass flow behaviour of the entire loop.

This method has been applied within the UTSG-3 code (Hoeld, 2011) for the simulation of the natural-circulation behaviour of the secondary steam generator loop. Similar considerations have been undertaken for a 3D case where the automatic mass flow distribution into different entrances of a set of parallel channels is asked (See e.g. Hoeld, 2004a and Jewer et al., 2005). The experience of such calculations should help to decide which of the different possible procedures should finally be given preference.

The 'open/closed channel concept' makes sure that measures with regard to the entire closed loop do not need to be taken into account simultaneously but (for each channel) separately. Its application can be restricted to only one 'characteristic' channel of a sequence of channels within a complex loop. This additional tool of CCM can in such cases help to handle the variety of closed loops within a complex physical system in a very comfortable way.

#### 4. Code package CCM

Starting from the above presented 'drift-flux based mixture-fluid theory' the (1D) thermal-hydraulic coolant channel module CCM could be established. It was derived with the intention to provide the authors of different and sometimes very complex thermal-hydraulic codes with a general and easily applicable tool needed for the simulation of the steady state and transient behaviours of the most important single- and two-phase parameters along any type of heated or cooled coolant channel.

The subdivision of such a (basic) channel (BC), characterized by an own key number (KEYBC), into different sub-channels (SC-s), characterized by its fluid type ( $L_{FTYPE}$ ), is done automatically within the module. Thereby the different SC-s will change from one SC type to another, i.e. two-phase flow follows single-phase flow and vice versa. SC-s can shrink to a single node or even disappear but also be created anew. The SC inlet boundary conditions are either identical to the entrance conditions of the BC or to the outlet parameters of the SC before.

The module CCM has been constructed in such a way that only input data with regard to the BC are demanded. These input data (for each channel KEYBC) will be transferred to the CCM by only two types of commons containing data established in the calling overall program, allowing thus a very easy handling of the code:

- The first common is only occupied by fixed BC geometry data (such as channel length, elevation heights, fixed or varying cross sections, hydraulic diameters).
- The second one has to contain
  - resulting data coming from the (overall) integration procedure (such as mean nodal coolant temperature or mean nodal steam void fraction values, boiling boundary and mixture level along the BC) and (in the case of a closed loop) the total mass flow term at BC entrance
  - and moreover
  - parameters representing the initial and boundary conditions of the system such as the nodal power profile (entrance power density  $q_{BCE}$  and mean nodal mean power values  $Q_{BMk}$ ), the coolant temperature, mass flow and pressure terms at BC entrance ( $T_{BE}$ ,  $G_{BE}$ ,  $P_{BE}$ ) and, in the case of steady state conditions or at transient situations with a BC being a part of an 'open channel', also the pressure term ( $P_{BE}$  or  $P_{BA}$ ) at BC entrance or outlet.

At the end of a recursion- or time-step characteristic parameters of all SC-s are transferred to the corresponding BC positions, thus yielding, for example, a final set of (non-linear) algebraic or (in the transient case) non-linear ordinary differential equations (ODE-s) of 1-st order together with the parameters following from the constitutive equations of CCM. The resulting sets of equations for different channels appearing in a complex physical system can be combined with other sets of algebraic equations or ODE-s coming from additional parts of such a complex model (considerations with respect to heat transfer, nuclear kinetics, top plenum, downcomer etc.). The final overall sets can then be solved by applying adequate algebraic solution methods or an appropriate time-integration routine (See, for example, Hoeld, 2011).

As output CCM will then yield all the wanted and needed characteristic thermal-hydraulic single- and two-phase BC (and thus also SC) parameters of such a general coolant channel. These are:

- Time-derivatives of the mean nodal coolant fluid temperatures
- time-derivatives of the mean nodal void fractions
- time-derivatives describing the movements of the boiling boundary or mixture level within the BC
- time-derivative of the total mass flow entering the BC (at least for the case that the BC is a part of a closed loop and thus being, for example, of interest for a thermal-hydraulic 3D representation),
- other constitutive nodal BC boundary parameters such as terms for total, water and steam mass flow, for pressure and pressure drop, coolant temperatures, void fraction etc.

The module CCM has been continuously expanded into a very efficient and mature version. To analyze transient situations at normal operational conditions sometimes also very simple codes ('pen' codes) can be applied. The quality of a code has, however, to be proved in the context of how reliably complex or limit cases can be handled. Thus much weight and effort has been placed on the question of how the performance of CCM, especially at extreme situations, can be judged, i.e., in cases where the mass flow ceases to stagnant conditions, the power input decreases to zero, abrupt pressure changes (for example due to a fast opening or closing of valves), the boiling boundary or mixture level disappear, the coolant channel starts to dry-out etc.

The special case of water or steam mass flow terms being exchanged at node boundaries between two parallel 'porous' coolant channels (with pressure differences as driving forces) has not yet been taken into account.

## 5. Verification and validation (V & V) procedures

During the course of development of the different versions of the code combination UTSG-3/CCM has gone through an appropriate verification and validation (V&V) procedure (with continuous feedbacks being considered in the continual formulation of the theoretical model).

CCM is (similar as done in the separate-phase models) constructed with the objective to be used only as an element within an overall code. Hence, further V&V steps could be performed only in an indirect way, i.e. in combination with such overall codes. This has been done in a very successful way by means of the U-tube steam generator code UTSG-3. Thereby the module CCM could profit from the experiences been gained in decades of years

work with the construction of an effective non-linear one-dimensional theoretical model and, based on it, corresponding digital code UTSG-2 for vertical, natural-circulation U-tube steam generators (Hoeld, 1978 and 1990) and now also the new advanced code version UTSG-3 (Hoeld 2002b, 2004).

The good agreement of the test calculations with similar calculations of earlier versions applied to the same transient cases demonstrates that despite of the continuous improvements of the code UTSG and the incorporation of CCM into UTSG-3 the newest and advanced version has still preserved its validity.

A more detailed description over these general V&V measures demonstrated on one characteristic test case can be found in (Hoeld, 2011).

## 6. Conclusions

The universally applicable coolant channel module CCM allows describing the thermal-hydraulic situation of fluids flowing along up-, horizontal or downwards channels with fluids changing between sub-cooled, saturated and superheated conditions. It must be recognized that CCM represents a complete system in its own right, which requires only BC-related, and thus easily available, input values (geometry data, initial and boundary conditions, resulting parameters from integration). The partitioning into SC-s is done automatically within the module, without requiring any special actions on the part of the user. At the end of a time-step the characteristic parameters of all SC-s are transferred to the corresponding BC positions, thus yielding the final set of ODE-s together with the parameters following from the constitutive equations of CCM.

In contrast to the currently very dominant separate-phase models, the existing theoretical inconsistencies in describing a two-phase fluid flowing along a coolant channel if changing between single-phase and two-phase conditions and vice versa can be circumvented in a very elegant way in the 'separate-region' mixture-fluid model presented here. A very unique technique has been established built on the concept of subdividing a basic channel (BC) into different subchannels (SC-s), thus yielding exact solutions of the basic drift-flux supported conservation equations. This type of approach shows, as discussed in (Hoeld, 2004b), distinct advantages vs. 'separate phase' codes, especially if taking into account

- the quality of the fundamental equations (basic conservation equations following directly from physical laws supported by experimentally based constitutive equations vs. split 'field' equations with artificial closure terms),
- the special solution methods due to the detailed interpolation procedure from PAX allowing to calculate the exact movement of boiling boundaries and mixture (or dry-out) levels (different to the 'donor-cell averaging' methods yielding mostly only 'condensed' levels),
- the possibility to take advantage of the 'closed-channel concept' (needed for example for thermal- hydraulic 3D considerations) allowing thus to decouple a characteristic ('closed') channel from other parts of a complex system of loops,
- the speed of the computation,
- the derivation of the theory in close connection with the establishment of the code by taking advantage of feedbacks coming from both sides,
- the considerable effort that has been made in verifying and checking the CCM (besides an extensive V & V procedure), with respect to the applicability and adjustment and also for very extreme situations,

- its easy applicability,
- the maturity of the module, which is continuously enhanced by new application cases.
- taking advantage of the fact that most of the development work for the coolant channel thermal-hydraulics has already been shifted to this module (including the special provisions for extreme situations such as stagnant flow, zero power or zero sub-cooling, test calculations for the verification and validation of the code etc.).

The existence of the resulting widely verified and validated module CCM represents an important basic element for the construction of a variety of other comprehensive thermal-hydraulic models and codes as well. Such models and modules can be needed for the simulation of the steady state and transient behaviour of different types of steam generators with special primary and secondary loops (vertical U-tube, vertical once-through or horizontal VVER-440 or -1000 assemblies). One main field of application will be (and is already) the simulation of a 3D thermal-hydraulic situation by a number of parallel channels (reactor cores, VVER steam generators etc.), the (basic) channels distinguished by different key numbers  $N_{\text{TYPES}}$ . It shows special advantages in view of the determination of the mass flow distribution into different coolant channels after non-symmetric perturbations see (Hoeld, 2004a) or (Jewer et al., 2005), a problem which is far from being solved in many of the newest 3D studies. It allows also studying the validity of the 'open channel' method in a very detailed form.

The introduction of varying cross sections along the  $z$  axis allows to take care also of thermal non-equilibrium situations by simulating the two separate phases by two with each other interacting basic channels (for example if sub-cooled water rays are injected into a steam dome).

The resulting equations for different channels appearing in a complex physical system can be combined with other sets of algebraic equations and ODE-s coming from additional parts of such a complex model (heat transfer or nuclear kinetics considerations, top plenum, main steam system and downcomer of a steam generator etc.). The final overall set of ODE-s can then be solved by applying an appropriate time-integration routine. See for example (Hoeld, 2011).

The enormous efforts already made in the verification and validation of the codes UTSG-3, its application in a number of transient calculations at very extreme transient situations (fast opening of safety valves, dry out of the total channel with SC-s disappearing or created anew) brings the code and thus also CCM to a very mature and (what is important) easily applicable state. However, there is not yet enough experience to judge how the potential of the mixture-fluid models and especially of CCM can be expanded to other extreme cases (e.g., water and steam hammer). Is it justified to prefer separate-phase models versus the drift-flux based (and thus non-homogeneous) mixture fluid models? This depends, among other criteria, also on the quality of the special models and their exact derivation. Considering the arguments presented above it can, however, be stated that in general the here presented module can be judged as a very satisfactory approach.

## 7. Nomenclature

$A_{Bk}$	$m^2$	BC cross sectional area (at BC node boundary $k$ )
----------	-------	--

$A_{Nn}, A_{Mn}$	$m^2$	SC cross sectional area (at SC node boundary n, mean value)
$C$	-	Dimensionless constant
$C_0$	-	Phase distribution parameter
$d_{HW}$	$m$	Hydraulic diameter
$f(z,t), f_{Nn}, f_{Mn}$	-	General and nodal (boundary and mean) solution functions
$f_{LIMCA}$	-	Upper or lower limit of the approx. function $f(z,t)$
$f_{ADD0}, f_{FMP0}$	-	Additive and multiplicative friction coefficients
$G, G_F = G/A$	$\frac{kg}{s}, \frac{kg}{sm^2}$	Mass flow, mass flux
$h, h^P, c_P = h^T$	$\frac{J}{kg}, \frac{m^3}{kg}, \frac{J}{m^3 kg}$	Specific enthalpy and its partial derivatives with respect to pressure and temperature (= specific heat)
$h_{SW} = h'' - h', h'', h'$	$\frac{J}{kg}$	Latent heat, saturation steam and water enthalpy
$K_{EYBC}$	-	Characteristic key number of channel BC
$L_{FTYPE} = 0, 1 \text{ or } 2$	-	SC with saturated water/steam mixture, sub-cooled water or superheated steam
$N_{BT}$	-	Total number of BC nodes
$N_{BCA} = N_{CT} + N_{BCE}, N_{BCE}$	-	BC node numbers containing SC outlet or entrance
$N_{CT} = N_{BCA} - N_{BCE}$	-	Total number of SC nodes
$P, \Delta P_T = P_A - P_E$	$Pa = \frac{J}{m^3} = \frac{kg}{ms^2}$	Pressure and pressure difference (in flow direction)
$Q_{BT}, Q_{Bk}$	$W$	Total and nodal BC power into channel k
$q_{Bk} = U_{Bk} q_{LBk} / A_{Bk}$	$\frac{W}{m^3}$	Nodal BC power density into the fluid (= volumetric heat transfer rate)
$q_{FBk} = A_{Bk} \frac{q_{Bk}}{U_{Bk}}$	$\frac{W}{m^2}$	Heat flux from (heated) wall to fluid
$q_{LBk} = U_{TWBk} q_{FBk} = A_{Bk} q_{Bk}$	$\frac{W}{m}$	Linear power at BC node k
$q_{Mn} = \frac{Q_{Mn}}{V_{Mn}}$ $= \frac{1}{2A_{Mn}} (q_{LNn} + q_{LNn-1})$	$\frac{W}{m^3}$	Nodal SC power density into fluid (= volumetric heat transfer rate)
$T, t$	$C, s$	Temperature, time
$U$	$m$	(Heated) perimeter of a heated wall
$V_{Mn} = \frac{1}{2} (A_{Nn} + A_{Nn-1}) \Delta z_{Nn}$	$m^3$	Mean nodal SC volume
$v$	$\frac{m}{s}$	Velocity

$X = \frac{G_S}{G}$ or $= \frac{h-h'}{h_{SW}}$	-	Steam quality (2-phase and expanded to 1-phase flow)
$z, \Delta z_{Nn} = z_{Nn} - z_{Nn-1}$	m	Local position, SC node length ( $z_{Nn-1} = z_{CE}$ at $n=0$ )
$z_{BA} - z_{BE} = z_{BT}, z_{CA} - z_{CE} = z_{CT}$	m	BC and SC outlet and entrance positions, total length
$z_{BB}, z_{ML}$	m	Boiling boundary and mixture level within a BC
$\alpha$	-	Void fraction
$\alpha_{TWk}$	$\frac{W}{m^2 \cdot C}$	Heat transfer coefficient along a BC wall surface
$\Delta$	-	Nodal differences
$\varepsilon_{DPZ}$	-	Coefficient controlling the additional friction part
$\varepsilon_{QTW}$	-	Correction factor with respect to $Q_{NOM,0}$
$\varepsilon_{TW}$	m	Abs. roughness of tube wall ( $\varepsilon_{TW}/d_{HW}$ = relative value)
$\Phi_{2PF}^2$	-	Two-phase multiplier
$\Phi_{ZG}$	-	Angle between upwards and flow direction
$\rho, \rho^P, \rho^T$	$\frac{kg}{m^3}, \frac{kg}{J}, \frac{kg}{m^3 \cdot C}$	Density and their partial derivatives with respect to (system) pressure and temperature
$\Theta$	s	Time constant
$\partial$	-	Partial derivative

Subscripts

0, 0 (=E or BE)	Steady state or entrance to SC or BC ( $n$ or $k=0$ )
A, E, T (=AE)	Outlet, entrance, total (i.e. from outlet to entrance)
B, S	Basic channel or sub-channel (=channel region)
A, S, F, D, X ( $P=A+S+F+D+X$ ) and G	Acceleration, static head, direct and additional friction and external pressure differences (in connection with $\Delta P$ ) and pressure differences due to changes in mass flux
Mn, BMk	Mean values over SC or BC nodes
Nn, Bk	SC or BC node boundaries ( $n = 0$ or $k = 0$ : SC or BC entrances)
D	Drift
S, W	Steam, water
P, T	Derivative at constant pressure or temperature
TW	Tube wall surface

Superscripts

/, //

Saturated water or steam

P, T

Partial derivatives with respect to P or T

(G<sub>s</sub>), (α), z, sPartial derivatives with respect to  
G<sub>s</sub>, α or z (=gradient), slope**8. References**

- Austregesilo H. et al. 2003. *ATHLET Mod 2.0, Cycle A, Models and methods*. GRS-P-1/Vol.4.
- Bencik,V.& Hoeld, A.1991. *Experiences in the validation of large advanced modular system codes*. 1991 SCS Simulation MultiConf., April 1-5, New Orleans
- Bencik,V.& Hoeld, A.1993. *Steam collector and main steam system in a multi-loop PWR NPP representation*. Simulation MultiConf., March 29-April 1, Arlington/Washington
- Bestion, D. 1990. *The physical closure laws in CATHARE code*. Nucl.Eng.& Design 124, 229- 245
- Burwell, J. et al. 1989. *The thermohydraulic code ATHLET for analysis of PWR and SWR system*, Proc.of 4-th Int. Topical Meeting on Nuclear Reactor Thermal-Hydraulics, NURETH-4, Oct.10-13, Karlsruhe
- Dunn, F.E. 1998. *Thermal-hydraulic calculations in the SAS-DIF3DK coupled reactor physics and thermal-hydraulics code*. International Topical Meeting on Safety of Operating Reactors, Oct.11-14, San Francisco
- Fabic, S. 1996. *How good are thermal-hydraulics codes for analyses of plant transients*. International ENS/HND Conference, 7-9 Oct. 1996, Proc.193-201, Opatija/Croatia
- Haar, L., Gallagher, J.S., Kell, G.S. 1988. *NBS/NRC Wasserdampftafeln*. London/Paris/New York 1988
- Hanna, B.N., 1998. *CATENA. A thermalhydraulic code for CANDU analysis*. Nucl. Eng. Des. 180 (1998) 113-131.
- Hoeld, A. 1978. *A theoretical model for the calculation of large transients in nuclear natural circulation U-tube steam generators (Digital code UTSG)*. Nucl. Eng. Des.(1978), 47, 1.
- Hoeld, A. 1988a. *HETRAC: A heat transfer coefficients package*. GRS-A-1446, May.
- Hoeld, A. 1988b. *Calculation of the time behavior of PWR NPP during a loss of a feedwater ATWS case*. NUCSAFE 88, 2-7 October, Proc. 1037-1047, Avignon, France.
- Hoeld, A.1990a. *UTSG-2. A theoretical model describing the transient behaviour of a PWR natural-circulation U-tube steam generator*. Nuclear Techn. 90, 98-118, April.
- Hoeld, A. 1990b. *The code ATHLET as a valuable tool for the analysis of transients with and without SCRAM*, SCS Eastern MultiConf,23-26 April, Nashville, Tennessee.
- Hoeld, A., Jakubowska, E., Miro, J.E & Sonnenburg,H.G. 1992. *A comparative study on slip and drift- flux correlations*. GRS-A-1879, Jan. 1992
- Hoeld, A. 1994. *Drift-Flux Paket MDS auf der Basis der SONNENBURG-Korrelation*. GRS, Technische Notiz , TN-HOD-01/94, Juni 1994.
- Hoeld, A. 1996. *Thermodynamisches Stoffwertpaket MPP für Wasser und Dampf*. GRS, Technische Notiz, TN-HOD-1/96, Mai.
- Hoeld, A. 1999. *An Advanced Natural-Circulation U-tube Steam Generator Model and Code UTSG-3*, EURO THERM-SEMINAR No.63, September 6-8, Genoa, Italy.
- Hoeld, A. 2000. *The module CCM for the simulation of the thermal-hydraulic situation within a coolant channel*. Intern. NSS/ENS Conference, September 11-14, Bled, Slovenia.



- Hoeld, A. 2001. *The drift-flux correlation package MDS*. 9-th International Conference on Nuclear Engineering (ICONE-9), 8-12 April, Nice, France.
- Hoeld, A. 2002a. *The consideration of entrainment in the drift-flux correlation package MDS*. 10-th Int. Conference on Nuclear Engineering (ICONE-10), April 14-18, Arlington, USA.
- Hoeld, A. 2002b. *A steam generator code on the basis of the general coolant channel module CCM*. PHYSOR 2002, October 7-10, Seoul, Korea.
- Hoeld, A. 2004a. *A theoretical concept for a thermal-hydraulic 3D parallel channel core model*. PHYSOR 2004, April 25-29, Chicago, USA.
- Hoeld, A. 2004b. *Are separate-phase thermal-hydraulic models better than mixture-fluid approaches. It depends. Rather not*. Int. Conference on Nuclear Engineering for New Europe 2004'. Sept. 6-9, Portoroz, Slovenia.
- Hoeld, A. 2005. *A thermal-hydraulic drift-flux based mixture-fluid model for the description of single- and two-phase flow along a general coolant channel*. The 11-th International Topical Meeting on Nuclear Reactor Thermal-Hydraulics (NURETH-11). Paper 144. Oct. 2-6, 2005, Avignon, France.
- Hoeld, A. 2007a. *Coolant channel module CCM. An universally applicable thermal-hydraulic drift-flux based mixture-fluid 1D model and code*. Nucl. Eng. and Design 237(2007), 1952-1967
- Hoeld, A. 2007b. *Application of the mixture-fluid channel element CCM within the U-tube steam generator code UTSG-3 for transient thermal-hydraulic calculations*. 15-th International Conference on Nuclear Engineering (ICONE-15). Paper 10206. April 22-26, 2007, Nagoya, Japan
- Hoeld, A. 2011. *The thermal-hydraulic U-tube steam generator model and code UTSG3 (Based on the universally applicable coolant channel module CCM)*. Intech Open Access Book 'Steam Generator Systems', ISBN 978-953-7619-X-X, InTech, Austria, Available from: [http://sciyo.com/articles/show/title/ The thermal-hydraulic U-tube steam generator model and code UTSG3 \(Based on the universally applicable coolant channel module CCM\)](http://sciyo.com/articles/show/title/The%20thermal-hydraulic%20U-tube%20steam%20generator%20model%20and%20code%20UTSG3%20(Based%20on%20the%20universally%20applicable%20coolant%20channel%20module%20CCM)).
- Ishii, M. 1990. *Two-Fluid Model for Two-Phase Flow*, Multiphase Sci. and Techn. 5.1, Hemisphere Publ. Corp.
- Ishii, M. and Mishima, K. 1980. *Study of two-fluid model and interfacial area*. NUREG/CR-1873 (ANL-80-111), Dec.
- Jewer, S., Beeley, P., Thompson, A. & Hoeld, A. 2005. *Initial version of an integrated thermal-hydraulic and neutron kinetics 3D code X3D*. ICONE13, May 16-20, Beijing. See also NED 236(2006), 1533-1546.
- Lerchl G. et al. 2009. *ATHLET Mod 2.2, Cycle B, User's Manual*'. GRS-P-1/Vol.1. Rev. 5, July
- Liles D. R. et al. 1988. *TRAC-PF1/MOD1 – Correlations and Models*. NUREG/CR-5069, LA-11208-MS, Dec.
- Martinelli, R.C., Nelson, D.B. 1948. *Prediction of pressure drop during forced-circulation of boiling water*. Trans. ASME 70, 695.
- Moody, N.L.F. 1994. *Friction factors for pipe flow*. Trans. ASME, 66, 671 (See also VDI-Wärmeatlas, 7.Auflage, 1994, VDI - Verlag).
- Schmidt, E. & Grigull, U. (ed.) 1982. *Properties of water and steam in SI-Units*. Springer-Verlag.
- Sonnenburg, H.G. 1989. *Full-range drift-flux model based on the combination of drift-flux theory with envelope theory*, NURETH-4, pp.1003-1009, Oct.10-13, Karlsruhe.

- Shultz, R.R. 2003. *RELAP5-3D code manual. Volume V: User's guidelines*. INEEL-EXT-98-00084. Rev.2.2, October.
- US-NRC. 2001a. TRAC-M/FORTRAN90 (Version 3.0). Theory Manual, NUREG/CR-6724, April
- US-NRC. 2001b. *RELAP5/MOD3.3. Code Manual*. Volume I, NUREG/CR-5535, December
- Wulff, W. 1987. *Computational methods for multiphase flow*, 2-nd Int. Workshop on Two-phase Flow Fundamentals, Rensselaer Pol. Inst., March 15-20.
- Zuber, N. & Findlay, J.A., 1965. *Average volume concentration in two-phase flow systems*, J. Heat Transfer 87, 453

# The Thermal-hydraulic U-tube Steam Generator Model and Code UTSG-3 (Based on the Universally Applicable Coolant Channel Module CCM)

Alois Hoeld

*Retired from GRS Garching/Munich  
Bernaysstr. 16A, D-80937 Munich  
F.R. of Germany*

## 1. Introduction

The development of effective theoretical models and (based on it) digital codes which have the potential to describe in a detailed way the overall transient and accidental behaviour of both the reactor core but also the main components of different NPP types has already very early been an important task in the field of reactor safety research.

Within this context an own special thermal-hydraulic model for one of these components, namely the natural circulation U-tube steam generator together with its main steam and feedwater systems, has been derived. The resulting digital code UTSG (Hoeld, 1978) could be used both in a stand-alone manner but also as a part of more comprehensive transient codes. As such an overall code the thermal-hydraulic GRS system code ATHLET (Burwell et al., 1989, Hoeld 1990b, later-on also Austregesilo et al., 2003 and Lerchl et al., 2009) has been chosen. Along with the ATHLET code a special high level simulation language has been derived too (Austregesilo & Voggenberger, 1990; Austregesilo & Hoeld, 1991), resulting in the basic module GCSM (General Control Simulation Module) provided for the flexible description of balance-of-plant (BOP) actions as caused, for example, by the control, limitation and protection systems of NPP-s, thereby connecting basic functional blocks (e.g., switches, function generators, adders, differentiators, integrators) in an appropriate way.

Due to the rising demands coming from safety-related research studies and based on the efforts of many years work of application both at the GRS but also at a number of other institutes of different countries the UTSG theory and code had to be and had been continuously extended, yielding in a first step as a very satisfactory version the code UTSG-2 (Hoeld 1990a).

From the experience gained during the continuous development of this code it arose after a while the question how to establish an own basic element which is able to simulate the thermal-hydraulic situation in a cooled or heated coolant channel in an as general as possible way so that it can be applied for any modular construction of complex thermal-hydraulic assemblies of pipes and junctions. As a result finally a theoretical model has been derived based on a theoretical drift-flux related three-equation mixture fluid approach. The

resulting (coolant channel module) package CCM should then allow to calculate automatically all the needed characteristic thermal-hydraulic parameters of a coolant channel within a complicated system of channels and loops and can thus be a valuable tool for the establishment of complex codes (Hoeld 2000a and b, Hoeld, 2007b).

By means of this generally applicable code package CCM the original digital code UTSG-2 (Hoeld, 1990a) could now be extended to a new advanced version, named UTSG-3. Thereby the module CCM has been implemented for the three characteristic channel elements of an U-tube steam generator, namely the primary and secondary side of the heat exchange region and the riser, distinguished by their key numbers (KEYBC = 1, 2 or 3). Besides this essential change the new UTSG version contains compared to the previous one a number of outstanding improvements, for example by providing a more advanced simulation of the top plenum, main steam line, feedwater injection and downcomer region together with a better simulation of the natural circulation situation. This new code could then also be (and has been) used to check the performance and validity of the code package CCM (and to verify it).

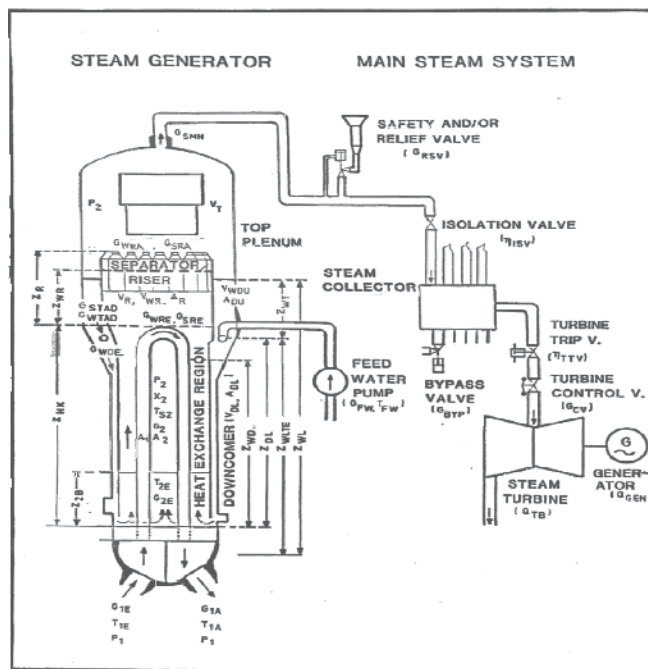


Fig. 1. Layout of a natural-circulation u-tube steam generator with its corresponding main steam system

The code UTSG-3 is, similarly as the code UTSG-2, based on the same U-tube and main steam system layout as sketched in fig.1. This means, the vertical natural-circulation U-tube steam generator is considered to consist of the following main parts:

- Primary or secondary heat exchange (HEX) region (evaporator)
- Bundle of U-tubes (index TW if restricting to a representative single U-tube)
- Riser (index R)
- Top plenum (index T) with its main steam system (index MS)

- Downcomer (index  $D=DU+DL$ ) with feedwater system (index FW)
- Closed secondary loop (natural circulation)

The HEX region is separated by a number ( $N_{TUBES}$ ) of vertical U-tubes into a primary and secondary loop, with the primary coolant flowing on the inner side (index 1) up and down, the secondary coolant on the outside (index 2) of these tubes upwards. The mixture flow from the HEX region is transported through a riser (index R) into the top plenum (TPL) where due to a separator the mixture flow is split into each phase, the water being yielded to the downcomer (DCM), the steam into the main steam system. The downcomer consist of an upper and (below the FW entrance) lower part (indices DU and DL). A feedwater system (index FW) transports sub-cooled water into the DCM where it is mixed with the downwards flowing saturated water from the TPL. To each of the U-tube steam generator systems (four in the case of a PWR) belongs a main steam line (with an isolation valve and a sequence of relief- and safety valves), all of them ending in a steam collector (SC) with steam lines to the bypass and steam turbine system (with steam bypass, turbine-trip and turbine control valves).

The flexibility of the finally established code combination UTSG-3/CCM will be demonstrated on a characteristic example by post-calculating with this combination a complicated transient situation after an initiation of the signal 'Loss of main feedwater in a PWR NPP with turbine trip and reactor scram'. A comparison with already existing (and tested out) UTSG-2 calculations for the same case has given an insight into the validity of the new code version UTSG-3 and helped thus to verify the general coolant channel module CCM too.

The here presented paper is concentrated on a very detailed description of the newest and advanced status of the theoretical U-tube steam generator model and its code version UTSG-3. Its theoretical background has already been partially published in (Hoeld, 2005 and 2007a). About the very important part of the UTSG-3 code, the coolant channel module CCM, here only a short review of its main elements can be given, an overall presentation will be placed in (Hoeld, 2011).

## 2. Basic equations of the thermal-hydraulic model

The thermal-hydraulic module CCM, part of UTSG-3, is based on the classical three-equation mixture fluid theory, starting from the conservation equations for mass, energy and momentum with respect to both single- and/or two-phase water/steam flow. Such conservation equations are mostly given in form of partial differential equations (PDE-s). In a closed loop further conservation equations are demanded, among them the 'volume balance equation', needed for the determination of the time-derivatives of the system pressure, and the TPL steam and water volumes. The solution of the momentum balance yields then local pressure difference terms over each channel element. It allows thus (in combination with the system pressure) to determine the behaviour of the (absolute) local pressure along a channel. A fifth physical law which is based on the fact that the sum of all pressure decrease terms along a closed loop must be zero. This gives the basis for the determination of the needed mass flow terms along a closed channel due to natural circulation by adapting these terms to the demand of this law.

The conservation equations are supported by adequate constitutive equations. These can be provided by tables for thermodynamic and transport properties of water and steam, a correlation package for single- and two-phase friction coefficients etc. In case of mixture

flow) the right choice of an adequate drift-flux package plays an important role among these constitutive equations, yielding not only the necessary equation for the fourth variable within the overall system of differential and constitutive equations but being also responsible for the possibility to simulate in a very detailed way stagnant or counter-current flow conditions or the appearance of entrainment within such a coolant channel.

## 2.1 Conservation equations for single- and two-phase flow

The three conservation equations (with a cross flow area  $A$  and perimeter  $U_{TW}$ ) describe both the steady state ( $L_{STS}=1$ ) and transient ( $L_{STS}=0$ ) behaviour of three or (at two-phase flow) four characteristic fluid variables. These are the total mass flow  $G$ , the fluid temperature  $T$  (or enthalpy  $h$ ) at single-phase or void fraction  $\alpha$  at two-phase conditions and the local pressure  $P$ . At two-phase conditions for a fourth variable, i.e. the steam mass flow  $G_S$ , an own relation is asked. This can, for example, be a drift-flux correlation which yields (together with an adequate correlation for the phase distribution parameter  $C_0$ ) the drift velocity  $v_D$  and thus also the steam mass flow  $G_S$ , hence closing the set of equations. They are interconnected by their definition equations.

### 2.1.1 Mass balance

$$\frac{\partial}{\partial t} \{A[(1-\alpha)\rho_W + \alpha\rho_S]\} + \frac{\partial}{\partial z} G = 0 \quad (1)$$

with the density terms  $\rho_W$  and  $\rho_S$  for saturated or sub-cooled water and saturated or superheated steam, the void fraction  $\alpha$  and the cross flow area  $A$  which can eventually be changing along the coolant channel. It determines, after a nodalization, the total mass flow  $G=G_W+G_S$  at node outlet in dependence of its node entrance value.

### 2.1.2 Energy balance

$$\frac{\partial}{\partial t} \{A[(1-\alpha)\rho_W h_W + \alpha\rho_S h_S - P]\} + \frac{\partial}{\partial z} (G_W h_W + G_S h_S) = q_L = U_{TW} q_F = A q \quad (2)$$

with the enthalpy terms  $h_W$  and  $h_S$  for saturated or sub-cooled water and saturated or superheated steam. As boundary values there have to be demanded either the 'linear power  $q_L$ ' or the 'heat flux  $q_F$ ' along the tube wall surface being directed (if positive) into the coolant, yielding thus the local 'power density term  $q$ ' (See also section 4.2.3).

As explained in very detail in connection with the establishment of CCM (Hoeld, 2011), after an appropriate finite-difference nodalization procedure it follows in the transient case then a set of nodal ordinary differential equations (ODE-s) of 1-st order for

- the mean nodal enthalpies ( $h_{WMn}$ ,  $h_{SMn}$ ) of either sub-cooled water (if  $L_{FTYPE}=1$ ) or superheated steam ( $L_{FTYPE}=2$ ) in the case of a single-phase flow situation and thus, by applying water/steam tables (for example the package MPP, see section 2.2.1), corresponding coolant temperature terms ( $T_{WMn}$ ,  $T_{SMn}$ ) too, or, at two-phase flow conditions ( $L_{FTYPE}=0$ ), the mean nodal void fraction  $\alpha_{Mn}$  over each node  $n$  and
- at the transition from single- to two-phase (and vice versa) for either the boiling boundary  $z_{BB}$  (if  $\alpha=0$ ) or the mixture (or dry-out) level  $z_{ML}$  (if  $\alpha=1$ ). Thereby it can be taken advantage

of the fact that these positions are marked by the fact that either the coolant enthalpy or temperature are limited by their saturation enthalpy or temperature values ( $h_W = h'$  or  $h_S = h''$  and  $T_W = T_{SAT}$  or  $T_S = T_{SAT}$ ), the void fractions by the limits 1 (or 0).

### 2.1.3 Momentum balance

$$\frac{\partial}{\partial t} (G_F) + \left( \frac{\partial P}{\partial z} \right) = \left( \frac{\partial P}{\partial z} \right)_A + \left( \frac{\partial P}{\partial z} \right)_S + \left( \frac{\partial P}{\partial z} \right)_F + \left( \frac{\partial P}{\partial z} \right)_X \quad (3)$$

describing either the pressure differences (at steady state) or (in the transient case) the change in the total mass flux ( $G_F = G/A$ ) along a channel.

The general pressure gradient ( $\frac{\partial P}{\partial z}$ ) can be determined in dependence of

- the mass acceleration

$$\left( \frac{\partial P}{\partial z} \right)_A = - \frac{\partial}{\partial z} [(G_{FW}v_W + G_{FS}v_S)] \quad (4)$$

with  $v_S$  and  $v_W$  denoting steam and water velocities,

- the static head

$$\left( \frac{\partial P}{\partial z} \right)_S = - \cos(\Phi_{ZG}) g_C [\alpha \rho_S + (1-\alpha) \rho_W] \quad (5)$$

with  $\Phi_{ZG}$  denoting the angle between upwards and flow direction. Then  $\cos(\Phi_{ZG}) = \pm |z_{EL}|/z_L$  with the relative elevation height  $z_{EL}$  being positive at upwards flow

- the single- and/or two-phase friction term

$$\left( \frac{\partial P}{\partial z} \right)_F = - f_R \frac{G_F |G_F|}{2 d_{HW} \rho} \quad (6)$$

with the friction factor derived from corresponding constitutive equations (See section 2.2.2) and finally

- the direct perturbations ( $\frac{\partial P}{\partial z}$ )<sub>X</sub> from outside arising either by operating an external pump or the pressure adjustment due to mass exchange between parallel channels.

For more details see (Hoeld, 2011).

### 2.1.4 Volume balance

Volume balance considerations yield, in the case of a closed loop, to a fourth conservation equation. This is based on the (trivial) fact that the sum of water and steam volume must be equal to the total available volume. This is required for the determination of an absolute pressure parameter, e.g., the system pressure  $P_{SYS}$  in the top plenum of a steam generator (see section 4.5). From the pressure differences over different nodes of the loop following the discretization of the momentum balance equation the transient behaviour of the (absolute) local pressure values can then, in combination with  $P_{SYS}$ , be determined.

### 2.1.5 Balance of pressure decrease over channels within a closed loop

In a network of channels within a closed loop (for example for the simulation of natural circulation or the case of a 3D representation) a fifth conservation equation has to be taken

into account. This is founded on the physical law that the sum of all pressure decrease terms over all these channels must be zero. This is the basis for the treatment of the thermal-hydraulics of a channel according to the 'closed channel concept' (For more details see section 3.4).

## 2.2 Constitutive equations

For the exact description of the steady state and transient thermal-hydraulic behaviour of single- or two-phase fluids there are needed, besides the conservation equations, a number of mostly empirical (and pseudo-stationary) constitutive relations. Naturally, any effective correlation package can be used for this purpose. A number of such correlations have been developed at the GRS, adapted to the special requirements of the models by the author and thoroughly tested, showing very satisfactory results (Here only a short review of them will be given, for more details see Hoeld, 2011).

### 2.2.1 Thermodynamic and transport properties of water and steam

The different thermodynamic and transport properties for water and steam demanded by the conservation and constitutive equations have to be determined by applying adequate water/steam tables. This is, for light-water systems, realized in the code package MPP (Hoeld, 1996). It yields the wanted values such as the saturation temperature  $T_{SAT}$ , densities ( $\rho'$ ,  $\rho''$ ), enthalpies ( $h'$ ,  $h''$ ) for saturated water and steam with respect to their local pressure ( $P$ ) and corresponding densities ( $\rho$ ) and enthalpies ( $h$ ) for sub-cooled water or superheated steam (index W and S) again with respect to their independent local parameters  $T$  and  $P$  (but also  $h$  and  $P$ ).

For the solution of the conservation equations also time-derivatives of these thermodynamic properties which respect to their independent local parameters are demanded. They get, for example for the case of an enthalpy term  $h$ , the form

$$\begin{aligned} \frac{d}{dt} h(z,t) &= \frac{d}{dt} h[T(z,t), P(z,t)] = \left( \frac{\partial h}{\partial T} \right) \frac{d}{dt} T_{Mn}(t) + \left( \frac{\partial h}{\partial P} \right)_{Mn} \frac{d}{dt} P_{Mn}(t) \\ &= h^T \frac{d}{dt} T_{Mn}(z,t) + h^P \frac{d}{dt} P_{Mn}(z,t) \end{aligned} \quad (7)$$

Hence the thermodynamic water/steam tables should provide also the derivatives ( $T_{SAT}^P$ ,  $\rho'^P$ ,  $\rho''^P$ ,  $h'^P$ ,  $h''^P$ ) for saturated water and saturated steam but also the partial derivatives ( $\rho^T$ ,  $\rho^P$ ,  $c_P = h^T$ ,  $h^P$ ) for subcooled water or superheated steam with respect to their independent parameters  $T$  and  $P$  (but also  $h$  and  $P$ ). Additionally, corresponding thermodynamic transport properties such as 'dynamic viscosity' and 'thermal heat conductivity' (and thus the 'Prantl number') are asked from some constitutive equations too as this can be stated, for example, for the code packages MPPWS and MPPETA (Hoeld, 1996). All of them have been derived on the basis of tables given by (Schmidt and Grigull, 1982) and (Haar et al., 1988). Obviously, the CCM method is also applicable for other coolant systems (heavy water, gas) if adequate thermodynamic tables for this type of fluids are available.

### 2.2.2 Single- and two-phase friction factors

In the case of **single-phase flow** with regard to equation (6) the friction factor  $f_R$  will, as recommended by (Moody, 1994), be set equal to the Darcy-Weisbach single-phase friction factor  $f_{DW}$  being represented by



$$f_R = f_{DW} = \frac{1}{\xi^2} \quad (\text{at single-phase flow}) \quad (8)$$

with the parameter  $\xi$  depending on the Reynolds number  $Re = Gd_H/(\Delta\eta)$  and the relative roughness  $(\varepsilon/d_H)$  of the wall surface. The factor  $\xi$  can be approximated by the relation

$$\begin{aligned} \xi &= 2 \log_{10} \left( \frac{d_H}{\varepsilon_{TW}} \right) + 1.14 & \text{if } Re > Re_{CTB} = 441.19 \left( \frac{d_H}{\varepsilon_{TW}} \right)^{1.1772} \\ \xi &= -2 \log_{10} \left( 2.51 \frac{\xi}{Re} + \frac{\varepsilon_{TW}}{3.71 d_H} \right) & \text{if } Re < Re_{CTB} \end{aligned} \quad (9)$$

For **two-phase flow** conditions this factor can be extended to

$$f_R = f_{DW} \Phi_{2PF}^2 \quad (\text{at two-phase flow}) \quad (10)$$

with the single-phase part  $f_{DW}$  to be determined under the assumption that the fluid moves with the total mass flow  $G$  (= 100 % liquid flow) and the two-phase multiplier  $\Phi_{2PF}^2$  as given by (Martinelli-Nelson, 1948) as measured curves (dependent only on steam quality and pressure). For more details see (Hoeld, 1996 and 2010)

### 2.2.3 Drift flux correlation

In the case of two-phase flow, the three conservation equations (1), (2) and (3) have to be completed by an additional two-phase relation in order to obtain an adequate representation of the needed fourth variable  $G_S$  (Note: These correlations can be seen as a 'bridge' between  $G_S$  and  $\alpha$ ). This purpose can be achieved by any two-phase correlation, e.g. a slip correlation. However, to take care of stagnant or counter-current flow situations too an effective drift-flux correlation seemed here to be more appropriate.

For this purpose an own drift-flux correlation package has been established, named MDS (Hoeld, 2001 and 2002a). It is based on the result of a very comprehensive study (Hoeld et al., 1992) and (Hoeld, 1994) comparing different slip (6) and drift-flux (3) correlations with each other and also with a number (5) of available experimental data in order to check their validity over a wide range of application and to find which of them is most suited for incorporation into the CCM. Due to different requirements in the application of CCM it turned out that the drift-flux correlation package in the form of the 'flooding-based full-range' Sonnenburg correlation (1989) should be preferred. This correlation combines the common drift-flux procedure, being formulated by (Zuber-Findlay, 1965), and expanded by (Ishii-Mishima, 1980 and Ishii; 1990 etc.), with the modern envelope theory. The correlation in the final package MDS had to be rearranged in such a way that also the special cases of  $\alpha \rightarrow 0$  or  $\alpha \rightarrow 1$  (where its absolute values but also their gradients are demanded by CCM) could be treated. It should be also possible to install an inverse form (needed for example for steady state considerations) or to take care of considerations with respect to a possible entrainment.

Having now calculated for the steady state case  $G_S$  in dependence of  $\alpha$  and in the transient situation  $\alpha$  in dependence of  $G_S$  then all the other characteristic local two-phase parameters can be determined too (as shown, for example, in the tables of Hoeld, 2001 and 2002a). Especially the determination of the steam mass flow gradient plays an important part for the case that the entrance or outlet position of a SC is crossing a BC node boundary ( $\alpha \rightarrow 0$  or  $\rightarrow$

1). This term is thus an indispensable part in the nodalization procedure of the mixture-fluid mass and energy balance.

### 2.2.4 Heat transfer coefficients along a tube wall

The needed heat transfer coefficients ( $\alpha_{TW1}$ ,  $\alpha_{TW2}$ ) along different flow regimes (into and out of a tube wall) can be calculated automatically if applying an appropriate heat transfer coefficient package.

Hence, in connection with the development of the UTSG code (and thus also CCM) for this purpose a method how to get the necessary correlations for heat transfer coefficients along different flow regimes within such a channel had to be established, yielding finally an own very comprehensive heat transfer coefficient package, called HETRAC (Hoeld 1988a or already 1978). It combines, for example, especially for this purpose chosen HTC correlations for each possible flow situation within LWR-s and steam generators (i.e., into or out of heated or cooled tube walls or fuel elements) in a very effective way. Thereby adequate correlations for the cases of sub-cooled water, sub-cooled and nucleate boiling, onset of critical heat flux, transient or instable film boiling, stable film boiling, onset of superheating and superheated steam for different geometry constellations and over a wide range of input parameters (pressures, total and steam mass flows, coolant temperatures, wall temperatures or heat fluxes etc.) had to be selected. Special attention had to be given also to the case of a counter-current flow situation within a mixture flow. Some correlations (and thus also the package) take not only heat transfer from wall to the different phases but also between these phases into account. This can, for example, be clearly explained on hand of the Chen correlation (being a part of the HETRAC package) for the case of nucleate boiling. There, because of different conditions with regard to the heat input and mass flow along the channel, the entire heat transfer consists of two overlapping fundamental mechanisms, a macro- and a micro-convective part. Thus it is distinguished between a heat transfer mechanism where in the first case heat is inserted directly into a thin water film along the wall and transported through it to the other part of the mixture flow or where (at small mass velocities) already along the wall surface void is produced transporting then the heat by means of bubbles into the inner region of the fluid until they collapse there. The Chen correlation has been tested versus a number of 10 test series with an average deviation between calculated and measured heat transfer coefficients of about  $\pm 12\%$ .

In contrast to this classic method in a 'separate-phase' approach the heat transfer into the entire mixture fluid has to be assumed to be split completely (and not only for special correlations) into different contributions, i.e., into a part which is transferred directly from the wall to each of the two possible phases but also an inner heat transfer between these phases. This arises then to the difficult question what such special heat transfer coefficients for each phase should look like.

### 2.2.5 Material properties of a metallic tube

Density ( $\rho_{TW}$ ) and specific heat ( $c_{TW}$ ) of a metallic tube wall (needed in section 4.2.1) can be assumed to be known from input. They are (almost) independent from changes in the wall temperature. Since the heat conduction coefficients ( $\lambda_{TW}$ ) show linear behaviour from tube wall temperatures their surface values can be described as

$$\lambda_{TWi}(z,t) \cong \alpha_{\lambda T} + \beta_{\lambda T} T_{TWi}(z,t) \quad (i=1, 2) \quad (16)$$

These parameters can then be determined on the basis of state parameters (temperatures, pressures etc.) taken from a recursion or time step before.

### 3. Coolant channel model and module CCM

The (double-precision) thermal-hydraulic coolant channel module CCM (and its single-precision version CCMS) belong to the essential parts of the UTSG theory and code. Within the code UTSG-3 this module is used for the description of the thermal-hydraulic situation of the single- and two-phase fluids flowing along the primary and secondary part of the HEX region and the riser.

The module has been developed with the aim to establish an effective and very universally applicable thermal-hydraulic digital code which should be able to simulate the thermal-hydraulic steady state and transient behaviour of a heated or cooled single- or a two-phase fluid flowing (in upwards, stagnant or even downwards direction) along a coolant channel and, normally, be also applicable for varying cross sections along the BC.

It can thus generally be an important basic element for the construction of complex thermal-hydraulic codes. Distinguished by corresponding key numbers (KEYBC =1, 2, etc.) it can, for example, be applied for the simulation of the steady state and transient behaviour of different types of steam generators with sometimes very complex primary and secondary loops (vertical U-tube, vertical once-through or horizontal VVER-440 ensembles) but also for the construction of 3D thermal-hydraulic codes which are needed for the simulation of non-symmetric single- or two-phase flow situations within large NPP (PWR or BWR) cores (Jewer et al., 2005). Special attention is given to the sometimes very complicated mass flow situations in these types. There the module can especially be significant for the main demand on such 3D codes, namely the automatic calculation of flow distribution into different parallel coolant channels after a non-symmetric perturbation of the entire system.

Together with the constitutive equations the discretization of the PDE-s yields a set of non-linear ordinary differential equations (ODE-s) of first order for the characteristic parameters of each of these SC and finally also BC nodes. This resulting set can then be combined with other sets of ODE-s and algebraic equations coming from additional parts of a complex theoretical model.

A very detailed description of the module CCM is given in (Hoeld, 2011), here only a short review of its main properties can be given.

#### 3.1 Basic channel, subdivided into sub-channels. Spatial discretization by means of the PAX procedure

One of the fundamental assumptions of the code package CCM is that a coolant channel, called 'basic channel (BC)', can, according to their flow characteristics, be subdivided into a number of 'sub-channels (SC-s)' with saturated ( $L_{FTYPE}=0$ ), sub-cooled ( $L_{FTYPE}=1$ ) and superheated ( $L_{FTYPE}=2$ ) flow conditions. All such SC-s can, however, belong to only two types of them, a SC with an only single-phase fluid (sub-cooled water or superheated steam) or a SC containing a saturated water/steam mixture. Theoretical considerations can thus be restricted to only these two types of subchannels.

Discretizing now (spatially) such a BC means that the main channel is further-on subdivided into a number ( $N_{BC}$ ) of (not necessarily equidistant) BC nodes. This has the consequence that

each of the ( $N_{SCT}$ ) SC-s within the BC is subdivided too, namely each of them into a number ( $N_{CT}$ ) of SC nodes. The corresponding conservation equations for mass, energy and momentum (given in form of PDE-s of 1-st order, as shown in section 2.1) can then be discretized along these SC by means of a special spatial 'modified finite volume method' with the consequence that also the possibility of either a time-varying SC entrance or outlet positions has to be considered. Integrating the PDE-s over these SC nodes three types of discretization elements can be expected:

- Integration of functions within the PDE-s yields nodal mean values,
- integration over a gradient yields functions values at the boundaries of the node and finally
- integration of time-derivatives over eventually time-varying nodal boundaries (marking the SC entrance or outlet positions) yields time-derivatives of mean function values together with time-derivatives of these positions.

Appropriate methods had to be developed to connect the relations between the mean nodal and the node boundary function values. There exist different possibilities and concepts to solve this problem in an adequate way. Within the scope of CCM this has been done by a specially developed quadratic polygon approximation procedure (named 'PAX'), based on the assumption that the solution function of a PDE along a SC can be approximated by a quadratic polygon function over a segment which reaches not only over its node length but also (in order to avoid saw tooth like behaviour) over the adjoining one.

The resulting PAX procedure plays a very important role for the establishment of CCM, especially with respect to the fact that boiling or superheating boundaries can (in the transient case) move along the coolant channel and then also cross BC boundaries (For more details see Hoeld, 2011).

### 3.2 Data transfer between the calling program and CCM

The list of the needed BC input parameters to CCM, demanded as boundary conditions, and the resulting output data to be transferred from CCM to the main program is presented in very detail in (Hoeld, 2007c and Hoeld, 2011). The allocation of these data to the input data of the different SC-s and the collection of the resulting SC data stored into corresponding BC output data is then done automatically within the module CCM. The user does not need to undertake any special actions in this context.

As a result of the integration procedure and the application of CCM the most characteristic steady state and transient SC (and thus BC) parameters of single- and two-phase fluid can be expected. Additionally, the transient calculation with CCM yields the time-derivatives

$$\frac{dz_{CA}}{dt} \text{ (for each SC within a BC), } \frac{dT_{BMk}}{dt} \text{ and } \frac{d\alpha_{BMk}}{dt} \quad (k=1, N_{BT}) \quad (12)$$

They are, together with other characteristic channel parameters, then needed within the overall set of differential and constitutive equations in the main code.

### 3.3 Pressure profile along a BC

An important chapter had to be devoted to the handling of the pressure distribution along the channel. Among a special renormalization procedure has been introduced in order to compensate also pressure drop contributions from spacers, tube bends etc., terms which are analytically difficult to be represented.

After having solved within each intermediate time step the mass and energy balance equations separately (and not simultaneously) from the momentum the (now exact) nodal SC and BC pressure difference terms ( $\Delta P_{Nn} = P_{Nn} - P_{Nn-1}$  and  $\Delta P_{BNn}$ ) can (for both single- or two-phase flow situations) be determined if discretizing the momentum balance eq.(3) by integrating over the corresponding SC nodes. The total pressure difference  $\Delta P_{BT} = P_{BA} - P_{BE}$  between BC outlet and entrance follows then from the relation

$$\Delta P_{BT} = \Delta P_{PBT} - \Delta P_{GBT} \quad (\text{Note: } \Delta P_{GBT,0} = 0 \text{ at steady state conditions}) \quad (13)$$

with the parameter

$$\Delta P_{PBT} = \Delta P_{SBT} + \Delta P_{ABT} + \Delta P_{XBT} + \Delta P_{FBT} + \Delta P_{DBT} \quad (14)$$

(Note:  $\Delta P_{PBT,0} = \Delta P_{BTIN,0}$  at steady state conditions)

consisting of terms from static head ( $\Delta P_{SBT}$ ), mass acceleration ( $\Delta P_{ABT}$ ), wall friction ( $\Delta P_{FBT}$ ) and external pressure accelerations ( $\Delta P_{XBT}$ , pump or other perturbations from outside) and (in the transient case) the term  $\Delta P_{GBT}$  taking care of the time-dependent changes in total mass flux along a BC.

Regarding, however, the friction correlations, there arises the problem how to consider correctly contributions from spacers, tube bends, abrupt changes in cross sections etc. as well. The entire friction pressure decrease ( $\Delta P_{FBT}$ ) along a BC can thus never be described in a satisfactory manner solely by analytical expressions. Hence, a special renormalization procedure had to be derived in order to compensate also pressure drop contributions from spacers, tube bends etc., terms which are analytically difficult to be represented. To minimize these uncertainties a further friction term will be included into these considerations having the form

$$\Delta P_{DBT} = (f_{FMP,0} - 1) \Delta P_{FBT} + \Delta P_{FADD} \quad (15)$$

This means that eq.(14) is either supplemented with an additive term (index FADD) or the friction parts are provided with a multiplicative factor  $f_{FMP,0}$ . Which of them should prevail can be governed from outside by an input coefficient  $\varepsilon_{DPZ} = \varepsilon_{DPZI}$ . Thereby, the additive part will be assumed to be proportional to the square of the total coolant mass flow (e.g., at BC entrance)

$$\Delta P_{FADD} = -f_{ADD,0} Z_{BT} \left( \frac{G_F |G_F|}{2\rho d_{HW}} \right)_{BE} \quad (16)$$

For steady state conditions the pressure difference term over the entire BC is given by the input ( $\Delta P_{BT,0} = \Delta P_{BTIN}$ ). Since  $\Delta P_{GBT,0} = 0$  the steady state total additional pressure term  $\Delta P_{DBT}$  follows from eq.(14). If defining the additive steady state pressure difference  $\Delta P_{FADD,0}$  to be the  $(1 - \varepsilon_{DPZ})$ -th part of the total additional friction term

$$\Delta P_{FADD,0} = (1 - \varepsilon_{DPZ}) \Delta P_{DBT,0} \quad (17)$$

the corresponding additive friction factor  $f_{ADD,0}$  follows directly from eq.(16), the multiplicative one ( $f_{FMP,0}$ ) from the combination of the eqs.(15) and (17).

The validity of both friction factors can, for example, be expanded to transient situations too by assuming that they should remain time-independent. Then, finally, the wanted nodal pressure decrease terms can be determined for both steady state but also transient situations. The absolute nodal pressure profile  $P_{Bk}$  along a BC (needed at the begin of the

next time step for the determination of the constitutive equations) can then finally be established by adding now the resulting nodal BC pressure difference terms to the (time-varying) system pressure  $P_{SYS}(t)$  (given from outside as boundary condition with respect to a certain position of the BC, e.g. at the TPL, see section 4.4)

In the transient case (as this can be seen from the momentum balance eq.(3)) a further pressure difference term ( $\Delta P_{GBT}$ ) has to be considered. This term has to take care of the time-dependent changes in total mass flux along a BC (caused by the direct influence of changing nodal mass fluxes). It can be described (in an approximate way) in dependence of the change of a fictive mean mass flux term ( $G_{FBMT}$ ) over the entire BC. The term  $\Delta P_{GBT}$  is defined as follows

$$\begin{aligned}\Delta P_{GBT} &= \int_0^{z_{BT}} \frac{d}{dt} G_{FB}(z,t) dz \cong \sum_{n=1}^{N_{SCT}} \sum_{n=1}^{N_{CT}} \Delta z_{Nn} \frac{d}{dt} G_{FBMn} \\ &= z_{BT} \frac{d}{dt} G_{FBMT} = \sum_{k=1}^{N_{BT}} \Delta z_{Bk} \frac{d}{dt} \frac{G_{BMk}}{A_{BMk}}\end{aligned}\quad (18)$$

As explained below, the resulting total pressure drop along the entire BC is then the key for the application of the module within an ensemble of channels.

### 3.4 BC entrance mass flow (Open and closed channel concept)

Normally, at transient conditions, the BC entrance mass flow  $G_{BE}=G_{BEIN}$  and one of the BC entrance or outlet pressure terms ( $P_{BEIN}$  or  $P_{BAIN}$ ) can be expected to be known from input. Then also the  $\Delta P_{GBT}$  can be determined according to eq.(18). This constellation can be seen as an 'open channel' situation, the procedure based on it as an 'open channel' concept. This allows then to calculate directly the nodal SC and thus also BC pressure profiles and, finally, from eq.(13), the total pressure difference  $\Delta P_{BT}$  over the entire BC, fixing then the second missing pressure term ( $P_{BE}$  or  $P_{BA}$ ) too.

In contrast to this normal situation a new concept has been implemented into CCM, called 'closed channel concept'. This concept should take care of special situations where only the two BC entrance and outlet pressure terms ( $P_{BEIN}$  and  $P_{BAIN}$ ) can be expected to be known from input, thus also the difference over the entire BC pressure ( $\Delta P_{BTIN} = \Delta P_{BT} = P_{BAIN} - P_{BEIN}$ ). Then, according to eq.(14), also the term  $\Delta P_{PBT}$  is given. Since now the BC entrance mass flow  $G_{BE}$  is not explicitly known this parameter has then to result from adequate considerations, by establishing a different concept (the 'closed channel concept'). This follows from eq.(18) by deriving a relation which is the centre of this concept', demanding that

$$z_{BT} \frac{d}{dt} G_{FBMT} = \Delta P_{GBT} = \Delta P_{PBT} - \Delta P_{BTIN} \quad (\text{'closed channel' conditions}) \quad (19)$$

This means that the total mass flow terms along a BC (and thus also at its entrance) must be adapted in such a way that this for the 'closed channel criterion' important condition remains valid. This means, if it is possible to find a relation between the term  $\frac{d}{dt} G_{FBMT}$  and  $\frac{d}{dt} G_{BE}$ , then the wanted mass flow time-derivative term at BC entrance can be determined. One practical method how this problem can, at present, be solved is shown for the case of the establishment of UTSG-3 code, later-on, in section 4.7.

It has to be noted that the application of the 'closed channel' method can, however, be restricted to only one 'characteristic' channel among a sequence of channels within a closed loop. The pressure drops of the remaining (eventually very complex) parts of the loop can then be calculated by means of the normal 'open loop' concept so that the demanded pressure decrease part of such a characteristic 'closed' channel is determined from the fact that the sum of all pressure decrease terms along the closed loop must be zero. It is thus equal to the sum of the negative values of the remaining terms of these channels.

This method makes sure that measures with regard the entire closed loop do not need to be taken into account simultaneously but can be treated separately. In contrast to this procedure in the most other thermal-hydraulic approaches (see for example the 'separate-phase' models) all the pressure differences have to be handled for all the elements of the entire closed loop (together with their BOP systems) together, with the consequence of a sometimes very CPU-time consuming method.

Similar considerations can be undertaken for the case that the automatic mass flow distribution into the different entrances of a set of parallel channels is asked. Thereby the friction coefficients can be determined with respect to a representative average channel. These factors can then be assumed to be valid for all the parallel channels (which will be of the same geometry and thus friction type). In order to obey the demands of the equal total pressure difference over these channels the wanted mass flow distribution can then be calculated by applying the above described 'closed channel criterion'. (See e.g. Hoeld, 2004a and Jewer et al., 2005).

## 4. Theoretical U-tube steam generator model

### 4.1 Primary and secondary HEX coolant channels

The heat exchange (or evaporator) region (HEX) is assumed to consist of a number of equidistant vertical U-tubes ( $N_{\text{TUBES}}$ ) of the (average) length of  $2z_{\text{HXU}}$ . The primary fluid flows on the inner side of these tubes (with the constant cross section  $A_1$ ) upwards and then downwards. The secondary side (with the total length  $z_{\text{HX}}$  and constant cross section  $A_2$ ) can be subdivided into  $N_{\text{ZHX}}$  equidistant nodes with the nodal (BC) length  $\Delta z_{\text{B2k}} = \Delta z_{\text{HX}} = z_{\text{HX}}/N_{\text{ZHX}}$  (with  $k=1, N_{\text{ZHX}}$ ). The primary nodes of the U-tubes have the same length except the two upper nodes ( $\Delta z_{\text{HXU}}$ ) which take the bend of the U-tubes into account.

In the here presented advanced UTSG-3 version the wanted differential (and constitutive) equations for the primary and secondary HEX coolant channels are now automatically determined by calling the coolant channel module CCM (Hoeld, 2000, 2001 and 2010). As already explained in chapter 3 for this purpose only a number of easily available boundary conditions have to be provided to the two CCM modules (distinguished by their key numbers KEYBC=1 and 2). These are

- the primary and secondary HEX inlet temperatures  $T_{1\text{E}}$  and  $T_{2\text{E}}$  (or enthalpies  $h_{1\text{E}}$  and  $h_{2\text{E}}$ ), mass flows ( $G_{1\text{E}}$  and  $G_{2\text{E}}$ ) and pressures ( $P_{1\text{E}}$  and  $P_{2\text{E}}$ ),
- the heat power profile along the primary and secondary HEX side (i.e., the mean nodal power values and the power densities at both sides of the HEX entrance, as determined in combination of the heat transfer considerations (explained in the section below) and (in the steady state case)
- the total nominal (steady state) heat power  $Q_{\text{NOM},0}$  (needed for normalization purposes).

Knowing the primary and secondary nodal HEX fluid temperatures the corresponding nodal primary and secondary heat flux values (into and out of a single U-tube) can then be determined (section 4.3.3 below) and thus also the nodal heat power terms being needed as input to the coolant channel module CCM.

#### 4.2 U-tube ensemble (Heat transfer between primary and secondary HEX side)

An effective description of the heat transfer between the primary and secondary HEX side (index 1 and 2) across a U-tube bundle has already very early been an interesting task within the theoretical treatment of steam generator models (Hoeld, 1978, 1990a, 2002b). Thereby the U-tube ensemble may consist of a number ( $N_{\text{TUBES}}$ ) of cylindrical U-tubes (now fixed inner and outer cross sections  $A_1$  and  $A_2$ ). The primary fluid is assumed to flow (both up- and then downwards) on the inner, the secondary fluid (only upwards) on the outer side of the tubes.

Among the U-tube bundle a representative single U-tube (index TW) has to be ascertained, subjected to the same discretization as applied for the primary HEX channel. This means its length ( $2z_{\text{HXU}}$ ) is subdivided axially in the same way, i.e., into  $2N_{\text{ZHX}}$  nodes ( $n=1, 2 \dots N_{\text{ZHX}}$ ). The node positions of the channels are then given by  $z_{\text{TW}in}$  (with  $i = 1, 2$  and  $n = 0, 1, N_{\text{ZHX}}$ ), having the node length  $\Delta z_{\text{TW}in} = \Delta z_{\text{HX}}$  (for both inner and outer tube wall sides  $i = 1, 2$ ) but, at the positions  $n = N_{\text{ZHX}}$  and  $n = N_{\text{ZHX}} + 1$  (where the tube bow has to be taken into account),  $\Delta z_{\text{TW}in} = \Delta z_{\text{HXU}}$ . The (metallic) wall of such a single U-tube (index TW) with the (now also fixed) inner and outer radii  $r_{\text{TW}1}$  and  $r_{\text{TW}2}$ , a wall thickness  $\Delta r_{\text{TW}} = r_{\text{TW}2} - r_{\text{TW}1}$  and the perimeters  $U_{\text{TW}1} = 2r_{\text{TW}1}\pi$  and  $U_{\text{TW}2} = 2r_{\text{TW}2}\pi$  can be assumed to consist of  $N_{\text{RT}}$  layers. The nodal inner and outer (wetted) surfaces of the tube wall over each axial node  $n$  can then be represented by

$$A_{\text{TW}2n} = A_{\text{TW}1n} \frac{r_{\text{TW}1}}{r_{\text{TW}2}} = U_{\text{TW}2} \Delta z_{\text{TW}n} \quad (n = 1, 2 \dots N_{\text{ZHX}}) \quad (20)$$

The original number of U-tubes can then be estimated from the known inner cross flow area

$$N_{\text{TUBES}} = \frac{A_1}{\pi r_{\text{TW}1}^2} \quad (21)$$

It will be assumed that (in correspondence with the BC node boundary positions) at each nodal position  $n = 0$  (=BE),  $1, 2 \dots N_{\text{ZHX}}$  heat will be transported from the primary coolant to the wall surface (with its temperature  $T_{\text{TW}1n}$ ), conducted through the wall and finally send from the secondary wall surface (with the temperature  $T_{\text{TW}2i}$ ) to the secondary coolant side. Characteristic nodal power parameters such as the 'nodal linear power values  $q_{\text{Lin}}'$ ' and thus also 'nodal heat flux values  $q_{\text{Fin}} = q_{\text{Lin}}/U_{\text{TW}i}$  (with  $i = 1, 2$  describing the inner and outer tube wall surface) have then to be determined from corresponding heat transfer considerations, based on heat transfer coefficients and material properties of the metallic wall as described in the sections 2.2.4 and 2.2.5.

##### 4.2.1 Fourier heat conduction equation

As input to the energy balance eq.(2) the 'linear power value  $q_L'$ ' (or the corresponding 'heat flux value  $q_F = q_L/U_{\text{TW}}$  along each nodal perimeter  $U_{\text{TW}}$ ) are demanded. They describe the heat transferred at a certain axial position  $z$  (for example at their node boundaries) into or



out of the coolant channel, i.e. from a heated or cooled surface (for example from or into an U-tube wall or out of the casing of a fuel rod). These terms, but also the radial tube wall temperatures  $T_{TW}(z,r,t)$ , can be determined by solving an adequate 'Fourier heat conduction equation'. This has (by neglecting the heat transfer in axial direction) the form

$$\rho_{TW} c_{TW} \frac{\partial}{\partial t} T_{TW}(z,r,t) = \frac{1}{r} \frac{\partial}{\partial r} [r \lambda_{TW} \frac{\partial}{\partial r} T_{TW}(z,r,t)] \quad (22)$$

with its initial condition

$$T_{TW}(z,r,t=0) = T_{TW,0}(z,r) \quad (\text{Index 0: Steady state}) \quad (23)$$

and the (for a tube wall characteristic) boundary conditions for a (single) U-tube. They can be represented together with the heat transfer relations at the inner and outer surfaces

$$-\lambda_{TW1} \frac{\partial}{\partial r} T_{TW1} = -\lambda_{TW1} T_{TW1}^{(r)} = q_{FTW1} = \alpha_{TW1} (T_1 - T_{TW1}) \quad (24)$$

$$-\lambda_{TW2} \frac{\partial}{\partial r} T_{TW2} = -\lambda_{TW2} T_{TW2}^{(r)} = q_{FTW2} = \alpha_{TW2} (T_{TW2} - T_2) \quad (25)$$

The mean tube wall temperature  $T_{TWM}$  (over the entire wall thickness  $\Delta r_{TW} = r_{TW2} - r_{TW1}$ ) can be defined by

$$\frac{1}{2} (r_{TW2}^2 - r_{TW1}^2) T_{TWM}(z,t) = \int_{r_{TW1}}^{r_{TW2}} r T_{TW}(z,r,t) dr \quad (26)$$

The (positive) local heat fluxes  $q_{FTW1}$  into and  $q_{FTW2}$  out of such a (single) TW, the local primary and secondary surface temperatures  $T_{TW1}$  and  $T_{TW2}$  and, in the transient case, the time derivatives of the mean tube layer temperatures are expected to result from the heat transfer procedure in dependence of the local primary and secondary fluid temperatures  $T_1$  and  $T_2$  to be known from outside.

#### 4.2.2 Heat transfer across a (representative) single cylindrical U-tube

To solve the partial differential eq. (PDE) of 2-nd order of the Fourier heat conduction eq.(22), the experience showed that for the special case of an U-tube steam generator it is sufficient to represent the tube by a single layer ( $N_{RT}=1$ ). It can even be assumed that in a transient situation, because of the relative thin tube wall and thus very small overall heat capacity of the material, the layer thickness  $\Delta r_{TW}$  can be neglected ( $N_{RT} = 0$ ). This means that (similar to the steady state solution,  $L_{STS}=1$ ) in this special case an overall heat transfer coefficient  $\alpha_{OV1}$  (or  $\alpha_{OV2}$ ) can be derived by setting the time-derivative of the mean tube wall temperature within the Fourier heat conduction eq.(27) equal to 0 without losing on exactness, i.e., it can be treated in a pseudo-stationary way. Examples for the case that a tube wall is subdivided into more than one layer, e.g.  $N_{RT}=2$  or 3, are presented by (Hoeld, 1978), heat transfer out of a fuel rod is described in (Hoeld, 2004).

Integrating now in the case  $N_{RT}=1$  the Fourier heat conduction eq.(22) over the layer thickness and inserting from the boundary conditions (24) and (25) yields finally the (ordinary) differential equation (ODE)

$$\frac{d}{dt} T_{TWM} = \frac{q_{FTW1} - \frac{r_{TW2}}{r_{TW1}} q_{FTW2}}{(1 + \frac{1}{2} \frac{\Delta r_{TW}}{r_{TW1}}) \Delta r_{TW} \rho_{TW} c_{TW}} \quad (L_{STS} = 0 \text{ and } N_{RT} = 1) \quad (27)$$

A special polygon approximation procedure had to be established in order to get a connection between the resulting mean and boundary layer values and thus to determine all the characteristic parameters of the tube wall ( $q_{FTW1}$ ,  $q_{FTW2}$ ,  $T_{TW1}$  and  $T_{TW2}$ ) and (in the transient case) also the time-derivative of the mean TW temperature, needed for the next integration step. Thereby it had been assumed that the radial temperature profile  $T_{TW}(r)$  along the TW can (for the cases  $N_{RT} \geq 1$ ) be approximated by a quadratic polygon.

If introducing the coefficients

$$C_{H1} = \frac{1}{2} \Delta r_{TW} \frac{\alpha_{TW1}}{\lambda_{TW1}} \quad (28)$$

$$C_{H2} = \frac{1}{2} \Delta r_{TW} \frac{\alpha_{TW2}}{\lambda_{TW2}} = C_{H1} \frac{r_{TW2}}{r_{TW1}} \frac{\alpha_{TW2}}{\alpha_{TW1}} \quad (29)$$

this procedure yields with regard to the boundary conditions (24) and (25) a relation connecting the heat fluxes  $q_{FTW1}$  and  $q_{FTW2}$  with the corresponding coolant temperatures  $T_1$  and  $T_2$

$$(1 + C_{H1}) \frac{q_{FTW1}}{\alpha_{TW1}} + (1 + C_{H2}) \frac{q_{FTW2}}{\alpha_{TW2}} = T_1 - T_2 \quad (L_{STS} = 0 \text{ and } N_{RT} = 1) \quad (30)$$

and if applying it to the definition eq.(26) for the mean layer temperature  $T_{TWM}$

$$(1 + \frac{1}{6} \frac{r_{TW2}}{r_{TW1} + r_{TW2}} C_{H1}) \frac{q_{FTW1}}{\alpha_{TW1}} - (1 + \frac{1}{6} \frac{r_{TW1}}{r_{TW1} + r_{TW2}} C_{H2}) \frac{q_{FTW2}}{\alpha_{TW2}} = T_1 + T_2 - 2 T_{TWM} \quad (L_{STS} = 0 \text{ and } N_{RT} = 1) \quad (31)$$

Hence, if replacing in eq.(31) the term  $q_{FTW2}$  by inserting from eq.(30) yields finally

$$\frac{q_{FTW1}}{\alpha_{TW1}} = \frac{(1 + \frac{1}{6} \frac{r_{TW1}}{r_{TW1} + r_{TW2}} C_{H2})(T_1 - T_2) + (1 + C_{H2})(T_1 + T_2 - 2 T_{TWM})}{(1 + C_{H1})(1 + \frac{1}{6} \frac{r_{TW2}}{r_{TW1} + r_{TW2}} C_{H2}) + (1 + C_{H2})(1 + \frac{1}{6} \frac{r_{TW1}}{r_{TW1} + r_{TW2}} C_{H1})} \quad (L_{STS} = 0 \text{ and } N_{RT} = 1) \quad (32)$$

and thus, by means of eq.(25), also a relation for the heat flux  $q_{FTW2}$  (Note: In the transient case and  $N_{RT}=1$  the mean tube wall temperature  $T_{TWM}$  is known from the integration procedure). Finally, from the eqs.(24) and (25) the surface temperatures  $T_{TW1}$  and  $T_{TW2}$  and also their temperature gradients and from eq.(27) the corresponding mean tube wall temperature time-derivative, needed for the next integration step, can be determined.

For the special case of a **steady state situation** but also for case  $N_{RT} = 0$  a pseudo-stationary treatment of the Fourier heat conduction equation (22) and thus of eq.(28) can be applied, setting there the time derivative equal to 0. This yields then

$$q_{FTW2} = \frac{r_{TW1}}{r_{TW2}} q_{FTW1} \quad (L_{STS} = 1 \text{ or } N_{RT}=0) \quad (33)$$

Hence, if starting from the boundary conditions (24) and (25) it is obvious that the (steady state) gradients of the TW entrance and outlet temperatures are then equal to

$$T_{TW1}^{(r)} = \frac{T_{TW2} - T_{TW1}}{\Delta r} = T_{TW2}^{(r)} = - \frac{q_{FTW1}}{\lambda_{TW1}} = - \frac{q_{FTW2}}{\lambda_{TW2}} \quad (L_{STS} = 1 \text{ or } N_{RT}=0) \quad (34)$$

This means that the shape of the radial temperature distribution can be represented for this case by a linear function. From the relations (33) and (34) it follows

$$\lambda_{TW2} = \lambda_{TW1} \frac{r_{TW1}}{r_{TW2}} \quad (L_{STS} = 1 \text{ or } N_{RT}=0) \quad (35)$$

Inserting from eq.(33) into eq.(35) allows deriving relations for  $q_{FTW1}$  and, if looking again at eq.(33), also for  $q_{FTW2}$

$$q_{FTW1} = \frac{r_{TW2}}{r_{TW1}} q_{FTW2} = \frac{\lambda_{TW1}}{\lambda_{TW2}} q_{TW2} = \alpha_{OV1} (T_1 - T_2) \quad (L_{STS} = 1 \text{ or } N_{RT}=0) \quad (36)$$

Thereby an 'overall heat transfer coefficient'  $\alpha_{OV1}$  has been introduced having the form

$$\frac{1}{\alpha_{OV1}} = \frac{1}{\alpha_{TW1}} + \frac{1}{2} \frac{\Delta r_{TW}}{\alpha_{TW1}} \left(1 + \frac{r_1}{r_2} \frac{\lambda_{TW1}}{\lambda_{TW2}}\right) + \frac{r_{TW1}}{r_{TW2}} \frac{1}{\alpha_{TW2}} \quad (L_{STS} = 1 \text{ or } N_{RT}=0) \quad (37)$$

Now, from the boundary conditions (24) and (25) the corresponding (steady state) surface temperatures  $T_{TW1}$  and  $T_{TW2}$  can be determined too.

Rearranging eq.(31) by inserting for the power flux terms  $q_{FTW1}$ ,  $q_{FTW2}$  and  $C_{H1}$  from the eqs.(33), (37) and (29) yields finally the relation for the (steady state) mean layer temperature

$$\begin{aligned} T_{TWM} &= \frac{1}{2} (T_{TW1} + T_{TW2}) - \frac{1}{24} \frac{\Delta r_{TW}}{r_{TW1} + r_{TW2}} (T_{TW1} - T_{TW2}) \\ &= \frac{1}{2} (T_{TW1} + T_{TW2}) - \frac{1}{24} \frac{\Delta r_{TW}}{r_{TW1} + r_{TW2}} \frac{\Delta r_{TW} q_{FTW1}}{\lambda_{TW1}} \quad (L_{STS} = 1 \text{ or } N_{RT}=0) \end{aligned} \quad (38)$$

Knowing now the nodal 'linear power' terms  $q_{LTWin}$  and if assuming a linear behaviour of this linear power within a BC node the nodal power terms  $\Delta Q_{TW1n}$  and  $\Delta Q_{TW2n}$  (per node  $n=1, 2N_{ZHX}$ ) into the inner side of a (single) tube wall surface  $A_{TW1n}$  and out of its outer surface  $A_{TW2n}$  are then given by

$$\Delta Q_{TWin} = \frac{1}{2} \Delta z_{TWin} (q_{LTWin} + q_{FLWin-1}) = \frac{1}{2} (U_{TWin} q_{FTWin} + U_{TWin-1} q_{FTWin-1}) \quad (i=1,2 ; n=1, 2N_{ZHX}) \quad (39)$$

yielding finally the corresponding total power terms into and out of a single tube

$$Q_{TWi} = \sum_{n=1}^{2N_{ZHX}} \Delta Q_{TWin} \quad (i = 1, 2) \quad (40)$$

#### 4.2.3 Nodal and total power out and into the adjoining coolant channels

There are always uncertainties in describing the heat transfer coefficients analytically in an exact way. This is, for example, very often caused by the very complicated geometrical situation within a complex system so that it is not possible to take care in a sufficient way of the influence of all the spacers, tube bends. It can thus be expected that the resulting primary and secondary total heat power terms (based on these HTC calculations) will not be able to simulate the real situation. Hence, to circumvent these difficulties, the number of U-tubes ( $N_{TUBES}$ ) will be provided with a normalization factor  $\varepsilon_{Q_{TW}}$  which should help to adapt the power terms in a correct way. Thereby it can be taken advantage from the fact that at steady state (index 0) these power terms have to correspond to a given nominal power term  $Q_{NOM,0}$ , usually equal to the from input known steady state power terms  $Q_{1,0} = Q_{2,0}$ . Hence, this factor can be determined from this steady state considerations as

$$\varepsilon_{Q_{TW}} = \frac{Q_{NOM,0}}{N_{TUBES} Q_{TW1,0}} \quad (41)$$

Since the nodal power terms  $\Delta Q_{TWin}$  depend on the heat transfer and heat conduction coefficients which in turn are functions of the tube wall (and coolant channel) temperatures the parameters  $\Delta Q_{TW1n}$ ,  $Q_{TW2n}$  and thus also  $\varepsilon_{Q_{TW}}$  have (in the steady state start calculation) to be determined in a recursive way. After the convergence the renormalization factor  $\varepsilon_{Q_{TW}}$  will then be assumed to remain valid also for the transient case.

Applied these results to the U-tube bundle of the here presented steam generator yields the nodal heat flux values  $q_{Fin}$  (with  $i=1$  if  $KEYBC=1$  and  $i=2$  if  $KEYBC=2$ ) taken from the primary HEX channel at each BC node  $n$ , transported across the  $N_{TUBES}$  U-tubes and inserted into the second HEX coolant channel

$$q_{Fin} = \varepsilon_{Q_{TW}} N_{TUBES} q_{FTW1n} \quad (n = 0, 1, 2*N_{ZHX}) \quad (42)$$

and (because of the co- and counter-current contributions of the U-tube to the secondary side)

$$q_{F2k} = \varepsilon_{Q_{TW}} N_{TUBES} (q_{FTW2k} + q_{FTW2j}) \quad (k=0, 1, N_{ZHX} \text{ and } j = 2*N_{ZHX} - k) \quad (43)$$

the nodal power terms

$$\Delta Q_{1n} = \frac{1}{2} A_{TW1n} (q_{F1n} + q_{F1n-1}) \quad (n = 0, 1, 2*N_{ZHX}) \quad (44)$$

$$\Delta Q_{2k} = \frac{1}{2} A_{TW2k} (q_{F2k} + q_{F2k-1}) \quad (k = 0, 1, N_{ZHX}) \quad (45)$$

and finally the total primary power terms  $Q_1$  and  $Q_2$

$$Q_1 = \sum_{n=1}^{2*N_{ZHX}} \Delta Q_{1n} \quad (46)$$

$$Q_2 = \sum_{k=1}^{N_{ZHX}} \Delta Q_{2k} \quad (47)$$

leaving the primary and being inserted into the secondary HEX coolant channel.

In order to establish the connection to the heating (or cooling) power terms of the primary and secondary BC channels in CCM (see Hoeld, 2011, section 3.4) one has to be aware that in CCM a power term leaving a coolant channel has to be provided with a negative sign.

Because of a sometimes very steep increase of the heat transfer coefficients at the transition from single to two-phase flow and steep decrease at changing to dry-out conditions the assumption of linearity of the linear power terms within a BC node is in these seldom cases somehow problematic. Then adequate precautions are to be advised (e.g., choosing a better nodalization for these nodes).

### 4.3 Riser

The riser (index R) is the third element within the UTSG-3 code which will be described by the coolant channel module CCM (thus setting KEYBC=3). It will be assumed to be represented by a (non-heated) coolant channel (with a constant cross section  $A_R$  and a length  $z_{RT}$ ) which can be subdivided into  $N_{RT}$  nodes. Applying CCM the wanted time derivatives and characteristic steady state and transient parameters can be determined in a similar way as for the secondary HEX region, having a zero power profile.

Thereby the 4 characteristic steady state and transient parameters at secondary HEX outlet (coolant temperature, pressure, total and steam mass flow) are yielded directly to the entrance of the riser. Hence it can be stated:  $T_{RE} = T_{HA}$ ,  $P_{RE} = P_{HA}$ ,  $G_{RE} = G_{HA}$  and  $G_{SRE} = G_{SHA}$ .

The entrance void fraction  $\alpha_{RE}$  can, however, be different from the HEX outlet value  $\alpha_{2H}$  if  $A_{RE} \neq A_{2A}$ . This term ( $\alpha_{RE}$ ) will then be estimated within CCM from the known value  $G_{SRE}$  ( $=G_{2SH}$ ) by applying the inverse drift-flux correlation of the package MDS (see section 2.2.3).

At special situations the riser can start to dry-out with the superheating boundary  $z_{RSPH}$  ( $=$  mixture level) to be provided by CCM. This boundary can even move into the secondary HEX region ( $z_{2SPH}$ ). Usually the overall parameter  $z_{SPH}$  will be equal to  $z_{HX} + z_{RSPH}$  but it can be also  $z_{SPH} = z_{2SPH}$  if  $z_{2SPH} < z_{HX}$ . Similar considerations can be performed for the boiling boundary  $z_{BB}$  ( $=z_{2B}$  but  $z_{BB} = z_{RB}$  if  $z_{2B} \geq z_{HX}$ ) if moving into the riser.

### 4.4 Top plenum (with steam separator)

The top plenum (with its total, steam and water volumes  $V_T = V_{ST} + V_{WT}$  and the pressure in the TPL being taken as system pressure, i.e.  $P_{2SYS} = P_2 = P_T$ ) will be assumed to consist of a steam crest together with the entire main steam system and (as to be described in section 4.6) the upper part of the DCM ( $V_{DU} = V_{WDU} + V_{SDU}$ ), i.e. the DCM volume above feedwater entrance. The TPL water volume is thus equal to the volume of this upper section ( $V_{WT} = V_{WDU}$ ). The main steam volume  $V_{SMN}$  is counted as the volume of the steam pipe (i.e. the volume from the isolation valve on to the entrance to the steam collector, SC). Hence, in case of a trip of the isolation valve, the corresponding steam and thus total top plenum volume have of course to be diminished by  $V_{SMN}$ .

The two-phase flow mixture leaving the riser enters the top plenum (TPL) with the mass flows  $G_{WTE} = G_{WRA}$  and  $G_{STE} = G_{SRA}$  and their enthalpies  $h_{WTE} = h_{WRA}$  and  $h_{STE} = h_{SRA}$  (Note: Allowing  $h_{WTE} < h'$  or  $h_{STE} > h''$  means that also single-phase flow with sub-cooled water or superheated steam can be included into the considerations). By means of a separator (being situated within the top plenum entrance) which is assumed to show an ideal separation effect the entire water is yielded (as sketched in fig.1) to the upper part of the DCM, the entire steam to the main steam system. From the steam collector on the steam is then either directed to the turbine or to the steam turbine bypass system (see section 4.6).

The separator adds to the overall pressure decrease terms an additional (friction) contribution ( $\Delta P_{FRSP}$ ) which can be treated in the same way as done later-on with the additional terms of chapter 3.3, assuming its steady state value  $\Delta P_{FRSP,0}$  being given either as input or to be already included in the overall additional part.

Caused by the natural circulation flow and the ceasing injection of feedwater it can happen that the TPL (and thus DU) water volume  $V_{WDU}$  diminishes, i.e. the DCM water level  $z_{WD}$  falls below the position ( $z_{DL}$ ) of the feedwater injection. Then dry-out of the DCM can be stated ( $L_{DCDRY}=1$ ). Hence, the originally constant TPL volume  $V_T$  has to be extended to the now time dependent parameter  $V_{TEX}$  by taking into account that

$$\begin{aligned} V_{TEX} &= V_T + V_{SDL} = V_{ST} + V_{WT} && (\text{if } L_{DCDRY}=0) \\ \text{with } \frac{d}{dt} V_{TEX} &= \frac{d}{dt} V_T = 0, \quad \frac{d}{dt} V_{ST} = -\frac{d}{dt} V_{WT}, \quad \frac{d}{dt} V_{SDL} = \frac{d}{dt} V_{WDL} = 0 \quad \text{and } V_{SDL} = 0 \\ &= V_{ST} = V_T + V_{SDL} && (\text{if } L_{DCDRY}=1) \quad (48) \\ \text{with } \frac{d}{dt} V_T &= \frac{d}{dt} V_{TEX} = \frac{d}{dt} V_{ST} = \frac{d}{dt} V_{DL} = -\frac{d}{dt} V_{WDL} \quad \text{and } V_{WT} = 0 \end{aligned}$$

The term  $V_{SDL} = V_{DL} - V_{WDL}$  depends on the amount of water and steam ( $G_{WTDE}$ ,  $G_{SIDE}$ ) leaving the TPL in direction to the lower DCM entrance (or, if having a negative sign, entering it) and the amount  $G_{2E}$  leaving the DCM at its outlet in connection with the natural-circulation flow.

Only at non-dry-out situations water (with  $G_{WTAD}$  and the enthalpy  $h_{WTAD} = h$ ) can leave the top plenum (in direction to DL), dependent on the natural circulation and the addition of feed water mass flow.

The dynamic situation of the characteristic parameters within the TPL and main steam system is governed by the, for both the non- dry-out and dry-out case, valid balance of in- and outgoing water and steam mass flows. Hence, the ODE-s for the change in TPL (and thus applied as system) pressure ( $P_2 = P_{2SYS}$ ), steam and water volumes ( $V_{ST}$  and  $V_{WT}$ ) within the top plenum can then be derived from corresponding conservation equations for volume, as already presented in eq.(49), and mass and energy

$$\frac{d}{dt} (V_{ST} \rho'' + V_{WT} \rho') = \Delta G_{ST} + \Delta G_{WT} = \Delta G_T \quad (49)$$

$$\frac{d}{dt} (V_{ST} \rho'' h'' + V_{WT} \rho' h') - V_{TEX} \frac{d}{dt} P_2 = h'' \Delta G_{ST} + h' \Delta G_{WT} - (h' - h_{FW}) G_{FWSAT} + Q_{IPL} \quad (50)$$

introducing an auxiliary power term  $Q_{IPL}$

$$Q_{IPL} = (h_{STE} - h') G_{STE} - (h' - h_{WTE}) G_{WTE} \quad (51)$$

This term can take care also of possible special cases where instead of a mixture flow pure superheated steam (with  $h_{STE} > h'$ ) or sub-cooled water (with  $h_{WTE} < h'$ ) enter the TPL.

From the combination of the eqs. (64) and (65) it follows then the general valid differential equation

$$B_{VP} \frac{d}{dt} P_2 - (\rho' - \rho'') \frac{d}{dt} V_{ST} = \Delta G_T \quad (L_{DCDRY} = 0 \text{ or } 1) \quad (52)$$

with the coefficient

$$B_{VP} = V_{WT} \rho^P + V_{ST} \rho'^P \quad (53)$$

Eliminating the  $\frac{d}{dt} V_{ST}$  in the eqs.(49) and (52) by inserting from eq.(48) yields finally the wanted relation for the time-derivative of the system pressure  $P_2$

$$B_{GP} \frac{d}{dt} P_2 = [\Delta G_{ST} + \frac{\rho''}{\rho'} \Delta G_{WT} + (1 - \frac{\rho''}{\rho'}) \Delta G_{VP}] / [1 + (C_{VP} - 1) \frac{\rho''}{\rho'}] \quad (L_{DCDRY} = 0 \text{ or } 1) \quad (54)$$

with the coefficients

$$B_{GP} = \frac{1}{h_{SW}} [V_{ST} \rho'^P h_{SW} + \rho'' h'^P] + V_{WT} \rho' h^P - V_{TEX} \quad (55)$$

$$C_{VP} = \frac{B_{VP}}{B_{GP}} \quad (56)$$

The corresponding time-derivatives of the TPL steam volume  $V_{ST}$  resp., if the DCM is drying out, of the extended steam volume  $V_{TEX} = V_{ST}$  follows then from eq.(49), for the water volume from eq.(48).

#### 4.5 Main steam system (with steam collector, bypass resp. steam turbine system)

As sketched in fig.1 the main steam system will be assumed to be composed (for each secondary loop, i.e. each steam generator) of a steam pipe (beginning at the position after the isolation valve) with an isolation, a sequence of relief and safety valves. The steam of all these loops is then collected into a (single) steam collector which is split afterwards into a bypass and steam turbine line with corresponding bypass resp. turbine trip and turbine control valves governing thus the steam mass flow into the steam turbine with consequences for the steam generator (See also Hoeld, 1990a).

The steam mass flow entering the main steam system (with the steam mass flow  $G_{SMN}$  and enthalpy  $h_{SMN}$ ) is governed by changes in the steam mass flow due to the closing of the isolation or turbine trip valves (characterized by the multiplication factors  $\eta_{ISV}$  and  $\eta_{TTV}$ ) or restricted through a number of  $N_{RSV}$  relief or safety valves, the bypass valve  $G_{RSV}$ , the opening and closing of the turbine control valve  $G_{TCV}$  (regulating the steam mass flow  $G_{STB}$  into the steam turbine) but also by feedbacks coming from the steam turbine resp. steam generator. Additionally, in the case of a multi-loop representation (see, for example Bencik et al., 1993) the steam collector can, in turn, be also influenced by eventually non-symmetric perturbations due to irregular steam mass flow extractions coming from or going into the other loops. The sum of all these contributing mass flow terms (for example by simulating corresponding balance-of-plant actions on these valves) is then determining

$$G_{SMn} = \sum_{n=1}^{N_{RSV}} G_{RS}(n) + \eta_{ISV} G_{BYP} + G_{STB} \quad (57)$$

If the system pressure exceeds a given threshold pressure setting,  $P_{OP}(n)$ , the relief and safety valves  $n$  begin with a certain time delay  $t_{DOP}(n)$  and an opening time  $t_{OP}(n)$  to release steam. The corresponding mass flow at a fully open valve  $G_{RS}(n)$  can be approximated by the function

$$G_{RS}(n) = S_{RSV}(n) P \quad (n = 1, N_{RSV}) \quad (58)$$

with the valve discharge rate  $S_{RSV}(n)$  of each valve (with respect to the system pressure  $P$ ) to be known. A decreasing system pressure initiates then the closing of the valves  $n$  when reaching the pressure value  $P_{CL}(n)$  with the delay and closing times  $t_{CDL}(n)$  and  $t_{CL}(n)$ .

The isolation and turbine trip valves can be closed at a certain starting time  $t_V = t_{ISV}$  or  $t_{TTV}$  with a closing time  $t_C = t_{ISC}$  or  $t_{ITC}$  represented by the multiplication factor  $\eta = \eta_{ISV}$  or  $\eta_{TTV}$ , with a value  $\eta = 1$  or  $0$  if  $t \leq t_V$  or  $t \geq t_V + t_C$  and a value in between if within the closing status.

Steam mass flows  $G_{STB}$  and  $G_{TCV}$  through the turbine bypass and turbine control valves are treated as outside perturbation values, e.g., given in form of corresponding polygons or as a result of corresponding BOP actions.

The steam mass flow  $G_{STB}$  through the steam turbine can be (roughly) estimated from the 'cone law' for condensation turbines

$$\frac{G_{STB}}{\sqrt{\rho_2^{//} P_2}} = \text{const.} = \frac{G_{STB,0}}{\sqrt{\rho_{20}^{//} P_{2,0}}} \quad (59)$$

Thus, defining  $G_{TCV}$  as steam mass flow through the turbine control valve at constant (i.e., steady-state) system pressure conditions, it follows the general relation

$$G_{STB} = \eta_{ISV} \eta_{TTV} G_{TCV} \frac{\sqrt{\rho_2^{//} P_2}}{\sqrt{\rho_{20}^{//} P_{2,0}}} \quad (60)$$

Then the steam-induced power can (very roughly) be estimated as

$$Q_{STB} = (h_{TSPH} - h_{STB,0}) G_{STB} \quad (61)$$

If neglecting thereby the change in the enthalpy of the expanded steam within the turbine system it can be set  $h_{TSPH} \approx h_{TSPH,0}$  and  $h_{TSPH,0}$  be determined from the fact that at steady state conditions it can be set  $Q_{STB,0} = Q_0$ .

From the fact that the turbine power  $Q_{STB}$  is responsible for the acceleration of the rotating masses of the steam generator and thus for the electrical power  $Q_{GEN}$  this term can finally be estimated by a first-order differential equation

$$\frac{d}{dt} Q_{GEN} = \frac{1}{\Theta_{GEN,0}} (\eta_{QSTB0} Q_{STB} - Q_{GEN}) \quad (62)$$

The characteristic time constant  $\Theta_{GEN,0}$  can be determined either from theoretical considerations (using a more comprehensive theoretical model) or from adequate measurements. The efficiency  $\eta_{QSTB0}$  of the turbine system (which is assumed to remain unchanged also during the transient) is then defined as the ratio of  $Q_{GEN,0}/Q_{GEN}$ .

#### 4.6 Downcomer and feedwater system

As already pointed-out the downcomer (DCM) is assumed to be subdivided into an upper and lower section (indices DL and DU), separated either by the entrance of the feedwater line (at the position  $z_{DL}$ ) or, in the case of a drying-out DCM, the upper head of the water



column ( $z_{WDE}$ ). The upper DCM section (with the volume  $V_{DU}$ , the length  $z_{DU}$  and water level  $z_{WDU}=z_{WD}-z_{DL}$ ) will be treated, within this theoretical approach, as a part of the top plenum (TPL). In the case of drying out of the lower DCM section, the original TPL volume ( $V_T$ ) will now be extended by the (time-dependent) steam volume  $V_{SDL}$  of the DL, hence  $V_{TEX} = V_T + V_{SDL}$  (see also eq.(48)). The lower section (DL) itself consists of an annulus with an outer and inner radius  $r_{DA}$  and  $r_{DI}$ , a flow area  $A_{DL}$ , the volume  $V_{DL}$  or, at dry-out conditions,  $V_{WDL}$  and the length  $z_{WDE}$  ( $= z_{DL}$  or  $= V_{WDL}/A_{DL}$ ).

Knowing (after the integration procedure) the transient behaviour of the TPL water volume  $V_{WT}$  ( $= V_{WDU}$ ) resp., in the case of DCM dry-out, extended TPL steam volume  $V_{SDL} = V_{TEX} = V_{ST}$  (as discussed in section 4.4) the movement of the water level ( $z_{WD} = z_{WL}$ ) along the upper and lower DCM section can be determined to be

$$\begin{aligned} z_{WD} = z_{WL} = z_{WDU} + z_{DL} \quad \text{with} \quad z_{WDU} = f(V_{WDU}, \dots), \text{ e.g., } z_{WDU} &= \frac{V_{WDU}}{A_{DU}} \quad (\text{if } L_{DCDRY} = 0) \\ &= z_{DL} - \frac{V_{SDL}}{A_{DL}} \quad (\text{if } L_{DCDRY} = 1) \end{aligned} \quad (63)$$

Saturated water which leaves the TPL (with the mass flow  $G_{WTAD}$  and enthalpy  $h_{WTAD}=h_{TA}'$ ) is mixed at FW entrance with feedwater (with the mass flow  $G_{FW}$  and enthalpy  $h_{FW}$ ) resulting in a mixture enthalpy  $h_{WDE}$ . Since the term  $G_{WDE}$  is determined, as explained below, from considerations with respect to DCM outlet mass flow, the density changes due to the movement of the enthalpy front and eventual flashing the term is given from the relation  $G_{WDE} = G_{WTAD} + G_{FW}$  with  $G_{WTAD} = 0$  at DCM dry-out.

From the fact that the amount of sub-cooling power at DCM entrance (due to the injection of sub-cooled feedwater into the DL) must be equal to the corresponding term at DCM outlet (=HEX entrance)

$$Q_{SCFW,0} = G_{FW,0} (h'_{T,0} - h_{FW,0}) = Q_{SC2E,0} = G_{2E,0} (h'_{2E,0} - h_{2E,0}) \quad (64)$$

the HEX entrance enthalpy  $h_{2E,0}$  and thus, if applying the package MPP (section 2.2.1) for thermodynamic properties of water/steam, also the steady state HEX entrance temperature  $T_{2E,0}$  can be determined.

The change in TPL (=DU) water volume  $V_{WDU}$  ( $=V_{WT}$ ) and thus movement of the water level ( $z_{WD}=z_{WDU}+z_{DL}$ ) within the upper DCM part (above feedwater entrance) is governed by the difference (and eventually deficit) between the entering (saturated) water coming from TPL ( $G_{WTAD}$  and  $h_{STAD}$ ), sub-cooled water coming from the feedwater system and water leaving the downcomer (due to natural circulation). If the water volume of the upper part reaches zero ( $V_{WDU} = V_{WT} = 0$ ), partial dry-out of the lower DCM section can be stated ( $L_{DCDRY}=1$ ). The water level ( $z_{WD}=z_{WDL}$ ) moves then within the DL part (marked by the upper end of the water column, index DE).

The difficult task of the moving enthalpy (and thus temperature) front along the downcomer will now, different to other methods, be simulated by an analytical approach (and not be described, as usual, by a set of ODE-s, i.e. the downcomer will not be treated as a coolant channel, simulated by CCM).

Beginning with the mixture enthalpy  $h_{WDE}$  at DL-E (= FEW) the enthalpy front of each water element will move, driven by the natural circulation mass flow, downwards along the DL

section and reach, after a certain time delay, the DL (=DCM) outlet ( $G_{WDA}$ ,  $h_{WDA}$ ,  $T_{WDA}$ ). This coolant is then assumed to be yielded immediately to the entrance of the HEX region ( $G_{2E}=G_{WDA}$ ,  $h_{2E}=h_{WDA}$ ,  $T_{2E}=T_{WDA}$ ). Different to other approaches this situation will be simulated by an analytical approach (and not be described, as usual, by a set of ODE-s). Thereby the lower DCM section is subdivided into a number of (maximal 50) nodes. The enthalpies at each (DL) node can then be determined by estimating for each of these nodes the length of the way the enthalpy front has attained during each time step  $\Delta t$ . Taking these new positions as basic points of a polygon the corresponding enthalpy changes at the original node boundaries (and thus also at DCM outlet) can now be estimated by interpolation. No smearing effects due to the movement of the enthalpy front along the DCM have to be expected (See, for example, fig.2C). The corresponding (water) mass flow parameters along the DL and thus also at its entrance ( $G_{WDE}$ ) or, in the case of DCM dry-out, at the upper end of the water column can then be determined in an analytical way too, but now by starting from the (given) DCM outlet mass flow ( $G_{WDA}=G_{2E}$ ).

If due to a decreasing secondary system pressure ( $P_{2SYS}$ ) the nodal saturation water enthalpy falls below some of the nodal DL water enthalpy values, flashing is initiated, i.e. producing steam in these nodes. This steam mass will be assumed to be transported directly to the next higher node, heating-up there eventually the still sub-cooled nodal water masses being transported to the next higher node, etc. By this very special procedure finally the amount of water flow  $G_{SFLS}$  can be estimated which disappears due to flashing from the water column (and enters directly the TPL). This term has also to be taken into account for the calculation of the mass flow ( $G_{WDE}$ ) at the top of the water column

On the other side, if in the case of a partial dry-out of the DCM (with  $z_{WDL} < z_{DL}$  and  $V_{SDL}=A_{DL}z_{WDL} > 0$ ) cold feedwater (with the mass flow  $G_{FW}$  and enthalpy  $h_{FW}$ ) is injected into the DL steam volume ( $V_{SDL}$ ) the possibility that a part of the feedwater ( $G_{FWSAT}$ ) is reacting directly with the steam in this compartment has to be taken into account. This part is then heated-up to saturation conditions, thereby condensing a corresponding part of the steam to saturated water (with the resulting condensed water mass flow  $G_{WDCND}$  being equal to the steam removed from the extended TPL). The condensed part is assumed to be mixed with the remaining feedwater part  $G_{FWSUB} (= G_{FW}-G_{FWSAT})$ , falling then directly and unperturbed to the top of the water column. This procedure is governed by the input parameter  $z_{DLMIX}$  which states at which falling length  $z_{DLMIX}$  the entire feedwater has condensed the steam to saturated water. This can be expressed by a mixing factor  $\varepsilon_{MIX} = z_{DLMIX}/z_{DL}$  with  $G_{FWSAT} = (1 - z_{WDL}/z_{DL}) G_{FW} = \varepsilon_{MIX} G_{FW}$ .

The total change in water (and thus also steam) volume ( $\frac{d}{dt} V_{WDL} = - \frac{d}{dt} V_{SDL}$ ) of a drying-out DL region ( $L_{DCDRY}=1$ ) has to be estimated from the balance of in- and outgoing water mass flows at the top of the water column. They are, as shown in eq.(48), equal to the corresponding time-derivative of the extended TPL volume.

The corresponding steam and water masses within DL (needed for the calculation of the natural circulation situation) are then:  $M_{WDL} = \rho_{WDL} V_{WDL}$  and  $M_{SDL} = \rho' V_{SDL}$ .

#### 4.7 Pressure decrease and natural circulation along secondary SG loop

The closed circuit of the secondary SG loop consists of the elements 'HEX secondary side', the riser, the top plenum and finally the downcomer. The sum of all pressure decreases should be equal to zero. Since the thermal-hydraulic behavior of the first two elements are simulated by corresponding CCM (distinguished by the logical KEYBC = 2 and 3). The

pressure decrease terms along this closed circuit are directly provided by the corresponding CCM-s. The corresponding terms for the top plenum and DCM section (mainly contributing by their static head) can be calculated in a similar way as done in CCM.

To determine in the transient case the natural circulation behaviour (for example by determining the time-derivative of the HEX entrance mass flow  $\frac{d}{dt} G_{2E}$ ) the HEX channel has to be applied as a 'closed loop' (as described in section 3.4 resp. Hoeld, 2011). This means the mass flow terms have to be adapted in such a way that the 'closed channel criterion' claimed by eq.(19) for the secondary HEX region is always fulfilled. For this purpose the term  $\frac{d}{dt} G_{BMT}$  can be taken directly as an independent variable within the entire set of ODE-s (estimating the entrance mass flow  $G_{2E}$  then after the integration from the resulting  $G_{FBMT}$ ) or it must a relation be found which connects the term  $\frac{d}{dt} G_{FBMT}$ , as defined in eq.(18), with the time-derivative of HEX entrance mass flow  $\frac{d}{dt} G_{2E}$ . At present it will be assumed that the change in the overall mass flow is almost equal  $\frac{d}{dt} G_{2E}$  (i.e., assuming  $\frac{d}{dt} G_{BMT} \approx \frac{d}{dt} G_{2E}$ ). Together with the fact that the secondary cross section is constant ( $A_{Bk} = A_2$ ) it follows from eq.(19)

$$\Delta P_{G2T} = \frac{Z_{HX}}{A_2} \frac{d}{dt} G_{BE} \quad (65)$$

This term can be eventually provided with a form factor which could help to fulfil (in a recursion procedure) the demand of eq.(24). Which of these procedures should be preferred will experience show.

As explained in chapter 3.2, the time-derivative for the overall natural circulation mass flow, for example at the entrance to the HEX region, follows from the facts that the sum of all pressure increase terms along the entire loop must be zero ( $\Delta P_{AE} = 0$ ), the differences in static head acting as driving force. If considering that a change in total mass flow is very fast propagating along the entire loop it can be estimated that

$$\frac{d}{dt} G_{2E} \cong d_{G2E} \Delta P_{GAE} \quad \text{with} \quad \frac{1}{d_{G2E}} = \frac{Z_{HX}}{A_2} + \frac{Z_R}{A_R} + \frac{Z_{DU}}{A_{DU}} + \frac{Z_{WDL}}{A_{DL}} \quad (66)$$

$$\text{and } \Delta P_{GAE} = \Delta P_{PAE} - \Delta P_{AE}, \Delta P_{PAE} = \Delta P_{STH} + \Delta P_{ACC} + \Delta P_{XIN} + \Delta P_{FR} + \Delta P_Z, \Delta P_{AE} = 0$$

The total pressure differences along the secondary HEX region and the riser are provided by the coolant channel code package CCM. The terms for the TPL and the DCM region have to be derived in a similar way. Knowing in the transient case the mass flow time-derivatives (which are assumed to be equal at each position of the loop) the pressure differences  $\Delta P_{GHAE}$ ,  $\Delta P_{GRAE}$  and  $\Delta P_{GDAE}$  and thus also the total pressure increase terms  $\Delta P_{HAE}$ ,  $\Delta P_{RAE}$  and  $\Delta P_{DAE}$  along the HEX, riser and DCM regions can be calculated too and, finally, in relation with the system pressure  $P_{2SYS}$ , also their absolute pressure parameters.

## 5. Digital code UTSG-3

Due to the rising demand on the thermal-hydraulic codes needed for comprehensive research studies in nuclear reactor safety the digital UTSG codes have been continuously expanded to the now very mature code version UTSG-3. Thereby it could be taken

advantage of the experiences gained during a variety of test-calculations (one example being presented in chapter 6) during the different stages of development through all the years. The resulting advanced code version UTSG-3 is based on the theoretical background as presented in the chapters above. It is, at present, applied in a stand-alone manner but is, however, constructed in such a way that it can be used also as a part of more complex transient codes.

As already discussed before, the code follows a layout as shown (and described) by fig.1. Thereby it has been assumed that the HEX region is axially subdivided into  $N_{ZHX}$  nodes (restricted by  $N_{ZHXMX}=7$ ) and the riser into  $N_{RIS}$  nodes (restricted by  $N_{RTMX}=5$ ). The heat transfer through a tube wall is simulated either by a single layer ( $N_{RT}=1$ ) or described by overall heat transfer coefficients ( $N_{RT}=0$ ). Obviously, a moving boiling (and eventually also superheating) boundary ( $z_{2B}$  and  $z_{2SPH}$ ) is taken into account too.

### 5.1 Input to UTSG-3

As already pointed-out, the primary and secondary side of the HEX region and the riser are simulated by the digital modules CCM, distinguished by the key numbers  $K_{EYBC}=1, 2$  and 3. Thereby it has to be noted that they demand as inputs only BC parameters. These will then (within CCM) be automatically translated into the needed corresponding SC parameters. Hence, the set of input data demanded by the code consists of the following parameters

- Steady state operational conditions (such as power, temperatures, pressures, mass flows etc.),
- geometry data (now with constant cross sections  $A_1$  and  $A_2$ ) and logicals consisting, for example, of the number of axial HEX and riser nodes ( $N_{ZHX}$  and  $N_{RIS}$ , restricted by  $N_{ZHXMX}=7$  and  $N_{RISMX}=5$ ) and the number of possible tube wall layers  $N_{RT} (\leq N_{RTMX}=1)$ ,
- characteristic data of the top plenum, downcomer and feedwater system,
- characteristic data of the valves along the main steam system,
- outside-perturbation signals

and

- option values governing the wanted output in form of tables and plots.

Looking at the (steady state) energy balance equation

$$Q_{1,0} = Q_{2,0} = G_{FW,0} (h_{T,0}'' - h_{FW,0}) \quad (67)$$

it is clear that from the 4 possible operational steady state input values  $Q_{SINP,0}$ ,  $G_{FWS,0}$ ,  $h_{FW,0}$  and  $P_{T,0}$  only 3 of them are required, otherwise the problem would be overestimated. Hence, a remaining fourth variable has to be replaced by a parameter which follows directly from the energy balance relation given above. This (and other normalization actions) will be done automatically by the code.

The entire natural-circulation U-tube steam generator system can, if operated in a stand-alone manner, be perturbed from outside by the following (transient) parameters:

- Primary HEX coolant inlet temperature  $T_{1E}$  (or enthalpy  $h_{1E}$ ), mass flow  $G_{1E}$  and pressure  $P_{1E}$ ,
  - perturbations coming from the main steam system (see section 4.5.2)
- and
- perturbations coming from the feedwater system (see section 4.6)

These outside perturbation signals can be described by means of polygons characterized by their basic points given as inputs.

If the code is a part of a more comprehensive code (for example the previous code version UTSG-2 used in combination with the thermal-hydraulic GRS system code ATHLET), entrance parameters of the primary side (temperature, total mass flow and pressure) are then taken from the main code, the resulting outlet parameters being transferred again back to it. If the overall code is operated in combination with balance-of-plant (BOP) actions the corresponding perturbation parameters of UTSG-3 are then directly provided with the corresponding BOP signals.

A more detailed input description of the code combination UTSG-3/CCM can be found in (Hoeld, 2007c).

## 5.2 Solution procedure

The corresponding steady state parameters will be determined by solving the resulting set of non-linear state equations by means of a linear algebraic solution procedure in a recursive way. These parameters are then needed as starting parameters for the transient calculation.

In the transient case a final system of state and differential equations has to be solved consisting of a set of maximal 53 (or 38, if choosing  $N_{RT}=0$ ) non-linear ODE-s of 1-st order for the variables

$$\begin{aligned} &T_{1M}(i_M, k), T_{2M}(i_M) \quad \text{with } i=1, N_{ZHX} \leq 7, i_M = i - \frac{1}{2}, k=1,2: \text{ up- and downwards flow} \\ &T_{TWE} \text{ and } T_{TWM}(i, k) \quad (\text{only if } N_{RT}=1) \quad \text{with } i_{RM}=1, N_{RT} \leq 5, i_{RM} = i_M - \frac{1}{2} \\ &\alpha_{2M}(i_M), \alpha_{RM}(i_{RM}) \\ &z_{2B}, z_{2SPH}, P_2, V_{WT}, G_{2E} \end{aligned} \tag{68}$$

Additionally, a number of state equations is required, describing total and nodal power terms, turbine power, nodal heat power fluxes, total and nodal steam mass flow, steam mass flow into main steam system, i.e. into steam relief and safety valves and into steam turbine, total and nodal pressure drops, steam volumes along HEX, riser, top plenum and DCM, dry-out boundary and movement of the enthalpy front along the DCM, etc.

The resulting set of equations (together with the corresponding contributions from the constitutive and momentum balance equations) can be combined with other sets of ODE-s and algebraic equations coming from additional parts of a complex model, e.g., from other basic channels which represent different thermal-hydraulic objects within an entire closed loop or a system of parallel channels, from heat transfer or nuclear kinetics considerations etc. Solving now directly the resulting set of ODE-s of such a complex physical system would have the effect that, if using an explicit integration procedure, the computation has due to the very fast pressure wave propagation to be performed with very small time steps ('stiff equation system'), with the consequence of high CPU values to be expected. This situation can partially be improved by choosing an implicit-explicit integration procedure, such as the 'forward-euler, backward-euler' routine FEBE developed by (Hofer, 1981), with a computing time being, however, still disagreeable. As already pointed out, in CCM and thus also UTSG-3 this time-consuming procedure could be circumvented by an approach which takes advantage of the fact that under the most circumstances the mass and energy balance equations can be treated separately from momentum balance without losing essentially on accuracy. Hence, if 'stiff' equations can be avoided in the final overall set of ODE-s then, for this purpose, the routine

DIFSYS can be recommended, based on a procedure established by (Bulirsch-Stoer, 1961) and (Stoer, 1974). Additionally, special precautions have been foreseen for the case that a variable is restricted (within an intermediate time-step) by a certain limit (For example a boiling boundary which should not fall below zero etc.). For more details see (Hoeld, 2000).

### 5.3 Output

Besides the print-out of the input data block and of the most important steady state parameters, as output governed by adequate input options interesting characteristic transient parameters (as absolute, absolute differences or relative differences) can be achieved in table form. It is, additionally, possible to store data needed for restart purposes and (if setting the input logical LSTORE > 0) to store at each time point TSTORE a selected number (NPARAM) of transient parameters in form of a 'Poly Plot Format' on the file LSTORE

WRITE(LSTORE,\*) NPARAM, TSTORE, (PSTORE(I),I=1,PARAM) (69)

Then their transient behaviour can be represented as plots (as this is demonstrated, for example, in fig.2).

## 6. Verification and validation procedure

The continuous adaption of the computer code version UTSG-2 (see for example Hoeld, 2005) and, later-on, of the code combination UTSG-3/CCM on the rising demands coming from the reactor safety research studies and the demand for the necessary quality of the codes has been accompanied by appropriate verification and validation (V&V) procedures (Bencik et al., 1991) with feedbacks to the formulation of the theoretical model. Thereby the judgment of the feasibility and exactness of the chosen theoretical model (compared with eventual other possible approaches) counted already to the first steps of the verification. A separate validation procedure of the applied packages for drift flux, single- and two-phase friction coefficients, heat transfer coefficients, thermodynamic properties of water and steam etc. represented the next one. By means of out-of-pile calculations these packages had to undergo a very thorough study (see Hoeld et al. 1992, Hoeld 1988a, 1994, 1996, 2001, 2002a) before being applied in CCM. It had to be made sure (again by out-of-pile calculations) that the applied mathematical methods are working satisfactory (integration routine, the PAX procedure together with the calculation procedure of moving boundaries). The development of the code with the intention to demand only easily applicable and available input data of the code and to provide the user with inner quality control parameters can help to avoid errors at the application.

Since CCM is constructed with the objective to be used (similarly as done in separate-phase models) only as an element within an overall code, V&V actions could be performed only in an indirect way, i.e. in combination with such an overall code. One of these verification steps was to take some of the most characteristic UTSG-2 calculations being previously done both in a stand-alone manner but also as a part of the overall modular GRS system code ATHLET as benchmark cases. Post-calculating them with the now advanced version (UTSG-3) means the verification of not only this advanced version but also of its most sensitive part, the CCM.

Within the scope of these tests, a number of PWR transients with different initiating events followed by process sequences according to the resulting 'balance-of-plants' (BOP) actions have been post-calculated. Some of the most characteristic cases were:

- 'Loss of feedwater with turbine trip and scram' (Hoeld, 1988b, 1990b, 1999 and 2002b). (See also test calculation below),
- 'loss of feedwater with turbine trip and ATWS' (anticipated transient without scram) (Hoeld, 1988b, 2000, 2007b) with or without boron injection (Frisch et al., 1989),
- 'station blackout with turbine trip and scram' (Hoeld, 1985),
- 'loss of preferred power with turbine trip and scram' (Austregesilo et al., 1991),
- 'loss of preferred power with turbine trip and ATWS' (Hoeld, 1990b).
- 'post-calculation of 3 out of 4 start-up tests' at a German NPP station such as the cases 'operational transient by changing the nominal power from 100 to 58%.', 'reactor scram (at 60 % nom. power) together with turbine trip' (Bencik et al., 1991) and (the non-symmetric case of) 'a loss of 1 out of 4 main circulation pumps in a multi-loop simulation' (Bencik et al., 1993),
- 'coupled thermal-hydraulic and neutron kinetics behavior of a 3D core' (Jewer et al., 2005),

The good agreement of the above presented test calculations with respect to similar calculations with earlier versions applied to the same transient cases demonstrates that despite of the continuous improvements of the code UTSG and the incorporation of CCM into UTSG-3 the newest and advanced version has still preserved its validity.

Besides the V&V actions for this code combination it has to be noted that an important verification step was based on the fact that UTSG calculations have always been accompanied with strong quality control measures. One of them is the comparison of the actual masses being present at any time in the HEX, RIS, TPL and DCM region of the secondary loop of an UTSG with masses to be expected due to the balance of in- and outgoing mass flows. Differences can give valuable hints to the quality of the study and thus the validity of the code. They can point to parts of the calculation where improvements in the theoretical model or in the realisation of the resulting set of equations of the code can be recommended (see fig.2H).

Additionally, accompanying calculations of pseudo-steady state parameters can be compared with the actual transient parameters and thus contribute to the quality control too (see, for example, the boiling boundary in fig.2G).

It is obvious that own V&V actions have to be foreseen for each special application case which can thus also contribute to the further maturation the module CCM too.

## 7. UTSG-3 /CCM test calculation

To demonstrate the properties and validity of the advanced code version UTSG-3 a number of earlier ATHLET/UTSG-2 calculations (see for example Hoeld 1988 or 1990a) have been taken as benchmarks and been successfully post-calculated by the UTSG-3 code. They can thus contribute to the verification process of this newest code version and also of the underlying coolant channel module CCM. The corresponding UTSG-3 tests had to be based on the same input data set, despite of the fact that the philosophy about the balance-of-plant (BOP) actions in a NPP may have partially changed during the years.

As an example the process sequence of an UTSG-3 stand-alone calculation of the case 'loss of main feedwater at a PWR NPP with turbine trip and scram' (at nominal conditions) will be presented. As a result of these calculations in the figs.2A-2H some selected and most characteristic parameters are plotted. The calculation is based on an ATHLET/UTSG-2 calculation (Hoeld, 1990a) which has been performed in connection with the establishment of an general standard input data set for the ATHLET/UTSG-2 code, using the general

control simulation language GCSM of ATHLET (see for example Austregesilo et al., 1991) for the description of BOP actions.

### UTSG-3 (CCM) STAND-ALONE CALCULATION

Loss of main feedw.(but EMFW), TUTRI/SCRAM, max.pr.c, prt.coold.

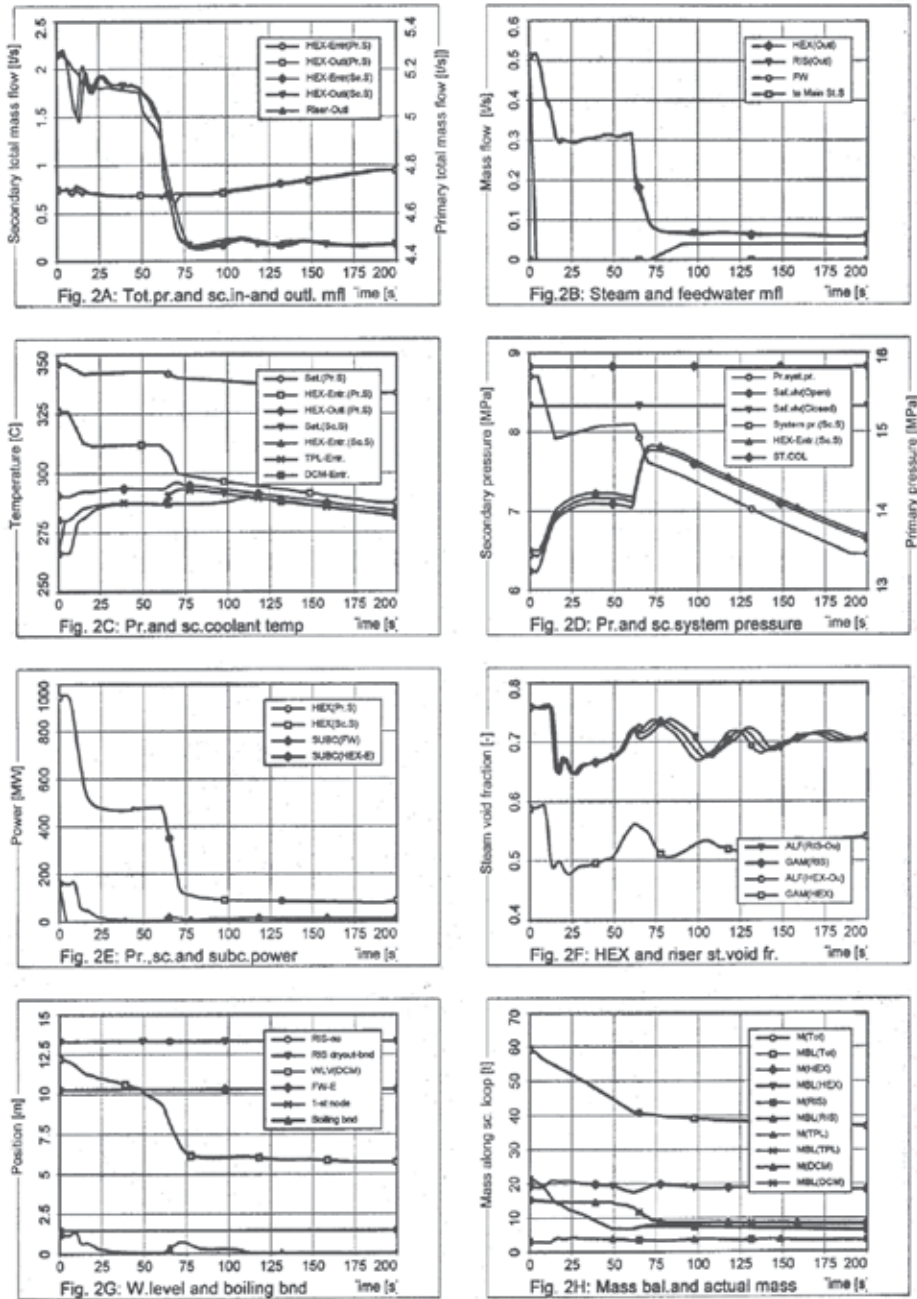


Fig. 2.



The following transient behaviour of these parameters can be observed:

- As initiating event the switch-off of all 2 (plus 1 reserve) main feedwater pumps had been assumed.
- The abrupt coast-down in main feedwater (falling within 4 s to zero, fig.2B) created the signal 'low-feedwater-flow' which in turn caused a number of BOP actions.
- In the first phase of the transient a signal for reactor power limitation (RELEB) is initiated, causing due to an adequate drop of control rods a reduction of the nuclear kinetic and thermal reactor power (and thus HEX power, fig.2E) to about 50%, resulting in a corresponding reduction of the primary HEX entrance temperature (fig.2C) and primary system pressure (fig.2C). The primary coolant mass flow remains almost unchanged (fig.2A).
- Simultaneously, a decrease in steam turbine power to about 55 % (fig.2E) is initiated by reducing, due to the 'maximum pressure control' procedure, in a controlled way the steam mass flow through the turbine-control valve (fig. 2B) yielding consequently to an (at the begin very steep) increase in secondary system pressure (fig.2D) and thus saturation temperature (fig.2C). The corresponding pressure set point curve is a function of the part-load diagram, is limited by a maximal increase rate of 2.0 MPa/min after having reached 7.7 MPa and is kept below 8.0 MPa.
- The temperature at DCM entrance is a mixture of saturated water coming from the riser/separator and the injected feedwater (with a temperature of 218 °C). Hence, the switch-off of the main feedwater pumps and increase in saturation temperature yielded to an abrupt increase in DCM entrance temperature, reaching saturation conditions. Its temperature (or enthalpy) front (fig.2C) is moving (due to natural circulation) along the DCM until it reaches (almost at the begin of the transient, i.e. after about 8 s) the HEX entrance.
- The decrease in feedwater flow causes also a decrease in sub-cooling power at feedwater and HEX entrance (fig.2E) and thus also a decrease in boiling boundary (fig.2G).
- From fig.2F the transient behaviour of the corresponding local and total HEX and riser steam void fractions can be seen.
- Due to the deficit in incoming (feedwater) and outgoing (steam) masses the downcomer starts to dry-out (see water level in fig.2G), crossing at about 45 s the position of feedwater nozzle. This means that in the model it had to be taken into account that feedwater, being injected after this time point, will act partially with the increasing steam content of the lower DCM section (i.e., will condense a part of it). The falling DCM water level causes at about 10.2 m (with a delay of about 10 s) the activation of the auxiliary FW pumps (fig.2B) and at 9.0 m a turbine trip (TUTRI) and a reactor scram, switching down the turbine and reactor power (fig.2E) (leaving only the power decay heating term), withdrawing, however, power from the primary loop due to steam removal through the bypass valve.
- Despite of turbine trip steam can still be removed through bypass valves (the valves being part of the main steam system, fig.1) . Steam mass flow through these valves is governed by the 'partial cool-down procedure'. It acts at first in combination with the 'maximum pressure control'. If the pressure exceeds 8.6 MPa the corresponding 'cool-down set point curve' is lowered from 8.6 to 8.3 MPa and decreases then in correspondence to its saturation temperature value with 100 K/h until it reaches the

mark 7.5 MPa, resulting in a pressure transient as can be seen from fig.2D. It should be noted that the difference between the secondary system pressure and the pressure at channel entrance (i.e. HEX entrance or DCM outlet) is an important basis for parallel channel assemblies. This difference stays in the first phase of the transient almost unchanged as long as no essential changes in the DCM (temperature, dry-out) appear. Hence the pressure difference between HEX outlet and steam collector entrance is still present but diminishing. This parameter plays an important role for the determination of different in- and outflows into the steam collector in case of a multi-loop application of the ATHLET/UTSG code (Bencik et al., 1991)

- The natural-circulation flow (e.g., at secondary HEX, fig.2A) is continuously decreasing, stagnant flow will, however, not be reached because of steam removal by the bypass valves.
- UTSG calculations have always been accompanied with strong quality control measures. The control of the actual masses being present at any time in the HEX, riser/separator, top plenum and downcomer regions with masses which should be expected due to the balance of in- and outgoing masses can give valuable hints to the quality of the calculations and thus the validity of the code. In fig.2H the total mass content along the secondary loop is split into its contributions from different regions and shows excellent agreement. This procedure has been a most valuable tool during the construction of the theoretical model.

The calculations showed, as expected, no noticeable differences in comparison to calculations with the code ATHLET/UTSG-2. That means, that the broad experience with the almost 20 years of UTSG application and the many verification runs with the ATHLET/UTSG-2 code combination could be transferred directly to this code and the module CCM. (See, for example, the case of a loss of one out of four main coolant pumps (see Bencik et al. [1]) within the series of post-calculations of start-up tests of a German PWR NPP).

## 8. Conclusions

The presented model fulfils the objective of constructing a reliable module which shows in many cases large flexibility with respect to other existing codes, can easier be handled (see the possibility of an automatic subdivision of a BC into SC-s) and has a much higher potential for further applications (e.g., if using it for parallel channel assemblies by taking advantage of the 'open and closed channel concept').

The procedure PAX and the drift flux correlation package are a central part of the theoretical model and module CCM and thus also of the advanced code version UTSG-3. The approximation procedure has to provide the model, apart from the above feature, also with gradients of the resulting approximation function needed for the determination of the time-derivatives of coolant temperature and void fraction and governs the movement of SC (= boiling or mixture) boundaries across BC node boundaries whereas an adequate drift-flux correlation package states in which way co- and counter-current flow in vertical, inclined or even horizontal coolant channels can be treated. In both cases it has, due to the availability of different input parameters, be distinguished between a steady state or a transient case and both methods had to be submitted to a thorough test phase outside of the code before being implemented into the code.

On hand of its application within the UTSG-3 concept it could be demonstrated that the presented theoretical drift-flux based thermal-hydraulic coolant channel model and the resulting module CCM can be a valuable element for the construction of complex assemblies of pipes and junctions. Simultaneously, it could be build a bridge to the verification status of the widely used UTSG-2 code. Experiences with other application cases will help to mature the present CCM module. As it turned-out the method to discretize PDE-s and connect the resulting mean and boundary nodal functions by means of the PAX procedure can be of general interest for similar projects too.

The knowledge of characteristic parameters of a U-tube steam generator allows also establishing some normalization procedures in order adjust the code to the real situation. Taking the steady state heat power as a nominal power helps to compensate the uncertainties in the determination of the heat transfer coefficients and the exact number of the U-tubes, the steady state natural circulation mass flow allows to adjust the pressure decrease over the entire secondary loop (see chapters 3.2 and 4.6) and, finally, from the given steady state sub-cooled power (being dependent on total power and pressure) an overestimation in feedwater entrance enthalpy or mass flow parameters can be avoided (chapter 4.4).

The resulting equations for different channels appearing in a complex physical system can then be combined with other sets of algebraic equations and ODE-s coming from additional parts of such a complex model (heat transfer or nuclear kinetics considerations, downcomer etc.). The final overall set of ODE-s can then be solved by applying an appropriate time-integration routine. Since 'stiff' equations could be avoided by treating the momentum balance separately from the energy and mass balance the integration routine DIFSYS can be recommended based on a procedure established by (Bulirsch-Stoer, 1961 and (Stoer, 1974). Otherwise an implicit-explicit integration procedure such as the 'forward-euler, backward-euler' routine FEBE (Hofer, 1981) can be chosen.

Several measures have been installed to control continuously the quality of the calculated results during a computational run. Parallel to the normal calculation a number of characteristic parameters can be called. These should then allow judging the quality of the run. Besides a high number of test-prints the presentation of characteristic pseudo-stationary parameters (such as boiling boundary, heat content values along the primary and secondary loop) turned out to be a very important tool for the comparison of the actual steam and water mass contents within the HEX, the riser and the DCM region with the mass contents as to be expected from the balance between the in- and outgoing mass flows. Already small deviations can grow during a transient and give a hint to the existence of some uncertainties in the model or in the realization in the code (see fig. 2H).

## 9. Nomenclature

$A$	$m^2$	Cross sectional area
$C, C_0$	-	Dimensionless constant, Phase distribution parameter
$d_{HW}$	$m$	Hydraulic diameter
$f_{ADD0}, f_{FMP0}$	-	Additive and multiplicative friction coefficients

$G, G_S, G_W$	$\frac{\text{kg}}{\text{s}}$	Total, steam and water mass flow
$G_F$	$\frac{\text{kg}}{\text{sm}^2}$	Mass flux
$h, h^P, c_P = h^T$	$\frac{\text{J}}{\text{kg}}, \frac{\text{m}^3}{\text{kg}}, \frac{\text{J}}{\text{kg} \cdot \text{C}}$	Specific enthalpy and their partial derivatives with respect to pressure and temperature (= specific heat)
$K_{EYBC}$	-	Characteristic key number of each BC
$L_{FTYPE} = 0, 1 \text{ or } 2$	-	SC with saturated water/steam mixture, sub-cooled water or superheated steam
$N_{BT}, N_{CT}, N_{RT}, N_{TUBES}, N_{ZHX}$	-	Total number of BC or SC nodes, of radial U-tube layers, of U-tubes and of HEX nodes
$P, \Delta P = P_A - P_E$	$P_a = \frac{W_s}{\text{m}^3} = \frac{\text{kg}}{\text{m} \cdot \text{s}^2}$	Pressure and pressure difference (in flow direction)
$Q_{SCE} = Q_{SCFE}$	$W = \frac{\text{m}^3}{\text{kg}}$	Subcooling power at HEX and FW entrance
$Q_i, Q_{NOM}, \Delta Q_{kn}$	$W = \frac{\text{m}^3}{\text{kg}}$	Total, nominal and nodal power into (!!) channel i
$q_{in} = q_{FTWin} A_{TWin} / U_{TWin}$ $= q_{FTWin} V_{Nn} / A_{Nn}$	$\frac{W}{\text{m}^3}$	Local nodal power density into and out of a single and thus also all U-tubes (i=1,2)
$q_{FTWin}$	$\frac{W}{\text{m}^2}$	Local nodal heat flux in- and out of a single U-tube
$r, \Delta r = r_2 - r_1$	M	Radial U-tube variable and thickness
$T, t$	C, s	Temperature, time
$U_{TW}$	M	(Heated) perimeter of a single U-tube
$V_{Bn} = 0.5(A_{Bn} + A_{Bn-1})\Delta z$	$\text{m}^3$	Nodal BC volume
$v$	$\frac{\text{m}}{\text{s}}$	Velocity
$X = G_S / G$	-	Steam quality
$z, \Delta z_{Nn} = z_{Nn} - z_{Nn-1}$	M	Local variable, SC node length ( $z_{Nn-1} = z_{CE}$ at $n=0$ )
$z_{BT}, z_{CA}, z_{CE},$	M	BC length, SC outlet and entrance positions
$\alpha$		Void fraction
$\alpha_{TWn}$	$\frac{W}{\text{m}^2 \cdot \text{C}}$	Heat transfer coefficient at inner and outer TW surface
$\Delta$	-	Nodal difference
$\epsilon_{DPZ}$	-	Coefficient for choice of additional friction
$E_{MIX} = z_{DLMIX} / z_{DL}$	-	Mixing coefficient governing the condensation of saturation steam along DL due to the injection of subcooled feedwater
$\epsilon_{QIW}$	-	Correction factor with respect to $Q_{NOM,0}$
$\epsilon_{TW}$	M	Absolute roughness of tube wall ( $\epsilon_{TW} / d_{HW} = \text{rel.value}$ )

$\Phi_{DW}$	-	Darcy-Weisbach two-phase multiplier
$\eta_{ISV}, \eta_{TTV}$	-	Multiplication factor (opening or closing of valves)
$\lambda_{TW}$	$\frac{W}{mC}$	Heat conductivity along tube wall
$\rho, \rho^P, \rho^T$	$\frac{kg}{m^3}, \frac{kg}{mJ}, \frac{kg}{m^3C}$	Density and their partial derivatives with respect to (system) pressure and temperature
$\partial$		Partial derivative

### Subscripts

0, 0 (=E)	Steady state or entrance to the HEX region (U-tubes)
A, E	Outlet, entrance
B, S	Basic or subchannel
A,F,Z,S,X	Acceleration, direct and additional friction, static head or external pressure difference (if in connection with $\Delta P$ )
D	Drift
HEX, R,T,MN, DU,DL,TAD	Heat exchanger (evaporator), riser/separator, top plenum, main steam system, upper and lower DCM part, out of TPL to DCM
i=1,2	Primary and secondary HEX side (containing all tubes)
Mn, BMk	Mean values over SC or BC nodes
Nn, Bk	SC or BC node boundaries
D	Drift
RS, ISV, BYP, STB	Relief/safety, isolation, bypass and turbine control valves
S, W	Steam, water
P, T	Derivative with respect to constant pressure or constant temperature
TW, TWIn	Tube wall and primary or secondary nodal tube wall surface of a single U-tube

### Superscripts

‘, ‘ ‘	Saturated water or steam
P, T	Partial derivatives with respect to P or T

## 10. References

- Austregesilo H. & Voggenberger T. 1990. *The General Control Simulation Module GCSM within the ATHLET Code*. GRS Report GRS-A-1660, 1990
- Austregesilo H. et al. 1991. The simulation of balance-of-plant actions during normal and abnormal transients in PWR-s with the GRS system code ATHLET. GRS. Internal report. Oct. 1991

- Austregesilo H. et al. 2003. *ATHLET Mod 2.0, Cycle A, Models and methods*. GRS-P-1/Vol.4.
- Bencik,V.& Hoeld, A. 1991. Experiences in the validation of large advanced modular system codes. 1991 SCS Simulation MultiConf., April 1-5, New Orleans
- Bencik,V.& Hoeld, A. 1993. *Steam collector and main steam system in a multiloop PWR NPP representation*. Simulation MultiConf., March 29-April 1, Arlington/Washington
- Bulirsch, R. & Stoer, J. 1961. Num. treatment of ODE-s by extrapolation methods. Num.Math., 8,1.
- Burwell, J. et al. 1989. *The thermohydraulic code ATHLET for analysis of PWR and SWR system*, Proc.of 4-th Int. Topical Meeting on Nuclear Reactor Thermal-Hydraulics, NURETH-4, Karlsruhe, Oct.10-13, 1989
- Frisch, W. & Hoeld, A. 1989. Beurteilung von DWR-Transienten mit starkem Druckanstieg anhand des ATWS-Falles 'Ausfall der Hauptspeisewasserversorgung'. GRS-A-1532, März.
- Haar, L., Gallagher, J.S., Kell, G.S. 1988. *NBS/NRC Wasserdampf Tafeln*. London/Paris/New York 1988
- Hoeld, A. 1978. A theoretical model for the calculation of large transients in nuclear natural circulation U- tube steam generators (Digital code UTSG). Nucl. Eng. Des.(1978), 47, 1.
- Hoeld, A. 1985. UTSG-2 calculation describing the transient behaviour of a PWR NPP after a station black-outwith reactor scram. GRS, Technische Notiz, TN-HOD-85/2, März.
- Hoeld, A. 1988a. *HETRAC: A heat transfer coefficients package*. GRS-A-1446, May.
- Hoeld, A. 1988b. Calculation of the Time Behavior of PWR NPP during a Loss of a Feedwater ATWS case. NUCSAFE 88, 2-7 October, Avignon, France, Proc. 1037-1047.
- Hoeld, A.1990a. UTSG-2. A theoretical model describing the transient behaviour of a PWR natural-circulation U-tube steam generator. *Nuclear Techn.* 90, 98-118, April.
- Hoeld, A. 1990b. The Code ATHLET as a Valuable Tool for the Analysis of Transients with and without SCRAM, *SCS Eastern MultiConf*,23-26 April, Nashville, Tennessee.
- Hoeld, A., Jakubowska, E., Miro, J.E & Sonnenburg, H.G. 1992. *A comparative study on slip and drift- flux correlations*. GRS-A-1879, Jan. 1992
- Hoeld, A. 1994. *Drift-Flux Paket MDS auf der Basis der SONNENBURG-Korrelation*. GRS, Technische Notiz, TN-HOD-01/94, Juni 1994.
- Hoeld, A. 1996. *Thermodynamisches Stoffwertpaket MPP für Wasser und Dampf*. GRS, Technische Notiz, TN-HOD-1/96, Mai.
- Hoeld, A.1999. An Advanced Natural-Circulation U-tube Steam Generator Model and Code UTSG-3, *EUROTHERM-SEMINAR* No.63, 6-8 September, Genoa, Italy.
- Hoeld, A. 2000a. The module CCM for the simulation of the thermal-hydraulic situation within a coolant channel. *Int. NSS/ENS Conf.*, 11-14 September, Bled, Slovenia.
- Hoeld, A. 2000b. The drift-flux based thermal-hydraulic coolant channel model and its realization in the code package CCM, *8-th Int.Conference on Nuclear Eng.*, ICONE-8049, April 2-6, 2000, Baltimore, USA.

- Hoeld, A. 2001. *The drift-flux correlation package MDS*. 9-th Int. Conference on Nuclear Engineering (ICONE-9), 8-12 April, Nice, France.
- Hoeld, A. 2002a. *The consideration of entrainment in the drift-flux correlation package MDS*. 10-th Int. Conf. on Nuclear Eng. (ICONE-10), 14-18 April, Arlington, USA.
- Hoeld, A. 2002b. A steam generator code on the basis of the general coolant channel module CCM. PHYSOR 2002, October 7-10, Seoul, Korea.
- Hoeld, A. 2004. A theoretical concept for a thermal-hydraulic 3D parallel channel core model. PHYSOR 2004, April 25-29, Chicago, USA.
- Hoeld, A. 2005. A thermal-hydraulic drift-flux based mixture-fluid model for the description of single- and two-phase flow along a general coolant channel. *The 11-th Int. Topical Meeting on Nucl. Reactor Thermal-Hydraulics (NURETH-11)*. Paper 144. Oct. 2-6, 2005, Avignon, France.
- Hoeld, A. 2007a. Coolant Channel Module CCM. An universally applicable thermal-hydraulic drift-flux based mixture-fluid 1D model and code. *Nucl. Eng. and Design* 237(2007), 1952-1967
- Hoeld, A. 2007b. Application of the mixture-fluid channel element CCM within the U-tube steam generator code UTSG-3 for transient thermal-hydraulic calculations. *15-th Int. Conf. on Nuclear Eng. (ICONE-15)*. Paper 10206. April 22-26, 2007, Nagoya, Japan
- Hoeld, A. 2007c. Input card description of the digital code UTSG / Mod 3.GRS, Internal paper, January
- Hoeld, A. 2011. Coolant Channel Module CCM. An universally applicable thermal-hydraulic drift-flux based separate-phase mixture-fluid model. Intech Open Access Book 'Steam Generator Systems', ISBN 978-953-7619-X-X, InTech, Austria, Available from: [http://sciyo.com/articles/show/title/Coolant\\_channel\\_module\\_CCM](http://sciyo.com/articles/show/title/Coolant_channel_module_CCM). An universally applicable thermal-hydraulic drift-flux based separate-region mixture-fluid model.
- Hofer, E. 1981. *An A( $\alpha$ )-stable variable order ODE-solver*. Topical Meeting on Advances in Math. Methods, Munich April 1981
- Ishii, M. 1990. *Two-Fluid Model for Two-Phase Flow*, Multiphase Science and Technology, 5.1, Hemisphere Publ. Corp.
- Ishii, M. and Mishima, K. 1980. *Study of two-fluid model and interfacial area*. NUREG/CR-1873 (ANL-80-111), Dec.
- Jewer, S., Beeley, P., Thompson, A. & Hoeld, A. 2005. *Initial version of an integrated thermal-hydraulic and neutron kinetics 3D code X3D*. ICONE13, Beijing, May 16-20. See also NED 236(2006), 1533-1546.
- Lerchl, G. et al. 2009. *ATHLET Mod 2.2, Cycle B, User's Manual*. GRS-P-1/Vol.1. Rev. 5, July
- Martinelli, R.C., Nelson, D.B. 1948. Prediction of pressure drop during forced-circulation of boiling water. *Trans. ASME* 70, 695.
- Moody, N.L.F. 1994. *Friction factors for pipe flow*. *Trans. ASME*, 66, 671 (See also VDI - Wärmeatlas, 7.Auflage, 1994, VDI - Verlag).
- Schmidt, E. & Grigull, U. (ed.) 1982. *Properties of water and steam in SI-Units*. Springer-Verlag.
- Sonnenburg, H.G. 1989. Full-range drift-flux model based on the combination of drift-flux theory with envelope theory, *NURETH-4*, Oct.10-13, Karlsruhe, pp.1003-1009.

Stoer, J 1974. Extrapolation methods for the solution of initial value problems and their practical solutions. *Lecture Notes Math.*, 363

Zuber, N.& Findlay, J.A., 1965. *Average vol. conc. in two-phase flow systems*, J.Heat Transfer 87, 453



# Computation of Flows in Steam Generators

Dr Jonas Bredberg  
Epsilon UC Väst  
Sweden

## 1. Introduction

This chapter will be devoted to explain the foundations of Computational Fluid Dynamics (CFD), and its possible application to simulate flow conditions in steam generators of pressurized water reactors (PWR). Besides steam generator application simulations, test cases will be included to show the ability of CFD to faithfully reproduce some fundamental heat and flow phenomena

The common design of a PWR steam generator is a vertical standing U-tube heat exchanger divided into a number of stages with separator plates (baffles) in between, as seen in Fig. 1. Several thousands of tubes is not unusual which consequently puts significant strain on computational resources if all details are to be resolved. The multitude of tubes and several stages however facilitates the possibility to study characteristic sections of the heat exchanger with reasonable confidence on flow conditions (i.e. boundary condition) and with a required accuracy.

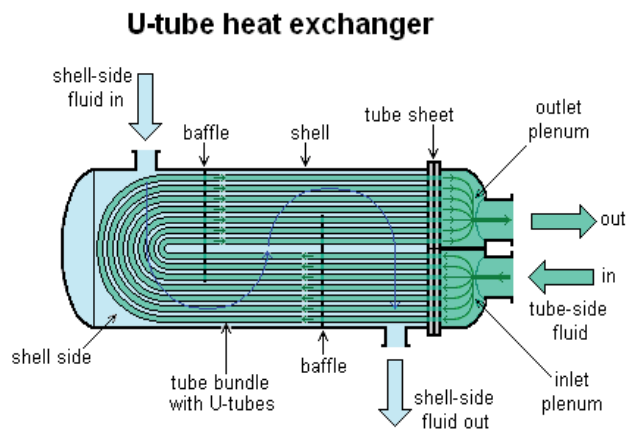


Fig. 1. Typical lay-out of U-tube heat exchanger, similar in concept to the design of steam generators as found in a PWR

The steam generator is divided into i) a primary side, where hot pressurized water from the reactor core flows, and ii) a secondary side, where relatively cold water is heated and evaporated to generate steam for the turbines. The division of the PWR into a primary- and secondary side (as opposed to a BWR, Boiling Water Reactor) is of major advantage for

safety reasons as the contaminated water on the primary side can be enclosed in a smaller and sealed off compartment.

In regards to simulating and predicting the conditions in the primary side, there is only minor obstacles, since the case of a single-phase fluid (superheated water), flowing in a pipe with external cooling (heating and boiling of the water on the secondary side) is a well defined and abundantly studied system. Pipe-flow is one of the cornerstones for developing numerics and models for CFD codes, and can now be considered to be mastered to a high degree of accuracy. The only part that may need some attention is the plenum with its inlet/outlet and the bend section with local effects from separation and secondary flow. The conditions within the pipe could even with little hesitation be estimated from well known correlation for internal pipe flow.

The flow on the secondary side need however to be more carefully treated, particularly as it includes two-phase boiling. To simulate this flow the CFD models and numerics need to capture:

- Wall interaction and shearing
- Streamline curvature
- Flow separation and re-attachment
- Heat transfer
- Boiling
- Buoyancy

In single-phase regimes the above criteria mainly put demands on turbulence modelling, particularly in the case of accurate heat transfer predictions, which obviously is of major importance in heat exchanger performance. Fortunately, turbulence theory and modelling has advanced significantly the last couples of decades and has now reached a mature level of predictability that, through proper choice can predict pressure drop and heat transfer within measurement accuracy. In the two-phase regime, the choice of multi-phase models is obvious of great importance, but also specific boiling models and bubble-dynamic models. CFD programs has not yet progress to a similar level of maturity for two-phase flow, although through a high-degree of mesh refinement and employing direct simulations (DNS/LES) all phenomena found in nature can be resolved, albeit at an extreme expense of computational resources. One is thus normally restricted to an engineering or global model for two-phase problems which are designed to capture the main characteristics of the flow, rather than all details. In forthcoming discussions, such models and examples of using them will not be included.

The following two sections are primarily based on the work performed by the author forming a basis for his Ph.D. (Bredberg, 2002). This introductory section and last sections are mainly based on the work within the ARTIST group (Güntay, et. al., 2004), (Berg et. al., 2008a) and (Berg et. al., 2008b)

## **2. Foundations of CFD**

### **2.1 Governing equations**

The equations that govern fluid motion and heat transfer are the continuity, momentum and energy equations. These equations, were independently derived by Navier (in 1822) and Stokes (in 1845) and are commonly referred to as the Navier-Stokes equations, albeit it was only the momentum equation that both Navier and Stokes were referring to. These

equations can be formulated in either a conservative form, or in a non-conservative, density normalized form.

### Continuity

The continuity equation states the conservation of mass, which for all but nuclear-reaction environments is valid. Its conservative form is:

$$\frac{\partial \rho}{\partial t} + \frac{\partial \rho U_i}{\partial x_i} = 0 \quad (1)$$

### Momentum

The momentum equation describes a force-balance, which – from Newtons second law - states that the mass times the acceleration is equal to imposed forces. The forces are divided into body force  $F_i$ , eg. the gravitational force, and surface forces,  $T_{ij}$ . The surfaces forces are normally written as a combination of pressure (normal stress) and viscous stresses (shear) as:

$$T_{ij} = -P\delta_{ij} + \tau_{ij} \quad (2)$$

Assuming a Newtonian incompressible fluid the momentum equations become:

$$\frac{\partial \rho U_i}{\partial t} + \frac{\partial \rho U_i U_j}{\partial x_j} = \rho g_i + F_i - \frac{\partial P}{\partial x_i} + \frac{\partial}{\partial x_j} (2\mu S_{ij}) \quad (3)$$

where  $F_i$  is any additional body-forces that can effect the fluid motion such as rotation, a magnetic- or electric-field etc.

### Energy

The first law of thermodynamics states that the exchange of energy in a system is the result of applied work and heat transfer through that region. In its most complete formulation the energy equations is given as (Panton, 1995):

$$\frac{\partial \rho E_0}{\partial t} + \frac{\partial \rho U_i E_0}{\partial x_i} = \rho U_i F_i - \frac{\partial q_i}{\partial x_i} + \frac{\partial}{\partial x_j} (U_i T_{ij}) \quad (4)$$

where  $T_{ij}$  is the surface forces similar to the viscous and pressure terms in the momentum equations.  $E_0$  is the total internal energy, including the kinetic energy. The energy equation as displayed above is however seldom used and instead the simplified temperature equation is applied:

$$\frac{\partial \rho C_p T}{\partial t} + \frac{\partial \rho C_p T U_i}{\partial x_i} = \frac{\partial}{\partial x_j} \left( \frac{\mu C_p}{Pr} \frac{\partial T}{\partial x_j} \right) \quad (5)$$

## **2.2 Flow models**

The Navier-Stokes equations are composed of non-linear partial differential equations with an intricate complex dependency within the equation system. Partial differential equations are apart from some specific cases, not solvable using known mathematical tools hence the NS-equations impose a severe obstacle to the physical world. There are only a very small

number of flows that entitle one to simplify the governing equations in such a way that it is possible to achieve an analytical solution. Consequently for most cases, one is referred to numerically solve the Navier-Stokes equations. The highest level of fidelity is given by Direct Numerical Simulations (DNS) and Large Eddy Simulations (LES). Numerical simulations performed using Reynolds Averaged Navier Stokes (RANS) solvers are apart from numerical approximations also affected by physical approximations - in the models for the turbulence field.

#### Direct Simulation (DNS/LES)

Direct Numerical Simulations (DNS) and Large Eddy Simulations (LES) both solve the equations in the four-dimensional room, time and space. The additional modelling in LES as compared to DNS is the introduction of a sub-grid scale (SGS) model (Smagorinsky, 1963) which legitimacy is based on the assumption of isotropy of the smallest scales. For a given cut-off wave-length, normally related to the grid-size, LES don't resolve the smallest length-scales but rather approximate them using the SGS-model. DNS are much appreciated as they are considered equally, or even more accurate than experiments. The numerical model enable unphysical although theoretical interesting flows to be simulated, with a degree of control unachievable in a laboratory. The numerical accuracy in DNS are usually much higher than the uncertainty in any measuring tool. A major drawback is however that the simulations are computational expansive and can only be performed on a limited number of flows, all with relatively low Reynolds numbers.

#### Reynolds Averaged Navier-Stokes (RANS)

Nearly all numerical simulations are performed using various RANS-models, as a consequence of the excessive computational resources needed for a DNS. Reynolds (Reynolds, 1895) proposed that the quantities in the Navier-Stokes-equation could be divided into a mean and a fluctuating part:

$$\phi = \bar{\phi} + \phi' \quad (6)$$

where the mean part is the time-average of a parameter over a certain time. The averaging time needs to be longer than the small turbulent fluctuation, however shorter than any mean flow oscillating period. If Reynolds decomposition is applied to the Navier-Stokes equation the result is an equivalent set of equations, the Reynolds Averaged Navier-Stokes equations. For a though and comprehensive analysis of the averaging see e.g. Hinze (Hinze, 1975). The difference between the former and the original are that the RANS equations not only involves time-averaged quantities but also produces an additional term, the Reynolds stresses:

$$\tau_{ij} = \overline{u_i u_j} \quad (7)$$

which are unknown and need to be modelled using a turbulence model. This is referred to as the closure problem with Reynolds averaging.

There are two distinct approaches to model the Reynolds stresses, either the eddy-viscosity models (EVM), or the Reynolds stress models (RSM). In the latter the actual stresses are solved, while in the former the Boussinesq hypothesis (Boussinesq, 1877) is employed to estimate  $\tau_{ij}$ . In its simplest form, the eddy-viscosity  $\mu_t$  is computed based on some geometrical/flow conditions. In the commonly employed two-equation turbulence models, the eddy-viscosity is computed using two turbulent quantities, the turbulent kinetic energy,

$k$ , and a length-scale determining quantity ( $\epsilon$ ,  $\omega$ ,  $\tau$  or  $l$ ). In a strive to enhance the performance of the two-equation EVMs researchers have proposed non-linear EVMs, which include, apart from the Boussinesq hypothesis, additional terms to determine the eddy-viscosity. The ASM and EARSM (or EASM) are different in that they compute the Reynolds stresses using algebraic equations. In ASM the convective and diffusion terms in the Reynolds stress transport equations are approximated using anisotropized versions of the same terms in the turbulent kinetic energy. The ASM thus only need to solve two transport equations, that for  $k$  and an additional secondary turbulence quantity. The Reynolds stresses could then be estimated using the constructed algebraic relations. This modelling approach is however prone to numerical instable solution and are seldom used. It is possible, through the use of the Cayley-Hamilton theorem to derive the complete tensorial relation for the Reynolds stresses, expression in the strain-rate tensor,  $S_{ij}$  and the rotation tensor,  $\Omega_{ij}$ . The complete set involves ten terms with their respective coefficients (Pope, 1975). Using these expressions the Reynolds stresses can, in a second moment closure sense, be exactly computed. EARSMs are thus theoretically more correct than non-linear EVMs, although the final expressions are often confusingly similar. They differ in the approach used for the coefficients in the tensor groups, which in EARSMs, at least for 2D-flows, can be based on derived analytic expressions (Wallin & Johansson, 2000).

### 2.3 Turbulence models

#### Reynolds Stress Models (RSM)

The Reynolds Stress Models (RSM) (Launder, 1989) solves the Reynolds stresses;

$$\tau_{ij} = \overline{u_i u_j} \quad (8)$$

using individual transport equations. RSM based RANS-codes thus include, apart from three momentum equation, six stress equation, and an additional length-scale determining equation. The transport equations for the Reynolds stresses are:

$$\frac{D\tau_{ij}}{Dt} = P_{ij} + G_{ij} + \Pi_{ij} - \epsilon_{ij} + \frac{\partial D_{ij}^T}{\partial x_k} + \frac{\partial D_{ij}^v}{\partial x_k} \quad (9)$$

where  $P_{ij}$  is the shear production term,  $\Pi_{ij}$  the pressure-strain term,  $\epsilon_{ij}$  the dissipation term,  $D_{ij}^T$  turbulent transport (diffusion) term,  $D_{ij}^v$  and the viscous diffusion term. For a complete derivation and expansion see e.g. Bredberg (Bredberg, 1999). The production terms, and the viscous diffusion term are exact in the context of a Reynolds Stress Model. The other terms need however be modelled. The exact formulation of the production terms is a fundamental advantage of the RSMs compared to the EVMs, e.g. for rotating flow.

#### Eddy-Viscosity Models (EVM)

The eddy-viscosity concept is based on similar reasoning that turbulence is a physical concept connected to the viscosity. It can be argued that similar to viscosity, turbulence affects the dissipation, diffusion and mixing processes. Thus it is reasonable to model the Reynolds stresses in a fashion closely related to the viscous term. The Reynolds stress term produced by the Reynolds-averaging is:

$$D_R = \frac{\partial \tau_{ij}}{\partial x_j} = \frac{\partial}{\partial x_j} (\overline{u'_i u'_j}) \quad (10)$$

A turbulent flow will, compared to a laminar flow, enhance the above properties, and thus a model for the Reynolds stress could be, as proposed by (Boussinesq, 1877):

$$-\overline{u'_i u'_j} = \nu_t \left( \frac{\partial U_i}{\partial x_j} + \frac{\partial U_j}{\partial x_i} \right) \quad (11)$$

where  $\nu_t$  is the eddy-viscosity, or the turbulent viscosity. It is computed using some turbulent quantities, such as the turbulent kinetic energy and the turbulent length scale:

$$\nu_t \approx \sqrt{k}l \quad (12)$$

In the commonly employed two-equation EVMs the turbulent kinetic energy is solved using a transport equation, whereas the turbulent length scale is computed using  $k$  and secondary (a length-scale determining) turbulent quantity. There exists EVMs based on the dissipation rate of turbulent kinetic energy,  $\epsilon$ , the turbulent time-scale,  $\tau$  or the specific dissipation,  $\omega$ . These quantities are solved using a transport equation, similar in construction to that shown in Eq. (9). A comprehensive study of two-equation EVMs could be found in (Bredberg, 2001).

## 2.4 Turbulent heat transfer models

Compared to the large amount of turbulence models for the flow field there exists only a relatively few heat transfer models. This may be a consequence of that the heat transfer model plays an inferior role compared to the turbulence model in predicting heat transfer data (private communication, Raisee, 1998). The coupled nature of the temperature and flow field, and thus the difficulties of accurately measure the heat transfer is however more to blame for the sparse work which has been done on heat transfer models. The appearance of DNS (e.g. Kawamura et. al., 1999) have however made it possible to construct new and more elaborated models, with improved predictability.

The simplest model is the SGDh (Simple Gradient Diffusion Hypothesis) which is based on similarities to the molecular heat transfer:

$$-\overline{u'_i t'} = \frac{\nu_t}{Pr_t} \frac{\partial T}{\partial x_i} \quad (13)$$

with  $Pr_t$  is the turbulent Prandtl number with a value 0,9 of for air. Kays (Kays, 1994) made a comprehensive review of alternatives to the constant  $Pr_t$ . A heat transfer model suitable when a RSM is employed for the flow field is the GGDH (Generalized Gradient Diffusion Hypothesis) which is an adaptation of the Daly-Harlow diffusion model (Daly & Harlow, 1972). The model can incorporate un-alignment effects in the relations for the heat flux vector and the temperature gradient:

$$-\overline{u'_i t'} = C_\theta \overline{u'_i u'_j} \frac{k}{\epsilon} \frac{\partial T}{\partial x_j} \quad (14)$$

The model however relies on similarities (an extended Reynolds analogy) to the flow-field for any transport effects in the heat flux vector as the GGDH is still a local model. A more fundamental heat transfer model similar to RSM has been developed by Launder et. al., which in a matured form can be found in (Launder, 1989).

## 2.5 Some numerical consideration of CFD

In the dominating majority of CFD-codes the solution method used for the governing equations, is the Finite Volume Method (FVM). Using this method the particular computational domain is divided into a number of control volumes. The differential versions of Navier-Stokes equations are discretized onto the computational mesh and numerically integrated over the control volumes and then solved until a convergence criteria is reached.

For the computations presented in the next section, the academic CFD-code CALC-BFC (Davidson & Farhanieh, 1995) is used. In the following section the commercial CFD-code ANSYS/Fluent is used (ANSYS, 2001). In either there is a selection of discretizing schemes, where hybrid (Spalding, 1972), central, van Leer (van Leer, 1974) and QUICK (Leonard, 1979) are examples of common used algorithms for pressure-based Navier-Stokes solvers (PBNS). The governing equation for a specific variable are after discretization expressed as:

$$a_p \phi_p = \sum_{nb} a_{nb} \phi_{nb} + S \quad (15)$$

where  $a_i$  are the coefficients from the convective and diffusive terms. Index  $p$  represents the nodal point and  $nb$  the contribution from the neighbouring nodes. Source terms in the governing equations are included in  $S$ . For a PBNS this equation system is solved iteratively using a Tri-Diagonal Matrix Algorithm (TDMA).

For incompressible flows the pressure needs to be carefully treated as the equation of state,  $P = \rho RT$ , is not suitable to use. In both CALC-BFC and ANSYS/Fluent the SIMPLE algorithms are used to deal with the velocity-pressure coupling (Patankar & Spalding, 1970) and (van Doormal & Raithby, 1984).

CALC-BFC uses Boundary-Fitted-Coordinates (BFC), with the nodes and grid points located in a non-staggered (ie. co-located) configuration. This procedure can induce a so-called checker-board solution, due to the velocity-pressure coupling, which is alleviated through the Rhie-Chow (Rhie & Chow, 1983) interpolation scheme.

## 2.6 Mesh dependencies and discretization schemes

The progress of computer power, which enables increasingly fine mesh to be employed, along with the development of highly accurate discretizing schemes, has reduced the numerical errors. The result of this have made CFD-workers believe that the results from their CFD-codes are purely an effect of the chosen flow models (turbulence models), boundary conditions etc. This is to a certain degree true, however in special cases and for sensitive quantities there is still an influence on the result from numerical approximations made in the CFD-codes and from mesh refinement. To visualize this, two different cases are selected: I) a backward-facing step (BFS) case and II) the heat transfer from a rib-roughened channel. The two cases were simulated using CALC-BFC with both the hybrid and the van Leer discretizing schemes and with different levels of mesh refinement.

### Backward facing step (BFS)

The BFS-case is the one studied by Gartling (Gartling, 1990). The Reynolds number is low enough to enable a laminar simulation to be performed. The demands on the discretizing scheme increases as a result, as any numerical (artificial) diffusion will be much more pronounced if it is not clouded by the turbulent diffusion. The geometrical condition is shown in Fig. 2. The expansion rate, i.e. the step-height to channel-height ratio, for this case

is  $h/H=2$ . Two different meshes were used in the computations: a  $100 \times 90$  mesh and a  $200 \times 180$  mesh (stream-wise by wall-normal). The inlet was specified as a parabolic profile in  $U$ , as in the benchmark (Gartling, 1990). The walls are well resolved on both meshes, with four and six nodes located within  $y^+=1$  for the  $100 \times 90$  and  $200 \times 180$  mesh, respectively. In the region of interest the meshes are un-stretched in the stream-wise direction, and only gently stretched in the wall-normal direction, with a maximum ratio, located at the walls of 4% and 1%. The discretizing schemes are here only compared for the predicted cross-stream ( $V$ ) velocity profiles at  $x/h=7$ . This station is located immediately downstream the re-attachment point, at  $xr/h=6,1$  (benchmark data).

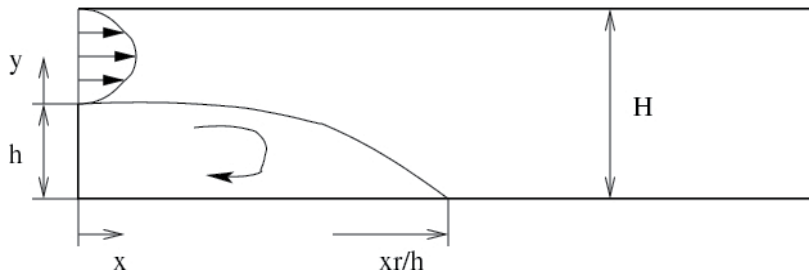


Fig. 2. Geometry of Gartling BFS (Gartling, 1990)

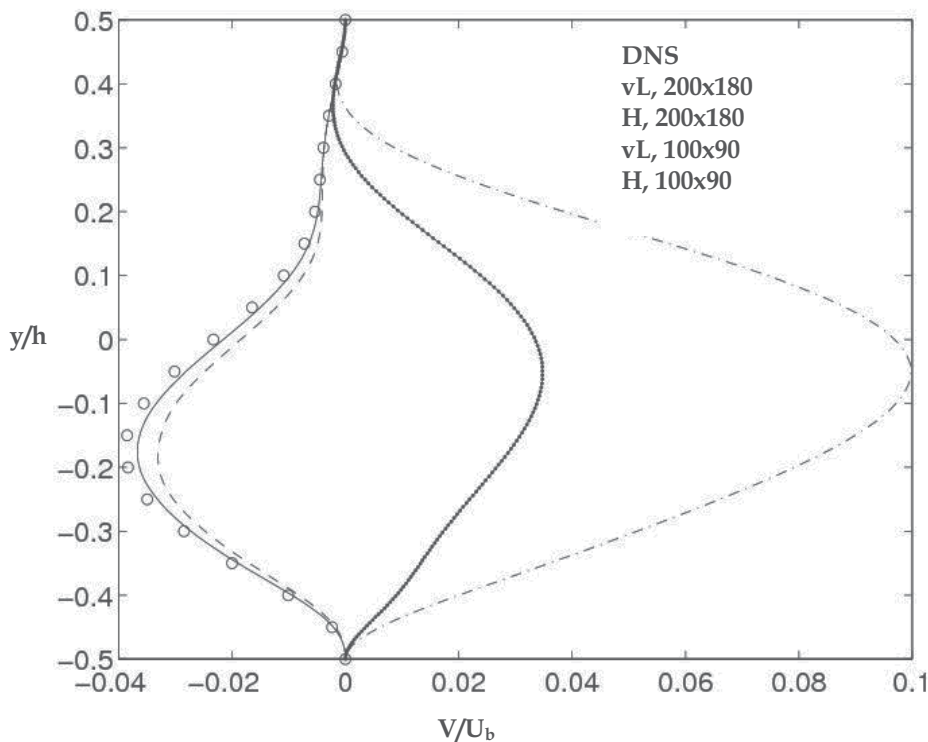


Fig. 3. Vertical velocity at  $x/h=7$ , Gartling BFS. Prediction using Hybrid (H) and van Leer (vL) discretization schemes



It is shown in Fig. 3 that the hybrid scheme is extremely sensitive to the used mesh, while the van Leer scheme predicts nearly identical profiles for both meshes, and also in close agreement with the DNS data.

### Rib-roughened channel

The rib-roughened channel is the one studied experimentally by Rau et. al. (Rau et. al., 1998) The Reynolds number based on the bulk velocity is  $Re_H=30.000$ . The ribs are square with a rib-size of  $e/H=0.1$ , and located along the bottom (south) wall with a pitch of  $P/e=9$ , see Fig. 4. A constant heat flux boundary condition was applied at the bottom wall, with the rib insulated. The measured and the predicted Nusselt numbers are normalized with the Dittus-Boelter equation (Dittus & Boelter, 1930), as introduced by McAdams (McAdams, 1942):

$$Nu_{\infty} = 0.023 Re^{0.8} Pr^{0.4} \quad (16)$$

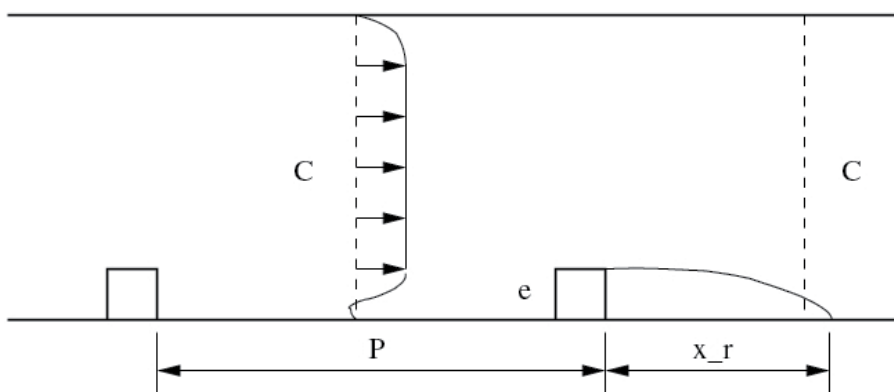


Fig. 4. Geometry, Rib-roughened channel (Rau et. al., 1998)

The computations were made using cyclic boundary conditions (C for cyclic in Fig. 4) at the stream-wise boundaries. Four different meshes were used: one with  $200 \times 240$  nodes, two with  $100 \times 120$  nodes and one with  $50 \times 60$  nodes (stream-wise  $\times$  wall normal). For the coarsest mesh the first interior computational node was located beyond  $y^+=1$ , although within the viscous sub-layer. It was thus of importance to use a turbulence model which is insensitive to the location of the first node. Using the conclusions from Bredberg (Bredberg, 2001), the AKN  $k-\epsilon$  turbulence model (Abe et. al., 1994) was selected.

The meshes with some predicted data are summarized in the table below:

Mesh	200x240	100x120*	100x120	50x60
$y_1/H$	0,00006	0,00012	0,0005	0,002
$y_1^+(\text{max})$	0,09	0,2	0,7	2,8
stretch	14%	30%	15%	12%
Nu (H)	n/a	190	192	188
Nu (vL)	186	190	191	192

Table 1. Mesh dependency on heat transfer, Nusselt number. Hybrid (H) and van Leer (vL) schemes

The first node distance from the wall is expressed both as  $y_1/H$  and normalized with local friction velocity  $y_1^+(\max)$ . The stretch is the growth in size of two successive cells, which should be less than 20% to ensure that the predictions are not corrupted by negligence of higher order terms in the estimation of gradients.

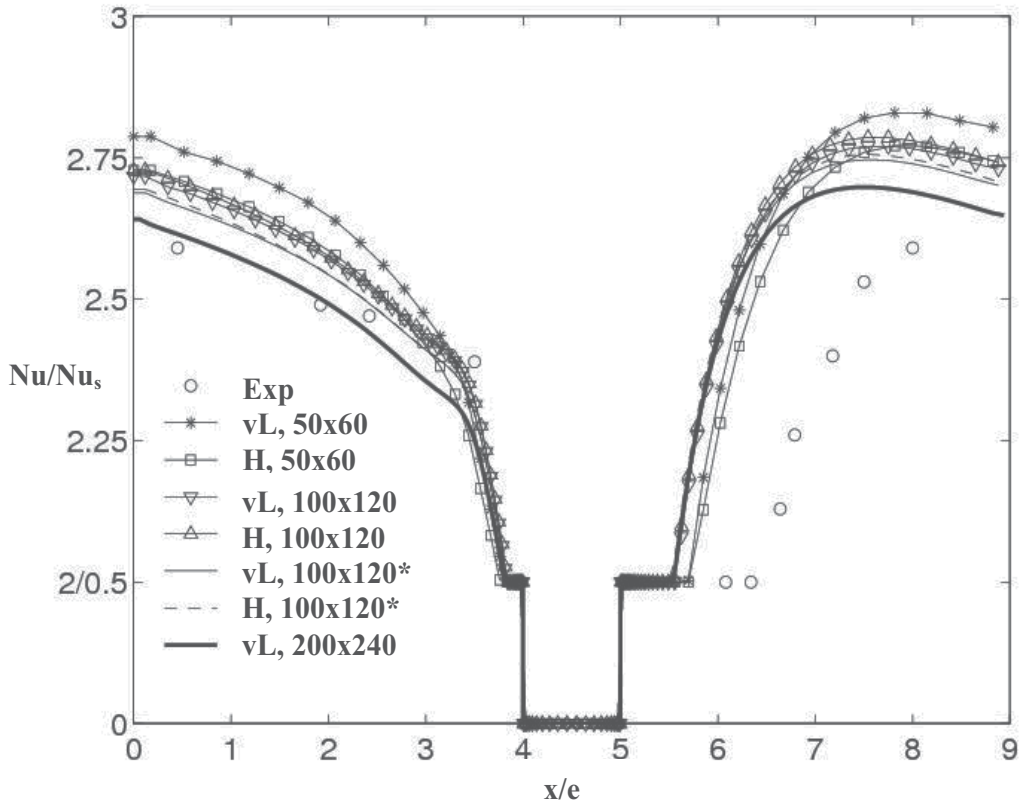


Fig. 5. Normalized Nusselt number for rib-roughened channel (Rau et. al., 1998). Predictions using Hybrid (H) and van Leer (vL) discretizing schemes. Observe the non-uniform y-axis

Fig. 5 gives the predicted variation of the normalized Nusselt number along the south, ribbed, wall. The insulated rib is located at  $4 < x/e < 5$ . To more clearly show the difference the graphs are cut for  $Nu/Nu_s < 2$ , which yield a visual impression that there are substantial difference between the predicted results. The maximum deviation is however a mere 5%, which is less than the deviation between two turbulence models as will be shown in the following section. Thus it can be concluded, that for a reasonable re-fined mesh the choice of numerical schemes are irrelevant for heat transfer predictions.

### 3. Numerical simulations of fundamental flows

A number of two-equations EVMs have been used to compute three different flows: fully developed channel flow, backward-facing-step (BFS) flow and rib-roughened channel flow. The models are: YS, Yang-Shih (Yang & Shih, 1993); AKN, Abe-Kondoh-Nagano (Abe et. al.,

1994); JL, Jones-Launder (Jones & Launder, 1972); C, Chien (Chien, 1982); LSY, Launder-Sharma-Yap (Launder & Sharma, 1974) and (Yap, 1987); WHR, Wilcox-high-Reynolds (Wilcox, 1988) and WLR, Wilcox-Low-Reynolds (Wilcox, 1993). The computations were made using the incompressible finite-volume method code CALC-BFC, (Davidson & Farhanieh, 1995), explained in section 2.5. For all cases only two-dimensional computations were made, to reduce computational costs. The test-cases have been chosen so that the difference between the predicted centreline values for a 3D mesh will be negligible as compared to the used 2D mesh.

### 3.1 Fully developed channel/pipe flow

The case is a 1D-flow, with a variation only in the wall normal direction. Due to its simplicity this was one of the first cases computed using DNS, and has since then become a standard case for turbulence model comparison. As DNS gives such a wealth of information most designers use these data-bases to improve their models. Thus it is not surprising that the accuracy of post-DNS models (from 1990 and later) are significantly higher than those prior to DNS. The DNS used as a comparison here are the data from Moser et. al. (Moser et. al., 1999), with a Reynolds number based on the channel half width and friction velocity of  $Re_\tau=395$ .

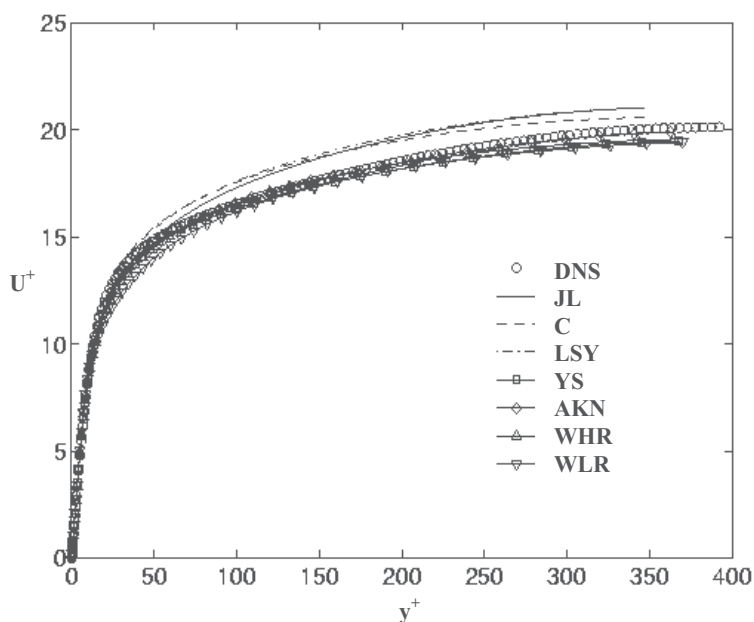


Fig. 6.  $U^+=U/U_\tau$  vs.  $y^+$ . DNS-data, Moser et. al. (Moser et. al., 1999)

The normalized friction velocity is listed in table 1 along with the predicted Nusselt number using a constant Prandtl number model. The Nusselt number is not available for the DNS-data and instead the Dittus-Boelter equation is used, see Eq. (16). All models predict the friction velocity fairly accurate. The largest deviation for the Nusselt number is given by the JL-model which under-predicts the value by 18%. Note that all turbulence models under-predict the Nusselt number, with the WLR-model yielding a correct value within 2%.

Model	YS	AKN	JL	C	LSY	WHR	WLR
$U_\tau^*$	58,1	57,3	54,8	55,0	54,3	57,5	58,5
Nu	40,1	38,9	33,9	35,6	34,9	38,2	40,4

Table 2. Friction velocity and Nusselt number. DNS,  $Re_\tau=395$ :  $U_\tau^* = 1000 \times U_\tau/U_b = 56,9$  and  $Nu_{DB}=41,1$

The predicted  $U^+=U/U_\tau$  profiles are compared in Fig. 6. The difference between the models is only minor, however some models slightly under-predict the friction velocity with a resulting over-prediction of  $U^+$ . Progressing to the turbulent kinetic energy,  $k^+=k/U_\tau^2$  the profiles are compared in semi-log plots, Fig. 7. The spread between the turbulence models is significantly larger for this quantity as compared to the velocity profiles. Generally the predictions improve the newer the model is. To quantify the models, the predicted maxima are shown in tables 3. Only the JL, LSY and WHR-models give  $k^+$  values that deviate significantly from DNS data. The WLR-model improves the result substantially compared with the WHR, using the added damping functions. However as noticed later, an improvement in the predicted turbulent kinetic energy don't automatically improve results for other quantities.

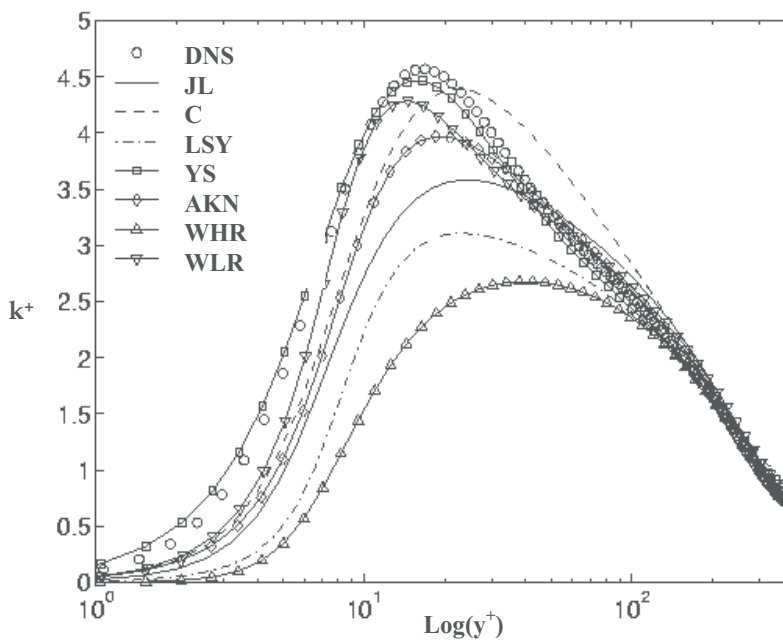


Fig. 7.  $k^+=k/U_\tau^2$  vs.  $y^+$ . DNS-data, Moser et. al. (Moser et. al., 1999)

Model	YS	AKN	JL	C	LSY	WHR	WLR
$k^+$	4,47	3,97	3,58	4,39	3,11	2,68	4,29
$\varepsilon^+$	0,29	0,18	0,19	0,21	0,18	0,22	0,13

Table 3. Maximum value of  $k^+$  and  $\varepsilon^+$ . DNS,  $Re_\tau=395$ :  $k^+=4,57$  and  $\varepsilon^+=0,22$

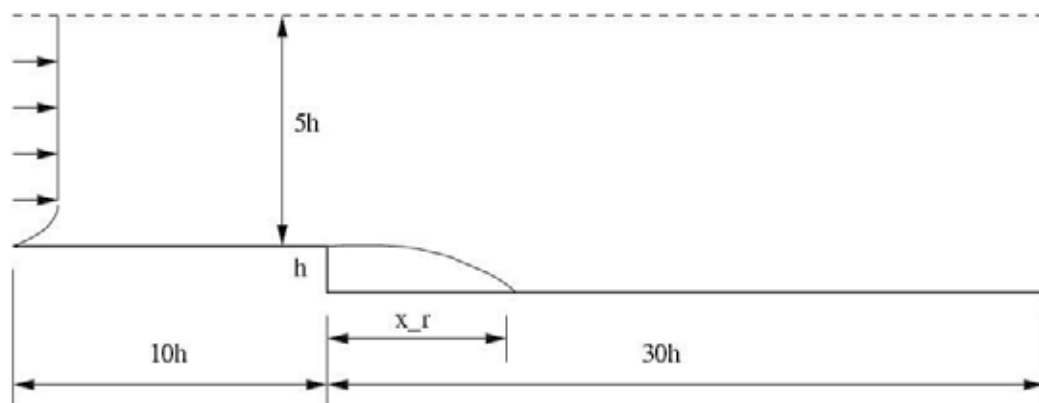


Fig. 8. Geometrical conditions, not to scale, BFS-case (Le et. al., 1997)

### 3.2 Backward-facing-step flow

In the backward-facing step case, the flow undergoes separation, re-circulation and re-attachment followed by a re-developing boundary layer. In addition, this flow involves a shear-layer mixing process, as well as an adverse pressure, thus the backward-facing step (BFS) is an attractive flow for comparing turbulence models. The case used here is the one that has been studied using DNS by Le et. al. (Le et. al., 1997) see Fig. 8. This case has a relatively low Reynolds number,  $Re_h=5.100$ , based on the step-height,  $h$ . In the present computation the inflow condition was specified using DNS data at  $x/h=-10$ . Neumann condition was applied for all variables at the outlet located at  $x/h=30$ . No-slip condition was used on the walls. The overall calculation domain ranges from  $x/h=-10$  to  $x/h=30$ , with the step located at  $x/h=0$ . The channel height is  $5h$  in the inlet section and  $6h$  after the step, yielding an expansion ratio of 1.2.

The inlet condition in the BFS-case is crucial for a critical evaluation and comparison. The DNS data of Spalart (Spalart, 1988) for the velocity profile and the  $k$ -profile, are directly applied at the inlet. The inflow  $\varepsilon$  or  $\omega$  was specified in such a way that the model prediction matches the DNS data at  $x/h=-3$ .

The skin friction coefficient, defined as  $C_f=2\tau_w/(\rho U_\infty^2)$ , is shown in Fig 9. The predicted friction coefficient varies from very good (LSY) to rather poor (JL and C). Although hardly discernible, the Chien-model reproduces a highly questionable  $C_f$  profile around the re-attachment point. The  $y^+$ -based damping functions is the main reason for this spurious behaviour, which also yields erroneous heat transfer in the rib-roughened case.

Model	YS	AKN	JL	C	LSY	WHR	WLR
$x_r/h$	4,62	5,65	6,17	5,86	6,83	7,46	7,96
$C_{f,max}$	3,68	3,35	4,04	4,05	3,13	2,56	2,30

Table 4. Re-attachment point and maximum friction coefficient. DNS:  $x_r/h=6,28$ ,  $1000 \times C_{f,max}=3,04$

One of the commonly used quantities to justify the accuracy of a turbulence model in a BFS-case is the re-attachment length of the main separation. Table 4 gives the re-attachment length,  $x_r$ , using the different models in comparison with DNS data,  $x_r/h=6,28$ . The model which yielded the most favourable values for  $\varepsilon^+$  at the wall in the channel flow case, YS

completely fail to capture the re-attachment point in this case, by as much as 26%. The Wilcox  $k-\omega$  models (WHR and WLR) don't give very accurate predictions either, with an overestimation of the re-attachment point of 19% and 27% respectively. Notable is that the improved WLR-model gives worse result.

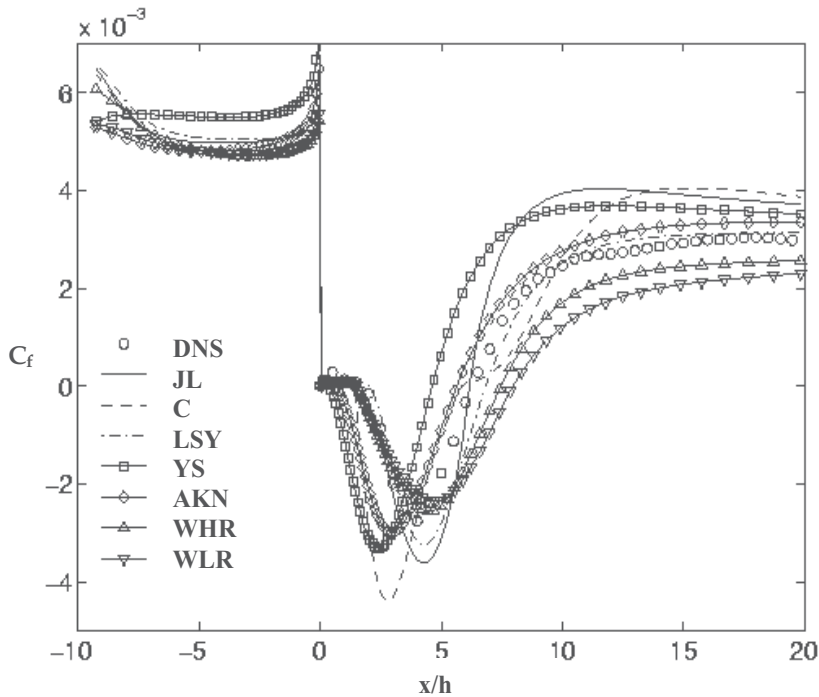


Fig. 9.  $C_f$  along lower wall. DNS-data, Le et. al. (Le et. al., 1997)

### 3.3 Rib-roughened channel flow

The heat transfer performance of the different models is evaluated in the rib-roughened case of Rau et. al. (Rau et. al., 1998) as used in the above mesh sensitivity study, see section 2.5. The Reynolds number, based on the mean velocity and the channel height is  $Re_H=30.000$ . The height-to-channel hydraulic diameter,  $e/H$ , is 0,1, and the pitch-to-rib-height ratio,  $P/e=9$ , see Fig. 4. The experiment provides both flow field and heat transfer measurements, however here only the centre-line Nusselt number is used in the comparison. The measured Nusselt numbers were normalized with the Dittus-Boelter equation see Eq. (16). The uncertainty in the resulting enhancement factor,  $Nu/Nu_0$  was estimated to be 5% for the experiment.

The computations were made using periodic boundary condition at the stream-wise boundaries, which was verified in the experiment to prevail in the test section. This reduces the uncertainty in the result due to the inlet boundary condition. No-slip condition and constant heat flux were applied at the walls. The rib was, as in the experiment, insulated.

Fig. 10 compare the Nusselt numbers predicted from the different turbulence models.

The AKN model give accurate predicted Nusselt number (+6%) although it yields too high values downstream the rib. The worst results are predicted with the JL and C-models,

especially the C-model, with a large over-prediction of the Nusselt number. The Wilcox models (WHR, WLR) under-predict the Nusselt number by a fair margin. The effect of the Yap-correction is apparent, with the LSY-model predicts less than half the Nusselt number as compared with the JL-model. The former is also in better agreement with the experimental data.

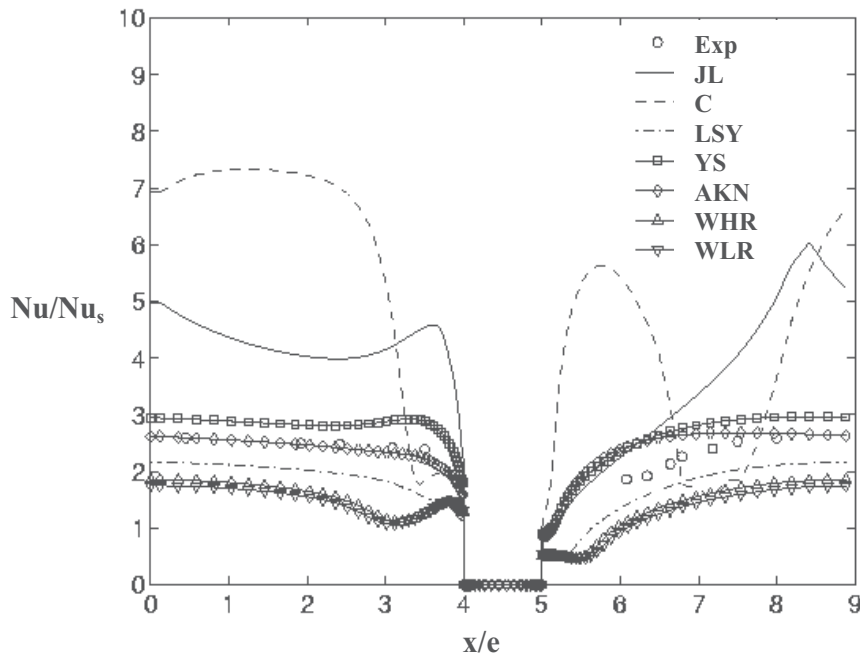


Fig. 10. Nu along lower wall. Experiment, Rau et. al. (Rau et. al., 1998)

Model	YS	AKN	JL	C	LSY	WHR	WLR
$Nu_{max}$	227	206	463	546	165	142	133
$\int Nu$	206	185	298	368	137	113	106
%	+18	+6	+71	+111	-21	-35	-39

Table 5. Nusselt number. Experiment:  $\int Nu \approx 174$ ,  $Nu_{max} = 198$

Table 5 give both the average and the maximum Nusselt number for each model along with the deviation of turbulence models from the experiment is also listed.

It is of interest to compare the predicted Nusselt number for the rib-roughened with the predicted skin friction in the BFS-case. In table 4 the maximum  $C_f$  in the re-developing zone, i.e. after the re-attachment point is listed.

Using Reynolds analogy it is reasonable to believe that models which underestimate the maximum friction coefficient will also underestimate the heat transfer coefficient. The JL- and C-models that severely over-predict the heat transfer in the rib-roughened case also give too large skin friction. The models that under-predict Nu (WHR, WLR) also gives low values of skin friction in the backward-facing step case.

#### 4. PWR applied CFD simulations

The three simulation cases presented below were all made at Epsilon UC Väst AB in support of Ringhals AB working with ARTIST (Güntay et. al. 2004). Aerosol Trapping In a Steam Generator (ARTIST) was an international project that investigates the consequences of a tube rupture in steam generators in nuclear power plants. A tube fracture in a steam generator could, in worst case, lead to a spread of nuclear substances to the atmosphere. It is therefore of great importance to investigate how such effects can be minimized, should a rupture take place. The ARTIST project was divided into seven phases, with the aim of each phase to investigate, both numerically and experimentally different parts of the steam generator, as visualized in Fig. 11. Note that the aim of the ARTIST project was to investigate the overall retention of nuclear particles in a steam generator, whereas the simulations presented here are all concerned with the flow distribution in a tube bundle. The system simulated is the state formed after a tube break has occurred when the coolant, on the secondary side, has evaporated and the gas from the primary side flows through the bundle.

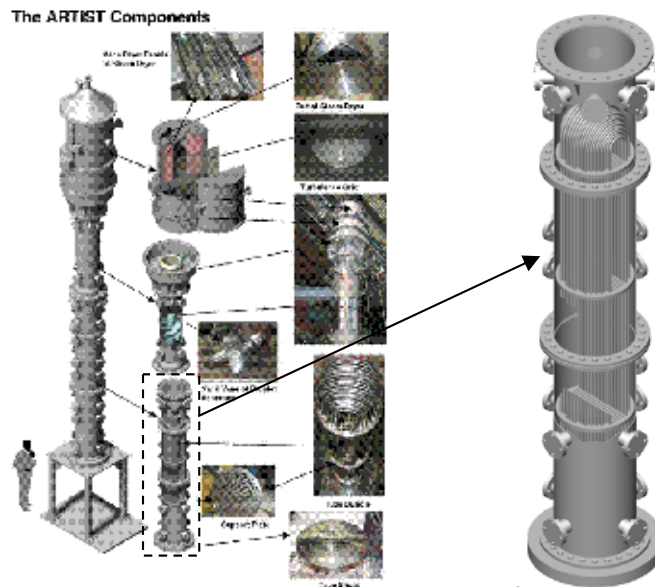


Fig. 11. ARTIST components with steam generator tube bundle enhanced. (Güntay et. al. 2004)

##### 4.1 Flow distribution in a steam generator with a tube failure

The ARTIST scaled-down steam generator, comprises one tube bundle divided into three tube stage, one separator and one dryer as seen in Figure 11. The three stages; break stage, stage 2 and stage 3 are separated by 30mm thick support plates, with a distance between each support plate according to Figure 12. The diameter of the tube bundle is 573mm. The total number of tubes in a fully occupied tube bundle is 270. The tubes have an inner-diameter of 16,8mm and an outer diameter of 19,08mm. The spacing between them is 27,43mm. In order to achieve a feasible CFD model, the geometry of the tube bundle is only



represented in the break stage, leaving stage 2 and 3 “empty” where porous media is defined. This is done since it is the flow distribution in the break stage that is of interest. The inside of the fractured tube is included in the computational domain.

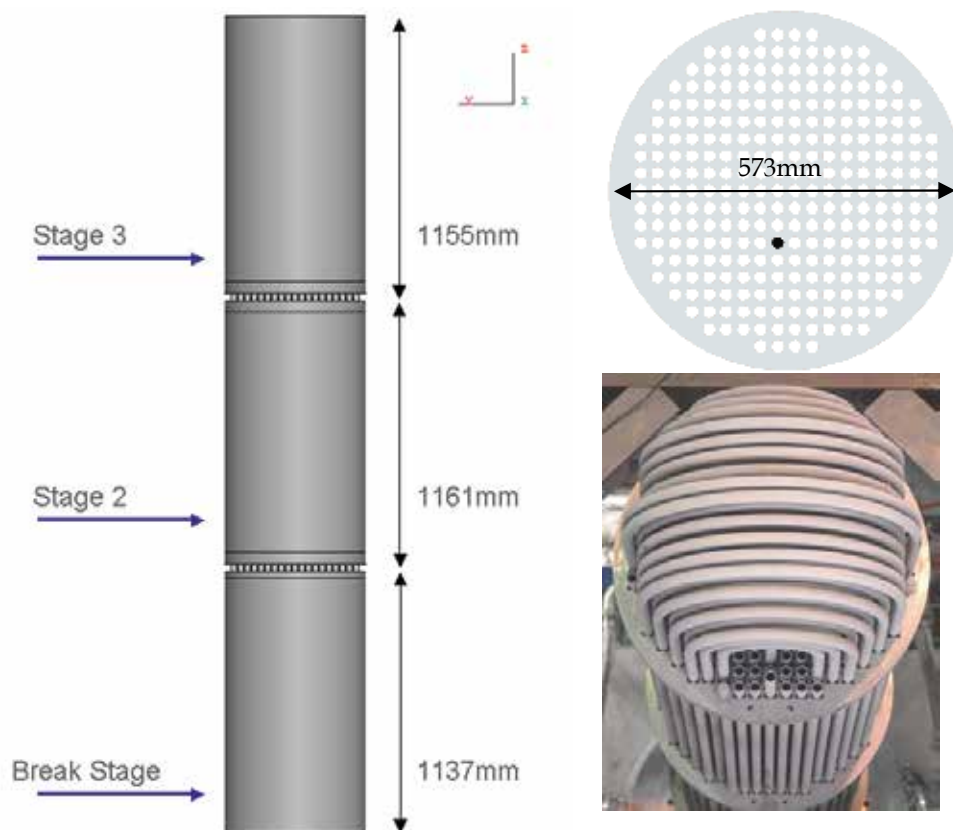


Fig. 12. Main dimension of the ARTIST scale-down steam generator rig. The filled hole in the upper-right figure represent the fractured tube

Figure 13 illustrates the mesh around guillotine break and the four support rods that stabilize the loose ends of the fractured tube. The longitudinal centre of the break is positioned 300mm from the bottom of the break stage. The box inside the break stage is the region close to the break containing the computational mesh shown in figure. This region is resolved with 800.000 computational cells. Total size of the volume mesh in the model is 5,6 million cells where 4,6 million cells are in the break stage and 1 million in the upper stages and support plates.

The CFD code used for solving the flow is ANSYS/Fluent version 6.3. For details of this code, the reader is referred to the users guide and theory guide (ANSYS, 2001). This case is solved with the pressure based RANS implicit iterative and segregated solver assuming steady state and adiabatic conditions. The fluid (nitrogen) is modelled as a compressible ideal gas with constant fluid properties taken at atmospheric condition at a temperature of 298K. The boundary conditions are; pressure at the inlet (4,6atm) and pressure at the outlet (1atm). The walls are modelled using no-slip condition. Stage 2 and 3 are modelled using

porous media for which the pressure loss coefficients are tuned to that of the flow along tubes. Turbulence is modelled using the standard  $k-\epsilon$  turbulence model, which is based on the work by Jones and Launder (Jones & Launder, 1972).

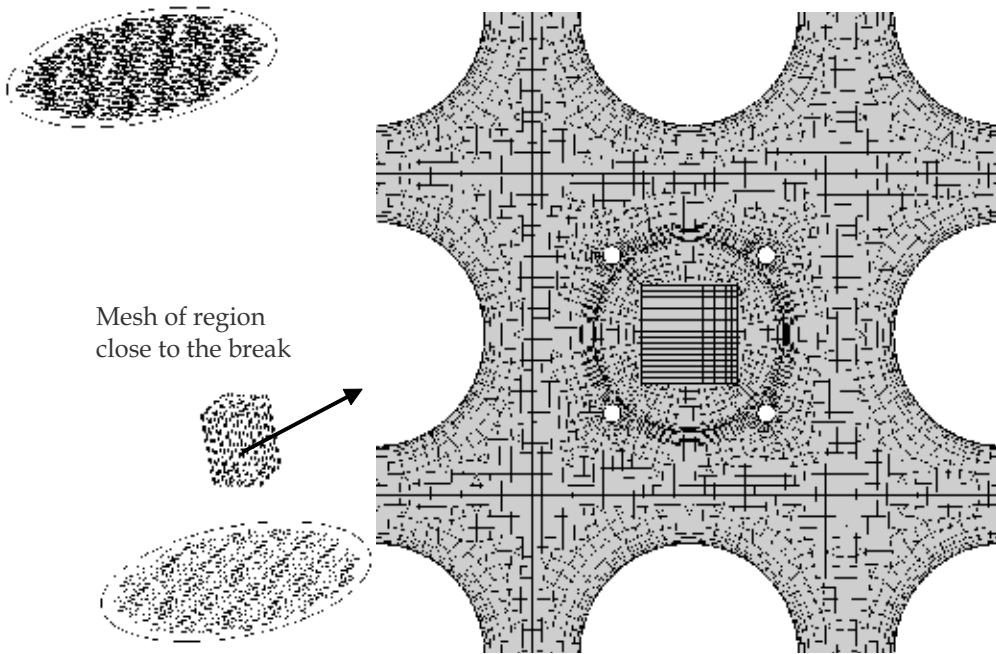


Fig. 13. Computational mesh around the break, including the support rods (voids)

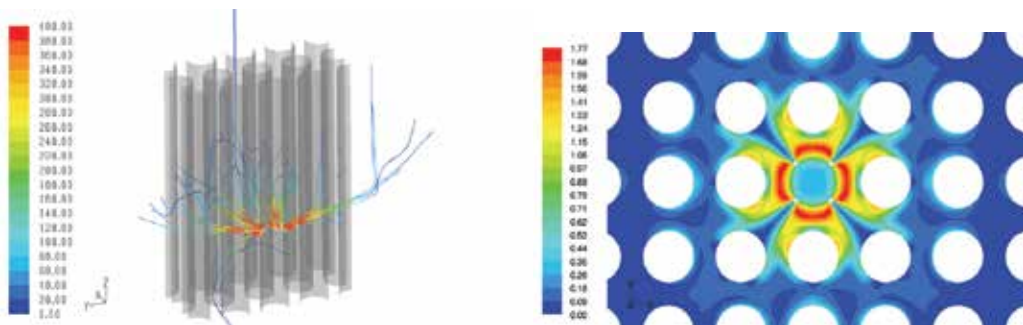


Fig. 14. Flow out from the fractured tube. Left picture; path-lines, coloured with velocity, right picture; contours of Mach-number in a plane through the break

The results focus on the flow distribution in the break stage and the pressure drop throughout the entire domain. The velocities in the upper stages are presented as well but are not physically true since the geometry of the tubes is represented with porous media.

Fig. 14 shows stream lines, coloured by velocity, released from the break and a contour plot of the Mach number at a  $xy$ -plane through the break. It is clear that the velocity field is affected of both the tubes and the support rods.

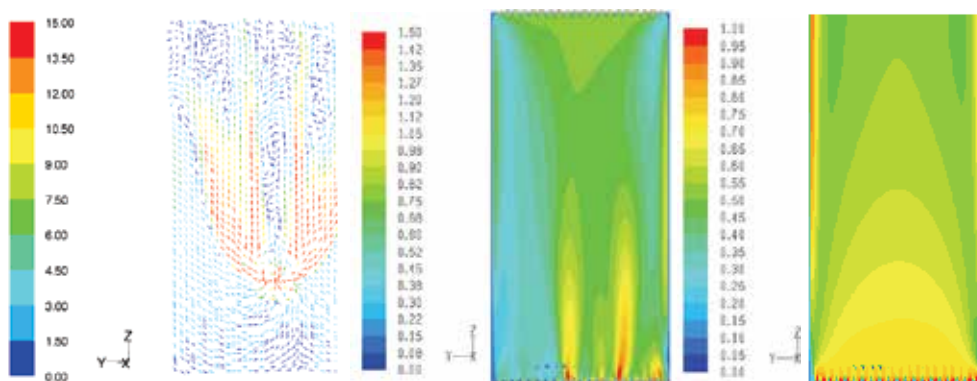


Fig. 15. Velocity variation through the tube bundle. From left to right; velocity vectors in the break stage; velocity contours in stage 2 and velocity contours in stage 3

The vertical velocity through the tube bundle is visualized in Fig. 15. Around the break there is a strong recirculation, illustrated the left in the figure as a vector plot on a  $xz$ -plane through the break stage. The computed velocity magnitudes in the upper stages (middle and right pictures in Fig. 15) are, as mentioned earlier, not physically correct since the geometry of the tubs is represented with porous media. The real open cross sectional area in the upper stages is  $0,181\text{m}^2$ , corresponding area in the CFD model is  $0,258\text{m}^2$ . The open area is thus 1,43 times larger in the CFD model. The contour plots below shows that stage 3 has a relatively homogenous velocity distribution. It is however expected that a homogenous distribution develops faster through a porous zone than through real bundle geometry.

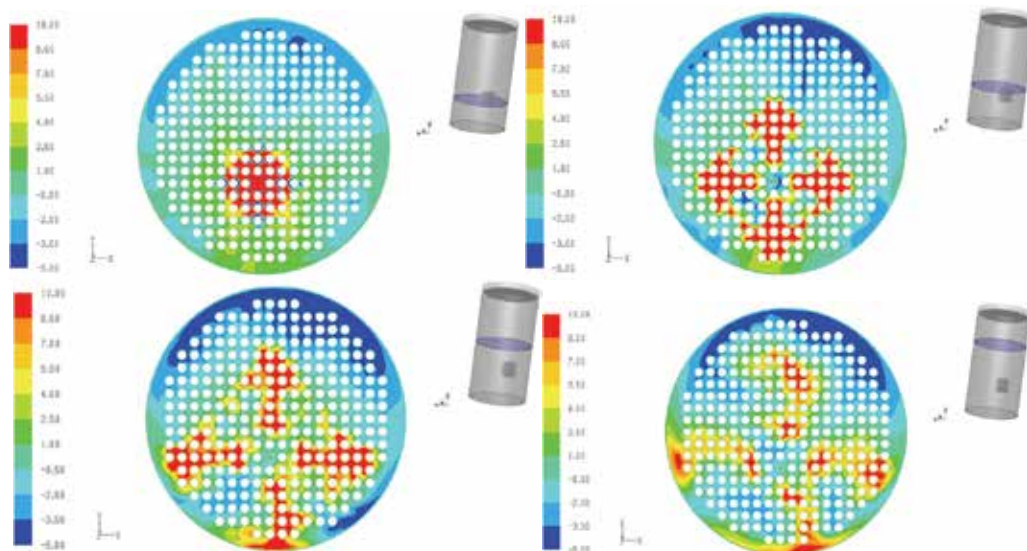


Fig. 16. Vertical velocity at selected horizontal planes. Upper-left: at break position, upper-right: 0,1m above break, lower-left: 0,3m above break and lower-right: 0,5m above break

The flow distribution in the break stage is here visualized with contour plots of vertical velocity ( $z$ -velocity) at 4 different planes, see Fig. 16. A sketch of the current plane position is

added beside each contour plot to illustrate where in the break stage the plots are generated. The plots above demonstrate how the flow from the guillotine break develops to four dominant flow streams upwards in the break stage. The region in the tube bundle where most of the recirculation, negative z-velocity, occurs is also visible in the plots. This “negative z-velocity flow” is concentrated to the zone most distant to the break, hence in the upper part of each of the plots above.

The most significant pressure drop occurs when the gas expands out from the broken tube but the pressure drop due to friction inside the tube, before the break, is also considerable. The table below lists the pressure losses throughout the whole tube bundle. It is clear that the pressure losses in the upper stages and in the support plates are insignificant compared to the losses in the break stage.

Section of the tube bundle	Pressure drop, total pressure
Break tube	20.5kPa
Break stage	338.2kPa
Support plate 1	17.8Pa
Stage 2	1.8Pa
Support plate 2	6.2Pa
Stage 3	1.7Pa

Table 6. Pressure drop in total pressure

#### 4.2 Flow simulation of a Beznau steam generator

In the ARTIST project the Beznau power plant (365MW, Westinghouse design) was chosen as the basis for investigation. Each steam generator at Beznau consists of close to 6500 tubes in a cylindrical shaped enclosure, while the test rig, consists of 274 tubes, in an octagonal box. This rig shares the same tube dimensions with the above steam generator rig, i.e. an outer diameter of 19mm and an inner diameter of 16,8mm. The guillotine break (horizontal cut) is positioned at roughly 1/4 of the height in a centrally located tube. The purpose of this rig is to enable velocity measurement using LDA, which was not possible in the above steam generator rig. The choice of an octagonal Plexiglas rig improved visibility and access, however reduced the maximum pressure. There are thus three different simulation using two different geometries:

- The Beznau steam generator with 6500 tubes, with a mass-flow of 650kg/h
- The ARTIST model with 274 tubes, with a mass-flow of 650kg/h
- The ARTIST model with 274 tubes, with a mass-flow of 360kg/h for comparison with LDA measured velocities

The two computational domains are shown in Fig. 18. For both cases a single stage (the break stage) is modelled. The Beznau mesh has 25 million cells, while the ARTIST model consists of 6 million cells.

The simulations were performed with the CFD-code ANSYS/Fluent (ANSYS, 2001), version 6.3.26. Similar to above the pressure based RANS implicit iterative and segregated solver assuming steady state and adiabatic conditions was used. The fluid (nitrogen) is modelled as a compressible ideal gas with constant fluid properties taken at atmospheric condition at a temperature of 298K. Two different turbulence models; k- $\epsilon$  (standard) (Jones & Launder, 1972) and Reynolds Stress Model (with wall reflection enabled) (Launder, 1989), both using enhanced wall treatment (hybrid wall functions). The presented results are converged to at

least 3 orders of magnitudes with second order (upwind-weighted) accurate discretization schemes. Due to numerical instability issues, the turbulence equations for the RSM were solved with first order schemes. Furthermore the flow shows tendencies of unsteadiness away from the break, and consequently a transient simulation was performed to visualize the effects of flow oscillation.

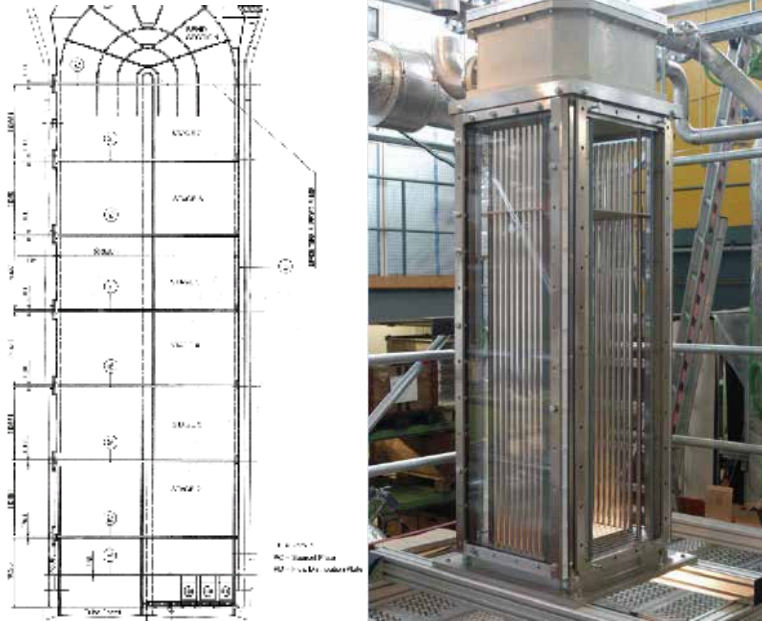


Fig. 17. Schematic drawing of the tube bundle of Beznau steam generator (left) and ARTIST test rig with a octagonal tube bundle for LDA measurements (right)

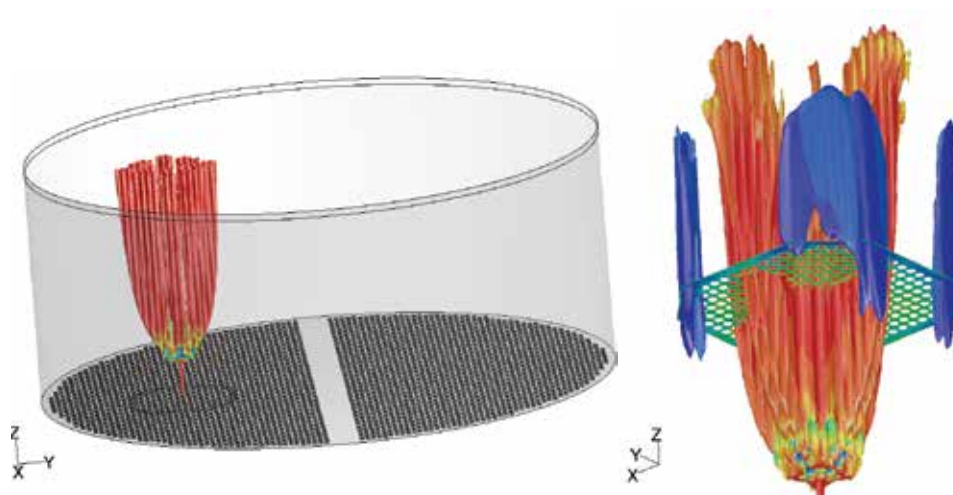


Fig. 18. Apprehension of the significant difference in size. Beznau (left) compared with ARTIST test rig (right)



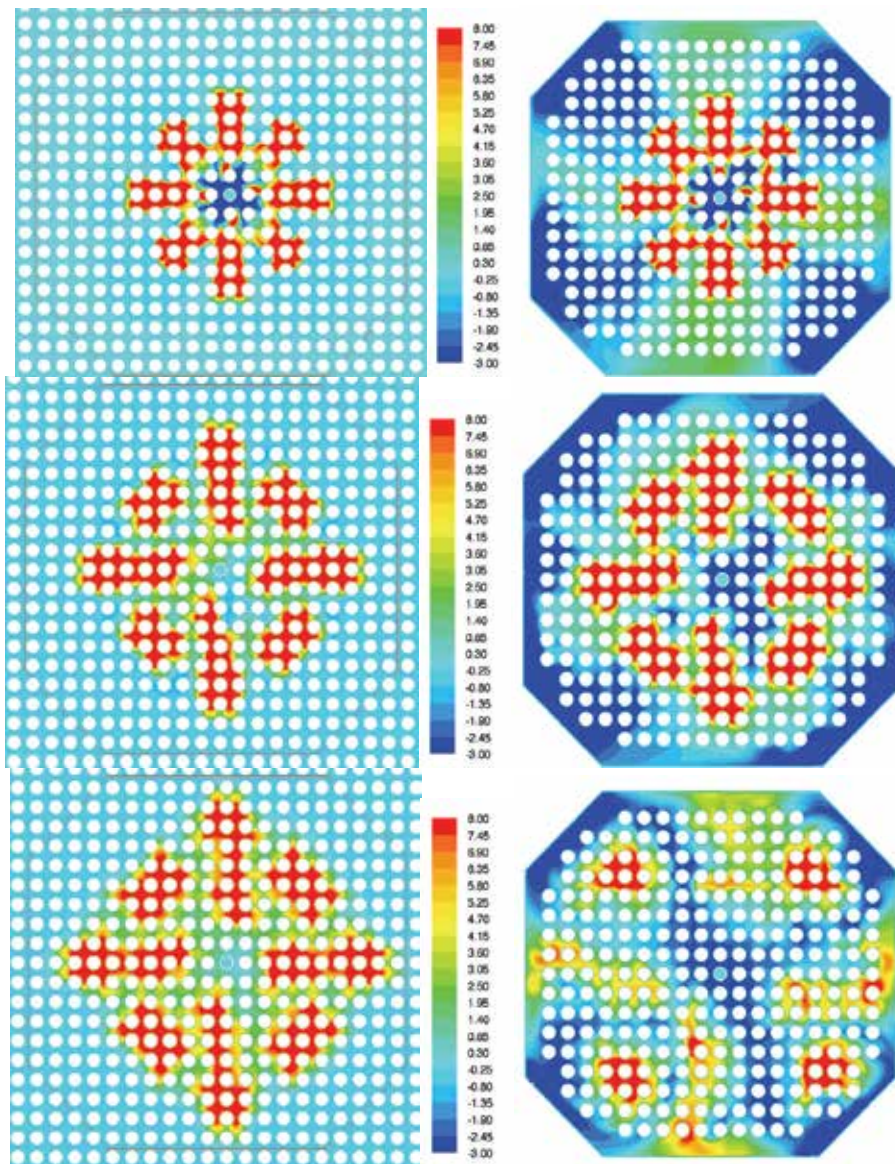


Fig. 19. Contours of vertical velocity for 650kg/h case at horizontal planes above the break. Left: Beznau case (domain cropped), right: ARTIST test rig. Upper row,  $\Delta z=100\text{mm}$ , middle row,  $\Delta z=350\text{mm}$  and lower row  $\Delta z=750\text{mm}$

Figure 19 compares the vertical velocity at selected horizontal planes above the break. The confinement of the test rig gives rise to larger variations, with alternating vertical velocities towards the walls. In contrast, the simulation of the Beznau steam generator shows a very small overall negative velocity, which is a consequence of continuity. The flow field in the vicinity of the break (the central tubes) is unaffected by the boundaries, hence the test rig simulation gives a faithful representation of the flow in this part of the Beznau steam generator.

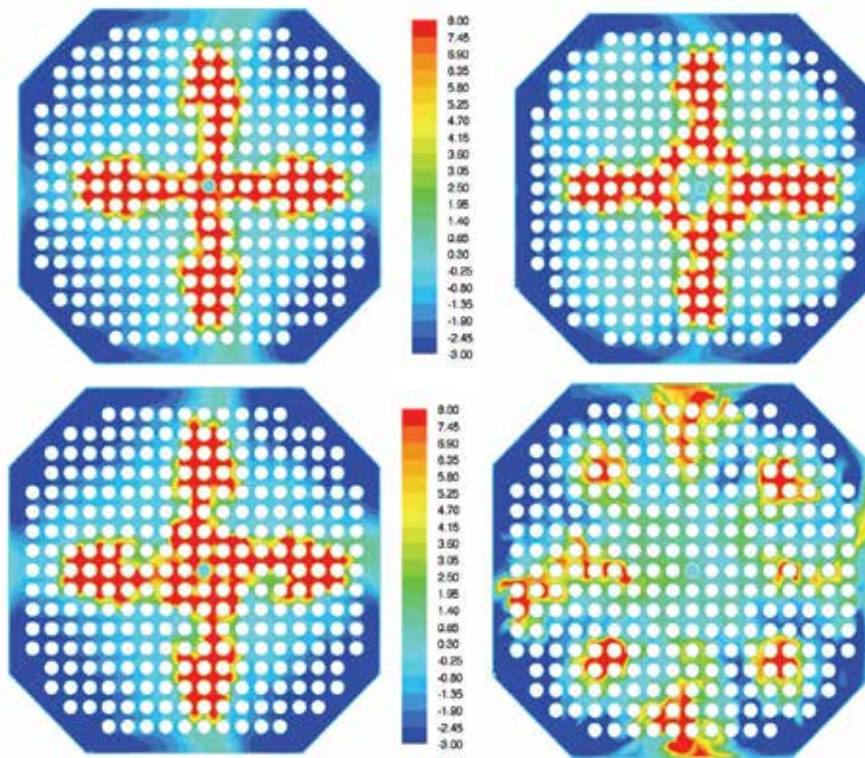


Fig. 20. Vertical velocity at  $\Delta z = 350\text{mm}$  for  $360\text{kg/h}$  case.  $k-\epsilon$  1:st order (upper left),  $k-\epsilon$  2:nd order (upper right), RSM 1:st order (lower left) and RSM 2:nd order (lower right)

The effect of turbulence model and order of discretization scheme can be seen in Fig. 20, where  $k-\epsilon$  is compared with the RSM for the test rig domain. Note that the mass flow is different as compared to Fig. 19. It is obvious that the discretization scheme has a more significant importance for the RSM than for the  $k-\epsilon$  turbulence model. A comparison between measurements and these turbulence models are presented in Fig. 21.

The measurements were carried out using LDA for a mass flow of  $360\text{kg/h}$ , along several lines at two different heights. Sampling was performed to ensure statistical invariance, with around 2000 samples for each measured point. Here comparisons along two lines at  $600\text{mm}$  height presents ( $\Delta z = 350\text{mm}$ , i.e.  $350\text{mm}$  above the break). The two lines are shown in Fig. 21, one positioned very close to the break tube (though  $350\text{mm}$  above the break), at  $y=13,7\text{mm}$ , and one closer to the boundaries at  $y=96\text{mm}$ .

The difference between measured and computed data is clearly notable in Fig. 21, especially for the results based on the  $k$ -epsilon turbulence model where the tendency is clearly wrong. Reynolds stress model does a better job, even though the amplitude is not correct. A major reason to the discrepancies between measured and computed data is the rather poor grid resolution in the CFD-model. The total cell count is 6 million cells, but there are still only 6 cell rows between each pair of tubes. This cell distribution combined with highly varying velocity magnitudes, results in  $y^+$  values between 0,1 and 256, which may be too demanding on the wall treatment model.

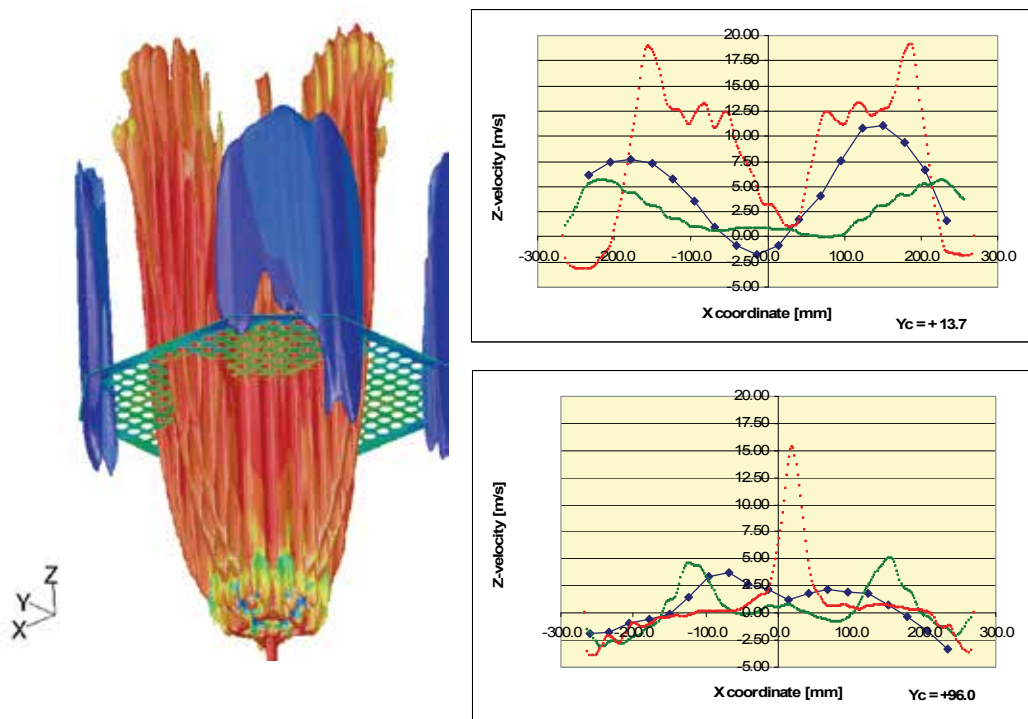


Fig. 21. Right: Z-velocity profile, k-epsilon (red), RSM (green) and measurements (blue). Left: location of measurements

## 5. References

- Abe, K.; Kondoh, T. & Nagano, Y. (1994). A new Turbulence Model for Predicting Fluid Flow and Heat Transfer in Separating and Reattaching Flows - I. Flow Field Calculations, *Int. J. Heat and Mass Transfer*, Vol 37, pp. 139-151
- ANSYS/Fluent (2001). *Users guide*, Fluent Inc.
- Berg, T.; Bredberg, J. & Dehbi, A. (2008a). Numerical Modeling of Flow in Dry Secondary Side of Steam Generator, *Proceedings of the 2008 International Congress on Advances in Nuclear Power Plants (ICAPP '08)*, ISBN: 0-89448-061-8, Anaheim, June 2008, American Nuclear Society
- Berg, T.; Bredberg, J. & Suckow, D. (2008b). CFD Simulation of ARTIST Break Stage and Comparison with Measured Data, *Proceedings of the 2008 International Congress on Advances in Nuclear Power Plants (ICAPP '08)*, ISBN: 0-89448-061-8, Anaheim, June 2008, American Nuclear Society
- Boussinesq, T.V. (1877). *Mém. pres Acad. Sci.*, 3rd ed Paris XXIII, pp. 46
- Bredberg, J. (1999). *Prediction of flow and heat transfer inside turbine blades using EARSM,  $k-\epsilon$  and  $k-\omega$  turbulence models*, Thesis for the Degree of Licentiate of Engineering, Dept of Thermo and Fluid Dynamics, Chalmers University of Technology, Gothenburg
- Bredberg, J. (2001). *On Two-equation Eddy-Viscosity Models*, Internal Report 01/8, Dept of Thermo and Fluid Dynamics, Chalmers University of Technology, Gothenburg



- Bredberg, J. (2002). *Turbulence Modelling for Internal Cooling of Gas-Turbine Blades*, Ph.D. Thesis, Dept of Thermo and Fluid Dynamics, Chalmers University of Technology, Gothenburg
- Chien, K.Y. (1982). Predictions of Channel and Boundary-Layer Flows with a Low-Reynolds-Number Turbulence Model, *AIAA Journal*, Vol 20, pp. 33-38
- Daly, B.J. & Harlow, F.H. (1970). Transport equation in turbulence, *Physics of Fluids*, Vol 13, pp. 2634-2649
- Davidson, L. & Farhanieh, B. (1995). *CALC-BFC*, Internal Report 95/11, Dept of Thermo and Fluid Dynamics, Chalmers University of Technology, Gothenburg,
- Dittus, F.W. & Boelter, L.M.K. (1930). Heat transfer in automobile radiators of the tubular type, *Univ. of Calif. Pubs. Eng.*, Vol 2, 1930, pp. 443-461
- Doormal (van), J.P. & Raithby, G.D. (1984). Enhancement of the SIMPLE Method for Predicting Incompressible Fluid Flows, *Numerical Heat Transfer*, Vol 7, pp. 147-163
- Gartling, D.K. (1990). A test problem for outflow boundary condition - flow over a backward-facing step, *Int. J. Numerical Methods in Fluids*, Vol 11, pp. 953-967
- Güntay S., Suckow, D., Dehbi, A. & Kapulla, R. (2004). ). Artist: Introduction a first results, *Nuclear Engineering and Design*, Vol 232, pp. 109-120
- Hinze, J.O. (1975) *Turbulence*, McGraw-Hill Inc.
- Jones, W.P. & Launder, B.E. (1972). The prediction of laminarization with a two-equation model of turbulence, *Int. J. Heat and Mass Transfer*, Vol 15, pp. 301-314
- Kawamura, H.; Abe, H. & Matsuo, Y. (1999). DNS of Turbulent Heat Transfer in Channel Flow with Respect to Reynolds and Prandtl Number Effects, *Int. J. Heat and Fluid Flow*, Vol 20, pp. 196-207
- Kays, W.M. (1994). Turbulent Prandtl number - where are we?, *J. Heat Transfer*, Vol 116, pp. 284-295
- Launder, B.E. (1989). Second-Moment Closure: Present... and Future?, *Int. J. Heat and Fluid Flow*, Vol 10, No 4, December 1989, pp. 282-300
- Launder, B.E. & Sharma, B.I. (1974). Application of the energy-dissipation model of turbulence to the calculation of flow near a spinning disc, *Letters in Heat and Mass Transfer*, Vol 1, pp. 131-138
- Le, H.; Moin, P. & Kim, J. (1997). Direct numerical simulation of turbulent flow over a backward-facing step, *J. Fluid Mechanics*, Vol 330, pp. 349-374
- Leer (van), B. (1974). Towards the ultimate conservative difference Monotonicity and conservation combined in a second-order scheme, *J. Computational Physics*, Vol 14, pp. 361-370
- Leonard, B.P. (1979). A Stable and Accurate Convective Modelling Procedure based on Quadratic Upstream Interpolation, *Comp. Meth. Appl. Mech. Eng.*, Vol 19, pp. 59-
- McAdams, W.H. (1942). *Heat Transmission*, McGraw-Hill, New York
- Moser, R.D.; Kim, J. & Mansour, N.N. (1999). Direct Numerical Simulation of Turbulent Channel Flow up to  $Re=590$ , *Physics of Fluids*, Vol 11, pp. 943-945
- Panton, R.L. (1995). *Incompressible flow*, John-Wiley and Sons Inc.
- Patankar, S.V. & Spalding, D.B. (1970). *Heat and Mass Transfer in Boundary Layers*, Intertext Books, London
- Pope, S.B. (1975). A more general effective-viscosity hypothesis, *J. Fluid Mechanics*, Vol 72, pp. 331-340

- Rau, G., Cakan, M., Moeller, D. & Arts, T. (1998). The effect of periodic ribs on the local aerodynamic and heat transfer performance of a straight cooling channel, *J. Turbomachinery*, Vol 120, pp. 368-375
- Reynolds, O. (1895). On the Dynamical Theory of Incompressible Viscous Fluids and the Determination of the Criterion, *Ph. Trans. Royal Soc. London, Series A*, Vol 186, pp. 126-
- Rhie, C.M. & Chow, W.L. (1983). Numerical Study of the Turbulent Flow Past an Airfoil with Trailing Edge Separation, *AIAA Journal*, Vol 21, pp. 1525-1532
- Smagorinsky, J. (1963). General Circulation Experiments with the Primitive Equations I. The Basic Experiment, *Monthly Weather Review*, Vol 91, 1963, pp. 99-165
- Spalart, R.P. (1988). Direct Simulation of a turbulent boundary layer up to  $Re=1410$ , *J. Fluid Mechanics*, Vol 187, pp. 61-98
- Spalding, D.B. (1972). A novel finite difference formulation for differential expressions involving both the first and second derivatives, *J. Numerical Methods Eng.*, Vol 4, pp. 551-559
- Wallin, S. & Johansson, A. (2000). An Explicit Algebraic Reynolds Stress Model for Incompressible and Compressible Turbulent Flows, *J. Fluid Mechanics*, Vol 403, pp. 89-132
- Wilcox, D.C. (1988). Reassessment of the Scale-Determining Equation for Advanced Turbulence Models, *AIAA Journal*, Vol 26, pp. 1299-1310
- Wilcox, D.C. (1993). Comparison of Two-Equation Turbulence Models for Boundary Layers with Pressure Gradient, *AIAA Journal*, Vol 31, pp. 1414-1421
- Yang, Z. & Shih, T.H. (1993). New Time Scale Based k- $\epsilon$  Model for Near-Wall Turbulence, *AIAA Journal*, Vol 31, pp. 1191-1198
- Yap, C.R. (1987). *Turbulent heat and momentum transfer in recirculation and impinging flows*, Ph.D. Thesis Dept. of Mech. Eng., Faculty of Technology, Univ. of Manchester

# Semi Analytical Analysis of Steady State Condition of Steam Generator

Zaki Su'ud

*Nuclear Reactor Research Group, Bandung Institute of Technology,  
Jl. Ganesha no 10, Bandung  
Indonesia*

## 1. Introduction

Steam generator is an important device in power plant. Steam generator use the heat to produce steam which then used to drive turbine for producing electricity. Various thermal related processes occurs in steam generator during its normal operation and also during abnormal or accident condition. Therefore perfect treatment of steam generator will include various complex mathematical model which need computational fluid dynamics. However in this chapter we will simplify the model which still give reasonable results. There are many types of steam generators. Figure 1 shows an example of counter flow type steam generator in which hot liquid flow outside the cylinders from top to the bottom while the water-steam flows inside the pipes from the bottom to the top of the steam generator.

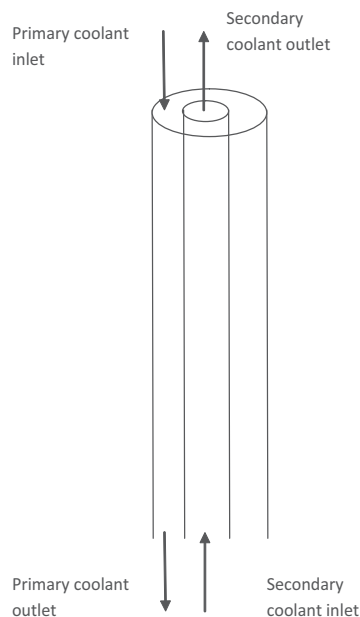


Fig. 1. Simplified schematic of counter flow heat exchanger

## 2. Mathematical model

The mathematical model of steam generators includes energy conservation equations, momentum conservation equations, and mass conservation equations.

### 2.1 Energy conservation equations

$$\begin{aligned}
 c_{p,p}W_p \frac{\partial T_p}{\partial z} - A_p \frac{\partial}{\partial z} \left( k_p \frac{\partial T_p}{\partial z} \right) &= -h_p S_p (T_p - T_W) \\
 -\pi(r_{w0}^2 - r_{wi}^2) \frac{\partial}{\partial z} \left( k_w \frac{\partial T_w}{\partial z} \right) &= h_p S_p (T_p - T_W) - h_s S_s (T_W - T_s) \\
 c_{p,s}W_s \frac{\partial T_s}{\partial z} - A_s \frac{\partial}{\partial z} \left( k_s \frac{\partial T_s}{\partial z} \right) &= -h_s S_s (T_W - T_s)
 \end{aligned} \tag{1}$$

### 2.2 Momentum conservation equation

$$\begin{aligned}
 \frac{\partial}{\partial z} \left( \frac{G_p^2}{\rho_p} \right) &= -\frac{\partial p_p}{\partial z} - \frac{f_p}{2\rho_p} D_p |G_p| G_p - \rho_p g \\
 \frac{\partial}{\partial z} \left( \frac{G_s^2}{\rho_s} \right) &= -\frac{\partial p_s}{\partial z} - \frac{f_s}{2\rho_s} D_s |G_s| G_s - \rho_s g
 \end{aligned} \tag{2}$$

### 2.3 Mass conservation equation

$$\begin{aligned}
 \frac{\partial G_p}{\partial z} &= 0 \\
 \frac{\partial G_s}{\partial z} &= 0
 \end{aligned} \tag{3}$$

## 3. Analytic solution of stead state condition of steam generator

In steam generators, liquid in the primary side is in single phase condition while the liquid in the secondary side change from sub cooled condition, then saturated condition, and then entering super heated steam condition in the last stage.

We will first discuss the analytical solution for single phase counter flow heat exchanger system. The results will be used to analyse some part of steam generator segments.

### 3.1 Analytical solution of counter flow single phase heat exchanger

Energy conservation equations for single phase counter flow heat exchanger is

$$\begin{aligned}
 c_{p,p}W_p \frac{\partial T_p}{\partial z} - A_p \frac{\partial}{\partial z} \left( k_p \frac{\partial T_p}{\partial z} \right) &= -h_p S_p (T_p - T_W) \\
 -\pi(r_{w0}^2 - r_{wi}^2) \frac{\partial}{\partial z} \left( k_w \frac{\partial T_w}{\partial z} \right) &= h_p S_p (T_p - T_W) - h_s S_s (T_W - T_s) \\
 c_{p,s}W_s \frac{\partial T_s}{\partial z} - A_s \frac{\partial}{\partial z} \left( k_s \frac{\partial T_s}{\partial z} \right) &= -h_s S_s (T_W - T_s)
 \end{aligned} \tag{4}$$

If the wall is thin and has good heat conduction capability we can simplify the model by eliminating the wall and include its effect in the overall heat transfer coefficient.

$$\begin{aligned} c_{p,p}W_p \frac{\partial T_p}{\partial z} - A_p \frac{\partial}{\partial z} \left( k_p \frac{\partial T_p}{\partial z} \right) &= -h_{eff}S_p(T_p - T_s) \\ c_{p,s}W_s \frac{\partial T_s}{\partial z} - A_s \frac{\partial}{\partial z} \left( k_s \frac{\partial T_s}{\partial z} \right) &= -h_{eff}S_s(T_p - T_s) \end{aligned} \quad (5)$$

Where  $h_{eff}$  is overall heat transfer coefficient from primary side to secondary side including the effect of the wall.

In normal condition, usually the effect of heat conduction is small so that we can further simplify the model into:

$$\begin{aligned} c_{p,p}W_p \frac{\partial T_p}{\partial z} &= -h_{eff}S_p(T_p - T_s) \\ c_{p,s}W_s \frac{\partial T_s}{\partial z} &= -h_{eff}S_s(T_p - T_s) \end{aligned} \quad (6)$$

In this stage we set the analytic solution of the above model as

$$\begin{aligned} T_p(z) &= Ae^{kz} + Be^{-kz} \\ T_s(z) &= Ce^{kz} + De^{-kz} \end{aligned} \quad (7)$$

Substituting equation (7) into (6) we get

$$\begin{aligned} A &= \frac{h_p S_p}{kc_{p,p}W_p + h_p S_p} C \\ B &= \frac{h_p S_p}{h_p S_p - kc_{p,p}W_p} D \end{aligned} \quad (8)$$

And,

$$\begin{aligned} h_{eff}^2 S_p S_s &= (kc_{p,p}W_p + h_{eff}S_p)(kc_{p,s}W_s + h_{eff}S_s) \\ k &= \frac{1}{c_{p,p}W} + \frac{1}{c_{p,s}W} \end{aligned} \quad (9)$$

Now we apply boundary condition:

$$\begin{aligned} T_p(0) &= T_{p_{in}} \\ T_s(H) &= T_{s_{in}} \end{aligned} \quad (10)$$

And we get

$$\begin{aligned} A + B &= T_{p_{in}} \\ Ce^{kH} + De^{-kH} &= T_{s_{in}} \end{aligned}$$

Substituting A,B, C and D we get

$$\begin{aligned}
C &= \frac{T_{p,in}e^{-kH} - \eta_2 T_{s,in}}{\eta_1 e^{-kH} - \eta_2 e^{kH}} \\
D &= \frac{\eta_1 T_{s,in} - T_{p,in}e^{kH}}{\eta_1 e^{-kH} - \eta_2 e^{kH}} \\
\eta_1 &= \frac{h_{eff} S_p}{kc_{p,p} W_p + h_{eff} S_p} \\
\eta_2 &= \frac{h_{eff} S_p}{h_{eff} S_p - kc_{p,p} W_p} \\
A &= \eta_1 C \\
B &= \eta_2 C
\end{aligned} \tag{11}$$

### 3.2 Analytical solution of counter flow steam generator

In steam generator we can in general divide it into three regions: sub cooled region, saturated region, and super heated region, see figure 1. In sub cooled region the water-steam side is in the form of water and the steam generator can be treated using the method developed in section 2.1

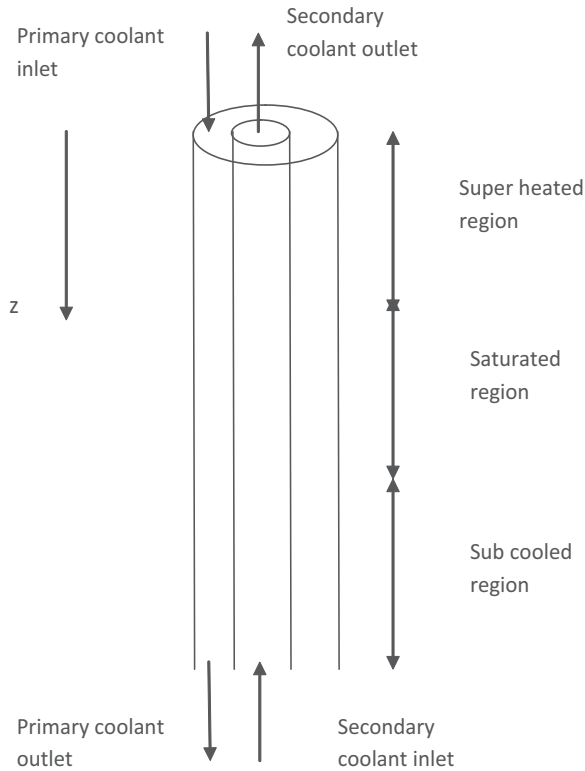


Fig. 2. Simplified model of single channel concentric tubes

In saturated region the water-steam side of SG experiences boiling process, a conversion of water into steam at constant temperature. After all water has been converted into steam then in the super heated section the water-steam side is in the form of steam which experiences temperature increase as it receive heat from the primary side. In this region we can also apply the method developed in section 2.1.

The boundary position between sub cooled region and saturated region and between saturated region and superheated region are influenced by many parameters such as inlet temperature of primary and secondary sides, flowrates in primary and secondary sides, thermal properties of primary and secondary sides, pipes properties, etc. Therefore we use iterative method to determine these boundary positions.

The method to determine these boundary positions is as follows. First we guess these two boundaries and based on these assumption we perform energy balance analysis for this simplified model.

Then we start with upper part in which the primary inlet temperature is  $T_{p_{in}}$  and while the secondary inlet temperature is just water saturation temperature. Using the formulated in 2.1 we get primary and secondary temperature distribution. From this stage we get primary outlet temperature.

Next we move to the saturated region. Based on the just previous calculation we use the previous primary outlet temperature as primary inlet temperature in saturated region. The secondary inlet temperature is water-steam saturated temperature in which the water is started to boil. From this stage of calculation we get primary and secondary temperature distributions.

Finally we can set primary site inlet temperature for the sub cooled region from the primary outlet temperature in the saturated region. The secondary outlet temperature in the subcooled region is just the water channel inlet temperature. Therefore we can get temperature distribution for the sub cooled region and therefore we now get for all regions.

Now we must check energy balance consistency in sub cooled and saturated regions. First we check whether or not the heat received by secondary side in the sub cooled region is exactly same with that needed to change the intake sub cooled water to the start of saturation condition.

In case that the heat from the primary side is not enough to increase the sub cooled temperature into saturated temperature then we need to shift the assumption of boundary between sub cooled and saturated regions to be higher than the current position. On the other hand if the saturated condition of water-steam side has been reached before the current sub cooled - saturated regions then we should decrease the boundary.

Similar judgment must be taken for boundary between saturated and super heated regions. For the saturated region, the energy balance equation can be written as

$$\begin{aligned}
 c_{p,p}W_p \frac{\partial T_p}{\partial z} &= -h_{eff}S_p(T_p - T_s) \\
 c_{p,s}W_s \frac{\partial T_s}{\partial z} &= -h_{eff}S_s(T_p - T_s) \\
 T_s &= \text{saturated temperature}
 \end{aligned}
 \tag{12}$$

We can rearrange the equation (12) as

$$\begin{aligned}
 c_{p,p}W_p \frac{\partial T_p}{\partial z} + h_{eff}ST_p &= h_{eff}ST_s \\
 c_{p,p}W_p \frac{\partial T_p}{\partial z} e^{\alpha z} + h_{eff}ST_p e^{\alpha z} &= h_{eff}ST_s e^{\alpha z} \\
 \frac{d}{dz}(\beta T_p e^{\alpha z}) &= h_{eff}ST_s e^{\alpha z}
 \end{aligned} \tag{13}$$

where

$$\begin{aligned}
 \beta &= c_{p,p}W_p \\
 \alpha &= \frac{h_s S}{c_{p,p}W_p}
 \end{aligned} \tag{14}$$

Solving (13) we get

$$T_p(z) = T_s + \frac{C}{\beta} e^{-\alpha z}$$

Introducing boundary condition  $T_p(0)=T_{P0}$  then we get

$$T_p(z) = T_s + (T_{P0} - T_s) e^{-\frac{h_s S}{c_{p,p}W_p} z}$$

where C is a constant.

Note that z is assumed started at the boundary between saturated and super heated region.

For the sub cooled region as in super heated region we can use the method describe in the section of 2.1.

### 3.3 Algorithm and program for semi analytical method of steam generator analysis

The algorithm to solve counter flow steam generator system is as follows

- Set an assumption of boundary between sub-cooled region and saturated region and also between saturated region and super heated region.
- Calculate temperature distribution in the superheated region using the method described in the section 2.1 and using inlet primary liquid temperature as  $T_{p,in}$  and water saturated temperature as secondary side inlet temperature
- Calculate temperature distribution along primary side of saturated region using the method describe in the section 2.2 using primary side outlet temperature of super heated section as primary inlet temperature
- Calculate temperature distribution in the sub-cooled region using the method described in the section 2.1 and using primary side outlet temperature of saturated region as  $T_{p,in}$  and water inlet temperature secondary side inlet temperature
- Check consistency of the assumed boundary. Is secondary side in sub-cooled region reach transition between sub-cooled and saturated region at the end of this region? Is secondary side of saturated region reaches transition between saturated region and super heated region at the end of this region?



- f. If the consistency check in e. is fail then we have to readjust the assumption considering the results in e, other wise the boundaries are right and the calculation is finished.  
Here the program in Fortran language to solve this problem.

For initialization process:

```

c
c This subroutine is to calculate thermohydraulic of Steam Generator
c using semi analytical method
c
  subroutine semansg
  INCLUDE "common1.f"
  write(6,*)'enter anasg routine:tp,ts',tpin,tsin
  astp=ssgs
  psys=psyst
  tsat=temsw(psys)-273.15
  enthfl=entw(psys)
  enthgs=entstv(psys)
  enthfg=enthgs-enthfl
  tpout=tsin
  tsout=tpin
  mxz=maxsub+maxsat+maxsph
  mx2=maxsub+maxsat
  gp=wp
  gs=ws
  tsin=tsin0
c
c superheated region preparation, setting parameters
c
  tsin=tsat
  tpav=(tpin+tsat)/2.0
  tsav=(tsout+tsat)/2.0
  tpsav=(tpav+2.0*tsav)/3.0
  hshv=entshv(psys,tsav)
  cpp=cpc(tpav)
  cps=cpsv(hshv,psys)
  cpp1=cpp
  cps1=cps
  diam=2.0*ro
  a1=3.0**0.5/4.0*pitcsg**2-3.14159*diam**2/8.0
  pw1=3.14159*diam/2.0
  dep=4.0*a1/pw1
  de=dep
  des=2.0*ri
  rep=gp/asgp*dep/visc(tpav)
  prp=visc(tpav)*cpc(tpav)/conc(tpav)
  pecp=rep*prp

```

```

pod=pitcsg/diam
xnusp=7.55*pod-6.3/pod**(17*pod*(pod-0.81))
xnusp=xnusp+0.0174*(1.0-exp(-6.0*(pod-1.0)))*(pecp-200.0)**0.9
hpp=xnusp*conc(tpav)/dep
res=gs/asgs*des/visshv(hshv,psys)
prs=visshv(hshv,psys)*cpshv(hshv,psys)/conshv(hshv,psys)
xnus=0.024*res**0.8*prs**0.4
hss=0.5*xnus*conshv(hshv,psys)/ri
hmt=2.0*3.14159*conm(tpsav)/alog(ro/ri)
u=1.0/(1.0/hpp+1.0/hss+astp/hmt)
u1=u
tmp1=-6.28*ro*u*ztsg*(1.0/(gs*cps)-1.0/(gp*cpp))
tmp2=-6.28*ro*u*(1.0/(gs*cps)-1.0/(gp*cpp))
tsin=tsat
aa=(tpin-tsin)/(exp1(tmp1)-gp*cpp/(gs*cps))
bb=tpin-(tpin-tsin)/(1.0-gp*cpp/(gs*cps)/exp1(tmp1))
bb1=tsin-gp*cpp/(gs*cps)*aa

```

```

c
c   saturated region preparation, setting parameters
c

```

```

tpav=(tsgp(mx2)+tsat)/2.0
tsav=tsat
tpsav=(tpav+2.0*tsav)/3.0
cpp=cpc(tpav)
cpp2=cpp
rep=gp/asgp*dep/visc(tpav)
prp=visc(tpav)*cpc(tpav)/conc(tpav)
pecp=rep*prp
pod=pitcsg/diam
xnusp=7.55*pod-6.3/pod**(17*pod*(pod-0.81))
xnusp=xnusp+0.0174*(1.0-exp(-6.0*(pod-1.0)))*(pecp-200.0)**0.9
hpp=xnusp*conc(tpav)/dep
hmt=2.0*3.14159*conm(tpsav)/alog(ro/ri)
u2=1.0/(1.0/hpp+astp/hmt)

```

```

c
c   subcooled region preparation, setting parameters
c

```

```

tpav=(tsgp(maxsub)+tsin0)/2.0
tsav=(tsgp(maxsub)+tsin0)/2.0
tpsav=(tpav+2.0*tsav)/3.0
tsub=(tsin0+tsat)/2.0
hsbw=entsbw(psys,tsub)
cpp=cpc(tpav)
rep=gp/asgp*dep/visc(tpav)
prp=visc(tpav)*cpc(tpav)/conc(tpav)
pecp=rep*prp

```

```

pod=pitcsg/ diam
xnusp=7.55*pod-6.3/pod**(17*pod*(pod-0.81))
xnusp=xnusp+0.0174*(1.0-exp(-6.0*(pod-1.0)))*(pecp-200.0)**0.9
hpp=xnusp*conc(tpav)/dep
cpp3=cpp
cps3=cpw(hsbw,psys)
res=gs/asgs*des/visw(hsbw,psys)
prs=visw(hsbw,psys)*cpw(hsbw,psys)/conw(hsbw,psys)
xnus=0.024*res**0.8*prs**0.4
hss=0.5*xnus*conw(hsbw,psys)/ri
hmt=2.0*3.14159*conm(tpsav)/alog(ro/ri)
u3=1.0/(1.0/hpp+1.0/hss+astp/hmt)

```

The following iteration routine is used to calculate temperature distribution across steam generators iteratively until the consistency check become successful.

```

c
c  searching routine
c
  tsgpa=tsat
  tsgsa=tsat
  tsgpb=tsat
  tsgsb=tsat
  tsgpo=tsin
  tsgso=tpin
  aboun0=aboun
  bboun0=bboun
  numblp=0
c
c  super heated region -> iteration
c
50 tsin=tsat
  tpav=(tpin+tsgpb)/2.0
  tsav=(tsgso+tsat)/2.0
  tpsav=(tpav+2.0*tsav)/3.0
  cpp1=cpc(tpav)
  hshv=entshv(psys,tsav)
  cps1=cpshv(hshv,psys)
  cpp=cpc(tpav)
  cps=cpshv(hshv,psys)
  cpp1=cpp
  cps1=cps
  rep=gp/asgp*dep/visc(tpav)
  prp=visc(tpav)*cpc(tpav)/conc(tpav)
  pecp=rep*prp
  xnusp=7.55*pod-6.3/pod**(17*pod*(pod-0.81))
  xnusp=xnusp+0.0174*(1.0-exp(-6.0*(pod-1.0)))*(pecp-200.0)**0.9

```

```

hpp=xnusp*conc(tpav)/dep
res=gs/asgs*des/visshv(hshv,psys)
prs=visshv(hshv,psys)*cpshv(hshv,psys)/conshv(hshv,psys)
xnus=0.024*res**0.8*prs**0.4
hss=0.5*xnus*conshv(hshv,psys)/ri
hmt=2.0*3.14159*conm(tpsav)/alog(ro/ri)
u1=1.0/(1.0/hpp+1.0/hss+astp/hmt)
write(6,*)'tpav,tsav,xnus,hpp,hss,hmt,u1:'
write(6,*)'tpav,tsav,xnus,hpp,hss,hmt,u1

```

c

c saturated region -> iteration

c

```

tpav=(tsgpa+tsgpb)/2.0
tsav=tsat
tpsav=(tpav+2.0*tsav)/3.0
cpp2=cpc(tpav)
rep=gp/asgp*dep/visc(tpav)
prp=visc(tpav)*cpc(tpav)/conc(tpav)
pecp=rep*prp
pod=pitcsg/diam
xnusp=7.55*pod-6.3/pod**(17*pod*(pod-0.81))
xnusp=xnusp+0.0174*(1.0-exp(-6.0*(pod-1.0)))*(pecp-200.0)**0.9
hpp=xnusp*conc(tpav)/dep
hmt=2.0*3.14159*conm(tpsav)/alog(ro/ri)
u2=1.0/(1.0/hpp+astp/hmt)
write(6,*)'tpav,tsav,xnus,hpp,hmt,u2:'
write(6,*)'tpav,tsav,xnus,hpp,hmt,u2

```

c

c subcooled region -> iteration

c

```

tpav=(tsgpo+tsgpa)/2.0
tsav=(tsat+tsin0)/2.0
tpsav=(tpav+2.0*tsav)/3.0
tavsb=(tsin0+tsat)/2.0
hsbw=entsbw(psys,tavsb)
cpp3=cpc(tpav)
cps3=cpw(hsbw,psys)
res=gs/asgs*des/visw(hsbw,psys)
prs=visw(hsbw,psys)*cpw(hsbw,psys)/conw(hsbw,psys)
xnus=0.024*res**0.8*prs**0.4
hss=0.5*xnus*conw(hsbw,psys)/ri
cpp=cpc(tpav)
rep=gp/asgp*dep/visc(tpav)
prp=visc(tpav)*cpc(tpav)/conc(tpav)
pecp=rep*prp
xnusp=7.55*pod-6.3/pod**(17*pod*(pod-0.81))

```

```

xnu sp=xnu sp+0.0174*(1.0-exp(-6.0*(pod-1.0)))*(pecp-200.0)**0.9
hpp=xnu sp*conc(tpav)/dep
hmt=2.0*3.14159*conm(tavsb)/log(ro/ri)
u3=1.0/(1.0/hpp+1.0/hss+astp/hmt)
write(6,*)'tpav,tsav,xnus,hss,hpp,hmt,u3:'
write(6,*)tpav,tsav,xnus,hss,hpp,hmt,u3
tmp1=-6.28*ro*u1*(ztsg-bboun)*(1.0/(gs*cps1)-1.0/(gp*cpp1))
tmp2=-6.28*ro*u1*(1.0/(gs*cps1)-1.0/(gp*cpp1))
aa1=(tpin-tsav)/(exp1(tmp1)-gp*cpp1/(gs*cps1))
bb1=tpin-(tpin-tsav)/(1.0-gp*cpp1/(gs*cps1)/exp1(tmp1))
tsgpb=(tpin-tsav)/(exp1(tmp1)-gp*cpp1/(gs*cps1))+bb1
tmpsat=6.28*ro*u2/(gp*cpp2)*(bboun-aboun)
tsgpa=tsav+(tsgpb-tsav)*exp1(-tmpsat)
tmp3=-6.28*ro*u3*aboun*(1.0/(gs*cps3)-1.0/(gp*cpp3))
tmp4=-6.28*ro*u3*(1.0/(gs*cps3)-1.0/(gp*cpp3))
aa3=(tsgpa-tsin0)/(exp1(tmp3)-gp*cpp3/(gs*cps3))
bb3=tsgpa-(tsgpa-tsin0)/(1.0-gp*cpp3/(gs*cps3)/exp1(tmp3))
tsgsa=(tsgpa-tsin0)/(exp1(tmp3)-gp*cpp3/(gs*cps3))*
&      gp*cpp3/(gs*cps3)*exp1(tmp4*aboun)+bb3
hqq=(tsgpb-tsav)*gp*cpp2*(1.0-exp1(-tmpsat))/gs
aa=(tsgpa-tsin0)/(exp1(tmp3)-gp*cpp3/(gs*cps3))
bb=tsgpa-(tsgpa-tsin0)/(1.0-gp*cpp3/(gs*cps3)/exp1(tmp3))
zzz=0.0
tsgpo=(tsgpa-tsin0)/(exp1(tmp3)-gp*cpp3/(gs*cps3))*
&      exp1(tmp4*zzz)+bb
aa=(tpin-tsav)/(exp1(tmp1)-gp*cpp1/(gs*cps1))
bb=tpin-(tpin-tsav)/(1.0-gp*cpp1/(gs*cps1)/exp1(tmp1))
zzz=ztsg
tsgso=(tpin-tsav)/(exp1(tmp1)-gp*cpp1/(gs*cps1))*
&      gp*cpp1/(gs*cps1)*exp1(tmp2*zzz)+bb
errp=1.0+errstd
errm=1.0-errstd
c
c Checking the consistency
c
c
c if (hqq.lt.errm*enthfg) then
c   if (tsgsa.gt.errp*tsat) then
c     aboun=aboun-daboun
c   else
c     bboun=bboun+dbboun
c   endif
c   if (tsgsa.lt.errm*tsat) then
c     aboun=aboun+daboun
c   endif
c endif

```

```

if (hqq.gt.errp*enthfg) then
  if (tsgsa.gt.errp*tsat) then
    aboun=aboun-daboun
    bboun=bboun-dbboun
  else
    bboun=bboun-dbboun
  endif
endif
endif
c
c If all consistent then finish, otherwise readjust the boundary between
c sub-cooled region and saturated region and between saturated region and
c super heated region
c
  if ((abs(tsgsa-tsats).lt.errstd*tsats).and.
& (abs(hqq-enthfg).lt.errstd*enthfg)) goto 90
  if ((abs(hqq-enthfg).lt.errstd*enthfg).and.
& (tsgsa.gt.errp*tsats)) aboun=aboun-daboun
  if ((abs(hqq-enthfg).lt.errstd*enthfg).and.
& (tsgsa.lt.errm*tsats)) aboun=aboun+daboun
  if (aboun.lt.0.0) aboun=0.0
  if (bboun.lt.0.0) aboun=0.0
  if (aboun.gt.ztsg) aboun=ztsg
  if (bboun.gt.ztsg) bboun=ztsg
  numblp=numblp+1
write(6,*)'loop number :',numblp,maxlop
  if (numblp.gt.maxlop) goto 90
  if (numblp.eq.1) then
    tsgsao=tsgsa
    hqqo=hqq
    goto 50
  endif
  tcheck=(tsgsao-tsats)*(tsgsa-tsats)
  qcheck=(hqqo-enthfg)*(hqq-enthfg)
  if (numblp.eq.2) then
    tsgsao=tsgsa
    hqqo=hqq
    tcheco=tcheck
    qcheco=qcheck
    goto 50
  endif
  tcheco=tcheck
  qcheco=qcheck
  if ((tcheck.lt.0.0).and.(tcheco.lt.0.0)) then
    daboun=daboun/2.0
  endif
  if ((qcheck.lt.0.0).and.(qcheco.lt.0.0)) then

```

```

    dbboun=dbboun/2.0
endif
tsgsao=tsgsa
hqqo=hqq
goto 50
c
c After convergent calculate final temperature distribution across
c primary and secondary sides and also estimation of wall temperature
c distribution
c
90 max1=int(aboun/ztsq*mxz)
  if (zsg(max1+1).lt.aboun) max1=max1+1
  max2=int(bboun/ztsq*mxz)
  if (zsg(max2+1).lt.bboun) max2=max2+1
  aa=(tsgpa-tsin0)/(exp1(tmp3)-gp*cpp3/(gs*cps3))
  bb=tsgpa-(tsgpa-tsin0)/(1.0-gp*cpp3/(gs*cps3)/exp1(tmp3))
  do 60 i=1,max1
    zzz=zsg(i)
    tsgp(i)=(tsgpa-tsin0)/(exp1(tmp3)-gp*cpp3/(gs*cps3))*
&      exp1(tmp4*zzz)+bb
    tsgs(i)=(tsgpa-tsin0)/(exp1(tmp3)-gp*cpp3/(gs*cps3))*
&      gp*cpp3/(gs*cps3)*exp1(tmp4*zzz)+bb
    tsgm(i)=(tsgp(i)+tsgs(i))/2.0
c  write(6,*)i,zzz,tsgp(i),tsgs(i),tsgm(i)
60 continue
  do 70 i=max1+1,max2
    zzz=(zsg(i)-bboun)/(bboun-aboun)
    tsgp(i)=(tsgpb-tsata)*exp1(tmpsat*zzz)+tsata
    tsgs(i)=tsata
    tsgm(i)=(tsgp(i)+tsgs(i))/2.0
70 continue
  aa=(tpin-tsata)/(exp1(tmp1)-gp*cpp1/(gs*cps1))
  bb=tpin-(tpin-tsata)/(1.0-gp*cpp1/(gs*cps1)/exp1(tmp1))
  do 80 i=max2+1,mxz
    zzz=zsg(i)-bboun
    tsgp(i)=(tpin-tsata)/(exp1(tmp1)-gp*cpp1/(gs*cps1))*
&      exp1(tmp2*zzz)+bb
    tsgs(i)=(tpin-tsata)/(exp1(tmp1)-gp*cpp1/(gs*cps1))*
&      gp*cpp1/(gs*cps1)*exp1(tmp2*zzz)+bb
    tsgm(i)=(tsgp(i)+tsgs(i))/2.0
c  write(6,*)i,zsg(i),tsgp(i),tsgs(i),tsgm(i)
80 continue
  i=1
  write(6,*)i,zsg(i),tsgp(i),tsgs(i),tsgm(i)
  i=mxz
  write(6,*)i,zsg(i),tsgp(i),tsgs(i),tsgm(i)

```

```

    call pdrsg
100 format(i5,f8.2,2x,f12.4,2x,f12.4)
    return
end
c

```

This is the end of the program.

### 3.4 Examples of calculation results

In this example the primary side is lead-bismuth eutectic liquid metal while the secondary side is water-steam system. The system parameters are shown in the following table

Parameter	Value
Height (m)	4
Inner radius of pipe (cm)	1.1
Outer radius of pipe (cm)	1.25
Pipe pitch(cm)	4
Primary side flow rate (kg/s)	2250
Secondary side flow rate (kg/s)	30
Number of bundles	200
Secondary side inlet temperature (C)	225
Primary side inlet temperature (C)	510
System pressure( MPa)	7

Table 1. Steam generator parameters for calculation example

The calculation results is shown in the following figure



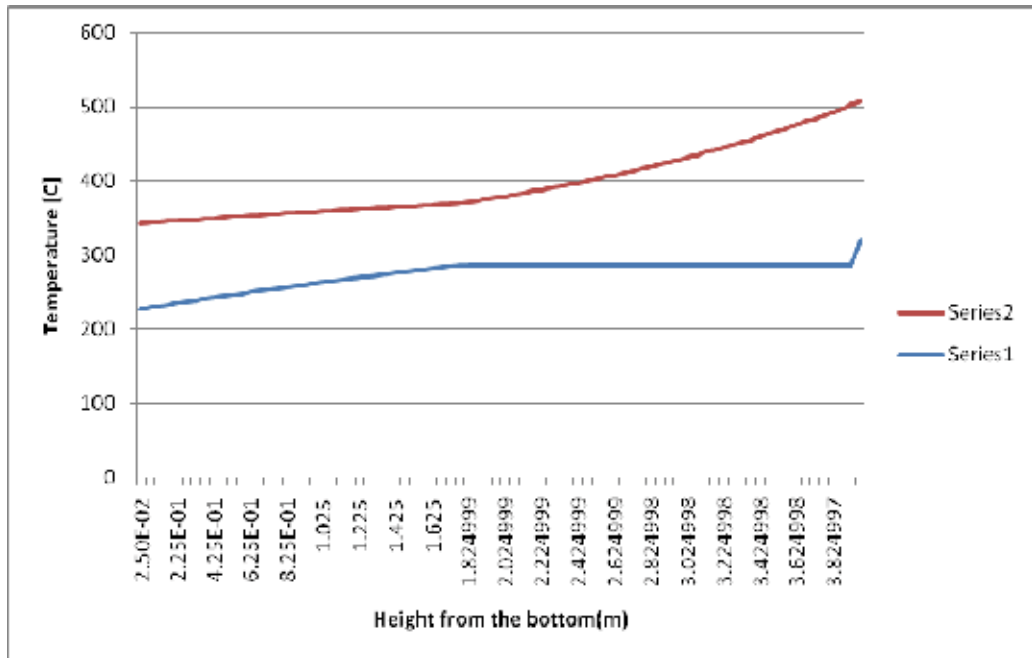


Fig. 3. Example of heat exchanger semi analytical analysis

### 3.5 Discussion and application

It is important to note that many thermal-hydraulic related constants for liquid metal Pb-Bi and water-steam system must be obtained and used during analysis. Such data can be obtained from references, e.g references number 1-5. In the program given in section 2.3 some thermal hydraulic constants are calculated using specific function such as

temsw(P) : to calculate water-steam system saturated temperature

entshv(psys,tsav): to calculate enthalphy of super heated vapour

cpc(tp):to calculate specific heat of primary coolant

conc(tp):to calculate thermal conductivity of primary coolant

visshv(hshv,psys): to calculate viscosity of super heated vapour

conshv(hshv,psys): to calculate thermal conductivity of super heated vapour

To calculate the pressure drop across the pipe inner and outer we can integrate the momentum balance equation. In general we have gravitational, friction, acceleration, and form related pressure drop components and we need specific correlation for friction and form pressure drop. To calculate this we can use the correlation from the references: 1,3,4,5. The data from the third reference is useful especially when we have the flow regime is in transition between laminar and turbulence.

The semi analytical analysis of steam generator in a certain level can be used for transient analysis of power system for example as long as the transient is relatively slow so that quasi-static approach can be adopted.

To get more accurate steam generator analysis we can use direct numerical solution of equations 1-3 and use the result of semi analytical analysis as initial guess of primary and

secondary side temperature distributions. In general the results from semi analytical analysis has good accuracy compared to that from direct numerical calculations.

#### 4. References

- [1] Kakac, S. et al. (1997) Handbook of Single-Phase Convective Heat transfer, John Wiley & Sons.
- [2] Raznjevic (1976) Handbook of Thermodynamic Tables and Charts, Hemisphere, Washington.
- [3] Cheng, S.K., Todreas, N.E., (1986) Hydrodynamic models and correlations for bare and wire-wrapped hexagonal rod bundles, *Nucl. Eng. Des.*, 92, 227.
- [4] Coffield, R.D., Markley, R.A., (1980), Natural convection analysis and verification for LMFBR cores, *Nucl. Eng. Des.*, 62, 181-198.
- [5] Guppy, J.G., (1993), Super System Code, NUREG/CR-3169.
- [6] Zaki S., Sekimoto, H. (1996), Accident Analysis of Lead or Lead-Bismuth Cooled Small Safe Long-Life Fast Reactor using Metallic or Nitride Fuel, *J. Nucl. Eng. And Design*, 162, Elsevier Science, 205-222.

## **Part 4**

# **Safety and Maintenance Management**



# Issues for Nuclear Power Plants Steam Generators

Lucia Bonavigo and Mario De Salve  
*Politecnico di Torino  
Italy*

## 1. Introduction

Steam Generators (SGs) are one of the big metal components in nuclear power plants. The function of Steam Generators is the removal of the thermal power generated into reactor core and its transfer to the secondary side of the tubes where secondary coolant flows. The preservation of the complete separation between the primary and secondary fluid is of capital importance in order to avoid radioactive contamination of secondary fluid and small loss of coolant also.

Mainly two designs have been developed for nuclear thermal power plants: vertical U-tubes with upstream and downstream flow for primary water, and horizontal steam generators. Also once through design can be found, but vertical U-tubes steam generators prevail.

A brief focus on operating life, of inspections and maintenance, and of water conditions is presented. Water conditions both at the primary and secondary side of the steam generator are of primary importance. During operating life, cooling radioactive contamination occurs, but water conditions must be maintained inside specific ranges. A typical PWR isotopic composition of contamination inside primary circuit components is presented. To avoid unwanted degradation of water conditions and of thermal exchange, specific inspections and interventions are applied.

Problems associated with Steam Generators in nuclear power plants are tube denting, wastage, thinning, corrosion, flow-induced vibrations, cracking and deformation of U-tube bend, or of support plates, tube leakage, fractures. We consider the case of a leakage, a rupture which would compromise the integrity of separation between radioactive and not-radioactive fluid, and the main symptoms and interventions.

The periodical inspections of SG have shown localized corrosion and mechanical wear problems on some SG tubes and degradation of SG lifetime (Bezdkian 2009). A replacement management program is necessary to achieve 40 years lifetime.

According to Wade (1995) in the United States 35 steam generators had been replaced in 12 plants and a list of 23 units are identified as potential candidates for steam generators replacement or shutdown.

When approaching end of life, decontamination and decommissioning of Steam Generators must be planned. Decommissioning is the end of life of a facility. It implies many issues: strategic, technological and scientific, measurement, environmental, legislation, and economic issues.

Finally, we focus just on Steam Generators degradation problem and decommissioning issues. We consider the step of radiological characterization and the characteristics of the available techniques for decontamination and cutting.

Steam Generators material should be managed with an eye toward reuse, recycling and clearance of all material and scrap. Steam Generators are typically the primary circuit components which the greater contaminated surface belongs. Decontamination can be performed by washing, heating, chemical or electrochemical action, mechanical cleaning, or other techniques.

## 2. Design of steam generators

The current status of the nuclear industry (2010) shows 441 nuclear power reactors in operation with a total net installed capacity of 374.692 GW(e), 5 nuclear power reactors in long term shutdown, 60 nuclear power reactors under construction (Power Reactors Information System, <http://www.iaea.org/programmes/a2/index.htm>).

The 2010 new connection to the grid are: Rostov 2 (950 MW(e), PWR-VVER (Pressurized Water Reactor Russian Design), Russia, (Rostov is a new official name of Volgodonsk reactor units); Rajasthan 6 (202 MW(e), PHWR (Pressurized Heavy Water Reactor), India; Lingao 3 (1000 MW(e), PWR, China; Qinshan 2-3 (610 MW(e), PWR, China; Shin Kori 1 (960 MW(e), PWR, S. Korea. Figure 1 shows their locations.

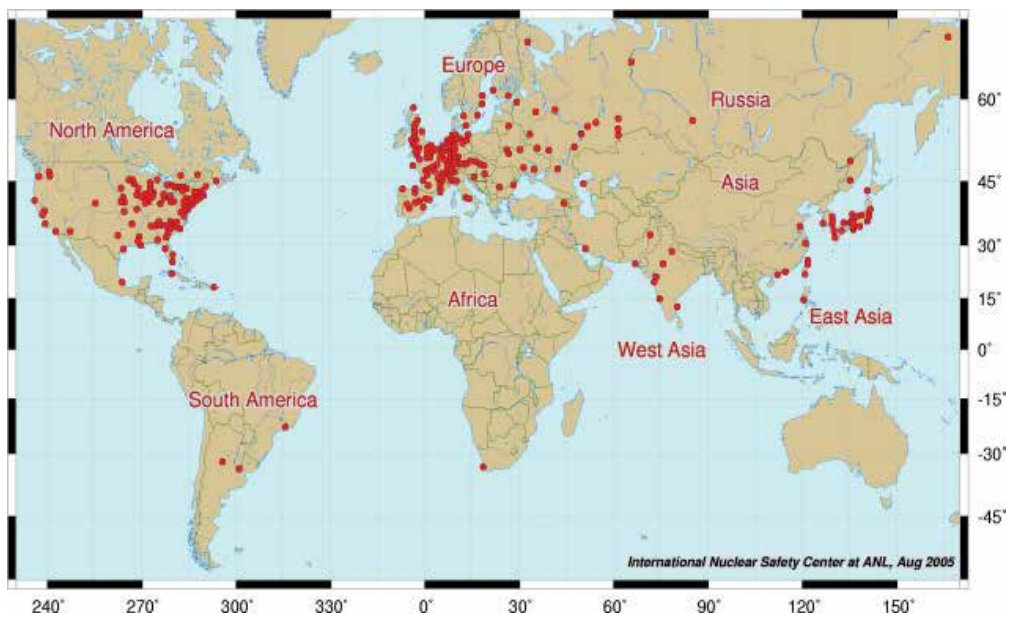


Fig. 1. Locations of Power reactors in the world (International Nuclear Safety Center, operated by DOE)

In the world there are 46 PHWR units for 22840 MWe power and 269 PWR units for 248295 MWe power.

In these plants Steam Generators raise very important issues about the design, the operation, the periodi inspections, the ageing management and the decommissioning.

In this chapter we will consider water reactors.

The function of Steam Generators (SG) in water reactors nuclear power plants is the heat transfer from the reactor cooling system, also called primary system, to the secondary side of the tubes which contain feedwater.

Primary coolant water receives heat passing through the core, then flows through the steam generator, where it transfers heat to the secondary coolant water to make steam (Green & Hetsroni, 1995). The steam then drives a turbine connected to an electric generator to produce energy.

The steam is then condensed and returns the steam generator as feedwater. PWR power plants have two, three or four SG and are called two-loop, three loop or four loop units. A general schematic view of a PWRs with 4 primar circuits is shown in figure 2. In contrast to a boiling water reactor (BWR), pressure in the primary coolant loop prevents the water from boiling within the reactor. In BWRs (Boiling Water Reactors), primary water produces steam directly, thus these concerns do not subsist anymore, and steam generators are not used.

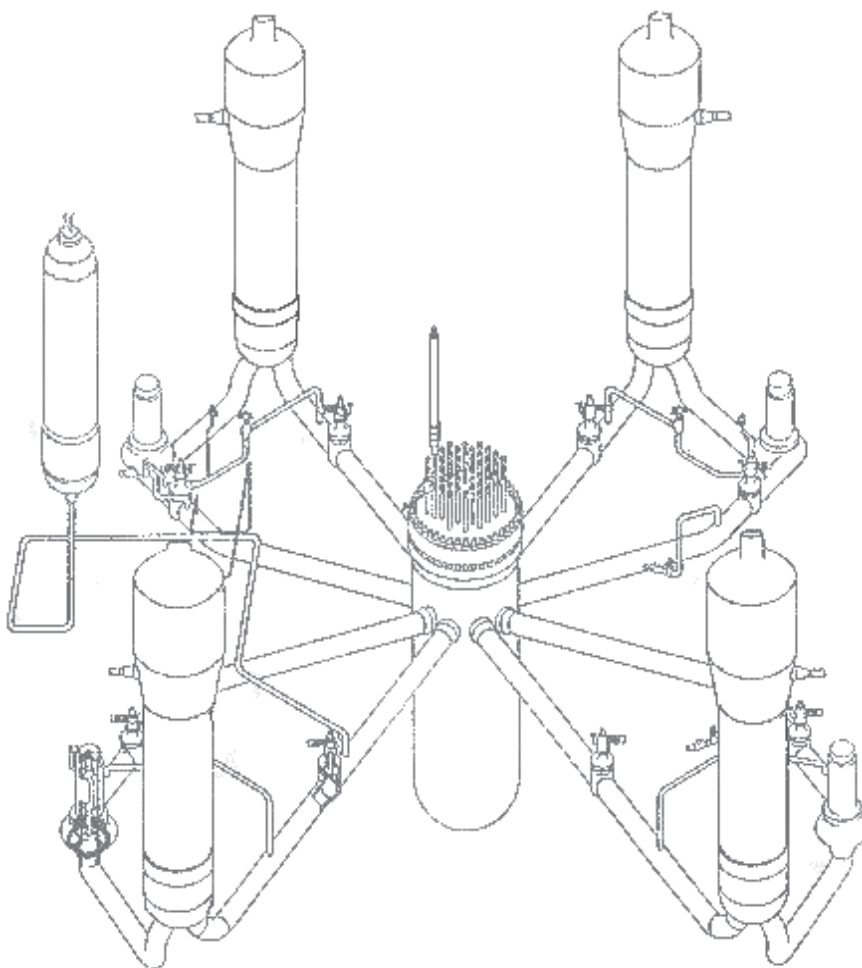


Fig. 2. General scheme of PWR primary circuit

Notice that the steam that flows from the steam generator must be pure and not contain any radioactive material, as it flows out of the containment structure. Conversely, the primary fluid does contain many radioactive material: the preservation of the complete separation between the two fluids is of capital importance. The integrity of tubes must be maintained. These tubes have an important safety role because they constitute one of the barriers between the radioactive and non-radioactive sides of the plant. For this reason, the integrity of the tubing is essential in minimizing the leakage of water between the two sides.

The integrity of the primary system must be assured in any case.

The steam generators may also contain a steam separation region.

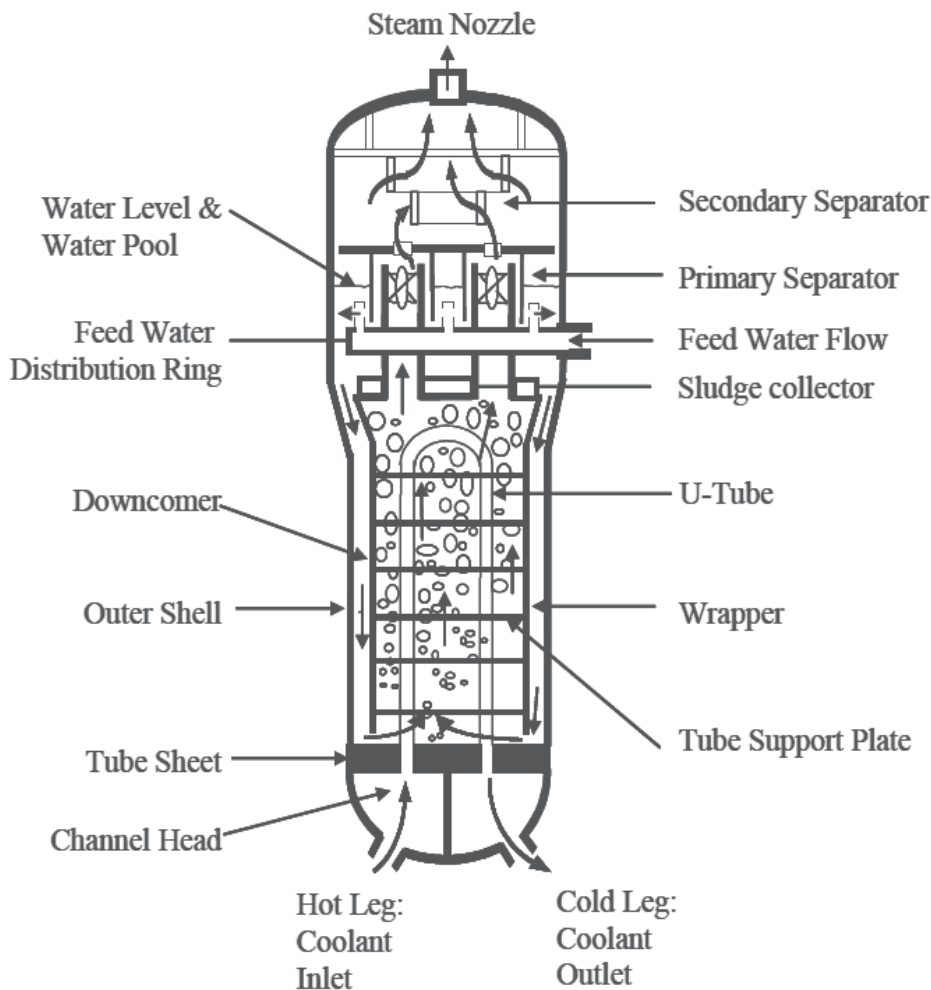


Fig. 3a. Schematic of a vertical PWR steam generator

Mainly two designs have been developed: vertical U-tubes with upstream and downstream flow for primary water (fig. 3a), and horizontal steam generators (fig. 3b). Also once through design can be found (fig. 3c).



In a horizontal design (fig. 3b) the steam generator have a horizontal cylindrical housing and horizontal coils. The steam is dried at the top of the housing by gravitational separation.

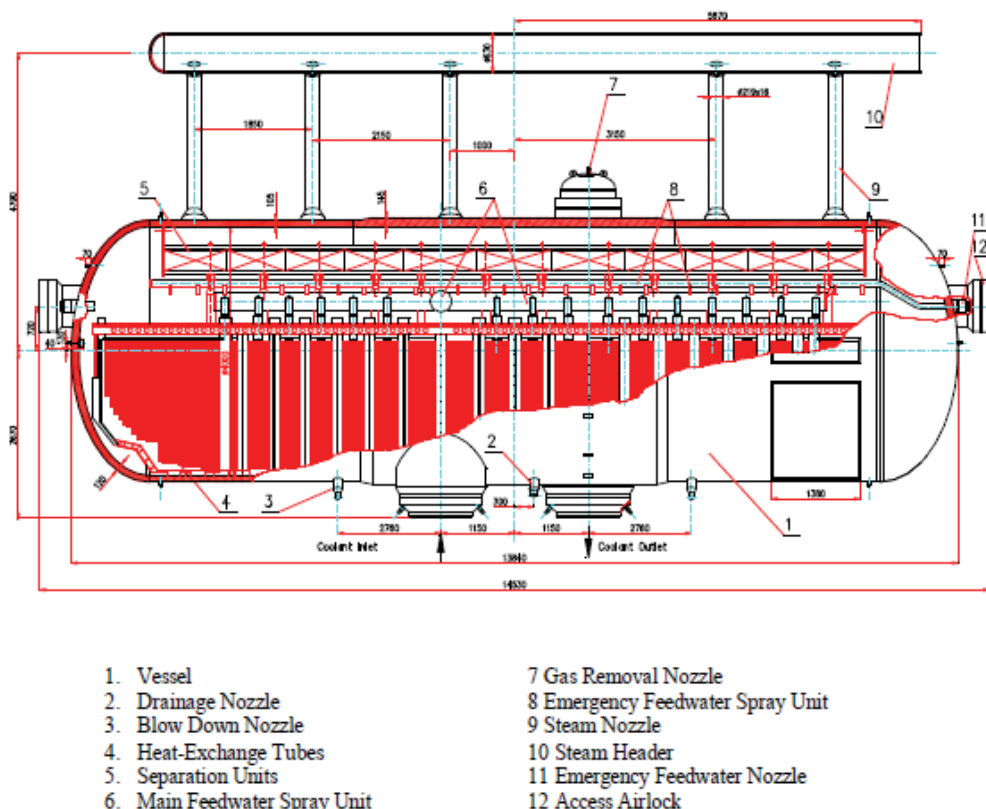


Fig. 3b. Typical Horizontal Steam Generator of the VVER-1000 Plant (Sánchez-Espinoza 2009)

In a once through design, the primary-side water enters at the steam generator at the top, flow through the generator in unbent tubes end exits at the bottom (fig. 3c).

According to the Power Reactor Information System (PRIS) of International Atomic Energy Agency (IAEA 2005) the steam generators of a power plant are described by the following data: type of SG (vertical, horizontal), steam output (saturated or superheated steam), number of steam generators (from two to six), number of drum separator (if present), tub shape (U tube or straight), tube material, SG shell material, drum separator shell material, design thermal capacity for single SG, design heat transfer surface.

Other important data, not present in PRIS database, are the nominal thermal power, the steam production rate, the steam pressure and temperature at the exit, the exit moisture content of the generated steam, the water store, the outer diameter of housing, and the hosing length. Important data of heat exchange of tubes are materials, number of tubes, average length, diameter, wall thickness, heat-exchange surface, metal mass without and with supports.

SG performance, degradation, lifetime and management program are strongly dependent of design data and operating experience.

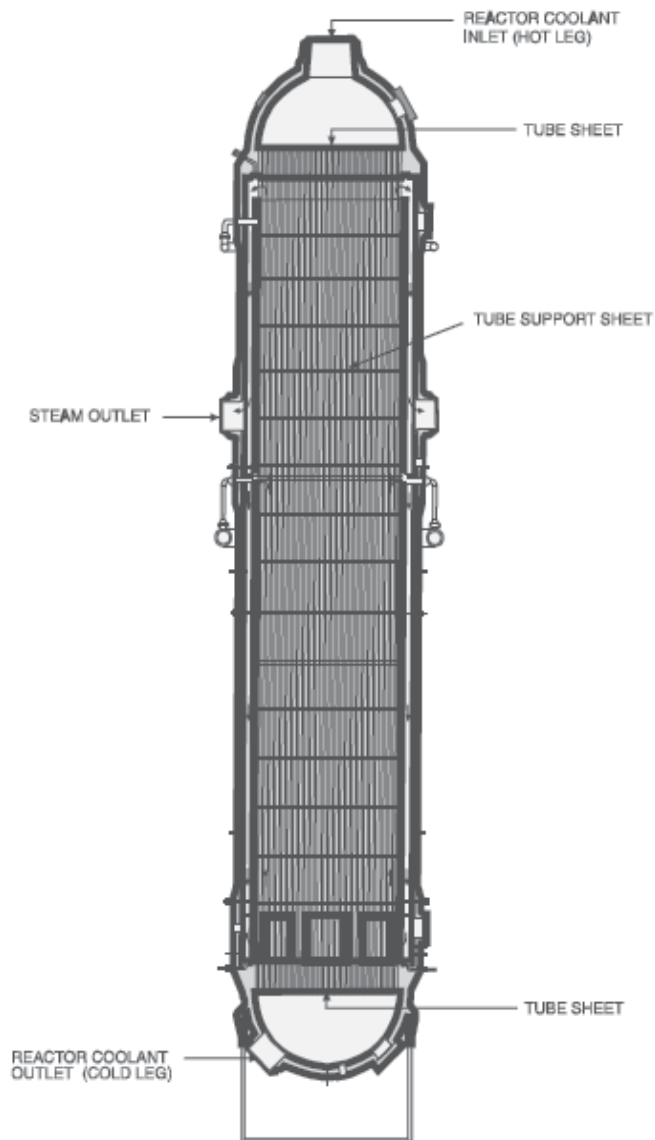


Fig. 3c. Typical Babcock & Wilcox Once through steam generator

The horizontal design is considered to be less susceptible to degradation than the vertical U-tube one. More specifically, the orientation of a tube has effects on boiling and on occurrence of boiling crisis causing differences on their behaviour to stress conditions (Merilo, 1977).

On the basis of operating experience gained over many years, horizontal steam generators have advantages over vertical steam generators, the main ones being (Trunov et al, 2008): moderate steam load (steam outflow rate from the evaporation surface 0.2–0.3 m/sec); simple gravity-based separation scheme;

- moderate velocity of the medium in the second loop (up to 0.5 m/sec), preventing any danger of vibrations of the heat-exchange tubes and damage from foreign objects;

- validated serviceability of the 08Kh18N10T austenitic steel tubes (the maximum operational age is 38 years for
- PGV-440 and 23 years for PGV-1000);
- vertical arrangement of the first-loop collectors, preventing accumulation of sludge deposits on their surfaces,
- thereby decreasing the danger of corrosion damage to the heat-exchange tubes in the region where the tubes are
- built into the tube sheet;
- larger store of water in the second loop, enabling cool-down of the reactor via the steam generator in the case where normal and emergency water feeding has stopped;
- the principle of stepped evaporation, making it possible to maintain an admissible concentration of dissolved impurities in the critical zones and increasing the reliability from the standpoint of corrosion effects;
- horizontal arrangement of the heat-exchange surface, enabling reliable natural circulation of the first-loop coolant even with a massive water level below the top rows of the heat-exchange tubes;
- convenient access to the tube sheet for servicing and checking from the first- and second-loop sides; there are no heat-exchange tubes at the bottom of the housing, so that sludge is more easily removed through the purge system;
- presence of equipment for disconnecting the collectors from the main circulation pipelines, making it possible to decrease the time required to perform scheduled-preventative maintenance work and to increase the installed capacity utilization factor by performing work simultaneously on several steam generators and refueling the reactor.

Mainly, vertical U-tubes steam generators are used. The steam generator consists of a heat exchange section and a steam drum section. The heat exchange section consists of a vertical, inverted U-tube bundle with the tube plate and the channel head. The steam drum portion consists of the internal moisture separating equipment and the enclosing pressure shell. In operation, primary coolant from the nuclear reactor vessel is circulated through the U-tubes. During this passage, the coolant gives off heat to the secondary water on the shell side of the steam generator, causing it to boil to steam. This steam, in turn, is passed through the moisture separating equipment in order to reduce the entrained moisture content and produce essentially dry steam.

## 2.1 Detailed description

Coolant enters the inlet nozzle from the reactor and circulates through the U-tubes and out of the outlet nozzle into the coolant pumps suction line. Heat is transferred through the walls of the tubes from the coolant, thus boiling the water on the shell side and generating steam.

Feedwater to the steam generator enters just below the normal water level and joins the water being recirculates as it flows downward to the bottom of the shell through the annular downcomer between the shell and the tube bundle wrapper. At the bottom of the active tube surface, this mixture of recirculated water and feedwater is introduced uniformly into the tube bundle. It then flows upward by natural convection through the bundle absorbing heat and leaves the top of the active tube surface as a steam water mixture. Moisture is separated from the mixture, essentially dry steam is discharged through the steam outlet nozzle.

Separation of liquid water from the steam-water mixture is done in the upper part of steam generators, and usually consists of three phases:

- Primary separation, normally done by means of centrifugal separators.
- Gravity separation, which occurs in the space between the primary separators and the driers.
- Secondary separation, normally done by means of corrugated shape separators, or driers.

The efficiency of steam separation and the pressure drop are the two most important features of steam separators.

The vessel shell consists of a barrel fabricated of carbon steel plate, welded to an hemispherical head of the same material. The shell or secondary side nozzles consist of the feedwater inlet nozzle, liquid level indicator and liquid level control connections, surface and bottom blowdown connections, shell drain connection, pressure test connection, steam sample connection, and steam offtake connection.

The tube plate consists of a carbon steel clad on the primary side with stainless steel, and contains holes whose number is the double of the number of tubes. In our case study the number of tubes is 1662. The tube plate separates the primary and secondary fluids and contains the U-tubes which extend into the secondary or shell side of the steam generator.

Many support plate designs are available (drilled, without flow holes, broached-trefoil, quatrefoil, egg-create...) (Green and Hetsroni, 1995).

The vertical steam generator is supported by means of a lower set of trunnions. The upper trunnions are provided for emergency support and may also be used for lifting purposes.

A general scheme of a U-tube vertical SG is shown in figure 3.

## 2.2 Operating phase

During a nuclear plant operation, cooling radioactive contamination is caused by the presence of:

- Fission products,
  - Uranium and Transuranium elements,
- (caused by fuel rod cladding insulation defects), as well as:
- fuel fission products,
  - Uranium and Transuranium elements,
- (originating from free Uranium particles which undergo fission outside fuel cladding), or finally from
- relevant fuel rod cladding insulation defects.

These may cause direct contact between primary coolant and fuel. The last two mechanisms are also called 'recoil phenomenon'.

Corrosion products may be:

- Corrosion products which have been activated while flowing through the reactor core.
- Activated corrosion products, which belong to corrosion of activated reactor materials.

All these materials create particular conditions for steam generators management, inspection, cleaning, maintenance, and decommissioning.

During operating phase, some precautions must be considered. For example, in the case of excessive carryover, correction should be made immediately or permanent damage to the turbine may result. This condition may be caused by either a high water level or a high solids concentration in the boiling water: correction may be either lowering the water level or blowing down.

The water level must be observed periodically, as well as temperature limitation to the steam side and the maximum heating or cooling rate to the primary coolant, all in concordance with the specific plant operating instructions.

Some of the observed material degradations for primary side SG are (Riznic 2009):

- Fatigue;
- Pitting;
- Stress corrosion cracking and intergranular attack (a form of corrosion occurring when the boundaries of crystallites of the material are more susceptible to corrosion than their insides);
- Fretting;
- Degradation of primary header divider plates;
- Tube plugs;
- SG tube magnetite build-up (degradation of thermal efficiency, and possible safety related impact on inspection capabilities);
- Presence of foreign materials.

The degradation of primary header divider plates doesn't lead to major safety impacts, but can lead to loss of thermal efficiency. Degradation permits hot reactor outlet header fluid to by-pass the tube bundle. An increase in reactor inlet header temperature has been observed.

When the primary header divider design is the 'segmented', or 'lap joint' designed (plate segments bolted to each other), leakage may occur:

- Around periphery between plate segments and seat bars;
- Between plate segments;
- Through bolt holes;
- Around corner filler blocks

When the primary header divider design is the welded floating plate designed (welded construction, no bolted lap joints), there are no leakage at bolted lap joints, but leakage still possible around periphery of the plate.

Geometry issues and magnetite in primary water may lead to flow assisted corrosion in carbon steel elements at periphery of plates. In any case, no significant degradation of this nature has been experienced to date.

A possible mitigation intervention is the application of Inconel overlays to segmented / lap joint divider plates on hot leg side, but this could lead to notable drop in reactor inlet header temperature (RIHT).

Concerning tube plugs, a general practice is to visually inspect Hot Legs and Cold Legs tube plug during outages. Leaking tube plug welds are normally identified during inspections. Tubes with poor plug welds could become pressurized and fail due to tube degradation if it progressed. This problem contributes to primary to secondary leakage if tube contained a leaking defect.

Tube fouling may lead to decrease in solubility of magnetite from in heavy water with decreased temperature, causing:

- Magnetite deposits in SG tubes;
- From a thermal performance perspective, increases in RIHT may occur;
- From a safety perspective, deposits can impact tube inspection capabilities (tubes may become obstructed preventing tool passage, and magnetite deposits may affect flaw detectability and sizing )

Foreign materials left in primary side of SGs could introduce scratches on tubes, and constitute a possible initiation sites for in-service degradation, so leading to possible damage to other primary side SG internals. Moreover, materials could be transported through the circuit and into reactor.

Some of the observed material degradations for secondary side SG are (Riznic 2009):

- Tube support degradation;
- Secondary side deposits and sludge piles;
- Foreign materials;
- Tube degradation mechanisms.

Tube supports made of carbon steel have been subject to a variety of degradation mechanisms, as:

- Under deposit corrosion and cracking or degradation of U-bend bar supports;
- Corrosion of tube support plates leading to tube denting and loss of tube support;
- Tube fretting at supports.

Secondary side deposits are associated to:

- Generally pitting at supports or along straight legs;
- Deposits contain higher concentrations of impurities than secondary side water and form crevices;
- Pitting observed at tube supports.

In this case, mitigation strategies include secondary side chemistry control, secondary side chemical cleaning and finally waterlancing. Waterlancing is a common SG cleaning technique; it is done routinely at many plants. It entails directing a high-pressure water jet between the tubes from the (central) tube-free lane. The jet oscillates in a vertical plane. It requires access through the shell and the downcomer shroud.

Foreign materials is associated to debris fretting. Sources of debris identified include:

- Welding electrodes;
- Wire;
- Screws;
- Gasket material

Some materials may have been left behind during construction.

It is known that degradation of the heat-exchange tubes in the steam generators in nuclear power plants with VVER reactors (Trunov et al. 2008) occurs during operation for the following reasons:

- the presence of copper-containing materials in the second loop, which, in the first place, makes it impossible to
- increase the pH of the feed water above 9.2 in order to reduce the amount of the products of corrosion of iron entering from the second loop to a minimum and, in the second place, results in deposits on the heat-exchange surfaces of the steam generators of, together with iron compounds, a substantial quantity of copper and its compounds and engenders local forms of corrosion;
- breakdown of the water-chemistry regime;
- ill-timed chemical laving;
- corrosion of the heat-exchange tubes in downtime regimes.

The defects which result in degradation of heat-exchange tubes include pitting, corrosion pits, and cracks of different depth and length, right up to through cracks.

### 2.3 Inspections and cleaning

Commercial PWR steam generators have experienced reliability problems within the first decade of operation associated with material degradation, one of the causes of which is particle deposition and tube fouling. As a result steam generators often require costly outages for inspection and cleaning of fouling deposits (Srikantiah & Chappidi, 2000).

In-service inspections are critical in maintaining steam generator tube integrity. The scope and frequency of these inspections vary from plant to plant based on each facility's operating experience. The purpose of inspection is to determine the condition of the apparatus and to locate any defects which may require repairs.

The components comprising separator, purifier, piping and drains may require servicing. Check all internal surfaces for corrosion or erosion and note unusual conditions is essential. Damage is often indicated by the presence of scale, grit, or other foreign matter.

Access to the inside of the primary channel may be accomplished by means of two manways. Prior to performing any work, the area around the steam generator should be carefully monitored to determine the radiation level. Workers and radiation field must be measured and controlled as stated by the Health Physics Department of the plant.

Other than inspection purpose, another repair work could be the plug leaking tubes.

During plant operation, the thickness of the tubes can be measured, in order to insulate those tubes which are affected by deterioration. Insulation consists in welding plugs on both sides of the U-tube.

Cleaning shall consist of the removal of slag, grease, paint or any other foreign matter when present. It is important to remove all organic materials since they would decompose and contaminate, and remove all particles of dust from heated surfaces. Cleaning must be extended at least to all heated surfaces. Various chemical and mechanical methods may be used (chemical methods, vapour cleaning, brushing...).

### 3. Water conditions

Water conditions both at the primary and secondary side of the steam generator are of primary importance.

Water conditions are intended to define the conditions under which the steam generator will operate properly. The condition of the boiling water should be tested by sampling at least once a day or as required by the operating instructions. The values of alkalinity and solids in excess of those specified may cause scaling of the steam generator tubes.

Feedwater must be maintained as free from impurities as possible. This requirement involves careful attention to the entire system through which the water flows, either in the form of steam or water, for even though water is used as feedwater be pure at the same time of its entry into the system, it may absorb impurities from the various parts of the installation. Specific attention should be directed to possible points of water leakage from the service water system, as in the main and auxiliary condensers. Feedwater must be treated to maintain the required water conditions.

The parameters to observe are, for the primary side:

- Impurity content, not considering the presence of inhibitors and chemical additives, which are necessary to the operation of the plant.
- Total dissolved solid, which is one of the causes of performance degeneration.
- pH.
- Hydrogen.
- Dissolved oxygen.

- Chlorides.
- Boric acid (with chemical shim<sup>1</sup> or without chemical shim).

The parameters to observe for the secondary side, are:

- Total dissolved solid.
- pH.
- Dissolved oxygen.
- Chlorides.

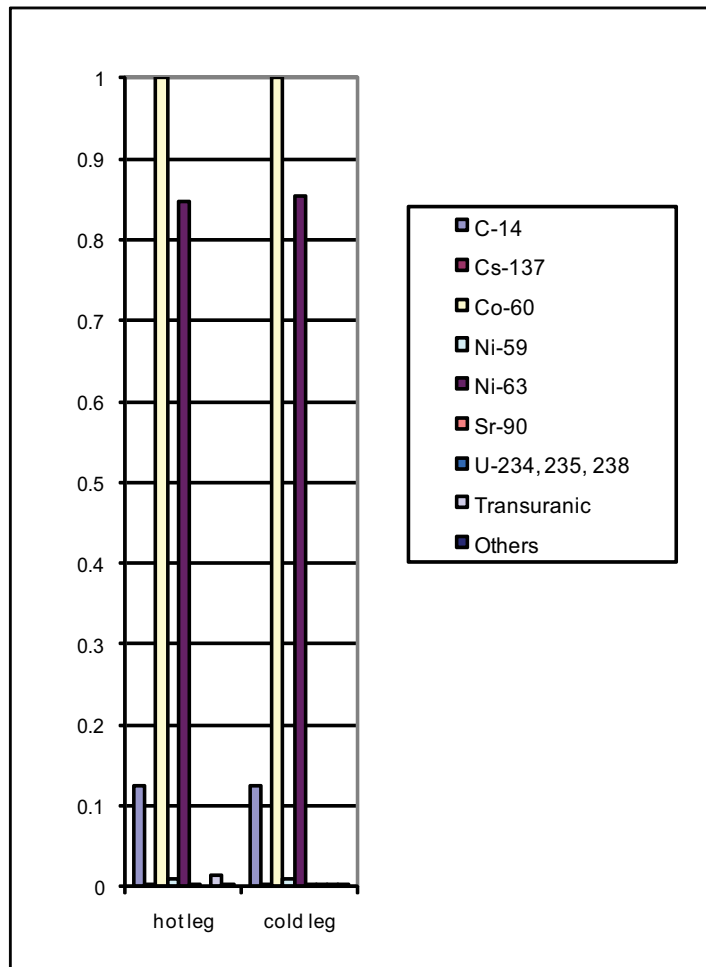


Fig. 5. Example of isotopic composition of contamination inside one of the steam generators of a decommissioned NPP

<sup>1</sup> The power level is controlled by control rods, temperature, and chemical shim. By chemical shim, we mean that boric acid is dissolved in the coolant/moderator. Boron-10 has a high neutron absorption cross-section and can be used to poison the chain reaction. If it is desired to increase power, then the boric acid concentration can be diluted, removing B-10 from the reactor core and decreasing its poisoning effect. Chemical shim is used in PWRs (Pressurized Water Reactors) and, to a small extent, in CANDUs. (Canada Deuterium-Uranium). Boric acid is not used in BWRs (Boiling Water Reactors).



Steam entering the main header from the steam offtake nozzle will have a moisture content not exceeding a determined value (usually a percentage of the steam flow under certain conditions, like constant power steam generation, or power increasing or decreasing up to a percent of full power).

In pressurised water reactor nuclear power plants it is necessary to filter corrosion products transported by the main flow, as well as radioactive particulate.

Activity must be controlled: fission products must be detected, as well as noble gases and iodines or activation products. Gamma spectra are acquired at many locations along the circuit. Gasborne activity is measured by means of coolant samples (e.g. fission gases isotopes of krypton and xenon). In the composition of primary coolant activity monitoring system, there are devices to detect Iodine volume activity. Isotopic composition of contamination inside primary circuit components comprises: C-14, Cs-137, Co-60, Ni-59, Ni-63, Sr-90, U-234, 235, 238, Transuranics, and, to a small degree, Nb-94, Cl-36, Tc-99, I-129 (figure 5).

For purifying primary coolant, ion exchange resins are utilised, as well as demineralizers.

Spent ion exchange resins constitute the most significant fraction of the wet solid waste produced at power reactors. They are wet solid waste arising during operation of a nuclear power plant.

The main wastes arising during the operation of a nuclear power plant are components which are removed during refuelling or maintenance (mainly activated solids, e.g. stainless steel containing cobalt-60 and nickel-63) or operational wastes such as radioactive liquids, filters, and ion-exchange resins which are contaminated with fission products from circuits containing liquid coolant. Powdered resins are used in PWRs, but are commonly used in BWRs with pre-coated filter demineralizers.

The make-up water for the steam generation system is similar to fossil fuel power plants: pre-treatment is followed by reverse osmosis system.

#### 4. Ruptures and maintenance

Problems associated with Steam Generators in nuclear power plants are tube denting (denting results from the corrosion of the carbon steel support plates and the corrosion product in the crevices between tubes and the tube support plates), wastage, thinning, corrosion, flow-induced vibrations, cracking and deformation of U-tube bend, or of support plates, tube leakage, fractures.

Considering a leakage, which would compromise the integrity of separation between radioactive and not-radioactive fluid, the main symptoms are:

- Low level alarm for primary circuit pressurizer.
- Low pressure alarm for primary coolant.
- Low level alarm for low pressure expansion tank.
- High level alarm for activity in steam generator purge line.
- High level alarm for activity in turbine condenser void pumps discharge line.
- High level alarm in the steam generator.
- Imbalance between steam flow and feedwater.

The Steam Generator should be then insulated, and the part of system discharged, when needed, and maintenance operations must be carried out.

When a certain percent of the tubes have been plugged as described above, heat transfer deteriorates too much and a final intervention is needed. Typically it requires up to 60 days to replace a Steam Generator.

Replacement of Steam Generators is a practice followed by nuclear power stations across the world to ensure longer life to the plant. During the 40 year initial license period of a power plant, normally steam generation replacement is not considered. To achieve license extension, and extend operating life, this practice has become of wide application all over the world. Some examples are the reactors of: Three Miles Island Unit 1 (U.S.A.), Angra 1 (Brasil).

Referring to French power plants, localized corrosion and mechanical problems are observed on some SG tubes (Bezdikian 2009). During the 80's, the thermal aging phenomenon was confirmed, so French Utility and the Manufacturer decided to take measurements to predict the metallurgical aging mechanism to assess for:

- 1st step 40 years evaluation,
- 2nd step 60 years prediction.

The objectives was to assess the ability of the cast elbows in existing plants to withstand continued and to maintain components in operating respect safety requirements. The strategy applied was to combined Elbows replacement with Steam Generators replacement. After studies based on economic and technical criteria, EDF set up a Steam Generator replacement program in compliance with the safety rules. These operations are classified into exceptional maintenance operations (all maintenance operations programmed nationally, on large number of NPPs usually carried out once during the lifetime of units), and have therefore significant cost and impact on availability. They are integrated in new routine maintenance program.

All units in study were classified into groups:

- Group 1. Units with SG affected by important degradations and Steam Generator replacement will be carry out in future;
- Group 2. Units with SG lifetime evaluation is with incertainties, evolution of degradations is unknown;
- Group 3. Units with SG Lifetime equal to Plant lifetime.

Before removal from the reactor building, all decommissioned SG openings are closed up by welding metal plates to make up sealed sources, and thereby preventing the release of contamination.

After removal, EDF adopted a standard building project suitable for all French sites, equipped with a concrete roof, walls from 50 to 80 cm thick, for environmentally-safe site storage. This building can accommodate the 3 decommissioned SG of a unit without causing any pollution of the air, water or soil, without generating any waste.

## 5. Decontamination and decommissioning of steam generators

When approaching end of life, decontamination and decommissioning of Steam Generators must be planned. Decommissioning is the end of life of a facility. It implies many issues: strategic, technological and scientific, measurement, environmental, legislation, and economic issues. In this chapter we focus just on Steam Generators decommissioning issues.

Steam Generators are one of the big metal components in decommissioning nuclear power plants. Their material should be managed with an eye toward reuse, recycling and clearance of all material and scrap (Anigstein et al., 2001; IAEA, 2004; IAEA 2000; NEA, 2008; Nieves et al, 1998).

Surface contamination and volume activity must be controlled.

When activity decreases below clearance levels, then legal constraints on material can be eliminated (IAEA, 2004; IAEA, 2000). Clearance levels are a set of requirements on radionuclides concentrations below which radioactive waste is no longer considered a radioactive hazard.

Levels for unrestricted release of material are not internationally harmonized, but in any case have to comply with radiation protection principles.

Clearance levels are recommended by EC (European Commission) and other international organizations. Although some cost-effective options to clearance exist, in the long term clearance is the best waste management choice internationally accepted (NEA, 2008).

When decontamination is possible and justified, metal material will undergo decontamination process in order to fit clearance levels or to reduce occupational exposure of workers, limiting potential releases and exposures, or to allow material reuse and make its management easier. The remaining metal will undergo the process of characterization as radioactive waste.

During the decommissioning of nuclear power plants large metallic components like steam generators (or reactor pressure vessels) play a relevant role. Depending on their radiological properties a disposal or a recycling is possible.

Different strategies are used. These strategies are planned considering economic costs, radiological protection or the site situation. A relevant aspect is the possible clearance of the waste material which can be achieved after decay storage if necessary or after a decontamination process.

Based on these conditions different strategies are resulting. Large components can be dismantled on site with the objective of a final storage. Another strategy is achieving the clearance of at least a part of the large components material.

This can typically be achieved by treatment of the fragmented or entire large components, eventually including decay storage before or after fragmenting.

Three main strategies for big metal components are usually considered:

- transport to an external treatment facility (option number 1)
- transport to an interim storage on site and treatment after decay (option number 2)
- in situ treatment (option number 3)

As an example of in situ treatment (option number 3) we can cite Gundremmingen nuclear power plant. The Steam Generators were filled with water, frozen and cut in situ by a band saw. The main advantage is that the pieces could be treated directly on site, avoiding the transport of heavy parts. On the other hand, it took a time of several years.

As an example of transport to an external treatment facility (option number 1) we can cite the Steam generator of the nuclear power plant Stade (Germany). They have been transported to Studvik Radwaste (Sweden) for: dismantling, melting and clearance of material. The large components are leaving the plant at an early stage, allowing the use of the empty place for the dismantling of other parts. Moreover, the decommissioning will be accelerated. In any case, the transport has to be planned very carefully, considering national law prescriptions, and it is cost intensive.

An example of transport to an interim storage on site and treatment after decay is the Decay storage of several reactor pressure vessels and steam generators in the interim storage Nord (Lubmin / Germany) (option number 2). The aim is to achieve the clearance of these components after cutting but without melting. In fact, the decay storage reduces the activity and allows an easier clearance of material without decontamination or other treatment. It

avoids component transport. This strategy is very sensitive for changes in clearance regulations during the decay time (Bauerfeind & Feinhals 2010).

### 5.1 Decontamination techniques

Decontamination is the removal of contamination from surfaces of facilities or equipment. It can be performed by washing, heating, chemical or electrochemical action, mechanical cleaning, or other techniques.

Decontamination is one of the main decommissioning activities. The objectives of decontamination are:

- reduce radiation exposure;
- reduce the volume of equipment and materials requiring radioactive waste management;
- remove loose radioactive contaminants and fix the remaining contamination in place in preparation for further activities;
- reduce the magnitude of the residual radioactive source.

Decontamination process will produce much secondary waste, thus a facility for secondary waste treatment is needed (processing chemical solutions, debris, etc...). Liquid waste and, in general, concentrated waste, must be solidified for disposal, or treated for waste reduction or recycling.

When a treatment is undertaken, there may be an increase in: occupational exposure rates, potential for a release or uptake of radioactive material. These may be higher than to those due to removing, packaging and disposal of the radioactive material without decontamination treatment. All interventions must be defined after an economic / technical / environmental assessment of treatment.

Prior to performing actions, the appropriate knowledge on the presence, kind and distribution of radioactivity inside the item should be known. This stage is the radiological characterization step.

Radiological characterization and radioactivity inventory for decommissioning purpose is an evaluation of systems internal contamination and activation in order to plan the best procedure of intervention.

Radiological characterization of a facility starts from the historical analysis of plant operating life and of conditions that could lead to accidental contaminations. Representative components for each system can be identified and the materials belonging to these systems can be grouped into: contaminated/ activated/not contaminated or activated.

This first classification is followed by dose rate measurement campaign and radiochemical analysis campaign on representative components in order to detect the level of specific contamination, its isotopic composition, and correlation factors between easily-measured radionuclides and other critical nuclides.

Dose rate measurements should be performed on each component, with radiometric survey to detect superficial removable contamination lying on outer surfaces. To evaluate the deposition of contamination on components inner surface, calculation codes are applied. SGs are typically the primary circuit components which the greater contaminated surface belongs.

A complete description of decontamination techniques may be found in literature (IAEA 2006, NEA 1999).

For our purpose, just a brief introduction to the available techniques will be presented. After that, a practical example will be provided.

Washing, swabbing, foaming, abrasive blasting, grinding, scarifying, are some examples of physical (mechanical) decontamination techniques. These last techniques are most applicable to the decontamination of structural surfaces. Usually give very high decontamination factors.

Decontamination factor is used to express the capability of a process to remove decontamination. It is defined as the ratio of radiation level of the material or component prior to the treatment, and the level of the same measured immediately after decontamination.

These techniques are not applicable for complicated surfaces.

Chemical decontamination is based on the use of chemical reagents in contact with the contamination layer to remove, in this case, to dissolve. Generally, the process may be continued or repeated until the required decontamination factor is achieved, taking care of the material involved. Chemical decontamination is often carried out by circulating the selected reagents in the system, while segmented parts may be decontaminated by immersing them into the reagent. Application of specific chemical decontamination depends on many factors, e.g., complexity of shape and dimensions of the item to be treated, kind and characteristics of the chemical reagents, type of material and contamination, availability of proper process equipment, and so on. It may be mild or aggressive, which involves the dissolution of the base metal.

Chemical flushing is recommended for remote decontamination of intact piping systems. It is also suitable for use on complex geometries as well as for a uniform treatment of piping surfaces. These techniques, however, require efficient recycling of reactive chemicals.

Compliance with basic health and safety practices regarding chemical agents is required, in addition to the radiological safety aspects. As a minimum, workers – suitably trained - will be equipped with the proper DPI (individual protection devices) such as glasses, full-body protective coveralls, impermeable gloves and foot covers.

Additional safety equipment depends on the toxicity of contaminants.

When a chemical decontamination is assisted by an electrical field, we speak about an electrochemical decontamination. It usually involves the immersion of the item in electrolyte bath or using a pad. The electric current causes an anodic dissolution and removal of metal and oxide layer from the surface in treatment. It may be only applied to conductive surfaces.

Melting may also be considered as a decontamination method, although generally limited by specific national law constraints. It homogenizes a number of radionuclides in the ingots and concentrating others in the slag. It is used often for complex geometries, avoiding the problem for inaccessible surfaces.

Also many hybrid technologies between those cited above are in use (Kinnunen 2008).

## 5.2 Dismantling techniques

A wide range of dismantling techniques, both mechanical and thermal, are developed and tested during decommissioning of plants (IAEA 1999; Cumo et al., 2002; Eickelpasch et al., 1997; Klein et al., 2001; Steiner et al., 1997), often supported by European Community research programmes. There is a large variety of dismantling techniques that are state of the art and in use.

They can be grouped into mechanical (sawing, shearing, milling, diamond wire sawing, pipecutting...), usually used for activated component cutting, thermal (oxy-fuel cutting, lance cutting, plasma-arc cutting, laser beam cutting...) and hydraulic (water jet cutting, abrasive water jet cutting).

Technique	Applicability	Secondary emissions	Underwater Cutting	Specific hazards	Cost	Remote operated handling
Oxy-fuel cutting	Steel, mild steel, low alloys. It cuts a max. thickness greater than 2000 mm	Hot oxides, fumes, aerosols	Yes, with reduced cutting speed	Preheating flame and hot oxide ejected from the cutting zone	Low	Yes
Lance cutting	All kind of material (reinforced concrete and thermal resistant materials included). It cuts a max. thickness of 2000 mm of concrete	Gaseous and solid products, dust	Yes, but the lance must have been lighted before	High gaseous emissions, fumes and solid products ejected from the cutting zone	Low	No
Plasma cutting	All conductive materials (ferrous and not ferrous). It cuts a max. thickness of 170 mm of stainless steel.	Gaseous products and dust	Yes	Fire hazard, electric discharge, brightness, gas and fumes emission	Medium	Yes
Laser	All kind of material. It cuts a max. thickness of 110 mm of stainless steel	Gaseous products and dust	Yes	Laser beam, fumes and aerosols	Medium-high	Yes
Water jet	Many kinds of material, also sandwiches of different compositions. It cuts a max. thickness of 1 mm of steel	Fluid products and dust	Yes, but performances are reduced	Effluents should be collected and treated	High	Yes
Mechanical	All kind of material. It cuts a max. thickness greater than 2000 mm	Scraps, burrs, dust	Yes	Noise and vibrations	Medium-high	Yes

Table 1. Characteristics of some main cutting techniques

Table number 1 proposes a classification of cutting techniques for metal for decommissioning purposes. A complete description of these techniques may be found in literature (EPRI, 2008; EPRI, 2007; EPRI, 2005; EPRI, 2001; EPRI, 2000).

Also many hybrid technologies between those cited above are in use. An interesting example is the case of the dismantling of the SG in unit A at Gundremmingen nuclear power plant (Germany) (Steiner et al. 1997). To perform this segmentation, the use of thermal cutting would cause a large amount of radioactive and metal aerosol, moreover it is performed in direct contact with the item, thus exposing the operator to a high radiation field. The presence of non-fixed single tubes excludes the application of a sawing machine. The tube bundle would vibrate excessively. The solution chosen for this cutting is called the 'ice sawing technique'. The heat exchanger has been filled up with water on the secondary side and the whole component has been freezed down to about  $-20^{\circ}\text{C}$  by blowing cold air through the primary side. After freezing it has been possible to cut through the whole component by a suitable band saw. The advantages of this technique are: reduction of the local dose rate, fixing of the heat exchangers tubes, minimizing the aerosol generation during cutting phase, cooling of the saw blade.

Waste will contain radionuclides with different radio-toxicity levels (radio-toxicity classes are set by Italian law in the *Decreto Ministeriale del 27 luglio 1966*). Radio-toxicity is the potential capacity to cause harmful effects on living tissues because of radionuclide inhalation, ingestion or intake by skin and wounds. Radio-toxicity level is influenced by the kind of radiation, its energy, physical and biological half time, radio-sensibility of tissue or organ. The greater part of radionuclides present in decommissioning waste belongs to high radio-toxicity classes of nuclides.

Contamination spread as consequence of metal cut can normally be overcome by the use of individual radioprotection devices and devices for protection of respiratory track, as emissions retaining rooms, filtering systems, masks, gloves and suits (Bonavigo et al. 2009).

## 6. Conclusion

Steam Generators are one of the main components in nuclear systems. Their management poses many issues.

The steam that flows from the Steam Generator must be pure and not contain any radioactive material, as it flows out of the containment structure. The primary fluid contains many radioactive material: the preservation of the complete separation between the two fluids is of capital importance. In this chapter we considered the issue of contamination of secondary system and we analysed how to preserve the separation between the two fluids, considering the main kind of inspections and maintenance, and the kind of interventions which are applied.

An interesting observation is that life of nuclear power plants all over the world is approaching its end. The goal of license extension is cost effective and postpones all decommissioning operations, and new plant construction. Typically, extension is 20 years. In the U.S.A., more of the half of the plants have applied for, or are in the process of applying for, license extensions for another 20 years under the NRC's License Renewal Rule. License extensions for existing power plants are considered as crucial to the nation's ability to maintain a continuous supply of cost-effective energy as the nuclear energy industry transitions to the next generation of nuclear power plants. Often, the substitution of some

components may be applied in order to achieve this task, inside the refurbishment process. Steam Generators are the main component to which this concept refers.

When approaching end of life, decontamination and decommissioning of Steam Generators must be planned. During the decommissioning of nuclear power plants large metallic components like steam generators (or reactor pressure vessels) play a relevant role. Depending on their radiological properties a disposal or a recycling is possible.

We considered some different approaches to this issue, showing European examples.

The step of radiological characterization should be broadened to ensure the best operation planning and material management.

We considered the main issues concerning decontamination and cutting of this metal component.

We focused on some possible techniques.

In any case, reuse, recycle and clearance of material are key-concepts and should always be applied. They are stressed by all international institutions concerning nuclear installations safety and radioprotection.

High decontamination factors may be achieved. On the other hand, contamination spread as consequence of metal cut can be overcome by the use of individual radioprotection devices and devices for protection of respiratory track, as emissions retaining rooms, filtering systems, masks, gloves and suits.

## 7. References

- Anigstein R., Thurber W. C., Mauro J. J., Marschke S. F., and Behling U. H. (2001), Potential Recycling of scrap metal from nuclear facilities. *U.S. Environmental Protection Agency EPA Technical Support Document*, Washington D.C.
- Bauerfeind M., Feinhals J. (2010) The Disposal of Large Components Strategies TÜV NORD SysTec GmbH & Co. KG, report for IAEA, available online.
- Bezdekian G. (2009), Steam Generators and heavy components replacement strategy in French NPPs, *IAEA Technical Meeting Heavy components Replacement on NPPs*, Lynchburg Virginia May 26 - 28, 2009.
- Bonavigo L., De Salve M., Annunziata D., Zucchetti M., (2009) Radioactivity release and dust production during the cutting of the primary circuit of a nuclear power plant. The case of E. Fermi NPP, *Progress in Nuclear Energy* 2009, Vol. 52, pagine da 359 a 366, ISSN: 0149-1970.
- Cumo M., Tripputi I., Spezia U. (2002), *Nuclear Plants Decommissioning* - Università di Roma La Sapienza - Scuola di Specializzazione in Sicurezza e Protezione, Roma.
- Eickelpasch N., Kalwa H., Steiner H., Preismeyer U. (1997), The application of mechanical and thermal cutting tools for the dismantling of activated internals of the reactor pressure vessel in the Versuchsaatomkraftwerk, Kahl and the Gundremmingen Unit A. *Nuclear Engineering and Design* 170, 175-182.
- EPRI (2008), Rancho Seco Reactor Vessel Segmentation Experience Report. *Electric Power Research Institute EPRI Final Report* 1015501.
- EPRI (2007), Reactor Internals Segmentation Experience Report: Detailed Experiences 1993 – 2006. *Electric Power Research Institute EPRI Final Report* 1015122.
- EPRI (2005), Maine Yankee Decommissioning- Experience Report: detailed Experiences 1997- 2004. *Electric Power Research Institute EPRI Final Report* 1011734.



- EPRI (2001), Decommissioning: Reactor Pressure Vessel Internals Segmentation. *Electric Power Research Institute EPRI Final Report 1003029*.
- EPRI (2000), Decommissioning Technology Experience, *Electric Power Research Institute EPRI Final Report 1000884*.
- Green S. J., Hetsroni G. (1995). PWR steam generators. *International Journal of Two-phase flow*, 12, Suppl. Pp. 1-97.
- IAEA (2006), Management of Problematic Waste and Material Generated During the Decommissioning of Nuclear Facilities. *International Atomic Energy Agency IAEA Technical reports series*, ISSN 0074-1914 ; no. 441
- IAEA (2005), The Power Reactor Information System (PRIS) and its extension to non electrical applications, decommissioning and delayed projects information, *Technical Reports Series no. 428*.
- IAEA (2004), Practical Use of the concepts of exclusion, exemption and clearance. *International Atomic Energy Agency IAEA Safety Standards Series No. RS-G-1.7*, Vienna.
- IAEA (2000), Practical Use of the Concepts of Clearance and Exemption, Guidance on General Clearance Levels for Practices. *International Atomic Energy Agency IAEA Radiation Protection series 122*, Vienna.
- IAEA (1999), Decommissioning of Nuclear Power Plants and Research Reactors. *International Atomic Energy Agency IAEA Safety Standards Series No. WS-G-2.1*, Vienna.
- Kinnunen P. (2080) ANTIOXI Decontamination techniques for activity removal in nuclear environments EURATOM FP6 Programme RESEARCH REPORT NO VTTR0029908 12.3.2008
- Klein M., Dadoumont J., Demeulemeester Y., Massaut V. (2001), Experience in decommissioning activities at the BR3 site. *Fusion Engineering and Design* 54, 443-449.
- Merilo, M. (1976). Critical heat flux experiments in a vertical and horizontal tube with both freon-12 and water as coolant. *Nuclear Engineering and design*, 44, Issue 1, Pp. 1-16.
- NEA (1999) *Decontamination Techniques Used in Decommissioning Activities*, Nuclear Energy Agency NEA Report of the Task group on decontamination, available on web.
- NEA (2008), Release of radioactive material and buildings from regulatory control. *Nuclear Energy Agency NEA N. 6403*, ISBN 978-92-64-99061-6.
- Nieves L. A., Chen S. Y., Kohout E. J., Nabelssi B., Tilbrook R. W. and Wilson. S. E. (1998), Analysis of Disposition Alternatives for Radioactive Contaminated Scrap Metal. *Journal of the Franklin Institute* 335, (6), 1089-1103.
- Power Reactors Information System, <http://www.iaea.org/programmes/a2/index.htm>
- Sánchez-Espinoza V. (2009), Investigations of the VVER-1000 Coolant Transient Benchmark with the Coupled Code System RELAP5/PARCS, *Report NUREG/IA-0217*.
- Srikantiah G., Chappidi P. R. (2000). Particle deposition and fouling in PWR steam generators. *Nuclear Engineering and Design*, 200, Pp. 285-294.
- Steiner H., Eickelpash N., Tegethoff H. (1997), Experience with the dismantling of three secondary steam generators in unit A in Gundremmingen by the ice-sawing technique. *Nuclear Engineering and Design* 170, 165-173.
- Stiepani C., Bertholdt H. (2005) Full system decontamination with HP/CORD UV fot decommissioning of the german PWR Stade, *Proceedings of the 18th International Conference on Structural Mechanics in Reactor Technology (SMiRT 18)* Beijing, China, August 7-12, 2005 SMiRT18-W02-7

- Trunov N.B., Lukasevich B.I., Veselov D.O.; Yu Dragunov G. (2008), Steam generators- Horizontal or Vertical (which type should be used in nuclear power plants with VVER ?), *Atomic Energy*, vol. 105, No. 3.
- Riznic J. (2009), Steam Generator Ageing Management in Canada - current practices and related Issues. *IAEA Consultancy Meeting on Ageing Management of Steam Generators*, IAEA, June 15-18, 2009, Vienna.
- Kennect Chuch Wade K. C. (1995), Steam generator degradation and its impact on continued operation of pressurized water reactors in the United States, *Energy Information Administration/Electric Power Monthly*.

# Shielding Analysis of the Secondary Coolant Circuit of Accelerator Driven Systems

Toshinobu Sasa and Hiroyuki Oigawa  
*Japan Atomic Energy Agency  
Japan*

## 1. Introduction

Disposition of radioactive waste is one of the key issues to make nuclear energy as a sustainable power resource for future power generation. To solve this issue, a long-term program for research and development on partitioning and transmutation called “OMEGA” (Options Making Extra Gains from Actinides and fission products) was adopted in 1988 by the Japan Atomic Energy Commission (Japan Atomic Energy Commission, 2009). The aims of the OMEGA Program are to widen options for future waste management and to explore the possibility to utilize high-level radioactive wastes as useful resources. To proceed the OMEGA program, partitioning and transmutation (P-T) is a key technology to reduce environmental impacts and source terms contained in the high level radioactive waste which was discharged from commercial nuclear power reactors. By using partitioning technology, the long-lived radioactive nuclides such as minor actinides (MAs) and long-lived fission products (LLFPs) can be extracted from high level radioactive waste. From the mass balance study performed under the OMEGA program, the lifetime of final disposal site can be prolonged 3 to 10 times more than current designed lifetime (Oigawa, et al. 2005). Under the framework of the OMEGA program, Japan Atomic Energy Agency (JAEA) has proposed a double-strata fuel cycle concept (Takano, et al. 2000) which consists of two fuel cycles; one is a commercial fuel cycle including current LWR cycle and also future FBR fuel cycle and the other is a small fuel cycle dedicated to the transmutation of MA and LLFP. By the double-strata fuel cycle shown in Fig. 1, long-lived radioactive nuclides are confined into the second-stratum small fuel cycle that includes an innovative nuclear system which is optimized to the transmutation of MA and LLFP. JAEA carries out research and development of accelerator-driven transmutation systems (ADS) as an innovative dedicated transmutation system under the OMEGA Program.

In the P-T, the most effective reaction to transmute MA separated from high level radioactive waste by partitioning process into short-lived/stable nuclides is fission reaction. By fission reaction, target MA nuclides can be directly transmuted into short or stable nuclides. However, to make fission reaction as dominant reaction in the nuclear reactor, the reactor core should be formed a fast neutron spectrum field. It requires rather large fuel inventory and diminishes some safety characteristics such as Doppler coefficient and delayed neutron fraction. Another point of view, MA discharged from current light water power reactors is roughly composed of 55% of neptunium, 40% of americium and 5% of

curium. Each nuclide has several difficulties to handle within the current fuel cycle because of their own physical/chemical characteristics. Neptunium requires special separation processes at reprocessing because the chemical properties of neptunium are similar to those of uranium and plutonium. Americium and curium can be easily separated from the other actinides but have several problems related to their physical properties such as decay heat release and particle emission. These nuclides also give the chemical instability, namely the low vapor pressure of americium which harms the soundness of burnup fuel pellet properties. It means that it is not easy to stabilize americium and curium in MOX type fuel (Sasa, et. al, 2009). From these reasons, JAEA proposes the dedicated transmutation system instead of the transmutation by commercial nuclear power reactors to keep the safety requirements and cost effectiveness of the commercial reactors.

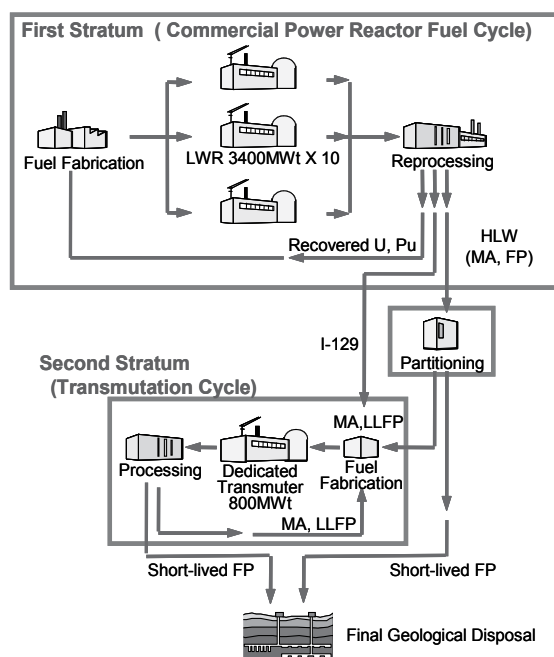


Fig. 1. Double-strata fuel cycle concept

ADS is one of the innovative nuclear systems that is a hybrid system composed of a high-intensity proton accelerator and a subcritical fast core. By using a subcritical core, the safety issues caused by the characteristics of MA can be compensated. However, to realize the ADS, there are some technical problems such as stable operation of accelerator, interface components between an accelerator and a reactor core, properties of MA fuels, adoption of liquid metal coolant, and so on (Sugawara, et al., 2009). This chapter mentions the issues related to the radiation protection from irradiated components installed in the tank-type subcritical core of a JAEA-proposed lead-bismuth cooled ADS.

## 2. Outline of ADS

Figure 2 shows a conceptual view of a JAEA-proposed ADS. MA is extracted from the spent fuel of commercial reactors and used as a dominant fuel component for ADS.

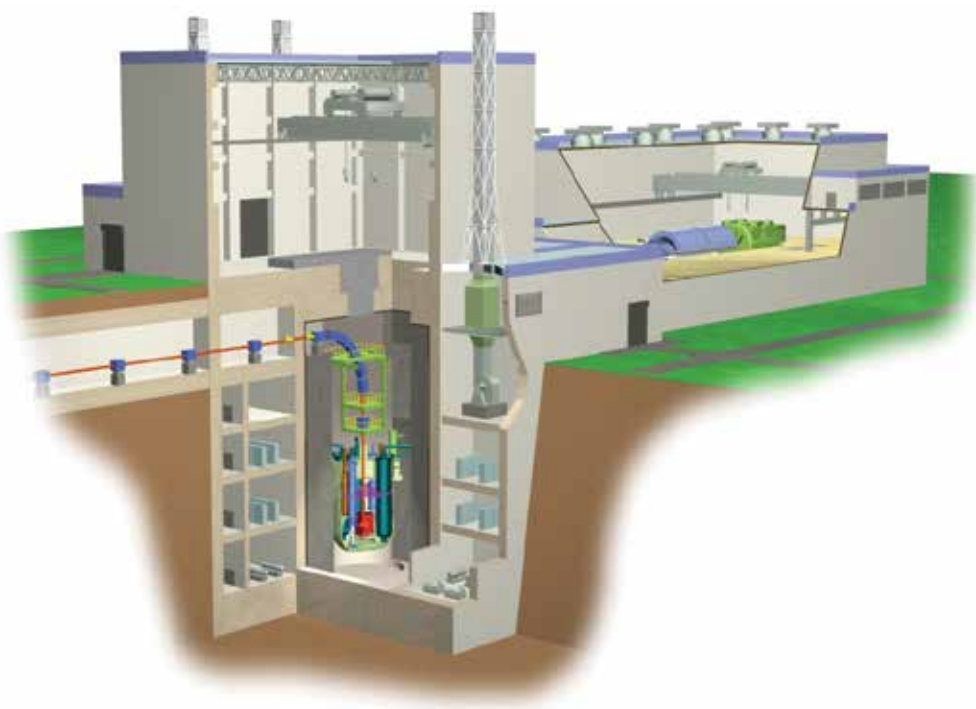


Fig. 2. Conceptual view of ADS plant

The system is mainly composed of a high intensity proton accelerator and a fast neutron spectrum subcritical core. Accelerated protons are injected into the subcritical core through the spallation target zone which is located at the center of the subcritical core. The subcritical core is driven by neutrons generated by spallation reaction of protons delivered from an accelerator with heavy metal target nuclides. To obtain enough efficiency of neutron production by spallation reaction, proton energy is set about 1 GeV to 1.5 GeV. In the case of JAEA-proposed ADS, proton energy is set at 1.5 GeV to reduce the proton beam current density. The vacuum zone inside the accelerator beam duct and the subcritical core was separated by the beam window. The beam window is fabricated by thin steel plate and formed like semi-sphere shape to sustain mechanical stress caused by the irradiation and heat deposition of protons and static pressure of lead-bismuth, simultaneously. Optimization of the beam window structure is one of the key issues of ADS design. To improve the soundness of beam window, effective and stable cooling is indispensable. From the preliminary design, a guide tube and an inlet nozzle are equipped to the beam duct. The inlet temperature of primary coolant is set at low value, 300°C to achieve effective cooling of the beam window.

The subcritical core is driven by the spallation neutrons. Because the core is set to subcritical condition, the fission chain reaction is not kept without the external neutron source. Released energy from fission reaction in the subcritical core is converted to electric power and used for the operation of the own accelerator. Residual electricity can be supplied to the power grid. The output electric power is about 250 MW, which means the ADS can be a self-sustaining system providing the efficiency of the accelerator is more than 15%. The block diagram of a power generation system and heat balance is illustrated in Fig. 3.



for effective transmutation of MA. Moreover, when the ADS fuel is fabricated as a nitride, dry process is applicable for reprocessing of spent ADS fuels. For avoiding the production of radioactive  $^{14}\text{C}$ , however,  $^{15}\text{N}$  enriched nitrogen shall be used in the nitride fuel.

### 3. Specification of ADS components

The subcritical core of JAEA-proposed ADS is designed as a tank type layout because of the application of Pb-Bi coolant. Two units of primary pump and four units of steam generator are installed in the reactor tank. The proton beam power and reactor thermal output are specified to about 30MW and 800MW, respectively. The reactor outlet/inlet temperature of the primary coolant at rated operation is set to 407/300 °C. Steam generators can be directly inserted in the reactor vessel because Pb-Bi is chemically compatible with water. Turbine steam condition is set to the saturated steam turbine at 4.9 MPa.

#### 3.1 Design of primary circulation pump

The primary circulation pump is operated at 300°C and flow amount is 94500 t/h (152 m<sup>3</sup>/min) according to the heat balance at rated operation. NPSH<sub>av</sub> (Net Positive Suction Head) is 2.5 m and suction specific speed is set to 1150 rpm·m<sup>3</sup>/min·m. To specify the actual head, the pressures loss in primary circuit is set as follows,

Fuel bundle section	0.25MPa,
Core bottom structure	0.03MPa,
Steam generator	0.09MPa,
Coolant piping in reactor	0.03MPa, and
Total	0.4MPa.

From the specification, the actual head pressure loss of the primary circuit was specified to H=4.0m. The rotation frequency N is derived from the Suction specific speed S, NPSH<sub>av</sub> and flow rate.

$$N = S \frac{H_{SV}^{3/4}}{\sqrt{Q}} = 185.5 \text{ rpm} \quad (1)$$

Impeller rim speed  $U_2$  at lifting coefficient  $\phi=0.3$  is delivered from following equation.

$$U_2 = \sqrt{\frac{gH}{\phi}} = 11.4 \text{ m/s} \quad (2)$$

And then, diameter of the impeller  $D_2$  are specified as follows.

$$D_2 = \frac{60U_2}{\pi V} = 1.21 \text{ m} \quad (3)$$

#### 3.2 Specification of steam generator

Heat transfer tube for steam generator is set to 12Cr steel which has good heat transfer rate and high strength. Outer diameter of heat transfer tube is set to 31.8 mm, which is as same as Japanese prototype fast breeder reactor "Monju". The thickness of the tube was set to 1.6

mm considering required strength determined by outer pressure, margin for corrosion by Pb-Bi or water and margin for manufacturing.

Heat transfer area is determined by considering the depth of the beam window and height of the heat transfer region (3.6 m). From the analysis with the conditions mentioned above, the number of the heat transfer tube is 255 which is assembled in 15 layer of helical pipes. The effective heat transfer area and effective heat transfer height of helical coil are 569 m<sup>2</sup> and 3510 mm, respectively. The specification of steam generator is summarized in Table 1.

Type, Number of units		Helical coil type with free fluid surface, 4 units
Total heat exchange quantity		205 MW
Rated flow volume	Pb-Bi side	47,250 t/h
	Steam side	782.8 t/h
Rated operation temperature	Pb-Bi (Inlet/Outlet)	407 °C/300 °C
	Steam (Inlet/Outlet)	243.8 °C / 275.4 °C
Steam outlet pressure/Enthalpy		6MPa / 1998.8kJ/kg
Maximum temperature (Pb-Bi / Steam)		430 °C/410 °C
Maximum pressure (Pb-Bi / Steam)		0.8 MPa / 7.5 MPa
Thermal conductivity for 12Cr steel		27.78 W/mK at 350 °C
Inner surface roughness of heat transfer tube		0.05mm
Effective heat transfer area		120% of required heat transfer area
Effective heat transfer area		569 m <sup>2</sup>
Effective heat transfer height		3510 mm
Pressure loss (Pb-Bi/Steam)		0.09 MPa / 0.25 MPa
Helical coil pitch (radial/axial) and angle		0.5mm/0.5mm, 9.04°

Table 1. Main parameters of the steam generator

Heat transfer section is designed as a helical coil type. A water/steam flows inside of the heat transfer tube and Pb-Bi circulates outside of the heat transfer tube. The Pb-Bi at hot-leg temperature enters the steam generator through the window located at the upper section of steam generator. After the heat exchange with water, Pb-Bi flows out of the bottom of steam generator. Water is supplied from the water supply room at the upper section of steam generator and goes down through the inner piping of the steam generator. Then, water goes up through the inside of the heat transfer tube and heat of the Pb-Bi is exchanged. From the current R&D activities, the most suitable candidate material for Pb-Bi cooling system is not decided. Then, structural material is tentatively set to Modified 12Cr Steel.



From the result of heat transfer analysis, water inlet pressure should be set below 6.5 MPa, and maximum operation pressure of heat-transfer pipe is set to 7.5 MPa. From these pressure conditions, the pipe wall thickness is specified. The outer diameter and wall thickness of heat-transfer pipe is set to 31.8mm and 0.8 mm, respectively, to bear these water pressure specifications. To reserve the margin for corrosion by Pb-Bi (0.64 mm), pipe wall thickness is finally set to 1.6mm.

When the number of the heat-transfer tube and layer number of helical coil are set to 255 and 15, respectively, heat transfer area is 621 m<sup>2</sup> and height of the helical coil is 3830 mm. After further optimization according to the layout of reactor tank, final design parameters was adjusted as follows; the number of the heat-transfer tube is 220 and layer number of the helical coil is 14. Total length of steam generator is 12.39 m and heat transfer area is 606 m<sup>2</sup>. Conceptual view of steam generator unit based on the analysis results is illustrated in Fig. 4.

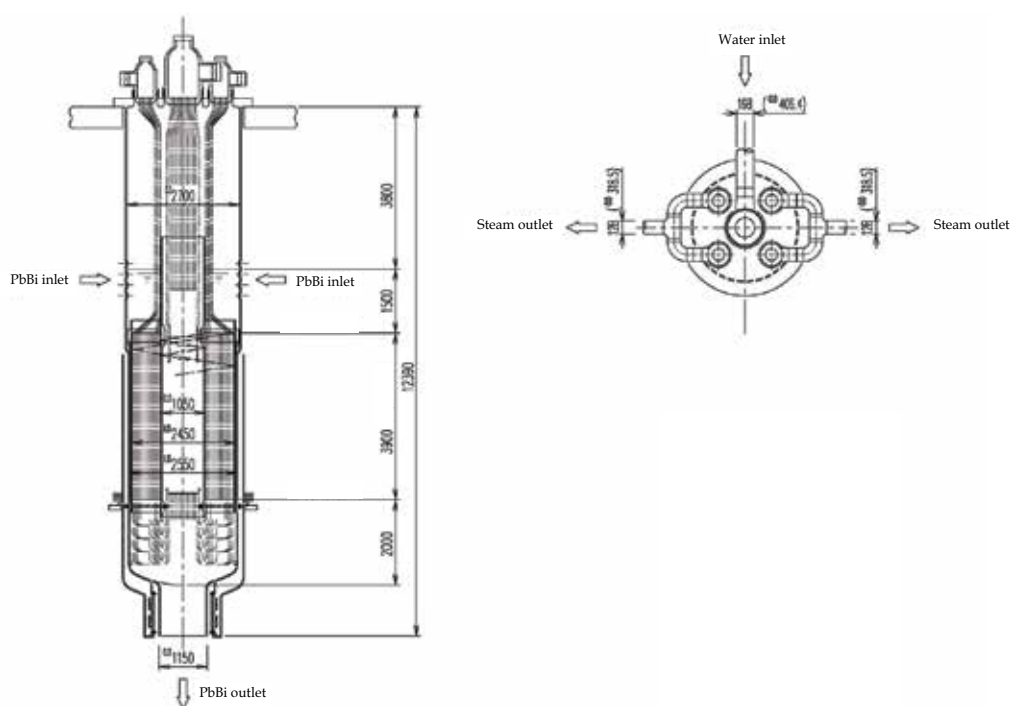


Fig. 4. Conceptual view of steam generator

ISI and maintenance of the heat transfer tube is performed by removing the top section of the steam generator. The steam generator itself can also be exchanged by extracting the device easily.

#### 4. Shielding analyses around steam generator

For the maintenance of steam generator, irradiation of the structures located at the upper section of ADS subcritical core should be considered. Structure of the core and beam injection part is illustrated in Fig.5.

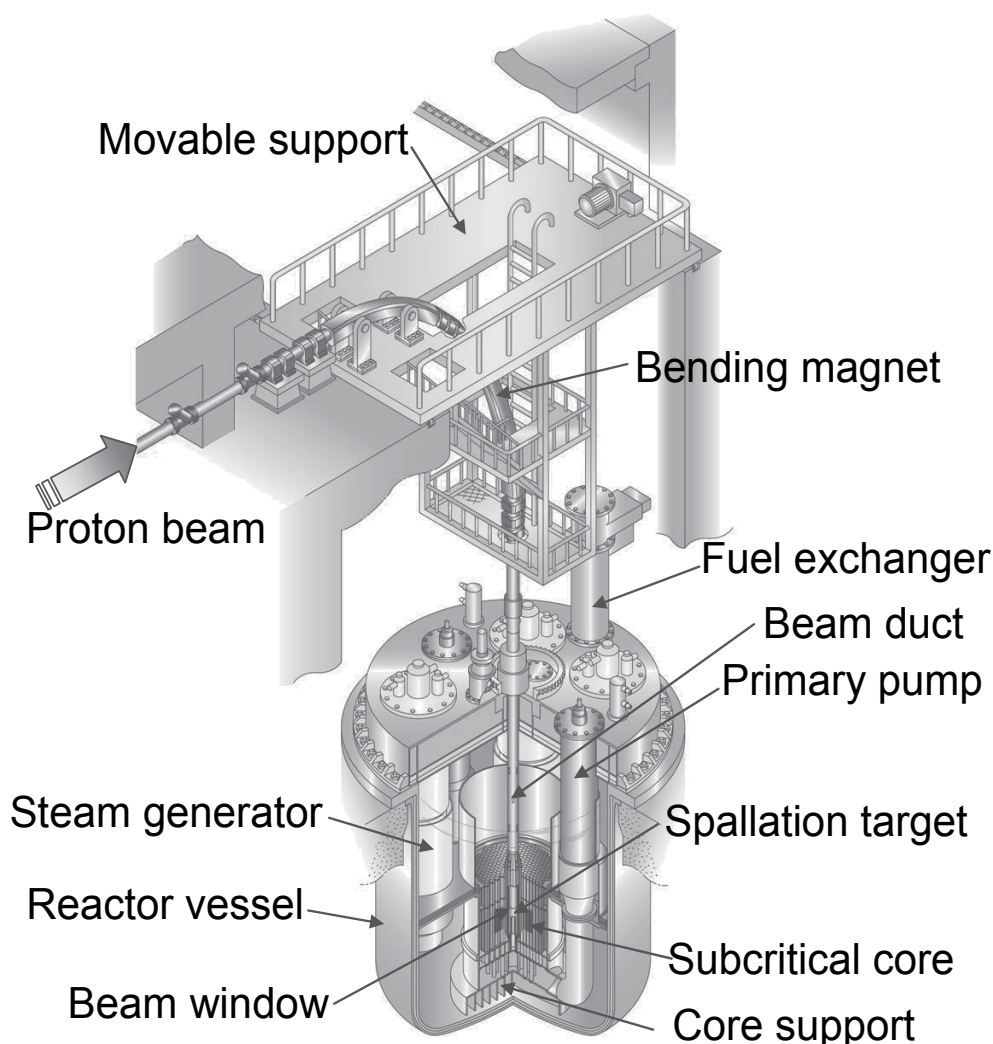


Fig. 5. Conceptual view of ADS subcritical core

Focusing magnets are the major component of beam transport line of ADS and are located at the upper part of the reactor vessel. Because the beam duct acts as a streaming path of the particles generated in the subcritical core, mainly neutron and photon, those magnets are heavily irradiated. To access the upper area of the subcritical core, the area locates a top section of steam generator, it is important to estimate the radiation dose from focusing magnets accurately.

Another point of view for radiation shielding, the system has four units of steam generator and then, secondary coolant, namely the water/steam, is also irradiated by secondary particles from subcritical core. It is also important to evaluate the radiation from irradiated secondary coolant through the piping to confirm the leakage radiation level satisfies the limitation of radiation non-controlled area.

#### 4.1 Subcritical core configuration for modeling

Fuel loading pattern and structure of fuel assembly are shown in Figs. 6 and 7, respectively. Parameters for fuel assembly are summarized in Table 2.

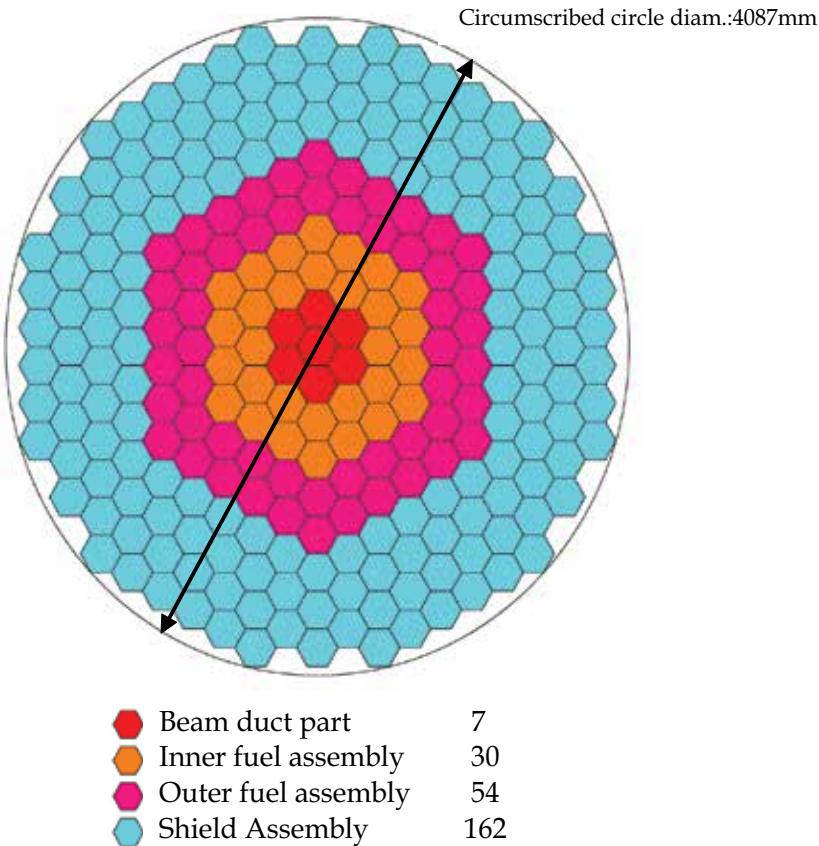
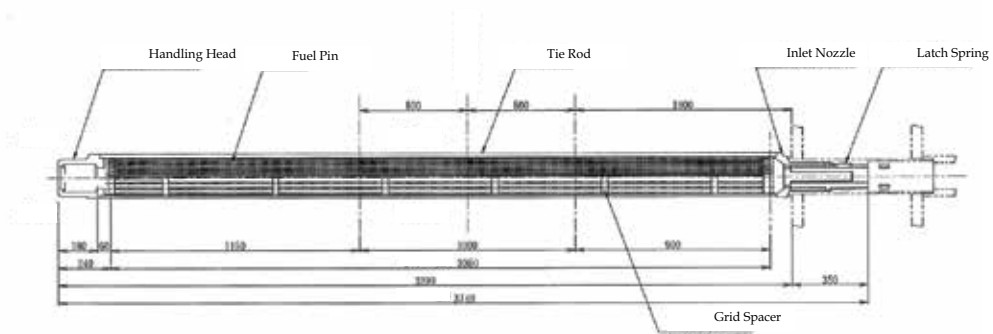


Fig. 6. Fuel loading pattern of ADS subcritical core



Number of fuel assemblies	84
Core equivalent radius	117.1 cm
Fuel composition	(MA, Pu) mono-nitride
Inert matrix	ZrN
Initial loaded Pu ratio	36 wt%
Inert matrix ratio	47.2 wt%
Fuel pellet density	95%TD (TD: Theoretical Density)
Pellet smear density	85%
Fuel pellet outer diameter	0.632 cm
Fuel-clad gap width	0.0165 cm
Clad outer diameter	0.765 cm
Clad thickness	0.05 cm
Actual fuel zone length	100 cm
Fuel pin pitch	1.148 cm
Fuel pin pitch/Clad OD (P/D)	1.5
Fuel assembly pitch	23.39 cm
Fuel pin number	391 pins/assembly
Tie rod number	6 rods/assembly

Table 2. Fuel assembly specification

As for the radial core layout, beam duct is located at the center of the core. Area of the beam duct is close to the area for 7 fuel assemblies. Around the beam duct, 84 fuel assemblies are located (30 inner fuel assemblies and 54 outer fuel assemblies). 162 units of reflector and shield assemblies (29 Pb-Bi assemblies, 33 SUS reflector assemblies and 100 B<sub>4</sub>C shield assemblies) are located around the fuel zone. Pitch of the fuel assembly is 23.39 cm. A core vessel is made of Mod.9Cr-1Mo steel with 420 cm of inner diameter and 5 cm thick. A reactor vessel, which is also made of Mod.9Cr-1Mo steel, has 1120 cm of inner diameter and 5 cm thick. Radial distance of the center axis of steam generator is 390 cm from core center. The outer radius of the steam generator is 245 cm. Density of Pb-Bi coolant is 10.2 g/cm<sup>3</sup> at the temperature of 430 °C.

As for the core layout along to the axial direction, length of the fuel assembly and fuel pin are 374 cm and 305 cm, respectively. Effective fuel length is 100 cm. Upper side of the fuel

meat, a 100 cm of gas plenum and a 15 cm shield are located. A 90 cm of SUS shield is attached at lower side of fuel meat. At the top of the reactor vessel, 200 cm thick shield plug made by concrete is located.

#### 4.2 Design criteria for shielding

Design criteria of shielding is assumed as follows,

1. Radiation dose rate around secondary coolant piping should be lower than  $6 \mu\text{Sv/h}$  during rated operation,
2. Radiation dose by gamma ray to magnet cable is limited below 10 MGy, and
3. Radiation dose rate at the upper section of the core is less than 2 mSv/h.

To obtain radiation dose from particle flux, energy dependent dose conversion factor, which is illustrated in Fig.8 was used (Sakamoto & Yamaguchi, 2001).

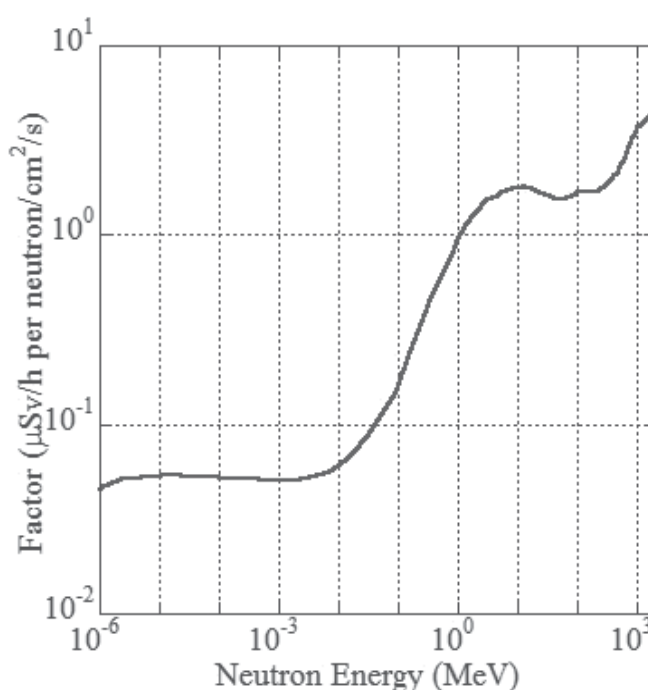


Fig. 8. Dose conversion factor for neutron

#### 4.3 Streaming analysis through the beam duct

The 1.5 GeV proton beam is injected into the Pb-Bi spallation target that is located at the center of the core region, and generates spallation neutrons. These neutrons drive the subcritical core by fission chain reaction at the fuel region of the core. However, part of the neutrons escape from the core and are captured at the outside of the core zone and some of escaping particles runs through the beam duct, which is ordinarily kept in vacuum condition, without the attenuation. Based on these specifications discussed in section 3.1, calculation model for the streaming analysis was set as Fig.9 (Sasa, Yang & Oigawa, 2005).

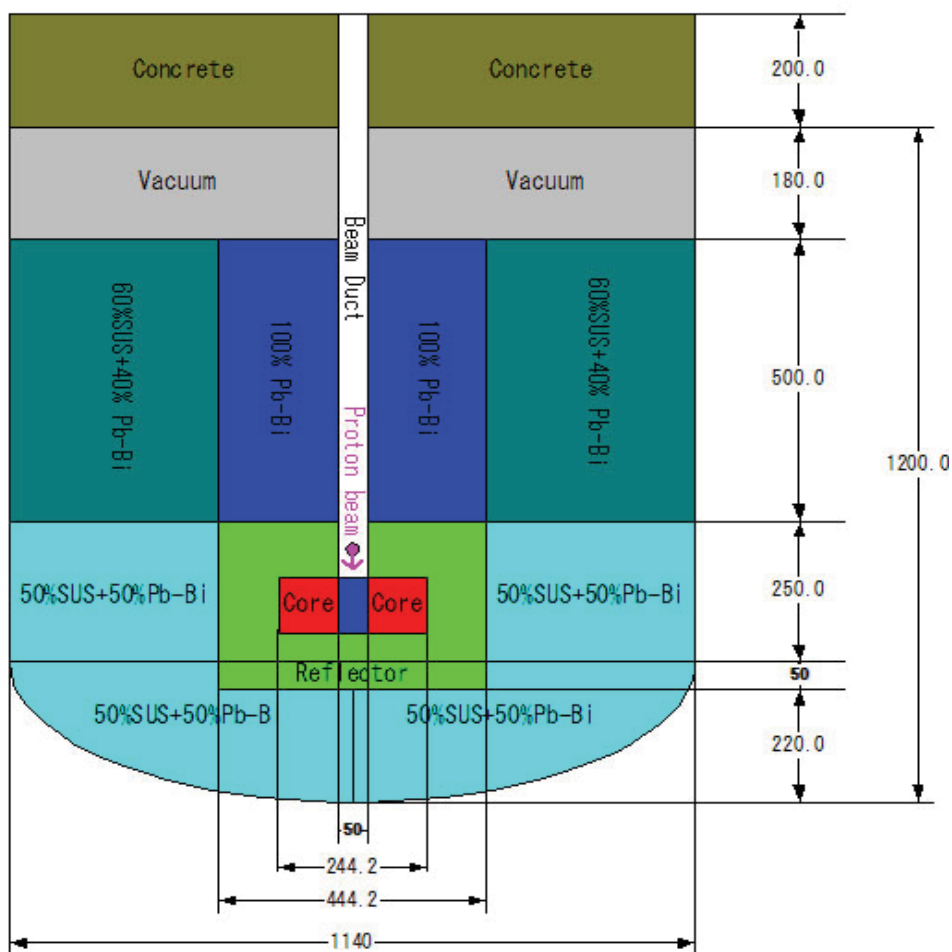


Fig. 9. Calculation model for streaming analysis

Before obtaining the activation of upper section devices, a leakage particle spectrum through the beam duct was calculated by MCNPX (CCC-705, 1999) with the Weight Window technique. For the analysis of secondary photons, the cross sections of almost all MA were substituted with those of plutonium because of lack of gamma-production cross section in JENDL-3.2 (Nakagawa et al., 1995). Figure 10 summarizes axial distributions of the radiation dose rates caused by neutrons and photons with (Duct case) and without (Bulk case) the beam duct during the rated operation.

From Fig.10, radiation doses at the bulk case give rather low value because of the large amount of the Pb-Bi at the upper plenum region. However, at the top of the subcritical core, the neutron radiation dose through the beam duct gives about 20 orders higher value than that of the bulk case. Some modifications are required to suppress the leakage particle such as application of narrower beam duct. To apply a narrow beam duct, optimization of the beam transport components especially for the beam expansion section must be performed simultaneously.

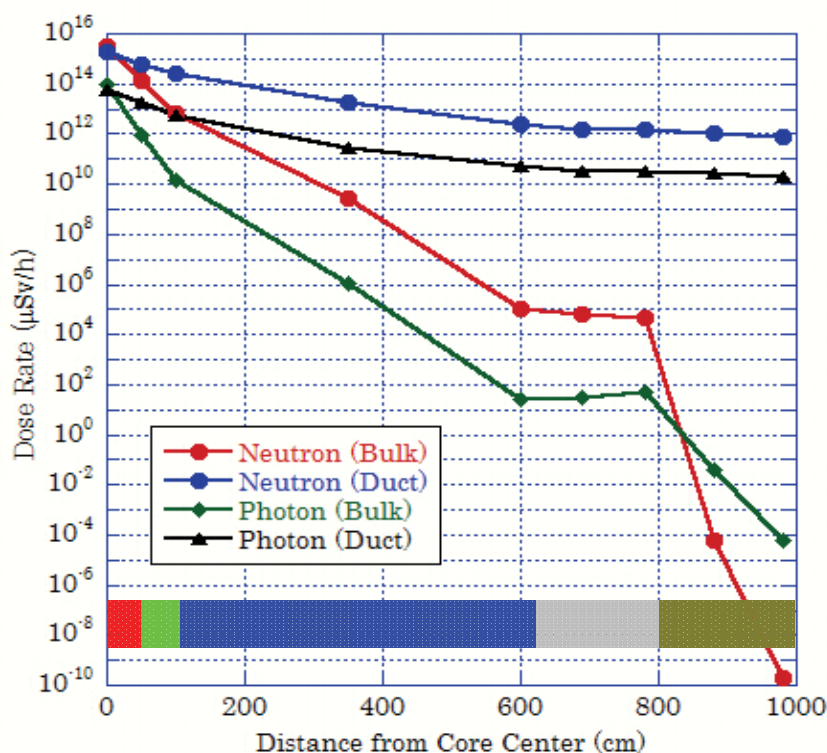


Fig. 10. Axial radiation dose distribution

Activation of the bending magnet, focusing magnets and shield plug was analyzed by PHITS (Iwase et al., 2002) and DCHAIN-SP (Kai et al., 2001) using the leakage neutron spectrum mentioned above. Two-dimensional calculation model and the calculation results are shown in Figs. 11 and 12, respectively. The proton beam power and operation period are 1.5 GeV/20 MW and 600 days, respectively. Figure 12 indicates that the radioactivity of the shield plug is  $10^{15}$  Bq after 600 days of rated operation. It is almost the same value as those of beam window of the Pb-Bi target/cooled ADS (Nishihara and Sasa, 2001). Focusing magnets also have high radioactivity. Additional shield must be required to reduce the irradiation by streaming particles.

Using these activated sources, gamma-ray transport analysis was performed to determine the radiation dose of the workers during maintenance period. The radiation doses at three kinds of time period, ten days, thirty days and one year after system shutdown were analyzed. Figure 13 shows the trends of radiation dose level after system shutdown in unit of mSv/h. From the figure, maximum radiation dose are observed around additional steel shield plug (exceed 1 Sv/h) and nearby the magnets are in order of 1 to 100 mSv/h. These high radiation doses are caused from components closed to the reactor, namely an additional shield plug and a lower part focusing magnet. These conditions are kept through one month because of the contribution of Fe-55 (2.7 years of half-life) and Mn-54 (312 days half-life) generated from (n,p) reaction of Fe-54.



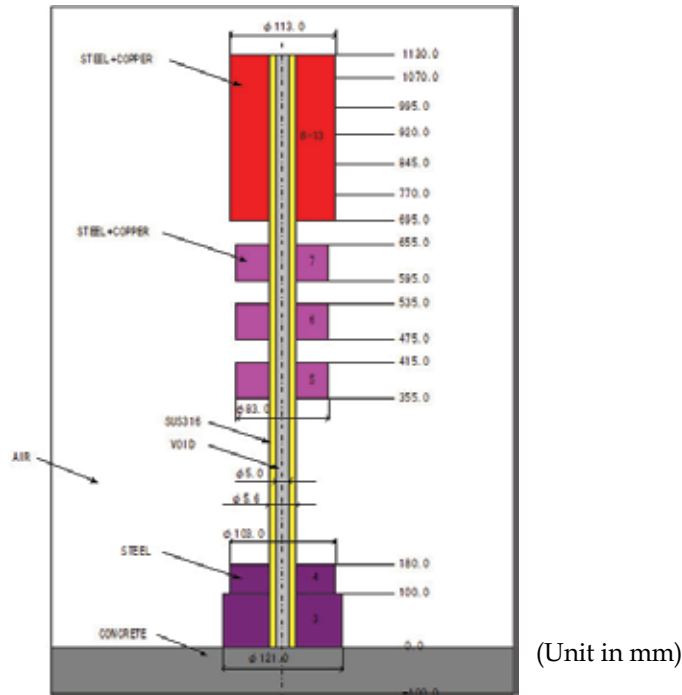


Fig. 11. Analysis model for activation analysis

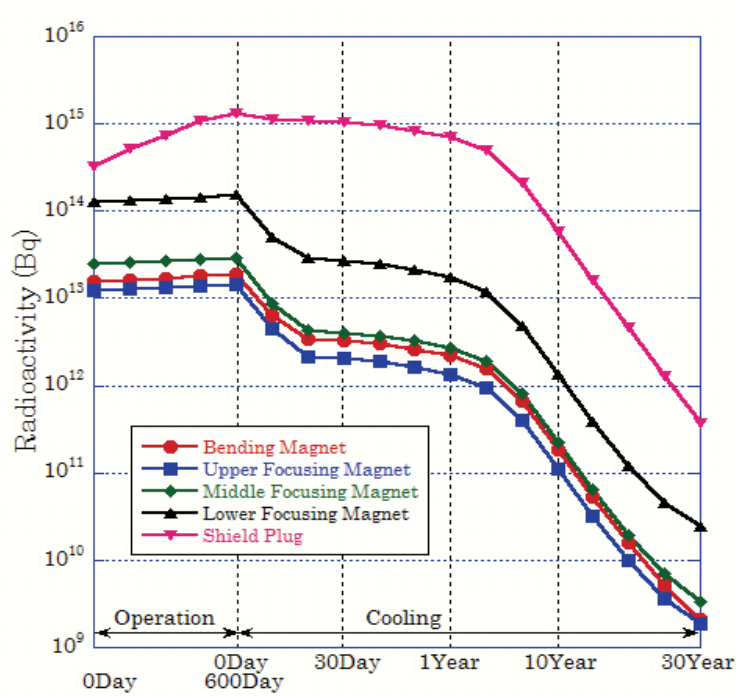


Fig. 12. Time evolution of radioactivity



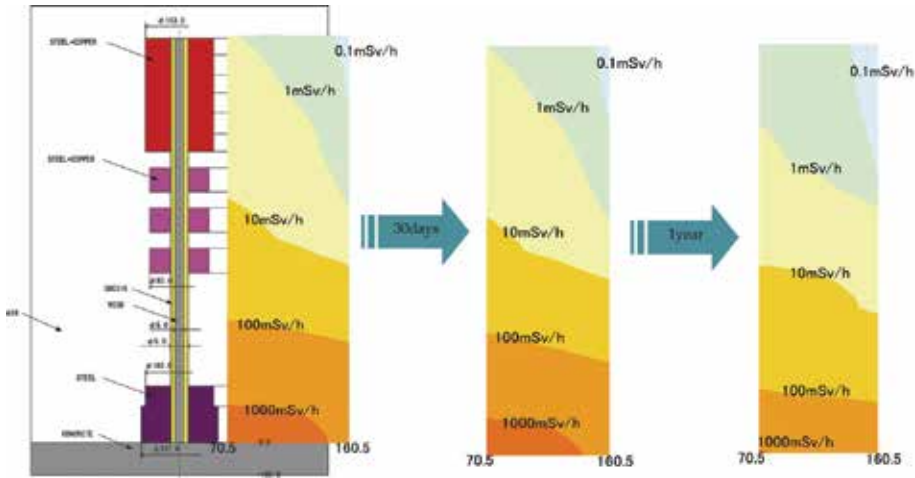


Fig. 13. Trends of radiation dose after shutdown

Compared with limitation of radiation exposure in Japan, the radiation dose near the magnets gives two or three order higher values. To suppress the radiation exposure of workers, the additional shield plug should be removed before maintenance period by remote operation. After the removal of additional shield plug, about ten to thirty minutes of maintenance time is applicable according to the maintenance positions.

#### 4.4 Shielding analysis of the secondary coolant circuit

Because of the heavy weight of lead and bismuth, the JAEA-proposed ADS adopt a tank-type reactor vessel and then, cooling circuit components are located nearby the core barrel. The size of the steam generator is slightly larger than the similar-scale sodium-cooled fast reactor by the limitation of maximum operation temperature to suppress the corrosion of structural materials. Considering these conditions, the activation of secondary coolant might be larger than that of other fast reactors. The analysis using MCNPX code with LA150 and JENDL-3.2 based cross section libraries, was performed to specify the requirement of secondary coolant circuit shielding.

To define the leakage neutrons reaching the steam generator, inside the core barrel was modeled in detail. Material compositions of the inner structure of the core barrel were homogenized by referring to the fuel assembly structure and assembly layout. To conserve the computation time, steam generator was modeled in homogenized annular shape by taking into account the volumetric ratio of lead-bismuth, water and structural material. At first, reaction rates of  $^{16}\text{O}$  (mainly a  $^{16}\text{O}(n,p)^{16}\text{N}$  reaction) were calculated and then, following formula was used to calculate radioactivity of reaction products;

$$A_i = \sum_g N_i \cdot \sigma_g \cdot \phi_g \cdot \frac{1 - e^{-\lambda_i t_0}}{1 - e^{-\lambda_i t}} \quad (4)$$

where

$A_i$  : Activity of nuclide in steam generator (Bq/gram),

$g$  : Energy group number,

$N_i$  : Number density of nuclide ( $10^{24}$ /gram $\text{H}_2\text{O}$ ),

- $\sigma_g$  : Activation cross section of nuclide (barn),  
 $\phi_g$  : Neutron flux in steam generator ( $\text{n}/\text{cm}^2\cdot\text{s}$ ),  
 $\lambda_i$  : Decay constant of decay products of nuclide ( $\text{s}^{-1}$ ),  
 $t_0$  : Round time of coolant in secondary loop (s), and  
 $t$  : Secondary coolant transit time in steam generator (s).

Figure 14 indicates the two-dimensional cylindrical calculation model for MCNPX.

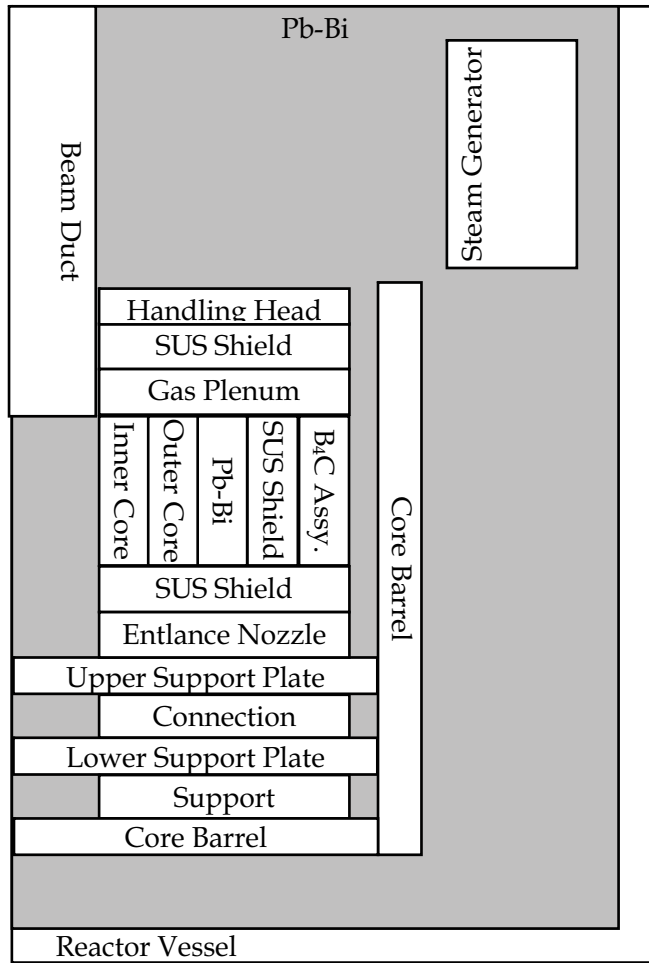


Fig. 14. Analysis model for secondary coolant activation by MCNPX

For the analysis of the radiation dose around the secondary loop, the dose rate calculation at the exit piping of the steam generator was performed using MCNPX code because of the short life time of  $^{16}\text{N}$  (7.1 seconds half-life) by one dimensional cylindrical model. Figure 15 shows the neutron spectrum around the steam generator. Because the statistical error is not enough in high energy region, the neutron flux in 0.5 MeV is extrapolated above 2 MeV energy region to determine the reaction rates. By using the above mentioned formula, neutron reaction cross section of  $^{16}\text{O}$  shown in Fig.16, and neutron flux information,  $^{16}\text{N}$

concentration is delivered to 0.12 Bq/gramH<sub>2</sub>O. Figure 17 illustrates the gamma-ray radiation dose around the piping caused by <sup>16</sup>N accumulation. It is shown that the radiation dose at the outside of the piping is 0.002  $\mu$ Sv/h and then, no specific shields are required for secondary cooling circuits.

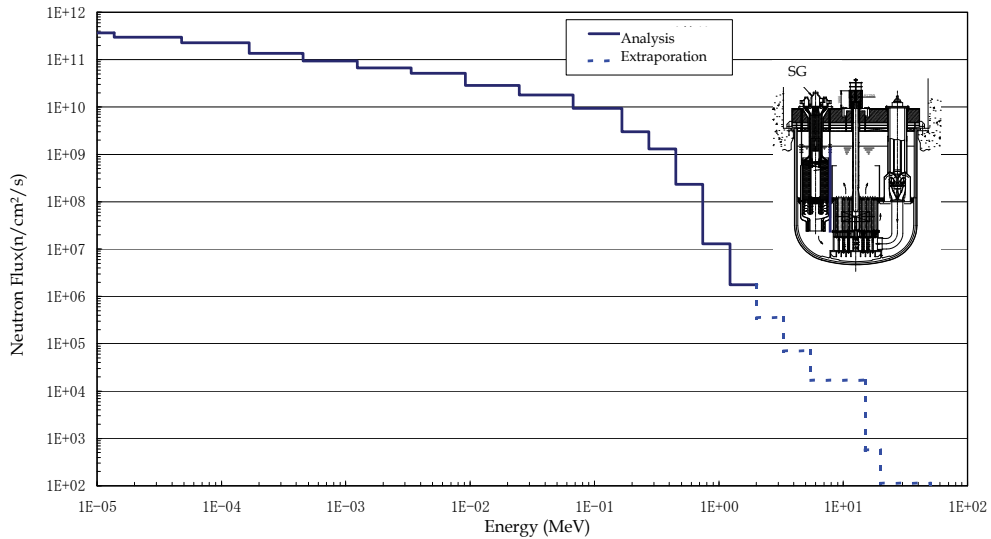


Fig. 15. Neutron energy spectrum at the outer surface of the steam generator

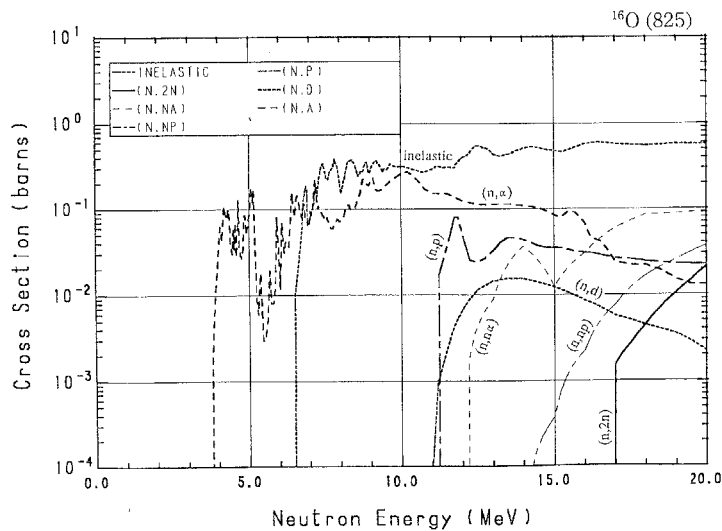


Fig. 16. Neutron reaction cross section for <sup>16</sup>O

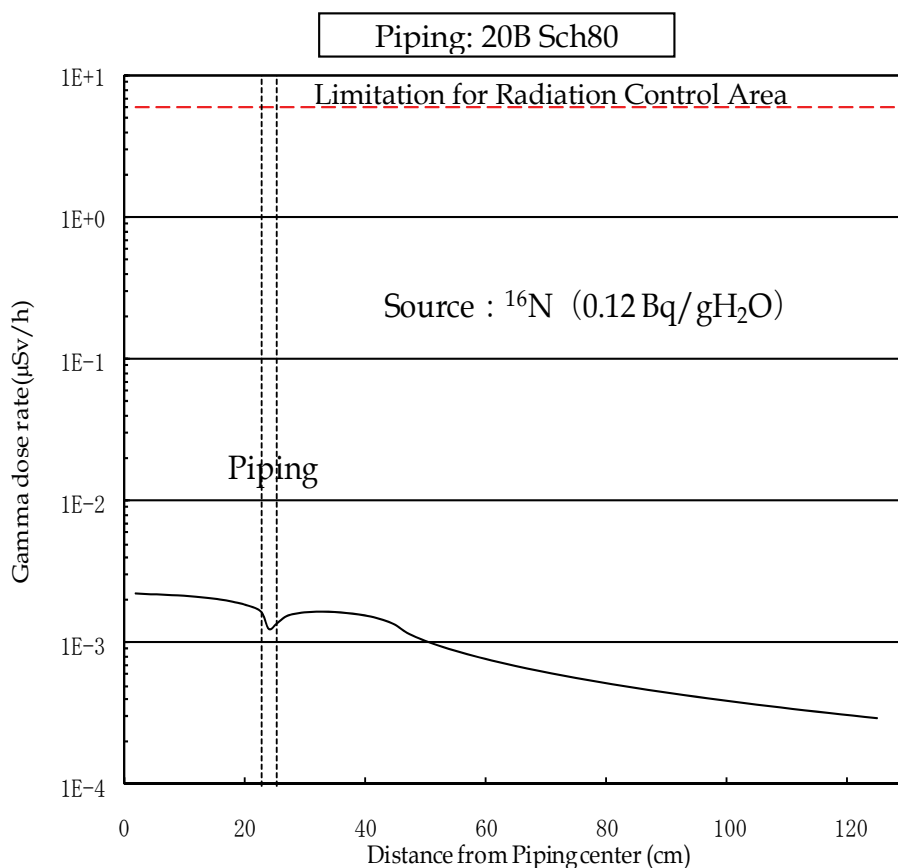


Fig. 17. Radiation dose rate distribution at secondary coolant piping

## 5. Conclusion

JAEA proceeds the research and development for partitioning and transmutation technology under the framework of the OMEGA program conducted by Japan Atomic Energy Commission since 1988.

To transmute long-lived radioactive nuclide, especially for the MA such as neptunium, americium and curium, fission chain reaction is suitable even thier physical and chemical characteristics is not necessarily compatible with other materials. To solve the problems to use minor actinides, JAEA promotes ADS which is an innovative nuclear system composed of high power proton accelerator and subcritical core.

To realize ADS, there are many technical issues to be solved. One of the issues is a shielding of high energy particles caused by spallation reaction of protons. In this chapter, we focused the influence of radiation exposure to the workers in two different viewpoints, activation of components set on the upper section of subcritical core including steam generator and radiation from secondary coolant which is irradiated in steam generator located in reactor vessel.

From Fig.10, the neutron radiation dose through the beam duct gives high activation dose than that of bulk case. To suppress the leakage particle, narrower beam duct might be effective. However, to apply a narrower beam duct at the shield plug position, optimization of the beam transport components especially for the beam expansion section must be performed simultaneously. In this study, it was found that the components set on the reactor vessel is heavily irradiated. It is indispensable to isolate shield plug before maintenance to access the upper section. Even the shield plug is isolated, allowable maintenance time for individual workers are limited within 30 minutes for hands on maintenance.

The analysis of the activation of secondary coolant was performed. Even using the detailed core configuration, which takes into account the closed layout of secondary cooling circuit to the fuel region, radiation dose caused by the activation of water/steam, namely an accumulation and circulation of  $^{16}\text{N}$ , was not so high and satisfy the limitation of the regulation for radiation non-control area as shown in Fig. 17. In this case, Pb-Bi in reactor vessel acts as a shield. It results that no additional shield is needed for secondary cooling circuits.

## 6. References

- Japan Atomic Energy Commission (2009). Concerning the Report Entitled “*Current Status and a Way Forward to Promote the Research and Development of Partitioning and Transmutation Technologies*”, Japan
- CCC-705 (1999), MCNPX version 2.1.5, RSICC Computer Code Collection, Oak Ridge National Laboratory.
- Iwase H. et al. (2002), Development of General-Purpose Particle and Heavy Ion Transport Monte Carlo Code, *Journal of Nuclear Science and Technology*, Vol.39, pp.1142.
- Kai T. et al. (2001), DCHAIN-SP2001: High Energy Particle Induced Radioactivity Calculation Code, *JAERI-Data/Code* 2001-016.
- Nakagawa T. et al. (1995), JENDL-3 Version2, *Journal of Nuclear Science and Technology*, Vol. 32, pp.1259.
- Nishihara K. and Sasa T. (2001), Estimation of Activity and Toxicity for Spallation Product from the Target for Accelerator-Driven Transmutation System, *JAERI-Research* 2001-015 [in Japanese]
- Oigawa, H., et al. (2005). Parametric Survey on Possible Impact of Partitioning and Transmutation of High-level Radioactive Waste, *Proc. of GLOBAL2005, International Conference Nuclear Energy System for Future Generation and Global Sustainability*, Tsukuba, Japan, October 9-13, 2005.
- Sakamoto Y. and Yamaguchi Y. (2001), Dose Conversion Coefficients in the Shielding Design Calculation for High Energy Proton Accelerator Facilities, *JAERI-Tech* 2001-042.
- Sasa, T., Yang, J.A. and Oigawa, H. (2005), Shielding analysis at the upper section of the accelerator-driven system, *Radiation Protection Dosimetry*, Vol.116, No.1-4, pp.256.
- Sasa, T. et al. (2009), Liquid-fuelled accelerator-driven transmutation system, *Proceedings of 10th OECD/NEA Information Exchange Meeting on Actinide and Fission Product Partitioning and Transmutation* (CD-ROM)

- Sugawara, T. et al. (2009), Recent activities for accelerator driven system in JAEA, *Proceedings of International Conference on Advanced Nuclear Fuel Cycle; Sustainable Options & Industrial Perspectives* (Global 2009) (CD-ROM)
- Takano, H. et al. (2000), Transmutation of Long-Lived Radioactive Waste Based on Double-Strata Concept, *Progress in Nuclear Energy*, Vol.37, pp.371.
- Tsujimoto, K. et al. (2004), Neutronics Design for Lead-Bismuth Cooled Accelerator-Driven System for Transmutation of Minor Actinide, *Journal of Nuclear Science and Technology*, Vol.41, pp.21.

# Starting Fast Reactors Again

Didier Costes

*Ingénieur Général Honoraire des Ponts et Chaussées  
France*

## 1. Introduction

Fast reactors (FRs), or surgenerators, or "breeders", transmute U238 (99,3% of natural uranium) into fissionable plutonium Pu239. For a given uranium mass, 60 to 100 times more energy may be produced, relatively to light water cooled reactors. At higher temperature, FRs allow better thermal efficiency. Increase of uranium ore cost would open access to huge uranium reserves. Planet energy needs could be satisfied for thousands of years. First fuel for these reactors may be Pu239 produced by LWRs, or U235 enriched uranium. FRs transmute actinides, created in the fuel, into shorter live fission products.

Sodium, their preferred coolant, liquid between 98°C and 883°C, reacts with air and water.

Their energy price is considered low for fuel cycle and high for construction, conducting to 2040 or 2050 before general use, when uranium prices have been increased due to shortage. To reduce energy price and increase safety, allowing an earlier extension, we propose the cold bottom resting vessel and other innovations.

In a "pool reactor", the vessel contains the primary circuit with pumps and exchangers to a secondary circuit, while in a "loop reactor", external pipes connect them. Several sodium vessel designs were proposed :

- vessel with a rounded bottom supporting the core diagrid, suspended to the concrete vault top ( pool reactors Phénix, Superphénix, European Fast Reactor project, loop reactor Monju), all the vessel in tension, needing climatization in hot regions (550°C), by sodium cooled in the exchangers (400°C).
- half resting vessel ( Russian pool reactors BN-600 and BN-800), the upper cylindrical wall and the roof resting on a ring supported by the basement. A diagrid slab anchored to this ring supports the core, above a rounded bottom in hydrostatic tension. No vessel climatization is needed.
- cold resting bottom vessel. The vessel bottom cooled at less than 90°C rests on the concrete basement and supports the core diagrid through vertical skirts, in a thick space of sodium in thermal gradient. No climatization is needed.
- hot resting bottom vessels, on rollers.

This paper describes innovations for the cold resting bottom in pool sodium reactors:

- diagrid extended on full vessel diameter and also borne in periphery by the cylindrical wall,
- lower space in thermal gradient containing heavy and refractory materials,
- exchangers-pumps vertically driven in the diagrid around the core,
- three handling pits around a cell above the vessel roof, where is lifted the control block,
- supplementary area obtained on the diagrid for used elements decrease.

The concrete vault contains the reactor under ground level. Advantages are cited:

- general robustness by rigid fixation of the diagrid and elimination of climatization structures,
- reduced vessel diameter, simplification and lesser weight of structures, easier repairs,
- protection against core fusion accident and bottom attack by hot mix flow of fuel and steel,
- sodium leaks frozen before penetrating in the concrete, no empty spaces outside the vessel,
- limited accident consequences, by resistant exchangers-pumps fixed on two levels,
- reduced thermal exchanges between "cool" and hot primary sodium, providing better efficiency,
- reduced cost.

Innovations proposed by the author, which may in some points differ from these here described, are currently examined by the CEA, French Commissariat à l'Energie Atomique, and could contribute to allow earlier extension of fast reactors.

## 2. Situation

Fast Reactors (FRs), or surgenerators or "breeders", where neutrons are not slowed by a moderator, transmute uranium U238 (99,3% of natural uranium) into fissionable plutonium Pu239. They may produce, for a given uranium mass, 60 to 100 times more thermal energy than moderated reactors like LWR's, light water cooled reactors, with a better thermal efficiency due to a higher temperature. An increase of uranium ore cost would not compromise economy production, and would open access to huge uranium reserves. Fission nuclear energy could then satisfy our planet energy needs of for thousands of years.

The fast neutron flux in surgenerators, like the moderated flux in LWRs, creates fission products subject to a relatively short half-life (about 300 years), more fissile plutonium and much less minor actinides, heavier than uranium, constituting long half-life wastes. Then the problem of wastes stockage, until raising the current level of radioactivity on our planet, is made much easier. Moreover, their fast flux is able to convert LWR produced minor actinides, introduced in their fuel, into energy and fission products easily stocked. For introduction of a series of fast reactors, they may use LWR-produced Plutonium, or U235 enriched Uranium, the price of which remains acceptable. For current use, they burn only natural uranium or depleted uranium, reserves of which are very important. Use of Thorium is not presently foreseen.

Sodium cooled reactors (SFRs) take advantage of factors like:

- coolant temperatures largely below boiling point, preventing core dry-out by coolant evaporation,
- very good heat transfer capability and natural circulation behaviour of the sodium coolant,
- an argon pressure slightly above atmospheric pressure, sufficient on sodium surface,
- use of ductile structural materials allowing leak detection before rupture,
- a stable core with negative reactivity feedback to power increase,
- high combustion rates before fuel subassemblies cladding failure,
- as shown by extended studies, a low energy produced in case of accidental bursts,
- a large experience, which allowed to eliminate several dysfunctions.

About twenty sodium cooled fast reactors have been or are constructed in the world. Phenix and Superphenix in France, now stopped, showed excellent fuel elements reliability and ease of control;. In Russia, BN-600 performs satisfactorily since 1980 and should operate until 2025. BN-800 is under construction.



Phenix performed well with exception to problems in steam generators, quickly mastered. Superphenix was lengthly stopped due to problems on secondary parts, equally mastered, and to extended administrative procedures. Overcosts appeared due to some options and to the number of technical actors. "Ecological" campaigns, based on the Tchernobyl accident, in a moderated reactor inherently unsafe and incorrectly operated, and a loss of secondary sodium to air on the Monju breeder in Japan, led the French government to stop Superphenix in 1998, in an unmotivated decision ; it is now being dismantled. Nuclear opponents still claim that surgenerators are dangerous and cannot become economical, in a context of, they suppose, uranium scarcity and renewable energy abundance.

On the contrary, we think that the world needs much energy, without limited recourse to fossil fuels. Fast reactors are clearly to be developed. Decisions for starting them again shall evidently be based on advantages for safety and overall economy. Low probability risks of aggressions by terrorism or by earthquakes shall be taken into account and their consequences prevented. Simplified designs and reduction of steel and sodium masses shall be sought.

The international Forum "Generation IV", launched in 2001 by USA, Japan and France, followed by some fifteen countries, defined tracks for improved nuclear reactors. Japan and France will conduct the research on sodium cooled fast reactors. Japan will reactivate the 250 MWe Monju breeder reactor stopped in 1995. For 2020, France will build the sodium cooled 600 MWe Astrid, which should validate new technical features and by transmutation reduce radioactive waste. Larger units should follow.

Running expenses of sodium cooled surgenerators should become low relatively to LWR's, when fuel reprocessing units will be ready, but their construction cost is deemed high: a supplement over 20% on the installed kW has been cited. Resulting profitability versus LWRs is often foreseen only for about 2040, when uranium price will be sufficiently increased due to demand. Surgenerators safety remains debated. In order to reduce their cost and to establish an evident safety, several innovations are here proposed, based on the concept of the cold resting bottom vessel with a diagrid support in thermal gradient, and on new propositions.

### 3. Present Sodium cooled fast reactors

Main features of to-day reactors will be recalled. Temperatures are rounded.

The steel sodium vessel of pool SFRs is suspended in a safety vessel which for EFR project (1998), along our 1978 proposition, became a concrete caisson or "vault", with internal cooled steel skin, imbedded in soil or resting on parasismic supports. The sodium vessel top contains, below an argon cover, a primary sodium at 550°C ("hot" temperature) coming from the core. This sodium enters exchangers, which heat the secondary sodium directed to external generating units for electricity production, and is discharged in a lower plenum at "cool" temperature (400°C). Taken by primary pumps, this sodium is injected under pressure (about 0,5 MPa or 5 atmospheres) in the diagrid, a flat hollow structure resting on the vessel bottom and supporting fuel subassemblies. In pool option, heat exchangers and pumps are contained in periphery of the sodium vessel. Direct reactor cooling loops (DRC) using natural convection are added for emergency cases.

The sodium vessel is usually suspended in periphery to the vault top. In Phenix, Superphenix and EFR, an internal wide-mouthed vessel extends from diagrid to the sodium vessel top and, completed by baffles, directs a flow of cool sodium to climatize the vessel wall, before mixing in hot sodium.

In Russian reactors, the concrete basement supports by articulated plates (BN600) or by a cylindrical shell (BN800 in construction) a resisting ring on which are fixed the wall

cylindrical part, a full diameter slab supporting the diagrid, and a rounded bottom. No climatization is needed in the wall, due to elimination of vertical tensile stresses.

The diagrid surface is loaded by fuel subassemblies and other elements, contained in identical hexagonal vertical wrapper tubes fixed to cylindrical spikes to be inserted in holes of the diagrid along a triangular net. Fuel subassemblies contain in median part uranium-plutonium pins heating the sodium and, above and below, axial blanket uranium pins to be transmuted into plutonium, and shielding materials. The core also receives wrapper tubes for control rods driven by vertical bars from an upper controlling block and left in lower position for nuclear arrest, when this block is displaced for allowing fuel elements transfers. The diagrid external part is loaded by breeding and shielding elements lowering the flux transmitted to exchangers and to the vessel. Spent fuel elements are stored in periphery for one or two years before discharge and treatment. Inserted spikes receive sodium by inlet ports around the shroud tubes, and individual sodium flows are controlled by gagging pieces in the spikes and by adaptation of inlet ports. Element take-off by pressure on spikes is prevented by openings to the lower space. A leak of "cool" sodium is admitted to the lower plenum, allowing an ascending flow along the vessel for climatization.

In "pool reactors", intermediary heat exchangers (IHx) with secondary sodium stand around the core, suspended to the vault roof by concentric secondary sodium pipes. For suspended vessels, exchangers penetrate the internal wide-mouthed vessel without leaks, using bell-shaped argon joints or solid segments, before feeding cool sodium down in the plenum. Pumps, of which columns arrive to the plenum through this internal vessel, drive sodium into the diagrid by side connected pipes.

In "loop reactors", pipes through the roof conduct hot sodium to external exchangers with secondary sodium, heating steam generators, and pumps reinject the cooled sodium to the reactor. For direct heating of mechanical energy cycles by primary sodium, steam generators with double exchange tubes have been proposed. Gas cycles without secondary sodium were also proposed..

The two excentered plugs system is usually used for handling subassemblies while bars commanding the control rods are left in place. Two vertical handling columns are used, one takes place in the control block on the smaller plug, for the inner handling zone of the core, and the other one on the large plug with a rotating lateral arm, for the outer handling zone. Subassemblies are exchanged between the diagrid and a lateral rotor, covered by a fuel handling flask for exchanges with external halls. These two plugs are fixed to the roof during reactor operation. Leak-tightness during rotations was given by skirts immersed in circular channels filled with a melted alloy, but now would be obtained using solid segments. This system with only rotations allows to keep at constant level the bar control block and the detectors placed on the top of the core.

For these sodium cooled breeding reactors, special risks are attached to:

- chemical reactions of sodium in case of contacts with air or water,
- the fact that the core is not in its most reactive configuration and that a lack of cooling flow could induce a sodium void with reactivity burst and fusion of a part of the core, producing a hot "corium" finally able to pierce the vessel bottom.

For LWR's, lack of cooling flow would not lead to nuclear excursion but could also induce a fusion. Vessel integrity is essential for both types of reactors. Applying the "defence in depth" principles, these risks are addressed by successive protection levels, not detailed here. Innovations below would contribute to these protections.

The European Fast Reactor (EFR) project, published in 1998, will be taken as reference to innovations. It is described in Part 6.

#### 4. Proposition for a cold resting bottom vessel with integral diagrid

The author has proposed (French patent 80 27759) for sodium cooled pool reactors a vessel with a flat bottom, resting on the bottom of a concrete vault imbedded in soil, maintained "cold" at about 90°C (melting sodium temperature 98°C).

In the cited patent, an empty lower space for inspection by detectors and potential reparability was indicated between the vessel bottom and the vault bottom steel skin, but is to be suppressed, along the french patent 88 11370 concerning a loop reactor. Better robustness is obtained by direct vessel support on the thick concrete and elimination of empty spaces favorizing leaks below the core. The here proposed sodium vessel bottom is only constituted by the vault steel skin, thick of about 4 cm, maintained by welded bars to a layer of sodium resisting concrete, cooled by fluid circulation in tubes, and monitored against cracks. A leak through any crack is prevented by sodium freezing above the skin. It has been asked to allow its reparability but this should not introduce empty spaces: after a very low probability disorder, it would remain possible to freeze sodium and cut a passage for repair through the concrete.

An "integral diagrid" is now patented (**Figures 1 and 2**). The entirely cylindrical wall of the sodium vessel itself constitutes the lateral wall of the full diameter flat diagrid, also supported by concentric steel skirts at about 2 meters height. Temperature remains "cool" to 400°C on the diagrid thickness.

In this closed space below the diagrid, the space is filled by stratified sodium, without forced circulation, in gradient between 90°C and 400°C. A 150°C/m gradient would give in pure sodium (conductivity 140W/m°) a flux of 21 kW/m<sup>2</sup>, not easily evacuated by the bottom cooling system. Solid refractory materials are added, detailed in Part 7. The flux could be reduced to less than 5 kW/m<sup>2</sup>, transmitting 715 kW on a section of 143 m<sup>2</sup> for a diameter of 13.5m.

The diagrid receives fuel subassemblies and other elements, and feeds them under pressure by cool sodium. It is made of three plates, the bottom one leaktight, defining an upper layer at high pressure and a lower one at smaller pressure, precluding elements taking-off. Central elements are fed by the upper layer, with leaks to the lower layer feeding peripheric elements. Above the diagrid, the vessel wall temperature increases, until reaching the hot sodium temperature (550°C), progressively due to the isolation produced by lateral elements and exchangers on the diagrid periphery. Like in other SFRs, an argon cover separates the sodium surface from the vault roof maintained at about 150°C in order to avoid a mesos (sodium oxides) accumulation. A steel plate is fixed below the roof for insulation, by means excluding fall of pieces.

The annular space between vessel wall and the cooled skin of the vault is filled by argon and may contain isolating panels, possibly renewable through upper trap-doors, using rotation displacements around the vessel. In case of accidental temperature jump in the vessel, sodium may be injected in this space, allowing a contribution of the vault cooling net. Such an injection, or a temporary heating, could clean this space after a mesos deposition.

Vessel wall dilatations induce displacements in height and diameter of its hot circular board, which could possibly be joined to the vault roof, maintained at 150°C, by a leak-tight bellow. If exchangers penetrate the roof at his limit, such a bellow should extend externally.

It is preferred to shape the vessel upper part along a short external cone (**Figure 3**), the slope of which corresponds to dilatation direction. This cone remains at short distance of a corresponding internal cone around the vault roof, with a clearance filled by a side by side collection of sectors in metallic isolating matter applied to the roof cone and protected below

by a steel flexible sheet which could slide on the external cone under a low stress. These sectors are assembled to curved chocks forming a ring, compressed by the roof weight and by tie-rods. The isolating matter and the sheet could be renewed with corresponding chocks, after a limited elevation of the roof by jacks. A leak-tight belt is wound around the chocks. As the thin space between cones is not leak-tight, a small argon flow penetrates from the annular space around the vessel to the space below the roof. This flow is purified and re-injected.

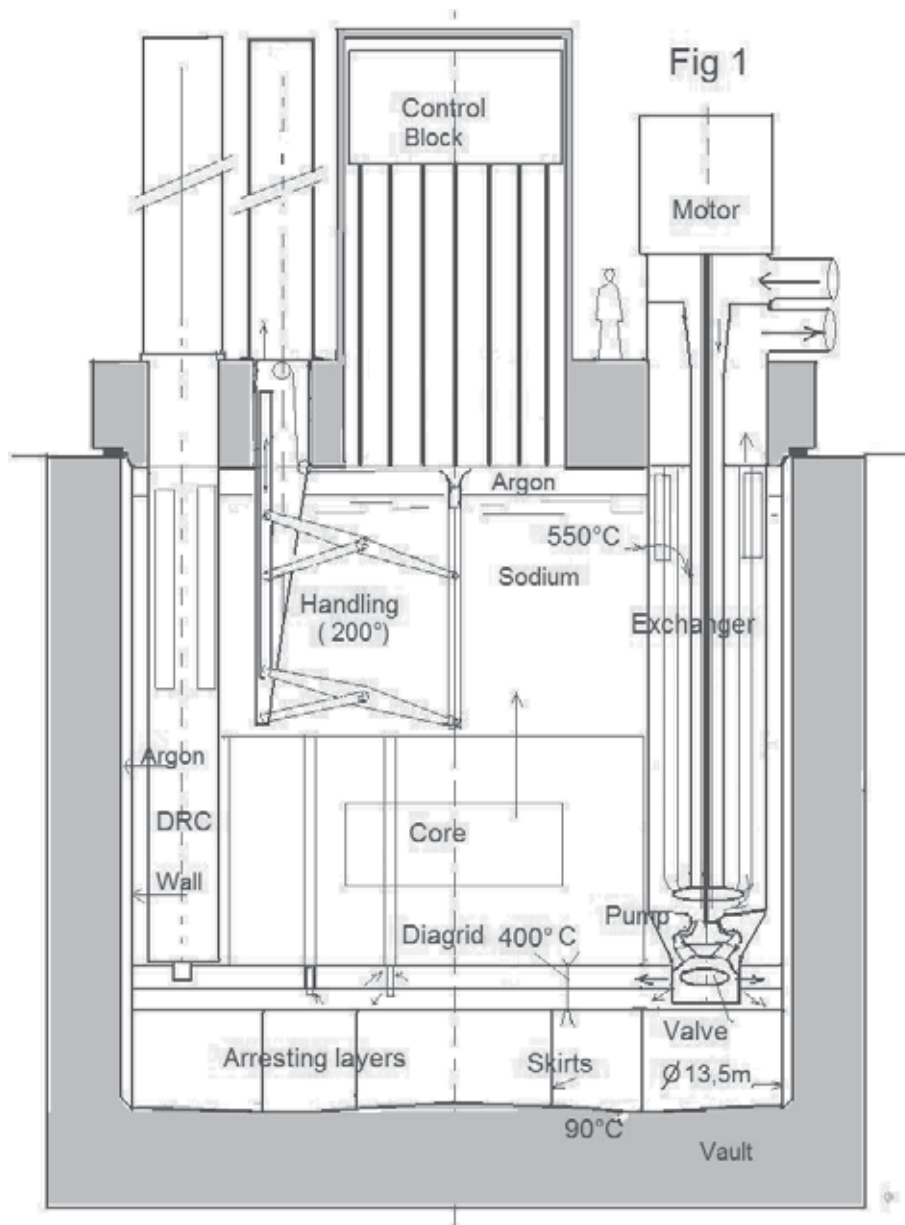


Fig. 1.

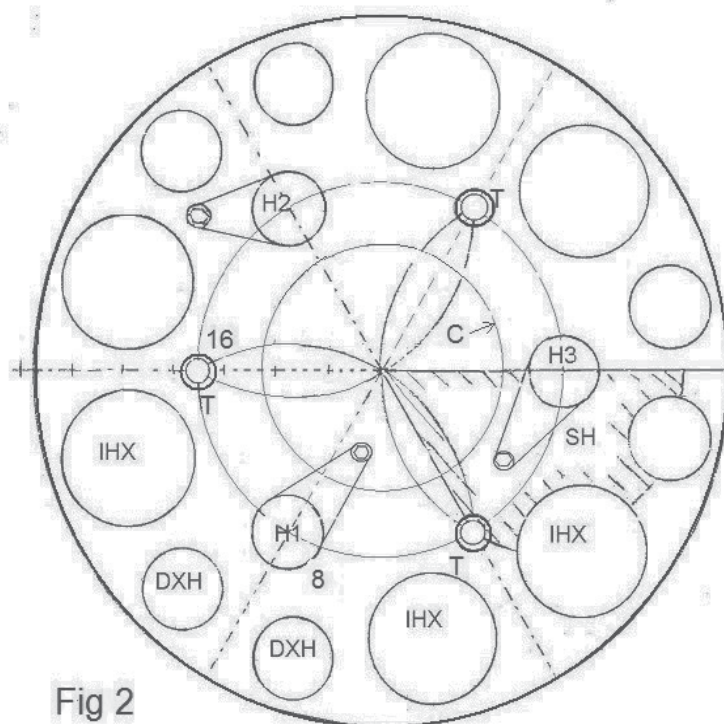
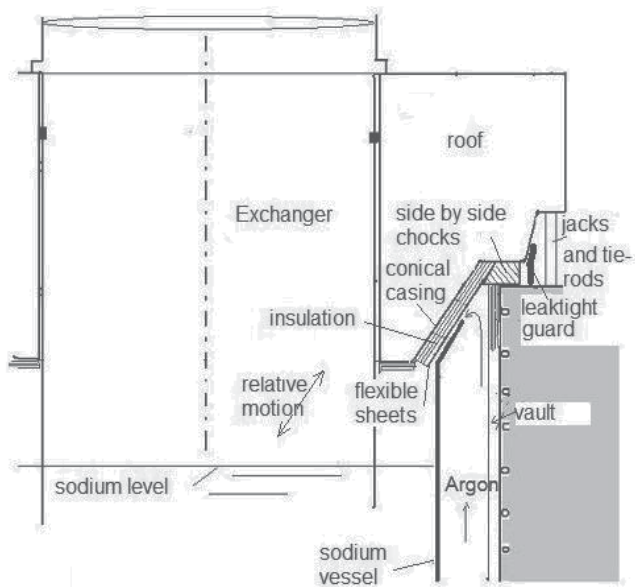


Fig. 2.

Vault-cover junction, between cones along dilatation displacements



Fatigue behaviour in the vessel wall due to temperature variations of the diagrid is here examined. Vessel bottom and bottom plate of the diagrid are assumed rigid. For half variation of  $150^\circ$  in the diagrid of radius 6.75m, the radial displacement reaches 12 mm, inducing in the 2 m high wall embeddings a curvature of radius 53m. For a thickness of 4 cm, flexural stress reaches 90 MPa without fatigue effect at  $400^\circ\text{C}$ . Internal skirts are less stressed. The height could be reduced if exceeding the need for protecting the bottom.

Above the diagrid, the vessel wall must in operation resist laterally only to the sodium hydrostatic pressure and may reach the hot sodium temperature, with a thickness for instance of 3cm. In case of accidental loading and specially of earthquakes, this vessel wall resists due to its centering at bottom, and at top by conical contact toward the robust vault roof. Dynamic effects are limited by friction of sodium to rigid exchanger walls in vessel periphery, centered on two levels, and as proposed below, by butting of core elements on their walls.

This resting bottom and the integral diagrid appear as robust and resisting to accidents. The flat bottom cylindrical shape allows a better arrangement of internals relatively to suspended vessels with a rounded bottom, and reductions on overall volume, weight and price.

## 5. Proposition for exchangers-pumps

Leaving intermediate exchangers, the sodium usually arrives in a plenum around and below the diagrid, before being taken by pumps and injected into the diagrid. Here exchangers-pumps are proposed, excluding such a plenum. Each one, comprising a vertical exchanger and a pump fixed below, injects cool sodium ( $400^\circ\text{C}$ ) down into the diagrid. The loss of charge in exchangers, no more limited by the height difference, usually of a few meters, between hot sodium level on vessel top and entry level in the pumps, may reach almost the exchanger height, about 10 m. Accepting an increased loss of charge may allow an optimization with smaller or more efficient exchangers.

A secondary sodium circuit comprises an inlet pipe connecting the external secondary pump to the exchanger, and an outlet pipe from the exchanger to the steam generator. These pipes, vertical and concentric in the roof, separate above, becoming horizontal. In the exchanger envelope, the secondary sodium arrives to an annular distributor for exchange tubes going to an upper annular collector. In the axis of the inlet pipe, the pump is driven by an upper motor and a shaft contained in an axial tube, with hydrostatic bearings fed along the shaft by primary sodium under pressure, in sufficient number to avoid vibrations,

At sodium vessel top, the primary hot sodium emitted by the core enters the exchanger-pump by upper peripheral ports. Once cooled and taken by the pump, this sodium is injected into the diagrid upper space by ports of a vertical large pump foot, penetrating in the lower space to preclude lifting effects like for fuel elements. Leaks contribute to feed this low pressure space with flow for peripheral elements. In the pump, a purging valve collects gas possibly carried by the flow and sends it up to vessel cover, avoiding cooling disorder in the core.

In the light of the EFR project (1500 MWe), equivalent circuits for the same power may, for the cold resting bottom reactor, use six exchanger-pumps IHXP's with a height of 12 m. Each of them is suspended by a rim in a pit in periphery of the roof and planted into the diagrid, leak-tightness being provided by piston rings. Six decay heat exchangers DHX's for safety, working in natural convection for both their lower sodium circuit and their upper air circuit,

are also centered in the roof periphery and in the diagrid. These rigid components, centered at two levels, reduce the charge on the wall in case of accidents.

All resting elements may be extracted for examination and repairs, and the diagrid inner space may be examined using the holes for exchanger-pumps.

In order to increase the stocking area for used elements it is interesting that the handling system would access the full area of the integral diagrid, between the exchangers.

## 6. Proposition for the handling system

The handling system, working normally in sodium cooled at about 200°C, should cover the large integral diagrid shown above, including allowable areas between exchangers in periphery. The usual two rotating plugs handling system covers an insufficient diameter, and, with a rotor proposed in the vessel for vertical exchanges, needs a large surface on the roof. It makes it difficult to examine the lower surface of the rod controlling block, where hot sodium, arriving from many core channels, creates thermal cycling and fatigue. This system gave however satisfaction in several reactors and remain compatible with other innovations here proposed.

Another system is here proposed, for which the space above the core is made free from commands to the control rods. While these rods are left in the core, commanding bars are independently lifted through pits in the vessel roof, under action of their mechanisms situated above this roof in a leak-tight cell, allowing examination and repairs. This gives space below the roof for three manipulators, centered in three pits around the cell. Each manipulator comprises a rotating column from which an articulated "pantograph" projects horizontally a vertical handling tube containing a lifting hook to cover positions on relevant part of the diagrid.

Before introduction of a subassembly or element in a channel on the diagrid, it is necessary to orient the hexagonal tube. On the handling tube is used an hexagonal funnel, mechanically oriented before projection, its rounded edge allowing sliding of the cables suspending the hooks.

Between manipulator pits, at intersections of their maxima projections, three transit pits pierce the roof, above three unoccupied locations on the diagrid in the blanket area, encircled by steel hexagonal elements. Transfer of elements between any location on the diagrid and a given transit pit is obtained using only one manipulator, or two manipulators and an intermediary unoccupied location. One transit pit could be chosen for evacuating cooled fuel subassemblies after a lengthy stockage, using large flasks filled by gas for several elements, while a second pit would be chosen for experimental or presumed faulty individual elements, needing earlier discharge under liquid sodium. This second pit would use on the diagrid a larger channel between blanket elements for containing a leak-tight sodium pot in which a subassembly may be kept during the full transit way to examination halls, inside a special flask. These transit ways through two pits appear to need less installations than usual systems, but the third pit could also be equipped for transits, in order to reduce operation delays.

The two types of hooks for subassemblies or for the sodium pot use differential motions of their two cables, coming from a winding-drum in the manipulator pit. These cables are guided in the pantograph angles by the funnel and by a pulley near the manipulator axis.

When the pantograph is retracted, the full manipulator may be lifted in a leak-tight container fixed on its pit, where it is kept out of flux under gas at moderate temperature. For

maintenance, this container is disconnected, and transported above the roof. Connection of a manipulator container or of a transport flask on a pit may use a gas bag inserted through a narrow lateral inlet and inflated for leaktightness, while lids are exchanged.

Manipulators may receive cameras for observing the space above the diagrid, or tools for repairs, for instance in case of malfunction in one of them. They may also be used for placing butting steel elements between some blanket elements resting on the diagrid and the robust exchangers in periphery, rigidly centered on two levels, able to prevent large displacements of all elements in case of accidents or earthquakes. These butting elements are placed before introduction of exchangers.

Manipulators are largely dimensioned for obtaining the necessary rigidity and precision. They are operated under automatic and visual control.

## 7. General implantation

The 1500 MWe EFR project, taken as reference, is described below.

Its thermal power is 3600 MW and electric power 1470 MWe. The sodium vessel is suspended in periphery of the vault top. Vessel height is 16,2m (8,6m for the cylindrical part, 7,6m for the rounded bottom), below a 0,85m thick steel roof. Diameters are 18m internally for the vault, 17,2 m for the vessel, 16,25m for internal wide-mouthed vessel, 8,2m for diagrid with a surface of 53 m<sup>2</sup>, 7.2m for the handling machine large plug. The diagrid is supported by a steel strongback resting on the rounded vessel bottom. Six intermediary heat exchangers, heating independently six external steam generating units, have a diameter of 2,3m in the exchanging part and 2,85m in the roof pit (6,4 m<sup>2</sup>) for a height of 7,7m in exchanging part and 13,2m between bottom and roof surface. Three primary pumps, for a flow rate of 19 tons/s, penetrate the roof through 2m diameter pits. Six smaller DRC (direct reactor cooling) exchangers, using natural convection in sodium and air, remove heat in case of unavailability of the main cooling system..

Figure 2 proposes a plan for the same reactor core with a vessel reactor diameter reduced to 13.5m, six exchangers (IHX), shown with a diameter of 2.5m, and six DRCs assumed to a diameter of 1.7m. Distance of these components to the vessel wall is 0.25m. The three handling systems H1, H2, H3 are shown with a pit diameter of 1.2m. The projection radius is taken at 3.5 m. The diameter CB of 4.5 m needed in the cell for the EFR conical skirt around the control block could be kept.

Area SH corresponds to half the area covered by one manipulator. Total covered surface reaches 77 sqm instead of 53 sqm for EFR, allowing for the same power a large extension of stockage in reactor, delays before discharge being increased for instance to three years.

Before a detailed project is established, it is clear that proposed innovations allow a very reduced vessel section, for a given power SFR.

The vessel height would be reduced by about 2m below the diagrid due to the cylindrical general shape without rounded bottom. The diagrid thickness is maintained to 1.15m. IHX's height must be increased by the pump height for about 2m. Then the overall height would not be modified, but above the roof by the cell receiving the control block.

## 8. Safety aspects

Safety as related to these innovations for sodium cooled reactors is shortly discussed here.



It was precedently admitted that the core disruptive accident (CDA) producing corium was limited to seven fuel subassemblies. It is now deemed that, even with large preventing measures, a core catcher should be able to cope with a full core fusion. This was one reason for proposing the cold resting bottom vessel with a thick refractory lower space excluding the risk of vessel piercing, other reasons being economy and robustness.

In this lower space designed to stop an important hot corium flow, an horizontal core catcher may be extended below the full diagrid surface, using for instance graphite pieces with a very high melting temperature, coated by steel in order to avoid chemical effects in normal run. Upper windows in supporting skirts allow communications. The large surface reduces the melt corium thickness and favors its cooling, by sodium vaporization, by transmission to bottom, and by mixing with granular refractory or absorbing materials, preventing recriticality.

Core catchers have been extensively studied for LWR's, assuming large corium flow. They were also examined for sodium cooled reactors. Tests used simulation of corium by chemically produced hot materials. It seems that reactions in case of core melting would be less explosive with sodium than in water reactors, and that core catcher cooling is more efficient with sodium than with water. Such studies should be extended to structures as proposed here.

Solid horizontal layers below the diagrid may use steel plates (conductivity  $82 \text{ W/m}^\circ$ , fusion  $1200^\circ$  to  $1500^\circ$  depending on composition), graphite ( $100 \text{ W/m}^\circ$ ,  $3850^\circ$ ), other refractory materials like alumina ( $8 \text{ W/m}^\circ$ ,  $2054^\circ$ ), depleted uranium oxide, and lead allowing corium flotation, in pieces coated by steel. These layers with different conductions would favour horizontal extensions of temperatures and reduce concentrated effects. A conical shape of skirts may prevent displacements of light pieces.

Cracks are not to be expected in the skin submitted to compression, under cold sodium. They could be however detected below the welds, using channels in the concrete, normally plugged by sand. In operation, sodium leaks through bottom cracks are prevented by sodium freezing.

Fusion in the core is normally prevented in each fuel element by fitting up fuel pins without obstacles to the sodium flow, using for instance helicoidal spacers.

The cold resting bottom with integral diagrid provides rigidity and robustness, preventing resonances of suspended vessels and probably avoiding recourse to parasismic supports below the vault. The strongly supported diagrid may resist large accidental loads.

Deliberate aggressions should also be taken into account. They would be excluded only by deeper and costly installations beneath the ground, to be justified by probabilistic assessments. A protection is given by above roof structures. Insertion of the vault and of the full primary sodium into the ground gives protection against primary sodium fires. It is recommended that the secondary sodium circuits, with parts above reactor roof for allowing natural convection, would be protected by partial digging and embankment surrounding. Frequent incidents came from water-sodium contacts in steam generators. No innovation is here presented.

## 9. Advantages for these innovations

1. Large simplification, with reductions of steel and sodium masses and consequently of construction cost. A minimum sodium volume could however remain required to provide a sufficient thermal inertia in case of accidents.

2. The space below the diagrid may contain cold and refractory materials in large thicknesses, preventing any piercing by corium.
  3. Robustness provided by simplified cylindrical structures fixed on two levels.
  4. Embedding the vault in ground protects against aggressions, accidents and earthquakes.
  5. Bottom leak-tight to cracks, due to sodium freezing.
  6. Voids exclusion below the core protects against core dry-out.
  7. Thermic losses reduced and efficiency correspondingly increased
  8. Negative reactivity coefficient added by opposite dilatations of structures and control bars.
  9. Large area diagrid allowing a several years decay for used elements.
  10. Only one circulation of neutral gas (argon).
  11. An emergency cooling obtained by replacing argon around the vessel by sodium.
  12. Cooled sodium in the bottom space, under low circulation, may trap sodium oxides.
  13. The handling system may reduce delays and allow easier observations and repairs.
  14. At reactor end of life, the vault remains available for new structures or waste stockage.
- Proposed innovations, allowing better safety, easier inspections and repairs, and lower costs, could give advantages of SFRs to LWRs and allow shorter delays before a large utilization.

The author would appreciate to receive comments to his propositions.

Other innovations are currently proposed to French Commissariat à l'Energie Atomique.

## 10. References

- [1] D. COSTES. "Réacteur nucléaire refroidi par un métal liquide et comprenant une cuve posée à fond froid" French patent 80/27759 (1980)
- [2] D. COSTES "A cold bottom supported vessel for sodium-cooled reactor". Nuclear technology Vol 67 Oct. 1984
- [3] D. COSTES "Concepts on sodium-cooled and water-cooled reactors". ENC'94 paper 4.32.
- [4] EFR Associates, European Fast Reactor, Outcome of design studies, 1998
- [5] D. COSTES "A Loop Sodium Reactor with a cold resting bottom Vessel". ICAPP 2007 Paper 7567.
- [6] D. COSTES "Système de manutention pour réacteur refroidi au sodium". French Patent 10/03351 (2010)
- [7] D. COSTES "Sommier étendu pour réacteur refroidi par métal liquide". French Patent 10/03352 (2010).
- [8] D. COSTES "Collecteur torique pour réacteur à neutrons rapides". French Patent 10/04519 (2010)



*Edited by Valentin Uchanin*

The book is intended for practical engineers, researchers, students and other people dealing with the reviewed problems. We hope that the presented book will be beneficial to all readers and initiate further inquiry and development with aspiration for better future. The authors from different countries all over the world (Germany, France, Italy, Japan, Slovenia, Indonesia, Belgium, Romania, Lithuania, Russia, Spain, Sweden, Korea and Ukraine) prepared chapters for this book. Such a broad geography indicates a high significance of considered subjects.

Photo by User2547783c\_812 / iStock

**IntechOpen**

